The Transport and Deposition of Molybdenum in Porphyry Ore Systems

Edward T. Spencer

A thesis submitted for the degree of Doctor of Philosophy

Department of Earth Science and Engineering
Imperial College London

Submitted March 2015

Supervisor 1:
Dr Jamie Wilkinson
Research Leader
Earth Sciences Department
Natural History Museum
London SW7 5BD, UK
+44 (0)20 7942 5334
j.wilkinson@nhm.ac.uk

Supervisor 2:
Dr Andrew Berry,
Senior Fellow
Research School of Earth Sciences,
Australian National University,
Canberra
andrew.berry@anu.edu.au

Declaration

The work presented in this thesis is my own or is appropriately referenced throughout. No portion of this work has been submitted in support of an application for a qualification at any other university or institute of learning.

The copyright of this thesis rests with the author and is made available under a Creative Commons Attribution Non-Commercial No Derivatives licence. Researchers are free to copy, distribute or transmit the thesis on the condition that they attribute it, that they do not use it for commercial purposes and that they do not alter, transform or build upon it. For any reuse or redistribution, researchers must make clear to others the licence terms of this work.

EDWARD SPENCER **20/03/2015**

Abstract

Approximately 99% of Mo is obtained from porphyry deposits (e.g. Sillitoe, 2010), representing the strongest association of any metal with a single deposit type. Despite this, the controls on the formation of Mo-rich porphyries and the spatial-temporal decoupling of Mo from Cu in these systems remain poorly understood. By combining fieldwork, Re-Os molybdenite dating and a fluid inclusion study at one of the world's largest Cu-Mo porphyries (El Teniente, Chile), this project assesses the magmatic-hydrothermal evolution of the system to help constrain the processes controlling Mo enrichment.

Results indicate that deposit-wide Mo grades of <0.06 wt.% are principally controlled by the abundance of main mineralisation-type quartz-molybdenite veins, that develop outwards and upwards into Cu-rich vein types. Parental ore fluids had low salinities (~6.5 wt.% $NaCl_{eq}$) and were exsolved at depth following the emplacement of multiple intrusions that acted as short-lived (<100,000 years) conduits for mineralising fluids between 6.3 and 4.6 Ma. The decoupled deposition of Mo and Cu surrounding each temporally separate intrusion is attributed to the sequential deposition of Mo then Cu in response to decreasing temperature followed by intermittent fluid boiling and increasing fluid pH in response to sericitic alteration of the mafic host-rocks.

Mo grades >0.06 wt.% correspond to the presence of late mineralisation-type veins and breccias produced by the exsolution of Mo-rich brines ±aqueous fluids from a highly fractionated magma source. Mineralisation in this stage was short-lived and occurred in all parts of the deposit at ~4.6 Ma. The relatively Cu-poor nature of this stage is attributed to the prior preferential extraction of Cu from the underlying magma chamber in earlier mineralising events. In accordance with data from other Mo-rich porphyry systems, results indicate that Mo-Cu decoupling is controlled by both changes in magma chemistry as well as by the evolving P-T-X properties of hydrothermal fluids.

Acknowledgements

Firstly I would like to thank my supervisors Dr Jamie Wilkinson and Dr Andrew Berry for firing ideas at me, monitoring my progress and helping me get my fieldwork and experiments up and running. I would particularly like to thank Jamie for his meticulous editing of draft chapters and papers over the past few months. I would also like to thank Jack Nolan, who was instrumental in helping me with my initial experiments, Robin Armstrong for his support throughout this project and Matt Genge and Dan Smith for their comprehensive reviews of this thesis and appendices.

At CODELCO, I would like to thank José Seguel for his expertise and guidance while working at El Teniente, his enthusiasm for this research project and his kind and generous hospitality whenever I visited Chile. I extend my gratitude to other members of CODELCO Superintendencia de Geología, El Teniente, especially Patricio Zuñiga and Felipe Celhay, for providing access to the mine, drillcore samples and grade data. We would also like to thank CODELCO Division El Teniente for granting permission to publish this research.

For my experimental work I would like to thank Clara Wilkinson and Anton Kearsley of the Natural History Museum, London, who guided me through my LA-ICP-MS and SEM-CL analysis work. I would also like to acknowledge the University of Alberta Radiogenic Isotope Facility for their invitation to complete my Re-Os molybdenite dating study in their labs. The guidance of Dr Robert Creaser and the assistance of Barbara Ziger, Mark Simms and Krystle Moore in completing this work made this a thoroughly successful and rewarding part of my PhD.

I would like to thank Imperial College London, Department of Earth Science and Engineering, for granting me a Janet Watson Ph.D. scholarship to complete this study. The fieldwork and laboratory work completed in this study would not have been possible without the generous financial support of CODELCO Division El Teniente, The Institute of Materials, Minerals and Mining bursary scheme (2012-2013), the Society of Economic Geologists Hugh E. McKinstry Fund (2012-2013), The Society of Economic Geologists travel bursary scheme (2012), The Society for Geology Applied to Mineral Deposits travel bursary scheme (2011), the Geological Society, Geochemistry Group travel grant scheme (2012) and student awards from the Geological Society, Mineral Deposits Studies Group (2013), and the Society for Geology Applied to Mineral Deposits (2011).

Finally, I would like to thank my friends and family who have supported me throughout this process, particularly Frances, who has been so kind and patient throughout.

Table of Contents

Declaration i

Abstract ii

Acknowledgements iii

Table of Contents and Appendices iv

List of Figures ix

List of Tables xv

Abbreviations xvi

Chapter 1. Introduction 1

1.1 Introduction 1

1.2 Aims and Objectives 7

Chapter 2. The Formation of Mo-rich Porphyry Deposits 11

2.1 Introduction 11

2.2 Global Distribution and Timing 12

2.3. Magmatic Evolution 15

2.3.1 Magma Generation and Mo Source 15

2.3.2 MASH-Zone and Crustal Interactions 15

2.3.3 Magma Ascent and Magma Chamber Emplacement 17

2.3.4 Mo Solubility and Speciation in Magmas 19

2.3.5 Cu Solubility and Speciation in Magmas 20

2.3.6 Magmatic Sulphide Saturation 22

2.3.7 Mo Melt-Crystal Partitioning 24

2.3.8 Cu Melt-Crystal Partitioning 25

2.4 Hydrothermal Evolution 26

2.4.1 Magma Volatile Exsolution 26

2.4.2 Mo Fluid-Melt Partitioning 29

2.4.3 Cu Fluid-Melt Partitioning 33

2.4.4 Mo Vapour-Brine Partitioning 35

2.4.5 Cu Vapour-Brine Partitioning 36

2.4.6 Mo Speciation in Hydrothermal Fluids 39

2.4.7 Cu Speciation in Hydrothermal Fluids 41

2.5 Ore Mineral Precipitation 43

2.5.1 Mo Deposition 45

2.5.2 Cu Deposition 47

2.5.3 Metal Remobilisation and Supergene Enrichment 48

2.6 Closing Statements 49

Chapter 3. The El Teniente Cu-Mo porphyry deposit 51

3.1 Introduction 51

3.2 Regional Geology and Tectonic Evolution 53

3.3 Deposit Formation and Geology 55

3.3.1 The Teniente Mafic Complex (TMC) 56

3.3.1 The Teniente Mafic Complex 58

- The Sewell Quartz Diorite 58

- The A-Porphyry 58

- The Diorite Pipes 60

- The Grueso Porphyry 61

- The Teniente Dacite Porphyry 61

- Latite Dykes 62

- Lamprophyre Dykes 63

3.3.3 El Teniente Breccias 64

- Igneous Breccias 64

- Biotite Breccias 64

- Anhydrite Breccias 66

- Diorite intrusions 66

- Tourmaline Breccias 66

- The Braden Breccia Pipe 67

3.3.4 Mineralisation 68

- Hypogene Mineralisation 68

- Supergene Enrichment 69

3.4 Structural Geology and Structural Evolution 70

3.5 Vein Classification Schemes 75

3.6 Fluid Inclusion Studies 81

3.6.1 Premineralisation stage 82

3.6.2 Main mineralisation stage 84

3.6.3 Late mineralisation stage 87

3.7 Re-Os Molybdenite Geochronology 88

3.8 Closing Statements 92

Chapter 4. The distribution and timing of molybdenite mineralisation at El Teniente 93

4.1 Introduction 93

4.2 Grade Distributions 94

4.3 Methods 98

4.3.1 Drillcore Logging 98

4.3.2 Petrography 100

4.3.3 Geochronology 100
4.4 Results 103
4.4.1 Breccia Distributions and Petrography 103
4.4.2 Vein Distributions and Petrography 106
- Premineralisation Veins 108
- Main Mineralisation Veins 111
- Late Mineralisation Veins 119
4.4.3 Breccia-Vein Relationships 120
4.4.4 Reverse Crosscutting Relationships 122
4.4.5 Geochronology 124
- Timing of Mineralisation 124
- Molybdenite Re Contents and Validity of Results 127
4.5 Discussion 129
4.5.1 Geochronological Constraints on the Evolution of El Teniente 129
4.5.2 Controls on Decoupling of Mo and Cu Mineralisation 135
4.5 Conclusions 141

Chapter 5. Magmatic-Hydrothermal fluid evolution at El Teniente 143
5.1 Introduction 143
5.2 Methods 144
5.2.1 Sample Collection and Preparation 144
5.2.2 Microthermometry 146
5.2.3 SEM-CL petrography 147
5.2.4 LA-ICP-MS analysis 147
5.3 Microthermometry and fluid inclusion petrography 151
5.3.1 Fluid Inclusion Types 151
5.3.2 Appraisal of Microthermometric Measurements 151
5.3.3 Premineralisation Veins and Breccias 153
- Type 3 Veins and Biotite Breccias 153
- Type 4a veins 155
5.3.4 Main mineralisation Veins and Breccias 156
- Anhydrite Breccias and Type 5 Veins 156
- Type 6a veins 158
- Type 6b veins 165
- Type 8 veins 168
5.3.5 Late Mineralisation Veins and Breccias 171
- Tourmaline Breccias and Type 9 Veins 171
- Anhydrite-Carbonate ±Gypsum Breccias and Type 10 Veins 173

5.3.6 Fluid Inclusion Densities and Minimum Trapping Pressures 175
- Premineralisation Type Veins and Breccias 176
- Main Mineralisation Type Veins and Breccias 176
- Premineralisation Type Veins and Breccias 177
5.3.7 Spatial-Temporal Variations in Microthermometric Properties 179
5.3.7 Evolution of Fluids in Each Mineralised Centre 183
5.4 LA-ICP-MS Fluid Chemistry 184
5.4.1 Appraisal of LA-ICP-MS Method 184
5.4.2 Premineralisation Type Veins and Breccias 188
5.4.3 Main Mineralisation Type Veins and Breccias 195
- Type 5 Veins 195
- Type 6a to Type 8 Veins 197
5.4.4 Late Mineralisation Type Veins and Breccias 203
- Type 9 Veins 203
- Type 10 Veins 208
5.4.5 Spatial-Temporal Variations in Fluid Chemistry 212
- Variations in Primary Fluid Chemistry 212
- Overall Variations in Brine Composition 216
5.5 Discussion 218
5.5.1 Premineralisation Type Vein and Breccia Development 218
5.5.2 Main Mineralisation Type Vein and Breccia Development 222
5.5.3 Late Mineralisation Type Vein and Breccia Development 230
5.5.4 Magmatic Evolution 232
5.6 Conclusions 234

Chapter 6. Discussion 236
6.1 Introduction 236
6.2 Magmatic Controls on the Formation of Mo-rich Porphyries 237
6.2.1 Source Magma Composition and Intrusion Emplacement 237
6.2.2 Magmatic Controls on Mo-Cu Decoupling 238
6.3 Fluid Exsolution and Metal Partitioning in Mo-rich Porphyries 241
6.3.1 Premineralisation-Type Fluid Exsolution 241
6.3.3 Main Mineralisation-Type Fluid Exsolution 241
6.3.5 Late Mineralisation-Type Fluid Exsolution 244
6.4 Crystal Fractionation as a Key control on the Formation of Mo-rich Porphyries 249
6.5 The Hydrothermal Transport of Metals in Mo-rich Porphyries 254
6.5.1 The Speciation and Transport of Mo 254
6.5.2 The Speciation and Transport of Cu 255

6.6 Vapour-Brine Partitioning in Mo-rich Porphyries 256
6.6.1 Mass and Volume Proportions 256
6.6.2 Vapour-Brine Partitioning of Mo 258
6.6.3 Vapour-Brine Partitioning of Cu 261
6.6.4 Post-Entrapment Modification of Cu Partition Coefficients 263
6.7 Mo Deposition in Porphyry Systems 265
6.7.1 Main Mineralisation-Type Mo Deposition 265
6.7.2 Late Mineralisation-Type Mo Deposition 269
6.8 Cu Deposition in Porphyry Systems 271
6.7.1 Main Mineralisation-Type Cu Deposition 271
6.7.5 Late Mineralisation-Type Cu Deposition 274
6.9 Metal Remobilisation 276
6.10 Conclusions 277

Chapter 7. Conclusions 279
7.1 Main Conclusions 279
7.1.1 The Evolution of El Teniente 279
7.1.2 Magmatic Controls on the Formation of Mo-rich Porphyries 280
7.1.3 Hydrothermal Controls on the Formation of Mo-rich Porphyries 281
7.1.3 The Decoupled Mineralisation of Mo and Cu 282
7.2 Future work 283
7.2.1 The Evolution of El Teniente 283
7.2.2 Magmatic Controls on the Formation of Mo-rich Porphyries 284
7.2.3 Hydrothermal Transport of Mo 284

References 285

Appendices

Appendix I: Compiled Geochronology (Excel)

Appendix II: Analysed Sample Catalogue (Pdf)

Appendix III: Vein Distribution Data (Excel)

Appendix IV: El Teniente - Compiled Fluid Inclusion Microthermometry (Excel)

Appendix V: El Teniente - Compiled Fluid Inclusion LA-ICP-MS Data (Excel)

Appendix VI: Compiled Porphyry LA-ICP-MS (Excel)

List of Figures

Chapter 1

Figure 1.1: Schematic sketch showing the processes and variables that govern the formation of porphyry deposits. 5

Chapter 2

Figure 2.1: World map showing the location of major porphyry belts and provinces. 14

Figure 2.2: Degree of fractional crystallisation (approximated by Fe wt.%) versus redox state for Intrusions associated with different mineralised systems. 15

Figure 2.3: Box and whisker plots of the emplacement depths of different porphyry Cu deposit subtypes. . 18

Figure 2.4: Evolution of magmas as a function of fO_2 and temperature in different magmatic and ore deposit systems. 22

Figure 2.5: Mechanism for the generation of fertile porphyry intrusions by the melting of zones of previously saturated sulphides. 23

Figure 2.6: Models for the exsolution of different fluid types from magmas intruded at different depths. .. 28

Figure 2.7: Schematic sketch showing the post-entrapment modification of Cu^+ and H^+ concentrations in low density vapour and brine inclusions..... 38

Figure 2.8: Schematic diagram showing the generalised alteration and mineralisation zonation in porphyry Cu-Mo system. 43

Chapter 3

Figure 3.1: Location map of the El Teniente Cu-Mo porphyry deposit and other major porphyry Cu-Mo and Cu systems in Chile. 51

Figure 3.2: Simplified geological map of El Teniente at mine level 2165 m asl showing igneous intrusions and breccia bodies. 57

Figure 3.3: Compiled geochronology for the crystallisation of intrusions and molybdenite mineralisation at El Teniente. 59

Figure 3.4: Example photographs of different breccia types at El Teniente. 65

Figure 3.5: Schematic map of sulphide zonation at El Teniente based on grade distribution data. 69

Figure 3.6: Regional and local structural geology of the El Teniente mine area. 71

Figure 3.7: Photographs showing evidence of fault displacement at El Teniente. 72

Figure 3.8: Schematic model showing the structural evolution of El Teniente proposed by Cannell *et al*. (2005) based on vein orientations and field observations. 73

Figure 3.9: Examples of vein crosscutting relationships observed during this study. 76

Figure 3.10: Pre-existing vein classification schemes for the El Teniente. 77

Figure 3.11: Vein chronology of Vry *et al*. (2010) with example photographs of each vein type. 78

Figure 3.12: Classification scheme for fluid inclusion types used in this study. 82

Figure 3.13: Pressure-composition phase diagram illustrating the evolution of fluids at El Teniente according to Vry (2010). 83

Figure 3.14: Simplified geological map of El Teniente showing the locations of 18 samples previously dated In Re-Os molybdenite dating studies. 90

Chapter 4

Figure 4.1: Simplified geological map of El Teniente at an elevation of 2165 m asl displaying drillcores and Re-Os samples analysed during this study. 96

Figure 4.2: Grade distribution map of Mo and Cu at a deep mine level (1890 m asl). 96

Figure 4.3: Grade distribution map of Mo and Cu at an intermediate mine level (2170 m asl). 97

Figure 4.4: Grade distribution map of Mo and Cu at a shallow mine level (2350 m asl). 97

Figure 4.5: Photographs of typical Cu and Mo sulphides associated with the three most intensely mineralised breccia types. 103

Figure 4.6: Number of veins of each vein type per 100 m in transects 1-4. 108

Figure 4.7: Sample photographs and cross-polarised and reflected light photomicrographs of sulphides present in different vein stages. 109

Figure 4.8: Total number of type 3 veins versus average Mo and Cu grades in 6 metre drillcore intervals in transects 1-4. 111

Figure 4.9: Total number of type 5 veins versus average Mo and Cu grades in ~6 metre drillcore intervals in transects 1-4. 112

Figure 4.10: Number of main mineralisation veins (type 6a-8) versus average Mo grades in ~6 metre drillcore intervals in transects 1-4. 113

Figure 4.11: Number of main mineralisation veins (type 6a-8) versus average Cu grades in ~6 metre drillcore intervals in transects 1-4. 114

Figure 4.12: Mo and Cu grades versus lithology and the abundances of type 6a, 6b and type 8 veins along transect 2. 117

Figure 4.13: Total number of type 9 and type 10 veins versus average Mo and Cu grades for ~6 meter intervals in the two shallowest transects. 118

Figure 4.14: Mo and Cu grades plotted against host lithology and the abundances of type 5 and type 10 veins for ~6 metre intervals along transect 2. 120

Figure 4.15: Mo and Cu grades plotted against host lithology and the abundances of type 9 veins for ~6 meter intervals along transect 4. 121

Figure 4.16: Mo and Cu grades plotted against host lithology and the abundance of type 10 veins for ~6 meter intervals along transect 3. 121

Figure 4.17: Matrix of vein crosscutting relationships recorded at El Teniente. 122

Figure 4.18: Grade distribution map showing Re-Os molybdenite sample ages recorded during this (red squares) and two previous studies. 126

Figure 4.19: Time versus depth plot showing the magmatic-hydrothermal evolution of El Teniente based on field observations and geochronology. 130

Figure 4.20: Mo versus Cu grades for different lithologies in transects 1-4. 136

Figure 4.21: Schematic diagram showing the potential spatial evolution of quartz-dominated type 6a veins into outboard Cu-rich type 6b, 7b and type 8 veins. 138

Chapter 5

Figure 5.1: Geological map of El Teniente at 2165 m asl showing the sections and areas studied in this and previous fluid inclusion studies. 145

Figure 5.2: Example ablation signal of a high salinity (49.8 wt.% $NaCl_{eq}$) fluid inclusion. 148

Figure 5.3: Example ablation signal of a microwell-hosted standard solution. 148

Figure 5.4: Fluid inclusion microthermometric data for type 3 veins and biotite breccias. 153

Figure 5.5: Quartz SEM-CL image and plane polarised light photomicrographs of fluid inclusions in a biotite breccia associated with type 3 veins. 154

Figure 5.6: Fluid inclusion microthermometric data for different inclusion types in a type 4a vein sample. 155

Figure 5.7: Fluid inclusion microthermometric data for different fluid inclusion types in type 5 veins and associated anhydrite breccias. 156

Figure 5.8 Transmitted light photomicrographs of fluid inclusions hosted in type 5 veins and associated anhydrite breccia cements. 157

Figure 5.9: Fluid inclusion total homogenisation temperatures versus salinity plots for different fluid inclusion types in type 6a veins from various depths. 159

Figure 5.10: SEM images and fluid inclusion photomicrographs of type 6a veins from various mine levels. 160

Figure 5.11: SEM images and fluid inclusion photomicrographs of a typical shallow type 6a vein proximal to the Teniente Dacite Porphyry. 162

Figure 5.12: Summary fluid inclusion microthermometric data for transitional type 6a-7a veins associated with the A-Porphyry and Northern Diorite. 163

Figure 5.13: SEM-CL images and reflected and transmitted light and photomicrographs of transitional 6a-7a veins. 164

Figure 5.14: SEM images and reflected and transmitted light and photomicrographs of type 6b veins. 166

Figure 5.15: Summary fluid inclusion microthermometric data for different fluid inclusion types in type 6b veins associated with several intrusions. 167

Figure 5.16: SEM images, sample photographs and fluid inclusion photomicrographs of type 8 veins containing variable sulphide abundances. 169

Figure 5.17: Summary fluid inclusion microthermometric data for different fluid inclusion types in type 8 veins containing chalcopyrite, bornite and molybdenite. 170

Figure 5.18: SEM images, sample photographs and fluid inclusion photomicrographs of type 9 veins and breccias. 171

Figure 5.19: Summary fluid inclusion microthermometric data for different fluid inclusion types in type 9 veins and breccias. 172

Figure 5.20: Summary fluid inclusion microthermometric data for different fluid inclusion types in the type 10 veins and associated anhydrite-carbonate ±gypsum breccias. 173

Figure 5.21: SEM images, sample photographs and fluid inclusion photomicrographs of type 10 veins and anhydrite-carbonate ±gypsum breccias. 174

Figure 5.22: Pressure-temperature projection of isochore T_h (L–V) lines calculated for the H_2O-NaCl system using a numerical model (Lecumberri-Sanchez *et al.*, 2012) and previously proposed halite liquidus isopleths. 176

Figure 5.23: Fluid inclusion density versus minimum trapping pressure plots for different main mineralisation vein types and fluid inclusion types. 178

Figure 5.24: Fluid inclusion density versus minimum trapping pressure plots for different late mineralisation vein and breccias types and fluid inclusion types. 178

Figure 5.25: Fluid inclusion salinity versus total homogenisation temperature plots for similar main and late mineralisation type veins from different mineralised intrusions. 180

Figure 5.26: Average fluid inclusion type densities in type 6a veins from different intrusions and different mine levels calculated from microthermometric data from this and a previous study (Vry, 2010). 182

Figure 5.27: Schematic diagram showing the different fluid regimes that operate in each intrusion. 183

Figure 5.28: Example of a poor ablation signal obtained for a small, shallow, low salinity A_L inclusion. 185

Figure 5.29: Example of an ablation signal obtained for a large, deep A_V inclusion hosted in anhydrite. 185

Figure 5.30: Selected element concentrations calculated using different internal standards (microwell standard solution and NIST-612 glass) for primary A_{ID} inclusions in a deep level type 6a vein. 187

Figure 5.31: LA-ICP-MS major element geochemistry for different fluid inclusion types in a biotite breccia proximal to the A-Porphyry. 193

Figure 5.32: LA-ICP-MS major element geochemistry for fluid inclusions in a type 3 vein proximal to the Southern Diorite. 194

Figure 5.33: Major element geochemistry of fluid inclusions in type 5 veins from the margins of the A-Porphyry and North Central Diorite. 196

Figure 5.34: Major element ratios in different fluid inclusion types in type 6a veins from variable depths, type 6b veins and type 8 veins. Figure shows fluid inclusion data from multiple intrusive centres. 198

Figure 5.35: Minor element ratios in different fluid inclusion types in type 6a veins from variable depths, type 6b veins and type 8 veins. Figure shows data from multiple intrusive centres. 199

Figure 5.36: Mo and Cu concentrations in different fluid inclusion types in type 6a veins from variable depths, type 6b veins and type 8 veins. 201

Figure 5.37: Major and trace element concentrations of different fluid inclusion types in type 9 vein to the south and east of the Braden Breccia pipe at various mine levels. 206

Figure 5.38: Mo and Cu concentrations in different fluid inclusion types in type 9 vein to the south and east of the Braden Breccia pipe at various mine levels. 208

Figure 5.39: Major and trace element concentrations of different fluid inclusion types in different host minerals in type 10 veins and anhydrite-carbonate ±gypsum breccias. 209

Figure 5.40: Mo and Cu concentrations in different fluid inclusion types in different host minerals in type 10 veins and anhydrite-carbonate ±gypsum breccias. 211

Figure 5.41: Major element ratios in primary inclusions associated with different vein types in multiple intrusions. 214

Figure 5.42: Minor and trace element ratios in primary inclusions associated with different vein types in multiple intrusions. 215

Figure 5.43: Compositions of primary brine inclusions in premineralisation, main mineralisation and late mineralisation (blue) type veins and breccias. 217

Figure 5.44: Pressure versus temperature plot showing the different homogenisation modes of fluid inclusions in the premineralisation type veins and breccias. 219

Figure 5.45: Models for the exsolution of different fluids from a magma intruded to varying depths. 220

Figure 5.46: Pressure versus salinity phase diagram for the NaCl-H_2O system (after Driesner and Heinrich, 2007) illustrating the evolution of pre- and main mineralisation type fluids. 221

Figure 5.47: Summary of microthermometric data showing the temperature-salinity evolution of fluids in type 6a-8 veins. 224

Figure 5.48: Pressure versus temperature plot showing alternative evolution pathways for main mineralisation type fluids. 225

Figure 5.49: Quartz solubility in pure water as a function of temperature and pressure showing the general interpreted fluid evolution pathways for the development of pre- and main mineralisation vein types in each mineralised centre. 228

Figure 5.50: Pressure versus temperature plot showing the likely evolution pathways for late mineralisation type fluids. 230

Figure 5.51: Schematic diagram summarising different magmatic-hydrothermal fluid regimes during the emplacement and mineralisation of the North Central Diorite, the Teniente Dacite Porphyry and the Braden Breccia pipe. 235

Chapter 6

Figure 6.1: Mo, Cu and Cs versus Na concentrations for different inclusion types in the premineralisation-type, main mineralisation-type and late mineralisation-type fluid inclusion assemblages at El Teniente. ... 240

Figure 6.2: Mo and Cu versus Na concentrations for the main mineralisation-type and late mineralisation-type fluid inclusion assemblages at El Teniente and from other porphyry systems. 246

Figure 6.3: Average fluid inclusion assemblage metal concentrations versus total homogenisation temperature and average chlorine concentrations calculated using microthermometry. 248

Figure 6.4: Average Cs versus Mo and Cu concentrations for fluid inclusion assemblages in type 6a veins associated with different intrusions at El Teniente. 250

Figure 6.5: Mo/Na versus Cs/Na concentrations for fluid inclusions from several porphyry Cu-Au, Cu-Mo and Mo deposits. 253

Figure 6.6: Cu versus Mo and Cu/Na versus Mo/Na ratios for vapour and brine inclusions at El Teniente and in a series of porphyry Cu±Au, porphyry Cu-Mo±Au and porphyry Mo deposits. 259

Figure 6.7: Individual fluid inclusion LA-ICP-MS data for different fluid inclusion types in quartz-chalcopyrite (type 6b) veins and sericite-altered quartz-chalcopyrite (type 8) veins at El Teniente. 264

Figure 6.8: Total homogenisation temperature versus individual fluid inclusion element concentrations for type 6a, 6b and type 8 veins as a proxy for the temperature-controlled deposition of elements. 267

Figure 6.9: Total homogenisation temperature versus fluid inclusion type Mo and Cu concentrations for late mineralisation-type veins and breccias. 270

Figure 6.10. Copper and molybdenum concentrations as a function of homogenisation temperature and fluid inclusion type in main mineralisation-type veins. 272

Figure 6.11. Summary of the main processes and variables that govern the formation of Mo-rich porphyries over Cu-rich and Mo-poor porphyries. 278

List of Tables

Chapter 1

Table 1.1: Average Mo concentrations in rocks derived from different environments in increasing order of enrichment. 1

Table 1.2 Comparison of the main characteristics of the three major types of Mo-rich porphyries. 2

Chapter 2

Table 2.1: Experimental studies designed to determine the solubility of Mo in magmatic fluids with varied compositions, fO_2, temperature and pressure that are assumed to prevail in porphyry ore systems. 21

Table 2.2: Experimental studies designed to determine the partitioning behaviour of Mo (and Cu) between magmas and exsolved fluids of varied compositions. 30

Table 2.3: Experimental studies of the solubility of different Mo-species in hydrothermal fluids and vapours under a range of physical and chemical conditions. 31

Chapter 3

Table 3.1: Summary of the different names given to units at El Teniente in previous studies. 56

Table 3.2: Previously determined Re-Os molybdenite dates for El Teniente. 89

Chapter 4

Table 4.1: Summary information for drillcores analysed during this study. 98

Table 4.2: Summary of the compositions, occurrences and key petrographic features of the seven different breccia types at El Teniente. 104

Table 4.3: Summary of grade data for drillcores in transects 1-4 showing average Mo and Cu grades for each host lithology. 105

Table 4.4: Summary of the mineralogy, occurrences and typical sulphide abundances of vein types observed in the 15 studied drillcores. 107

Table 4.5: Summary of Re-Os data for the 11 molybdenite samples dated during this study. 125

Chapter 5

Table 5.1: Classification scheme of fluid inclusion types found at El Teniente based on phases present and vapour fraction at room temperature. 152

Table 5.2: Average LA-ICP-MS element concentrations and standard deviations for all fluid inclusion types in the premineralisation and main mineralisation type veins and breccias. 189

Table 5.3: Average LA-ICP-MS element concentrations and standard deviations for all fluid inclusion types in the late mineralisation type veins and breccias. 204

Chapter 6

Table 6.1. Summary of porphyry deposits with available fluid inclusion LA-ICP-MS data. 239

Table 6.2: Average fluid inclusion microthermometric properties and Mo concentrations for three apparent boiling assemblages in type 6b-8 veins and quartz- and anhydrite-dominated type 10 veins. 257

Abbreviations

The following abbreviations are used throughout this thesis. This page acts as a guide for quick reference for the reader. Abbreviations are given in alphabetical order.

General Abbreviations

CL	Cathodoluminescence
DDH	Diamond drill-hole
LA-ICP-MS	Laser ablation-inductively coupled plasma-mass spectrometry
Ma	Millions of years before present
MASH zone	Melting, Assimilation, Storage and Homogenisation zone for magmas
asl	Above sea-level
MI	Methylene iodide
MVP	Magmatic volatile phase
PPL	Plane polarised light
SEM	Scanning electron microscope
SHRIMP	Super high-resolution ion microprobe
XPL	Cross polarised light

Fluid Inclusion Abbreviations

A_{ID}	Intermediate density fluid inclusion
A_{IDO}	Intermediate density fluid inclusion with opaque daughter mineral
A_{L}	High density, salt-undersaturated fluid inclusion
A_{LO}	High density, salt-undersaturated fluid inclusion with opaque daughter mineral
A_{V}	Low density, salt-undersaturated vapour inclusion
A_{VO}	Low density, salt-undersaturated vapour inclusion with opaque daughter mineral
B_{H}	Salt-saturated brine inclusion
B_{HO}	Salt-saturated brine inclusion with opaque daughter mineral
B_{M}	Salt-saturated brine inclusion with multiple opaque daughter minerals
FIA	Fluid inclusion assemblage
ID	Intermediate density (fluid)
T_h	Homogenisation temperature
T_t	Trapping temperature

Regional and Deposit Geology Abbreviations

NVZ	Northern Volcanic Zone
SVZ	Southern Volcanic Zone
TMC	Teniente Mafic Complex

Mineralogical Abbreviations with Chemical Formulae

act	Actinolite	$(Ca_2(Mg,Fe)_5Si_8O_{22}(OH)_2)$
anh	Anhydrite	$(CaSO_4)$
bio	Biotite	$(K(Mg,Fe)_3(AlSi_3O_{10})(F,OH)_2)$
bor	Bornite	(Cu_5FeS_4)
chl	Chlorite	$([Mg,Fe]_3(Si,Al)_4O_{10}(OH)\ (Mg,Fe)_3(OH)_6)$
cb	Carbonate	(CO^{2-}_3)
cpy	Chalcopyrite	$(CuFeS_2)$
epi	Epidote	$(\{Ca_2\}\{Al_2Fe^{3+}\}[O\|OH\|SiO_4\|Si_2O_7])$
gyp	Gypsum	$(CaSO_4{\cdot}2H_2O)$
k-spar	K-feldspar (orthoclase)	$(KAlSi_3O_8)$
mag	Magnetite	(Fe_3O_4)
mo	Molybdenite	(MoS_2)
plag	Plagioclase	$(NaAlSi_3O_8$ to $CaAl_2Si_2O_8$
py	Pyrite	(FeS_2)
qtz	Quartz	(SiO_2)
ser	Sericite (white clay alteration)	$(KAl_2[Si_3AlO_{10}](OH,F))$
ten	Tennantite	$(Cu_{12}As_4S_{13})$
tour	Tourmaline	$(Ca,K,Na)(Al,Fe,Li,Mg,Mn)_3(Al,Cr,Fe,V)_6(BO_3)_3(Si,Al,B)_6O_{18}(OH,F)$

Chapter 1. Introduction

1.1 Introduction

Molybdenum (Mo) is a transition element and one of the 4d series of metals found within period 5 of the periodic table. Its high resistance to corrosion, thermal expansion and thermal softening make it an extremely useful component in high-strength steel alloys and in engineering applications that involve intense heat. Worldwide Mo production is currently ~250,000 tonnes/annum; accounting for a global market value of approximately five billion pounds GBP (Polyak, 2013). This, combined with the ever-increasing demand for Mo in modern engineering applications, makes understanding its enrichment in ore deposits of paramount importance.

Due to the refractory and highly incompatible nature of Mo, it displays trace concentrations in almost all geological reservoirs (Table 1.1). Mo can, however, be enriched to concentrations of >3000 ppm in the ore zones of porphyry-type deposits. These are defined as large volumes (10−100 km^3) of hydrothermally altered rock centred on porphyritic stocks or intrusions (e.g. Sillitoe, 2010) and can be classified based on their contained metal resources (e.g. porphyry Cu-Mo and porphyry Mo deposits: Table 1.2).

Table 1.1: Average Mo concentrations in rocks derived from different environments in increasing order of enrichment.

Reservoir	Conc. (ppm)	References	Reservoir	Conc. (ppm)	References
PM	**0.06**	Sun and McDonough, 1989	**Crustal Granites**	**2.0**	Kuroda and Sandell, 1954
N-MORB	**0.31**	Sun and McDonough, 1989	**Ocean Island Basalts**	**2.4**	Sun and McDonough, 1989
E-MORB	**0.47**	Sun and McDonough, 1989	**Arc Granites**	**2.4**	White *et al*., 1981
Lower Crust	**0.60**	Wedepohl, 1995	**Peralkaline Rhyolites**	**30**	Lowenstern *et al.,* 1993
Cl chondrite	**0.92**	Sun and McDonough 1989	**Porphyry Cu-Au ore veins**	**90**	Cox and Singer, 1988
Basalts	**1.0**	Kuroda and Sandell, 1954	**Porphyry Cu-Mo ore veins**	**200**	Cox and Singer, 1988
Upper Crust	**1.4**	Wedepohl, 1995	**Low F type deposit veins**	**500**	Audétat, 2010
Crustal Average	**1.5**	Kuroda and Sandell, 1954	**Climax type deposit veins**	**3000**	Westra and Keith, 1981

Abbreviations: PM = Primitive mantle; N-MORB = Normal mid-ocean ridge basalts; E-MORB = Enriched-MORB; Grey cells = Mo concentrations for porphyry ore samples that were obtained from Mo-rich ore shells associated with stockwork veining. Low-F and Climax-type deposits = Porphyry Mo deposits.

Table 1.2 Comparison of the main characteristics of the three major types of Mo-rich porphyries.

	Porphyry Mo Deposits (Mo:Cu >1)		**Porphyry Cu Deposits** (Mo:Cu <0.1)
Characteristic	**Climax Type Deposits**	**Low-F Type Deposits**	**Porphyry Cu-Mo deposits**
Other Names	Granite Mo type Granite-related porphyry Mo	Quartz monzonite type Calc-alkaline stockwork type	Calc-alkaline porphyry Cu-Mo (Porphyry Cu-Mo-Au)
Source Magma	Granite	Quartz monzonite	Mo-rich Cu deposits: Granite-diorites
Magma Geochemistry	High silica, alkali-calcic series peralkaline magmas, F-rich (>0.1 wt.% F)	Calc-alkaline series, low F content (<0.1wt.% F)	Calc-alkaline quartz granodiorite and monzonite
Alteration	Intense core of potassic alteration and silicification with broad upper zones of phyllic and propylitic alteration with quartz-sericite alteration. Minor greisen below orebody?	Potassic core with outward gradation into propylitic alteration. Phyllic zone commonly has a propylitic overprint. Minor peripheral argillic alteration is observed in most systems.	Potassic core with outward gradation into sericitic alteration and large outer propylitic halo. Variable amounts of outboard advanced argillic alteration. Typically a large leached lithocap.
Tectonic Setting (Key locations)	Rift zones in extensional tectonic settings within thick cratonic crust. (Colorado Mineral Belt, USA)	Subduction zone arcs related to continent-continent collision or oceanic subduction. (West Coast Canada and Alaska)	Continental arcs at convergent boundaries linked to oceanic crust subduction. (Chilean Andes and North American Cordillera)
Typical Ages	Paleozoic to Tertiary, common in Mid Tertiary	Archean to Tertiary, common in Late Tertiary	Paleozoic-Pliocene, common after Palaeocene
Typical Depths	Deep, usually in excess of 4 km	High level, usually between 1-3 km	Most at 2-3 km but up to depths of 5 km
Ore Controls	Quartz stockwork ore zone exploiting brittle fractures forming cupolas draped over small stocks formed by multiple stages of intrusion, fracturing and mineralisation.	Quartz veinlet and fracture stockwork zones superimposed on intermediate to felsic intrusive rocks and extending into the surrounding country rocks.	Quartz stockwork veins related to multiple intermediate-felsic intrusions with significant ore also in magmatic-hydrothermal breccias. Minor disseminations.
Ore Minerals	**Molybdenite,** wolframite, cassiterite, sphalerite	**Molybdenite**, scheelite, chalcopyrite, galena	**Chalcopyrite, Molybdenite**, bornite, tennantite (malachite+Azurite)
Gangue Minerals	Quartz, pyrite, topaz, fluorite, rhodochrosite, biotite, calcite, anhydrite and clays	Quartz, pyrite, K-feldspar, biotite, sericite, calcite, anhydrite and clays	Quartz, K-feldspar, biotite, sericite, magnetite, anhydrite, K-feldspar and clays
Mo Grades **Cu:Mo ratio**	**0.3-0.45 wt.% Mo = primary metal** **1:100 to 1:50**	**0.1-0.2 wt.% Mo = primary metal** **1:30 to 1:1**	**0.02 wt.% Mo typical = by-product** **1:0.04 typical**
Tonnage	**Variable - 50 to 1000 Mt**	**Moderate: 100 Mt typical**	**Very high and variable: 1000 Mt-12 Gt**
Famous Examples	Climax and Henderson, Colorado Questa and Victorio, New Mexico and Pine Grove, Utah and Butte, Montana	Endako and Boss Mountain, British Columbia, Red Mountain, Yukon, Quartz Hill, Alaska, Jinduicheng, China, East Kounrad, Kazhakstan	Chuquicamata and Escondida, northern Chile El Teniente, Los Bronces, central Chile Bingham, Utah and Pima, Arizona

Notes: Primary ore minerals, Mo grades and typical Mo tonnages are displayed in bold. Data obtained from White *et al.,* (1981), Westra and Keith (1981), Cox and Singer (1988), Mcmillan and Panteleyev (1988), Carten *et al.,* (1993), Panteleyev (1995), Sinclair (1995, 2007), Misra (2000), Cooke *et al.*, (2005), Ludington and Plumlee (2009). For the distributions of different types of Mo-rich porphyry systems refer to Figure 1.1.

In this study, 'Mo-rich porphyries' are defined as any porphyry deposit in which Mo is obtained as a primary target metal (as in porphyry Mo deposits) or as a major co- or by-product (as in porphyry Cu-Mo systems). Approximately 50% of Mo is obtained from porphyry Mo deposits in which Mo:Cu ratios are >1 and Mo grades exceed 0.05 wt.% (e.g. Westra and Keith, 1981; Sinclair, 2007). These deposits can be subdivided into Climax and Low-F type end-members, which have distinct mineral associations, tectonic settings and metal grades (Table 1.2). The remaining Mo is obtained as a co- or by-product of Cu mining in porphyry Cu-Mo systems (McCready, 2007; Sillitoe 2010). These deposits have Mo:Cu ratios of <<0.1 (Audétat, 2010) and typical hypogene ore grades of 0.5 to 1.5 wt.% Cu and 0.01 to 0.04 wt.% Mo (Sillitoe, 2010: Table 1.2). Although grades in these systems are a magnitude lower than those found in porphyry Mo deposits, the greater abundance of Cu-Mo porphyries and their typically higher ore tonnages account for their equivalent global production values.

Approximately 99% of Mo is obtained from porphyry deposits (Richards, 2003; Sillitoe, 2010), which represents the strongest association of any metal with a single deposit type. These deposits also produce 50-75% of the world's Cu (Richards, 2003; Seedorf *et al*., 2005; Sillitoe, 2010), 20% of the world's Au (Sillitoe, 2010) and are also significant repositories of W, Ag, Pd, Bi Te, Se, Zn, Pb and Re (Sillitoe, 2010). The polymetallic endowment and high metal tonnages of porphyry deposits have made them the focus of numerous ore deposit studies (e.g. Lowell and Gilbert 1970; Burnham, 1979; Dilles, 1987; Richards 2003; Halter *et al*., 2005; Williams-Jones and Heinrich, 2005). However, the fact that Mo is commonly obtained as a by-product means that little attention has focused specifically on the controls on Mo-enrichment within these systems.

Porphyry deposits form by a complex sequence of events (Figure 1.1), starting with the generation of hydrous magmas in arc-related settings and ending with the precipitation of ore minerals from sulphur-rich hydrothermal fluids in the shallow crust (e.g. Burnham, 1979; Burnham and Ohmoto, 1980; Dilles, 1987; Williams-Jones and Heinrich, 2005; Pettke *et al*., 2010; Sillitoe, 2010). During these processes, Mo is typically concentrated by 2-3 orders of magnitude relative to its magmatic source (Table 1.1). Understanding this enrichment

requires a detailed knowledge of Mo solubility in ascending magmas, its partitioning behaviour into hydrothermal fluids and its transport characteristics under the variable physical and chemical conditions that exist in porphyry systems (pressure-temperature-composition-pH-oxygen fugacity). Several studies have helped form an understanding of the solubility and partitioning behaviour of Mo in magmas (e.g. Isuk and Carmen, 1981; Holzheid *et al*., 1994; Tacker and Candela, 1987; Candela and Bouton, 1990; Štemprok, 1990; Farges *et al*., 2006a, 2006b) and hydrothermal fluids (Ivanova *et al*., 1975; Kudrin, 1985; Wood *et al*., 1987; Cao, 1989; Audétat and Pettke, 2003; Klemm *et al.,* 2008; Ulrich and Mavrogenes, 2008; Audétat, 2010; Seo *et al*., 2012; Zhang *et al*., 2012). However, the physical and chemical complexity of porphyry systems, the multiple oxidation states of Mo (Mo^0-Mo^{6+}: e.g. Farges *et al*., 2006a), and the fact that experimental studies are intrinsically restricted to simplified and often inappropriate chemical systems mean that several areas of uncertainty remain regarding the formation of Mo-rich porphyries:

- It is unclear whether the magmas associated with Mo-rich porphyry systems are particularly Mo-rich or whether the formation of Mo-rich deposits purely relies on large volumes of magma or long-lived magmatic-hydrothermal systems. Understanding this requires a better understanding of the temporal relationships between intrusion emplacement, crystallisation, molybdenite deposition and alteration remain poorly constrained;
- It is unclear whether Mo is extracted from melts by dense magmatic brines, low density vapours (or supercritical fluids) or coexisting brines and vapour. In addition the volumes of different fluid types remain poorly constrained raising opposing views on whether large volumes of Mo-bearing vapours (e.g. Rempel *et al*., 2006) or smaller volumes of Mo-rich brines (e.g. Klemm *et al*., 2008) are the most important Mo-transporting fluids;
- Previous studies have also failed to ascertain whether vapour-brine partitioning plays an important role in Mo-enrichment and/or deposition. In addition, the timing of Mo deposition relative to fluid boiling remains poorly constrained;
- The likely speciation of Mo in hydrothermal fluids of varying densities and chemical compositions remains speculative and as a result the most important physical and chemical controls on its precipitation remain poorly understood.

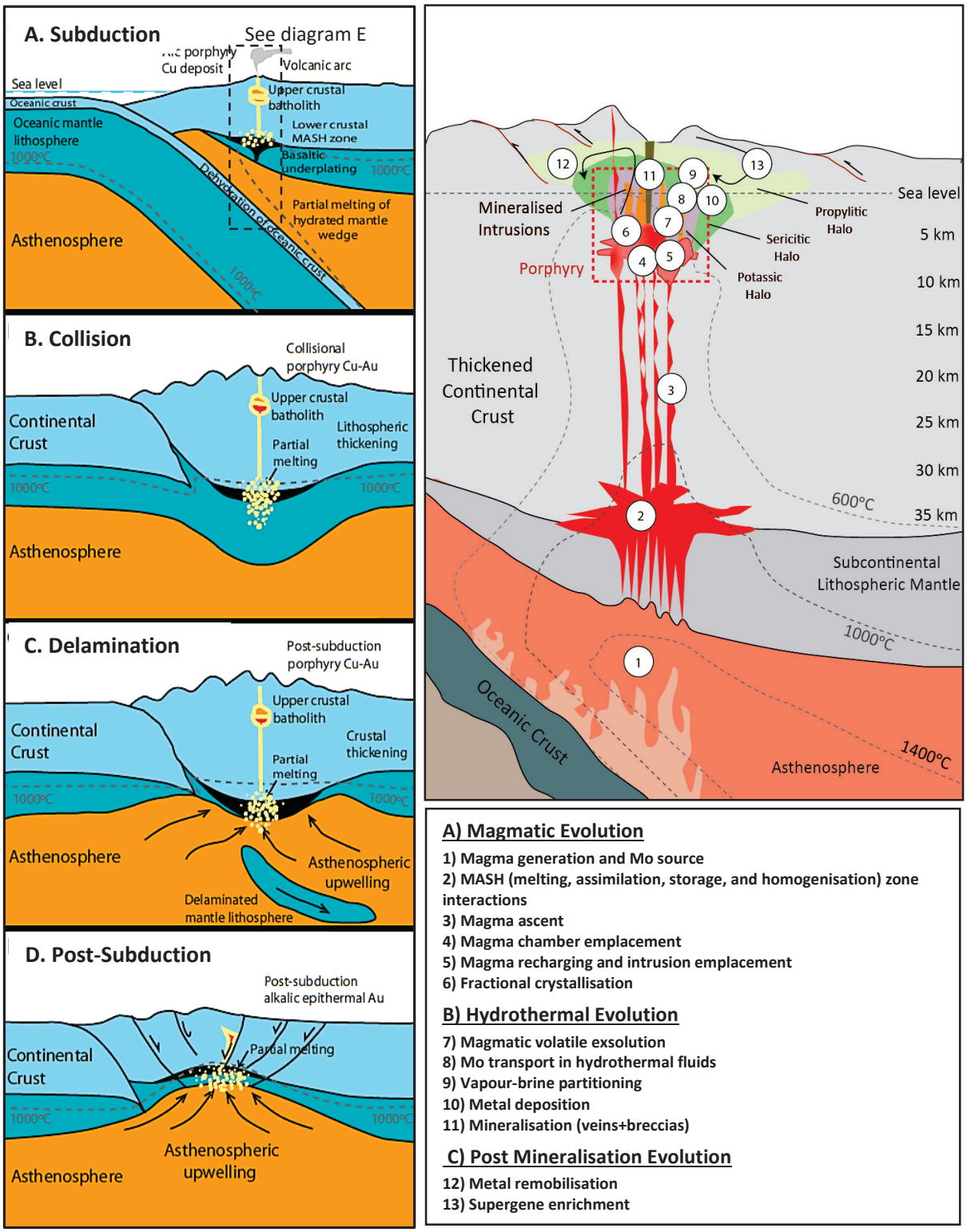


Figure 1.1: Processes and variables that govern the formation of porphyry deposits. (A-D) Schematic diagrams showing the evolution of a subduction zone after Richards (2003). Mo-rich porphyries can form throughout the progression: (A) Typical juvenile subduction zone setting; (B) Collisional magmatism under maximum compression; (C) Delamination of subduction slab and associated asthenospheric upwelling; (D) Post-subduction extensional setting with stretching and rifting of the continental rifting. (E) Schematic diagram of the 13 main magmatic (red), hydrothermal (green) and post-mineralisation (blue) features and processes that need to be considered in the study of porphyry ore formation. MASH: zone of magma melting, assimilation, storage and homogenisation (Hildreth and Moorbath, 1988).

Another major shortfall in the current understanding of porphyry systems is why there is typically a pronounced decoupling in the mineralisation of Mo and Cu. This trend has been recognised in a number of Cu-Mo deposits, but has yet to be conclusively explained (Gustafson and Hunt, 1975; Ulrich and Heinrich, 2001; Rusk *et al*., 2008; Landtwing *et al*., 2010; Redmond and Einaudi, 2010; Sillitoe, 2010; Vry *et al*., 2010; Seo *et al*., 2012). It has been attributed to several superimposed element-fractionating processes with the most popular hypothesis being that Cu is preferentially partitioned into low-density vapours during the separation of hydrothermal fluids into vapours and brines (e.g. Heinrich *et al*., 1999). Despite this, recent experimental studies failed to reproduce the favourable transport of Cu in vapour (Lerchbaumer and Audétat, 2011; Seo and Heinrich, 2012) and, as a result, the reasons for Mo and Cu decoupling remain elusive. Understanding the extents and causes of this decoupling is of paramount importance as it will not only improve our conceptual understanding of how porphyry systems form, but may also lead to the identification of new Mo resources in Cu-rich districts and porphyry systems.

1.2 Aims and Objectives

This study aims to form a better understanding of the transport and deposition of Mo in porphyry systems and the controls on the decoupled mineralisation of Mo and Cu by combining detailed fieldwork at a world-class Cu-Mo porphyry deposit with high-precision geochronology and fluid inclusion microanalysis. For this study, the El Teniente Cu-Mo porphyry was selected as the ideal deposit based on the following criteria:

- It is one of the world's largest known resources of both Cu and Mo, containing a current and mined resource total in excess of 95 Mt Cu and 1.4 Mt Mo. These metals exhibit clearly decoupled mineralisation patterns (Vry *et al*., 2010);
- The system is geologically very young in age (8-3 Ma) limiting the potential effects of post-mineralisation exhumation, alteration, oxidation and overprinting by metamorphic and later magmatic fluids;
- Molybdenite is the third most abundant hypogene ore mineral (behind chalcopyrite and bornite) and occurs in several different vein and breccia assemblages;
- It has a well-defined and constrained vein chronology (Vry *et al*., 2010) which is essential for carrying out vein distribution analysis at the deposit and identifying the veins and breccias that are principally responsible for controlling grade distributions;
- It has been extensively drilled allowing for the sampling of all intrusions, breccia bodies, vein types and alteration zones from depths of up to 3 km from the current erosional surface.
- It has multiple intrusions and breccias that have highly variable amounts of associated mineralisation, possibly indicating overriding magmatic controls on the distribution and timing of Mo mineralisation to be assessed;
- It contains a number of minerals including quartz, anhydrite and gypsum, which contain fluid inclusions suitable for analysis;
- It has pre-existing data sets for fluid inclusions (Cannell, 2004; Klemm *et al*., 2005; Vry, 2010) and geochronology (Cannell, 2004; Maksaev *et al*., 2004), which allow for a highly detailed comparative study to be completed.

The first part of this study (Chapter 2) aims to provide a detailed review of the current understanding of the formation of Mo-rich porphyry deposits from both a magmatic and

hydrothermal perspective. This involves an assessment of the magmatic precursors responsible for the formation of Mo-rich porphyries. However, this section will predominantly focus on the magmatic-hydrothermal processes that follow the emplacement of a parental porphyry intrusion (Figure 1.1) and typically concentrate Mo by 2-3 orders of magnitude (Table 1.1). Previous work on the magmatic-hydrothermal evolution of El Teniente is also reviewed (Chapter3) in order to identify any significant gaps or discrepancies in the current understanding of the deposit.

The second part of this study aims to form a better understanding of the evolution of El Teniente and the controls on the distribution and timing of Mo and Cu mineralisation by combining detailed fieldwork with thin section petrography and high precision Re-Os molybdenite dating (Chapter 4). In this part of the study the main objectives were to:

- Compare the distribution of Mo and Cu grades at different mine levels to assess the spatial relationships of each metal with different intrusions and breccias and identify any clear similarities and differences in metal distributions;

- Assess the validity of the previously determined vein chronology for El Teniente (Vry *et al*., 2010) and complete a detailed vein and breccia distribution study at different mine levels in order to quantitatively assess which veins and breccias are the most important with respect to Mo and Cu mineralisation;

- Collect a suite of samples on which to complete thin section petrography, Re-Os molybdenite dating and fluid inclusion analyses;

- Assess the typical sulphide abundances within different vein and breccia generations and the relative timing of Mo and Cu sulphides by completing detailed conventional and reflective light petrography on samples from multiple intrusion centres;

- Date molybdenite mineralisation associated with several intrusions in order to assess whether or not there is a deposit-wide evolution in vein and breccia formation. Compare results with previously collected geochronological data (e.g. U-Pb zircon and Ar-Ar sericite) in order to assess the relationship of molybdenite mineralisation with different intrusions and alteration regimes;

- Propose a refined model for the temporal evolution of El Teniente by comparing previous evolution models with new geochronological and vein distribution data.

This study then aims to constrain the most important magmatic and hydrothermal controls on the transport and deposition of Mo and Cu at El Teniente by combining detailed fluid inclusion petrography, microthermometry and LA-ICP-MS analysis (Chapter 5). In this part of the study the main objectives were to:

- Identify the different fluid inclusion types present within different veins and breccias and assess their relative proportions and relative timing with different gangue and sulphide minerals. Results can then be combined with detailed SEM-CL petrography to form a better understand of the spatial and temporal evolution of fluids within each sample and how these vary in different parts of the deposit;
- Analyse fluid inclusions from multiple vein and breccia generations using microthermometry and LA-ICP-MS to determine their P-T-X characteristics (salinity, temperature, density, composition) and assess which fluids are critical for the transport and deposition of Mo and Cu;
- Ascertain the effects of fluid phase separation on the decoupled partitioning of Mo and Cu and assess whether this process is the most important control on the decoupling of Mo and Cu within the different hydrothermal fluids present;
- Compare the P-T-X properties of Mo- and Cu-bearing inclusions to identify the key controls on metal solubility and sulphide deposition across the deposit;
- Assess the timing and main physical characteristics of overprinting fluids using combining SEM-CL petrography and fluid inclusion microthermometry. Assess the origin of these fluids and use LA-ICP-MS to determine whether or not these fluids remobilised and potentially enriched Mo and Cu grades at the deposit;
- Assess changes in fluid inclusion chemistry with time to determine whether any changes in magma chemistry affect shallow level Mo mineralisation and Mo-Cu decoupling.
- Propose a refined model for the hydrothermal evolution of El Teniente by comparing fluid inclusion data with geochronological data with previously proposed magmatic-hydrothermal models for El Teniente.

This study then aims to assess which magmatic and hydrothermal processes and variables are the most important with respect to Mo transport and Mo-Cu decoupling in porphyry systems. This is done by combining results from the previous chapters with previously collected natural and experimental data. The main objectives were to:

- Compare results with data from a number of porphyry Cu-Mo, Cu-Au, Mo and barren systems to assess which processes (Figure 1.1) are the most important in forming Mo-rich deposits.
- Compare natural results with experimental results to assess whether there are any universal physical or chemical parameters that strongly influence the formation of Mo-rich systems;
- Determine the likely dissolved species of Mo and Cu in hydrothermal fluids with different salinities and compositions and quantitatively assess which processes and variables are the most important with respect Cu-Mo decoupling.
- Assess whether or not metal remobilisation plays an important role in redistributing and enriching Mo grades in porphyry ore systems.

Finally, this study will summarise the key findings regarding the evolution of El Teniente, the magmatic and hydrothermal controls on the formation of Mo-rich porphyries and the controls on the decoupled mineralisation of Mo and Cu. This study will then outline any further work that will be beneficial to our understanding of the formation of Mo-rich porphyry deposits.

Chapter 2: The Formation of Mo-Rich Porphyry Deposits

2.1 Introduction

This chapter provides an introduction to the global distribution and tectonic settings of Mo-rich porphyry deposits and summarises the current understanding of the processes and variables that govern their formation from magma source to ore trap (Figure 1.1). In order to achieve this results are combined from a number of experimental and natural solubility and partitioning studies. Particular attention is paid to any clear discrepancies in the evolution of porphyry Mo and Cu-Mo deposit systems. The identification of these characteristics is necessary for comparative work to be completed between the studied Cu-Mo porphyry (El Teniente) and other Cu-Mo, Climax type and Low-F type deposits (Table 1.2). To date, little comparative work of this nature has been undertaken and therefore it is still unclear whether the speciation and transport of Mo is significantly different in each deposit type.

Information provided in this chapter will form the basis for the assessment of the evolution magmatic-hydrothermal evolution of El Teniente, the relative importance of different magmatic and hydrothermal processes in enriching Mo, and the reasons for Mo-Cu decoupling in porphyry systems.

2.2 Global Distribution and Timing

Porphyry deposits show clear spatial-temporal relationships with active continental margins where compressional tectonics, crustal thickening, uplift and erosion have taken place (e.g. Lindgren, 1933; Lowell and Guilbert, 1970; Kesler, 1973; Burnham, 1979; Hedenquist and Lowenstern, 1994; Richards, 2003; Cooke *et al*., 2005; Sillitoe, 2010; Munoz *et al*., 2012). In these settings, generation of oxidised magmas (e.g. Sillitoe, 1973) can lead to the formation of porphyry deposits, potentially at any point during subduction zone evolution (Richards, 2003, 2009; Figure 1.1A-D). Studies of the distribution of porphyry systems show clear provinciality with respect to contained metal concentrations (e.g. Kesler 1973, Clark, 1993; Sillitoe, 2002; Cooke *et al*., 2005). For example, Mo and Cu-Mo porphyries are predominantly found in thickened cratonic arcs, whereas Au-rich porphyries usually occur in juvenile island arc settings (e.g. Kesler 1973: Figure 2.1). Different deposit types also show different modal formation ages and age ranges (e.g. Table 1.2) as a function of their different settings and preservation potentials (e.g. Cooke *et al*., 2005).

Porphyry Cu-Mo deposits are principally found in Palaeozoic to Pleistocene continental collisional arcs in numerous countries (Figure 2.1A). Most abundant and notable examples occur in Chile (e.g. El Teniente, Los Bronces), Peru (e.g. Toquepala), China (e.g. Dexing) and the USA (e.g. Bingham, Utah). These countries produce nearly 75% (approximately 160,000 tonnes) of global Mo (Figure 2.1B) and are also the top four Cu producers (Figure 2.1C), highlighting the importance of Cu mining in global Mo production. This relationship is particularly strong in Chile, which hosts the highest concentration of Cu-rich porphyries in the world (Camus, 2002) and obtains its Mo almost exclusively as a by-product of Cu mining. The relatively shallow formation depths of Cu-Mo porphyries relative to Cu-Au porphyries (Table 1.2) and their abundance in young collisional belts such as the Chilean Andes means that most known deposits formed in the Palaeogene and Neogene. However a wider range of ages between the Palaeozoic and late Pliocene is reported (e.g. Cooke *et al*., 2005).

Low-F type deposits occur in similar continental collision settings to porphyry Cu-Mo systems but are comparatively restricted in terms of their global distribution (Figure 2.1A). Most Low-F type deposits occur in the North American Cordillera in western Canada (e.g.

Endako and Kitsault, British Columbia), northwest USA (e.g. Thompson Creeek, Idaho) and Alaska (e.g. Quartz Hill), where they may be interspersed between Cu-Mo porphyries (Figure 2.1A). Only a few notable examples are found outside North America, including East Kounrad, Russia, Compaccha, Peru and Jinduicheng, China. Due to their abundance in the North American Cordillera and relatively shallow formation depths (Table 1.2), Low-F type deposits probably have lower preservation potential and therefore display modal ages in the mid- to late Tertiary. However, mineralisation ages ranging from the Archean (e.g. Setting Net Lake, Ontario) to late Cretaceous (e.g. Red Mountain, Yukon) have been reported (e.g. Sinclair, 2007).

Climax type deposits are typically found further from cratonic margins (Sinclair, 2007) than Low-F type and Cu-Mo deposits, forming within post-collisional extensional settings (e.g. Audétat, 2010: Figure 1.1D). These deposits display strong provinciality and are typically found in close proximity to one another in localised clusters or belts. For example, Climax, Henderson and Mt Emmons, Colorado; Mt Hope, Nevada; and Questa, New Mexico, all occur proximal to each other within the Colorado Mineral Belt (Figure 2.1). These deposits also occur close to several large Cu-Mo porphyries including Butte, Montana and Bingham, Utah, which means that several of the world's largest Mo resources occur within 1% of the Earth's land surface (Singer *et al*., 2005; Pettke *et al*., 2010). Previously, Ludington and Plumlee (2009) recognised 13 known Climax type deposits, all of which occur in western North America. However, a cluster of large Climax type deposits are also now recognised in China, including the Jindulcheng and Nannihu deposits (Figure 2.1), allowing it to become the world's top Mo producer (Figure 2.1B). Due to their formation in back-arc settings at greater depths, Climax-type deposits typically display older modal ages than porphyry Cu-Mo-rich deposits, with most being Palaeozoic in age (Table 1.2).

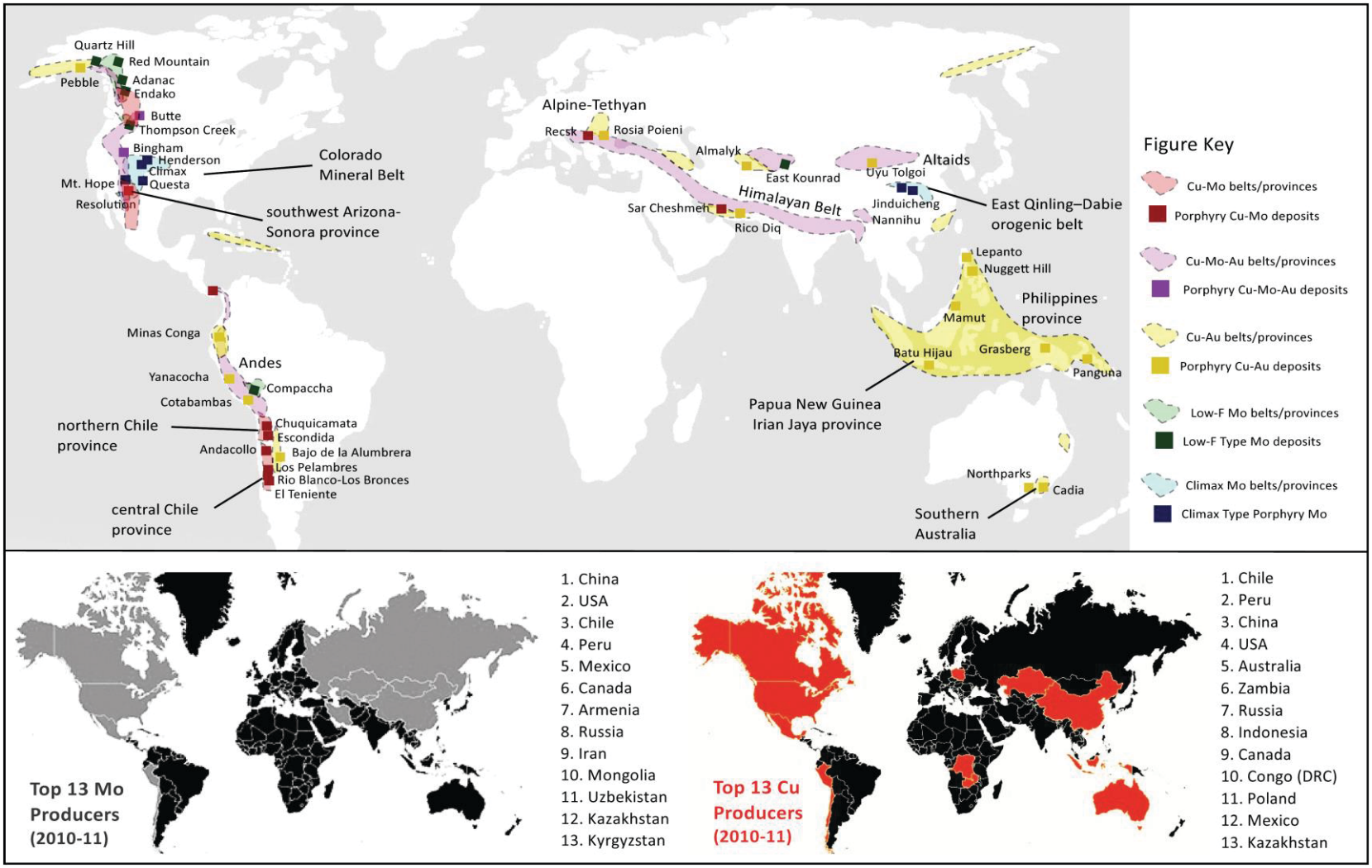


Figure 2.1: (A) World map showing the location of major porphyry belts/provinces and example deposits from each region. Different deposit types and districts are represented by different colours: Red = Cu-Mo porphyry deposits; Purple = Cu-Mo-Au deposits; Yellow = Cu-Au deposits; Green = Low-F type deposits, Blue = Climax type porphyry Mo deposits. Figure adapted from (Singer *et al.*, 2005; Cooke *et al.*, 2005; Vry, 2010; Sillitoe, 2010). (B-C) Top 13 countries for Mo production (pale grey countries) Cu production (pink countries) based on estimated mine productions in 2010-2011. Data obtained from the (Polyak, 2013).

2.3 Magmatic Evolution

2.3.1 Magma Generation and Mo Source

In subduction zones, magmas are generated by melting of metasomatised mantle wedge as a result of dehydration of the subducting oceanic slab (e.g. Richards, 2003) and melting of its veneer of sediments and possibly the plate itself (e.g. Best and Christiansen, 2001). The release of oxidising components such as H_2O, CO_2 and Fe^{3+} (Mungall, 2002; Frost and McCammon, 2008) has been argued to produce magmas with high fO_2 (Figure 2.2) that can oxidise residual sulphides to more fluid-mobile sulphate, allowing for the liberation of sulphide-bound elements such as Cu and Mo (Sillitoe, 1997). Cu and Au are believed to be directly sourced from the mantle wedge, whereas Mo is generally considered to be derived from melting of overlying, thickened continental crust (e.g. Farmer and DePaolo, 1984).

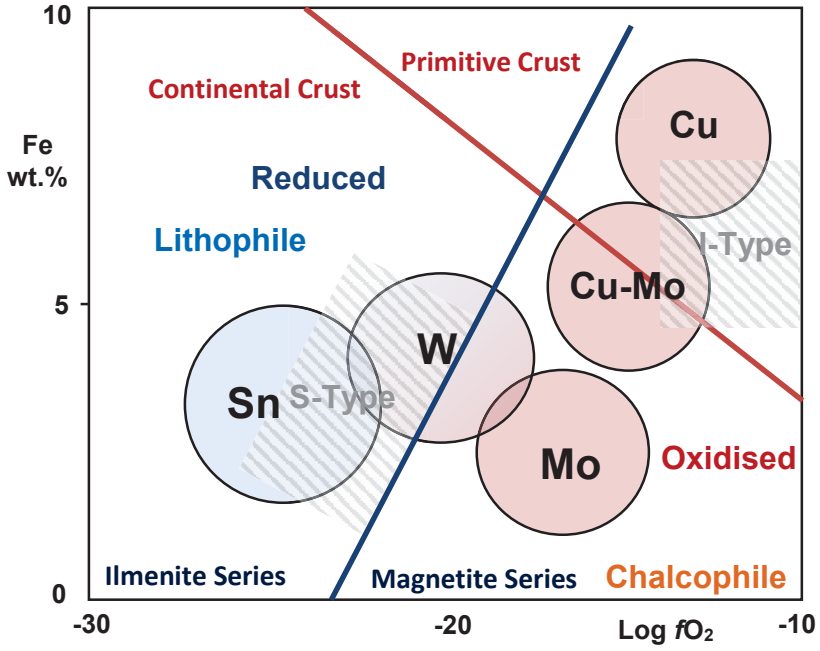


Figure 2.2: Fe wt.% as a proxy for degree of fractional crystallisation versus redox state (log fO_2) for Intrusions associated with different mineralised systems (Sn–W and Cu–Mo). S-type and I-type granites are displayed in striped grey areas. Mo deposits are plotted in magnetite series granites associated with I-type magmas with a continental crustal affinity. Figure adapted from Blevin (2003) and Vigneresse (2007).

2.3.2 MASH-Zone and Crustal Interactions

Metal- and sulphur-rich magmas generated in continental subduction zones buoyantly rise to the base of the thickened continental crust (e.g. Richards, 2003). Due to the greater density of basaltic magmas than lower crustal rocks, ascending magma is interpreted to underplate or pool in the deep continental crust in zones of melting, assimilation, storage, and homogenisation (MASH zones; c.f. Hildreth and Moorbath, 1988) or hot zones (c.f.

Wilkinson, 2013). Similar zones may also occur beneath Climax type deposits as a result of rift-related asthenospheric upwelling (Figure 1.1D). In these zones, the assimilation of lower crustal rocks and fractionation of primitive basaltic magma produces silica-rich (andesitic to dacitic) arc magmas (Annen *et al*., 2006; Hildreth and Moorbath, 1988; Richards, 2003, 2009). It has been suggested that these sulphur-rich magmas become progressively enriched in chalcophile elements and volatiles in this region during repeated cycles of magma input and fractionation (e.g. Wilkinson, 2013). Metal concentrations may also increase as a result of the scavenging of additional chalcophile elements from the lower crust (e.g. Richards, 2003). This may be particularly important with respect to Mo (e.g. Farmer and DePaolo, 1984).

Petrological and isotopic evidence in several porphyry Cu-Au, Cu-Mo and Low-F type systems indicate that metals and sulphur are sourced from multiple injections of subduction zone magma into compositionally-zoned magma chambers underlying the ore bodies (e.g. Keith *et al.,* 1986; Audétat and Pettke, 2003; Klemm *et al.,* 2008; Audétat, 2010). Similar interactions are suggested for Climax type systems (Keith *et al*., 1986; Carten *et al*., 1993), although evidence tends to be far more subtle than in porphyry Cu-Mo systems (Audétat, 2010). This, combined with the provinciality of Climax type deposits (e.g. Table 1.2; Figure 2.1A), led to the hypothesis that Mo may be enriched by local interactions with upper crustal rocks (Sinclair, 2007; Zhu *et al*., 2009). Despite this, recent sulphur, Pb, Nd and Sr isotope and trace element ratio studies at Climax, Colorado, Questa, New Mexico, and Cave Peak, Texas, reveal that Mo is likely enriched at far greater depths (Audétat, 2010; Pettke *et al.,* 2010; Audétat *et al*., 2011). One possibility is that Climax type deposits are underlain by significant Mo anomalies created by subduction of reduced, sulphide-rich shales during periods of intensive continental construction (Pettke *et al.,* 2010). Mo is then acquired by highly silicic, peraluminous melts generated by asthenospheric upwelling and melting in the sub-continental lithospheric mantle (Pettke *et al.,* 2010). Alternatively, Mo may be derived from protracted periods (i.e. 100 million years) of rift-related magmatism, where ascending mafic magmas undergo extreme degrees of elemental fractionation (Audétat, 2010). Both theories may explain the close association of Climax-type deposits with highly siliceous quartz monzonite and alkali granite intrusions (Table 1.2) that are characterised by strong continental crustal signatures (e.g. White *et al.,* 1981; Figure 2.2).

2.3.3 Magma Ascent and Magma Chamber Emplacement

Evolved arc magmas buoyantly rise through the crust to form mid- to high-level magma chambers at typical depths of 4-10 km (e.g. Singer *et al*., 2008; Wilkinson, 2013). The depth to which magma can ascend is a function of the extent of fractionation and volatile degassing that take place during ascent (Annen *et al*., 2006). These interlinked processes lead to large increases in magma viscosity that lead to stalling and construction of large magma chambers that ultimately crystallise to form batholiths. Extensive crystallisation commences when an ascending magma intersects its H_2O-saturated liquidus and releases magmatic volatiles. This is initiated by depressurisation, but is strongly controlled by magma composition and initial water content (e.g. Murakami *et al.,* 2010). Experimental studies by Cloos (2001) demonstrated that 8% H_2O in silicate magma causes saturation at ~3 kbar (9-12 km), 4% H_2O at ~1 kbar (3-4 km), and 2% H_2O at ~0.25 kbar (1-2 km).

Petrological and geochronological studies of porphyry intrusions and their associated volcanic rocks indicate that magma chambers are composite bodies that evolve over protracted periods of >100 kyr to several million years (e.g. Audétat and Pettke 2003; Maksaev *et al*., 2004; Halter *et al*., 2005; Audétat 2010; Sillitoe, 2010; von Quadt, 2011). This longevity is not possible without thermal rejuvenation by the input of numerous batches of intermediate to mafic magma (Wilkinson, 2013). Repeated pulses of magma input increase the amount of metal and sulphur available for mineralisation in the overlying deposit. For example, It has been suggested that Cu and sulphur concentrations at the El Teniente Cu-Mo porphyry are indicative of a long-lived, composite parental magma chamber with a volume in excess of 600 km^3 (Skewes and Stern, 2007). Protracted periods of mineralisation in Climax-type systems have also been attributed to multiple injections of rift-related magma (Audétat, 2010), suggesting that magma recharging is a ubiquitous process in the formation of all Mo-rich systems.

Multiple pulses of magma input and fractionation leads to the accumulation and buoyant escape of low-density, volatile-rich magmas from top of the magma chamber (Burnham, 1981; Blevin and Chappell, 1992; Hattori and Keith, 2001; Wilkinson, 2013). These crystallise to form volumetrically minor porphyry bodies and dikes at typical depths of 1-4 km (e.g.

Wilkinson, 2013). These are often surrounded by halos of alteration and mineralisation (Lowell and Guilbert 1970; Sillitoe, 2010; Vry *et al*., 2010) suggesting that they act as important conduits for multiple pulses of ascending, metal-bearing fluids.

Stratigraphic relations, erosion level estimates, alteration sequences, and fluid inclusion pressure estimates have all been used to estimate the final emplacement depths of intrusions in a number of porphyry systems (e.g. Redmond *et al.,* 2004; Rusk *et al.,* 2008; Singer *et al*., 2008; Seo *et al*., 2009; Murakami *et al*., 2010). Results show that intrusions in porphyry Cu-Au systems generally form at shallower crustal levels than in Cu-Mo systems (Figure 2.3). Porphyry Mo intrusions usually form at even greater depths, with most Climax-type deposits associated with magma emplacement at >3 km (Kesler, 1973). This implies that the felsic and viscous magmas associated with Mo-rich systems tend to reach H_2O saturation at greater depths. This may be due to their greater initial water content, but is more likely a function of their extreme degrees of fractionation (e.g. Ulrich and Mavrogenes, 2008), as documented by the more felsic (e.g. Sillitoe, 1997) and evolved nature of their intrusions (Figure 2.2).

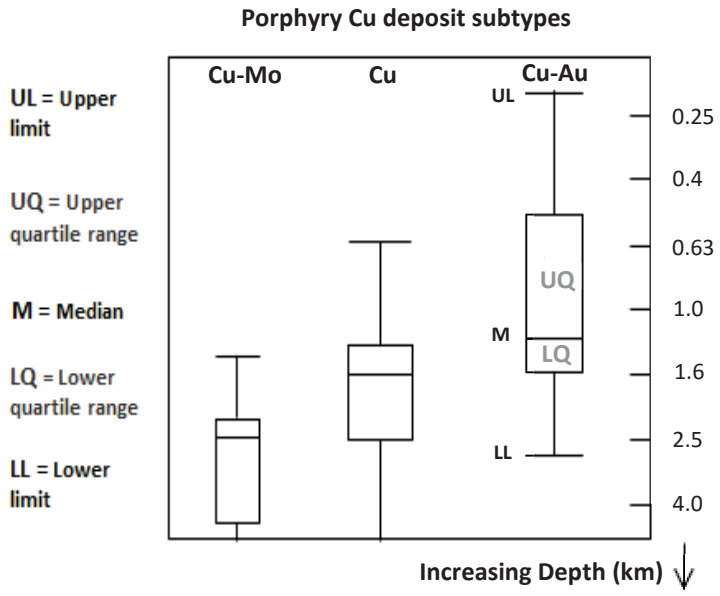


Figure 2.3: Box and whisker plots of the emplacement depths of different porphyry Cu deposit subtypes based on emplacement depth estimates for 51 Cu-Mo deposits, 256 Cu deposits and 115 Cu-Au deposits. Adapted from Singer *et al*. (2008).

Although a broad distinction is observed between different porphyry deposit types, within each group there is significant variation in intrusion emplacement depths. For example, intrusions at the porphyry Cu-Mo deposits of Bingham Utah, and Butte, Montana, are interpreted to have formed at 2-3 and 7 km respectively (Redmond *et al.,* 2004; Rusk *et al.,*

2008). The similar parental magma compositions in these deposits indicate that other factors may also play direct roles in controlling porphyry emplacement depths. For example, the exploitation of major crustal-scale fault zones has been observed in several deposits (e.g. Sillitoe, 1997).

2.3.4 Mo Solubility and Speciation in Magmas

The amount of Mo that is successfully delivered to the porphyry environment is a function of its solubility in the melt during ascent and its partitioning behaviour into separating silicate, sulphide and magmatic volatiles phases (see sections 2.3.6 to 2.4.3). The close relationship between the geochemical signatures and contained metal contents of porphyry intrusions (Figure 2.2) suggests that magma composition plays an important role in controlling metal solubilities during ascent. In addition, the close association of Mo with highly oxidised granites (Figure 2.2) suggests that high fO_2 (i.e. >NNO+1) must be maintained during ascent to form Mo-rich porphyries (e.g. Dilles, 1987; Streck and Dilles, 1998; Field *et al.,* 2005).

A number of experimental studies have been undertaken to evaluate the controls on Mo solubility and speciation in silicic magmas (Table 2.1). These reveal that Mo is readily soluble in silicate melts over a broad range of temperature and pressure (e.g. Holzheid *et al*., 1994; Štemprok, 1990; O'Neill and Eggins, 2002). Several studies demonstrate that Mo solubility increases with increasing fO_2 (Tacker and Candela, 1987; Candela and Bouton, 1990; Lowenstern *et al*., 1993; Holzheid *et al.,* 1994; Farges *et al*., 2006a; Table 2.1). This was attributed to the predominance of Mo^{6+} under oxidised conditions, which is interpreted to be more soluble in silicate melt than other Mo cations (Mo^{2+} to Mo^{5+}). The speciation of Mo in silicate melts remains speculative. The high solubility of Mo in oxidised, H_2O-bearing melts led to the suggestion that Mo is dissolved as MoO_3 (Štemprok, 1990) or Mo-hydroxyl complexes (Candela and Holland, 1984; Webster, 1997). Isuk and Carman (1981) suggested that Mo solubility is independent of dissolved CO_2 but may be enhanced by dissolved $Na_2Si_2O_5$ and $K_2Si_2O_5$ concentrations. This led to the suggestion that Mo may also be dissolved as silicate and hydroxylated silicate complexes. In contrast, O'Neill and Eggins (2002) stated that complexation with Ca (i.e. as $CaMoO_3$ and $CaMoO_4$) is far more likely to

enhance Mo solubility in oxidised melts. Studies of the partitioning of Mo between fluids and melts have also shown that increased melt NaF (Bai and Koster van Groos, 1999) and HCl concentrations (e.g. Keppler and Wyllie, 1991) may also increase Mo solubility in melts. This was attributed to the formation of Mo-hydroxyl-halide complexes.

Although these species are plausible, many of the older solubility studies could not evaluate the relative abundances of different Mo cations or the possibility of polynuclear Mo complexes (e.g. Candela and Holland, 1984). Recent speciation studies using X-ray absorption fine structure (XAFS) spectroscopy of silicate and fluid-bearing glasses (Farges *et al*., 2006a, 2006b), reveal that halogens do not complex with Mo, but may promote its tetravalent coordination in oxidised melts. This increases the solubility of Mo as dissolved molybdate species [$Mo^{6+}O_4^{2-}$] (Farges *et al.,* 2006a). This speciation is interpreted to be present over a broad range of fO_2 at temperatures of 1100 to 1700°C (Farges *et al*., 2006a, 2006b), whereas species involving Mo^{4+} and Mo^{5+} prevail in more reduced systems (e.g. fO_2 = IW to IW–3 at 1300°C). XAFS analyses also indicate that Mo can also interact with sulphur in silicate melts (Farges *et al*., 2006b). These disconnected (mobile) thio-oxo-molybdate (e.g. MoO_2S_2 and MoO_3S_3) complexes are interpreted to be present at moderate oxygen and sulphur fugacities (Farges *et al*., 2006a).

2.3.5 Cu Solubility and Speciation in Magmas

To date, little work has focused specifically on the speciation of Cu in magmas. However, experimental studies have shown that Cu is soluble in magmas with a wide range of compositions (e.g. Rybachikov *et al*., 1981, Candela and Holland, 1984). Similar to Mo, Cu shows a close affinity for oxidised intrusions (Figure 2.2), suggesting that it is preferentially transported in systems with high magma fO_2. This relationship has led to the suggestion that Cu is likely transported as monovalent Cu^+ ("$CuO_{0.5}$") complexes (e.g. Holzheid and Lodders, 2001). This speciation is supported by a recent solubility study of Cu in hydrous andesitic melts at 1000 °C and 200 MPa which also showed that Cu chloride complexes are unlikely to form (Zajacz *et al*., 2012). Despite this, it has been hypothesised that Cu^{2+} complexes may prevail in more oxidised magmas (Johnston and Chelko, 1966; Candela and Holland, 1984).

Table 2.1: Experimental studies designed to determine the solubility of Mo in magmatic fluids with varied compositions, fO_2, temperature and pressure that are assumed to prevail in porphyry ore systems.

Experimental Study	Composition	fO_2	T (°C)	P (kbar)	Key Conclusions	Reference
Solubility of molybdenite in alkali silicate melts **(H)**	$Na_2Si_2O_5$ - $K_2Si_2O_5$ MoS_2 4-40 wt.% H_2O	Between NNO and MH	450-850	0.34-1.36	There is a positive pressure dependency on the solubility of MoS_2. Maximum solubility = 650°C. Molybdenite solubility is enhanced by $Na_2Si_2O_5$ - $K_2Si_2O_5$. Mo silicate and/or Mo-hydroxylated silicate complexes are likely dissolved species.	Isuk and Carman (1981)
Mo Solubility in Silicate Melts **(H)**	Anorthite-diopside Eutectic composition	~FMQ-1 to IW - 2.5	1349-1438	0.001	Mo changes its valence state from Mo^{4+} to Mo^{6+} at ~IW-1 making it more soluble. Mo solubility shows a significant increase correlating with increasing temperature.	Holzheid *et al.,* (1994)
Mo partitioning between magnetite and melt **(H)**	High silica (78%) rhyolitic glass	GM to NNO+0.5	800	1.0	Increased oxidation significantly decreases the partitioning of Mo into magnetite from melts.	Tacker and Candela (1987)
Solubility of Mo in felsic magmas **(D)+(H)**	quartz-albite-orthoclase eutectic	No Buffer	750-800	1.5	Mo is readily soluble in felsic magmas under these conditions, likely to be as Mo^{6+} over a range of fO_2. OH groups are not important ligands of Mo^{6+}.	Štemprok (1990)
Mo partitioning between ilmenite and melt **(H)**	High silica rhyolitic glass and ilmenite	GM to NNO	800	1.0	Mo is more soluble in melt at higher fO_2 of NNO+0.5. Reduction aids loss of Mo from the melt during ilmenite crystallisation.	Candela and Bouton (1990)
The effects of melt composition on activity coefficients of Mo-oxides (melt furnace experiments)	19 different melt compositions: CaO - MgO -$Al2O_3$- SiO_2-TiO_2 system + MoO_2 and MoO_3	CO –CO_2 controlled Log fO_2 = $10^{-9.6}$ $10^{-11.7}$	1400	Air	Mo is readily soluble in melts of variable composition and fO_2. Activity coefficients of MoO_2 and MoO_3 vary by factors of 20 and 60 and show a good correlation with melt CaO concentrations suggesting that $CaMoO_3$ and $CaMoO_4$ are key dissolved species.	O'Neill and Eggins (2002)
Study of the speciation of Mo in silicate glasses and melts (**XANES** analysis).	H_2O- to near H_2O-saturated glasses of anorthite- albite, diopside, rhyolite, and basaltic compositions.	Air to IW-4	1104-1600	0.001	$Mo^{6+}O_4^{2}$ is the predominant functional group over a range of compositions. Below the IW buffer, Mo^{6+} is reduced to Mo^{4+} and Mo^{5+} resulting in reduced solubility at all temperatures.	Farges *et al.,* (2006a)
Study of the speciation of Mo in silicate glasses and melts (**XANES** analysis).		NNO+3 to IW-1	832-1478	0.001 - 7.0	Halogens can enhance Mo concentrations in melts by promoting the tetravalent coordination of Mo. Sulphur is found to complex molybdenum at moderate oxygen and sulphur fugacities. This may lead to its sequestration from the melt as sulphides.	Farges *et al.,* (2006b)
Partitioning of Mo between Rhyolitic melt pyrrhotite and an immiscible Fe-S-O melt Furnace experiments **(D)**	Combined silicate melt, magnetite- pyrrhotite and immiscible Fe–S–O	NNO	1042	0.5-1.0	Mo readily partitions into an Fe-S-O melt and pyrrhotite under the experimental conditions. $DMo^{Fe\text{-}S\text{-}O/melt}$ = 90 ±10. $DMo^{Pyr/melt}$ = 35 ±3. Overall Mo partitioning into sulphide phases is less prominent than most other metals including Cu, Au and Ag.	Mengason *et al.,* (2011)

Notes: Shaded blocks represent the key variables explored in each study. Experiments were given run times that were believed to be sufficient to attain equilibrium. (H) = Hydrothermal experiments in cold seal vessels. (D) = Dry experiments. (TA) = Titanium autoclave experiments. XANES = X-ray absorption near-edge structure spectroscopy. Redox buffers used: NNO = Nickel-Nickel Oxide, FMQ = Fayalite-Magnetite+Quartz, GM = Graphite-Methane, MNO = Manganese-Manganese Oxide, MH = Magnetite-Hematite, RRO = Rhenium-Rhenium Oxide.

2.3.6 Magmatic Sulphide Saturation

During magma cooling and fractionation, magma fO_2 decreases with temperature following the trends of the usual redox buffers, such as MH, NNO and FMQ (Figure 2.4). Porphyry Cu-Mo and Cu-Au melts follow similar fO_2-temperature evolution paths, falling just above the SO_2-H_2S reaction curve (Figure 2.4). Under these conditions, a parental magma contains abundant dissolved sulphate, which optimises the uptake and transport of chalcophile elements (e.g. Mungall, 2002).

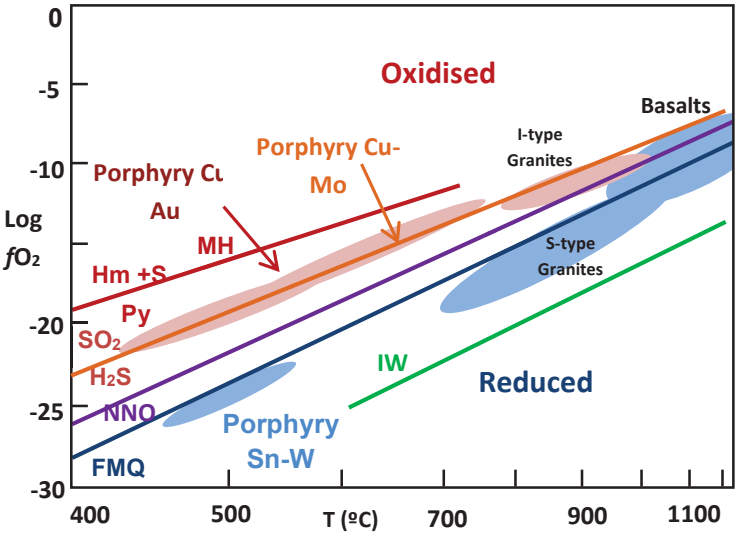


Figure 2.4: Evolution of magmas as a function of fO_2 and temperature in different magmatic and ore deposit systems. Pink = oxidising regime; blue = reduced environment. Proposed area of fO_2 - temperature space for porphyry Cu-Mo deposits is within the dashed orange region. Commonly used buffers, such as nickel–nickel oxide (NNO), fayalite–magnetite–quartz (FMQ) and magnetite–hematite (MH) are indicated as solid lines. Hm = Haematite, Py = Pyrite. Figure after Vigneresse, 2007.

Several recent studies have suggested that a small drop in fO_2 in the magma chamber may dramatically affect sulphide speciation and solubility (e.g. Liang *et al*., 2009; Jenner *et al*., 2010; Richards, 2013; Wilkinson, 2013). Jenner *et al.,* (2010) suggested that magnetite crystallisation in magmas may be sufficient to lower fO_2 so that most dissolved sulphate (SO_4^{2-}) is converted to sulphide (S^{2-}). Alternatively, the assimilation of reducing rocks, such as carbon-rich shales, may also significantly decrease fO_2 of an ascending magma (e.g. Cloos, 2001). These processes may lead to sulphide saturation within the porphyry magma chamber, which could trigger the sequestration of chalcophile metals in separate sulphide phases (e.g. Candela and Holland, 1986; Liang *et al*., 2009; Audétat *et al.,* 2011; Simon and Ripley, 2011; Wilkinson, 2013). This is interpreted to occur during the latter stages of magma fractionation (i.e. >55 wt.% SiO_2: Liang *et al.,* 2009).

It has been suggested that reduction of magma may polymerise mobile thio-oxo-molybdate complexes into hydrophobic Mo-S units (Farges *et al*., 2006b), leading to molybdenite

saturation and nucleation in the melt (Candela and Holland, 1986; Candela and Bouton, 1990; Mengason *et al*., 2011; Audétat *et al*., 2011). This may explain why reduced magmatic rocks, such as peralkaline rhyolites, typically contain higher Mo concentrations than unaltered granitic rocks in mineralised systems (e.g. Lowenstern *et al.,* 1993). The strong association of Mo with oxidised intrusions (Figure 2.2) that typically contain abundant anhydrite (e.g. Burnham and Ohmoto, 1980; Vry *et al.,* 2010; Audétat *et al*., 2011) suggests that high fO_2 in throughout crystal fractionation may play an important role in preventing molybdenite saturation. High fO_2 can be maintained by the early crystallisation of Fe-bearing silicate minerals, such as olivine and clinopyroxene, which increase magma fO_2 by removing Fe^{2+} (e.g. Audétat *et al*., 2011), limiting the partitioning of moderately siderophile Mo into iron sulphide phases (Lodders and Palme, 1991; Stimac and Hickmott, 1994). This may explain the strong association of Mo with silica-rich, Fe-poor intrusions (Figure 2.2).

Although sulphide saturation may remove Mo and Cu from the melt and therefore making them unavailable to exsolving ore fluids (e.g. Candela, 1997; Mengason *et al*., 2011), this process may create important metal-rich regions that could be scoured by later pulses of magmatic-hydrothermal fluids (Wilkinson, 2013). Ascending volatile-rich melts and/or fluids may have the potential to cannibalise zones of previously saturated sulphides, enhancing their chalcophile element concentrations (Figure 2.5). Theoretically these could then ascend to form small intrusions with anomalously high metal concentrations. This scavenging of a heterogeneous source may explain the highly variable metal endowments and metal associations of intrusions associated with the same parental magma chamber.

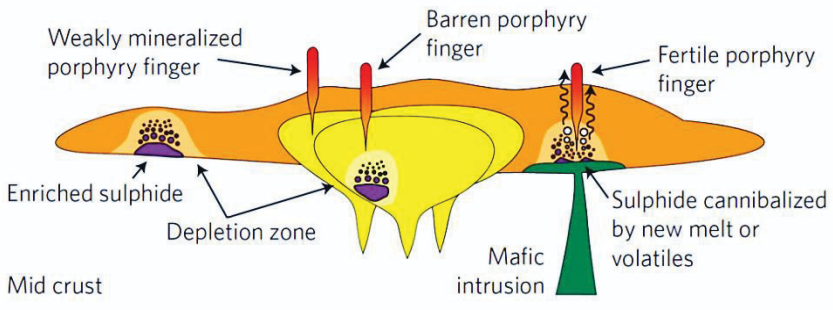


Figure 2.5: Mechanism for the generation of fertile porphyry intrusions by the melting of zones of previously saturated sulphides. In this model, siderophile and chalcophile metals, concentrated in the partitioned sulphide-melts, are stripped producing highly enriched melt or volatile phases. These can buoyantly rise to form mineralised finger porphyries (from Wilkinson, 2013).

2.3.7 Mo Melt-Crystal Partitioning

Intrusions associated with porphyry Cu-Mo and Mo deposits display high Rb/Sr ratios and low Fe contents (Figure 2.2), indicative of high degrees of crystal fractionation (e.g. Westra and Keith, 1981; Blevin, 2003; Vigneresse, 2007; Audétat, 2010). Crystallisation of silicate minerals leads to the generation of a residual melt phase, enriched in volatiles and incompatible elements such as Mo and Cu. Metal concentrations of residual melts are believed to be strongly controlled by temperature, pressure, melt composition, fO_2, fS_2 and water content (e.g. Blevin and Chappell, 1992; Candela and Piccoli, 1995; Audétat *et al*., 2011). These control the partitioning behaviour of metals between magma and crystallising mineral phases and dictate the degree of fractionation that can occur prior to the exsolution of metal-bearing magmatic volatiles (Candela, 1997).

Several experimental studies have investigated the partitioning behaviour of Mo between silicate melts and coexisting crystalline phases (e.g. Tacker and Candela, 1987; Candela and Bouton, 1990; Štemprok, 1990; Mengason *et al*., 2011). These show that Mo is incompatible in most crystal structures and, as a result, typically concentrates in residual melts during fractional crystallisation. Increased fO_2 has a negative effect on $D_{Mo}^{mineral/melt}$ partition coefficients for magnetite (Tacker and Candela, 1987) and ilmenite (Candela and Bouton, 1990) at 800°C and 1 kbar pressure (Table 2.1). This is attributed to the predominance of Mo^{6+}, which does not readily substitute into the crystal structures of most minerals. In contrast, Mo^{4+} displays near-identical ionic charge and radii to Ti^{4+}, thus allowing for its substitution into Ti-bearing phases, such as titanite and rutile, which are common in reduced, ilmenite series granites (Mahood and Hildreth, 1983; Candela and Holland, 1986; Lowenstern *et al.,* 1993; Candela 1997). In reduced systems, Mo can also efficiently partition into pyrrhotite, which may lead to >90% of Mo to be sequestered in fractionating I-type melts (Mengason *et al*., 2011) befire it has a chance to partition into exsolving magmatic volatiles This again may explain the higher typical Mo concentrations in reduced granitic systems (e.g. 30 ppm: Lowenstern *et al*., 1999) relative to oxidised ones (e.g. 2.4 ppm: White *et al*., 1981). It could also explain the association of Mo with melts that have high initial water contents (Ulrich and Mavrogenes, 2008), that permit the partitioning of Mo-rich fluids prior to the final stages of magma fractionation.

2.3.8 Cu Melt-Crystal Partitioning

Similar to Mo, Cu is incompatible in most crystal structures and displays high melt solubility in oxidised melts (e.g. Lynton *et al*., 1993). However, the smaller ionic radii and charges of Cu ($Cu\text{-}Cu^{4+}$) ions means that Cu displays more compatible behaviour than Mo. For example, Cu can partition far more readily from silicate melts into biotite, magnetite, amphiboles, feldspar and ilmenite (Ewart *et al*., 1973; Ewart and Griffin, 1994). Cu also displays far higher $D_{Cu}^{mineral/melt}$ values for partitioning into sulphide phases (e.g. Candela, 1997). For example, experimentally derived $D_{Cu}^{mineral/melt}$ values of 311 to 1530 were obtained for the partitioning of Cu between high silica rhyolites and pyrrhotite (Lynton *et al*., 1993). This indicates that even small amounts of pyrrhotite crystallisation may remove most dissolved Cu from a melt. Therefore, sulphide saturation is likely to be a key control on the availability of Cu to exsolving ore fluids.

2.4 Hydrothermal Evolution

2.4.1 Magmatic Volatile Exsolution

Intermediate arc magmas associated with porphyries typically contain 2.5-10 wt.% H_2O (Burnham, 1997; Halter *et al*., 2004; Annen *et al*., 2006; Loucks, 2014) as well as variable amounts of dissolved SO_2 and CO_2 (e.g. Giggenbach, 1997). As a result, they are likely to saturate at considerable depth (15-4 km) leading to the accumulation of low density aqueous fluids in the upper parts of the melt body (e.g. Wilkinson, 2013). If these fluids exsolve at depth, this could lead to considerable loss of metals from an ascending melt. For example, the deep exsolution of low salinity, CO_2-bearing fluids has been proposed in several Mo-rich systems (e.g. White *et al.,* 1981; Rusk *et al*., 2008). These fluids are interpreted to have the potential to extract covalently bonded sulphur complexes of Cu and Au, which are stable in weakly-ionised H_2O-CO_2 solvents (Pokrovski *et al*., 2008; Wilkinson, 2013).

Fractional crystallisation within porphyry magma chambers also leads to the accumulation of fluids in the residual melt phase. Andesitic to rhyolitic composition magmas contain far more dissolved H_2O than can be accommodated in the hydroxyl sites of crystallising mineral phases (Loucks, 2014). As a result, crystallisation of a magma chamber leads to an increase in melt fH_2O (e.g. Lowell and Guilbert, 1970; Burnham and Ohmoto, 1980; Loucks, 2014). Once fluid saturation of a melt is reached, sulphur-bearing hydrothermal fluids are exsolved, either as single-phase liquids or coexisting hypersaline liquids and vapours (e.g., Eastoe, 1978; Bodnar, 1995; Ulrich *et al*., 2001; Sillitoe, 2010). These magmatic volatiles contain highly variable concentrations of ore-forming metals (Mo, Cu, Au, Ag) and ligands, such as S and Cl (Candela and Holland, 1984, 1986; Cline and Bodnar, 1991).

The low concentrations of Mo and Cu in unaltered metalliferous granites in mineralised systems and the non-phenocrystic deposition of molybdenite and Cu-sulphides (e.g. White *et al*., 1981; Mutschler *et al.,* 1981) implies that magmatic volatile exsolution must efficiently extract metals during the latter stages of crystallisation (White *et al*., 1981; Candela and Holland, 1984; Webster, 1997; Heinrich *et al*., 1999; Zajacz *et al*., 2008; Ulrich and Mavrogenes, 2008; Audétat, 2010).

Identifying the hydrothermal fluids responsible for Mo and Cu transport and deposition has been the focus of numerous natural fluid inclusion studies over the past few decades (e.g. Roedder, 1971; Bloom, 1981; Hezarkhani and Williams-Jones, 1998; Ulrich *et al.,* 1999; Audétat and Pettke, 2003; Rusk *et al.,* 2004, 2008; Landtwing *et al*., 2005; Klemm *et al.,* 2008; Audétat, 2010; Vry *et al*., 2010). Detailed fluid inclusion petrography and microthermometric heating and freezing tests have helped identify the relative timing and types of fluids present in porphyry ore systems. By combining this information with microanalytical techniques for analysing single fluid inclusion compositions, recent studies have also identified the most important fluids with respect to metal transport. Laser ablation inductively coupled plasma mass spectrometry (LA ICP-MS) is now popularly utilised as a powerful tool for studying element concentrations in porphyry fluid inclusions (Ulrich *et al.,* 1999; Audétat and Pettke, 2003; Rusk *et al.,* 2004, 2008; Landtwing *et al*., 2005; Rempel *et al.,* 2006, 2009; Klemm *et al.,* 2008; Audétat, 2010; Pettke *et al.,* 2010; Vry *et al*., 2010).

Fluid inclusion studies revealed that hydrothermal fluids in porphyry systems can exist as single-phase, intermediate-density fluids or as low density vapours or high salinity brines that can coexist with one another. The types of fluids that exsolve are believed to be a strong function of pressure and therefore intrusion emplacement depths (Figure 2.6). For example, Mo-bearing fluids at the deeply emplaced (~7 km) Butte Cu-Mo deposit, Montana, are interpreted to have been exsolved as low salinity (<10 wt.% $NaCl_{eq}$), intermediate density fluids (Rusk *et al.,* 2008). In contrast, the shallower (~2-3 km) Au-rich and barren intrusions of Grasberg, Indonesia, and Bajo de la Alumbrera, Argentina, are interpreted to have exsolved low density vapours and brines (Ulrich *et al*., 1999; Heinrich *et al*., 2005). These may have been exsolved in the two-phase field (Figure 2.6B), been generated by the phase separation of a single-phase fluid or may have formed via the condensation of small volumes of brine from the vapour phase (e.g. Bodnar *et al*., 1985; Figure 2.6 D). The highly variable salinities of fluid inclusions in porphyry Cu-Mo and Mo systems are interpreted to have been generated by vapour-brine separation of moderate to low salinity parental fluids (e.g. Ulrich and Mavrogenes, 2008; Pettke *et al*., 2010). For example, microthermometric data and isotopic ratios of fluid inclusions at Bingham Canyon suggest that vapours and

brines were formed by the separation of a single-phase magmatic-hydrothermal fluid with a bulk salinity of ~7 wt.% $NaCl_{eq}$ (Pettke *et al.,* 2010).

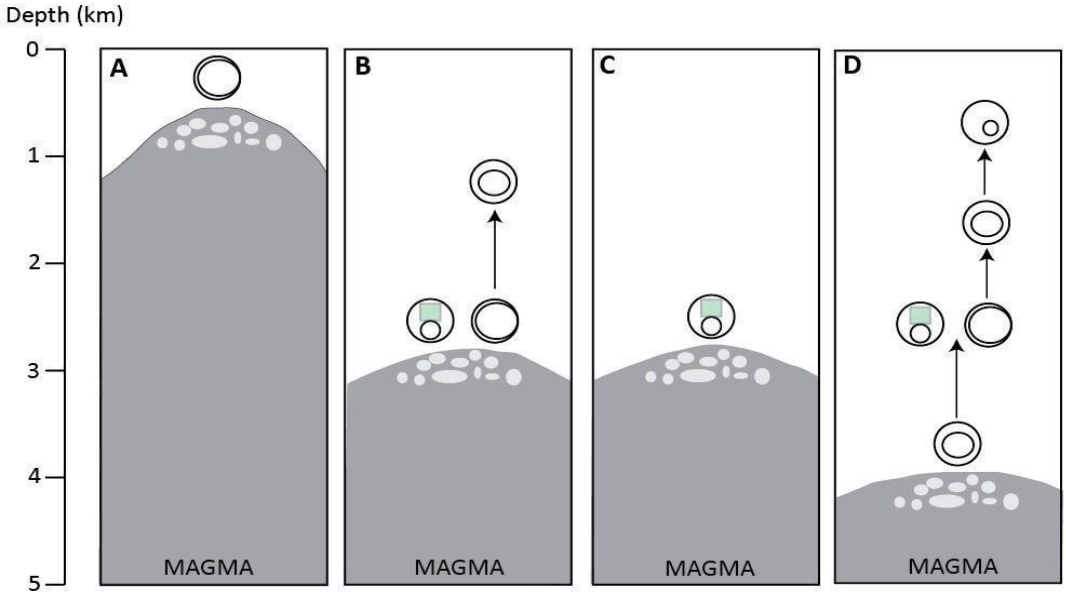


Figure 2.6: Models for the exsolution of different fluid types from magmas intruded at different depths (after Cline and Bodnar, 1991; Heinrich, 2007). The types of fluids that exsolve are a function of pressure, temperature and melt Cl concentration. (A) direct exsolution of a magmatic vapour at shallow depths; (B) direct exsolution of coexisting brine and vapour; (C) direct exsolution of a brine with high pressure and high Cl activity, also a function of degree of melt crystallisation; and (D) direct exsolution of a single-phase, intermediate density, low-salinity fluid and subsequent evolution during ascent.

Understanding Mo-enrichment and the decoupling of Mo and Cu precipitation in porphyry systems relies on a detailed understanding of the controls of Mo and Cu partitioning during magmatic and hydrothermal processes, i.e. between residual melts and magmatic volatiles (e.g. Candela and Holland, 1984, 1986; Audétat and Pettke, 2003; Audétat, 2010) and between vapours and brines generated during phase separation (e.g. Heinrich *et al.,* 1992, 1999; Ulrich *et al.,* 1999; Mavrogenes *et al.,* 2002; Seo *et al.,* 2009; Murakami *et al.,* 2010). Natural, coexisting melt and fluid inclusions and coexisting vapour and brine inclusions have been used to track this partitioning behaviour (e.g. Audétat and Pettke, 2003; Zajacz *et al.,* 2008; Audétat, 2010). Such fluid inclusion data have also constrained experimental studies designed to establish Mo and Cu speciation and the key controls on solubility (Tables 2.3-2.4).

2.4.2 Mo Fluid-Melt Partitioning

The partitioning of Mo between silicate melts and magmatic volatiles has been the focus of several solubility studies using cold seal vessels (Khitarov *et al*., 1982; Tingle and Fenn, 1984; Candela and Holland, 1984; Webster, 1997; Bai and Koster van Groos, 1999). These show that Mo is soluble between 650–1075°C and 0.2–4 kbar in hydrothermal fluids with ranging composition (Table 2.2-2.4). However, $D_{Mo}^{fluid/melt}$ values are relatively low (2.5 ±1.6: Candela and Holland, 1984; 7 ±1: Webster, 1997; 0.02-4.67: Bai and Koster van Groos, 1999).

Recent LA-ICP-MS analyses of coexisting melt and fluid inclusions have also been used to derive $D_{Mo}^{fluid/melt}$ values (Audétat and Pettke, 2003; Zajacz *et al.,* 2008; Audétat, 2010). These studies reveal consistently higher $D_{Mo}^{fluid/melt}$ values for the barren Rito del Medio pluton, New Mexico (17-20: Audétat and Pettke, 2003; 14-23: Zajacz *et al.,* 2008) and the Cave Peak Climax-type deposit, Texas (17-20: Audétat, 2010). The similar values for barren and mineralised systems suggest that melt enrichment may play a more important role than fluid-melt partitioning in the formation of Mo-rich porphyries. However, the lower $D_{Mo}^{fluid/melt}$ values recorded in experimental studies suggest that additional factors may enhance melt-fluid Mo partitioning in natural systems. One possibility is that the partitioning of metals is strongly influenced by the presence of key magmatic volatile components such as F, Cl, CO_2 and S (e.g. Bai and Koster van Groos, 1999). However, changes in physical properties including pressure temperature and redox potential of the system may also strongly influence metal partitioning (e.g. Khitarov *et al*., 1982; Tingle and Fenn 1984; Webster, 1997; Bai and Koster van Groos, 1999; Audétat and Pettke, 2003; Zajacz *et al.,* 2008).

Several experimental studies have shown that hydrous fluid F concentrations do not affect Mo partitioning into hydrothermal fluids (e.g. Tingle and Fenn, 1984; Candela and Holland, 1984; Keppler and Wyllie, 1991). However, as discussed previously, high melt NaF concentrations may reduce $D_{Mo}^{fluid/melt}$ values by enhancing Mo solubility in the melt (Bai and Koster van Groos, 1999). This may result in the late exsolution of extremely Mo- and F-rich fluids during the final stages of fractionation. This may explain why Climax Mo deposits are strongly associated with highly fractionated intrusions and F-rich fluids (Table 1.2).

Table 2.2: Experimental studies designed to determine the partitioning behaviour of Mo (and Cu) between magmas and exsolved fluids of varied compositions.

Experimental Study	Composition	fO_2	T (°C)	P (kbar)	D_{Mo}	Key Conclusions	Reference
Partitioning of Cu and Mo between silicate melt and aqueous coexisting fluid **(H)**	Haplogranite–H_2O-with variable $(Na,K)_2CO_3$ and HCl	NNO	700	2	0.06	Both metals partition into fluid, but Mo is unaffected by Cl concentrations. Cu partitioning is low and appears to be independent of $(Na,K)_2CO_3$ fluid concentrations	Khitarov *et al.*, (1982)
Partitioning of Mo between silicate melt and magmatic vapour/fluid **(H)**	Synthetic granites similar to Moly Mine. Varied F + S	No Buffer	1000	1.0	NA	Mo partitioning is independent of S and F content of magmas and exsolved fluid phase. However, S plays an important role in Mo deposition but does not affect partitioning.	Tingle and Fenn (1984)
Partitioning of Mo and Cu between silicate melt and magmatic vapour/fluid **(H)**	High silica (78%) rhyolitic glass with varied F + Cl	NNO and FMQ	750	1.4	1.0 - 4.0	Mo partitioning is independent of Cl and F content of magmas whereas Cu is preferentially partitioned into magmatic aqueous fluids with increased Cl. Mo^{6+} is likely cation at both fO_2 values.	Candela and Holland (1984)
Partitioning of Mo and Cu between haplogranite melts and F- and Cl-bearing fluids **(H)**	Haplogranite–H_2O-HCl Haplogranite–H_2O-HF	NNO	750	0.2	0.75 - 5.5	Mo and Cu partitioning is independent of F concentrations. Increasing fluid HCl concentration has a negative effect on the partitioning of Mo, whereas increased fluid Cl concentration increases Cu partitioning.	Keppler and Wyllie, 1991
Mo partitioning between silicic melts and saline volatile phase(s). **(H)**+SIMS	Haplogranites and rhyolites of varied Cl and initial H_20	~MNO	831–1075	0.5 - 2.0	8.0 – 80.0	Mo favourably partitions into highly saline brines but does not complex with Cl in aqueous fluids. Increased solubility may be a strong function of increased activity of Na and K in Cl-rich MVP. Pressure has negligible effect.	Webster (1997)
The distribution of Na, K, Rb, Sr, Al, Ge, Cu, W, Mo, La, and Ce between granitic melts and coexisting aqueous fluids. **(H)**	Haplogranites with fluids with variable HCl, NaCl, KCl, NaF, Na_2CO_3 + K_2CO_3	NNO	750-800	1.0 - 4.0	0.2 – 5.0	There is no clear correlation between fluid NaCl concentrations and Mo partitioning but high Cl and NaF concentrations in the melt generally lead to partitioning of Mo back towards the melt. Cl-bearing fluids strongly promote the partitioning of Cu relative to Mo. Mo partitioning is enhanced at elevated pressure. Pressure has no significant effect on the partitioning of Cu.	Bai and Koster van Groos (1999)

Notes: Shaded blocks represent the key variables explored in each study. D_{Mo} = range of fluid/melt partition coefficients reported for Mo in each study. Specific $D_{Mo}^{fluid/melt}$ values for specific conditions are given in the following text. All experiments were carried out under P-T-X conditions that can prevail in porphyry ore systems. Experiments were given run times that were believed to be long enough to attain equilibrium. (H) = Hydrothermal experiments in cold seal vessels. SIMS = Secondary-Ion-Mass-Spectrometry analysis. Redox buffers used in each study: NNO = Nickel-Nickel Oxide, FMQ = Fayalite-Magnetite+Quartz, MNO = Manganese-Manganese Oxide.

Table 2.3: Experimental studies of the solubility of different Mo-species in hydrothermal fluids and vapours under a range of physical and chemical conditions.

Experimental Study	Composition	fO_2	T (°C)	P (kbar)	D_{Mo}	Key Conclusions	Reference
Equilibrium study of MoO_3 in water over a range of temperature	MoO_3 - H_2O Sulphur-free system 0–0.5 M NaOH	NNO	25-300	Saturated vapour P	NA	Mo solubility increases as temperature is increased to 300°C. NaOH has a minor positive effect on Mo solubility.	Ivanova *et al.,* (1975)
Solubility of molybdenite in saline, CO_2- and S-bearing solutions **(CA)**	H_2O – CO_2 - (0-5%) NaCl + MoS_2 - pH 3-6 Sulphur-rich system	MPP	200-350	0.00269 0.287	NA	Mo solubility is broadly independent of Cl and CO_2 concentrations and may be transported as molybdic acid. No pH dependency on Mo solubility but Increased solubility with increasing temperature	Wood *et al.,* (1987)
Solubility of molybdenite in aqueous solutions	MoS_2 - H_2O - NaCl - KCl Sulphur-rich system	NNO	300-400	1.5	NA	Increased Mo solubility with increasing temperature and salinity. Sulphur greatly reduces the solubility of Mo and results in the precipitation of molybdenite.	Cao (1989)
Solubility of Mo in saline aqueous solutions	H_2O - NaCl - KCl + MoO_2 (varied acidity) Sulphur-free system	NNO - NNO-4	300-450	0.009-1.0	NA	Mo readily soluble at all temperatures. Solubility increases with increasing pH, fO_2, and salinity. MoO_2 solubility is almost doubled in the KCl system as opposed to NaCl only.	Kudrin (1989)
The solubility and speciation of Mo in water vapour **(TA)**	Varied vapour fH_2O composition + MoO_3 ± MoO_2 Sulphur-free system	MH	300–360	0.04–0.15	NA	Significant amounts of Mo can be transported in water vapour, particularly if fH_2O is high. The solubility of MoO_3 is ~ 20 orders of magnitude higher than that predicted from volatility data.	Rempel *et al.,* (2006)
Solubility experiments of Mo in fluids of different starting compositions **(S)**	S-free: MoO_3 - H_2O MoO_3 - KCl - H_2O Mo - KCl - H_2O pH= Kfsp–mus–qtz	NNO, MH and RRO	500-800	1.5-3.0	NA	Mo solubility in MVP increases steadily with increased temperature. Mo is readily soluble in MVPs of variable salinities even with low Cl. Mo may be soluble as Cl complexes, ion pairs or as molybdic acid as salinity decreases.	Ulrich and Mavrogenes (2008)
Partitioning of Mo^{6+} between aqueous liquid and Vapour **(TA)**	NaCl – H_2O – MoO_3 and MoO_3- NH_3 - H_2O pH 4-4.7 Sulphur-free system	<FMQ-2	300–370	0.085 - 0.192	0.006 – 3.4	Mo increases in vapour relative to liquid with increase pressure and temperature. In porphyry systems, a significant amount of Mo fractionates into the vapour over the liquid, especially if the pH of the liquid is below the muscovite–microcline reaction boundary.	Rempel *et al.,* (2009)
Solubility experiments of molybdenite in NaCl ±HCl-bearing aqueous fluids **(S)**	2-20 wt.% NaCl + H_20 1–3 mg MoS_2 Varied log fS_2 -4.0 to 0.4	MPP, CCO, NNO	600-800	2.0	NA	Mo concentrations range from 20 to 3000 ppm in synthetic fluid inclusions and increase with increasing temperature, salinity and oxygen fugacity, but decrease with increasing sulphur fugacity.	Zhang *et al.,* (2012)

Notes: Shaded blocks represent key variables explored in each study. D_{Mo} = range of vapour/brine Mo partition coefficients reported. Experiments were given run times believed to be long sufficient to attain equilibrium or to allow time for fracture healing in synthetic fluid inclusion experiments. Experimental methods: (H) = Hydrothermal experiments in cold seal vessels. (D) = Dry experiments. (TA) = Titanium autoclave experiments. (CA) = Chrome/gold autoclave experiments. (S) = Synthetic fluid inclusion analysis with LA-ICP-MS. Redox buffers used: NNO = Nickel-Nickel Oxide, FMQ = Fayalite-Magnetite+Quartz, GM = Graphite-Methane, MNO = Manganese-Manganese Oxide, MH = Magnetite-Hematite, RRO = Rhenium-Rhenium Oxide, CCO = Cobalt-Cobalt Oxide, MPP = magnetite–pyrrhotite–pyrite triple point.

The effects of fluid Cl concentrations on Mo partitioning are highly contested (Table 2.2). Khitarov *et al.* (1982) found consistent $D_{Mo}^{fluid/melt}$ values of 0.06 for solutions containing 0.1–1 *m*NaCl at 700°C and 2 kbar. Later experiments conducted at 0.1 kbar and 750°C (with both NNO and FMQ buffers) also yielded far higher yet relatively constant $D_{Mo}^{fluid/melt}$ values of 2.5 ±1.5 for fluids containing 0-4.5 *m*Cl (Candela and Holland, 1984). By contrast, $D_{Mo}^{fluid/melt}$ values of 8 to 80 have been reported in experiments at >800°C using high salinity NaCl brines (Webster, 1997). In addition, solubility studies at 750-800°C and 1-2 kbar conducted by Bai and Koster van Groos (1999) demonstrated that $D_{Mo}^{fluid/melt}$ values increase from 0.2 to 5 in solutions containing 0.0-2.7 *m*HCl. This suggests that Mo partitioning may be favoured in Cl-rich fluids, but only under acidic conditions. Despite this, Keppler and Wyllie (1991) showed that increasing HCl concentrations can actually decrease $D_{Mo}^{fluid/melt}$ values from 5.5 to 0.75 at a similar temperature of 750°C and lower pressure (0.2 kbar). This behaviour is consistent with LA-ICP-MS analysis of coexisting melt and fluid inclusions in a number of granitic intrusions (Rito del Medio, New Mexico; Mt. Malosa, Malawi; Ehrenfriedersdorf, Germany; Cuasso al Monte and Baveno, Italy: Zajacz *et al.,* 2008). This study revealed an apparent decrease in $D_{Mo}^{fluid/melt}$ values with increasing inclusion salinity, suggesting that Mo partitioning is independent of Cl and that Mo forms non-chloride (e.g., hydroxyl) complexes in exsolving fluids.

Sulphur appears to have a limited effect on the partitioning behaviour of Mo (e.g. Tingle and Fenn, 1984). This is surprising, considering that it is interpreted to complex with sulphur in oxidised magmas (e.g. Farges *et al*., 2006b). The presence of CO_2 in fluids also appears to have a relatively limited effect on Mo solubility (e.g. Bai and Koster van Groos, 1999; Pokrovski *et al*., 2008). However, Bai and Koster van Groos (1999) stated that Mo partitioning is consistently high in fluids with high $(Na,K)_2CO_3$ concentrations. This, and the presence of CO_2 in fluid inclusions in Mo-rich systems (Candela; 1997; Rusk *et al*., 2008), suggests that Mo-carbonate complexes may further contribute to the partitioning and hydrothermal transport of Mo.

As key volatile components are shown to have little effect on Mo fluid-melt partitioning, it has been suggested that Mo is predominantly transported by hydroxyl complexing (e.g. Candela and Holland, 1984) and therefore its partitioning may be closely controlled by fH_2O

(e.g. Rempel *et al.,* 2006; Ulrich and Mavrogenes, 2008), or total mass proportions of exsolving fluids (Williams-Jones and Heinrich, 2005). This is in accordance with solubility studies that show a general increase in $D_{Mo}^{fluid/melt}$ values with increasing temperature and pressure (Khitarov *et al*., 1982; Webster, 1997; Bai and Koster van Groos, 1999). For example $D_{Mo}^{fluid/melt}$ values calculated at 860°C and 0.55 kbar for coexisting silicate melt and saline fluids increased tenfold as temperature and pressure were increased to 1075°C and 2.0 kbar (Webster, 1997). Increased fH_2O may explain the higher $D_{Mo}^{fluid/melt}$ values recorded in deeply formed natural systems (e.g. Audétat, 2010).

The effects of fO_2 on the partitioning behaviour of Mo have not been studied in great detail (Table 2.2). However, $D_{Mo}^{fluid/melt}$ values are very low in the relatively oxidised natural and experimental systems studied (Tingle and Fenn, 1984; Audétat and Pettke, 2003; Zajacz *et al.,* 2008). This is attributed to the speciation as more melt-soluble Mo^{6+}, which delays Mo partitioning into magmatic volatiles (Candela and Holland, 1984). This may result in the late exsolution of Mo-rich fluids during the final stages of magma fractionation, but may also result in the failed partitioning of Mo in the most oxidised systems. This could explain the strong association of Mo with moderately oxidised systems (Figure 2.2).

2.4.3 Cu Fluid-Melt Partitioning

Similar to Mo, Cu is soluble in fluids of variable composition (Table 2.2), but generally displays higher $D^{fluid/melt}$ values than Mo in both experimental (e.g. Candela and Holland, 1984, 1986; Webster 1997; Bai and Koster van Groos, 1999) and natural systems (e.g. Audétat and Pettke, 2003; Audétat, 2010). For example, $D_{Cu}^{fluid/melt}$ values derived from coexisting melt and fluid inclusions at Cave Peak, Texas, are an order of magnitude greater than $D_{Mo}^{fluid/melt}$, indicating that Cu is more mobile, even in porphyry Mo systems (Audétat, 2010). Unlike Mo, $D_{Cu}^{fluid/melt}$ values are relatively constant with changes in temperature (e.g. Khitarov *et al*., 1982). In addition, Bai and Koster van Groos (1999) suggested that increasing pressure may inhibit Cu partitioning by enhancing its solubility in residual melts. Given this, it is likely that decreasing pressure may enhance Cu partitioning relative to Mo.

The role of CO_2 in Cu partitioning remains unclear. Although Cu is interpreted to be stable in carbonic solvents (Pokrovski *et al*., 2008), experimental studies have shown that Cu

partitioning is independent of fluid $(Na,K)_2CO_3$ concentrations (Khitarov *et al*., 1982). Cu partitioning also appears to be independent of fluid and melt fluorine concentrations (Candela and Holand 1984; Keppler and Wyllie, 1991; Bai and Koster van Groos, 1999).

The effects of sulphur concentration on Cu partitioning remain highly contested. Sulphide has been interpreted as a potential ligand in enhancing Cu partitioning into hydrothermal fluids (Mountain and Seward, 2003; Seo *et al*., 2009). Experimental studies by Simon *et al.,* (2006) showed that partitioning of Cu increased by a factor of 2 to 5 in favour of the fluid phase in the presence of dissolved sulphur. HS^- is interpreted to complex with Cu^+ under reduced, near-neutral to alkaline conditions with high total S concentrations (Shea and Helz 1988; Thompson and Helz 1994; Mountain and Seward, 2003). This may lead to the early extraction of Cu in reduced systems before it is significantly concentrated in the residual melt phase. However, in oxidised and acidic fluids, Cu is unlikely to complex with S because it will be present as H_2S and SO_2 (Giggenbach, 1987). Furthermore, thermodynamic studies indicate that Cu partitioning may be favoured by increasing fO_2 in both S-free, Cl-bearing and S-rich fluids (Candela and Holland, 1984; Candela, 1992). These results raise doubts concerning the importance of sulphide as a control on $D_{Cu}^{fluid/melt}$ values in highly oxidised Cu-porphyry systems (Figure 2.2).

The role of Cl also remains unclear. Recent, LA-ICP-MS data for natural coexisting melt and fluid inclusions in several granitic systems reveal highly variable $D_{Cu}^{fluid/melt}$ values that are commonly highest for vapour-like fluids with low chlorinities (Zajacz *et al.,* 2008). In contrast, a number of previous experimental studies showed that fluid Cl concentrations greatly enhance Cu partitioning into hydrothermal fluids (Table 2.2; Candela and Holland, 1984; Pokrovski *et al.,* 2005; Simon *et al*., 2006). For example, cold seal experiments at 0.1 kbar and 750°C (with both NNO and FMQ buffers) yielded a $D_{Cu}^{fluid/melt}$ value of 9.1 ±2.5 for fluids containing 4.5 moles/kg Cl (Candela and Holland, 1984), whereas fluids with Cl concentrations of 0.5 moles/kg Cl had far lower $D_{Cu}^{fluid/melt}$ of ~1.5. This therefore suggests that, Cu partitioning is enhanced where magmas evolve to higher Cl/H_2O ratios (e.g. Candela, 1992, 2007; Simon *et al*., 2006).

2.4.4 Mo Vapour-Brine Partitioning

Proton-induced-X-ray-emission (PIXE) and LA-ICP-MS analyses of co-existing vapour and brine fluid inclusions (boiling assemblages) have been used to calculate the $D_{Mo}^{vapour/brine}$ values during fluid separation in natural systems. These include studies at two porphyry Cu–Mo deposit (Bingham Canyon, Utah: Seo *et al.,* 2009; and Questa, New Mexico: Klemm *et al*., 2008), three porphyry Cu-Au deposits (Grasberg, Indonesia: Ulrich *et al*., 1999; Batu Hijau, Indonesia: Ryan *et al*., 2001.; and Bajo de la Alumbrera, Argentina: Seo *et al.,* 2009), two granite-related Sn–W vein deposits (Zinnwald, Germany: Heinrich *et al.*, 1999; and the Yankee Lode deposit, Mole Granite, Australia: Heinrich *et al*., 1992; Audétat *et al.,* 2000), a barren granitic intrusion (Rito del Medio: Audétat and Pettke, 2003) and a Pb-Zn skarn deposit (Bismark, Mexico: Baker *et al*., 2004). These studies reveal that vapour inclusions typically contain higher proportions of S, CO_2, Cu and Cs, whereas brine inclusions are richer in Na, Cl, K, Fe, Mn, Zn, Pb, and most of the heavy elements, including Mo (Heinrich *et al*., 1999, 2003; Ulrich *et al*., 1999; Wilkinson *et al*., 2009).

Results show that Mo is predominantly concentrated in high salinity brine inclusions (typically >25 wt.% $NaCl_{eq}$). Highest Mo concentrations are recorded for brine inclusions at Bingham Canyon, which are interpreted to have formed by the phase separation of a single-phase magmatic-hydrothermal fluid with a bulk salinity of approximately 7 wt.% $NaCl_{eq}$ (Landtwing *et al*., 2005; Pettke *et al.,* 2010). At Questa, boiling assemblages yield a $D_{Mo}^{vapour/brine}$ value of 0.32 and brine Mo/Cu ratios of 0.01 (Klemm *et al.,* 2008) where vapour-brine separation is interpreted to have occurred on decompression to ~0.3 kbar, and cooling to ~420°C. Even lower $D_{Mo}^{vapour/brine}$ values of 0.10 and ~0.08 are recorded for the Grasberg Cu-Au deposit, Indonesia (Ulrich *et al*., 1999) and for the Rito del Medio, barren pluton (Audétat and Pettke, 2003).

Although Mo appears to be preferentially transported by high salinity fluids, experimental studies have shown that, under high fluid pressure, vapour can also uptake significant amounts of Mo (Williams-Jones and Heinrich, 2005; Rempel *et al*., 2006). In addition, the ability of vapour to transport greater absolute quantities of metals may also occur as a function of the high ratio of vapour to brine inferred in many melt–vapour–brine systems

(cf. Candela and Piccoli, 1995; Williams-Jones and Heinrich, 2005; Simon *et al*., 2006; Rempel *et al*., 2006, 2009).

The potential importance of the vapour phase has been highlighted in a recent experimental study (Rempel *et al.,* 2006). Here it was theorised that a 5 million tonnes per annum flux of water vapour containing as little as 0.5 ppm Mo will transport approximately 2.5 tonnes of Mo each year. If such flow is sustained for 115,000 years (a realistic lifespan for a porphyry-hydrothermal system: c.f. von Quadt *et al*., 2011), and if Mo is trapped without significant loss (i.e. to the atmosphere), it could theoretically produce a porphyry Mo deposit with a similar grade and tonnage to Endako, British Columbia (336 Mt at 0.087% Mo). This is supported by recent fluid analysis at Bingham Canyon, where Mo concentrations in vapour and brines and mass balance calculations indicate that vapour may have transported 70% of the Mo and sulphur (Seo *et al*., 2012).

Therefore the relative volume and mass proportions of vapours and brines need to be constrained when assessing the most important phases with respect to metal transport and deposition in a two-phase fluid system. To date, few natural fluid inclusion studies have taken this into account. Furthermore, few studies have assessed whether significant metal deposition occurs prior to vapour-brine partitioning.

2.4.5 Cu Vapour-Brine Partitioning

The partitioning behaviour of Cu during phase separation is disputed. Analysis of boiling trails at Rito del Medio, Bingham Canyon and Bajo de la Alumbrera revealed that S and Cu are enriched in vapour inclusions relative to coexisting brines (Seo *et al.,* 2009). $D_{Cu}^{vapour/brine}$ values are particularly high in reduced systems, such as the Yankee Lode deposit, where average Cu concentrations in vapour-rich inclusions are 4300 ppm compared to only 250 ppm in high salinity brine inclusions (Heinrich *et al*., 1992; Audétat *et al*., 1998; Seo *et al*., 2009). If the brine was in equilibrium with the vapour at the time of trapping, the data yield $D_{Cu}^{vapour/brine}$ values of ~17. This is in close accordance with vapour and brine fluid inclusions in the Batu Hijau Cu-Au deposit, which contain 2.5 and 0.15 wt% Cu, respectively, yielding a calculated $D_{Cu}^{vapour/brine}$ value of approximately 17 (Ryan *et al*., 2001). Fluid inclusions from

high grade Cu-Au ore zones at Bajo de la Alumbrera and Grasberg yield lower $D_{Cu}^{vapour/brine}$ values of approximately 4 (Heinrich *et al*., 1999; Ulrich *et al*., 1999). A $D_{Cu}^{vapour/brine}$ value of approximately 4 was also obtained for co-existing vapour and brine inclusions from the Bismark Pb-Zn skarn (Baker *et al*., 2004).

Hydrothermal experiments exploring partitioning of Cu between saline liquids and vapour also showed that Cu partitioning into vapour is enhanced in sulphur-rich systems (Simon *et al*., 2006; Pokrovski *et al*., 2008; Frank *et al*., 2011), particularly where fluids are reduced (Figure 2.2). William-Jones and Heinrich (2005) also suggested that, similar to Mo, Cu solubility in vapour is a function of water fugacity. These results, combined with high Cu contents in vapour inclusions in numerous porphyry systems (e.g. Henley and McNabb, 1978; Audétat *et al*., 2000; Pokrovski *et al*., 2005, 2008; Williams-Jones and Heinrich, 2005; Simon *et al*., 2006; Murakami *et al*., 2010), led to the popular conclusion that reduced HS^- in vapours enhances Cu partitioning by the formation of volatile sulphur species (Cu^+HS^-) (Heinrich *et al.,* 1999; Mountain and Seward, 1999, 2003; Simon *et al*., 2006; Pokrovski *et al*., 2008; Seo *et al*., 2009; Landtwing *et al*., 2010).

Due to the apparent favourable partitioning of Cu over Mo into S-rich vapours, fluid phase separation has been adopted as a popular explanation for the decoupling of Mo and Cu in porphyry systems (e.g. Heinrich *et al*., 1999; Ulrich *et al*., 1999; Rusk *et al*., 2004, 2008; Landtwing *et al*., 2010). This included studies at El Teniente, where it was concluded that a substantial amount of Cu was transported by low salinity vapours (Klemm *et al*., 2007; Vry, 2010). However, with the exception of Nagaseki and Hayashi (2008), no experimental studies have managed to recreate $D_{Cu}^{vapour/brine}$ values >1 (Williams *et al.,* 1995; Simon *et al*., 2006; Pokrovski *et al*., 2008; Frank *et al*., 2011). For example, Williams *et al.,* (1995) obtained extremely low $D_{Cu}^{vapour/brine}$ values of 0.005 at 50 MPa and 850°C and 0.008 at 100 MPa and 800°C indicating strong brine partitioning of Cu. These results therefore suggest that Cu may preferentially partition into brines during fluid boiling.

The discrepancy in naturally and experimentally derived $D_{Cu}^{vapour/brine}$ values led to the suggestion that high Cu concentrations in vapour inclusions may be an artefact of post-entrapment modification (Figure 2.7: Lerchbaumer and Audétat, 2012). Recent studies have

shown that quartz-hosted fluid inclusions can be affected by Cu^+ diffusion (Zajacz *et al*., 2009; Lerchbaumer and Audétat, 2012; Seo and Heinrich, 2013). The mass balance of fluid inclusions is maintained via the loss of H^+, which readily diffuses outwards through diffusion channels in quartz. Reequilibration experiments of synthesised coexisting vapour and brine inclusions in quartz revealed that post-modification Cu diffusion is strongly controlled by the sulphur content of inclusions (Lerchbaumer and Audétat, 2012). This allows inwardly diffusing Cu to be precipitated as chalcopyrite ($CuFeS_2$) which in turn produces more H^+ that diffuses out. This process is interpreted to continue until the system reaches chemical equilibrium, explaining the 1:2 molar ratios of Cu and S recorded in natural quartz-hosted inclusion (Seo *et al*., 2009). As vapour inclusions contain high concentrations of H_2S, they are interpreted to be more prone to this effect. This is supported by a recent study of vapour inclusions hosted in topaz which yielded lower average Cu concentrations than apparently cogenetic inclusions in quartz, potentially due to its smaller diffusion channels (Seo and Heinrich, 2013). These results indicate that the reasons for Cu-Mo decoupling need to be readdressed at El Teniente and in other porphyry Cu-Mo systems.

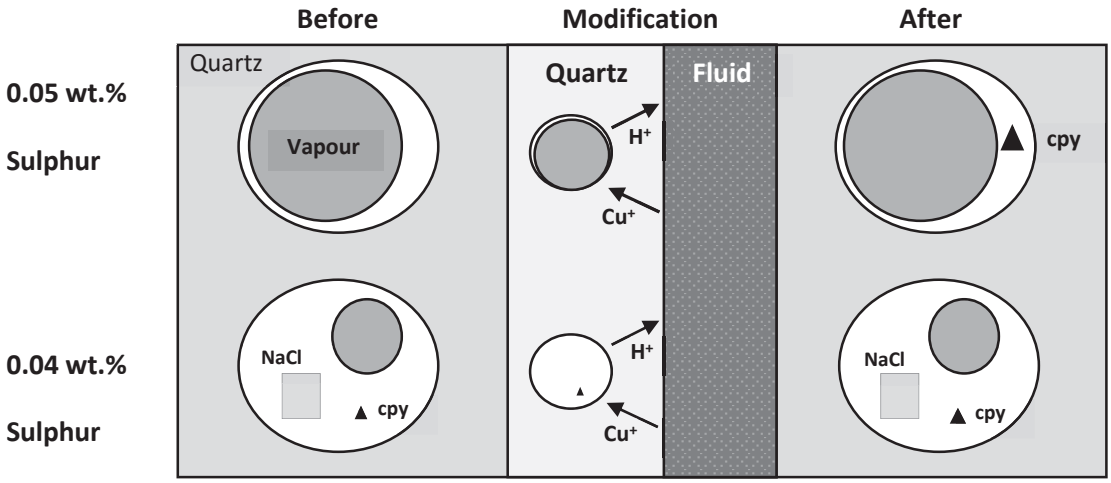


Figure 2.7: Schematic sketch showing the post-entrapment modification of Cu^+ and H^+ concentrations in low density vapour and brine inclusions. Diffusion relies on a gradient in fluid acidity which balances inward Cu+ diffusion. Incoming Cu is precipitated as chalcopyrite leading to net Cu gain. Due to the high initial H_2S concentrations of vapour inclusions relative to brine inclusions, these can acquire far larger quantities of Cu. After Lerchbaumer and Audétat (2012).

2.4.3 Mo Speciation in Hydrothermal Fluids

Although fluid composition appears to have a limited effect on $D_{Mo}^{fluid/melt}$ values, several experimental studies have shown that it can affect Mo solubility (Table 2.3). This has led to ongoing debate over the likely speciation of Mo in porphyry ore fluids. Mo solubility has been determined in a number of hydrothermal cold-seal experiments (Ivanova *et al*., 1975; Ryabchikov *et al*., 1981; Kudrin, 1985; Wood *et al*., 1987; Cao, 1989; Gu, 1993). These showed that Mo is readily soluble in the form of Mo, MoO_2, MoO_3 and MoS_2 in fluids with a broad range of compositions (Table 2.3).

The proposed partitioning of Mo from melts into $(Na,K)_2CO_3$-rich fluids led to the proposal that $Mo(HCO_3)_6^{2-}$ type complexes may be important for Mo transport (Bai and Koster van Groos, 1999). However, solubility studies conducted between 200 and 350°C indicate that Mo solubility is not greatly affected by CO_2 concentrations at these lower temperatures (Kudrin, 1989). Concentrations of up to 7 wt.% Mo have been documented in S-free, NaOH-bearing fluids (Ivanova *et al*., 1975), whereas Mo solubility appears to be significantly lower in sulphur-bearing, multicomponent experiments (Wood *et al*., 1987; Cao, 1989; Gu, 1993). As a result, it has been suggested that sulphur limits hydrothermal Mo mobility through the saturation of molybdenite (Bingen and Stein, 2003). The poor solubility of Mo in sulphur-bearing systems may also explain the low $D_{Mo}^{vapour/brine}$ values recorded in natural systems where sulphur preferentially partitions into the vapour phase (e.g. Heinrich *et al*., 1999).

The high Mo concentrations recorded in Cl- and S-free fluids suggests that Mo does not strongly complex with Cl^- and HS^- at temperatures of up to 450°C (e.g. Ivanova *et al*., 1975; Cao, 1989; Kudrin, 1989). Consequently, molybdic acid species such as $MoO_3.2H_2O$ and H_2MoO_4 may be the most important in oxidised hydrothermal fluids and low density vapours (Ivanova *et al*., 1975; Candela and Holland, 1984; Keppler and Wyllie, 1991; Rempel *et al*., 2006, 2009). Mo speciation has now been characterised using synchrotron-based X-ray absorption near-edge structure (XANES) spectroscopy (Ulrich and Mavrogenes, 2008; Table 2.3). Synthetic fluid inclusions synthesised in oxidised, S-free, MoO_3-H_2O experiments reveal distinct spectral peaks indicative of three or four Mo=O bonds. This provides strong evidence that Mo occurs in tetrahedral coordination, possibly as H_2MoO_4 as suggested by experimental predictions (e.g. Rempel *et al.,* 2006; Table 2.3). This speciation may explain

the strong association of Mo with fluids that have high fH_2O and low Cl/H_2O ratios (e.g. Bai and Koster van Groos, 1999; Ulrich and Mavrogenes 2008).

Recent experimental studies also show that the metal-transporting capacity of vapour also increases exponentially with increased water fugacity (fH_2O) within a P-T range of 300-360°C and 39-154 bars and with fO_2 buffered by MH (Rempel *et al*., 2006). This was previously interpreted to be due to the hydration of metal-ligand complexes to form gaseous species of the type $MeL.nH_2O$ (Williams-Jones and Heinrich, 2005). However, a more recent speciation study showed that vapour–liquid fractionation occurs between neutral species (Rempel *et al*., 2009). Given this it is theorised that vapours may also transport significant amounts of Mo as gaseous H_2MoO_4 (e.g. Ulrich and Mavrogenes, 2008), particularly in high temperature, oxidised fluids with high fH_2O (Rempel *et al*., 2009).

Although H_2MoO_4 is inferred to be a key dissolved species of Mo in low salinity fluids (Rempel *et al*., 2006, 2009; Ulrich and Mavrogenes, 2008), Mo solubility studies reveal a strong positive correlation with salinity in aqueous solutions containing 0.03 to 5 molal NaCl (Cao, 1989; Kudrin, 1989). This was interpreted to be due to the enhanced solubilities of ion pairs, including $KHMoO_4$, Na_2MoO_4 and K_2MoO_4, which may be the dominant Mo species in saline solutions at temperatures of 300 to 450°C (e.g. Cao, 1989). Alternatively Mo may be dissolved as species such as $NaHMoO_2S_2$ in S-rich fluids that have higher alkalinity and pH (Zhang *et al*., 2012). In accordance with these studies, a recent study of Mo in synthetic fluid inclusions formed between 500-800°C and 1.5-3.0 kbar (Table 2.3) revealed that Mo solubility increases from 0.8 wt.% in pure H_2O solution to 1.6 wt.% in KCl-bearing aqueous solutions (Ulrich and Mavrogenes, 2008). Based on the near 1:1 ratio of Mo and K it was suggested that the solubility of Mo was driven by reaction 1:

$$MoO_2\,(s) + KCl + 2H_2O \leftrightarrows KHMoO_4\,(aq) + HCl + 2H_2 \qquad (1)$$

In higher salinity (>20 wt.% KCl) fluids Mo solubility appears to be enhanced by the formation of dissolved Mo-oxo-chloride complexes (Ulrich and Mavrogenes, 2008). This is consistent with previous XANES analyses on the structure of Mo^{6+} in HCl solutions, which indicate the formation of MoO_2Cl^+, MoO_2Cl_2, or $MoO_2Cl_3^-$, depending on the number of Cl atoms surrounding the MoO_2^{2+} structure (Yokoi *et al*., 1993). In high salinity fluids the

formation of Mo-oxo-chloride complexes from dissolved ion pairs can be expressed by the following speciation equilibrium:

$$KHMoO_4\,(aq) + KCl + H_2O \leftrightarrows MoO_2Cl^+(aq) + 2K^+ + 3OH^- \qquad (2)$$

The formation of these species suggests that salinity may strongly control the amount of Mo that is dissolved in hydrothermal fluids. This may explain the presence of high Mo concentrations in natural brine inclusions and the low $D_{Mo}^{vapour/brine}$ values recorded in natural coexisting vapour and brine inclusions (e.g. Audétat and Pettke, 2003; Seo *et al*., 2009).

2.4.7 Cu Speciation in Hydrothermal Fluids

A number of volatile ligands have been suggested as potential Cu-complexing agents in hydrothermal fluids. XRF mapping and XANES analysis suggests that Cu can be volatilised as simple hydroxyl complexes (Mavrogenes *et al*., 2002), consistent with solubility experiments in S- and Cl-free systems (e.g. Bai and Koster van Groos, 1999). Mavrogenes *et al.,* (2002) proposed the formation of $[CuCl(H_2O)]$ in low temperature, Cl-bearing fluids (25°C) and $[Cu(H_2O)_6]^{2+}$ in vapours with high fH_2O. Cu is also interpreted to complex with HS^-, particularly in high temperature, reduced, alkaline, sulphur-rich vapours (Heinrich *et al.,* 1999; Mountain and Seward, 1999, 2003; Simon *et al*., 2006; Pokrovski *et al*., 2008; Seo *et al*., 2009; Landtwing *et al*., 2010). For example, Mountain and Seward (2003) suggested that formation of the linear $[Cu(HS)_2]^-$ complex may be an important speciation of Cu under typical porphyry P-T conditions. However, the transport of Cu in vapours is a contentious issue and the complexation of Cu with HS^- is yet to be confirmed by speciation studies using modern techniques.

Although these species are thermodynamically possible, the strong control of Cl^- on Cu partitioning and solubility suggests that Cu may be dissolved primarily as alkali chloride complexes (Candela and Holland, 1984, 1986; Bai and Koster van Groos, 1999; Archibald *et al*., 2002; Hack and Mavrogenes, 2006; Simon *et al*., 2006) such as $CuCl^0$ and $[CuCl_2]^-$. This is supported by numerous solubility and spectroscopic experiments, mostly completed at

temperatures below 400°C (e.g. Hemley *et al*., 1992; Seyfried and Ding, 1993; Liu *et al*., 2002; Archibald *et al*., 2002).

Recent X-ray absorption near-edge structure (XANES) spectroscopy analyses of Cu speciation confirms that solubility is strongly enhanced by the formation of metal–Cl complexes in brine inclusions synthesised between 200 and 700°C (Berry *et al*., 2006, 2009). In these experiments, Cu was interpreted to be predominantly dissolved as $[CuCl_2]^-$ or potentially as $CuCl_2H$ complexes in KCl-bearing solutions. X-ray fluorescence elemental maps also provide circumstantial evidence for the complexation of Cu as $[CuCl_4]^{3-}$ as previously proposed in experimental studies by Liu *et al.,* (2002) at lower temperatures. However, such highly charged Cu is considered unlikely in "supercritical" fluids due to the decrease in the dielectric constant of water with increasing temperature (Seward and Barnes, 1997; Mavrogenes *et al*., 2002). As a result, this speciation has been retracted as erroneous (Brugger *et al*., 2007). Despite this, the formation of other species, including H_3CuCl_4 (Hack and Mavrogenes, 2006), cannot be completely discounted.

2.5 Ore Mineral Precipitation

Ore deposition in porphyry systems is interpreted to occur due to changes in the physicochemical characteristics of magmatic-hydrothermal fluids as they migrate away from their magmatic source into surrounding host rock (Heinrich *et al*., 1999; Redmond *et al*., 2004; Harris *et al*., 2003; 2005; Landtwing *et al*., 2005; Sillitoe, 2010). These fluids alter the surrounding rock leading to characteristic shells of alteration and mineralisation (Figure 2.8). In order to form ore deposits, the fluids must be channelled through relatively small volumes of rock where metal precipitation occurs without too much dispersion (Wilkinson, 2013). In all porphyry deposit types mineralisation in porphyry systems typically occurs in stockwork veins and breccia cement with minor ore hosted as disseminated sulphides (Lowell and Guilbert, 1970; Sillitoe, 1973, 2010).

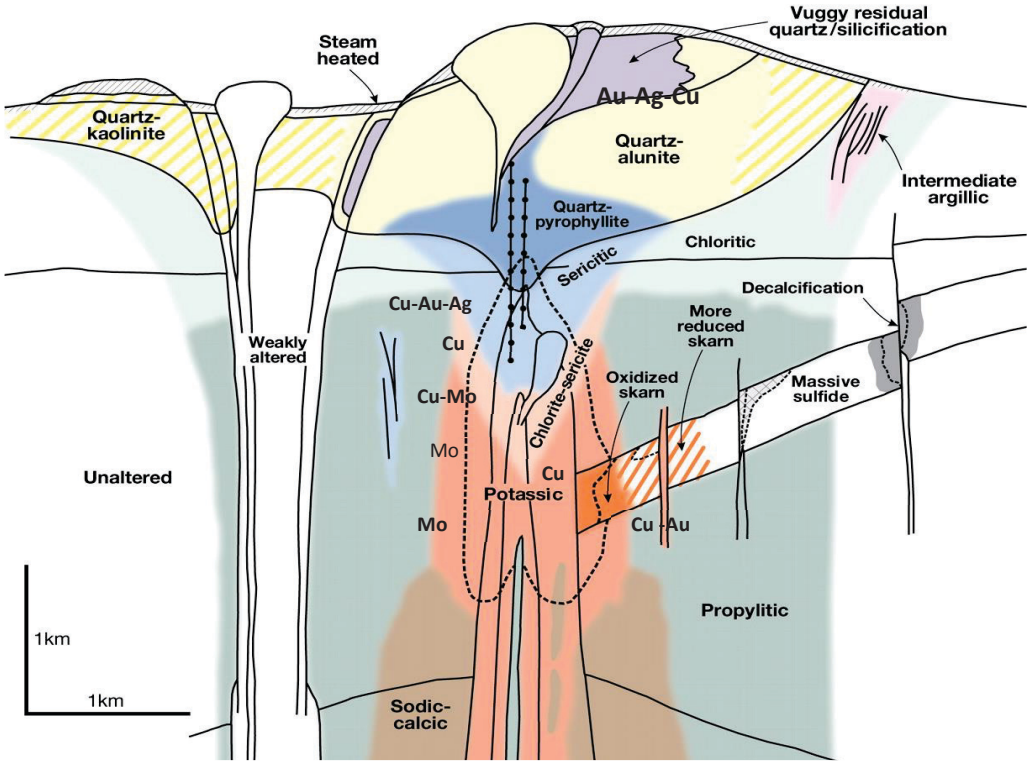


Figure 2.8: Schematic diagram showing the generalised alteration and mineralisation zonation in a telescoped porphyry Cu-Mo system. Shallow alteration-mineralisation types typically overprint deeper ones. The volumes of altered rocks and the morphology of alteration halos may vary significantly between deposits. Alteration associated with the lithocap and supergene enrichment zones is highly complex. Molybdenite mineralisation is typically found at the boundary of the potassic and sericitic alteration zones. Cu-sulphides typically occur outboard of molybdenite, but can also occur within the potassic zone. From Sillitoe (2010).

The mineralisation potential of porphyry deposits may be partly controlled by lithology. Many porphyry deposits are hosted within reduced shales and mafic intrusion complexes, suggesting that ferrous Fe-rich rocks can be important chemical traps for the precipitation of Cu and Mo (e.g. Sillitoe, 2010; Richards, 2013). For example, it has been suggested that 80% of the mineralisation at El Teniente is hosted by basaltic-andesite country rocks (Skewes *et al*., 2002; Cannell *et al*., 2005; Rabbia *et al*., 2009). This is also the case at the giant Resolution porphyry Cu-Mo deposit in Arizona, where high-grade mineralisation is predominantly hosted by a doleritic sill complex (Manske and Paul, 2002). Tholeiitic basalt also hosts some of the highest metal concentrations within the Oyu Tolgoi district, Mongolia (Kirwin *et al*., 2005; Sillitoe, 2010). Host rock permeability may also affect the ore grades of porphyry systems. For example, the formation of the Grasberg Cu-Au deposit may in part be attributed to its emplacement into impermeable limestones, which limited metal dispersion (Wilkinson, 2013). The precipitation of metal sulphides within a confined rock volume may also be facilitated by the redissolution of pre-existing quartz vein networks as a function of retrograde quartz solubility by cooling, depressurising hydrothermal fluids (Fournier, 1999; Landtwing *et al.,* 2005).

The mineralisation potential of porphyries may also rely on the presence of long-lived magmatic systems. Increased ore grades may result from episodic intrusion, brecciation and mineralisation events that create zones of intense overlapping mineralisation (e.g. Vry *et al*., 2010). This can lead to the formation of ore shells with concentrations of up to 3000 ppm Mo and several wt.% Cu (e.g. Westra and Keith, 1981). However, tectonic perturbations may disrupt potentially long-lived magmatic plumbing systems resulting in the relocation of magma conduits and thereby limiting the extent of superimposed mineralisation (Loucks, 2014).

Recent LA-ICP-MS analyses of fluid inclusions in porphyry systems indicate that fluids contain sub-equal proportions of sulphur and chalcophile elements, including Mo, Cu and Fe (Seo *et al*., 2009). This suggests that competition for sulphur may play a significant role in the decoupled precipitation of Mo and Cu (e.g. Heinrich, 2007; Ulrich and Mavrogenes, 2008). Recent fluid inclusion studies have demonstrated that a variety of physical and chemical parameters may affect the solubility of Mo and Cu leading to their selective

precipitation. (e.g. Klemm *et al.*, 2008; Vry, 2010; Seo *et al*., 2012). Such processes include rapid drops in pressure and temperature (e.g. Ulrich and Mavrogenes, 2008), changes in pH and fO_2 due to cooling and fluid-wallrock interactions (e.g. Hedenquist and Richards, 1998; Seo *et al*., 2012), and mixing of fluids with groundwater e.g. Lowell and Guilbert, 1970). Fluid phase separation has also been proposed as a possible mechanism for metal deposition (e.g. Burnham and Ohmoto, 1980) via the destabilisation of metal-sulphide complexes as a result of the loss of acidic volatile species. These processes may be coupled with quartz redissolution, which creates free accommodation space for metal-sulphide deposition (Landtwing *et al*., 2005).

2.5.1 Mo Deposition

Molybdenite is by far the most important Mo-bearing ore mineral with only minor amounts of wulfenite ($PbMoO_4$), powellite ($CaMoO_4$) and molybdite (MoO_3) reported in porphyry systems. In molybdenite, Mo is present as Mo^{4+} whereas Mo^{6+} is the predominate cation in silicate melts (e.g. $[MoO_4]^{2-}$: Farges *et al*., 2006a, 2006b), and most aqueous species likely to be present in oxidised porphyry systems, including H_2MoO_4, MoO_2Cl_2 (Ulrich and Mavrogenes, 2008), and $MoO_3.H_2O$ (Candela and Holland, 1984; Rempel *et al*., 2009). This combined with the deposition of sulphur as sulphides suggests that reduction must play an important role in the deposition of Mo in porphyry systems. This is supported by solubility experiments between 200-700°C which reveal a strong linear relationship between Mo solubility and fO_2 at constant pH (Kudrin, 1985; Cao, 1989; Ulrich and Mavrogenes, 2008). Decreasing fO_2 may occur in porphyry systems as a function of the early deposition of Fe^{3+}-bearing oxide minerals, and interactions with more reduced wall rocks,

When pH was varied at constant fO_2, reveal that minimum Mo solubility occurred at pH values of 3 to 4 (at 450°C) and pH 2 (at 350°C), whereas Mo solubility increased at higher alkalinity (Kudrin, 1985). This suggests that dissociation of acids will drive Mo towards saturation. Cooling may also result in the disproportionation of dissolved magmatic sulphur dioxide (e.g. Giggenbach, 1992; Rye, 1993; Heinrich *et al*., 2004). This will increase fS^{2-} within the fluid, again favouring molybdenite saturation (e.g. Tingle and Fenn, 1984; Gu, 1993; Vigneresse, 2007). This may explain the precipitation of Mo over relatively narrow temperature ranges (360-440°C) associated with the transition from potassic to early

sericitic alteration in several porphyry systems (e.g. El Teniente: Vry *et al*., 2010; Questa: Klemm *et al*., 2008; Bingham Canyon, Utah: Landtwing *et al*., 2005; Endako, British Colombia: Selby *et al*., 2000). It is also likely to explain the strongly temperature-dependant solubility of Mo, MoO_2, MoO_3 and MoS_2 in saline fluids and vapours in experimental S-bearing systems (e.g. Ivanova *et al*., 1975; Cao, 1989; Ulrich and Mavrogenes, 2008; Rempel *et al*., 2009: Table 2.3).

Pressure also displays a strong positive linear relationship with the solubility of molybdenite between 1 bar and 3.0 kbar (e.g. Wood *et al*., 1987; Cao, 1989). This was attributed to the enhanced solubility of H_2MoO_4 at high fH_2O (Ulrich and Mavrogenes, 2008). This suggests that drops in pressure could also result in molybdenite saturation and mineralisation. For example, at Butte, Montana, molybdenite is inferred to precipitate in response to a pressure drop from near-lithostatic to near-hydrostatic conditions (Rusk and Reed, 2002; Rusk *et al*., 2008; Reed *et al*., 2013). Drops in pressure are also interpreted to be important in the formation of sulphide-dominated veins at El Teniente (Cannell *et al*., 2005). Given this, the formation of molybdenite-dominated veins in porphyry systems may result from sudden switches from lithostatic to hydrostatic pressure regimes.

Based on uncertainty regarding the speciation of Mo in hydrothermal fluids, Seo *et al.,* (2012) proposed several reductive reactions for the deposition of molybdenite from different oxy, hydroxyl and oxy-chloride complexes:

Deposition from aqueous fluids and vapours

$$MoO_3(aq) + H_2(aq) + 2H_2S(aq) \rightarrow MoS_2 + 3H_2O \quad (3)$$

$$MoO + 2H^+ + H_2(aq) + 2H_2S(aq) \rightarrow MoS_2 + 4H_2O \quad (4)$$

$$HMoO + H^+ + H_2(aq) + 2H_2S(aq) \rightarrow MoS_2 + 4H_2O \quad (5)$$

$$H_2MoO_4(aq) + H_2(aq) + 2H_2S(aq) \rightarrow MoS_2 + 4H_2O \quad (6)$$

Deposition from brines

$$MoO_2Cl+ + H_2(aq) + HS^- + H_2S(aq) \rightarrow MoS_2 + 2H_2O + HCl(aq) \quad (7)$$

$$MoO_2Cl_2(aq) + H_2(aq) + 2H_2S(aq) \rightarrow MoS_2 + 2H_2O + 2HCl(aq) \quad (8)$$

$$MoO_2Cl + H_2(aq) + 2H_2S(aq) \rightarrow MoS_2 + 2H_2O + 2HCl(aq) + Cl^- \quad (9)$$

2.5.2 Cu Deposition

Unlike Mo, Cu is precipitated as several different sulphide minerals in porphyry systems, the most common of which are chalcopyrite ($CuFeS_2$) and bornite (Cu_5FeS_4). These can both be deposited within the potassic alteration zone (e.g. Sillitoe, 2010), but are more commonly found in association with chlorite-sericite and sericitic alteration zones (Figure 2.8). Fluid inclusion studies of porphyry Cu-Au and Cu-Mo deposits suggest that drops in temperature and pressure are the principal driving forces for Cu ore deposition from vapours (e.g. Hezarkhani *et al*., 1999; Ulrich *et al*., 2002; Redmond *et al*., 2004; Seo *et al.,* 2009; Klemm *et al*., 2007). Similarly to Mo, Cu solubility experiments indicate that Cu-Fe sulphide saturation is reached in both Cu-bearing vapours and brines as temperature decreases below ~425°C (Williams-Jones and Heinrich, 2005).

Although Cu is likely to favourably partition into brines, significant amounts of Cu are still considered to be transported in coeval vapours (e.g. Candela and Holland, 1984; Simon *et al*., 2006; Williams-Jones and Heinrich, 2005; Simon and Ripley, 2011; Seo *et al*., 2012). This partitioning is inferred to play a key role in metal decoupling in several porphyry systems, including El Teniente (Vry, 2010). Based on previously proposed CuCl (e.g. Berry *et al*., 2006; 2009) and CuHS speciation (Pokrovski *et al*., 2008; Seo *et al*., 2009; Simon and Ripley, 2011), three reactions have been proposed for the deposition of chalcopyrite from brines and vapours (Seo *et al.,* 2012):

Deposition from Brines:

$$CuCl(aq) + FeCl_2(aq) + 2H_2S(aq) \rightarrow CuFeS_2 + 3HCl(aq) + 0.5\ H_2(aq) \qquad (10)$$

Deposition from vapours:

$$2Cu(HS)^{-2}(g) + 2FeCl_2(g) \rightarrow 2CuFeS_2 + 2Cl^{-}(g) + 2HCl(g) + H_2(g) \qquad (11)$$

$$2Cu(HS)(H_2S)(g) + 2FeCl_2(g) \rightarrow 2CuFeS_2 + 4HCl(g) + H_2(g) \qquad (12)$$

Similar to Mo, these reactions suggest that the deposition of Cu is also likely to be highly dependent on fluid fO_2 and pH (e.g. Landtwing *et al*., 2005; Seo *et al*., 2012). However, unlike Mo, these reactions imply that chalcopyrite saturation is promoted under oxidised (low H_2) and less acidic fluid conditions. This is consistent with previous studies that indicate that Cu is highly soluble (e.g. as $CuCl_2^-$) in reduced, acidic fluids (e.g. Hezarkhani and

Williams-Jones, 1998; Simon *et al*., 2006). Based on the contrasting solubilities of Mo and Cu as a function of redox and pH it has been suggested that small changes in these conditions may control the decoupling of Mo and Cu mineralisation (e.g. Seo *et al*., 2012). For example, if fluid conditions were initially highly oxidised and alkaline then Mo deposition may be delayed leading to the early deposition of chalcopyrite. This may explain the distal deposition of Mo relative to high temperature Cu deposition in some systems (e.g. Yerington, Nevada: Dilles and Einaudi, 1992). However, if fluid conditions are initially fairly reduced then Mo will saturate early. Chalcopyrite then may deposit in more distal settings as a result of increasing pH created by wall-rock alteration (e.g. Hemley *et al.,* 1992). This may explain the strong association of Cu with sericitic alteration in porphyry systems (e.g. Vry *et al*., 2010; Seo *et al*., 2012).

Phase separation as a function of decreasing temperature and pressure has also been forwarded as an effective mechanism for precipitation of Cu from vapours by destabilising Cu-complexes through volatile loss and by decreasing water fugacity with an associated decrease in fluid density (Pokrovski *et al*., 2005). This is suggested as an important factor in chalcopyrite deposition at Butte, whereas it does not appear to control the precipitation of molybdenite (Rusk *et al*., 2008).

2.5.3 Metal Remobilisation

Metal grades in porphyry deposits can be modified as the result of the remobilisation of elements by subsequent pulses of hydrothermal activity or by the ingress and circulation of meteoric or metamorphic waters. Field evidence indicates that Mo mineralisation in porphyry deposits is often closely related to igneous bodies that have been subject to intense alteration (e.g. Carten *et al*., 1988). As a result, it has been suggested that Mo grades may be enhanced through the alteration of metal-bearing silicate minerals during cycling of late stage magmatic fluids and/or meteoritic fluids (e.g. Taylor, 1974). Metal remobilisation from pre-existing sulphides has also been proposed as a potential factor in the generation of high metal grades in late stage fluids at El Teniente (Klemm *et al*., 2007; Vry, 2010). However, no definitive evidence for this has been provided and to-date no study has systematically assessed the potential effects of metal remobilisation during progressive stages of magmatic-hydrothermal activity.

2.6 Closing Statements

This chapter provides a summary of the current understanding of the formation of Mo-rich porphyries and the behaviour of metals within them. Although the evolution of these systems is fairly well understood in broad terms, there are still several areas of significant uncertainty regarding their magmatic-hydrothermal evolution and the reasons for the decoupling of Mo-Cu mineralisation. These include:

(1) A lack of understanding of the deep magmatic processes that govern the fertility and metal tenor of overlying porphyry systems.

- There is uncertainty regarding the source of Mo in the most enriched porphyry Mo systems: It remains unclear whether their formation relies on a Mo-enriched zone in the deep continental crust or subcontinental lithospheric mantle;
- It is unclear whether the formation of porphyry Mo and Cu-Au systems is related to deep magmatic processes or changes that occur during ascent and emplacement;
- It is unclear whether sulphide saturation occurs in magma chambers underlying porphyry deposits and whether this process can provide metal-rich sources for subsequent pulses of magmatic-hydrothermal activity;
- The effects of magma composition and fO_2 on the speciation and transport of Mo and Cu in magmas remain unclear;
- The timescales over which porphyry intrusions operate remain unclear. This is often poorly constrained but may control metal grades as a result of the superposition of multiple generations of metal-bearing fluids.

(2) Uncertainty regarding the effects of different element partitioning processes on Mo-Cu decoupling from both a magmatic and hydrothermal perspective.

- The processes that govern decoupled mineralisation remain elusive. This problem is particularly apparent given recent concerns regarding the validity of Cu concentrations in measured melt and fluid inclusions;
- Ascertaining the exact reasons is especially difficult as the formation of porphyry deposits relies on the superposition of several magmatic-hydrothermal element fractionation processes that may affect the partitioning and solubility of Mo and Cu in

different ways. Such processes include: the partitioning of metals from a crystallising magma into magmatic volatile fluids; the separation of metal bearing fluids into coexisting vapour and brine phases; the selective deposition of metals under different physical and chemical conditions; and the modification of mineralisation patterns by later pulses of fluid.

- Understanding the controls on Mo and Cu deposition requires a better understanding of the evolution of fluids as they ascend and/or migrate into surrounding host rock.

(3) Uncertainty regarding the speciation of both Mo and Cu in porphyry ore fluids.

- Most hydrothermal fluid experiments have been completed at temperatures and pressures lower than those expected in porphyry systems leading to uncertainty regarding the exact speciation and transport of Mo and Cu in porphyry ore fluids.
- The speciation of Mo in NaCl-rich fluids and the role of HS^- complexes in transporting Cu remains a contentious issue.
- Most ore deposit studies fail to provide clear constraints on the types of hydrothermal fluids present and their relative volumes. This information is vital in assessing the carrying capacities of vapours and brines and assessing how most metal is transported and deposited.

(4) Poor constraints on the controls on the deposition of Cu and Mo sulphides.

- It is unclear whether Mo and Cu are transported by the same hydrothermal fluids or are exsolved into separate fluids that mineralise in different parts of the deposit;
- The exact physical-chemical parameters responsible for deposition remain unclear. These could vary from deposit to deposit and may be strongly interrelated;
- Very little comparative work has been undertaken regarding the controls on Mo mineralisation in different porphyry Mo and Cu-Mo systems. It is unclear whether metals are deposited under similar conditions in these different deposit types.

Resolving these issues relies on the study of a deposit that displays distinct decoupled Cu and Mo mineralisation and is relatively well understood in terms of its magmatic evolution. For these reasons, the El Teniente provides an ideal study deposit.

Chapter 3. The El Teniente Cu-Mo porphyry deposit, Chile

3.1 Introduction

The El Teniente Cu-Mo porphyry deposit (34°05'S, 70°21'W) is located approximately 70 km southeast of Santiago on the western margin of the Andean Cordillera and within the confines of the central Chilean porphyry Cu-belt (Figure 3.1). This supergiant porphyry is the world's largest underground Cu mine, hosting a pre-mining resource total of approximately 100 Mt of fine Cu (Skewes *et al.*, 2002; 2005; Stern *et al.*, 2010). Mo, present as molybdenite, is obtained purely as a by-product of Cu mining with low typical ore grades of <0.03 wt.%. Despite this, the extremely high ore tonnage of El Teniente makes it historically the world's largest exploitable resource of Mo (Sillitoe, 2010). Total current and mined resource estimates are between 1.4 Mt (Cannell *et al.*, 2005) and 2.5 Mt (Camus, 2003).



Figure 3.1: Location map of the El Teniente Cu-Mo porphyry deposit and other major porphyry Cu-Mo and Cu systems in the central and northern Chilean porphyry Cu districts. Dotted red line = rough location of the boundary between the Central Volcanic Zone (CVZ) and The Southern Volcanic Zone (SVZ). Different colour circles correspond to deposit ages (See key). Figure adapted from Camus (2001), Vry *et al.* (2010) and supplementary data obtained from the USGS porphyry database (2008).

Mineralisation styles and the magmatic-hydrothermal evolution of El Teniente have been the focus of a number of studies over the last 90 years (Lindgren and Bastin, 1922; Howell and Malloy, 1960; Camus, 1975; Freydier *et al*., 1997; Skewes *et al*., 2002, 2005; Maksaev *et al*., 2004; Cannell *et al*., 2005; Skewes and Stern, 2007; Cannell *et al*., 2007; Klemm *et al*., 2007; Rabbia *et al*., 2009; Astudillo *et al*., 2010; Stern *et al*., 2010; Vry *et al*., 2010; Munoz *et al*., 2012). Further descriptive research and structural analysis have also been undertaken by mine geologists of CODELCO Division El Teniente and three detailed PhD studies (Cannell, 2004; Klemm, 2006; Vry, 2010). Combined, these have helped constrain the magmatic evolution of El Teniente and the nature of Cu mineralisation across the deposit. In contrast, comparatively little work has focused on the distribution and timing of Mo mineralisation or the types of hydrothermal fluids responsible for Mo mineralisation.

Understanding the controls on Mo mineralisation at El Teniente requires a detailed knowledge of the units and vein types present within the deposit and how they evolved in space and over time. This section provides an overview of:

- The regional geology of the central Chilean Andes and the tectonic precursors for the formation of El Teniente;
- The petrology and key morphological features of intrusions and breccias present within the deposit;
- The vein classification schemes used at El Teniente including notes on their main similarities and differences;
- The type of fluids present within the deposit as determined in previous fluid inclusion studies;
- The zonation of hypogene and supergene mineralisation at the deposit;
- The current models for the evolution of El Teniente from a magmatic-hydrothermal and structural perspective.

In this section, photographs of vein and breccia types taken during this study were used to show the different vein and breccia types present at El Teniente.

3.2 Regional Geology and Tectonic Evolution

The Chilean Andes host the highest concentration of Cu-rich porphyries of any arc setting with >450 Mt of fine Cu identified in 54 deposits (Camus, 2003). These include the three largest known Cu porphyry resources on Earth: El Teniente, Río Blanco-Los Bronces and Chuquicamata (Cannell, 2004; Figure 3.1). Porphyry deposits in the northern and central Chilean Cu districts can be divided into five metallogenic belts of different ages (Figure 3.1). Porphyry genesis is linked to the near-continuous subduction of the oceanic Nazca plate beneath South America since the Early-Cretaceous (e.g. Camus, 2002, 2003; Cooke *et al*., 2005). Pulses of porphyry formation (Figure 3.1) are believed to be closely controlled by changes in subduction geometry over time, which resulted in segmentation of the Andes large variations in crustal thickness and magma generation (Stern, 1989, 2004; Skewes and Stern, 1994, 1995; Stern and Skewes, 1995, 2005; Rosenbaum *et al*., 2005). The general trend of porphyry younging to the south and east reflects the overall migration of arc magmatism since the Cretaceous.

El Teniente occurs alongside the late Miocene to early Pliocene porphyry Cu-Mo deposits of Los Pelambres (>25 Mt Cu: Atkinson *et al*., 1996) and Rio Blanco-Los Bronces (>50 Mt Cu: Serrano *et al*., 1996; Frikken *et al*., 2005) within the confines of the central Chilean Cu-belt (Maksaev *et al*., 2004; Cannell *et al*., 2005). All three deposits lie proximal to the boundary between two major tectonic segments, the Central Volcanic Zone (CVZ) and the Southern Volcanic Zone (SVZ), separated at a latitude of approximately 33°30'S (Figure 3.1). The CVZ hosts the Rio Blanco-Los Bronces and Los Pelambres deposits and has a subduction angle of <10° (e.g. Cahill and Isaaks, 1992) and a crustal thickness of approximately 50 km (e.g. Introcaso *et al*., 1992). The SVZ hosts El Teniente, has a steeper subduction angle of approximately 30° (Cahill and Isaaks, 1992) and a crustal thickness of 35 to 40 km (e.g. Cannell, 2004). Unlike the CVZ, volcanism is still active in the SVZ but is now located to the east of El Teniente (e.g. the Planchón-Peteroa volcanic complex and the Copahue stratovolcano ~71°W).

The tectonic evolution of the central Chilean Cu belt has been the focus of numerous studies (e.g. Vergara *et al*., 1988; Stern, 1991; Introcaso *et al*., 1992; Skewes and Holmgren, 1993;

Skewes and Stern, 1994, 1995; Kurtz *et al*., 1997; Godoy *et al*., 1999; Charrier *et al*., 2002; Cannell 2004; Cannell *et al*., 2005; Kay *et al*., 2005; Stern *et al*., 2010). During the early Tertiary, the subduction zone underlying central Chile was moderately dipping and had a slow convergence rate. During this period, extensional tectonism in the back-arc led to crustal thinning (to 30-35 km; Charrier *et al*., 2002) and opening of a northward trending extensional graben (the Central Valley). In the Oligocene to early Miocene this was filled by volcanic deposits of the Coya-Machali Formation. No rocks of the Coya-Machali Formation are found at the El Teniente, but they do crop out to the north of the mine (e.g. Charrier *et al*., 2002; Parada *et al*., 2007). Here, exposed rocks consist of basaltic to dacitic lava flows interbedded with horizons of lacustrine and fluvial sediments that form a package that is likely to exceed 3,000 m in thickness (e.g. Charrier *et al*., 2002).

During the early Miocene, extension in the cordillera was replaced by compressional tectonics as a result of increasing subduction rates beneath central Chile (e.g. Charrier *et al*., 2002). Associated crustal thickening is interpreted to have the uplift and erosion of the Coya-Machali Formation between 23 and 15 Ma (Skewes and Holmgren, 1993; Kurtz *et al*., 1997; Godoy *et al*., 1999; Charrier *et al*., 2002; Stern, 2010). Following this, extensive volcanism resulted in the formation of a 2,500 m thick sequence of extrusive and intrusive rocks of basaltic to rhyolitic composition named the Farellones Formation (Skewes *et al.,* 2002, 2005) between 15 and 7 Ma (Cuadra, 1986; Kay and Kurtz, 1995; Maksaev *et al*., 2004). This volcanic package lies unconformably on top of the Coya-Machali Formation and includes the Teniente Mafic Complex (TMC), which hosts the majority of mineralisation at El Teniente (Skewes *et al*., 2002; Cannell *et al*., 2005; Vry *et al*., 2010). Lithological subdivisions for the Farellones Formation have been defined in a number of studies (e.g. Howell and Malloy, 1960; Kay and Kurtz, 1995; Cannell, 2004; Cannell *et al*., 2005).

During the late Miocene, continued decrease in the subduction angle beneath central Chile led to the eastward migration of the magmatic arc (Stern, 1989, 2004; Stern and Skewes, 1995, 2005; Kay *et al*., 2005). Between 10 and 12 Ma the angle is believed to have been significantly reduced by the subduction of the Juan Fernández ridge, leading to slab segmentation (e.g. Garrido *et al*., 2002; Gilbert *et al*., 2006). Crustal thickening to 50-60 km is interpreted to have led to the eventual termination of volcanism in the SVZ at ~7 Ma and

the formation of large crustal magma chambers, including the parental magma chamber inferred to lie beneath El Teniente (Cuadra, 1986; Kay and Kurtz, 1995; Stern *et al*., 2010). The amount of Cu within the deposit (approximately 95 Mt) has led to the suggestion that the parental magma chamber is likely to have had a volume in excess of 600 km^3 (Skewes and Stern, 1995, 2007; Stern and Skewes, 2005; Stern *et al*., 2010). The large volumes of water, sulphur and chlorine present in the system suggest that magmas were derived from a mantle source contaminated by altered oceanic crust and sediments (Stern, 1989, 1991; Skewes *et al*., 2005).

3.3 Deposit Formation and Geology

Between the late Miocene and Pliocene, intermittent escape of magmas from the inferred parental chamber led to the formation of a number of overlying, nested, felsic-intermediate intrusions termed the Teniente Intrusive Complex (e.g. Camus, 1975; Maksaev *et al*., 2004; Cannell, *et al*., 2005; Stern *et al*., 2010; Vry *et al*., 2010). The presence of intense mineralisation associated with brecciated sections of the TMC led some authors to reclassify El Teniente as a supergiant breccia deposit (Skewes *et al*., 2002, 2005; Skewes and Stern, 2005; Skewes and Stern, 2007; Stern *et al*., 2007). This interpretation is more akin to the models developed for the neighbouring porphyry Cu deposits of Rio-Blanco-Los Bronces (e.g. Serrano *et al*., 1996) and Los Pelambres (Atkinson *et al*., 1996: Figure 3.1).

Although mineralised breccias are an important characteristic of El Teniente, numerous studies have suggested that the majority of mineralisation is hosted in stockwork veins that surround the felsic-intermediate porphyry intrusions (Camus, 1975; Cannell, 2004; Cannell *et al*., 2007; Vry *et al*., 2010). Geochronology (Maksaev *et al*., 2004; Cannell *et al*., 2005; Cannell *et al*., 2007), petrology, vein chronology, fluid chemistry (Camus, 1975; Cannell *et al*., 2005; Cannell *et al*., 2007; Klemm *et al*., 2007, Vry *et al*., 2010), hydrothermal rutile data (Rabbia *et al*., 2009) and palaeomagnetic data (Astudillo *et al*., 2010) provide an abundance of evidence to suggest that El Teniente is a large, nested porphyry Cu deposit (e.g. Vry *et al*., 2010). This is consistent with Howell and Molloy (1960) who described a 'circular configuration' of alteration and mineralisation that is typical of porphyry Cu-Mo systems.

A number of petrological and geochronological studies have been completed at El Teniente which provide detailed descriptions of the units present and a general framework for deposit evolution (Clark *et al*., 1983; Cuadra, 1986; Skewes *et al*., 2002; Maksaev *et al*., 2004; Cannell *et al*., 2005; Vry *et al*., 2010: Appendix 1). In this study, the intrusion names used are consistent with the CODELCO mine classification (Table 3.1) and, with the exception of the diorite porphyries, are the same as those used by Vry *et al*. (2010).

Table 3.1: Summary of the different names given to units at El Teniente in previous studies.

This Study - Mine Classification	Cannell *et al*. (2005)	Skewes and Stern (2007)	Vry *et al*., (2010)
Teniente Mafic Complex	Teniente Host Sequence	Teniente Mafic Complex	Teniente Mafic Complex
Sewell Quartz Diorite	Sewell Tonalite	Sewell Tonalite	Sewell Quartz Diorite
A-Porphyry	Gray porphyry	A porphyry igneous breccia	A-Porphyry
Diorite porphyries	Dacite pipes	Quartz diorite porphyries	Dacite porphyries
Grueso Porphyry	Marginal Porphyry	-	Grueso Porphyry
Teniente Dacite Porphyry	Dacite porphyry dike	Teniente Dacite Porphyry	Teniente Dacite Porphyry
Latite dikes	Latite dikes	Dacite ring dike	Latite dikes

Notes: Names from (Cannell *et al*., 2005; Skewes and Stern, 2007; Vry *et al*., 2010). Names adopted for this study are shaded grey.

3.3.1 The Teniente Mafic Complex (TMC)

The TMC hosts the felsic-intermediate intrusions at the deposit (Figure 3.2). Whole-rock analyses including major element and immobile element data suggest that rocks are predominantly of basaltic to andesitic composition (Cannell *et al*., 2005; Vry *et al*., 2010). However, the major element data at least are likely to have been modified significantly by widespread and pervasive biotitisation and sericitisation. Intense alteration also makes it difficult to identify the original textures or boundaries of different lithological horizons within the TMC. However, a number of authors have noted a clear heterogeneity in rocks from aphanitic (± phenocrysts) to coarse equigranular (Howell and Molloy, 1960; Skewes *et al*., 2002; Cannell, 2004; Cannell *et al*., 2005; Vry 2010; Vry *et al*., 2010). Skewes *et al*. (2002) suggested that the Teniente Mafic Complex is predominantly composed of mafic to intermediate intrusive rocks including gabbro, diabase, basalt and andesite. Additional

lithotypes were recognised by Cannell *et al*., (2005), including the presence of altered dioritic intrusions, and interbedded ash and heterolithic volcaniclastic breccias (Cannell, 2004). These were interpreted to have formed by the intrusion of mafic stocks and sills into a mid-late Miocene andesitic volcano-plutonic complex (Cannell *et al*., 2005). Several dating techniques have been undertaken on the TMC yielding emplacement ages between 15.2 and 7.5 Ma (Cuadra, 1986; Skewes *et al*., 2002).

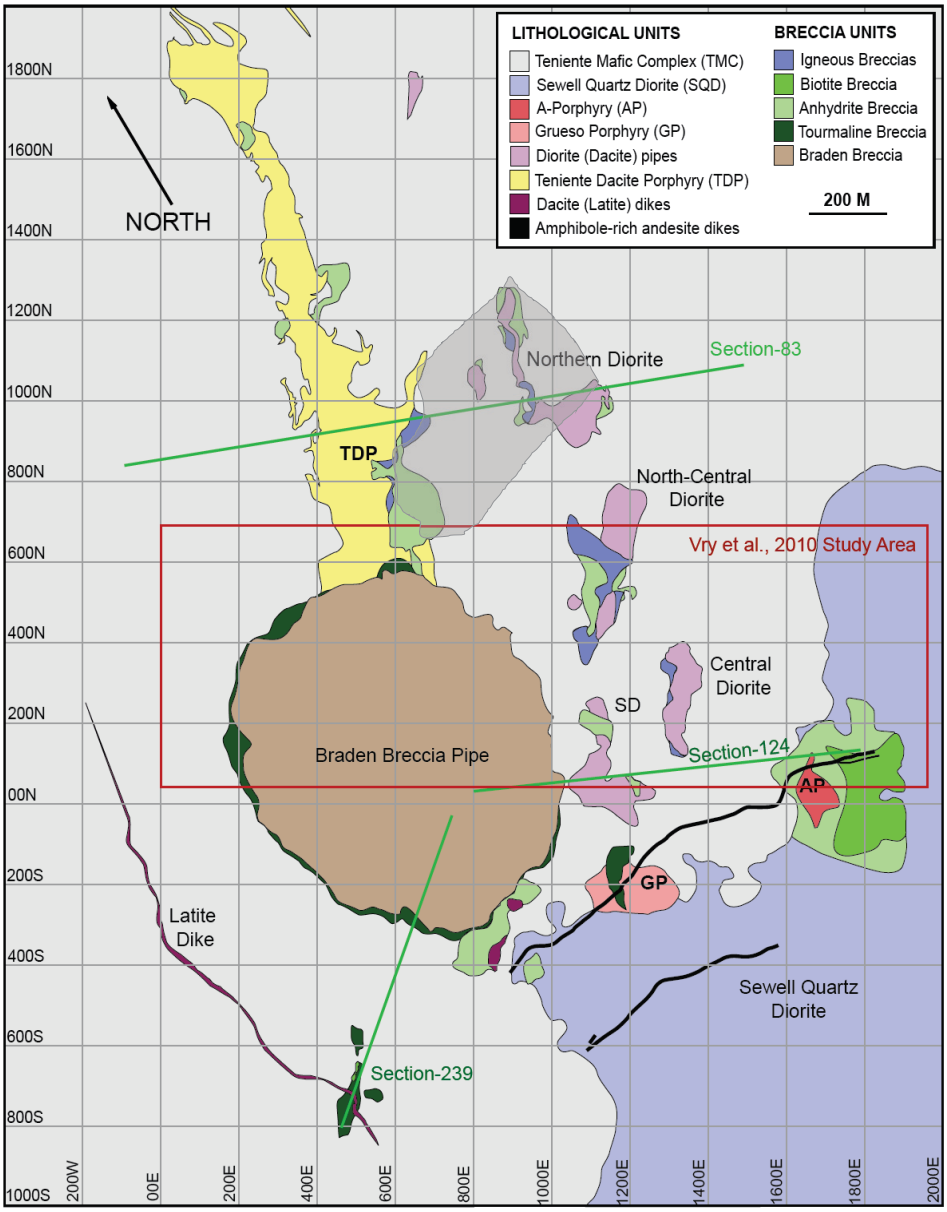


Figure 3.2: Simplified geological map of El Teniente at mine level 2165 m asl showing igneous intrusions and breccia bodies. Local mine grid is oriented 14.5°E of geographic north. Green lines (sections 83,124 and 239) are the drillcore cross-sections studied by Cannell (2004) to determine vein chronology and for fluid inclusion analysis. Grey shaded area represents the sampling region utilised by Klemm *et al*. (2007) for their fluid inclusion study. Red box shows the extent of the study area of Vry *et al*. (2010) in which E-W trending cross sections were analysed for every 50 m northing to determine vein chronology.

3.3.2 The Teniente Intrusive Complex

The Sewell Quartz Diorite

The Sewell Quartz Diorite is the oldest unit of the Teniente Intrusive Complex and forms much of the south-eastern quadrant of the mine area (Figure 3.2). This unit is equigranular to porphyritic and displays minor compositional variations of quartz-diorite to tonalite (e.g. Skewes *et al*., 2002; Vry *et al*., 2010). The lithology comprises andesine to oligoclase plagioclase and minor K-feldspar, biotite, quartz and altered amphibole (Skewes *et al*., 2002). The textural and mineralogical variations within the Sewell Quartz Diorite have been interpreted to be induced by differential cooling rates within the intrusion with porphyritic tonalite representing the chilled margins (Cuadra, 1986). However, other authors argue that it is composed of at least two intrusions (e.g. Guzmán, 1991).

The Sewell Quartz Diorite is thought to have been emplaced between 12.4 and 7.0 Ma (Cuadra, 1986, 1992; Kay and Kurtz, 1995; Rivera and Falcón, 1998; Skewes *et al*., 2002). In contrast, Cannell *et al*. (2005) proposed a slightly younger crystallisation age based on clusters of U-Pb zircon dates that fall between 6.7 ±0.6 and 5.5 ±0.6 Ma (Figure 3.3: Maksaev *et al*., 2004). It is evident that the Sewell Quartz Diorite was emplaced prior to significant mineralisation at El Teniente (e.g. Howell and Malloy, 1960; Maksaev *et al*., 2004; Vry *et al*., 2010).

The A-Porphyry

The A-porphyry was emplaced along the contact between the Sewell Quartz Diorite and the TMC at the eastern side of the deposit (Figure 3.2). This unit is essentially a magmatic breccia (Skewes *et al*., 2002) consisting of abundant TMC and Sewell Quartz Diorite clasts in an altered matrix of biotite, K-feldspar, plagioclase, anhydrite, and quartz (Cannell, 2004; Vry *et al*., 2010). Recent immobile and mobile element analyses indicate that the A-Porphyry matrix is predominantly andesitic in composition (Vry *et al*., 2010). The unit is affected by zones of intense biotite alteration and minor sericitisation creating a marked enrichment in K_2O and reduction in silica contents to as low as 46 wt.% (Vry *et al*., 2010). The nature of anhydrite in the matrix of the A-Porphyry igneous breccia is disputed, with

contrasting hypotheses that it is magmatic in origin (Stern *et al*., 2007) or that it is precipitated from later hydrothermal fluids (Cannell *et al*., 2005; Vry *et al*., 2010).

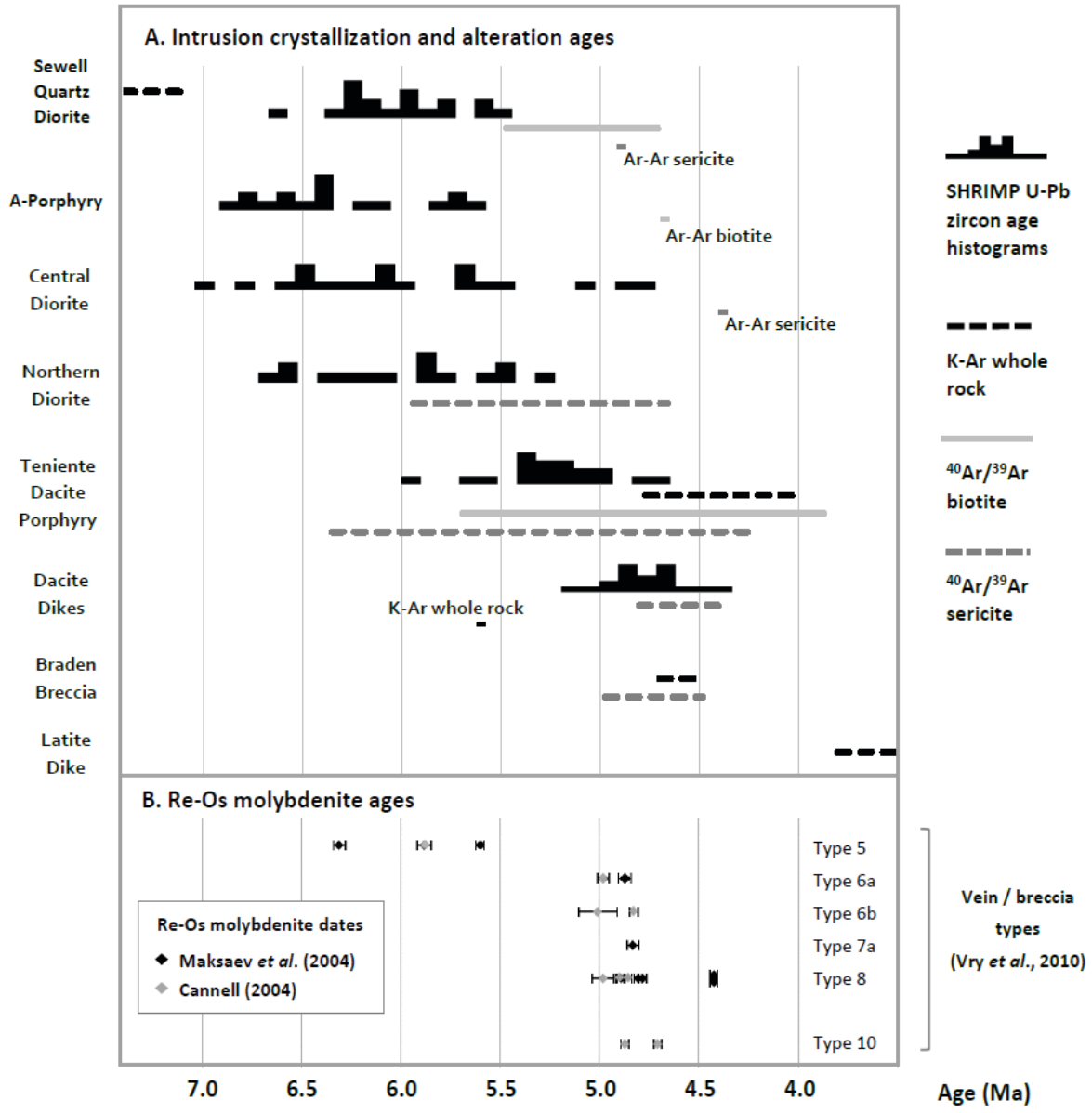


Figure 3.3: Compiled geochronology for the crystallisation of intrusions and molybdenite mineralisation at El Teniente. (A) Intrusion crystallisation, biotite and sericite alteration (Quirt, 1972; Clark *et al*., 1983; Cuadra, 1986; Maksaev *et al*., 2004). Intrusions are listed in order of formation as reported in previous studies (Maksaev *et al*., 2004; Cannell *et al*., 2005; Vry *et al*., 2010). Histograms show temporal distribution of previously collected U-Pb zircon ages (Maksaev *et al*., 2004) divided into 0.1 Ma intervals and ignoring any clearly anomalous outliers. $^{40}Ar/^{39}Ar$ step-heating and total fusion ages are combined. (B) Re-Os molybdenite ages for vein types collected in two previous studies (Maksaev *et al*., 2004; Cannell 2004). Vein types are given according to the vein classification scheme of Vry *et al*. (2010) discussed in subsequent sections. For intrusion locations refer to Figure 3.2.

U-Pb dating of zircons from the A-Porphyry yielded ages of 6.9 to 5.7 Ma (Figure 3.3; Maksaev *et al*., 2004). These suggest that the unit may have formed in multiple intrusion and brecciation pulses centred at approximately 6.2 Ma, or that it contains inherited zircon from the Sewell Quartz Diorite and was actually emplaced nearer 5.7 Ma. Only one ^{40}Ar-^{39}Ar biotite date of 4.69 ±0.16 Ma has been obtained (Maksaev *et al*., 2004). This young age suggests there was overprinting of the A-Porphyry by potassic alteration related to later intrusive pulses, or that the system remained above the closure temperature for Ar diffusion in biotite (~310°C: e.g. Miyashiro, 1994) until this time.

The Diorite Pipes

Four diorite pipes of roughly equal size are found to the east of the Braden Breccia pipe (Figure 3.2), named the Northern, North-Central, Central and Southern Diorites. These units have also been referred to as dacite pipes/finger porphyries (Cannell *et al*., 2005; Cannell *et al*., 2007; Vry *et al*., 2010), tonalite pipes (Klemm *et al*., 2007) and quartz diorite-tonalite stocks (Maksaev *et al*., 2004). The intrusions have relatively consistent diameters of ~200 m at all mine levels indicating that they are volumetrically small, finger-shaped bodies of significant vertical extent. All the diorites are porphyritic, containing 30-50% phenocrysts of feldspar and 5-15% phenocrysts of amphibole and biotite in a fine-grained aplitic matrix of quartz, plagioclase and minor K-feldspar. Plagioclase phenocrysts are predominantly albite in composition (Vry *et al*., 2010) and have often been altered to chlorite, sericite and quartz (Cannell, 2004; Vry *et al*., 2010). The plutonic "diorite" terminology was used throughout this study as requested by CODELCO Division El Teniente in order to maintain consistency with the mine classification and to provide a clear distinction from the Teniente Dacite Porphyry further to the north and west.

Relatively consistent SHRIMP U-Pb zircon ages have been obtained for the Northern and Central diorites (Figure 3.3) suggesting that they formed contemporaneously (Maksaev *et al*., 2004). Most dates cluster at approximately 5.6 Ma suggesting that these units formed soon after intrusion of the A-Porphyry. However, the large range in zircon crystallisation ages from 7.0 Ma to 4.8 Ma make the determination of the emplacement age difficult. ^{40}Ar-^{39}Ar sericite dates in and near the Northern and Central Diorites fall between 5.94 ±0.44 and

4.4 ±0.24 Ma (Maksaev *et al*., 2004). However, it is known that this system is reset by high-temperature (>350°C) fluid circulation (e.g. Selby and Creaser, 2001). These dates may therefore represent alteration associated with the intrusion of the nearby Teniente Dacite Porphyry. No zircon crystallisation ages have been obtained for the North Central and Southern Diorites. As a result, the inferred synchronous formation of these units with the other diorites (e.g. Maksaev *et al*., 2004) is based purely on their similar mineralogy and close proximity.

The Grueso Porphyry

The Grueso Porphyry is located to the southeast of the Braden Breccia pipe, along the margin of the Sewell Quartz Diorite (Figure 3.2). This unit is described as having a porphyritic texture comprising a plagioclase-quartz ground mass, biotite phenocrysts and quartz eyes (Vry *et al*., 2010). Overall, the unit is mineralogically and geochemically similar to the nearby diorites (Vry *et al*., 2010). However, the Grueso porphyry appears relatively fresh compared to these units, possibly related to its southern location. Although alteration is less intense, some mineralisation is present including 2-3% disseminated pyrite and chalcopyrite. To date, no U-Pb zircon ages or alteration ages have been obtained for the Grueso porphyry.

The Teniente Dacite Porphyry

The Teniente Dacite Porphyry is an elongate, dike-like intrusion that extends approximately 1,600 m north of the Braden Breccia pipe (Figure 3.2). Small underground exposures of the Teniente Dacite Porphyry also occur to the south of the Braden Breccia pipe indicating that the unit is cut by the pipe. The Teniente Dacite Porphyry is composed of phenocrysts of oligoclase-andesine plagioclase, biotite and amphibole in a fine- to medium-grained groundmass of quartz, albite, K-feldspar, and biotite (Skewes *et al*., 2002; Maksaev *et al*., 2004). Recent immobile element data show that it is dacitic in composition. Unlike most other units at El Teniente, the Teniente Dacite Porphyry has not been subjected to significant amounts of biotite alteration (Vry *et al*., 2010). However, elevated K_2O and SiO_2 contents reflect variable quartz-sericite alteration (Vry *et al*., 2010). This alteration is particularly abundant at shallow mine levels along the margins of the intrusion (Skewes *et al*., 2005; Cannell, 2004; Vry *et al*., 2010).

The observation of distinct textural boundaries within the Teniente Dacite Porphyry led to the conclusion that it is composed of multiple intrusive phases (Ossandón, 1974; Duarte, 2000; Rojas, 2002; Skewes *et al*., 2002; Rojas, 2003; Maksaev *et al*., 2004; Cannell *et al*., 2005; González, 2006; Hitschfeld, 2006). It can be divided into two intrusive subtypes: the 'euhedral phase' is composed of euhedral plagioclase phenocrysts in a fine-grained aplitic matrix and comprises the northern end and eastern side of the dike. The 'subhedral phase' forms the rest of the unit and contains resorbed plagioclase phenocrysts in a coarser aplitic matrix (Ossandón, 1974; Duarte, 2000; Rojas, 2002; Cannell *et al*., 2005). Rojas (2003) suggested that the euhedral phase was intruded later as it contains xenoliths of the subhedral phase. The presence of at least two separate intrusions is supported by a large range in zircon and alteration ages associated with the Teniente Dacite Porphyry. U-Pb zircon dates for the unit show a range of 1.3 Ma (Maksaev *et al*., 2004: Figure 3.4) and exhibit an overall younging to the north (Baker *et al*., 2011). ^{40}Ar-^{39}Ar biotite and sericite dates appear bimodal suggesting at least two separate phases of potassic and phyllic alteration.

Latite Dykes

Latite dikes are found in concentric rings surrounding the Braden Breccia pipe with additional, minor, northeast-trending dikes that cut other intrusions (Figure 3.2). These dikes are rarely more than 5 m wide and are porphyritic, consisting of a very fine groundmass of quartz and feldspar supporting phenocrysts of sericitised albite, biotite and altered amphibole (Skewes *et al*., 2002; Cannell *et al*., 2005). Whole rock immobile element data suggest that the dikes are compositionally similar to the diorites found to the east of the Braden Breccia pipe (Vry *et al*., 2010). This is supported by K-Ar whole rock dates such as 5.76 ±0.23 Ma (Cuadra 1986) and 5.62 ±0.23 Ma (Quirt, 1972), which correlate well with U-Pb dates for the diorites. Despite this, U-Pb zircon ages for late dacite dikes proximal to the Teniente Dacite porphyry, to the North of the Braden Breccia pipe yield ages that cluster between 5.0 and 4.4 Ma (Maksaev *et al*., 2004). These young ages suggest that numerous dacitic dikes were emplaced during and after the emplacement of Teniente Dacite Porphyry.

Lamprophyre Dykes

All units at El Teniente are cut by a number of post-mineralisation dikes, referred to as lamprophyre (Skewes *et al*., 2002; Rabbia *et al*., 2009; Vry *et al*., 2010) or amphibole-phyric andesite dikes (Maksaev *et al*., 2004). These unaltered dikes occur on roughly eastward trends and cut mineralisation (Figure 3.2). Dikes are composed of a fine groundmass of glass, alkali feldspars and biotite, and abundant amphibole containing plagioclase phenocrysts (Skewes *et al*., 2002; Vry *et al*., 2010). K-Ar hornblende and K-Ar whole rock dates for these dikes have yielded ages of 2.9 ±0.6 Ma and 3.8 ±0.3 Ma respectively (Cuadra, 1986) confirming that they were the last intrusions at El Teniente.

3.3.3 El Teniente Breccias

A number of magmatic and hydrothermal breccias occur within, and/or surround, all of the intrusions at El Teniente (Figure 3.2). Understanding these breccias is important as they are important hosts of Mo and Cu mineralisation (e.g. Skewes *et al*., 2002). Five principal breccia types have been identified at the deposit: igneous-, biotite-, anhydrite- and tourmaline-cemented, and rock flour breccias (CODELCO Division El Teniente). Other localised breccias include actinolite-, magnetite-, K-feldspar-, quartz- and gypsum-cemented breccias (Skewes *et al*., 2002; Seguel *et al*., 2006; Vry *et al*., 2010). Examples of each of the breccia types observed during this study are shown in Figure 3.9.

Igneous Breccias

Igneous breccias (Figure 3.4A) formed in association with all of the major intrusive events, commencing with the formation of the A-Porphyry and ending with the Teniente Dacite Porphyry (Cannell *et al*., 2005, 2007; Vry *et al*., 2010). These are typically composed of 30-60% TMC clasts (± tonalite and diorite), 3-60 mm in diameter, in a matrix of biotite-quartz-feldspar- anhydrite. Skewes *et al*. (2002) reported an abundance of chalcopyrite in the matrix of the igneous breccias which may account for the high Cu (and Mo) grades observed along the boundaries of the El Teniente intrusions (Cannell *et al*., 2005, 2007; Vry *et al*., 2010).

Biotite Breccias

Biotite breccias (Fig. 3.4B) are inferred to be early magmatic-hydrothermal breccias that formed at the onset of the premineralisation stage (e.g. Vry *et al*., 2010). These predominantly occur at depth proximal to the A-Porphyry and, to a lesser extent, the diorites and the Teniente Dacite Porphyry, and consist of TMC and porphyry rock fragments cemented by coarse biotite and interstitial quartz (Cannell *et al*., 2007; Vry *et al*., 2010). Skewes *et al*. (2002; 2005) suggested that biotite breccias formed throughout the TMC but have been obscured by intense overprinting during later vein development and hydrothermal alteration. However, recent studies have found little evidence to support this contention (Cannell *et al*., 2007; Vry *et al*., 2010).

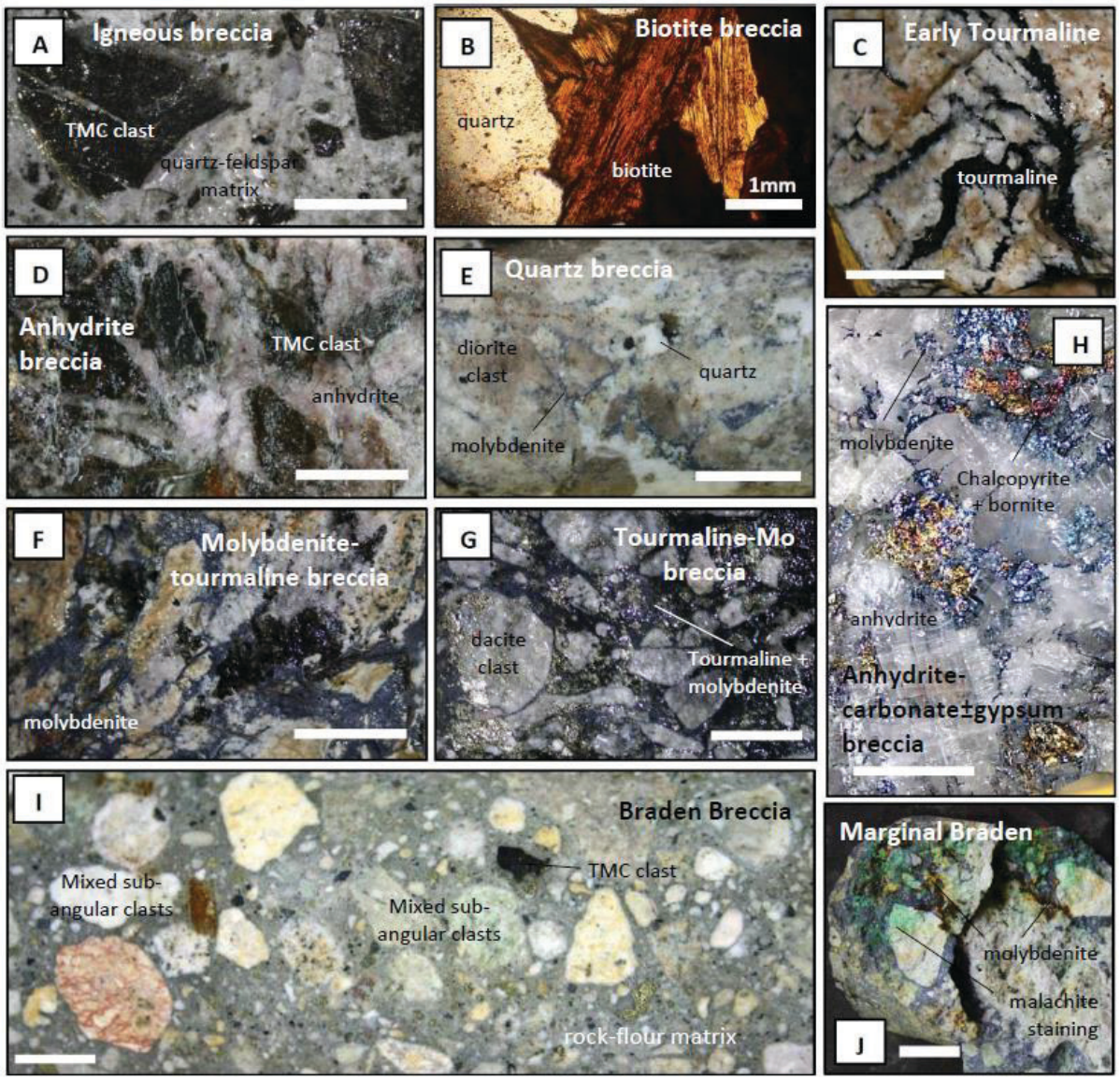


Figure 3.4: A-J Magmatic and hydrothermal breccia types observed at El Teniente. (A) Igneous breccia showing angular TMC clasts in a quartz-feldspar matrix (1754-127.1). (B) Plane-polarised light photomicrograph of a biotite breccia sample proximal to the A-Porphyry with 2-5 mm long biotite laths in a fine biotite-quartz matrix (sample Bt Bx 1). (C) Early (premineralisation stage), barren, tourmaline-cemented crackle breccia sampled at a shallow mine level to the east of the Braden Breccia pipe (1754-317.5). (D) Anhydrite-cemented breccia associated with the carapace of the Southern Diorite at shallow mine levels (2083-262.2). (E) Quartz-cemented breccia with minor K-feldspar and anhydrite cement surrounding clasts of the North Central Diorite (2215-49.8). Molybdenite mineralisation predominantly occurs at the clast-matrix boundary. (F) Late mineralisation stage tourmaline-cemented breccia to the east of the Braden Breccia pipe consisting of a molybdenite-rich matrix supporting highly altered diorite and TMC clasts (1754-285.9). (G) Marginal tourmaline breccia with tourmaline +molybdenite cement found at the western rim of the Braden Breccia pipe (2672-92.35). (H) Anhydrite-carbonate- and minor gypsum-cemented breccia supporting abundant bornite-chalcopyrite-molybdenite mineralisation found in the southern section of the mine area (2672-103.05). (I) Braden Breccia sample containing sub-angular to rounded clasts of several different lithologies in a rock flour matrix that contains fragmented chalcopyrite (2716-72.0). (J) Oxidised and altered hand specimen of the marginal breccia within the western rim of the Braden Pipe (2716-75.5). Matrix is molybdenite-rich with minor chalcopyrite oxidised to malachite. Scale bars = 1 cm in length.

Anhydrite Breccias

Anhydrite breccias (Figure 3.4D) are found surrounding the carapaces of the A-Porphyry, diorites and Teniente Dacite Porphyry (Figure 3.2). These breccia bodies are considered to have formed in conjunction with porphyry emplacement but they overprint the igneous and biotite breccias and contain angular TMC and porphyry clasts up to 100 mm in diameter (Vry *et al*., 2010). Breccia cements consist of anhydrite with minor quartz and feldspar. A number of studies have demonstrated that these breccias are well-mineralised (Skewes *et al*., 2002; Cannell *et al*., 2005, 2007; Vry *et al*., 2010), leading to the suggestion that their formation marks the onset of the main mineralisation stage. Some anhydrite cements are replaced by quartz (Figure 3.4E) which is inferred to have occurred during a change from anhydrite dominant to subsequent quartz-dominant precipitation (e.g. Vry, *et al*., 2010)

Tourmaline Breccias

The presence of large tourmaline breccia bodies is a notable feature of El Teniente and other deposits of the central Chilean porphyry-Cu belt (Los Pelambres and Los Bronces: Figure 3.1). At least two separate episodes of tourmaline breccia development were recognised in this study, consistent with previous breccia categorisations (Camus, 1975; Skewes *et al*., 2002). Early tourmaline breccias (Figure 3.4C) are found along the upper margin of the Sewell Quartz Diorite at shallow mine levels and form caps over other intrusions such as the Grueso Porphyry (e.g. Camus, 1975). These breccias have poorly-mineralised tourmaline cements and are inferred to have formed at a similar time to the biotite and anhydrite breccias. Late tourmaline breccias (Figure 3.4F-G) occur in a ring surrounding the Braden Breccia pipe (Figure 3.2). These breccias are clast supported and polymictic, containing 60-90% angular clasts of 10-100 mm diameter in a cement of tourmaline ± sulphides, sulphates and sulphosalts (Skewes *et al*., 2002). These breccias are associated with strong sericitic alteration and are inferred to have formed in the latter stages of deposit evolution.

Anhydrite-Carbonate ±Gypsum Breccias

At shallow mine levels, some anhydrite-dominated breccias contain variable amounts of gypsum and carbonate in their cements (Figure 3.4H). Unlike the earlier anhydrite breccias,

these predominantly occur in close proximity to the Braden Breccia pipe and are associated with quartz-sericite alteration (Vry *et al*., 2010).

The Braden Breccia Pipe

The Braden Breccia pipe dominates the centre of the deposit (Figure 3.2) and has a surface diameter of approximately 1,200 m. The pipe walls dip steeply inwards at approximately 60-80° (Cannell *et al*., 2005) creating a funnel-shaped structure extending to more than 2100 m below the surface (Skewes *et al*., 2002). The pipe has a diameter of >600 m at the deepest drillcore level (Skewes and Stern, 2007) and it is suggested that between 700-1400 m of diatreme has been eroded since its formation (Skewes and Holgrem, 1993; Stern *et al*., 2010). Given this, it is likely that the full vertical extent of the pipe was in excess of 3.5 km.

The Braden Breccia (Figure 3.4I) is a well-consolidated, polymictic breccia consisting of altered diorite, dacite and mafic clasts in a rock flour matrix (Howell and Malloy 1960; Maksaev *et al*., 2004; Cannell, 2004). The pipe can be subdivided into two breccia facies: the mineralised marginal breccia, rich in tourmaline and sulphides; and the largely barren rock flour breccia that forms the bulk of the fill. The Braden Breccia pipe is interpreted to be a diatreme (e.g. Maksaev *et al*., 2004), which based on K-Ar sericite dates was interpreted to have formed between 4.7 and 4.6 Ma (Cuadra, 1986). Several studies have suggested that the Braden Breccia pipe is mostly barren with respect to sulphide mineralisation and that its formation marked the end of significant economic mineralisation at the deposit (Cannell *et al*., 2005, 2007; Vry *et al*., 2010). However, Skewes and Stern (2007) predicted that it contains >1 Mt of Cu at grades of >0.7 wt.%. Cu, and >5 Mt Mo at an average grade of 0.4 wt.%. Evidence of mineralisation is particularly abundant towards the pipe walls, where the cement commonly contains molybdenite and minor Cu-oxide staining (Figure 3.4J).

3.3.4 Mineralisation

Hypogene Mineralisation

Chalcopyrite, bornite and molybdenite are the three most abundant hypogene ore minerals at El Teniente (e.g. Camus, 1975). These predominantly occur in zones of intense stockwork veining surrounding intrusion-breccia complexes (e.g. Maksaev *et al*., 2004, 2009; Vry *et al*., 2010). It has been estimated that 60 to 80% of mineralisation is hosted within these veins with only minor additional disseminated sulphides found throughout the altered TMC (Camus, 1975; Cannell, 2004; Cannell *et al*., 2007; Vry *et al*., 2010). The remaining 20-40% is interpreted to be hosted within felsic intrusions and in the cements of the igneous and hydrothermal breccias (Skewes *et al.,* 2002; Cannell *et al.,* 2005).

Previous studies concluded that Cu mineralisation is broadly zoned around the relatively barren cores of the Teniente Dacite Porphyry and Braden Breccia pipe (e.g. Camus, 1975; Cannell, 2004; Figure 3.5). This distribution has been interpreted as a classic porphyry zonation, centred on the Teniente Dacite Porphyry (Howell and Molloy, 1960; Cannell, 2004; Klemm *et al*., 2007). However, it has also been suggested that the Teniente Dacite Porphyry truncates earlier mineralised breccias (Skewes *et al*., 2002; Skewes *et al*., 2005; Stern *et al*., 2007). In addition, high Cu grades also occur within and surrounding other intrusions, including the diorites and the A-Porphyry (Vry *et al*., 2010). This led to the suggestion that coalesced vein halos associated with multiple intrusions are the primary control on Cu grade distributions.

Mo forms a near-continuous concentric ring surrounding the Braden Breccia pipe with highest grades (~0.1 wt.%) occurring at approximately 100-250 m outboard of its contact with the TMC (Cannell, 2004; Figure 3.13). Mo highs are also recognised in peripheral and deeper parts of the deposit proximal to the A-Porphyry, the Central Diorite and the North-Central Diorite leading to the suggestion that these intrusions were linked to Mo introduction (e.g. Vry *et al*., 2010). A detailed comparison of Mo and Cu grade distributions is presented in the following chapter.

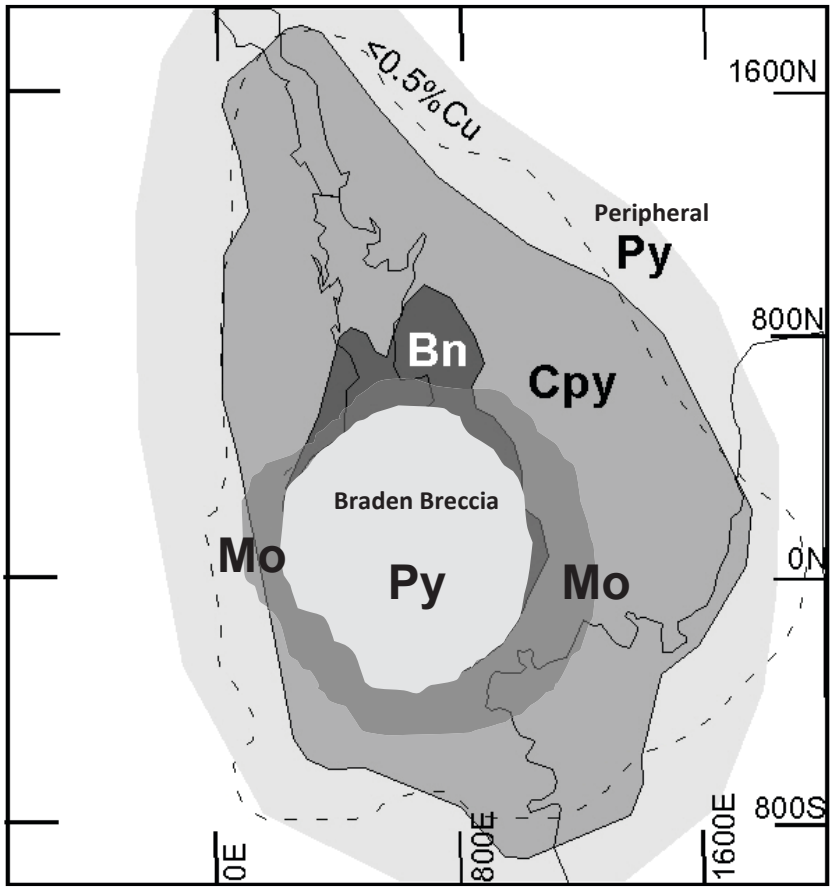


Figure 3.5: Sulphide zonation at El Teniente based on the grade distribution database of Arevalo and Floody (1995). Bornite (Bo) occurs proximal to and within the Teniente Dacite Porphyry and grades outwards into chalcopyrite (Cpy) and peripheral pyrite (Py) zones. Pyrite is also the predominant sulphide within the Braden Breccia pipe. This is surrounded by a zone of abundant molybdenite (Mo) that forms a zone of high Mo grades outside the Braden Breccia pipe (e.g. Vry, 2010). Figure adapted from Cannell (2004).

Supergene Enrichment

A zone of supergene enrichment originally overlay hypogene mineralisation at El Teniente, at approximately 100-600 m below the premining surface (e.g. Cuadra, 1986). This was composed of an upper leached zone containing abundant Cu oxide minerals including chrysocolla, malachite, azurite, cuprite, brochantite and chalcophyllite (Cuadra, 1986). Secondary Cu sulphides including chalcocite and covellite are dominant in the lower portions of the supergene zone. Development of these minerals was accompanied by argillic alteration which was most intense in the southern section of the ore body at the contact of the Sewell Tonalite and the TMC (Camus, 1975). Supergene Mo products are rare at the deposit with only minor ferrimolybdite ($Fe_2(MoO_4)_3 \cdot 8H_2O$) reported in the leached zone (Camus, 1975).

3.4 Structural Geology and Structural Evolution

El Teniente lies at the junction between the northeast-trending Teniente Fault Zone and the northwest-trending Codegua Fault (Figure 3.6A). The Teniente Fault Zone comprises a series of anastomosing strike-slip faults that form a 3 km wide zone of deformation and argillic alteration that extends over 14 km (Camus, 1975; Cuadra, 1986; Garrido *et al*., 1994; Skewes *et al*., 2002; Cannell *et al*., 2005). Surface expressions of the crustal-scale Codegua Fault are yet to be observed (Camus, 1975; Cannell *et al*., 2005). However, its trend is clearly represented by the alignment of several relict volcanic centres (Figure 3.6A) that are predominantly late Miocene in age (Rivera and Falcón, 2000; Cannell, 2004).

Evidence of large fault displacements is rare within the El Teniente mine area. However, displacement is documented by offset veins, fault breccias and slickensides (Figure 3.7). A number of east-northeast-trending faults that follow the trace of the Teniente Fault zone have been recognised by CODELCO Division El Teniente (Figure 3.6B). In addition, a number of tourmaline-anhydrite breccia zones, thick quartz veins and lamprophyre dikes follow similar trends, leading to the suggestion that that their formation is linked to the Teniente Fault Zone (Garrido *et al*., 1994). The sub-parallel alignments of the Teniente Dacite Porphyry and diorite finger porphyries with the Codegua Fault suggest that it may have played an important role in their emplacement. In addition, several other faults follow similar trends to the Codegua Fault, including the molybdenite-rich B-Fault (Figure 3.6B). Mine geologists have reported right-lateral, strike-slip displacement along faults in this zone, which has created slickensides on molybdenite that coats fault planes (Figure 3.7B-C). Recent local seismic activity suggests that the Codegua Fault is still active (Garrido *et al*., 1994).

Although both major faults have been implicated in the formation of El Teniente, analysis of vein orientations reveals that most veins do not follow sub-parallel trends (Cannell *et al*., 2005). Instead, they appear to be randomly oriented or occur in concentric and radial configurations centred on the Braden Breccia pipe (Figure 3.6B). Consequently, it was concluded that far-field stress regimes were not important during mineralisation (Cannell *et al*., 2005).

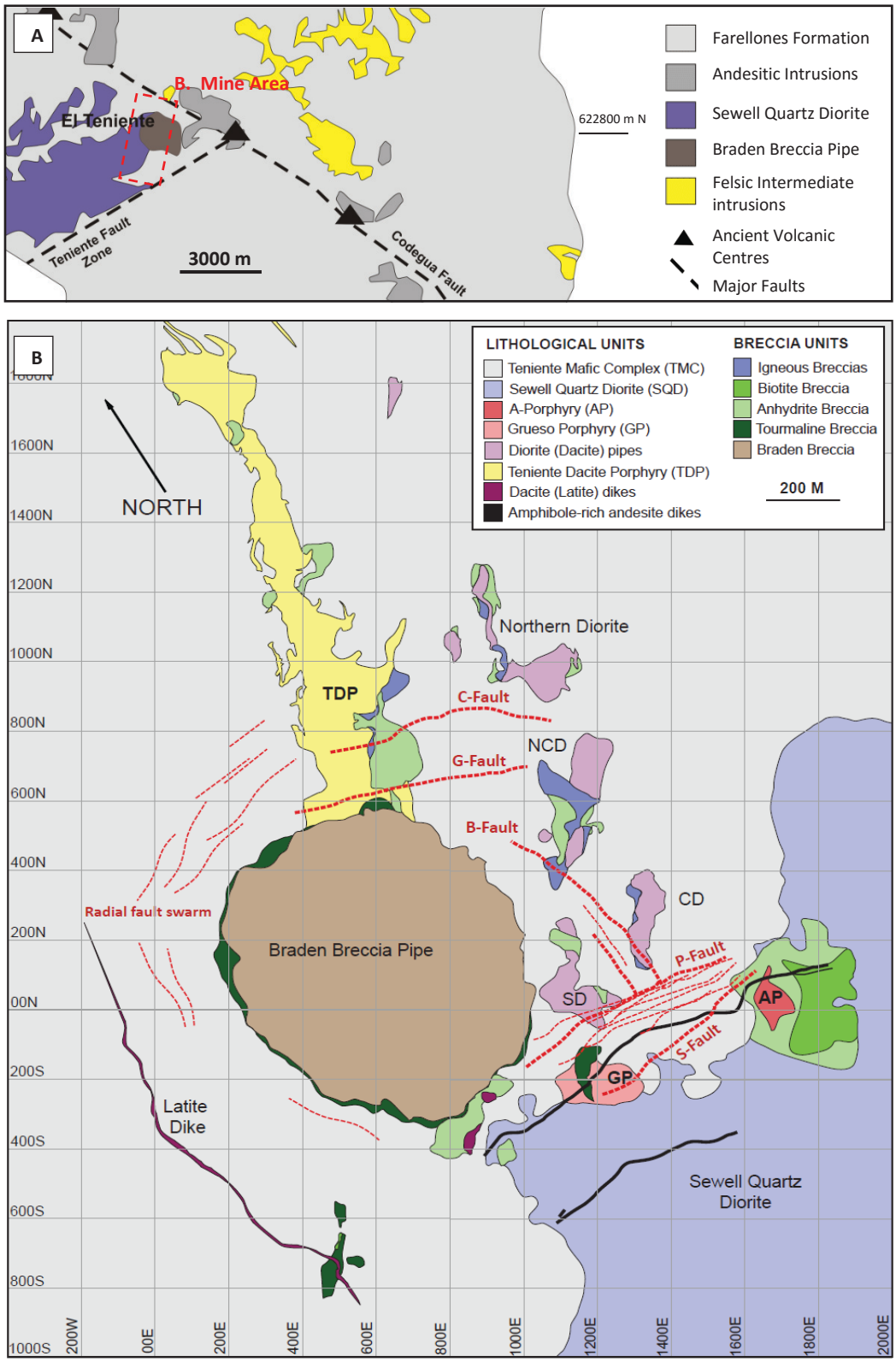


Figure 3.6: Regional and local structural geology of the El Teniente mine area. (A) Geology of the Teniente district (after Cannell *et al.*, 2005, adapted from Vry, 2010) showing the locations of the Teniente Fault Zone and interpreted trend of the Codegua Fault, as indicated by the alignment of volcanic centres (Rivera and Falcón, 2000). The El Teniente mine area is indicated by the red box. (B): Geological map of the El Teniente mine area at an elevation of 2165 m above sea-level (asl). Dotted red lines = faults. Large faults (thick lines) are labelled according to the mine classification of CODELCO Division El Teniente.

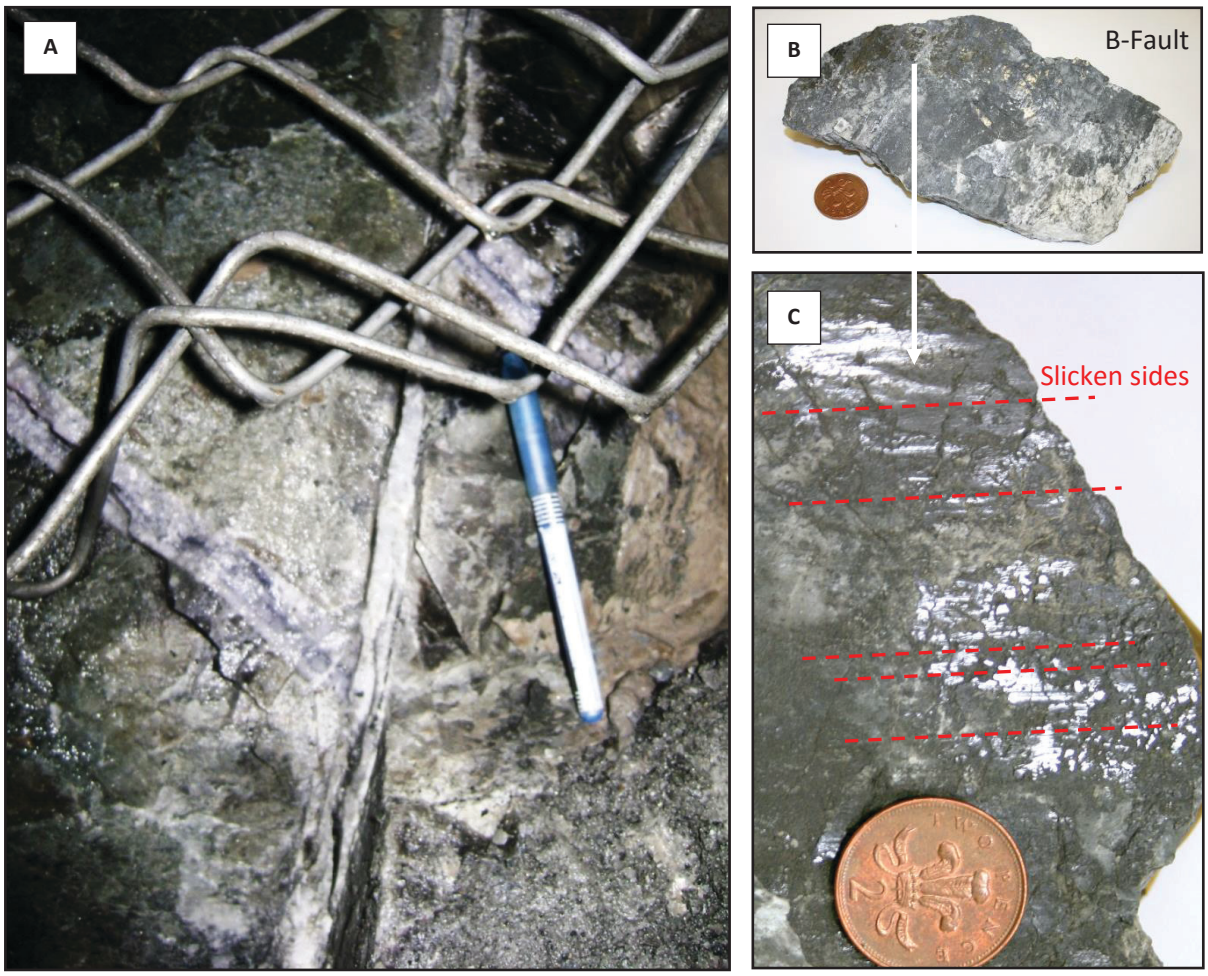


Figure 3.7: Photographs showing evidence of fault displacement at El Teniente. (A) Displaced quartz-molybdenite vein in underground mine face. Photograph courtesy of CODELCO Division El Teniente. (B-C) Whole rock sample from the northwest-trending B-Fault (Figure 3.6) containing slickensides that overprint molybdenite mineralisation.

Based on vein distributions and field observations, Cannell *et al*. (2005) proposed a three-stage structural evolution for El Teniente (Figure 3.8). This commenced with the emplacement of a deep level pluton which led to doming and the formation of inwardly dipping late magmatic and principal hydrothermal veins centred on the middle of the deposit (Figure 3.8A). During this period, the emplacement of multiple finger porphyries is interpreted to have resulted in the formation of dense vein halos, possibly as a result of local fluid pressures exceeding stresses induced by the intruding magma (e.g. Burnham, 1979). These veins correspond to the main- mineralisation stage veins classified by Vry *et al*. (2010). This was followed by an inferred period of magma withdrawal. Subsidence related to this event led to the development of steeply dipping, concentric fractures that surround the

current position of the Braden Breccia pipe (Figure 3.8B). These were exploited by fluids to form late hydrothermal veins, thought to form during a period of low magma pressure (Koide and Bhattacharji, 1975; Cannell *et al*., 2005).

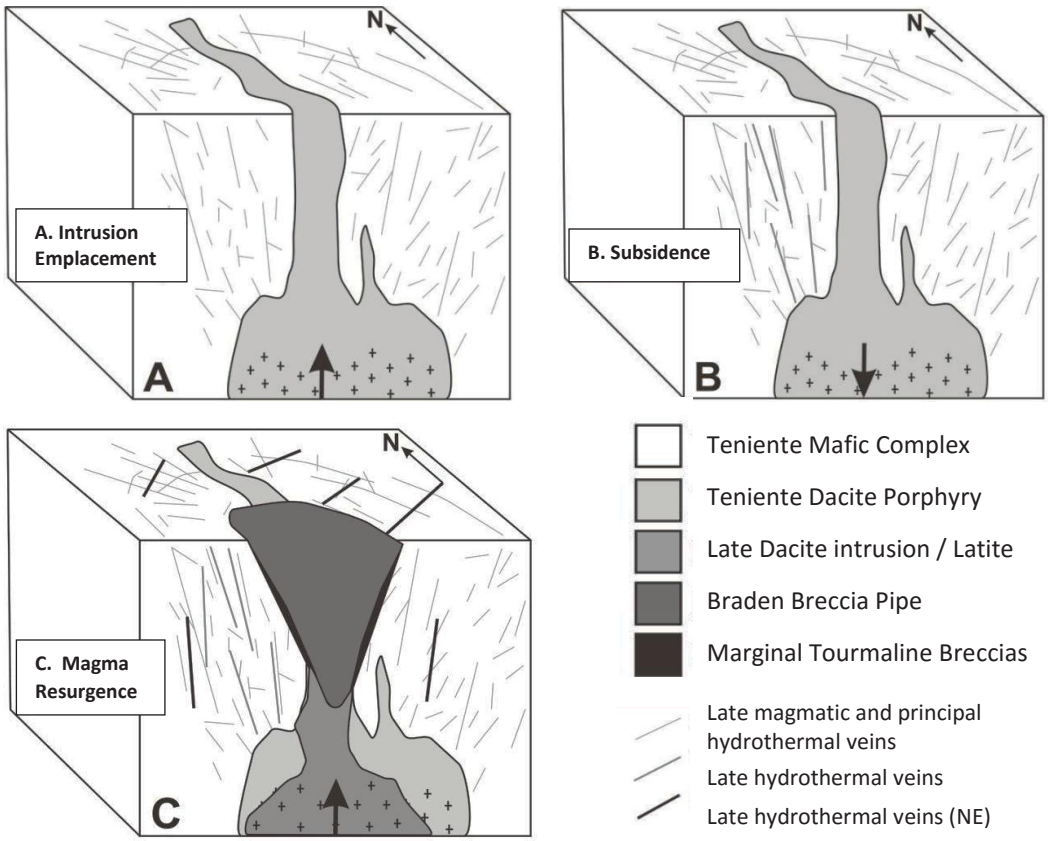


Figure 3.8: Schematic model showing the structural evolution of El Teniente proposed by Cannell *et al*. (2005) based on vein orientations and field observations. (A) Doming related to the emplacement of a magma chamber. (B) Magma withdrawal and related subsidence stage. (C) Magma resurgence and Braden Breccia pipe formation. Figure adapted from Cannell *et al*. (2005) and Vry (2010).

A major magmatic resurgence is then interpreted to have reactivated the concentric faults in reverse, leading to the emplacement of latite dikes and marginal breccia zones (Figure 3.8C). Eventually, lithostatic pressure was exceeded by late stage fluid and/or magmatic pressure, leading to the explosive formation of the Braden Breccia pipe. Based on the presence of brecciated tourmaline within the Braden diatreme, this is interpreted to have occurred after the formation of the marginal tourmaline breccias (Cannell *et al*., 2007). Finally, the late northeast- trending faults and lamprophyre dykes (Figure 3.2) were formed in response to renewed movement along the Teniente Fault Zone as the system waned.

This model implicates underlying magmatism as the key control on the structural evolution and vein orientations at El Teniente. However, it does not discount the possibility that the larger fault structures played important roles in the emplacement of intrusions. Furthermore, constraints on the timing of some faults remain speculative, including the northeast-trending and molybdenite-rich B-Fault. It is also unclear whether the dense vein halos surrounding each intrusion were formed by localised stress perturbations (Cannell *et al*., 2005) or are purely a manifestation of the intrusions acting as effective conduits for multiple pulses of hydrothermal fluid (Vry *et al*., 2010). Finally, the lack of precise dating of the Braden Breccia event means that its relationships with the concentric and radial faults, the marginal tourmaline breccias and late mineralisation stage veins remain unclear.

3.5 Vein Classification Schemes

Crosscutting relationships have been used to determine the relative timing of vein and breccia development at El Teniente (Figure 3.9). To date, three vein classification schemes have been defined based on vein mineralogy, timing and associated alteration (Figure 3.10: Vry *et al*., 2010; Mine Classification, 2003; Cannell *et al*., 2005). In this study the classification of Vry *et al*. (2010) was adopted (Figure 3.10: Classification 1). This consists of 13 vein types (Figure 3.11) that comprise three paragenetic stages: (1) the premineralisation stage, associated with potassic alteration (K-feldspar alteration and biotitisation); (2) the main mineralisation stage, consisting of quartz and/or anhydrite veins with alteration halos grading from minor potassic (type 5) to none (6a to 7b) to sericitic (type 8); (3) the late mineralisation stage, consisting of veins containing tourmaline and sulphosalts, possibly related to the formation of the Braden Breccia pipe and its marginal breccia facies.

The classification of Vry *et al*. (2010) bears a number of similarities to the El Teniente Mine Classification (2003) documents 15 distinct vein generations (Figure 3.10, Classification 2: Cuadra, 1986; Valenzuela, 2003). This classification is divided into three main paragenetic stages of mineralisation: the late magmatic stage (associated with potassic alteration), the principal hydrothermal stage (associated with quartz-sericite alteration) and the late hydrothermal stage (associated with the breccias surrounding the Braden Breccia pipe and veins with intense quartz-sericite alteration). These stages are generally unaffected by supergene alteration except in shallow zones of mineralisation to the east of the Braden Breccia pipe at shallow mine levels (Cuadra, 1986; Valenzuela, 2003).

Cannell *et al*. (2005) presented an alternative classification composed of 13 distinct vein types, divided into 4 paragenetic stages (Figure 3.10: Classification 3). In this sequence a premineralisation stage was added before the late magmatic stage, which consists of vein types associated with intense potassic alteration. In contrast to the mine classification only one principal hydrothermal stage vein type is recognised (vein stage 3). This is interpreted to mark the onset of intense sericitic alteration that prevails throughout the late hydrothermal stage (4a-4d). The late mineralisation stage is also divided into four distinct vein types.

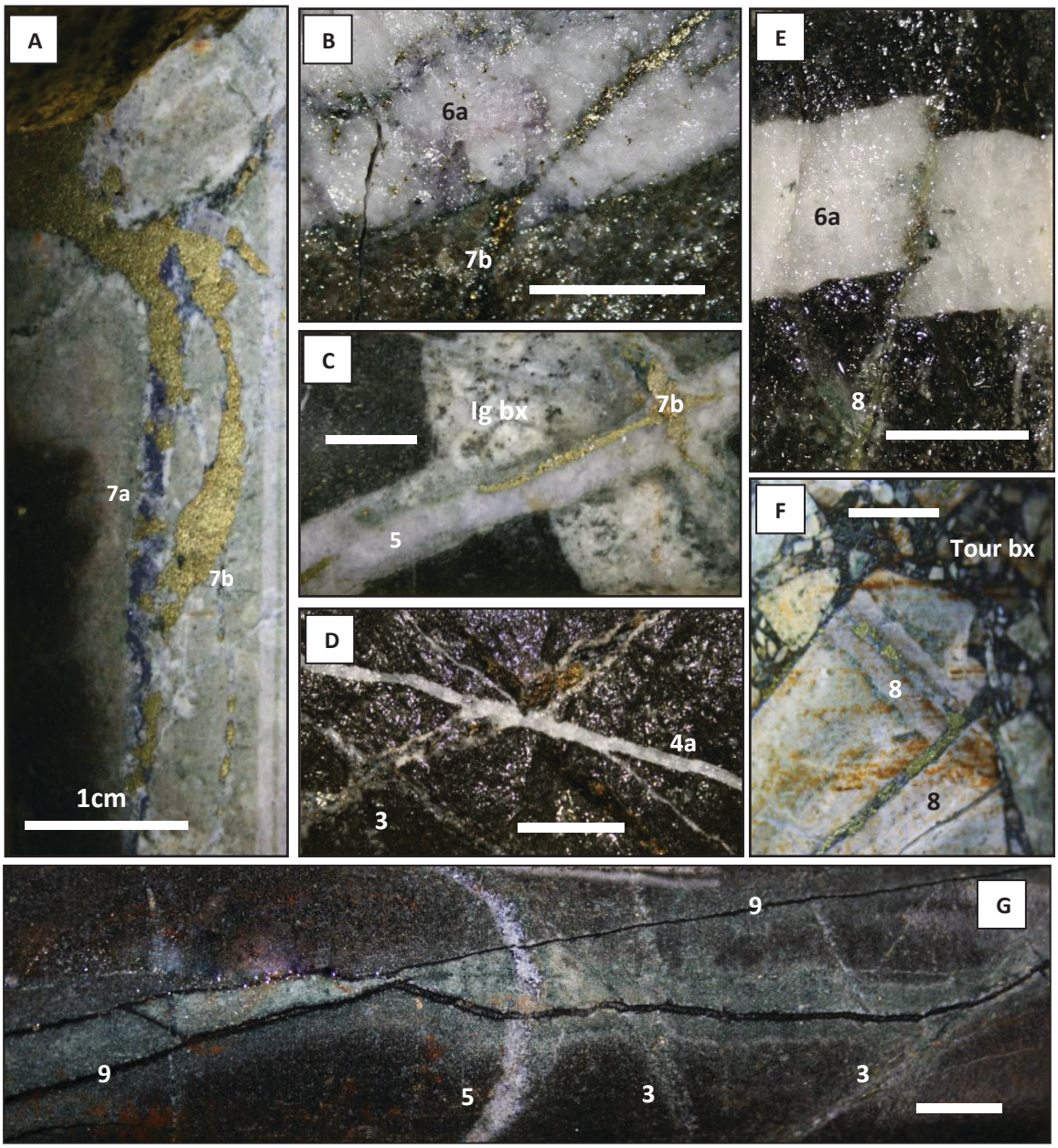


Figure 3.9: Examples of vein crosscutting relationships observed during this study. All vein types are labelled in accordance with the vein classification scheme of Vry *et al*. (2010). Scale bars = 1 cm. (A) Mo-rich type 7a vein overprinted by a Cpy-bearing type 7b vein (sample 2215-116.0). (B) Small type 7b vein with chalcopyrite cutting and offsetting a thick quartz-molybdenite type 6a vein alongside the Southern Diorite (1754-152.9). (C) Chalcopyrite-rich type 7b veins overprinting and replacing type 5 anhydrite veins that cut an igneous breccia at the western rim of the A-Porphyry (2305-121.0) (D) Thin, type 4a vein with no sulphides overprinting a type 3 biotite-quartz vein (1754-269.2) (E) Thick, type 6a vein cut and offset by a thin chalcopyrite-rich type 7b vein in the TMC proximal to the North Central Diorite (1034-899.1). (F) Type 8 veins in a clast of Teniente Dacite Porphyry truncated by type 9 tourmaline breccia at the western margin of the Braden Breccia pipe (2716-51.0). (G) Thin type 9 tourmaline veinlets with intense sericite alteration halos cutting and offsetting a 4 mm wide type 5 vein and several type 3 veins to the northwest of the Braden Breccia pipe, proximal to the Teniente Dacite Porphyry (2661-138.4). Abbreviations: Ig bx = igneous breccia, Tour bx = tourmaline breccia.

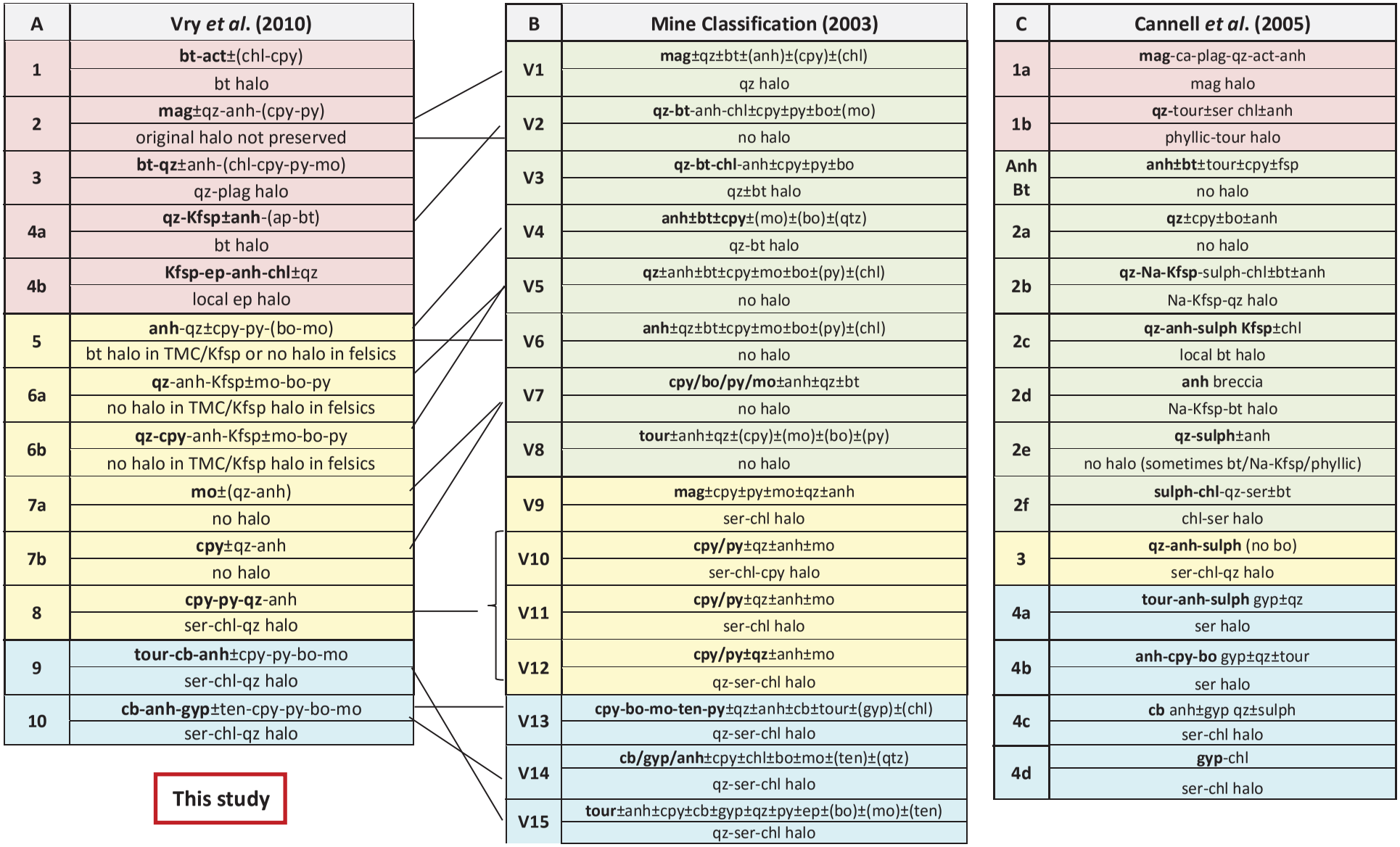


Figure 3.10: Pre-existing vein classification schemes for the El Teniente. (A) Classification 1: Defined by Vry *et al*. (2010). This sequence was selected for use during this study. (B) Classification 2: Pre-existing sequence used by mine geologists at the deposit. (C) Classification 3: Alternate scheme defined by Cannell *et al*. (2005). Paragenetic stages are shown in different colours: Red = Premineralisation stage veins; Green = late magmatic stage from El Teniente mine geologists (2003) and Cannell *et al*. (2005). Yellow = principal hydrothermal/main mineralisation; Blue = Late hydrothermal/late mineralisation stage.

Vein	Vein Mineralogy and alteration halos
1	**bt-act**±(chl-cpy)
	bt halo
2	**mag**±qz-anh-(cpy-py)
	original halo not preserved
3	**bt-qz**±anh-(chl-cpy-py-mo)
	qz-plag halo
4a	**qz-Kfsp±anh**-(ap-bt)
	bt halo
4b	**Kfsp-ep-anh-chl**±qz
	local ep halo
5	**anh**-qz±cpy-py-(bo-mo)
	bt halo in the TMC/Kfsp or no halo in felsics
6a	**Qz**-anh-Kfsp±mo-bo-py
	no halo in TMC/Kfsp halo in felsics
6b	**qz-cpy**-anh-Kfsp±mo-bo-py
	no halo in TMC/Kfsp halo in felsics
7a	**mo**±(qz-anh)
	no halo
7b	**cpy**±qz-anh
	no halo
8	**cpy-py-qz**-anh-mo
	ser-chl-qz halo
9	**tour-cb-anh**±cpy-py-bo-mo
	ser-chl-qz halo
10	**cb-anh-gyp**±ten-cpy-py-bo-mo
	ser-chl-qz halo

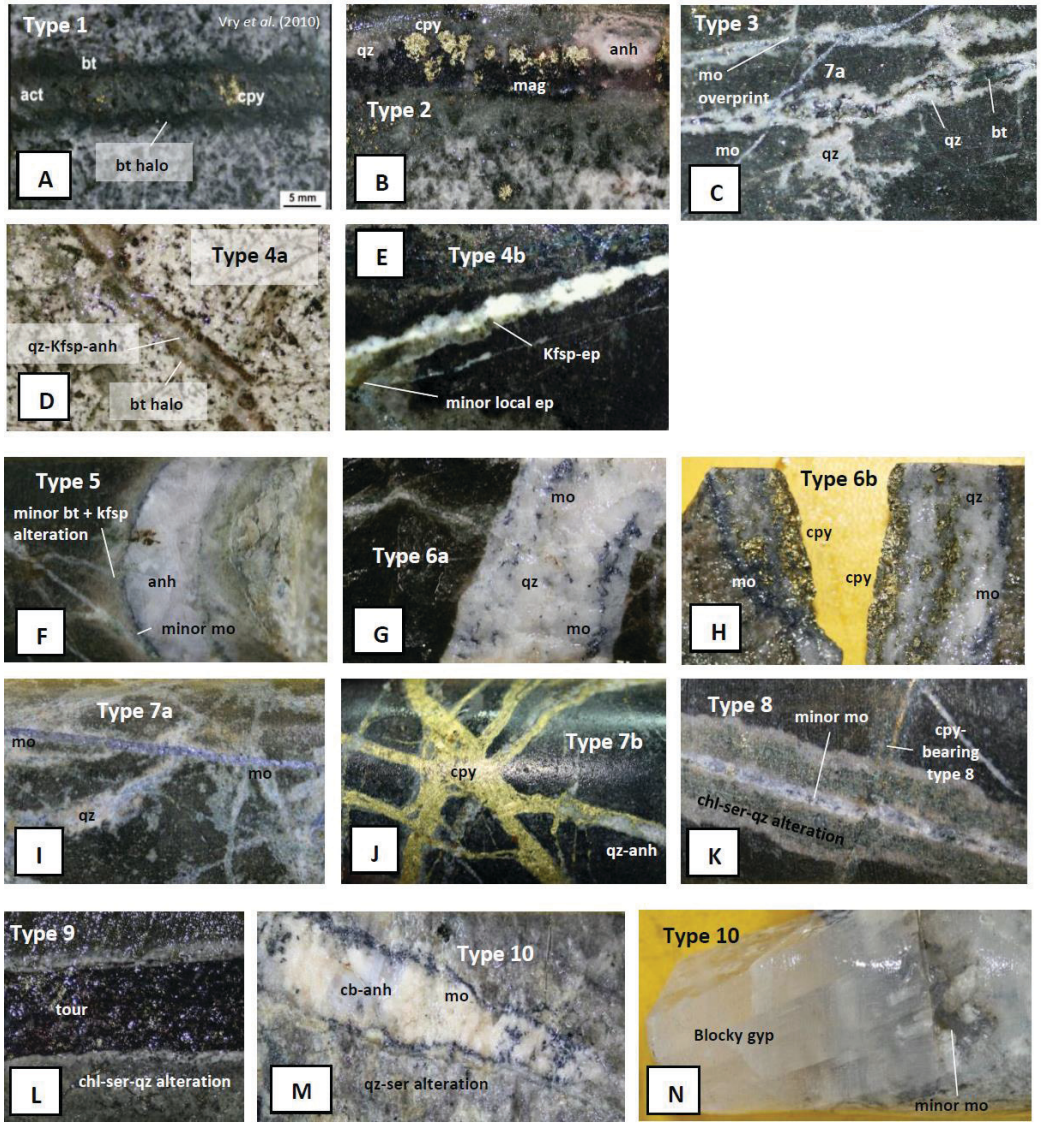


Figure 3.11 (previous page): Vein chronology of Vry *et al*. (2010) with example photographs of each vein type. The classification is divided into 3 main paragenetic stages: Red rows = Pre-mineralisation stage; Yellow = Main mineralisation stage; Blue = Late hydrothermal stage. Bold minerals = main constituents. Molybdenite mineralisation can be seen in type 3, 5, 6a, 6b, 7a, 8, 9 and 10 veins. (A) Type 1 Biotite-actinolite-chlorite vein with diffuse biotite halo in the Sewell Quartz Diorite (08/2483/13, DDH 2483, 294.90 m, courtesy of Vry *et al*. (2010); (B) Type 2 vein with magnetite and quartz overprinted and replaced by significant chalcopyrite mineralisation in the A-Porphyry (2305-178.1); (C) Quartz-biotite type 3 vein cut and overprinted by a molybdenite type 7a vein (2371-55.0); (D) Quartz-K-feldspar type 4a vein with wide, diffuse biotite halo in the A-Porphyry, cut and offset by small quartz type 6a veins (2305-57.95); (E) Type 4b vein with K-feldspar-epidote- anhydrite + minor chlorite within the TMC, proximal to the Sewell Quartz Diorite (1888-62.7); (F) Type 5 anhydrite vein with minor molybdenite in the Southern Diorite (2083-207.0); (G) Type 6a quartz vein with significant molybdenite mineralisation in the TMC at deep mine level (1805-381.3); (H) Type 6b quartz-chalcopyrite vein with early molybdenite at edges of vein and chalcopyrite in the centre proximal to the North Central Diorite (1754-258.3); (I) Type 7a molybdenite vein cutting type 3 and 4a veins in the TMC proximal to the North Central Diorite (2230-175.2); (J) Network of chalcopyrite-rich type 7b veins with minor quartz to the east of the North Central Diorite (2215-185.1); (K) Molybdenite-bearing type 8 anhydrite-quartz vein with sericitic alteration halo cut by a chalcopyrite-bearing type 8 vein proximal to the Teniente Dacite Porphyry (2661-174.4); (L) Type 9 tourmaline vein with minor molybdenite and chalcopyrite in sericite-altered section of the Teniente Dacite Porphyry south of the Braden Breccia pipe (2672-108.6). (M) Type 10 carbonate-anhydrite vein with quartz halo proximal to the Southern Diorite (2083-251.6); (N) Type 10 vein with large gypsum crystals from proximal to the Southern Diorite (2083-297.9). Mineral abbreviations: bt = biotite, act = actinolite, chl = chlorite, cpy = chalcopyrite, mag = magnetite, anh = anhydrite, py = pyrite, plag = plagioclase, Kfsp = K feldspar, ap = apatite, ep = epidote, mo = molybdenite, bo = bornite, tour = tourmaline, cb = carbonate, gyp = gypsum, ten = tennantite. ser = sericite.

Vein and breccia cross-cutting relationships reported by Cannell *et al*. (2005) and Vry *et al*. (2010) are generally consistent across the deposit. However, it is unclear whether this is due to the synchronous development of each vein type across the deposit or the diachronous development of similar cycles of veining, localised around each intrusion. The presence of reverse cross-cutting relationships, albeit rarely, would tend to imply that the latter model is more likely. In addition, the exact relationships between vein types remain poorly understood, in particular whether some developed coevally or cospatially, grading from one type into another.

Although the three vein classifications are broadly similar (Figure 3.10), there are some inconsistencies in the mineral assemblages and relative timing of formation. This is particularly apparent in the earliest and latest vein stages, possibly due to a lack of clear crosscutting relationships or as a function of intense overprinting and replacement. Contradictions may also be caused by vein reopening, which is likely to have created composite vein types that are not easily assigned to a particular vein stage (Vry *et al*., 2010).

This may explain the apparent repetition in magnetite- (V1 and V9), anhydrite- (V4 and V6) and tourmaline- (V8 and V15) veins reported in the mine classification (Classification 2: Figure 3.10).

Unlike the Mine classification (2003), Vry *et al*. (2010) combined mineralogically-similar vein types that occur at similar points in the sequence. For example, V4 and V6 veins in the Mine Classification are combined into a single, type 5, anhydrite vein stage. Sericite-altered V10, V11 and V12 veins in the Mine Classification are also grouped to create main mineralisation stage, type 8 veins. This was due to the fact that these veins appear to be from the same generation and only appear to be different due to their variable alteration halos which appear to be a function of host lithology. The early tourmaline + phyllic alteration stage identified in the Mine Classification (V8) and the Cannell *et al*. (2005) classification (type 1b veins) could represent an early tourmaline breccia-vein stage that predated the development of the mineralised system (c.f. Camus, 1975). This early stage is not present in the Vry *et al*. (2010) classification.

Vry (2010) suggested that discrepancies with the classification of Cannell *et al*. (2005) could be due to the fact that the Cannell *et al.* (2005) chronology was based on observations from only two relatively shallow drillcore transects (Figure 3.2). Because the pre-mineralisation stage veins are best preserved at depth (Vry *et al*., 2010), it is probable that this stage was not as well constrained as the later events. This, and the fact that the Cannell *et al*. (2005) classification displays several major discrepancies with the other two chronologies (Figure 3.10) led to it being discounted for use in this study.

The most important difference between the Vry *et al*. (2010) classification and the other classification schemes is that it separates main mineralisation stage type 6 and type 7 veins into molybdenite (6a-7a) and chalcopyrite (6b-7b) end-members. This distinction is imperative for a study of the decoupling of the two metals. These vein types are interpreted to have formed roughly synchronous (Vry *et al*., 2010), although it is noted that chalcopyrite-rich veins almost always overprint the molybdenite-rich veins in any given part of the deposit. This suggests that Mo deposition usually occurred before Cu-sulphide mineralisation at any one location, and that this sequence is consistent across the deposit.

3.6 Fluid Inclusion Studies

Several fluid inclusion studies have been completed at El Teniente (Ip, 1987; Kusakabe *et al*., 1990; Skewes, 1996, 1997; Skewes *et al*., 2002; Cannell 2004; Klemm *et al*., 2007; Vry, 2010). Three of these are relatively extensive microthermometric studies that provide reasonable constraints on the evolution of hydrothermal fluids at the deposit (Cannell, 2004; Klemm *et al*., 2007; Vry, 2010). These studies also helped constrain the chemical compositions of different fluids. Cannell (2004) used proton-induced X-ray emission (PIXE) microanalysis to study 32 inclusions in 7 samples from sections 124, 83 and 289 (Figure 3.2). The other two studies combined Scanning Electron Microprobe cathodoluminescence (SEM-CL) petrography with LA-ICP-MS analysis of individual fluid inclusions to determine the chemical evolution of fluids (Klemm *et al*., 2007; Vry, 2010). The study of Klemm *et al*. (2007) mainly sampled veins from shallow mine levels within and surrounding the Teniente Dacite Porphyry (Figure 3.2), based on the assumption that this intrusion was the most important intrusion with respect to Cu mineralisation. In contrast, Vry (2010) sampled inclusions from veins and breccias from several intrusive centres between 50N and 750N (Figure 3.2).

These studies revealed that a broad range of fluid types passed through the system, including vapours, aqueous liquids and brines of highly variable salinities, densities and chemical compositions. All studies recognised three major groups of inclusions: (1) undersaturated liquid-rich inclusions that homogenise to liquid; (2) vapour-rich inclusions that homogenise to vapour; and (3) salt-saturated inclusions that contain halite crystals at room temperature. Vry (2010) suggested that these can be divided into 8 separate fluid inclusion subtypes (Figure 3.12) based on their vapour fractions and contained daughter phases. Although similar classifications are provided by Cannell (2004) and Klemm *et al*. (2007) the nomenclature used in these studies is confusing (Figure 3.12). Throughout this study, the names of fluid inclusion types are presented in accordance with the style of Vry (2010) to avoid confusion. Where relevant, the results of Cannell (2004) and Klemm *et al*. (2007) are presented in accordance with the vein chronology and fluid inclusion classifications of Vry (2010) to allow for direct comparative analysis. Summaries of fluid inclusion microthermometric data and LA-ICP-MS results from these studies are given in Appendix 4 and Appendix 5 respectively.

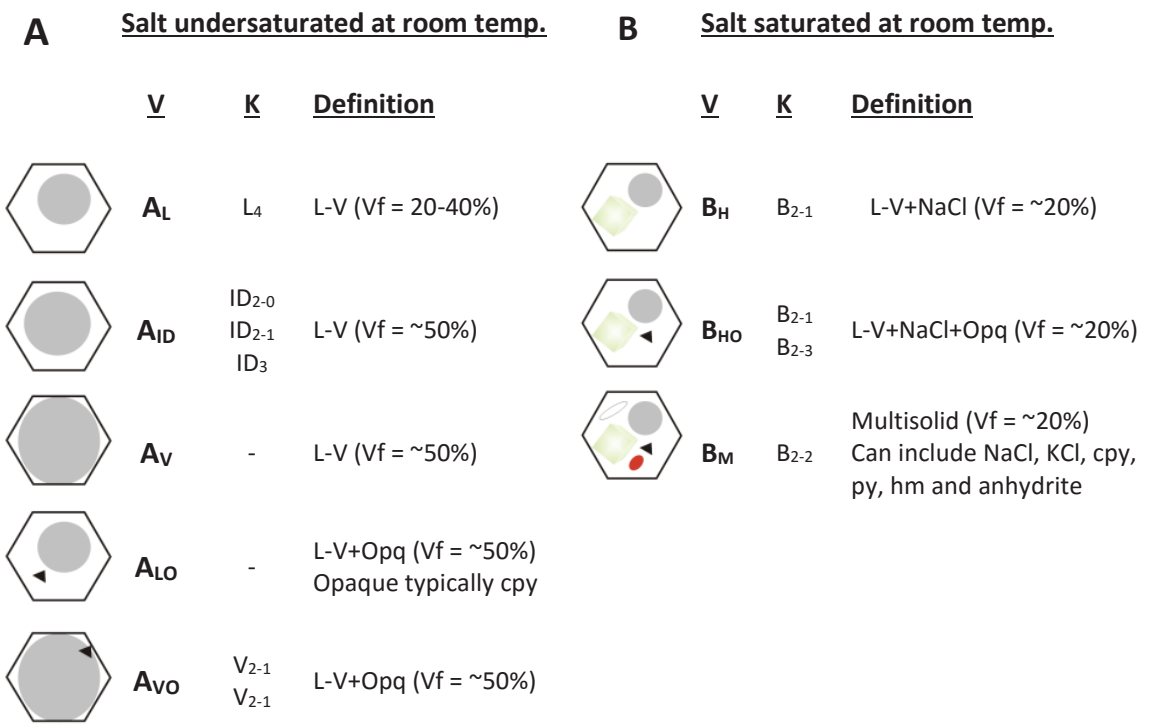


Figure 3.12: Classification scheme for fluid inclusion types at El Teniente according to Vry (2010) based on daughter phases and vapour fractions (Vf) at room temperature. Type A = salt undersaturated inclusions, subdivided by vapour fractions and the presence of opaque daughter crystals. Type B = salt saturated inclusions, subdivided by daughter phase assemblages. Bold acronyms = names according to Vry (2010) where subscript L = liquid-rich, ID = intermediate density, V = vapour-rich, H = halite-bearing, and M = multisolid-bearing. K = corresponding inclusion types according to Klemm *et al*. (2007). Abbreviations: cpy = chalcopyrite, hm = hematite. Figure adapted from Vry (2010).

3.6.1 Premineralisation Stage

Due to a lack of quartz and well-preserved fluid inclusions in pre-mineralisation stage veins and breccias, only 11 samples have been analysed (Klemm *et al*., 2007; Vry, 2010). These are dominated by high salinity brines (B_H + B_{HO} inclusions) that are interpreted to have formed at temperatures of >400°C and pressures >50 MPa (Vry, 2010). These are cut by trails containing moderate to low salinity A_L and A_{ID} inclusions that probably represent primary inclusions from the main mineralisation stage (Klemm *et al*., 2007; Vry, 2010). Based on consistent LA-ICP-MS results, Vry (2010) suggested that type 1-3 veins may have formed broadly synchronously across the deposit. Type 4a veins are constrained to be the first vein type to postdate emplacement of the A-Porphyry. These were interpreted to have formed at >330°C and >50-100 MPa (Vry, 2010). However, due to a lack of analysed samples, trapping condition estimates are poorly constrained.

LA-ICP-MS analysis of early brine inclusions reveals that they typically contain low concentrations of Cu and very low concentrations of Mo, indicating that they are not economically important fluids (Klemm *et al*., 2007; Vry, 2010). Vry (2010) also reported relatively low Zn and Mn concentrations in the brine inclusions. As these elements normally partition strongly into saline fluids during vapour-brine partitioning it was suggested that these fluids represent primary magmatic brines exsolved directly from the melt (Figure 3.13). Early brine inclusions also display negative correlations in K, Cs and Rb to Na from vein stages 1-5, attributed to the incorporation of these elements into K-feldspar (and potentially biotite) which replaced plagioclase during early potassic alteration (Vry, 2010). However, these trends were not identified in the previous PIXE and LA-ICP-MS studies (Cannell, 2004; Klemm *et al*., 2007).

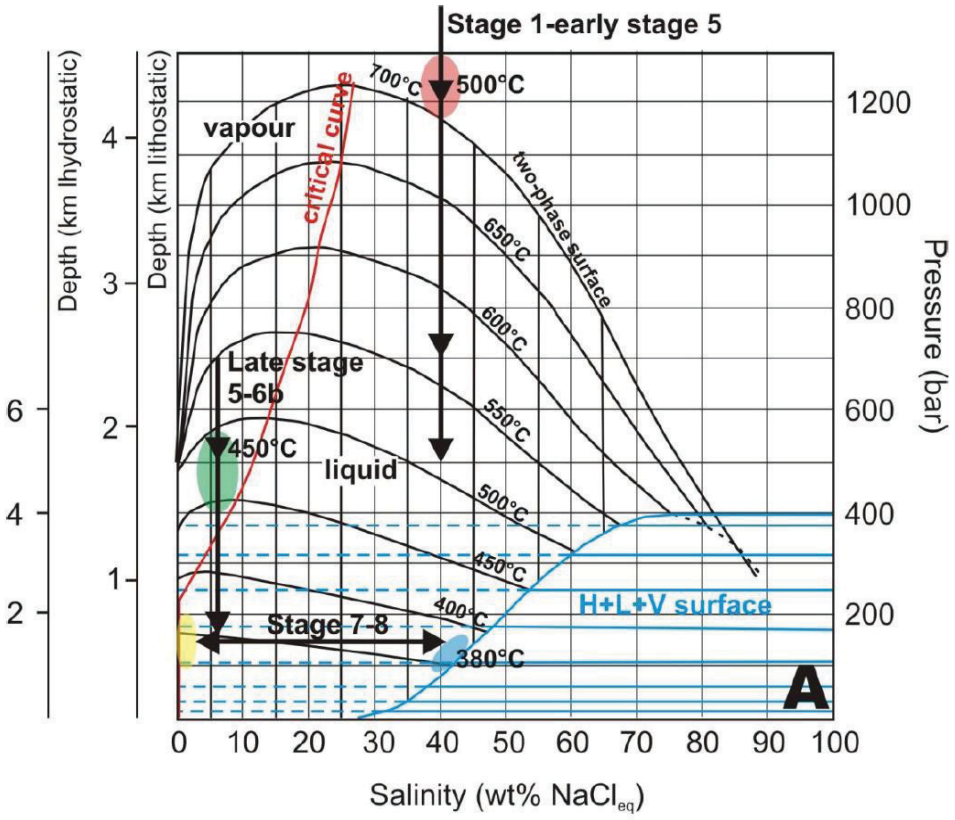


Figure 3.13: Pressure-composition phase diagram (after Driesner and Heinrich, 2007) illustrating the evolution of fluids at El Teniente according to Vry (2010). The critical curve defines the crest of the two phase surface and represents the locus of critical points for fluids of variable salinity. Stage 1-5 veins contain inclusions that were likely exsolved as single-phase, high salinity liquids (red). Main mineralisation stage fluids were likely exsolved as low-moderate salinity, liquid-like fluids (green) that crossed the critical curve above the two-phase field giving rise to intermediate density fluid inclusions. Continued decompression led to progressive boiling and the formation of coexisting brines and vapours in type 7 and 8 veins. Late stage brines could also be related to the input of new magmatic brines during the last stages of crystallisation. Figure from Vry (2010).

3.6.2 Main Mineralisation Stage

Vry (2010) suggested that there was a switch from the exsolution of primary high salinity (~40 wt.% $NaCl_{eq}$) fluids to the exsolution much lower density (~0.6 g/cm3), low salinity (~6 wt.% $NaCl_{eq}$) liquids during the type 5-6a vein stages (Figure 3.8). Cannell (2004) and Klemm *et al*. (2007) also reported a predominance of low salinity A_{ID} inclusions in type 6 veins. Laser Raman analysis of a limited number of inclusions detected only trace amounts (>0.1 mole %) of CO_2 (Cannell, 2004) and clathrate formation was only observed in a few A_{ID} inclusions (Klemm *et al*., 2007). Some of these A_{ID} inclusions appear to have coexisted with silicate melt inclusions, suggesting that they represent the primary magmatic fluid type. However, abundant hypersaline (60 wt.% $NaCl_{eq}$) brines that homogenise at higher temperatures have also been documented (Cannell, 2004), leading to the suggestion that the direct exsolution of magmatic brines may have continued into the main mineralisation stage (Vry, 2010).

Although A_{ID} inclusions are interpreted to represent the dominant primary fluid inclusion type in main mineralisation stage veins, low salinity vapours and aqueous inclusions that appear to coexist with high salinity brine inclusions have also been reported (Cannell, 2004; Klemm *et al*., 2007; Vry, 2010). SEM-CL petrography shows that these can occur on the same growth zones or as boiling trails where they exhibit consistent homogenisation temperatures (Cannell, 2004; Klemm *et al*., 2007; Vry, 2010). Unlike the premineralisation stage brines, these later brines are relatively enriched in Mn, Zn and Mo, whereas the vapour inclusions are enriched in As and Au suggesting that they were produced by phase separation (e.g. Vry, 2010). All three studies proposed broadly similar fluid evolution models for the main mineralisation stage, in which intermediate density (~0.6 g/cm^3), low salinity (6-7.5 wt.% $NaCl_{eq}$) fluids underwent phase separation as a result of decompression to form coexisting, low salinity (<3.7 wt.% $NaCl_{eq}$) vapours and high salinity (25-60 wt.%) liquids and brines (Figure 3.13). Based on Na concentrations, Klemm *et al*. (2007) suggested that phase separation led to the generation of approximately 70% vapour to 30% brine by mass.

Pressure(-temperature) fluctuations related to multiple cycles of fracture opening and chemical sealing by mineral precipitation within the system are then interpreted to have led to the entrapment of inclusions with varied fluid densities in different parts of the deposit

(Klemm *et al*., 2007). Such fluctuations may have resulted in pressure-temperature conditions passing through the retrograde solubility domain of quartz (ref.), leading to quartz redissolution and the creation of sulphide-dominated, type 7 veins (Vry, 2010).

Although fluid evolution models for the main mineralisation stage are similar, there are several key discrepancies. Klemm *et al*. (2007) reported relatively consistent K/Na, Fe/Na and Cs/(Na+K+Mn+Fe) ratios for fluid inclusions in the different vein types studied. This led to the conclusion that fluid evolution occurred contemporaneously across the entire deposit and was derived from a magma chamber that did not undergo a significant degree of fractionation during the main mineralisation stage. However, this interpretation was only based on LA-ICP-MS analysis of 49 fluid inclusions in vein samples from a small zone proximal to the Teniente Dacite Porphyry (Figure 3.2). A subsequent study by Vry (2010) on 550 inclusions revealed clear trends in fluid inclusion associated with each intrusion. For example, all fluid inclusion types from veins associated with the North Central Diorite exhibit an apparent enrichment in Mo, Ba and Sr suggesting that a system characteristic rather than an effect of element partitioning between different fluid types (Vry, 2010). This led to the suggestion that similar vein types in each system developed separately.

The timing of vapour brine separation also remains unclear. Klemm *et al*. (2007) suggested that it occurred early in the main mineralisation stage and occurred synchronously across the deposit at temperatures of ~410°C and pressures of 200-300 bars following pressure drops exceeding 150 bars. Progressive boiling is then inferred to have produced subsequent separate brine and vapour generations in response to pressure fluctuations related to multiple cycles of opening and sealing of the fracture system. Cannell (2004) proposed a similar model in which vapour-brine partitioning occurred early in the main mineralisation stage. Intermediate salinity fluids (5-20 wt.% $NaCl_{eq}$) were then interpreted to be produced by the partial re-equilibration of brines and vapours with low-salinity magmatic fluids (Cannell, 2004). These intermediate salinity fluids are thought to have undergone phase separation during the deposit-wide development of type 8 veins, coincident with a change to hydrostatic pressures and brittle conditions related to rapid uplift and erosion. Assuming boiling of a fluid with a salinity of <7.5 wt% $NaCl_{eq}$), coexisting vapour and brine inclusion properties imply formation depths of <2500 m at temperatures of approximately 380°C.

Vry (2010) also stated that boiling assemblages are most abundant in type 8 veins, where they homogenise between 340 and 380°C (Figure 3.13). These apparently coexisting vapour and brine inclusions were interpreted to have formed under low confining pressures of <200 bars (Vry, 2010; Figure 3.13). High salinity (>50 wt.% $NaCl_{eq}$) brine inclusions that homogenise by halite dissolution at temperatures >500°C were also recorded in some deep type 6a veins. These are similar to the high temperature brines interpreted to be the result of early vapour-brine partitioning by Cannell (2004) and Klemm *et al*. (2007). Given this, it is possible that apparent boiling trails in the type 8 veins represent resurgent boiling assemblages from contracted vapours created by boiling at greater depths. However, the general restriction of these brine inclusions to deep 6a veins led to the suggestion that they may represent evolved premineralisation brines (Vry, 2010).

LA-ICP-MS analysis of inclusions believed to have been trapped during the main mineralisation stage has revealed that Cu concentrations are sometimes very high (0.5-2 wt.%) in low salinity, sulphur-rich vapour inclusions (Klemm *et al*., 2007; Vry, 2010). In contrast, Mo concentrations are generally low (<50 ppm) in vapour inclusions but are typically high (100-10000 ppm) in the B_H, B_{HO} and B_M inclusions (Vry, 2010). Based on this, both studies proposed that the differential complexation behaviour of Mo and Cu during vapour-brine partitioning was the key control on Mo-Cu decoupling. However, both studies did not consider the possible effects of post-entrapment modification of fluid inclusions by Cu diffusion (Lerchbaumer and Audétat, 2012), which would have significantly increased Cu concentrations in S-rich vapour inclusions (Section 2.4.5). Klemm *et al*. (2007) stated that only the multisolid B_M inclusions contain very high Mo concentrations (600-1800 ppm) and therefore represent the most important fluid type with respect to Mo mineralisation. However, these fluid inclusions were the least abundant type recorded by Vry (2010).

All previous studies concluded that sulphide-dominated, type 7 veins are the most important with respect to Cu mineralisation at El Teniente. This is supported by their abundance across the deposit (Cannell 2004) and the fact that, relative to earlier vein stages, fluid inclusions in type 8 veins are depleted in Cu suggesting efficient deposition in the preceding stage (Klemm *et al*., 2007; Vry (2010). Cu sulphide precipitation is interpreted to have been primarily controlled by decreasing temperature (Klemm *et al*, 2007; Vry, 2010)

based in part on a roughly four-fold decrease in Cu/(Na+K+Mn+Fe) ratios between 410° and 320°C (Klemm *et al*. 2007). Unlike Cu, the most important veins and physical variables controlling Mo mineralisation are not well understood. Mo/(Na+K+Mn+Fe) ratios show a poor correlation with decreasing temperature, leading to the suggestion that this may not have been the main control on Mo mineralisation (Klemm *et al*., 2007).

3.6.3 Late Mineralisation Stage

To date, only a few late mineralisation stage veins have been analysed for their microthermometric properties. Both Klemm *et al*. (2007) and Cannell (2004) reported the presence of abundant, irregularly-shaped, type A_L inclusions. These exhibited slightly lower homogenisation temperatures (~325°C) than the main mineralisation stage and were interpreted to have been trapped at pressures below 170 bars (Cannell, 2004). Cannell (2004) also reported the presence of high salinity liquids and brines (10-67 wt.% $NaCl_{eq}$). The highly variable salinities and densities of these inclusions led to the proposition that late mineralisation stage fluids were produced by the mixing of late magmatic fluids with meteoric waters. Such fluid mixing may have played an integral role in the precipitation of base metal sulphides and sulphosalts in this stage.

No fluid inclusions hosted by late mineralisation stage veins or breccias have been studied using LA-ICP-MS analysis. However, SEM-CL petrography of main mineralisation stage veins indicated cross-cutting, liquid-rich inclusions that were interpreted to represent the latest fluids (Klemm *et al*., 2007). LA-ICP-MS analyses of these late stage liquid inclusions in two samples revealed the highest As/(Na+K+Mn+Fe) and B/(Na+K+Mn+Fe) ratios of all inclusion types (Klemm *et al*., 2007). Based on this, it was suggested that late mineralisation stage fluids were derived from fractionated vapours produced during the main mineralisation stage that contracted to liquids as the boiling front retracted during the waning of the hydrothermal system. However, Vry (2010) noted that the “late stage” fluid inclusion chemistry presented by Klemm *et al*. (2007) is considerably different to that measured in main mineralisation stage vapours. This led to the hypothesis that the late mineralisation fluids represent the final fluids exsolved from a highly evolved magma chamber.

3.7 Re-Os Molybdenite Geochronology

Both Re and Os are incorporated directly into the structure of sulphide minerals in variable proportions when they form (e.g. Stein *et al*., 2001). Molybdenite is particularly suitable for dating because it typically contains high concentrations of Re (ppm to wt.%) and no initial Os meaning that all Os present is essentially radiogenic ^{187}Os formed by the post-mineralisation β-decay of ^{187}Re (Stein *et al*., 1998; Selby and Creaser, 2001). Since molybdenite was first used in Re-Os isotopic dating studies (e.g. Hirt *et al*., 1963; Herr *et al*., 1967), techniques for sample preparation and analysis have become increasingly sophisticated allowing for the collection of highly reproducible mineralisation ages (e.g. Watanabe and Stein, 2000; Maksaev *et al*., 2004; Cannell 2003, 2004). Now, the Re-Os molybdenite geochronometer is an extremely accurate and precise technique for dating phases of sulphide mineralisation in ore deposits.

Unlike some of the other dating techniques used at El Teniente, including K-Ar the $^{40}Ar/^{39}Ar$ sericite systems, the Re-Os isotopic system typically displays closed-system behaviour during post-mineralisation hydrothermal alteration, ductile deformation and regional metamorphism (e.g. Stein *et al*., 1998; Selby and Creaser, 2001; Stein and Bingen, 2002; Bingen and Stein, 2003; Ootes *et al*., 2007; Bingen *et al*., 2008; Lawley and Selby, 2012). This, combined with the fact that molybdenite is the third most abundant ore mineral at El Teniente (Camus, 1975), makes Re-Os an ideal technique for dating mineralisation in this system. To date, a total of 18 molybdenite samples (Table 3.2; Figure 3.14) in two studies (Maksaev *et al*., 2004; Cannell 2004) have been dated at El Teniente. These include six of the eight molybdenite-bearing vein stages reported by Vry *et al*. (2010). Results reveal extensive mineralisation spanning a 1.8 My period.

The first Re-Os molybdenite study at El Teniente provided nine dates that were interpreted to represent five distinct episodes of Cu-Mo mineralisation at 6.30 ± 0.03, 5.60 ±0.02, 5.01–4.96, 4.89 ±0.08 to 4.78 ±0.03, and 4.42 ±0.02 Ma (Maksaev *et al*., 2004). These results were largely confirmed by Cannell (2004), who produced seven out of nine dates that fell within these five time periods. The close synchronicity of these pulses with U-Pb zircon ages for the A-Porphyry, Diorites and Teniente Dacite Porphyry led to the conclusion that mineralisation

was closely associated with the crystallisation of each of these intrusions (Maksaev *et al*., 2004; Cannell, 2004; Cannell *et al*., 2005).

Table 3.2: Previously determined Re-Os molybdenite dates for El Teniente.

Sample	DC	M	Original vein type description	VC	Date	Reference
2176	DDH 2176	73	Anh-bt breccia with cpy-mo hosted by Sewell Quartz Diorite with potassic alteration	**5**	**6.31±0.03**	Maksaev *et al*. (2004)
tt-Mo-1	DDH 1334	356	Anh breccia with cpy-mo hosted by Sewell Quartz Diorite with potassic alteration	**5**	**5.60±0.02** **5.60±0.02**	Maksaev *et al*. (2004)
TT-179	DDH 1556	551	Mo vein with pervasive qz-ser alteration in the Sewell stock	**8**	**4.89±0.08**	Maksaev *et al*. (2004)
tt-Mo-6	DDH 1514	185	Qz-mo vein with potassic alteration in the Teniente Dacite Porphyry	**6a**	**4.87±0.03**	Maksaev *et al*. (2004)
TT-174	DDH 2181	65	Mo vein hosted by bt altered TMC	**7a**	**4.83±0.03**	Maksaev *et al*. (2004)
TT-164	DDH 1303	229	Mo-cpy vein with ser halo hosted by Teniente Dacite Porphyry	**8**	**4.78±0.03**	Maksaev *et al*. (2004)
tt-Mo-5	DDH 1514	462	Mo-cpy vein with ser halo hosted by Teniente Dacite Porphyry ($^{40}Ar/^{39}Ar$ age 4.57±0.12 Ma)	**8**	**4.42±0.02**	Maksaev *et al*. (2004)
tt-Mo-7	DDH 1309	298	Qz-mo-cpy vein with pervasive qz-ser alteration in the Northern Diorite	**8**	**4.42±0.02**	Maksaev *et al*. (2004)
tt-Mo-8	DDH 1309	169	Qz-mo-cpy vein with pervasive qz-ser alteration in the Northern Diorite	**8**	**4.42±0.02**	Maksaev *et al*. (2004)
ET851	DDH 1529	9	Breccia surrounding A-Porphyry. Anh-bt-mo-cpy breccia cement	**5**	**5.883±0.036** **5.897±0.020**	Cannell (2004)
ET184a	DDH 1300	224	2c qz-mo-cpy vein without alteration halo cut by ET184b	**6a**	**5.006±0.096**	Cannell (2004)
ET184b	DDH 1300	224	3 qz-anh-mo-cpy vein with ser halo, cuts ET184a	**8**	**4.895±0.055**	Cannell (2004)
ET196	DDH 1134	273	2c/2e qz-mo vein without halo next to Teniente Dacite Porphyry	**6a**	**4.979±0.016** **4.960±0.016**	Cannell (2004)
ET215	DDH 1530	722	2e qz-mo-cpy vein with ser halo on deposit periphery	**6b**	**4.980±0.035**	Cannell (2004)
ET558	DDH 1666	390	2e qz-semi massive mo-cpy seam without alteration halo. Proximal to the Teniente Dacite Porphyry at depth	**6b**	**4.825±0.021** **4.805±0.016**	Cannell (2004)
ET144	DDH 1698	248	3 anh-mo-cpy-py vein with ser halo close to Northern Diorite	**8**	**4.854±0.018**	Cannell (2004)
ET783	DDH 1079	678	4c disseminated mo in anh breccia in ser altered deep late Teniente Dacite Porphyry close to Braden Breccia Pipe	**10**	**4.870±0.020** **4.835±0.016**	Cannell (2004)
ET404	DDH 1423	463	4c anh-mo-bn-cpy breccia with ser halo associated with late Dioritic (latite) dike	**10**	**4.705±0.076** **4.691±0.015**	Cannell (2004)

Notes: Samples with two dates are from replicate analyses of the same vein. DC= Drillcore studied. M = Meters along drillcore. VC = Vry *et al*., 2010 vein classification. For locations of each date see Figure 3.14.

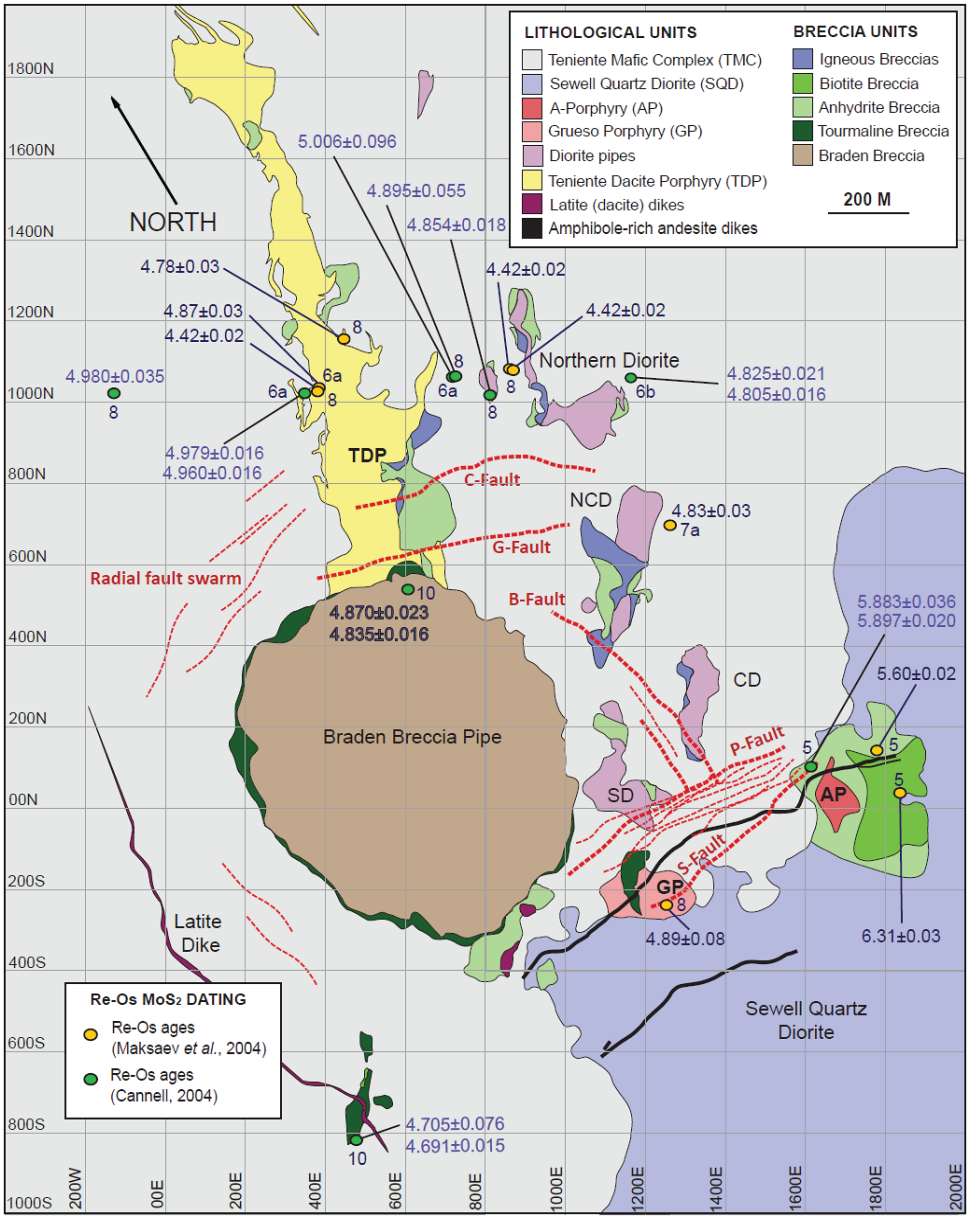


Figure 3.14: Simplified geological map of El Teniente at an elevation of 2165 m above sea-level (asl) showing the locations of the 18 vein and breccia samples dated in previous Re-Os molybdenite dating studies (Maksaev *et al*., 2004; Cannell 2004). Vein types are labelled in accordance with the classification of Vry *et al*. (2010), refer to Figure 2.3. Original map provided by CODELCO Chile Division El Teniente. Mine grid is oriented 14.5° from true north.

Despite this, subsequent attempts to correlate K-Ar and U-Pb zircon ages with Re-Os molybdenite ages have yielded highly variable interpretations (Skewes *et al*., 2002; Maksaev *et al*., 2004; Cannell, 2004; Skewes and Stern, 2007; Cannell *et al*., 2007). This is largely due to the large errors associated with previously collected U-Pb zircon dates (0.2-1.8 Ma: Maksaev *et al*., 2004) and the fact that single zircon grains from individual intrusions show a range of crystallisation ages (Figure 3.3) that probably indicate inheritance from an

underlying magma chamber. In addition, some intrusions have yet to be adequately dated, including the North Central Diorite and the Grueso Porphyry. As a result, the importance of each intrusion and the relationship between the timing of intrusion crystallisation and mineralisation remain unclear.

In both previous studies, the oldest molybdenite ages were recorded from type 5 veins and anhydrite breccias associated with potassic alteration (Table 3.2). In contrast, the youngest ages were found in type 8 and 10 veins associated with sericite alteration. This apparent younging with paragenetic stage led to the conclusion that there was a deposit-wide evolution in vein formation (Cannell *et al*., 2005) as proposed in several other studies (e.g. Cuadra, 1986; Arevalo *et al*., 1998; Klemm *et al*., 2007). In addition, it was suggested that the deposit underwent a switch into sericite-stable conditions at approximately 4.95 Ma (Cannell, 2004).

However, in both studies, the oldest veins are hosted by the oldest intrusions (the Sewell Quartz Diorite and the A-Porphyry) whereas the youngest veins analysed were spatially associated with the younger Teniente Dacite Porphyry and Braden Breccia pipe (Figure 3.14). As a result, these data alone cannot distinguish between a deposit-wide evolution in vein and breccia types or a cyclic history involving multiple hydrothermal pulses (e.g. Maksaev *et al*., 2004; Astudillo *et al*., 2010; Vry *et al*., 2010). Furthermore, almost all dated samples come from one shallow section cutting the Teniente Dacite Porphyry or from the carapace of the A-Porphyry (Figure 3.14) so that pulses of mineralisation elsewhere in the deposit may have been overlooked. This is supported by recent palaeomagnetic data which reveal numerous polarity reversals indicative of far more pulses of hydrothermal fluid activity than the five identified by Maksaev *et al.* (Astudillo *et al*., 2010).

Therefore, although these studies provide valuable insights into the overall timescale of Mo mineralisation at El Teniente, stages of Mo mineralisation associated with a number of intrusions, veins, breccias and fault zones still need to be assessed. Additional dates are required to assess the longevity of mineralisation associated with each intrusion and to facilitate a full comparative study between mineralisation and previously obtained crystallisation and alteration ages (Clark *et al*., 1983; Cuadra, 1986; Maksaev *et al*., 2004).

3.8 Closing Statements

This Chapter provided an overview of the current understanding of the magmatic-hydrothermal evolution of El Teniente and the controls on mineralisation at the deposit. Although previous studies have elucidated many aspects of the system, several factors still need to be assessed. These include:

- The exact timing relationships between intrusion crystallisation, fault development and Mo and Cu mineralisation, including the longevity of mineralisation in each individual hydrothermal system;
- The geochemical affinities of each intrusion and whether they show any definitive trends in chemistry or degree of fractionation with time and whether these changes affect the metal contents of exsolved hydrothermal fluids;
- The relative abundances of different vein and breccia types, their distributions across the deposit and at different mine levels, and whether there are any definitive spatial or temporal relationships between vein and breccia types and mineralisation;
- The validity of the new vein chronology proposed by Vry *et al*. (2010) and whether or not there is a deposit-wide evolution in vein types as previously suggested (e.g. Cannell *et al*., 2005; Klemm *et al*., 2007);
- Whether there is a corresponding deposit-wide fluid evolution and whether there is a genetic link between fluids in different vein types;
- The parental fluids responsible for Mo and Cu transport, their relative volumes and their evolution during ascent and migration into the TMC;
- The geochemistry and microthermometric properties of late mineralisation stage fluids need to be studied in order to ascertain the origin of these fluids and why they appear to be particularly Mo-rich.

By combining a detailed study of the distribution and timing of Mo mineralisation at El Teniente with an extensive fluid inclusion analysis study using LA-ICP-MS, the next two chapters address these areas of uncertainty, allowing for a subsequent discussion regarding the magmatic-hydrothermal evolution of Mo-rich porphyries and the controls on Mo transport and Mo-Cu decoupling in porphyry systems.

Chapter 4. The Distribution and Timing of Molybdenite Mineralisation at El Teniente

4.1 Introduction

A recent study at El Teniente highlighted the distinct decoupling in the mineralisation patterns of Mo and Cu (Vry *et al*., 2010). Similar decoupled zonation patterns have been recognised at a number of other porphyry deposits (Gustafson and Hunt, 1975; Ulrich and Heinrich, 2001; Rusk *et al*., 2008; Landtwing *et al*., 2010; Redmond and Einaudi, 2010; Sillitoe, 2010; Seo *et al*., 2012). At Bingham, Utah, this was attributed to reduction and an increase in acidity in the evolving fluid source region, allowing for the development of a late stage Mo overprint (Seo *et al*., 2012). However, at El Teniente, molybdenite-rich veins are commonly overprinted by chalcopyrite, suggesting different controls on decoupling (Vry *et al*., 2010). In order to identify these controls, better constraints on the distribution and timing of molybdenite mineralisation relative to Cu-sulphide deposition are required. These include accurate identification of the veins and breccias that are the most important hosts for Cu- and Mo-sulphides and their timing relationships in different parts of the deposit.

Using detailed drillcore analysis, this chapter aims to provide quantitative constraints on the abundances of different Mo-bearing vein and breccia types and their distributions across the deposit. By comparing results with grade distribution data provided by CODELCO Division El Teniente, an assessment of the key controls on the distribution of molybdenite mineralisation is made.

This chapter also attempts to provide better constraints on the timing of mineralisation across the deposit using the Re-Os molybdenite geochronometer. Here eleven geologically constrained vein and breccia samples from several Mo-rich zones were dated in order to address some of these limitations. These results, combined with field observations and additional geochronological evidence (Clark *et al*., 1983; Cuadra, 1986; Maksaev *et al*., 2004), provide further evidence for an episodic, multistage evolution of intrusion formation and mineralisation at El Teniente, involving at least four major pulses of magmatism and multiple pulses of related hydrothermal activity.

4.2 Grade Distributions

In order to identify the most important intrusions (Figure 4.1) with respect to Mo mineralisation and controls on Mo-Cu decoupling at El Teniente, Mo and Cu grade distribution data were obtained from CODELCO Division El Teniente from three mine levels (1890 m, Figure 4.2; 2200 m, Figure 4.3; and 2350 m above sea-level, Figure 4.4). Due to sloping topography, the current land surface is 2300 m asl at the western margin of the deposit area and approximately 3300 m asl on the eastern margin. Morphological reconstruction of a nearby volcanic centre (Rivera and Falcon, 1998), estimates of local exhumation rates (Skewes and Holmgren, 1993; Kurtz *et al*., 1997) and calculations of pressure using fluid inclusions (Cannell, 2004) indicate approximately 2000 m of erosion at El Teniente since it formed at approximately 5 Ma. Therefore, the deepest grade distribution slice examined is inferred to represent a depth of approximately 3 km below the paleosurface.

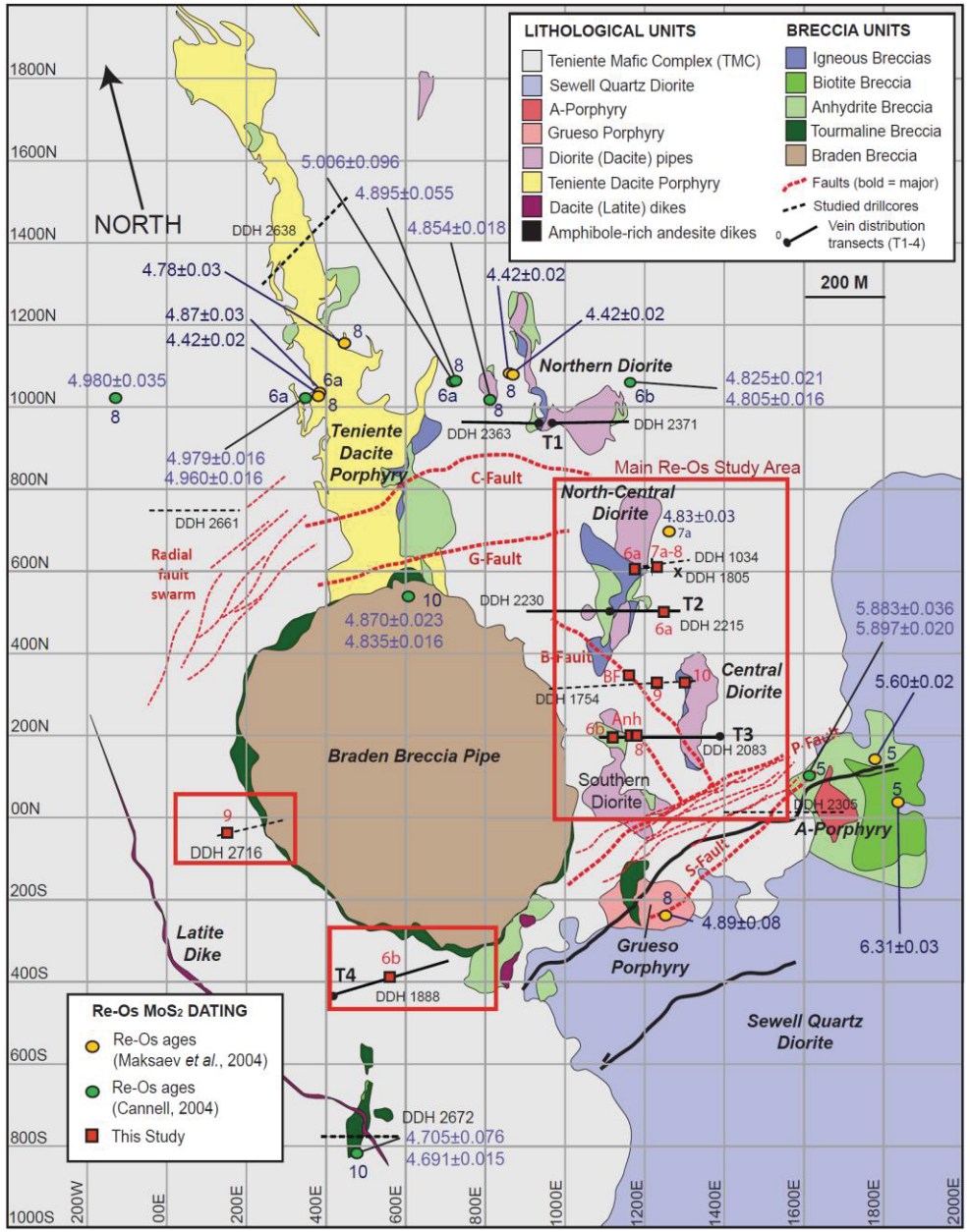
At the deepest mine level studied, Mo mineralisation displays a close spatial association with the diorite finger porphyries (Figure 4.2). Mineralisation is abundant within and surrounding these diorites, with the highest grades observed at their contacts with the TMC. Copper grades also show a clear spatial relationship with these intrusions with the 1.0 wt.% Cu contour surrounding all the diorite intrusions and enclosing zones of maximum Mo grade. High Mo and Cu grades also appear to show a relationship with igneous and anhydrite breccias surrounding the Northern Diorite and North Central Diorite and also to the south of the Braden Breccia pipe. Particularly high Mo:Cu ratios are found on the western and southern sides of the Braden Breccia pipe and proximal to the Southern Diorite. At this level, the centre of the Braden Breccia pipe, the Teniente Dacite Porphyry and A-Porphyry all show relatively low Cu and Mo grades (Figure 4.2).

At intermediate mine levels, the high grade Mo and Cu shells spatially associated with the diorites shift approximately 100 m to the west (Figure 4.3) maintaining a similar separation to that observed at 1890 m asl. This is likely to be a manifestation of post-mineralisation deformation, which tilted the diorites and Braden Breccia pipe towards the northwest (Figure 4.1). The highest Mo grades are associated with the western and eastern rims of the

Braden Breccia pipe with an additional Mo anomaly associated with a tourmaline breccia, which is crosscut by the southern tip of a northwest-trending latite dyke, south of the Braden Breccia pipe. Highest Cu grades are associated with the southern tip of the North Central Diorite and the northern tip of the Central Diorite. Elevated Cu grades also occur at the margins of the Teniente Dacite Porphyry, in particular associated with a large anhydrite breccia body to the north of the Braden Breccia pipe where grades exceed 2 wt.%.

At the shallowest mine level studied (2350 m asl), both Mo and Cu are concentrated within and surrounding the A-Porphyry, Northern Diorite, North Central Diorite and Southern Diorite (Figure 4.4). Unlike Cu, high grade Mo mineralisation also occurs in a near-continuous halo of >0.03 wt.%, approximately 100-250 m from the perimeter of the Braden Breccia pipe. This enriched halo appears to be a continuation of that seen at the intermediate mine level (Figure 4.3) and occurs outboard of the marginal tourmaline breccias that surround the breccia pipe. High Mo grades are also observed in association with smaller tourmaline breccia bodies at the southern tip of the latite dyke southwest of the Braden Breccia pipe and overlying the Grueso Porphyry (Figure 4.4). Zones of high Cu grade are found to the north of the Braden Breccia pipe and extend to the north and east where they display a spatial association with the North Central Diorite and the margins of the Teniente Dacite Porphyry. The Mo halo surrounding the Braden Breccia pipe appears to overprint Cu mineralisation associated with the Teniente Dacite Porphyry margins, suggesting that significant Mo deposition in this part of the deposit occurred later than Cu (Figure 4.4).

Figure 4.1 (next page): Simplified geological map of El Teniente at an elevation of 2165 m above sea-level with units and breccias listed from oldest to youngest in accordance with previous studies (Maksaev *et al*., 2004; Vry *et al*., 2010). Map shows the location of drillcores analysed during this study (dashed black lines) and transects selected for vein distribution analysis (solid black lines). The circles on the transect lines represent the start of each drillcore. DDH 1805 = vertical drillcore. The 18 vein and breccia samples dated in previous studies using the Re-Os molybdenite technique are shown (yellow circles = Maksaev *et al*., 2004; green circles = Cannell, 2004). Red squares = the 11 molybdenite samples dated during this study using the Re-Os molybdenite technique. The vein and breccia types are listed next to each dated sample in accordance with the classification of Vry *et al*. (2010). BF = B-Fault sample (a major Mo-rich fault zone trending towards the northwest). Original map provided by CODELCO Chile Division El Teniente. Mine grid is oriented 14.5° from true north.



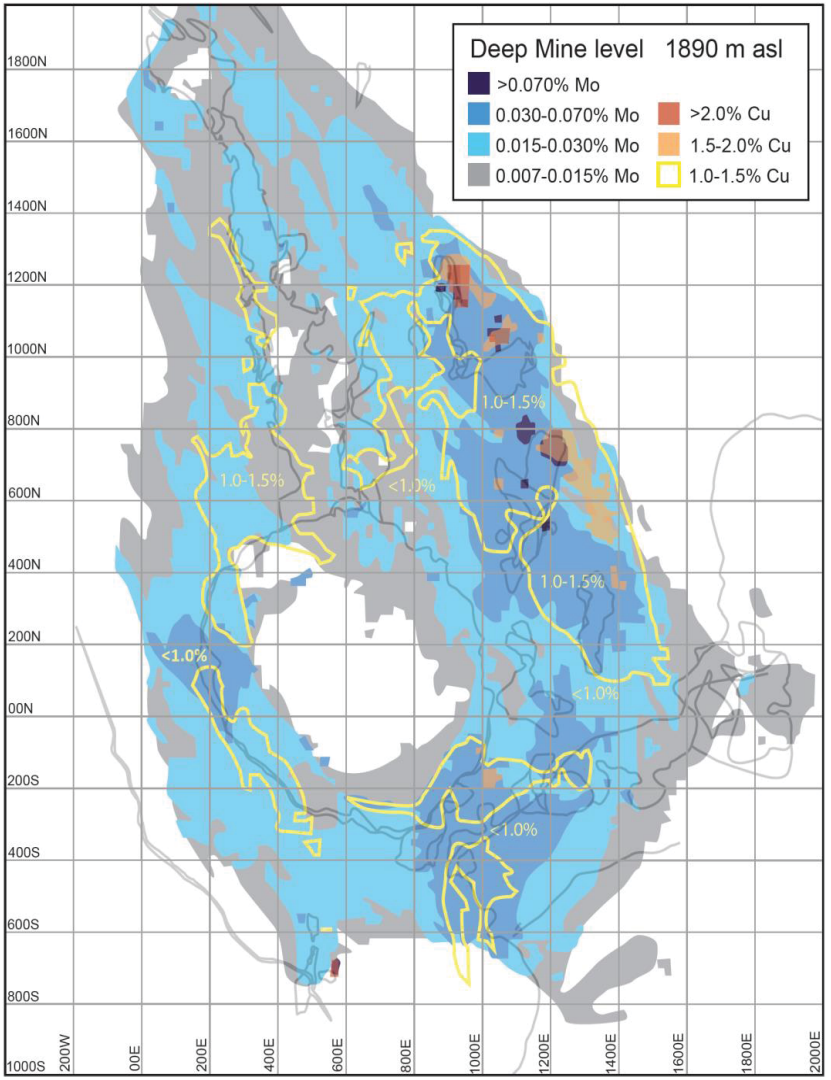


Figure 4.2: Grade distribution map of Mo and Cu (wt.%) at a deep mine level (1890 m asl). Outline map from Figure 4.1 is superimposed to show the relationship between mineralisation and geology. Original maps, Mo grades and Cu grades courtesy of CODELCO Division El Teniente.

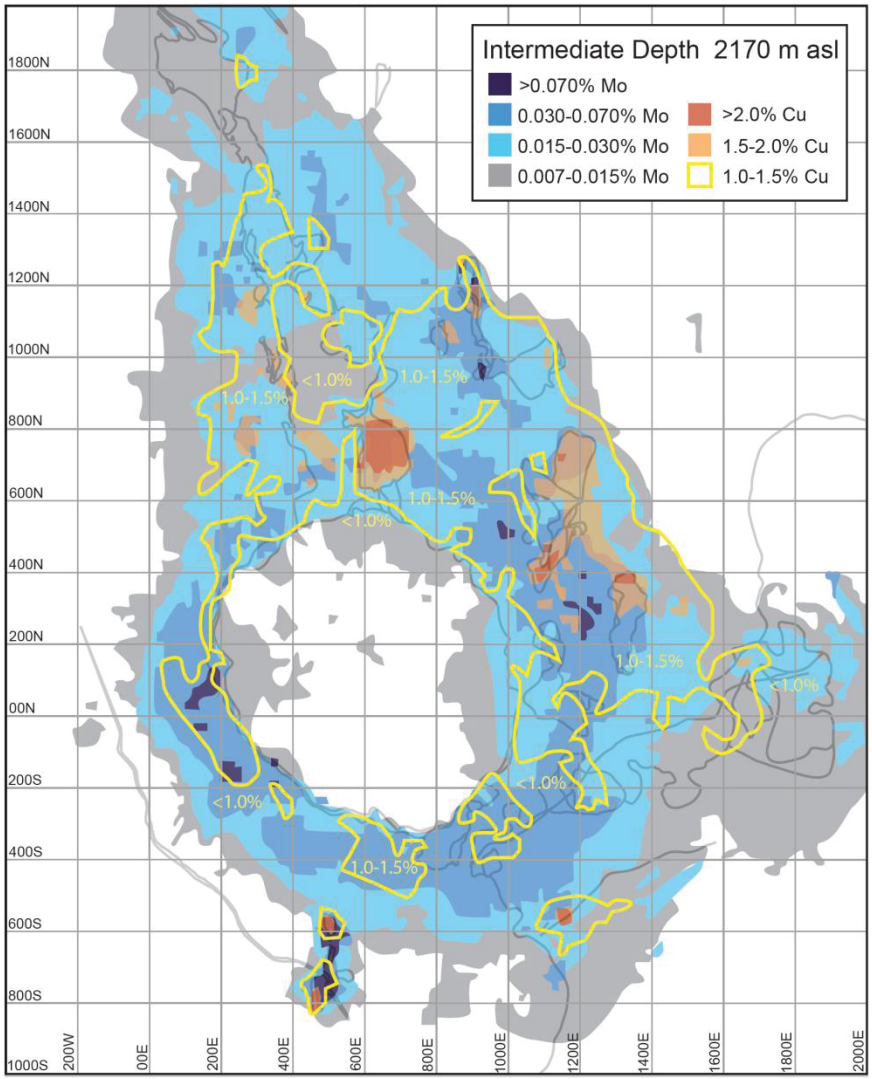


Figure 4.3: Grade distribution map of Mo and Cu (wt.%) at an intermediate mine level (2170 m asl). Outline map from Figure 4.1 is superimposed to show the relationship between mineralisation and geology. Original maps, Mo grades and Cu grades courtesy of CODELCO Division El Teniente.

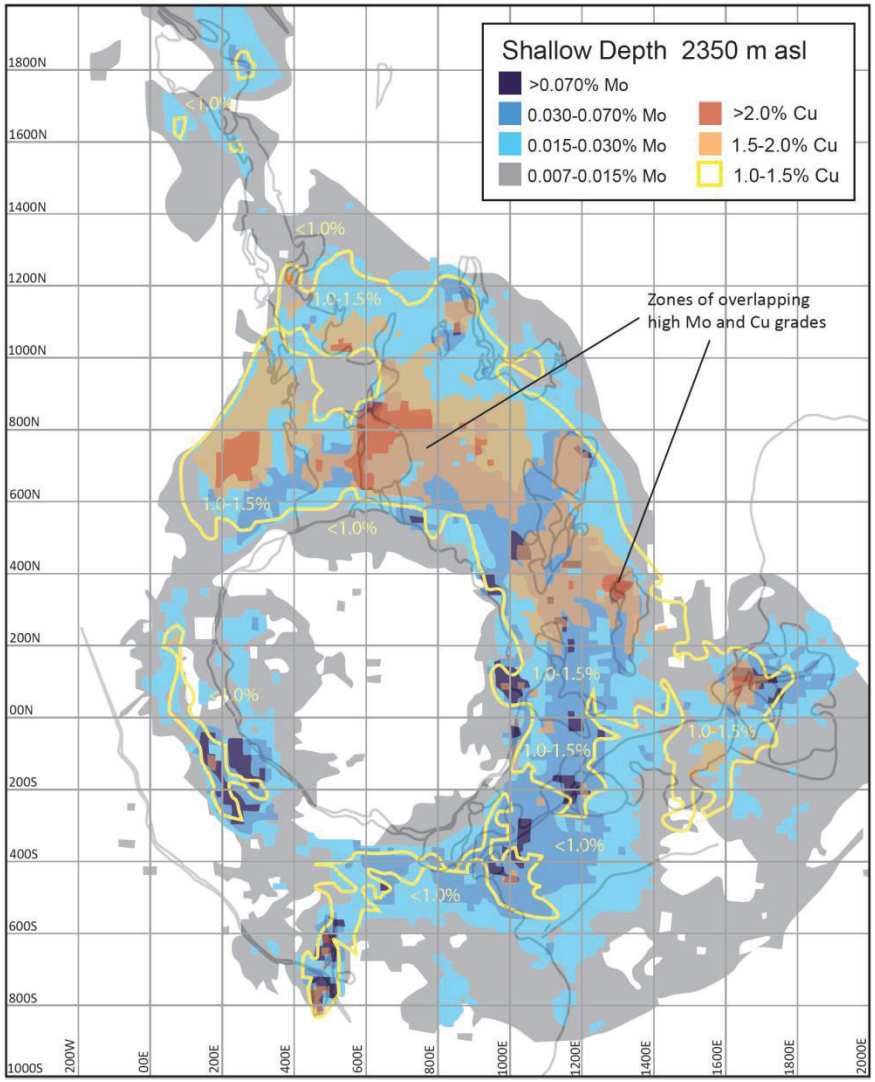


Figure 4.4: Grade distribution map of Mo and Cu (wt.%) at a shallow mine level (2350 m asl). Outline map from Figure 4.1 is superimposed to show the relationship between mineralisation and geology. Original maps, Mo grades and Cu grades courtesy of CODELCO Division El Teniente.

4.3 Methods

4.3.1 Drillcore Logging

Fieldwork was completed at El Teniente in two visits in Oct - Nov 2011 and Sept - Oct 2012. Fourteen drillcores were studied in order to analyse mineralisation and hydrothermal alteration assemblages associated with intrusions and breccias at various mine levels (see Table 4.1; Figure 4.1). Over 240 samples were collected for laboratory analysis. These included examples of each vein and breccia type hosted by different lithologies, samples suitable for fluid inclusion analysis, and well-constrained, Mo-rich samples for Re-Os dating.

Table 4.1: Summary information for drillcores analysed during this study.

	Drillcore	Starting Coordinates	Azimuth	Inclination (from horizontal)	Metres studied	Elevation m asl	Lithology
T1	DDH 2371	N 942.555 E 940.844	89.0°	-4°	0-200	2055.34	TMC-ND
	DDH 2363	N 942.041 E 921.751	270.6°	-6°	0-200	2054.28	ND-TMC
T2	DDH 2215	N 505.017 E 1115.823	90.0°	+15.3°	0-200	1987.88	TMC-NCD
	DDH 2230	N 505.062 E 1108.458	269.8°	-3.2°	0-200	1986.40	NCD-TMC
T3	DDH 2083	N 199.930 E 1380.040	270.0	+2°	0-300	2214.24	TMC-CD-SD
T4	DDH 1888	S 413.420 E 425.420	74.0°	-52°	0-300	2283.21	TMC
DDH 1805		N 602.511 E 1209.048	Vertical	-90°	0-533	1984.84	NCD-TMC
DDH 1034		N 619.285 E 1323.062	265°	-80°	0-990	2286.64	NCD-TMC
DDH 2638		N 1315.955 E 252.358	44.91°	-54.80	0-300	2166.72	TMC-TDP
DDH 1754		N 318.659 E 933.357	87°	-10.00	0-390	2384.00	TMC-CD
DDH 2305		N 36.786 E 1702.716	279.65°	-13.95°	0-300	2322.62	AP-TMC
DDH 2661		N 750.194 E 188.325	269.35°	-59.17°	60-360	2164.83	TMC-TDP
DDH 2672		S 775.516 E 565.298	270.67°	+28.80°	0-190	2192.81	TB-LD-TMC
DDH 2716		S 61.438 E 126.059	77.0°	+34.00°	0-120	2356.23	TMC-BB

Notes: For drillcore locations refer to Figure 4.1. T1-T4 = Transects 1-4 used for vein distribution analysis. ND = Northern Diorite, NCD = North Central Diorite, CD = Central Diorite, SD = Southern Diorite, TDP = Teniente Dacite Porphyry, AP = A-Porphyry, TB = Tourmaline Breccia, LD = Latite Dyke, BB = Braden Breccia pipe.

Based on Mo grade distribution maps, six drillcores were selected on which to complete detailed vein distribution analyses. These formed three, near-horizontal, E-W trending transects that cut the diorites at various depths (transects 1-3) and a final transect (transect 4) that cuts the Mo-rich halo and Teniente Dacite Porphyry to the south of the Braden Breccia pipe (Figure 4.1). Detailed notes on lithology, alteration and sulphide abundances were taken along each transect and the total number of veins of each type was recorded for

each metre interval following the vein classification of Vry *et al*. (2010). The lack of reverse cross-cutting veins and breccia relationships surrounding these intrusions (Vry *et al*., 2010) suggests that the main mineralisation stage veins in transects 1-4 are not likely to be formed by the overprinting of veins related to multiple mineralisation events. This means that the vein distribution analysis should either record overall vein abundances for a deposit-wide evolution in vein type or will allow for the study of vein abundances surrounding each intrusion.

Near horizontal transects were selected in order to intersect the majority of the veins surrounding the diorites and Braden Breccia Pipe which tend to have vertical or sub-vertical attitudes (e.g. Cannell *et al*., 2005). The majority of veins present in transects 1-4 cut the drillcores at near-perpendicular angles, rarely extending for lengths of >6 cm, and are therefore predominantly oriented roughly N-S. In the rare cases where veins ran along the drillcore for >10 cm, or branched into two separate veins each with lengths of >3 cm, they were recorded as two veins based on the assumption that they would exert a higher than normal control on Mo and Cu grades in their drillcore interval. Composite veins were counted as two separate veins, provided the separate vein generations could be identified. If this was not possible, the vein was classified by its predominant mineralogy. Due to the relatively uniform thickness of each vein type (discussed in subsequent sections) and the fact that the thickest veins are typically gangue-dominated (e.g. early barren quartz and anhydrite veins, and late gypsum veins), vein width was not taken into account. However, notes were made when unusually large, sulphide-rich veins were encountered. Veinlets with widths of <1 mm were not recorded. Results were compared against average Mo and Cu grades provided by CODELCO División El Teniente. Average grades are reported for six metre drillcore intervals along transects 1-2 whereas grades are given for 20 foot intervals along the earlier studied drillcores in transects 3-4. This was due to a switch from metric to imperial measurements between the collection of assay data for transects 3-4 and the later measured drillcores in transects 1 and 2.

In order to investigate the distribution of Mo with depth, two drillcores (DDH 1805 and DDH 1034) were selected in order to provide a near-vertical section proximal to the North Central Diorite (Figure 4.1, Table 4.1). These extend down to an elevation of 1300 m asl,

representing a vertical profile of approximately one kilometre that represents a maximum estimated paleodepth of 3.5-4.0 km. Six additional drillcores were studied (Figure 4.1, Table 4.1) to enable a deposit-wide analysis of molybdenite mineralisation by assessing cross-cutting relationships between vein types, breccias and intrusions and their association with Mo or Cu anomalies.

4.3.2 Petrography

Representative and well-constrained vein and breccia samples from several intrusions and the TMC were selected for petrographic analysis (Appendix 2). These were obtained from a range of depths and had highly contrasting sulphide abundances and associated alteration. Sixty polished thin sections were prepared with thicknesses of 32–150 μm. All samples were studied using conventional transmitted light petrography to confirm vein/breccia classifications and by reflected light microscopy in order to identify sulphides present, their relative abundances and their timing relationships.

4.3.3 Geochronology

Unlike the other dating techniques used at El Teniente, which may be susceptible to the effects of hydrothermal overprinting, the Re-Os isotopic system displays closed behaviour during post mineralisation alteration, ductile deformation and regional metamorphism (e.g. Stein *et al*., 1998; Selby and Creaser, 2001; Stein and Bingen, 2002 Bingen and Stein, 2003; Ootes *et al*., 2007; Bingen *et al*., 2008; Lawley and Selby, 2012). This, combined with the fact that molybdenite is the third most abundant ore mineral at El Teniente (Camus, 1975), makes it a suitable technique for dating mineralisation. Twenty samples were initially selected for Re-Os molybdenite dating based on their vein/breccia type, sample depth and geographic locations. Large composite veins and overprinted veins were avoided so that constrained age determinations could be made for single molybdenite generations in each vein. Consistent with their premineralisation stage classification, reflected light analysis revealed that the amount of molybdenite in all selected type 3-4b veins was either insufficient for dating or it was the result of overprinting by later vein generations. As a result, no samples from this paragenetic stage were dated in this study.

Eleven samples were selected for Re-Os molybdenite dating (Appendix 2) that include seven main mineralisation stage samples and four samples from the late mineralisation stage. Vein samples ranging from type 6a to type 10 were obtained from proximal to the Central Diorite and Southern Diorite in order to study the temporal evolution of veins within a single part of the deposit (Figure 4.1). Two type 6a vein samples with a difference in elevation of approximately 550 m were selected proximal to the North Central Diorite in order to assess the relationship between depth and timing of molybdenite mineralisation (1034-837.0, 2215-119.9). Additional samples analysed included a molybdenite-rich tourmaline breccia from the western rim of the Braden Breccia pipe (2716-8.0) and a type 6b vein associated with the southern tip of the Teniente Dacite Porphyry (1888-133.8). The final sample analysed was a sample from the B-Fault, an anastomosing NW-trending fault zone that coincides with a significant Mo anomaly to the east of the Braden Breccia pipe (Figure 4.1, Figure 4.4). Mine geologists report evidence for right-lateral, strike-slip displacement along this fault zone, which has created slickensides on the contained molybdenite. Although this indicates displacement following molybdenite mineralisation, the timing of Mo introduction remains untested. This information can be used to assess the relationships between fault activation, intrusion emplacement and crystallisation and mineralisation.

All samples were prepared and analysed at the University of Alberta Radiogenic Isotope Facility, Canada, using the method of Selby and Creaser (2001, 2004). Veins and breccia zones of interest were cut out of each sample to create molybdenite-rich specimens with weights of <20 g. Cut samples were crushed separately using a porcelain disk mill, collecting the fraction that passed through a 200–70 mesh sieve. Molybdenite was then separated using a Frantz isodynamic magnetic separator and heavy liquid (methylene Iodide). Due to the low abundance of molybdenite in sample 2083-184.1, molybdenite was separated using the hydrofluoric acid (HF) chemical separation technique of Lawley and Selby (2012) to maximise recovery. Lawley and Selby (2012) showed that this technique does not affect the Re and Os isotope composition of molybdenite and can be used to obtain accurate and reproducible age determinations for ultrafine molybdenite.

Previous Re-Os studies have shown that analysing large amounts of separated or hand-picked molybdenite (i.e. 10 mg) or small aliquots of separated molybdenite (<1 mg) can

both yield dates that significantly deviate from "true" sample ages (Stein *et al*., 1998, 2001; Creaser and Selby, 2002). In order to avoid anomalous results produced by the sampling of multiple generations of molybdenite, relatively small aliquots of molybdenite with weights of approximately 1.2 mg were separated. These were accurately weighed and dissolved together with a known amount of "mixed-double" spike (^{188}Os+^{190}Os+^{185}Re; Markey *et al.*, 2007) in a thick-walled Carius tube. Os and Re were separated using a combination of solvent extraction, microdistillation and anion chromatographic methods and analysed by N-TIMS using a Thermo Triton mass spectrometer and Faraday Collectors. Previous studies have shown this to be an effective technique for deriving highly precise, accurate and reproducible molybdenite ages (Selby and Creaser, 2001, 2004; Stein *et al*., 2001). Procedural blanks are less than 2 pg for Re and 3 pg for Os, and model ages were calculated using the ^{187}Re decay constant of $1.666x10^{-11}a^{-1}$ (Smoliar *et al*., 1996). Uncertainty in the Re-Os model ages includes uncertainty in the ^{187}Re decay constant, Re and Os concentrations as a result of weighing uncertainties (spikes and samples), spike calibration and mass spectrometry analytical uncertainties. All age uncertainties are reported at the 2σ level in the results section. Three samples were selected for replicate runs using the same mineral separate in order to assess the accuracy and reproducibility of results and confirm that these samples consisted of a single generation of molybdenite.

4.4 Results

4.4.1 Breccia Distribution and Petrography

Seven breccia types were observed in this study (igneous-, biotite-, anhydrite-, quartz-, tourmaline-, anhydrite-carbonate ±gypsum-cemented, and rock flour breccias). These are spatially associated with different intrusions and contain highly variable sulphide abundances as summarised in Table 4.2. Consistent with their premineralisation timing (Cannell *et al*., 2005; Vry *et al*., 2010), Mo and Cu-sulphides are rare in igneous and biotite breccias but are often present in the other breccia types which commonly contain 5-40% Cu-sulphides and 5-20% molybdenite (Table 4.2). Sulphides are sometimes concentrated where later vein stages cut the breccias (e.g. Figure 4.5A), but are also commonly present as isolated crystals (e.g. Figure 4.5B-C) or as fine or coarse crystals that are intergrown with gangue minerals (Figure 4.5D-E) or constitute much of the breccia matrix (Figure 4.5F).

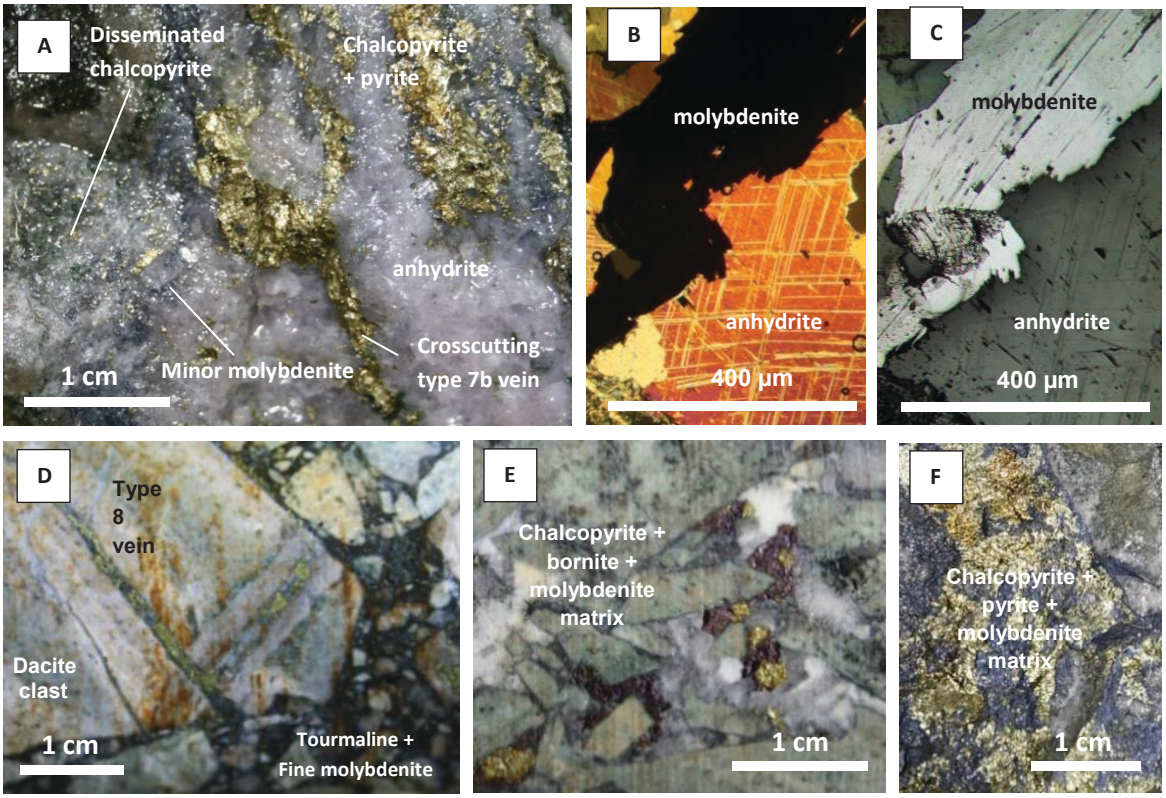


Figure 4.5: Typical Cu and Mo sulphides in the three most intensely mineralised breccia types. (A) Chalcopyrite mineralisation associated with type 7b veinlets that cut an anhydrite breccia within the A-Porphyry (2305-44). (B-C) Cross-polarised and reflected light photomicrographs of an isolated molybdenite crystal within the same sample (D) Teniente Dacite Porphyry clast containing chalcopyrite-bearing type 8 veins being truncated by a Mo-rich tourmaline breccia on the western margin of the Braden Breccia pipe (2716-51.0). (E) Anhydrite-carbonate cemented breccia containing molybdenite, chalcopyrite and bornite (2716-16.2). (F) Late stage breccia with sulphide-dominated cement (2672-238.0).

Table 4.2: Summary of the compositions, occurrences and key petrographic features of the seven different breccia types observed.

Breccia	Composition	Occurrence	Sulphides
Igneous	Plag phenocrysts +bt-qz-anh Clasts = Predominantly TMC ± Sewell Quartz Diorite, A-Porphyry	• Second most common breccia type observed. • Occur surrounding every intrusion at all mine levels suggesting that they are linked to the emplacement of each intrusion • Cut by all vein stages from 3 onwards and all other breccias	• Typically contain <1% mo and <2% cpy, <1% py and no bo • Sulphides interpreted to be the result of later vein stages and disseminations related to the main and late mineralisation stages.
Biotite	Plag phenocrysts +bt-qz-anh Clasts = Predominantly TMC ± SQD	• Only observed proximal to the A-Porphyry and SQD in DDH 2305. None observed in other intrusions. • Sample bt bx 1 was a supplementary sample obtained from a deep mine level where bt breccia preservation is inferred to be better.	• Minor cpy <3% observed in one sample (Bt Bx 1) • Opaque daughter minerals (cpy?) observed in large fluid inclusions.
Anhydrite	Plag phenocrysts +bt-qz-anh Clasts = Predominantly TMC + A-Porphyry + Sewell Quartz Diorite	• Most frequently observed breccia type during this study • Observed surrounding the A-Porphyry, diorites and Teniente Dacite Porphyry. Notable sulphide-rich examples recorded proximal to the A-Porphyry, North Central Diorite, Southern Diorite and to the south of the Braden pipe.	• Highly variable. Typically <5% mo, <10% cpy, <2% bo, <5% py • In rare cases can contain up to 40% mo at the clast-matrix contacts. • Contain a maximum of 50% blocky cpy found throughout anh cement
Quartz	qz with minor anh and K-fsp in cases Clasts = Predominantly TMC and altered diorite	• Rare occurrences observed at the contacts of the diorites in areas of intense qz stockwork veining. Best example observed proximal to the North Central Diorite. • Evidence that quartz is replaced anh cement, possibly during the type 6 vein stage.	• Typically contain minor mo ~5% (e.g. Figure 3.4E), usually found at cement-clast contacts. • Minor cpy <5% in all samples observed.
Tourmaline	Tour ± anh, often with abundant mo Clasts = Teniente Dacite Porphyry + TMC ± diorites	• Observed surrounding the Braden Breccia pipe in DDH 2716, DDH 2083 and DDH 1888 as well as cut by the latite dyke to the south of the Braden pipe (DDH 2672). • Crosscut the Teniente Dacite Porphyry and diorites and are cut by the Braden pipe	• Highly variable with examples containing 0-70% mo in cement • Several examples contain abundant cpy and py, possibly representing sulphide zonation surrounding the Braden pipe
Anhydrite-carbonate-±gysum	anh+cb±gyp ± sulphosalts Clasts = Teniente Dacite Porphyry + TMC + diorites	• Observed crosscutting the diorites and Teniente Dacite Porphyry In most drillcores. • Display an apparent spatial relationship with the presence of NW-trending and concentric faults surrounding the Braden pipe (see Figure 4.2).	• Typically contain abundant mo (5-50% and bo (5-20%), which appear to be coprecipitated. • cpy <10% in most samples • Minor sulphosalts in several samples (tennantite+enargite)
Rock flour	Plag phenocrysts +bt-qz-anh Clasts = All intrusions, TMC + brecciated tour and sulphides (cpy)	• Rock flour breccia composes the central portion of the Braden pipe surrounded by the marginal tourmaline breccias. • Recorded in drillcores DDH 2716 and at the start of DDH 1754 • Crosscuts the Teniente Dacite Porphyry and all other breccia types.	• Shattered fragments of cpy and py with minor mo and bo in matrix • Cpy-rich clasts of Teniente Dacite Porphyry and diorite truncated by breccia matrix.

Notes: Breccia names are derived from the primary components of cement/matrix. These are listed in an inferred idealised chronologic order proposed by Vry *et al*. (2010). Mineral abbreviations: refer to Figure 3.7.

In transects 1-4, igneous-, anhydrite-, tourmaline- and anhydrite-carbonate ±gypsum-cemented breccias were observed. Anhydrite breccias commonly form a shell surrounding the diorite pipes and contain elevated average Mo and Cu grades in transects 1, 3 and 4 (Table 4.3A-B). Despite this, average grades are lower in intervals of anhydrite breccia in transect 2, reflecting the locally variable sulphide abundances within their cements (Table 4.2).

Table 4.3: Summary of grade data for drillcores in transects 1-4 (T1-4) showing average Mo (Table A) and Cu grades (Table B) for each host lithology.

A. Mo		Veins		Grades (wt.%)	Lithology (Mo wt.% averages)						
T.	Drillcore	Common Veins	Veins/m	Average Mo	TMC	DIO	Teniente Dacite Porphyry	Ign Bx	Anh Bx	Tour Bx	A-C-G Bx
T1	DDH 2371	6a>8>6b	16.8	**0.039**	0.055	0.032		0.037			0.085
	DDH 2363	6b>8>6a	21.9	**0.024**	0.023	0.024			0.043	0.012	0.078
T2	DDH 2215	6a>6b>8	17.4	**0.037**	0.037	0.039		0.029			0.074
	DDH 2230	6a>6b>8	22.5	**0.030**	0.030	0.027			0.021		0.064
T3	DDH 2083	8>6a>6b	26.7	**0.045**	0.039	0.045		0.052	0.049	0.075	0.071
T4	DDH 1888	9>8>6a	33.3	**0.047**	0.040		0.024		0.071	0.105	0.072
Average all			23.1	**0.037**	**0.037**	**0.034**	**0.024**	**0.039**	**0.046**	**0.064**	**0.074**

B. Cu		Veins		Grades (wt.%)	Lithology (Cu wt.% averages)						
T.	Drillcore	Common Veins	Veins/m	Average Cu	TMC	DIO	Teniente Dacite Porphyry	Ign Bx	Anh Bx	Tour Bx	A-C-G Bx
T1	DDH 2371	6a>8>6b	16.8	**1.13**	1.36	1.04		1.13			1.21
	DDH 2363	6b>8>6a	21.9	**1.19**	1.20	1.32			1.23	1.48	1.06
T2	DDH 2215	6a>6b>8	17.4	**1.20**	1.33	0.86		1.17			1.93
	DDH 2230	6a>6b>8	22.5	**0.92**	0.92	0.63			0.88		1.52
T3	DDH 2083	8>6a>6b	26.7	**1.27**	1.24	1.27		1.66	1.52	0.95	1.34
T4	DDH 1888	9>8>6a	33.3	**0.99**	0.98		0.85		1.39	0.93	0.98
Average all			**23.1**	**1.12**	**1.12**	**1.03**	**0.85**	**1.32**	**1.26**	**1.12**	**1.34**

Notes: Common veins = three most common vein types recorded. T. = Transect, DIO = Diorite, Bx = Breccia, A-C-G = anhydrite-carbonate ±gypsum breccias. Grade data provided by CODELCO Division El Teniente.

Tourmaline- and anhydrite-carbonate ±gypsum-cemented breccias are abundant at shallow mine levels, where they cut all intrusions and truncate type 8 veins (e.g. Figure 4.5D). Mo-rich tourmaline breccias are particularly abundant surrounding the Braden Breccia pipe, where six metre drillcore intersections have average Mo grades of up to 0.35 wt.% (DDH 2716). In these breccias, fine-grained molybdenite commonly occurs throughout the tourmaline-dominated matrix. Mo-poor tourmaline breccias were also observed, predominantly occurring at deep mine levels and in distal positions relative to the Braden Breccia pipe. Intersections of tourmaline breccia are generally Cu-poor (Table 4.3B), although sections of chalcopyrite- and pyrite-rich tourmaline breccias were observed in transect 1, and in drillcores DDH 2716, 1888 and 2672.

Anhydrite-carbonate ±gypsum-cemented breccias are almost always enriched in Mo (e.g. Table 4.3A). Molybdenite is predominantly concentrated around clast margins where it commonly occurs as large, bladed crystals. Cu grades are generally low in the anhydrite-

carbonate ±gypsum-cemented breccias (Table 4.3B). However, some shallow-level anhydrite-dominated examples do contain significant chalcopyrite and bornite, accounting for the highly variable average Cu grades recorded (0.98-1.93 wt.%) for the transects studied (Table 4.3B). In some cases, Cu-sulphide mineralisation occurs alongside significant molybdenite in the breccia matrix (e.g. Figure 4.5E-F) suggesting that late stage Cu was introduced together with Mo.

4.4.2 Vein Distributions and Petrography

The abundance and distribution of each vein type and their typical sulphide associations are summarised in Table 4.4. The vein distribution analysis recorded a total of 33,723 veins at an overall average frequency of ~24 veins per metre in transects 1-4 (Appendix 3). Nearly 80% of veins are related to the main mineralisation stage, with approximately 10% belonging to each of the premineralisation and late mineralisation stages. Abundant sulphide mineralisation was observed in every vein stage with the exception of type 1 veins (Table 4.4). Of these, eight vein types (3, 5, 6a, 6b 7a, 7b, 8, 9 and 10) commonly contain molybdenite and chalcopyrite that is observable without the use of a hand lens. Although often present in the same veins, evidence for the apparent co-precipitation of Mo and Cu was rarely observed. Thin section analysis reveals that molybdenite typically occurs on separate vein growth zones to chalcopyrite and bornite, or is overprinted or truncated by later Cu-sulphides.

Total vein abundance is generally higher at shallower mine levels (e.g. Table 4.3A), largely due to increases in type 7b-10 vein frequency (Figure 4.6). No vein type displays a clear increased abundance at deep mine levels, although the relative proportion of molybdenite-rich type 6a and 7a veins generally increases with depth in the two deepest drillcores studied (DDH 1805 and 1034). Vein frequencies are lower within the finger porphyries than within the mafic complex rocks immediately surrounding them. For example, an average vein frequency of 16.31 veins/metre was recorded for the Northern Diorite in transect 1, whereas the TMC exhibits a frequency of 21.96 veins/metre. This is largely due to pronounced decreases in the abundances of type 3 and 8 veins within the finger porphyries.

Table 4.4: Summary of the mineralogy, occurrences and typical sulphide abundances of vein types observed in the 15 studied drillcores displayed in Figure 4.1.

Vein	Mineralogy	Occurrences	N	Sulphides
1	bt-act±(chl-cpy) bt halo	• No veins observed during study • Rare occurrences at deep mine levels associated with the Sewell Quartz Diorite and A-Porphyry (Vry *et al.*, 2010)	0 (0%)	• None observed during this study
2	mag±qz-anh-(cpy-py) No original halo	• Preserved at depth and present as pervasive magnetic patches at shallow mine levels (>2200) in the TMC • Typical thicknesses of 5-10 mm. • Rare occurrences in the A-Porphyry and diorites	113 (0.4%)	• Minor mo observed in a few samples (0-3%) • Many replaced by cpy (5-15%) or py (5-15%)
3	bt-qz±anh-(chl-cpy-py-mo) qz-plag halo	• The most abundant premineralisation stage vein, found throughout the TMC at all mine levels, • Typical thicknesses of 5-15 mm. • Rare, thin biotite veins (<2 mm) found in the A-Porphyry with extremely rare examples in the diorites	3347 (10.1%)	• By far the most sulphide-rich premineralisation stage vein • Up to10% mo in some samples • Most contain 5-30% cpy
4a	qz-Kfsp±anh-(ap-bt) bt halo	• Thin wavy veins (0.5-4 mm width) found in the TMC. • Rare occurrences within the A-Porphyry and to a lesser extent the diorites. None observed within the Teniente Dacite Porphyry • Observed grading into anh-rich veins	324 (0.9%)	• Minor primary mo <1% and cpy <1% observed in thin section only • No py or bo observed
4b	Kfsp-ep-anh-chl±qz local ep halo	• Very rare vein type, only observed within the TMC and to a lesser extent the A-Porphyry. Thicknesses of 1-5 mm • Well preserved at deep mine levels and are most frequently observed in the Sewell Quartz Diorite (Vry *et al.*, 2010)	54 (0.2%)	• None observed during this study
5	anh-qz±cpy-py-(bo-mo) bt in TMC/ Kfsp or no halo in felsics	• Occur throughout the TMC, surrounding the diorites and being cut by the Teniente Dacite Porphyry. Thicknesses of 1-15 mm • Most abundant surrounding and in the A-Porphyry (DDH 2305) • Appear to be spatial association with anhydrite breccias surrounding the A-Porphyry and diorites	1922 (5.8%)	• Extremely variable. • Typically 0-20% mo and 0-5% bo, usually at contacts • Can contain up to 30% cpy ± py in some isolated patches
6a	qz-anh-Kfsp±mo-bo no halo in the TMC/ Kfsp halo in felsics	• The most abundant vein type. Present in the TMC and every intrusion. Typical thickness = 1-30 mm. • Highest frequency observed within and immediately surrounding the diorites in dense stockworks • Slight decrease in abundance of mo-bearing examples with distance from the felsic-intermediate intrusions • Abundant at the deepest mine levels studied (1300 m asl) proximal to the diorites	6585 (21.0%)	• Most Mo rich vein type with 0-30% in most samples. • Mo-rich examples observed at the deepest mine levels. • Some contain minor bo, which appears to be co-precipitated with mo. • Always <5% cpy and <5% py
6b	qz-cpy-anh-Kfsp±mo-bo-py no halo in TMC/Kfsp halo in felsics	• Abundant throughout the TMC and crosscutting every intrusion. Typical thicknesses of 2-25 mm • Equally abundant in all the transects studied, but showed a slightly decreased abundance in the deepest mine levels studied, particularly in DDH 1805 • Typically found outboard of type 6a veins in surrounding the finger porphyries, but also overprinting type 6a veins	5961 (19.4%)	• Observed with highly contrasting sulphides • Typically contain 5-40% cpy and/or ~10% py. • ~25% contain mo (5-20%) at vein edges or overprinted by cpy. Typically <5% bo
7a	mo±(qz-anh) no halo	• Most observed within the felsic-intermediate intrusions or at distances <20 m from their contacts • Typically thin (0.5-3 mm) and often discontinuous • Some appear to transition from type 6a or type 10 veins.	1078 (3.6%)	• >70% molybdenite • often surrounded by cpy disseminations within 1 cm of vein edges
7b	cpy±qz-anh no halo	• Observed in every lithology except late breccias. Abundant in the TMC at shallow mine levels. • 0.2-20 mm thick with abundant, large examples found at 50-100 m from the contacts of the intrusions • Vast number of veins coat edges of broken drillcore	3670 (10.7%)	• >70 cpy. No coprecipitated mo present although • some show evidence of Mo overprinted by cpy in reflected light
8	cpy-py-qz-anh-mo ser-chl-qz halo	• Particularly abundant at shallow mine levels surrounding the Teniente Dacite Porphyry or in distal settings of the TMC from the diorites (>50 m from margins). Typical thicknesses = 2-15 mm. • Rare occurrences (<10% of total recorded) within the felsic-intermediate intrusions or at depths <1900 m asl	6479 (19.2%)	• Almost all contain cpy (5-60%) and/or py (5-30%) • Rare examples contain mo and bo (5-10%)
9	tour-cb-anh±cpy-py-bo-mo ser-chl-qz halo	• Abundant within 300 m of the Braden pipe margins, cutting all lithologies. Thicknesses of 1-20 mm. • Most commonly observed in the TMC in DDH 1888, 2716, 1754 and 2672, where they appear to be closely spatially associated with the presence of tour breccias	2837 (5.1%)	• Typically contain 0-25% mo with minor bo or 0-10% cpy + minor py (<5%) • Barren examples recorded, at deeper mine levels.
10	cb-anh-gyp±ten-cpy-py-bo-mo ser-chl-qz halo	• Found throughout the deposit with increased abundance at shallower mine levels. Crosscut all intrusions and are reported in the Braden pipe. Thicknesses are 5-50 mm • Show a good spatial relationship with NW-trending faults and concentric faults that surround the Braden pipe	1353 (3.6%)	• Contain 10-50% mo often with 10-20% bo, typically at vein margins • Some examples (<10%) contain cpy and/or py (5%)

Notes: N = number of veins of each type recorded with percentage proportions displayed in brackets below (total number of veins of each vein type/total veins recorded).

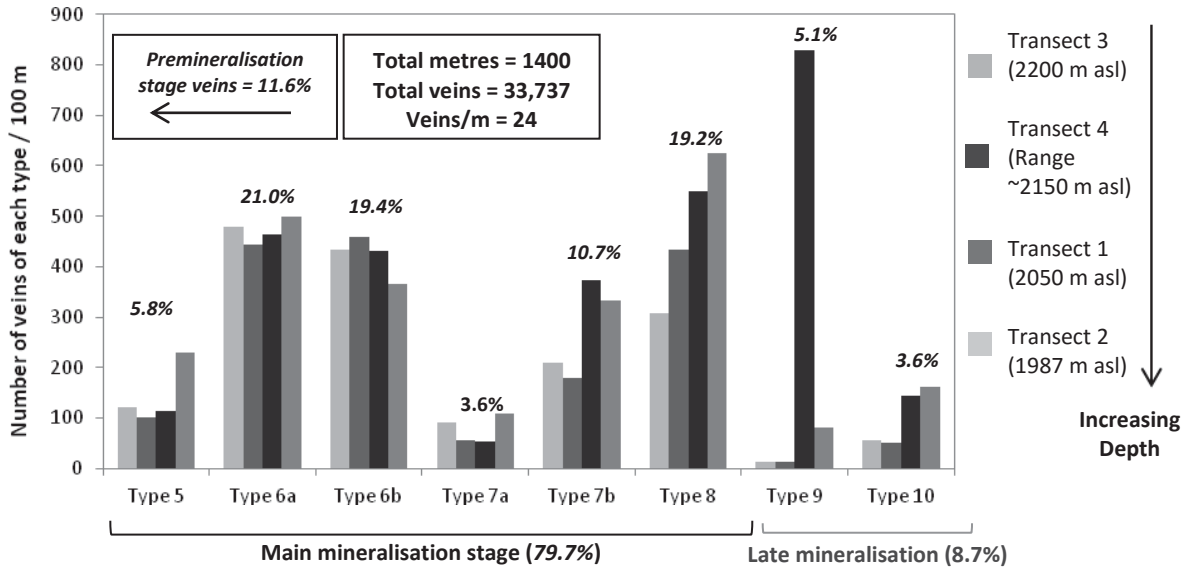


Figure 4.6: Average number of veins of each type in 100 m sections of transects 1-4. Main mineralisation veins account for ~80% of all veins recorded due to the high proportions of type 6a, 6b and 8 veins observed in all transects (Table 4.2). Premineralisation veins are not plotted due to low abundances and lack of sulphides. Overall relative vein type abundances (number of veins of type/total veins) are shown in italics.

Premineralisation Veins

Premineralisation stage veins are abundant within the TMC, the Sewell Quartz Diorite and, to a lesser extent, the A-Porphyry, but are extremely rare in the diorites and Teniente Dacite Porphyry. Of these, type 3 and 4a veins were the only abundant veins observed in transects 1-4 (Table 4.4). Type 3 veins have modal widths of approximately 8 mm and commonly contain abundant chalcopyrite ± minor molybdenite (Figure 4.7A-B). Despite this, the abundance of type 3 veins shows no clear relationship with Mo and Cu grades in transects 1-4 (Figure 4.8A-D). Type 3 vein abundance data fall in clusters relating to host rocks, with the TMC being typified by higher pre-mineralisation stage vein abundances and a slight bias towards higher Cu grades relative to Mo (Figure 4.8A-B). There is a weak negative correlation between type 3 vein abundance and Cu grades in the TMC (Figure 4.8D) suggesting that these veins are not economically important. Furthermore, thin section analysis reveals that molybdenite and chalcopyrite typically replace biotite in type 3 vein centres where they are sometimes accompanied by minor sericitic alteration. This suggests that sulphide-rich type 3 veins are the product of overprinting by later vein stages (e.g. Mo-rich type 7a veins: Figure 3.7C).

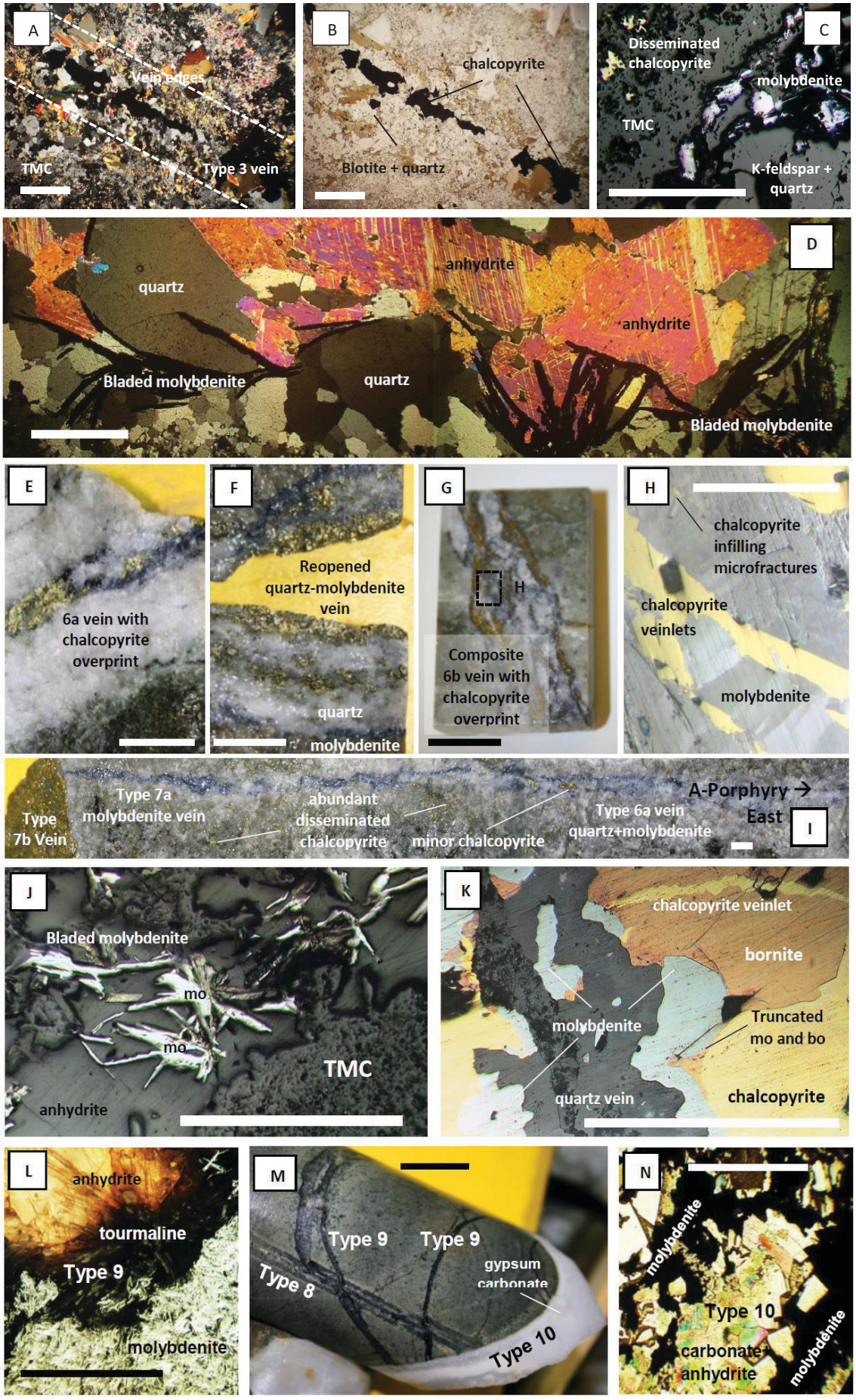

A
Vein edges
TMC
Type 3 vein
B
chalcopyrite
Biotite + quartz
C
Disseminated chalcopyrite
molybdenite
TMC
K-feldspar + quartz
D
quartz
anhydrite
anhydrite
Bladed molybdenite
quartz
Bladed molybdenite
E
6a vein with chalcopyrite overprint
F
Reopened quartz-molybdenite vein
quartz
molybdenite
G
H
Composite 6b vein with chalcopyrite overprint
H
chalcopyrite infilling microfractures
chalcopyrite veinlets
molybdenite
Type 7b Vein
Type 7a molybdenite vein
abundant disseminated chalcopyrite
minor chalcopyrite
Type 6a vein quartz+molybdenite
A-Porphyry →
East
I
J
Bladed molybdenite
mo
mo
TMC
anhydrite
K
chalcopyrite veinlet
bornite
molybdenite
Truncated mo and bo
quartz vein
chalcopyrite
L
anhydrite
tourmaline
Type 9
molybdenite
M
Type 9
Type 9
gypsum
carbonate
Type 8
Type 10
N
molybdenite
Type 10
carbonate
anhydrite
molybdenite

Figure 4.7 (previous page): Sample photographs and cross-polarised and reflected light photomicrographs of sulphides present in different vein types. (A-B) Plane and crossed polarised light photomicrographs of a type 3 vein containing abundant chalcopyrite in the TMC proximal to the A porphyry (2305-57.95). (C) Minor molybdenite and disseminated chalcopyrite at the edge of a K-feldspar+quartz type 4a vein to the south of the Braden Breccia pipe (1888-63.7). (D) Cross-polarised light photomicrograph of elongate molybdenite crystals developed along the border of a type 5 vein in the TMC (2406-14). (E-G) Type examples of 6b veins that contain abundant molybdenite. (E) Type 6b vein in which molybdenite is overprinted by chalcopyrite at the vein centre (2083-136.6). (F) Type 6b vein in which molybdenite is deposited at the vein edges and contains later quartz-chalcopyrite mineralisation at the vein centre (1754-258.3). (G) Composite type 6b vein formed by the overprinting of a type 6a vein by a series of anastomosing type 7b chalcopyrite veins (2371-183.25). (H) Reflected light photomicrograph of chalcopyrite overprinting molybdenite in the type 6b vein shown in photograph G. Chalcopyrite veinlets truncate tabular molybdenite crystals and is also present in microfractures that cut molybdenite (I) Photograph showing the transition within a single vein from a type 6a vein to a type 7a molybdenite vein in the A-Porphyry halo (2305-81.9-82.2). (J-K) Reflected light photomicrographs of a type 8 vein proximal to the Teniente Dacite Porphyry (2661-174.7), containing platy molybdenite (J) and compositionally zoned quartz-molybdenite sections surrounded by bornite that is truncated by chalcopyrite and overprinted by chalcopyrite veinlets (K). (L) Composite transmitted and reflected light photomicrograph of abundant molybdenite associated with the edge of a type 9 vein to the east of the Braden Breccia pipe. Most of the vein is composed of anhydrite with isolated radiating fans of tourmaline (1754-226.5). (M) Cross-cutting relationships showing a type 8 vein being cut by two type 9 veins, all of which are overprinted by a type 10 carbonate-gypsum vein (2672-163.0). (N) Cross-polarised light photomicrograph of a type 10 vein containing abundant carbonate and anhydrite overprinting molybdenite at the vein edges (1754-226.5). Straight gangue mineral crystal edges clearly overgrow the finer molybdenite and isolated fragments of molybdenite also occur within the gangue mineralisation. Scale bars in photographs = 1 cm; in photomicrographs = 1 mm.

Type 4a veins commonly have widths of <1 mm, accounting for their low abundance in the vein distribution analysis (Table 4.4). Reflected light analysis reveals that they typically contain <2% molybdenite and Cu-sulphides that do not appear to be the product of overprinting. Molybdenite usually occurs as small clusters of crystals, commonly occurring along the vein margins, and shows a stronger affinity for quartz-rich veins rather than those containing abundant K-feldspar (e.g. Figure 4.7C). The low primary sulphide abundances, combined with the low abundance of type 4a veins (Table 4.4) confirms the previous categorisation of type 4a veins as premineralisation stage veins (Vry *et al*., 2010).

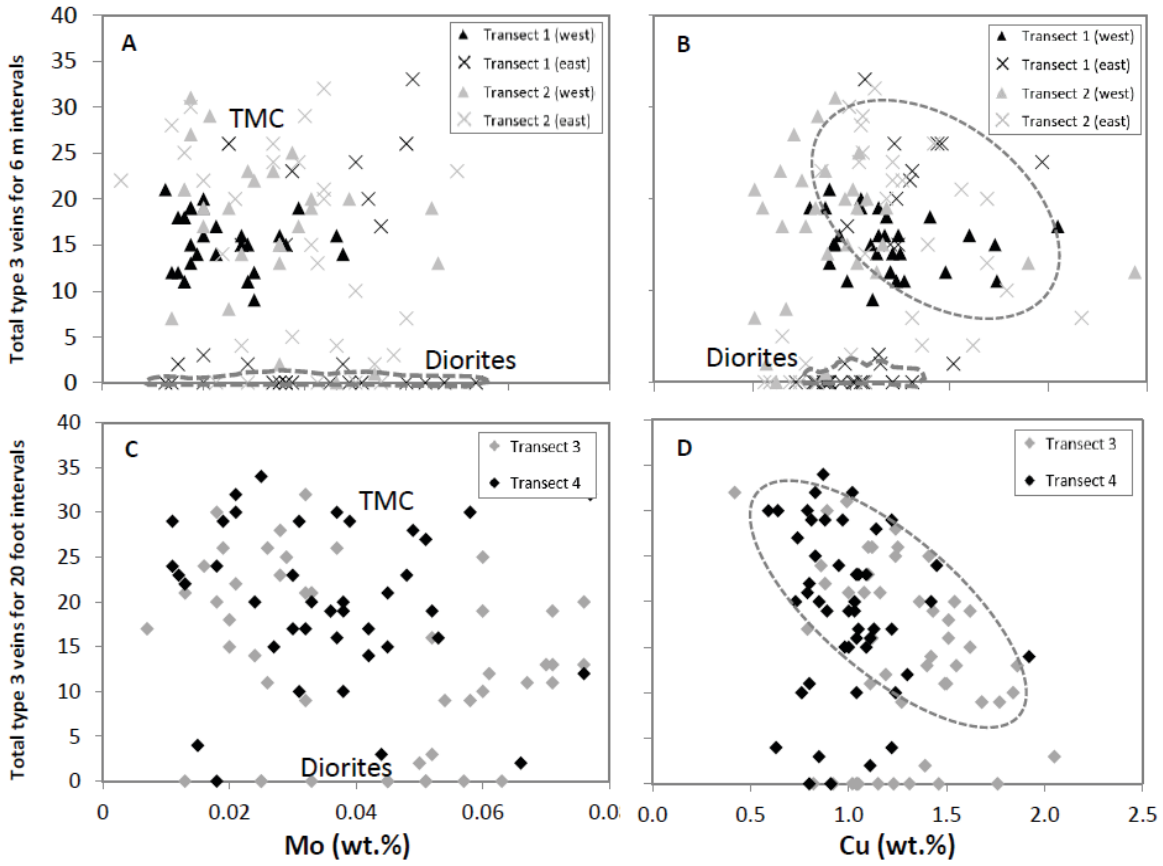


Figure 4.8: (A-B) Total number of type 3 veins versus average Mo and Cu grades for six metre intervals in the two deepest transects (transect 1 = black, transect 2 = grey). (C-D) Abundance of type 3 veins versus average Mo and Cu grades for 20 foot intervals in the two shallowest transects (Transects = grey diamonds, Transect 4 = black diamonds). Grade data courtesy of CODELCO Division El Teniente.

Main Mineralisation Veins

Main mineralisation stage veins occur throughout the TMC as well as within every intrusion at El Teniente. In accordance with previous studies (Camus, 1975; Cannell *et al*., 2005; Vry *et al*., 2010), these veins were found to be particularly abundant immediately surrounding the felsic-intermediate intrusions. Type 5 veins are abundant in the A-Porphyry, but less so in the diorites and Teniente Dacite Porphyry, suggesting that they predominantly formed prior to the final emplacement of these units in their respective parts of the deposit. Reflected light analysis of Mo-rich type 5 veins revealed that molybdenite is locally present as large, bladed crystals concentrated at vein margins, associated with quartz (e.g. Figure 4.7D). In contrast, Cu-rich examples typically exhibit large chalcopyrite crystals intergrown with anhydrite in sites that appear to represent the final stages of vein infill. Mo and Cu grades display no clear relationship with the abundance of type 5 veins in each drillcore interval

(Figure 4.9). This, combined with the fact that type 5 veins account for <6% of veins recorded (Figure 4.6; Table 4.4), indicates that they are of limited importance in controlling grade distributions in transects 1-4.

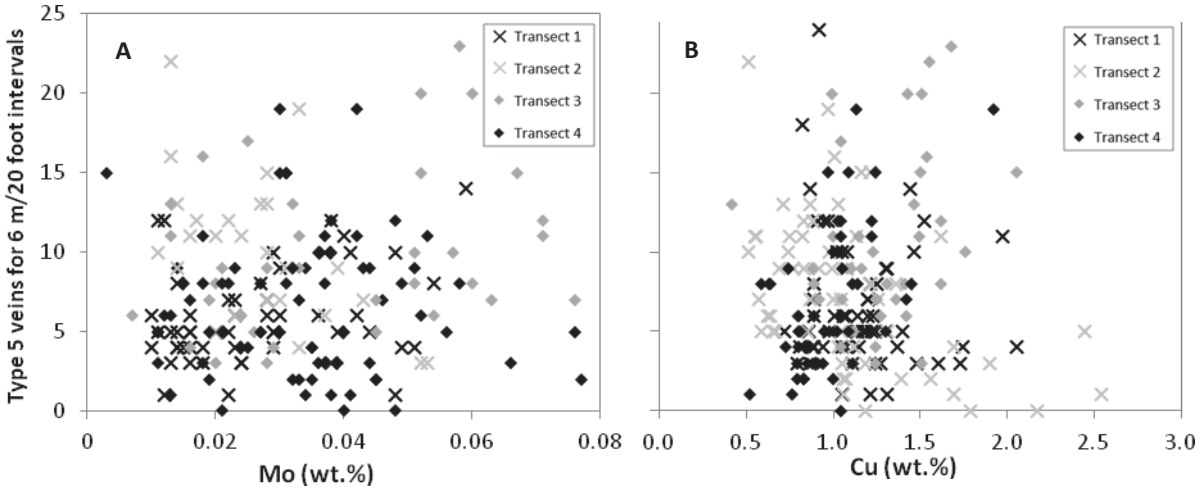
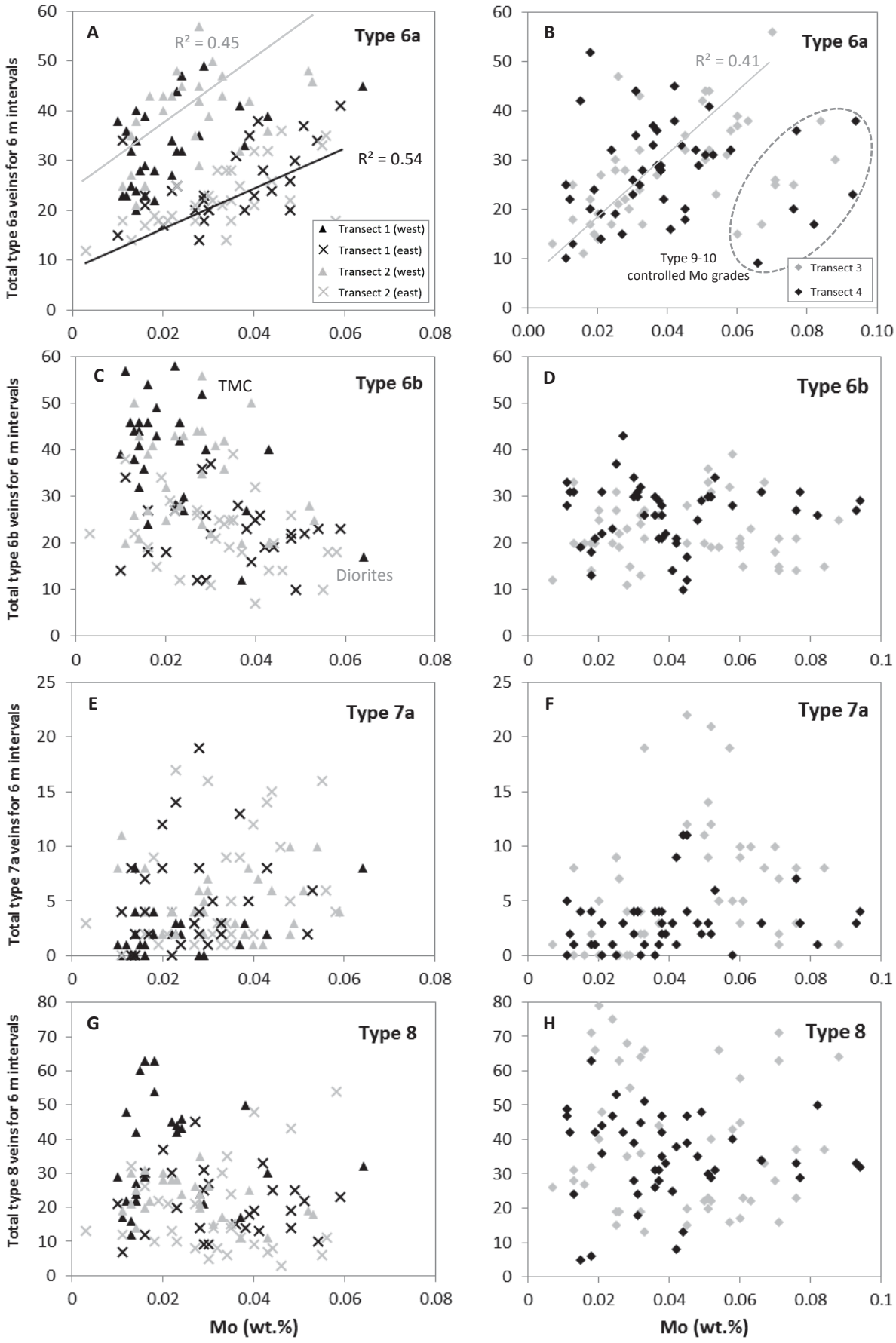


Figure 4.9: Total number of type 5 veins versus average Mo (A) and Cu (B) grades for six metre intervals in the two deepest transects (Transect 1 = black crosses and Transect 2 = grey crosses) and in the two shallowest transects (Transect 3 = grey diamonds and Transect 4 = black diamonds). Grade data courtesy of CODELCO Division El Teniente.

Quartz-dominated type 6 veins account for ~40% of all veins recorded and are observed throughout the TMC and within all intrusions (Table 4.4). These veins display similar abundances at all mine levels (Figure 4.6) but the proportion of Mo-rich type 6a veins generally increases with depth. Mo grades exhibit the strongest positive relationship with type 6a veins than with the abundances of any other vein type in transects 1 and 2 (Figure 4.10A-B). This relationship is particularly strong at deep mine levels in the drillcores that intersected the Northern and North Central Diorites (DDH 2371 = Transect 1-east and DDH 2215 = Transect 2-east). These drillcores contain fewer type 6a veins than the drillcores that traversed the TMC to the west, suggesting that Mo-poor type 6a veins also formed in more distal settings of the TMC relative to the diorites. However, Mo grades in the TMC still show a stronger relationship with type 6a vein abundance than any other main mineralisation vein type. This relationship is also apparent in transects 3 and 4 if the cluster of data with unusually high Mo grades is excluded (Figure 4.10B). These high grades are likely to be associated with paragenetically later Mo-rich vein and breccia types that occur at shallow mine levels (Table 4.3A).


A
Type 6a
R² = 0.45
R² = 0.54
Transect 1 (west)
Transect 1 (east)
Transect 2 (west)
Transect 2 (east)
Total type 6a veins for 6 m intervals
B
Type 6a
R² = 0.41
Type 9-10
controlled Mo grades
Transect 3
Transect 4
C
Type 6b
TMC
Diorites
Total type 6b veins for 6 m intervals
D
Type 6b
E
Type 7a
Total type 7a veins for 6 m intervals
F
Type 7a
G
Type 8
Total type 8 veins for 6 m intervals
H
Type 8
Mo (wt.%)
Mo (wt.%)

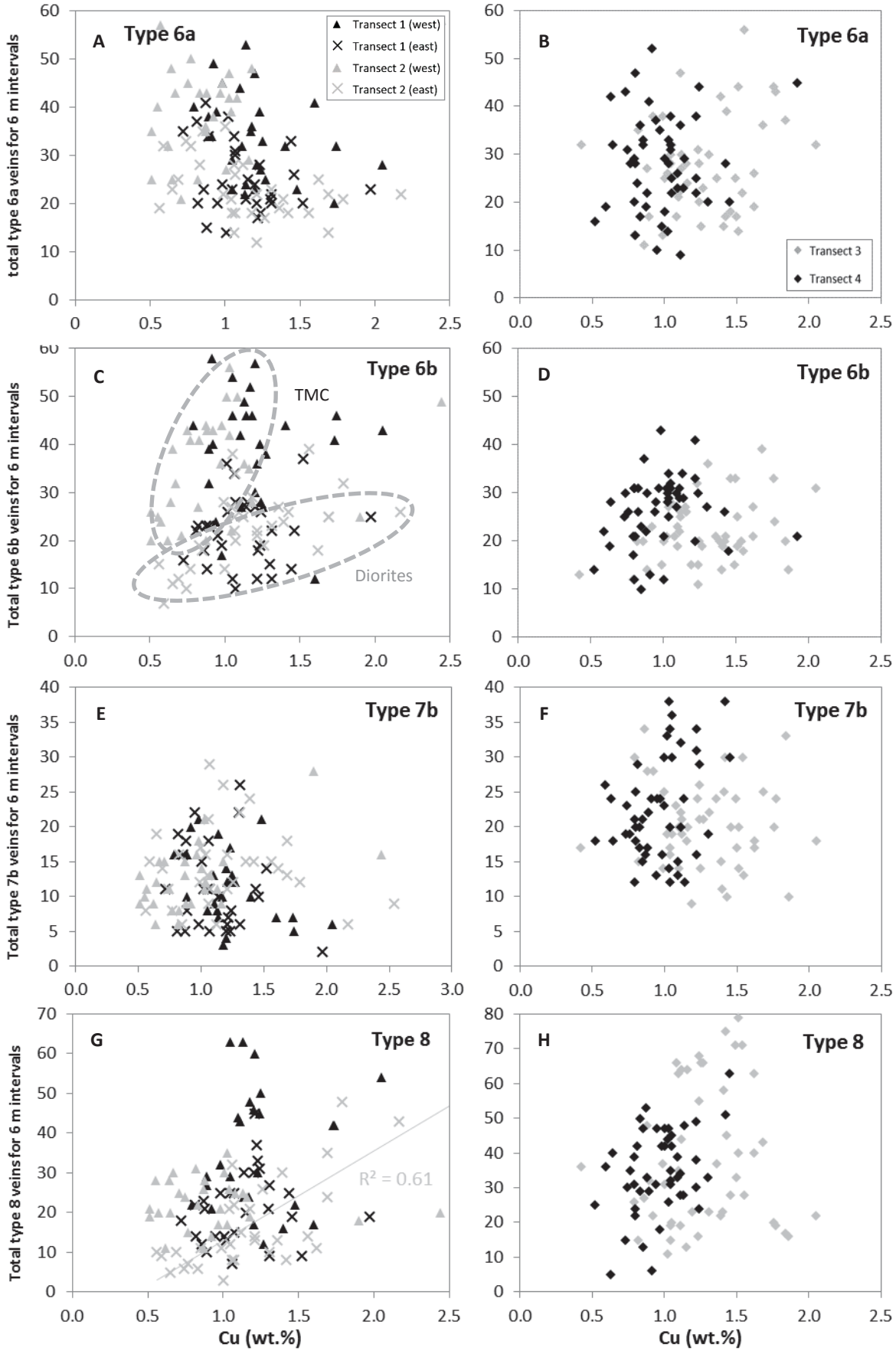

A
Type 6a
Transect 1 (west)
Transect 1 (east)
Transect 2 (west)
Transect 2 (east)
total type 6a veins for 6 m intervals
B
Type 6a
Transect 3
Transect 4
C
Type 6b
TMC
Diorites
Total type 6b veins for 6 m intervals
D
Type 6b
E
Type 7b
Total type 7b veins for 6 m intervals
F
Type 7b
G
Type 8
R² = 0.61
Total type 8 veins for 6 m intervals
Cu (wt.%)
H
Type 8
Cu (wt.%)

Figure 4.10 A-H: Total number of main mineralisation veins (type 6a-8) versus average Mo grades (wt.%) for six metre intervals in transects 1-2 and 20 foot intervals for transects 3-4. Transect 1 (2250 m asl) and transect 2 (1987 m asl) data are plotted on the left hand column. Transect 1-west = black triangles, transect 1-east = black crosses, transect 2-west = grey triangles, transect 2-east = grey crosses. Transect 3 (grey diamonds) and transect 4 (black diamonds) are plotted on the right. Due to their lack of contained molybdenite type 7b veins were not plotted. Type 6a veins show the strongest positive correlation with Mo grades of any vein type in all transects. Note the similar trends for drillcores that cut through the Northern Diorite and North Central Diorite (transect 1-east and transect 2-east), and the similar trends for drillcores that predominantly cut the TMC host rock to the west of the diorites (transect 1-west and transect 2-west). Brecciated drillcore intervals and drillcore intervals with >8 late mineralisation stage veins are not plotted. Grade data courtesy of CODELCO Division El Teniente.

Figure 4.11 A-H: Total number of main mineralisation veins (type 6a-8) versus average Cu grades (wt.%) for six metre intervals in transects 1-2 and 20 foot intervals for transects 3-4. Transect 1 (2250 m asl) and transect 2 (1987 m asl) data are plotted on the left hand column. Transect 1-west = black triangles, transect 1-east = black crosses, transect 2-west = grey triangles, transect 2-east = grey crosses. Transect 3 (grey diamonds) and transect 4 (black diamonds) are plotted on the right. Due to their lack of contained chalcopyrite and/or bornite type 7a veins were not plotted. Brecciated drillcore intervals and drillcore intervals with >8 late mineralisation stage veins are not plotted. Grade data courtesy of CODELCO Division El Teniente.

Copper grades display a weak negative correlation with the abundance of type 6a veins (Figure 4.11A-B) but show a clear positive correlation with the abundance of type 6b veins (Figure 4.11C-D). These chalcopyrite-rich veins are particularly abundant in the TMC in the deeper transects (DDH 2363 = T1-west and DDH 2230 = T2-west) where their frequency often exceeds 8 veins/metre (Figure 4.11C). Three, Mo-rich, type 6b vein subtypes are recognised in this study that showed clear evidence of early molybdenite mineralisation at the vein edges (e.g. Figure 4.7F-G), or at the vein centre with a chalcopyrite overprint (e.g. Figure 4.7E). Although these Mo-rich examples are relatively abundant within and surrounding all intrusions, type 6b vein abundance displays an inverse correlation with Mo grades in the two deepest transects (Figure 4.10B). This trend is similar to the inverse relationship displayed between Cu grades and type 6a vein abundances (Figure 4.11A).

Type 7a veins appear to be a transitional type from the quartz-rich type 6a and 6b veins (e.g. Figure 4.7I). However, the classification scheme of Vry *et al*. (2010) does not present a threshold sulphide abundance for this transition. Here type 7 veins are defined as those containing >70% sulphides that have no significant associated sericitic alteration. Molybdenite-dominated type 7a veins account for <5% of all veins recorded (Figure 4.6) and are typically thin (<2 mm) and commonly discontinuous. These predominantly occur within

or proximal to (<20 m) the felsic-intermediate intrusions, in part accounting for the high vein densities and Mo grades surrounding them. However, these veins display no clear relationship with Mo grade (Figure 4.10E-F), suggesting that they are of insufficient size and frequency to significantly control Mo grade distribution. Reflected light analysis of several type 7a veins revealed that they do not contain co-precipitated Cu, but are commonly surrounded by significant amounts of disseminated chalcopyrite in the wallrock (e.g. Figure 4.7I).

Chalcopyrite-dominated type 7b veins with widths >1 mm are approximately four times more abundant than type 7a molybdenite veins (Figure 4.6) and occur throughout the TMC where they have average thicknesses of 5-10 mm (Table 4.4). Despite this, plots of Cu grade against type 7b abundances also display no clear correlations (Figure 4.11E-F). This is largely attributed to the fact that, unlike other vein types, type 7b veins are commonly <1 mm thick and therefore a considerable proportion (20-40%) were not recorded. This undersampling is particularly likely in the deeper transects and within the felsic-intermediate intrusions where the number of recorded type 7b veins was typically less than 5 veins/metre even though chalcopyrite commonly coats fractured drillcore surfaces. This is therefore the most problematic limitation of the vein distribution analysis technique used.

Type 8 veins account for approximately 20% of the total number of veins recorded. These veins are particularly abundant at shallow mine levels (e.g. Figure 4.6) as well as within drillcores containing abundant TMC intervals (Figure 4.10G: DDH 2363 = Transect 1-west and DDH 2230 = Transect 2-west). Similar to type 6b veins, type 8 vein abundance generally increases with distance from the felsic-intermediate intrusions (e.g. Figure 4.12). These veins are typically composed of more anhydrite and less quartz than the type 6 veins and commonly host significant chalcopyrite, bornite and pyrite (e.g. Figure 4.7K). Molybdenite-bearing type 8 veins are relatively rare (e.g. Figure 4.7J), are typically more quartz-rich, and generally have narrow alteration halos in which unaltered feldspar can be observed. In rare cases where Mo-rich veins are surrounded by more intense sericitic alteration, reflected light microscopy revealed that molybdenite is typically overprinted by chalcopyrite and/or bornite (e.g. Figure 4.7K). This suggests that Mo was deposited prior to a copper sulphide + anhydrite-sericite overprint. Consistent with petrographic observations, Mo grades show no

relationship with type 8 vein abundances (Figure 4.10G-H). In contrast, type 8 veins display the clearest positive relationship with Cu grade of any vein type in all transects (Figure 4.11G-H). Peak Cu grades commonly coincide with peak type 8 vein abundance between 60 and 120 metres from the diorite intrusion margins (e.g. Figure 4.12).

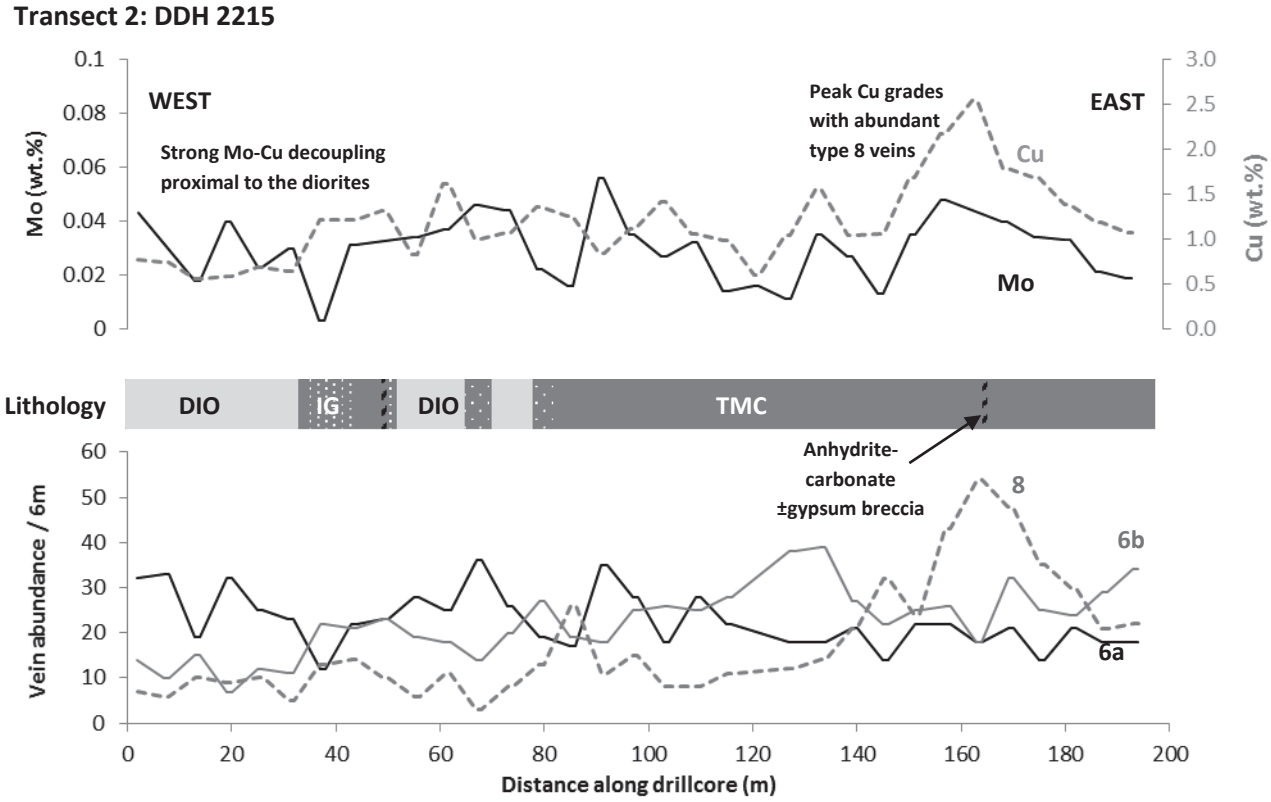


Figure 4.12: Mo and Cu grades (wt.%) versus lithology and the abundances of type 6a, 6b and type 8 veins along transect 2 heading to the east of the North Central Diorite (DDH 2215). Results show fluctuating Mo grades that correlate well with intervals containing abundant type 6a veins. There is a slight decrease in the abundance of type 6a veins and a general increase in type 6b and 8 vein abundances with distance from the intrusion. High Cu grades correlate well with peaks in type 6b and 8 vein abundances (e.g. 136 m and 165 m). Decoupling of Mo and Cu is most prominent within 40 m of the intrusion. Abbreviations: IG = igneous breccia, DIO = Diorite (North Central Diorite), TMC = Teniente Mafic Complex.

Late Mineralisation Veins

Type 9 tourmaline veins were observed throughout the deposit, cutting all intrusions. These accounted for <1% of veins recorded in transects 1-3 (Figure 4.6), but for a quarter of veins in transect 4 (Figure 4.6). Here they form an apparent vein halo surrounding the Braden Breccia pipe, in which veins commonly contain abundant molybdenite that is intergrown with, or overprints, large, acicular tourmaline crystals (e.g. Figure 4.7L). Consistent with this, type 9 vein abundance appears to exert a strong control on Mo grades in transect 4, but

displays no relationship in transect 3 (Figure 4.13A). In contrast, Cu grades tend to be low and consistent (0.6-1.2 wt.%) in transect 4 (Figure 4.13B) but are generally slightly higher in transect 3 (Figure 4.13B) where several chalcopyrite-bearing type 9 veins were observed.

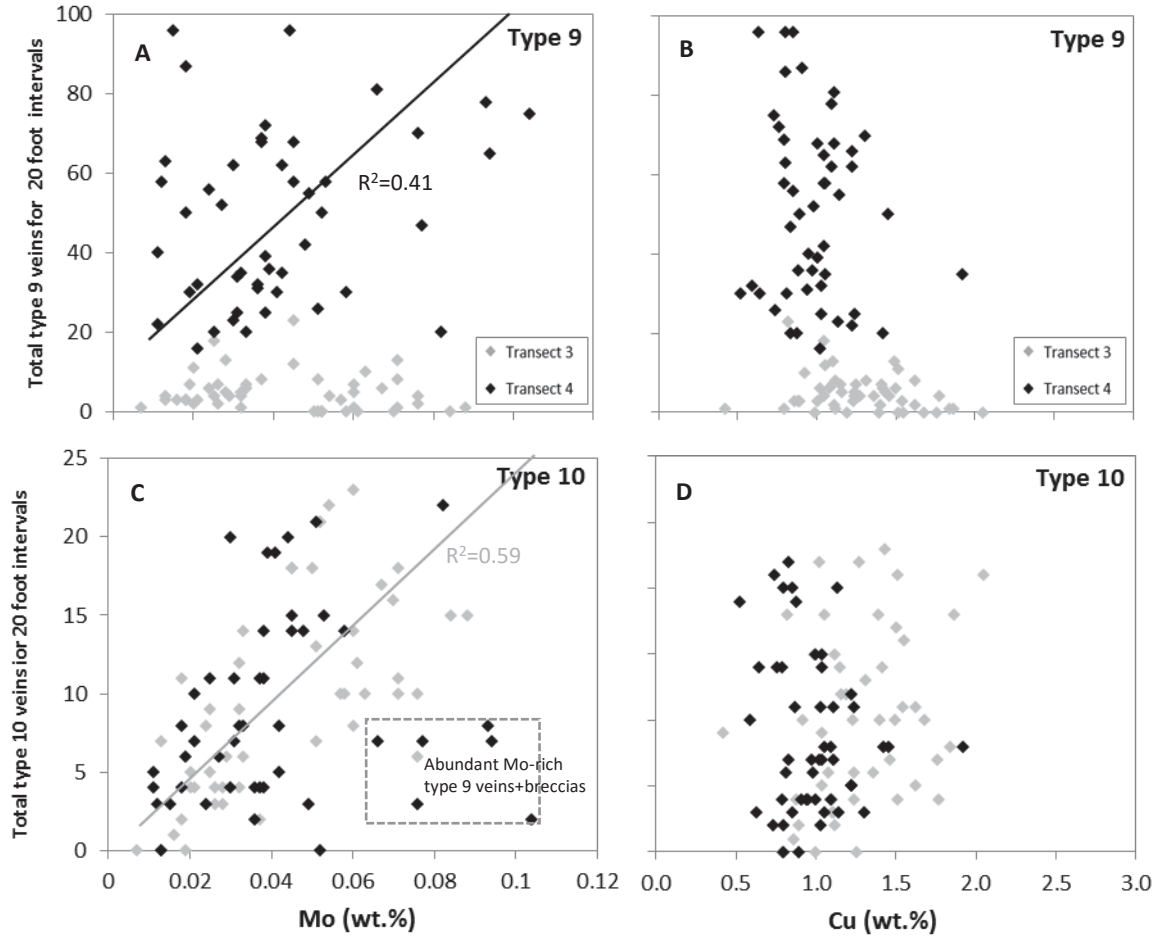


Figure 4.13: Total number of type 9 (A-B) and type 10 (C-D) veins versus average Mo and Cu grades for 20 foot intervals in the two shallowest transects studied (transect 3 = grey diamonds, transect 4 = black diamonds). Due to the extremely low number of type 9 and 10 veins recorded in the two deeper transects (transects 1-2), these veins are not considered important in controlling grade distributions at deep mine levels. As a result, late mineralisation stage vein abundances in transects 1-2 were not plotted. Type 9 vein abundances in transect 4 display a positive relationship with Mo grades (A) whereas type 10 veins show the strongest positive relationships with Mo grade of any vein type in transect 3 (C). Cu grades display no relationship with type 9 or 10 veins in both transects.

Type 10 anhydrite-carbonate ±gypsum veins were observed cross-cutting type 9 veins (e.g. Figure 4.7M) and appear to show a close spatial association with concentric and northwest-trending faults surrounding the Braden Breccia pipe (Table 4.4). Molybdenite is again abundant in these veins and typically occurs at the vein edges alongside variable amounts of bornite±chalcopyrite. Thin section analysis of a number of these veins revealed clear

evidence of reopening, with gypsum, anhydrite and carbonate overprinting sulphide mineralisation (e.g. Figure 4.6N). Isolated and tarnished fragments of bornite were also observed in several coarse gypsum veins. Although type 10 veins account for <4% of total veins recorded, their abundance displays a strong positive relationship with Mo grade in drillcore intervals in the shallow transects (Figure 4.13C). In contrast, Cu grades display a highly variable relationship with the abundance of type 10 veins (Figure 4.13D), as well as their associated anhydrite-carbonate ±gypsum breccias (e.g. Table 4.3). This probably reflects the highly variable amounts of contained chalcopyrite and bornite in this stage.

4.4.3 Breccia-Vein Relationships

Plots of vein abundance data against lithology for transects 1-4 reveal clear spatial relationships between the type 5, 9 and 10 veins and anhydrite-, tourmaline- and anhydrite-carbonate ±gypsum-cemented breccias respectively. For example, type 5 veins in transect 2 clearly represent vein halos around anhydrite-cemented breccia bodies (Figure 4.14). Strong spatial correlations are also observed between type 9 veins and tourmaline breccias in transect 4 (Figure 4.15) and between type 10 veins and anhydrite-carbonate ±gypsum breccias in transects 2 (Figure 4.14) and 3 (Figure 4.16). These breccias and their interpreted vein halos often spatially correlate with elevated Mo and Cu grades. This is particularly noteworthy for Mo, which is generally enriched in sections of drillcore that contain tourmaline- (type 9) and anhydrite-carbonate ±gypsum-cemented (type 10) breccias (Figures 4.14-4.16).

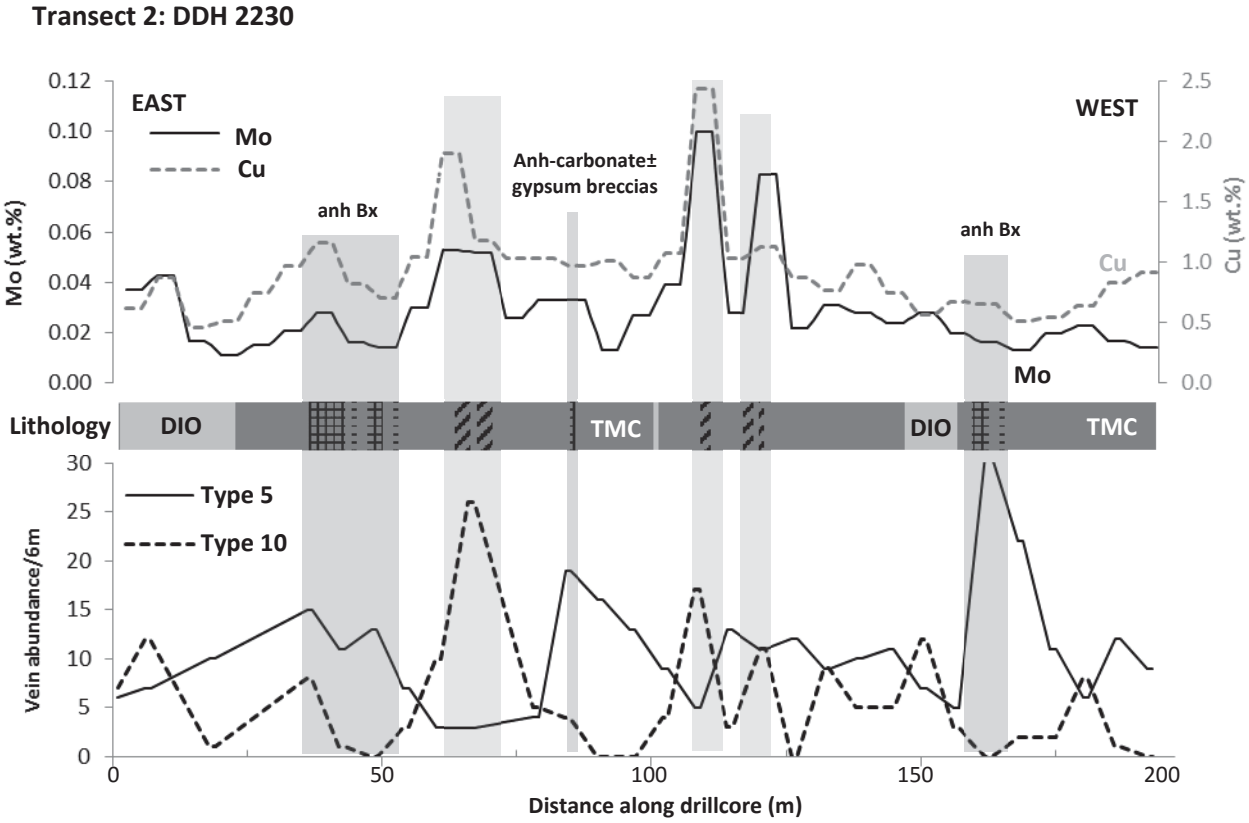


Figure 4.14: Mo and Cu grades (wt.%) plotted against host lithology and the abundances of type 5 and type 10 veins for 6 metre intervals along transect 2 west (DDH 2230). Results show a good spatial relationship between type 5 veins and inferred associated anhydrite breccias and type 10 veins and their inferred associated anhydrite-carbonate ±gypsum breccias (grey columns). Mo and Cu grades show a good spatial relationship with the presence of type 10 veins and their associated breccias.

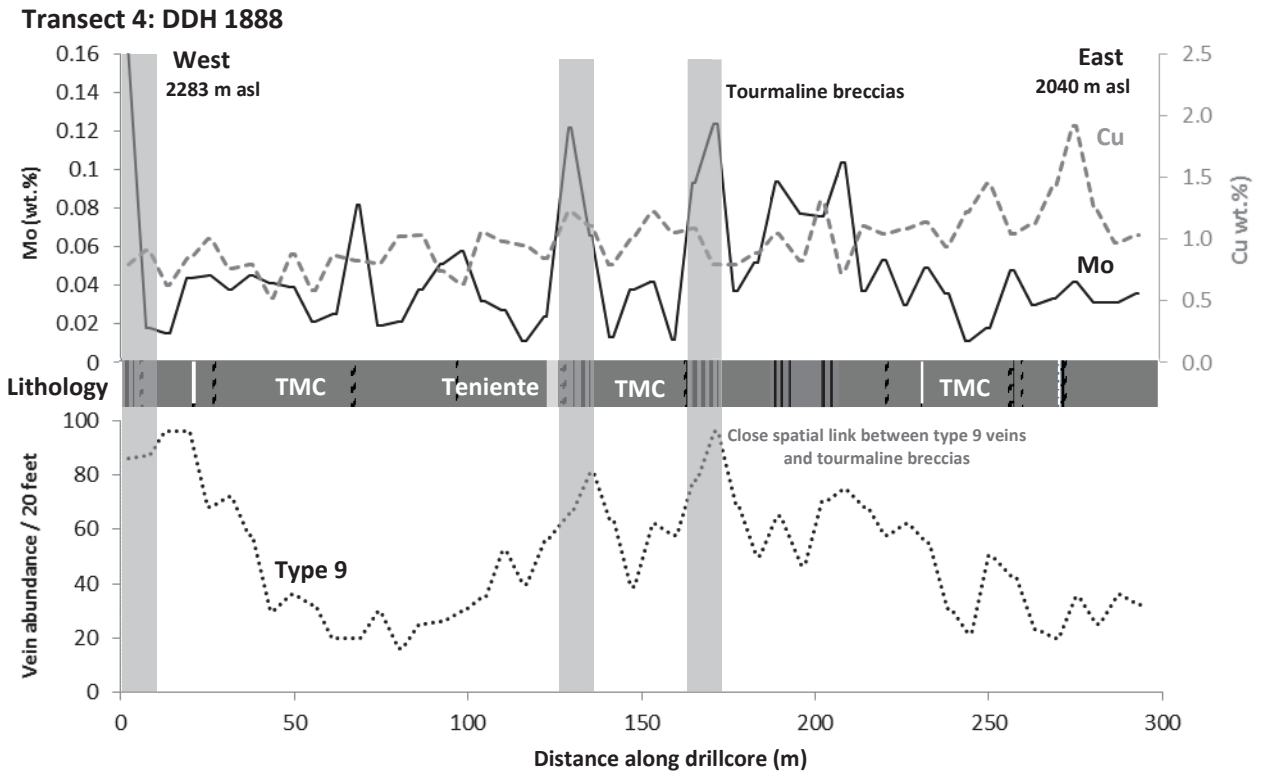


Figure 4.15: Mo and Cu grades (wt.%) plotted against host lithology and the abundances of type 9 veins for 20 foot intervals along transect 4 (DDH 1888). Results show a good spatial relationship between the presence of tourmaline breccias (grey columns) and the abundance of type 9 tourmaline veins. These correlate well with peak Mo grades whereas Cu shows no clear relationship with this vein/breccia stage.

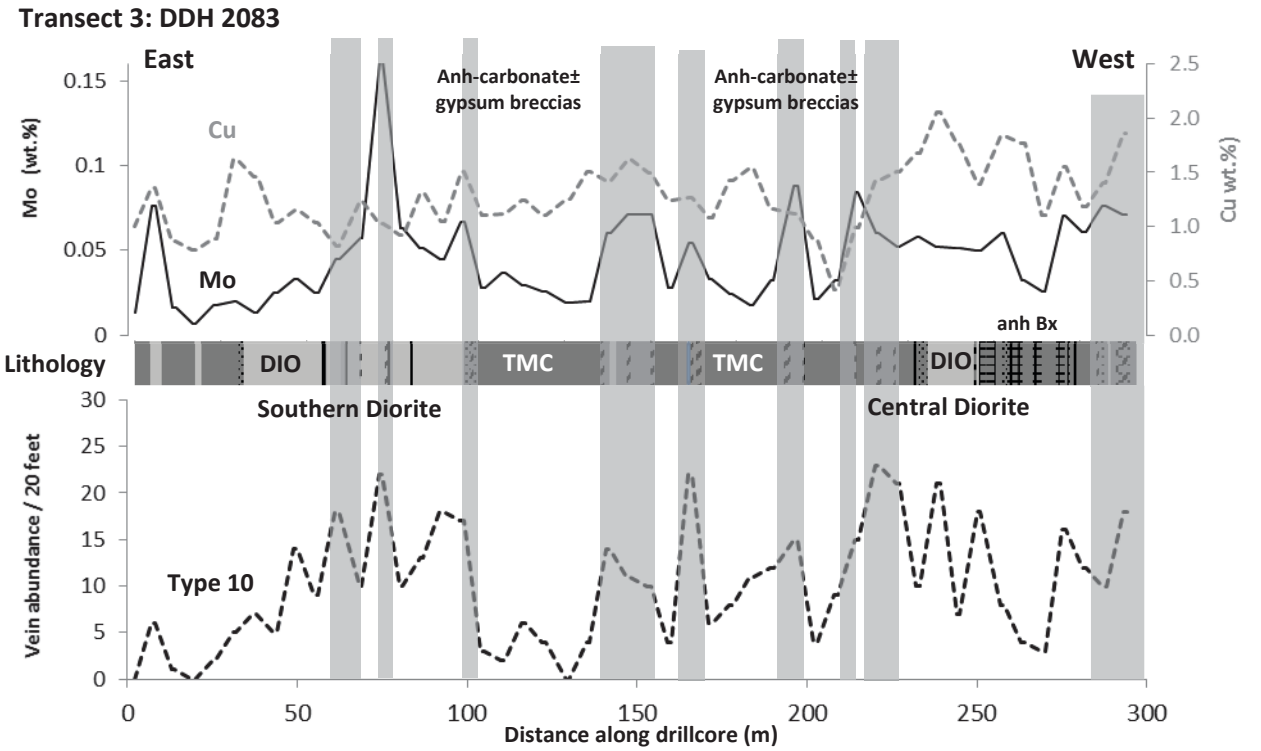


Figure 4.16: Mo and Cu grades (wt.%) plotted against host lithology and the abundance of type 10 veins for 20 foot intervals along transect 3 (DDH 2083). Peak Mo grades are well correlated with the presence of type 10 anhydrite-carbonate ±gypsum breccias (grey columns), whereas Cu grades show a strong spatial correlation with anhydrite breccias proximal to the Southern Diorite. Mo grades show a spatial association with peaks in the abundance of type 10 veins whereas Cu shows no clear relationship.

4.4.4 Reverse Crosscutting Relationships

The vein chronology of Vry *et al*. (2010) was defined by plotting observed vein and breccia cross-cutting relationships in the following matrix (Figure 4.17: black numbers). In order to test the validity of this sequence, reverse cross-cutting veins observed during this study were recorded (Figure 4.17: red numbers). Only 29 reverse cross-cutting vein relationships were identified suggesting that the classification scheme of Vry *et al*. (2010) is generally accurate and robust for use across the deposit. The majority of the reverse cross-cutting vein types involved pre-mineralisation stage type 3 veins (e.g. Figure 4.17A) and tourmaline veins (e.g. Figure 4.17C). By contrast, reverse cross-cutting relationships involving molybdenite-bearing type 6a-7a veins and chalcopyrite-bearing type 6b-7b veins were extremely rare (e.g. Figure 4.17B). This confirms that the deposition of these metals was consistently decoupled across the deposit (Vry *et al*., 2010).

Offsetting vein (older) \ Offsetting vein (younger)	1	2	3	4a	4b	bt bx	5	anh bx	6a	6b	7a	7b	8	9	10
1															
2															
3			15	4	1		5	9	36	1	9		14		4
4a						2		20	5		4		4		1
4b									1		1				
bt bx									1	1	1		1		1
5			2						2		3		6		3
anh bx			1						7		3	1	10	3	3
6a			1				2	2			7	1	20		5
6b							1		2	25		3			
7a										1		2			
7b															
8													2		5
9									3	2		1	7		2
10														4	

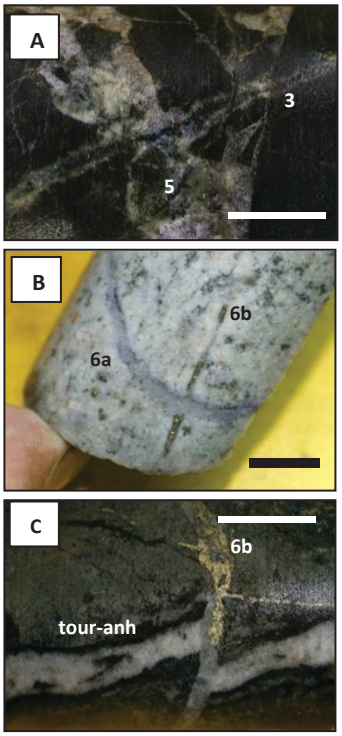


Figure 4.17: Matrix of vein crosscutting relationships recorded at El Teniente. Black numbers = crosscutting relationships recorded by Vry *et al*. (2010). Red numbers = reverse crosscutting relationships observed in this study. (A-C) = Example photographs of reverse cross-cutting relationships. (A) Type 3 vein crosscutting an anhydrite breccia to the east of the TDP (2230-42.8). (B) Type 6b vein with chalcopyrite crosscut by a molybdenite-bearing type 6a vein in the CD (2083-69.2). (C) Example of an early tourmaline vein cut by a type 6b vein to the south of the Braden pipe. Scale bars = 1 cm. Abbreviations: bt = biotite, bx = breccia.

The apparent reverse cross-cutting relationships involving tourmaline veins (e.g. Figure 4.17C) are likely to be a manifestation of multiple episodes of tourmaline brecciation and veining that were not recognised by Vry *et al*. (2010). The abundance of anhydrite and K-feldspar observed in some of these samples (e.g. Figure 4.17C) suggests that early tourmaline may have been deposited during the generation of type 4 and type 5 veins. This is in accordance with previous chronologies presented for El Teniente (Figure 3.6). The lack of contained sulphides and the relative rarity of these veins means that the omission of an early tourmaline vein stage is not considered important for this study. By contrast, the presence (albeit rarely) of reverse cross-cutting relationships involving premineralisation and main mineralisation stage veins and breccias (e.g. Figure 4.17A-B) supports the development of repeated cycles of the vein paragenesis, associated with successive intrusive centres. The infrequency of reverse cross-cutting relationships may be a manifestation of the spatial separation of the successive intrusive centres.

4.4.5 Geochronology

Timing of Mineralisation

The 11 molybdenite samples dated in this study by Re-Os document 0.83 million years of mineralisation between 5.411 ±0.022 Ma and 4.584 ±0.022 (4.580 ±0.019 Ma replicate: Table 4.5). This age range is shorter than the 1.9 My range presented by previous studies (Maksaev *et al*., 2004; Cannell, 2004), which include older Re-Os ages of 6.31 ±0.03 Ma and 5.60 ±0.02 Ma (Maksaev *et al*., 2004), and 5.897 ±0.020 Ma (Cannell, 2004) for anhydrite breccias associated with the older Sewell Quartz Diorite and A-Porphyry intrusions.

The oldest molybdenite ages recorded in this study are for main mineralisation stage veins within the Southern Diorite and to the north of the Central Diorite (Table 4.5; Figure 4.18). These type 6a, 6b, and type 8 veins cluster at ages between 5.411 ±0.022 and 5.322 ±0.022 Ma. Molybdenite hosted by the B-fault yields an age of 4.967 ±0.039 Ma, which coincides with the oldest main mineralisation stage veins spatially associated with the Teniente Dacite Porphyry and Northern Diorite (Figure 4.18). Previously dated main mineralisation stage veins in this part of the deposit cluster between 4.980 ±0.035 and 4.78 ±0.03 Ma (Figure 4.18), slightly older than the type 6b vein from the southern tip of the Teniente Dacite Porphyry dated in this study (4.718 ±0.023 Ma). These dates also coincide with a molybdenite age of 4.835 ±0.016 Ma from an anhydrite breccia to the north of the Braden pipe (Cannell, 2004). Although reported as a late mineralisation stage breccia (Figure 4.1), this sample may actually represent a type 5 breccia associated with the Teniente Dacite Porphyry that has been overprinted by sericitic alteration. These dates also coincide with a transitional type 7a-8 vein and a previously dated type 7a vein proximal to the North Central Diorite (Maksaev *et al.*, 2004), which yielded ages of 4.804 ±0.020 and 4.83 ±0.03 Ma respectively (Figure 4.18). These veins are, however, significantly older than a deep-level (1462 m asl), type 6a vein also from the margin of the North Central Diorite that yielded an age of 4.613 ±0.020 Ma in this study.

Table 4.5 (next page): Summary of Re-Os data for the 11 molybdenite samples dated during this study.

Notes: Replicates = complete new analysis of existing mineral separate. SEM = Os analysis completed using a Secondary Electron Multiplier (weak signal). Elev. = Elevation of sample in metres asl. The B-Fault sample was given an estimated depth as it was not obtained from one of the studied drillcores. For sample locations refer to sample Re-Os dates displayed on Figure 4.18.

Sample	Vein Type	Elev.	Aliquot Weight (mg)	Re ppm	± 2s	187Re ppb	± 2s	187Os ppb	± 2s	Total common Os pg	Model Age (Ma)	± 2s (Ma)	Sample Description
2215-119.9	6a	**2019.5**	1.17	353.4	0.91	222153	575	19.699	0.016	1.8	**5.322**	**0.022**	2 cm wide type 6a-7a vein containing abundant mo mineralisation, proximal to the North Central Diorite. Vein has no halo and minor cpy mineralisation (2%). Vein minerals are 50% qz and 8% anh, 40% mo 2% disseminated cpy.
1034-837.0 (SEM)	6a	**1462.4**	1.18	171.8	0.44	107993	279	8.301	0.011	3.3	**4.613**	**0.020**	14 mm wide type 6a vein of 80% qz and 5% anh proximal to the North Central Diorite at a deep mine level. Vein contains 15% molybdenite at the centre of vein. No cpy present and no discernible alteration halo.
2083-250.0	6b	**2222.9**	1.35	500.5	1.30	314613	815	28.364	0.021	1.2	**5.411**	**0.022**	1 cm wide type 6b vein with Mo at vein edges and cpy at vein centre in the Southern Diorite. Vein is 50% qz, 15% anh, 15% mo, 15% cpy and 5% Kfsp. No alteration halo but surrounding 4 mm contains disseminated cpy
1888-133.8	6b	**2177.8**	1.21	183.2	0.47	115126	298	9.049	0.024	2.8	**4.718**	**0.023**	Large composite type 6b vein with abundant mo and cpy mineralisation to the south of the Braden pipe. Vein is 70% qz, 5-10% anh, 5% cpy and 15-20% mo. Faint qz alteration halos with disseminated cpy.
1805-367.1	7a-8	**1617.7**	1.02	217.2	0.56	136538	353	10.929	0.012	2.9	**4.804**	**0.020**	6 mm wide transitional 7a-8 vein within the TMC proximal to the North Central Diorite with a diffuse qz+minor ser halo. Halo is still feldspathic and is 2 mm wide. Vein is 50% mo, 30% anh, 15% qz, 5% cpy and 1% bo.
2083-184.1	8	**2220.6**	0.98	1228.4	3.18	772118	1998	69.142	0.051	1.0	**5.375**	**0.022**	3mm wide mo-rich type 8 vein with a well-developed qz-ser alteration halo in the TMC proximal to the Southern Diorite and Central Diorite. Vein is 45% anh, 10% qz 38% mo, 5% cpy and 2% bo. Alteration halo contains disseminated bo, mo and cpy.
Replicate		**2220.6**	0.95	1203.6	3.11	756483	1957	68.071	0.078	2.7	**5.401**	**0.023**	
1754-285.9	9	**2334.4**	2.97	78.75	0.20	49498	128	3.780	0.006	2.4	**4.584**	**0.020**	Tour-mo cemented breccia sample with clusters of radiating tourmaline crystals found to the East of the Braden Breccia pipe. Clasts are dacitic in composition and have been aggressively altered by qz-ser
Replicate		**2334.4**	2.96	76.50	0.20	48086	124	3.669	0.004	1.4	**4.580**	**0.019**	
2716-8.0 (SEM)	9	**2360.7**	1.27	13.71	0.04	8614	22	0.660	0.003	1.5	**4.599**	**0.029**	Tour+mo+anh cemented breccia in the Mo-rich halo to the West of the BBP. Found in association with a type 10 pyrite-carbonate vein. Breccia matrix is 32% mo, 17% anh, 30% tour, 14% cb 5% qz, 2% py.
2083-201.2	10	**2221.2**	1.37	49.25	0.13	30954	80	2.423	0.018	2.5	**4.698**	**0.040**	1 cm wide anhydrite vein surrounded by type 10 qz-ser halo found in the TMC on the rim of the Southern Diorite proximal to a type 5 anhydrite breccia with no alteration. Vein contains 15% mo and <1% cpy mineralisation. No disseminated sulphides present.
Replicate		**2221.2**	2.94	49.00	0.13	30799	80	2.394	0.007	3.6	**4.666**	**0.023**	
1754-373.8	10	**2283.1**	1.38	176.3	0.46	110781	287	8.515	0.015	0.7	**4.613**	**0.020**	2 cm wide qz+mo+cb+anh type 10 vein in the TMC on the western rim of the Central Diorite. Vein is 35% qz, 15% anh, 25% cb and 20% mo, 3% bo, 1% cpy and 1% py. Sample has a diffuse 6mm qz-ser halo containing disseminated mo and cpy.
B-FAULT	None	**2210.0**	1.35	15.69	0.04	9864	26	0.816	0.005	1.7	**4.967**	**0.039**	Hand sample of fine grained mo+cb+and clay minerals with slicken sides associated with a large fault (B-Fault) running on a SW trend through the TMC near the North Central Diorite. Minor py 1% present. Mo has a pale blue-grey colour.

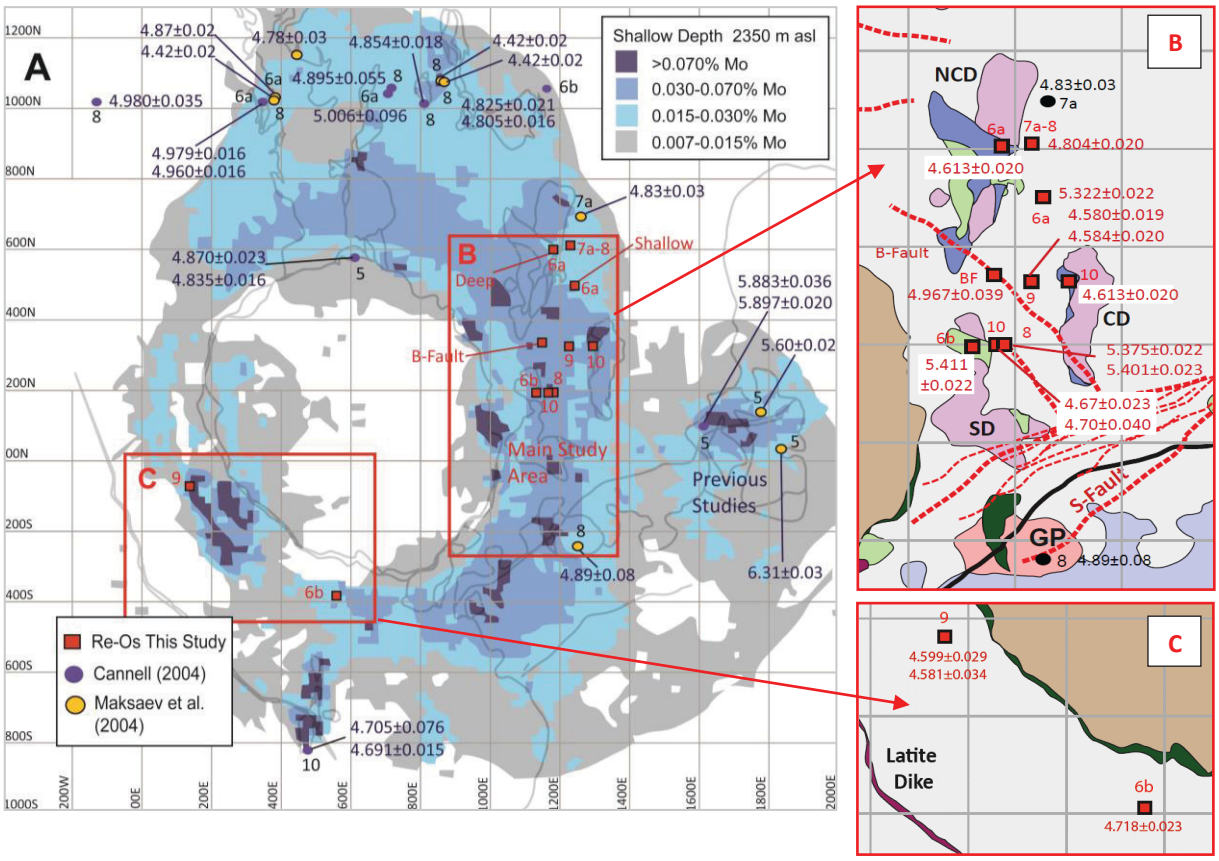


Figure 4.18: (A) Re-Os molybdenite ages recorded during this (red squares) and two previous studies (black circles: Cannell, 2004; Maksaev *et al*., 2004) superimposed on a Mo grade distribution map at mine level 2350 m asl. Vein and breccia types are displayed next to each sample location in accordance with the classification of Vry *et al*. (2010). Red boxes B and C contain samples dated during this study, the ages of which are shown on sections of geological map to the right (panels B-C). For sample descriptions and depths refer to Table 4.5.

Tourmaline breccias on opposite sides of the Braden pipe yield similar ages of 4.599 ±0.029 and 4.584 ±0.020 Ma (Figure 4.18). These dates are slightly younger than the type 10 vein samples from the western edge of the Central Diorite (1754-373.8) and Southern Diorite (2083-201.2) which yield similar ages of 4.613 ±0.020 and 4.698 ±0.023 Ma (4.666 ±0.023 Ma replicate). These ages are comparable with a previously dated, late mineralisation stage breccia associated with the latite dyke to the southwest of the Braden pipe (Figure 4.18; Cannell, 2004). The youngest Re-Os molybdenite ages at El Teniente are from three type 8 veins proximal to and within the Teniente Dacite Porphyry and Northern Diorite (Figure 4.16) dated by Maksaev *et al*. (2004; see Figure 4.18).

Molybdenite Re Contents and Validity of Results

The Re contents of the studied molybdenite samples are consistent for all the main mineralisation stage samples (171.8-500.5 ppm) with the exception of the type 8 vein sample, which contains highly elevated Re (1203.6-1228.4 ppm). This vein type accounted for the highest Re concentrations recorded in the two previous Re-Os dating studies, where Re concentrations of up to 829.7 ppm were recorded (Cannell, 2004; Maksaev *et al*., 2004). In contrast, Re concentrations in molybdenite in the late mineralisation stage veins and breccias and in the B-fault are consistently lower (13.71-176.3 ppm).

Stein *et al*. (2001) stated that variations in the Re contents of molybdenite are most likely explained by a simple mass balance phenomenon (Stein *et al*., 2001): as Re is highly compatible in molybdenite it will be effectively incorporated into the molybdenite crystal structure in preference to other sulphide species. Therefore, if only minor amounts of molybdenite and abundant copper-sulphides are precipitated, the molybdenite will contain higher Re concentrations. This explains the elevated Re concentrations in molybdenite-bearing type 8 veins which, in accordance with petrographic observations and vein distribution data, are commonly associated with abundant chalcopyrite ±bornite and only minor Mo mineralisation.

In contrast to type 8 veins, mineralisation in the B-Fault and in the late mineralisation stage type veins and breccias is dominated by molybdenite with only minor quantities of Cu-sulphides. This means that low Re concentrations could be a manifestation of Re dilution during abundant molybdenite crystallisation. This is consistent with a comparison study of Re in molybdenite from the Endako porphyry Mo deposit and the Nithi Mountain occurrence, British Columbia, where lower Re concentrations at Endako were attributed to the far greater extent of Mo mineralisation (Selby and Creaser, 2001). Similar observations have also been made in the Qinling belt, China (Stein *et al*., 1997), and in comparison studies between porphyry Cu-Mo and Mo deposits (Giles and Schilling, 1972), both of which showed decreasing Re concentrations in molybdenite deposited during Mo-rich stages.

Suzuki *et al*. (2000) suggested that the Re-Os molybdenite system may be disturbed in the presence of hot, low-salinity fluids (<1 wt% $NaCl_{eq}$). However, a recent study by Selby and Creaser (2001) concluded that the Re-Os system is undisturbed by low to moderately saline (1–15 wt% $NaCl_{eq}$) hydrothermal fluids. This, combined with the young age of El Teniente and the fact that the Re-Os molybdenite system shows closed system behaviour during ductile deformation and regional metamorphism (e.g. Stein *et al*., 1998; Selby and Creaser, 2001; Lawley and Selby 2012), suggests that the dates obtained during this study represent true mineralisation ages.

The three replicate samples yielded ages that agree within calculated uncertainty limits (Table 4.5) taking into account all procedural uncertainties. The reproducibility of these sample ages suggests that the technique used was effective in producing accurate age determinations and confirms that the reanalysed samples did not contain mixed generations of molybdenite. With the exception of two samples, all calculated uncertainties are ≤0.023 Ma (Table 4.5). However, one type 10 vein sample (2083-201.2) and the B-Fault sample have higher analytical uncertainties, mainly due to their low Re concentrations (Table 4.5). The replicate run for the type 10 vein sample yielded a lower degree of uncertainty, which was achieved by running a larger aliquot of molybdenite. Low Re concentrations are also documented for molybdenite in the tourmaline breccia samples from opposite sides of the Braden Breccia pipe. However, these samples yielded Re-Os ages that are within calculated uncertainties of one another as well as the tourmaline breccia replicate, thus suggesting that the technique used was effective in producing reproducible age determinations for molybdenite samples that contain very low Re concentrations.

4.5 Discussion

4.5.1 Geochronological Constraints on the Evolution of El Teniente

Mineralised vein and breccia distributions provide strong evidence that the A-Porphyry, diorites and Teniente Dacite Porphyry all played integral roles in controlling deposit-wide grade distributions as previously proposed (e.g. Cannell *et al*., 2005; Vry *et al*., 2010). The wide range of U-Pb zircon crystallisation ages recorded for these intrusions (Figure 3.3: Maksaev *et al*., 2004) may be due to age determinations made on zircon antecrysts that crystallised over an extended period of time in the underlying parental magma chamber and occasional younger ages due to zircon overgrowths or post-crystallisation lead-loss. It is therefore inferred that the youngest distributions of reliably dated, overlapping zircon ages (1σ) provide the best constraints for the timing of emplacement and final crystallisation of each intrusion (cf. von Quadt *et al*., 2011).

Geochronological data collected in this study are compared with the youngest reliable overlapping U-Pb zircon dates collected by Maksaev *et al*. (2004) and are summarised in Figure 4.19 to summarise the evolution of the system. The reinterpretation of U-Pb zircon data presented here still agree with Maksaev *et al*. (2004) that the crystallisation of the A-Porphyry is likely to have occurred between 6.0 and 5.7 Ma following the emplacement of the Sewell Quartz Diorite. However, the crystallisation of the Central and Northern Diorites is likely to have occurred between 5.6 and 5.3 Ma (Figure 4.19). This window correlates with the subordinate peak in U-Pb zircon ages recorded for these intrusions (Maksaev *et al*., 2004) and explains the presence of molybdenite Re-Os ages of 5.411 ±0.022 to 5.322 ±0.022 Ma for main mineralisation-type veins within and proximal to them. Based on petrological evidence and the spread of U-Pb zircon and Re-Os molybdenite ages associated with the Teniente Dacite Porphyry, this unit is interpreted to have a prolonged crystallisation history occurring in multiple intrusion-mineralisation pulses between 5.1 and 4.7 Ma (Figure 4.19). This age range is younger than the weighted average $^{206}Pb/^{238}Pb$ age of 5.28 ±0.10 Ma reported by Maksaev *et al*. (2004), which possibly incorporates older zircon antecrysts.

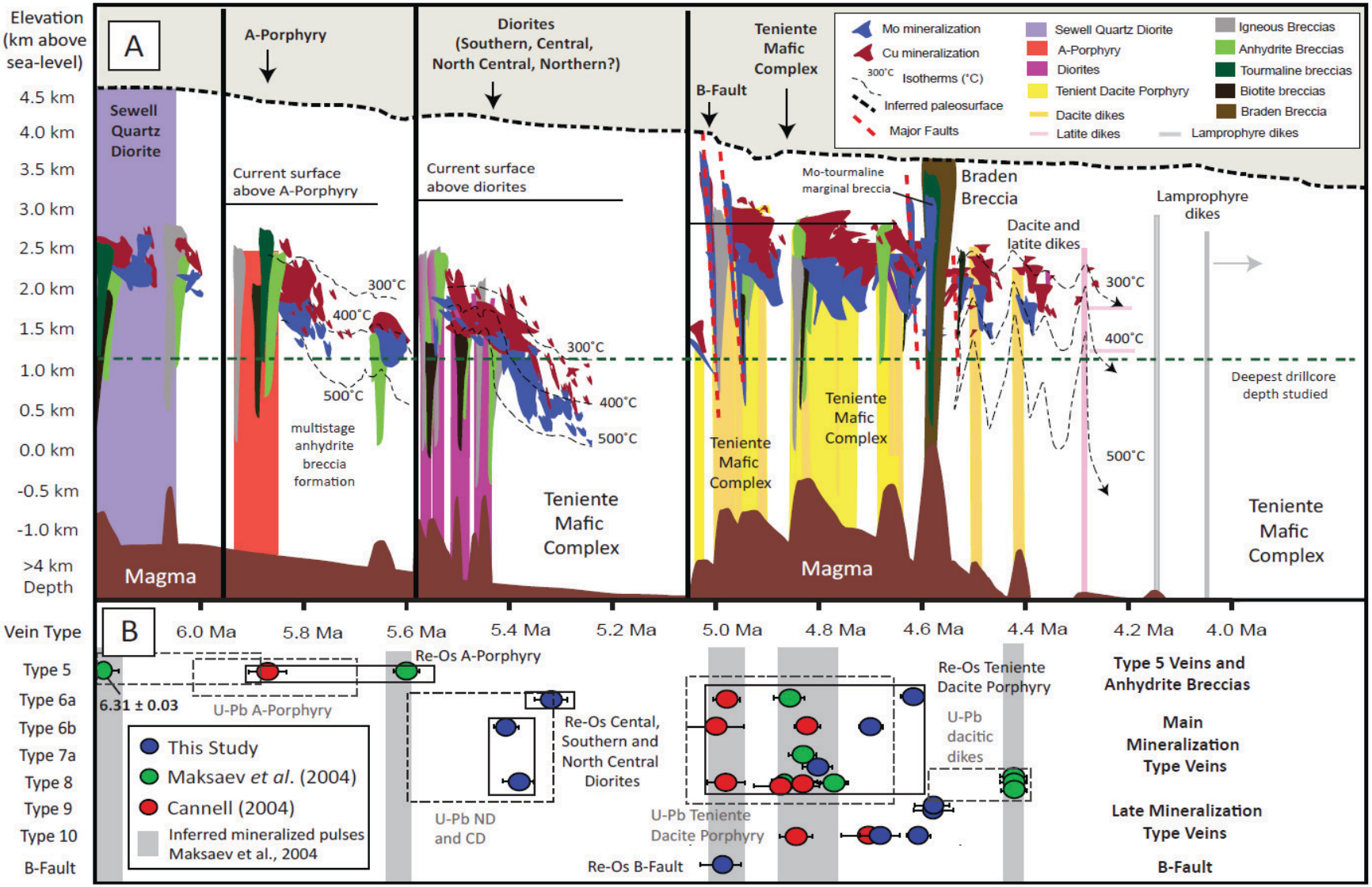

Elevation (km above sea-level)
4.5 km
4.0 km
3.5 km
3.0 km
2.5 km
2.0 km
1.5 km
1.0 km
0.5 km
0.0 km
-0.5 km
-1.0 km
>4 km Depth
A
Sewell Quartz Diorite
A-Porphyry
Diorites (Southern, Central, North Central, Northern?)
Teniente Mafic Complex
B-Fault
Mo mineralization
Cu mineralization
300°C Isotherms (°C)
Inferred paleosurface
Major Faults
Sewell Quartz Diorite
A-Porphyry
Diorites
Tenient Dacite Porphyry
Dacite dikes
Latite dikes
Igneous Breccias
Anhydrite Breccias
Tourmaline breccias
Biotite breccias
Braden Breccia
Lamprophyre dikes
Current surface above A-Porphyry
Current surface above diorites
Mo-tourmaline marginal breccia
Braden Breccia
Dacite and latite dikes
Lamprophyre dikes
300°C
400°C
500°C
multistage anhydrite breccia formation
Deepest drillcore depth studied
Magma
Teniente Mafic Complex
Vein Type
B
6.0 Ma
5.8 Ma
5.6 Ma
5.4 Ma
5.2 Ma
5.0 Ma
4.8 Ma
4.6 Ma
4.4 Ma
4.2 Ma
4.0 Ma
Type 5
Type 6a
Type 6b
Type 7a
Type 8
Type 9
Type 10
B-Fault
6.31 ± 0.03
U-Pb A-Porphyry
Re-Os A-Porphyry
Re-Os Cental, Southern and North Central Diorites
U-Pb ND and CD
Re-Os Teniente Dacite Porphyry
U-Pb dacitic dikes
U-Pb Teniente Dacite Porphyry
Re-Os B-Fault
This Study
Maksaev et al. (2004)
Cannell (2004)
Inferred mineralized pulses Maksaev et al., 2004
Type 5 Veins and Anhydrite Breccias
Main Mineralization Type Veins
Late Mineralization Type Veins
B-Fault

Figure 4.19: (A) Time versus depth plot showing the magmatic-hydrothermal evolution of El Teniente based on field observations and geochronology. Intrusion and breccia colours match geological map (Figure 4.1). The positions of Mo and Cu mineralisation relate to enriched ore zones (>0.03% Mo, >1.5% Cu) surrounding each intrusion and are based on grade distributions, vein cross-cutting relationships and Re-Os dates collected during this and the two previous studies (Cannell, 2004; Maksaev *et al*., 2004). The inferred paleosurface is a conservative estimate (max = 5300 m asl at 5 Ma). Dotted green line = deepest drillcore depth studied, below which significant Mo grades are interpreted to extend. (B) Re-Os dates from this study (blue circles) and the two previous studies (green and red circles). The five mineralising pulses of Maksaev *et al*. (2004) are shown in grey columns. Dotted boxes represent the youngest, reliable, overlapping U-Pb zircon dates previously obtained for each intrusion (Maksaev *et al*., 2004: Figure 3.3).

A younger crystallisation age between 4.6 and 4.4 Ma is also inferred for the late dacitic dyke encircling the Braden Breccia pipe. The late formation of such dykes may explain the younger Re-Os ages of type 8 veins in the northern part of the deposit dated at 4.42 ±0.02 Ma (Maksaev *et al*., 2004). Based on the overall younging of U-Pb dates from the Sewell Quartz Diorite and the A-Porphyry in the south to the Northern Diorite and the Teniente Dacite Porphyry in the north, a general northward progression of the locus of magmatism is inferred to have occurred during the ~1.6 My lifetime of the mineralising system.

The apparent correspondence between intrusion crystallisation ages and Re-Os ages determined in this and the two previous studies (Maksaev *et al*., 2004; Cannell *et al*., 2005) strongly supports the field evidence that mineralisation occurred in pulses during and after the emplacement of each of the main intrusions – the A-Porphyry, diorites and during several stages of emplacement and crystallisation of the Teniente Dacite Porphyry (Figure 4.19; Vry *et al*., 2010). The relative rarity of the reverse cross-cutting vein and breccia relationships that might be expected in a system involving repeated mineralisation cycles can be explained by the general northward progression of magmatism combined with the vertically elongate aspect-ratios of the A-Porphyry and diorites.

The deposit-wide vein paragenesis and associated fluid evolution espoused in several previous studies (e.g. Cannell *et al*., 2005; Klemm *et al*., 2007) is disproved by the new Re-Os ages presented here. For example, a type 6a-7a transitional vein between the Central Diorite and North Central Diorite has a relatively old age of 5.322 ±0.022 Ma, consistent with the inferred emplacement age range of the Central and Northern Diorites, whereas a deep type 6a vein from within the North Central Diorite has a significantly younger age of 4.613 ±0.020 Ma (Table 4.5; Figure 4.18). Some type 8 veins formed as early as 5.375 ±0.022

Ma (proximal to the Southern Diorite), clearly *before* a number of type 6 and 7 veins from the northern part of the deposit dated in this and previous studies (e.g. 4.805 ±0.016 Ma; Cannell, 2004). Early type 8 vein development in the southern part of the system refutes the argument that there was a deposit-wide transition into sericite-stable conditions (type 8 vein stage) at ~4.95 Ma (Cannell, 2004). Sericitic alteration is the result of the dissociation of acids and the disproportionation of magmatic sulphur dioxide (e.g. Giggenbach, 1992; Rye, 1993; Heinrich *et al*., 2004) in response to drops in temperature and pressure (Meyer and Hemley, 1967; Reed and Rusk, 2001; Reed *et al*., 2005; Rusk *et al*., 2008). Therefore, the presence of type 8 veins of different ages within and surrounding multiple intrusions implies several distinct episodes of decreasing temperature (and/or pressure) towards the end of each mineralising cycle (Figure 4.19). For example, a complete sequence of veins from type 6 to type 10 is documented at approximately 4.8 Ma (Figure 4.19).

The consistent breccia and vein parageneses for the main stage of mineralisation associated with each intrusion (Vry *et al*., 2010) are indicative of a relatively stable and fertile underlying magma chamber that fluxed geochemically similar pulses of metalliferous magmatic-hydrothermal fluids through each porphyry intrusion, synchronous with emplacement. The vein distribution analysis reveals that each intrusion developed similar vein halos, consisting of vein types that exhibit relatively uniform abundances and spatial configurations in each mineralised centre. Combining all Re-Os and U-Pb zircon ages, suggests that there were at least three major magmatic pulses, each separated by approximately 0.3 My (Figure 4.19). These pulses may consist of several emplacement events (as in the case of the composite Teniente Dacite Porphyry), with up to nine distinct mineralisation cycles identified (Figure 4.19). This interpretation is consistent with paleomagnetic data from the deposit that document complex polarity zonation, suggestive of numerous pulses of hydrothermal activity (Astudillo *et al*., 2010).

Molybdenite Re-Os dates from within and surrounding the Southern Diorite suggest that main mineralisation-type veins associated with this intrusion formed over a relatively short timescale, within around 100,000 years (Table 4.5; Figure 4.19). This age range is consistent with an ~80,000 year time gap between U-Pb zircon ages (closure temperature ~1000°C) and $^{40}Ar/^{39}Ar$ ages for hydrothermal biotite (closure temperature ~300°C) previously

recorded for a mineralised dacitic dyke at El Teniente (Maksaev *et al*., 2004). These age ranges are also in accordance with previous studies which concluded that the emplacement of an intrusion and the subsequent focusing of large fluid fluxes through it is likely to occur on a time scale of 10,000 to 100,000 years (Cathles, 1977, 2007; Driesner and Geiger, 2007; von Quadt *et al*., 2011). Relatively rapid heat loss in this environment can be attributed to significant heat advection by magmatic fluids and can explain the inward and downward overprinting of later, chalcopyrite-rich type 6b and 7b veins over molybdenite-rich type 6a and 7a veins. Thermal contraction during each mineralisation cycle may also explain the overprinting of high-temperature veins by sericite-altered type 8 veins. Although type 8 veins are most abundant in distal parts of the TMC relative to the felsic-intermediate intrusions, some examples were also observed overprinting type 6a veins within the mineralised intrusions and occurring at the greatest depths currently accessible.

Molybdenite Re-Os dates within and proximal to the Southern and Central Diorites cluster between 5.4 and 5.3 Ma and correlate well with crystallisation ages for the Central Diorite (Maksaev *et al*., 2004). Unfortunately, no emplacement ages currently exist for the Southern Diorite. Significantly younger molybdenite ages of ~4.8–4.6 Ma were obtained for main mineralisation-type veins within and proximal to the North Central Diorite and Northern Diorite (Figure 4.18). Based on these results, it is possible that these northern diorites were emplaced approximately synchronously with the Teniente Dacite Porphyry and mineralised approximately 0.6 My later than the diorites further south. However, this is contradicted by relatively old zircon ages obtained from the Northern Diorite, which fall between 5.3 and 6.7 Ma. To date, no crystallisation ages have been obtained for the North Central Diorite. Given this, it is currently not possible to say whether the Northern Diorite and North Central Diorite developed later. In addition, it is unclear whether zircons dated in the Northern Diorite reflect final crystallisation, or veins associated with older intrusions that were reactivated as hydrothermal fluid conduits during later pulses of magmatism and mineralisation accompanying emplacement of the Teniente Dacite Porphyry.

Mineralisation within the B-fault occurred at approximately 5.0 Ma and corresponds with the oldest Re-Os dates obtained for main mineralisation-type veins associated with the Teniente Dacite Porphyry (Figure 4.18). This suggests that the northwest-trending faults

may have developed synchronously with the emplacement of this intrusion (Figure 4.19). Evidence for right-lateral, strike-slip displacement is observed along several northwest trending faults at El Teniente, including the B-Fault. An E-W oriented minimum principal stress is consistent with dextral strike-slip motion on these faults and the opening of the N-S fractures that probably accommodated emplacement of the Teniente Dacite Porphyry dyke, and possibly the North Central Diorite and Northern Diorite. Thus, initiation of movement along the B-fault and related structures is interpreted to have been the trigger that rejuvenated shallow magmatism and hydrothermal activity following a hiatus of ~300,000 years (Figure 4.19). The orientation of the diorite intrusions along a similar northerly trend to the Teniente Dacite Porphyry suggests that a similar tectonic trigger could have been responsible for the earlier major pulses of magmatism.

Molybdenite within main mineralisation-type veins along the Teniente Dacite Porphyry dyke predominantly displays ages between 5.00 and 4.42 Ma (Figure 4.18). This extended (~580,000 year) period of mineralisation is attributed to the fact that the Teniente Dacite Porphyry formed as a composite intrusion composed of several overlapping dykes (Figure 4.19) as constrained by petrological observations, geochemical studies and previous geochronology that documents up to 1 My of magmatism along the dyke (Ossandón, 1974; Duarte, 2000; Skewes *et al*., 2002; Rojas, 2003; Maksaev *et al*., 2004; Cannell *et al*., 2005; Hitschfeld, 2006; Baker *et al*., 2013). The three, unusually young, type 8 veins proximal to the Teniente Dacite Porphyry and Northern Diorite (4.42 Ma: Maksaev *et al*., 2004) postdate all U-Pb zircon ages for the Teniente Dacite Porphyry by 0.3 My (Figure 3.3) but do coincide with the youngest ^{40}Ar-^{39}Ar sericite ages recorded in this part of the deposit. Given this, it is suggested that these veins represent minor, late pulses of hydrothermal activity related to the emplacement of small dacitic dykes during the waning of the magmatic system (Figure 4.19) in agreement with Maksaev *et al*. (2004).

The close spatial association of Mo-rich type 9-10 veins and breccias with the margin of the Braden Breccia pipe suggests that the late mineralisation stage is closely linked to this cataclysmic event. Concentric faults and fractures surrounding the Braden Breccia pipe (Figure 4.1) are interpreted to be the result of a period of subsidence related to magma withdrawal prior to the Braden Breccia event (Koide and Bhattacharji, 1975; Acocella *et al*.,

2000; Cannell *et al*., 2005). The close spatial association of these faults with the well-defined Mo-rich halo around the Braden Breccia observed at shallow mine levels (Figure 4.18) suggests that they were important in focusing late, Mo-mineralising fluids into the upper parts of the deposit to form type 9 and 10 veins. This occurred over a relatively short time period between 4.698 ±0.040 and 4.584 ±0.020 Ma (Figure 4.18; Table 4.5).

The formation of type 9 and 10 veins is likely to have been immediately followed by a major release of magmatic volatiles that formed the Braden Breccia pipe (e.g. Cannell *et al*., 2005). This major brecciation event cut the Mo-rich marginal tourmaline breccias leading to the formation of a large rock-flour breccia diatreme with a Mo-rich marginal facies. This evolution is supported by the absence of cross-cutting type 9 veins in the Braden Breccia itself and the presence of considerable amounts of brecciated type 9-related tourmaline within the diatreme margins. Type 10 veins are also absent in the Braden Breccia. However, cavities and fractures within the diatreme do contain considerable amounts of coarse grained gypsum, possibly generated by the ingress of circulating groundwater into the breccia pipe. U-Pb zircon ages for a ring dyke linked to the formation of the Braden Breccia pipe (Maksaev *et al*., 2004) and K-Ar sericite dates from within and surrounding the breccia diatreme (Cuadra, 1986) led to the interpretation that this formed between 4.82 and 4.60 Ma. However, the consistent molybdenite ages in the marginal tourmaline breccias on opposing sides of the Braden Breccia pipe (4.599 ±0.029 and 4.584 ±0.020 Ma; Table 4.5) suggest that it was emplaced at, or shortly after, 4.6 Ma (Figure 4.19).

4.5.2 Controls on Decoupling of Mo and Cu Mineralisation

Vein and grade distribution data conform to previous suggestions that approximately 80% of the Cu at El Teniente is hosted within veins and as minor disseminations in the TMC (Camus, 1975; Vry *et al*., 2010) suggesting that this mafic host rock sequence is an effective physical and chemical trap for copper sulphide deposition. Approximately 10% of the Cu is hosted by breccias (Cannell *et al*., 2005, 2007) and the remaining 10% Cu occurs within the intrusions that acted as conduits for mineralising fluids. In contrast, grade distribution data reveal that Mo grades are generally more elevated in the intrusions (e.g. Figure 4.20) as well as in the cements of late mineralisation stage breccias (e.g. Figures 4.14-4.16). Based on intrusion

and breccia volumes, and their elevated Mo-grades relative to Cu at different mine levels, it is likely that up to 20% of the Mo is hosted within breccias and approximately 20% is hosted within the felsic-intermediate intrusions. The remaining 60% occurs in veins in the TMC, predominantly in type 6a veins surrounding each mineralised intrusion and in late mineralisation stage veins that surround the Braden Breccia pipe at shallow mine levels.

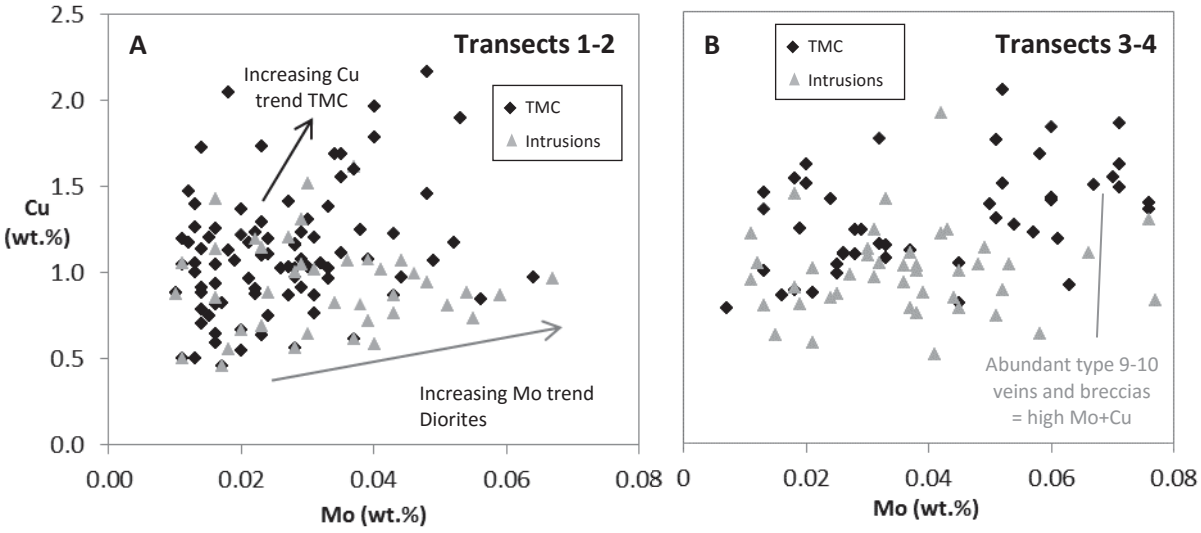


Figure 4.20: Mo versus Cu grades for different lithologies in transects 1-4. (A) Grades for six metre drillcore intervals in transects 1-2 where intrusions (grey triangles) are the Northern and North Central Diorites. (B) Mo versus Cu grades for 20 foot intervals in transects 3-4, where intrusions are the Teniente Dacite Porphyry and the Central and Southern Diorites. Mo:Cu ratios are generally high in the intrusions and low in the TMC.

The relative rarity of sulphide-bearing, premineralisation stage veins indicates that only minor mineralisation accompanied potassic alteration and biotitisation of the TMC, as previously proposed (Camus, 1975; Cuadra 1986; Maksaev *et al*., 2004; Cannell *et al*., 2005; Vry *et al*., 2010). The first paragenetic stage containing elevated Mo and Cu relates to the formation of anhydrite breccias (Table 4.3A-B) that cap the felsic-intermediate intrusions. Although these breccias may be well mineralised, the poor relationship between the abundance of the type 5 anhydrite veins and Cu and Mo grades (Figure 4.9) suggests that most sulphides during stage 5 were precipitated proximal to the intrusions and that the ore within the surrounding TMC is controlled by later main stage-type veins.

The overlap of Mo and Cu grade halos (e.g. Figures 4.2-4.4) and the comparable Re-Os dates for Mo- and Cu-rich type 6a-8 veins surrounding the porphyry intrusions (Figure 4.18) suggest that both metals were deposited during the same pulses of magmatic-hydrothermal

activity and are not entirely decoupled in time. Vein distribution data indicate that most Mo was precipitated in type 6a veins within and proximal to the intrusions (Figure 4.10A), whereas Cu is principally hosted by outboard type 6b, 7b and 8 veins. The general increase in the abundance of these Cu-rich vein types with distance from the felsic-intermediate intrusions, coupled with a comparable decrease in the abundance of type 6a veins (e.g. Figure 4.10), can be interpreted in terms of an outward/upward transition from type 6a veins into type 6b and then type 7 and/or type 8 veins (Figure 4.21). This considered, it is suggested that main mineralisation stage Mo and Cu were predominantly transported by the same fluids and were sequentially deposited leading to their decoupled mineralisation shells surrounding the intrusions.

The development of Cu-rich veins from Mo-rich type 6a veins is supported by previous fluid inclusion LA-ICP-MS studies that documented high Mo and Cu concentrations in fluid inclusions within type 6a veins, whereas fluid inclusions in type 6b and 8 veins typically remain Cu-rich but are Mo-depleted (Klemm *et al.*, 2007; Vry, 2010). Cooling and consequent downward telescoping of main mineralisation-type veins within each magmatic-hydrothermal cycle (Figure 4.19) can explain the overprint of "later" Cu-rich veins over paragenetically "earlier" Mo-rich ones. However, it is likely that several of the main mineralisation stage vein types formed synchronously at different depths and distances from the intrusions. There are several ways in which Mo-rich 6a veins may have evolved spatially into type 6b, 7a, 7b and type 8 veins (Figure 4.21). Further fluid inclusion analysis of these vein types at different mine levels and distances from the intrusions is required to assess these potential evolution pathways.

Several factors are likely to have influenced Mo and Cu solubility during the development of type 6a-8 veins. The general restriction of Mo-rich veins to within and immediately surrounding the porphyry intrusions suggests that Mo was deposited at relatively high temperatures. Previous fluid inclusion analysis of type 6a veins suggests likely deposition temperatures in excess of 380°C (e.g. Vry, 2010). In contrast, the close association of Cu with type 8 veins (e.g. Figure 4.11G-H) suggests that it was usually deposited at lower temperatures under which significant sericite alteration occurred.

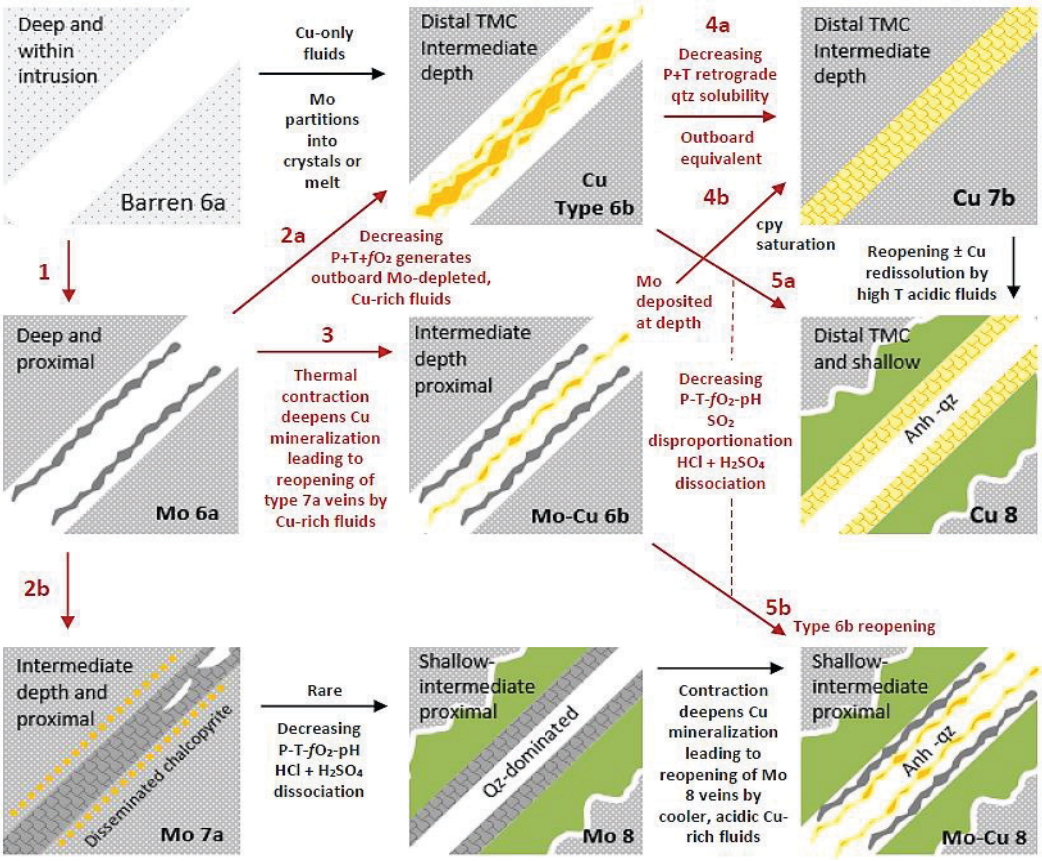


Figure 4.21: Schematic diagram showing the potential spatial evolution of quartz-dominated type 6a veins into outboard Cu-rich type 6b, 7b and type 8 veins. The most likely and commonly occurring evolution pathways are shown in red (1-5b) as a function of temperature (T), pressure (P), oxygen fugacity (fO_2) and acidity (pH) during the migration of fluids through the TMC. Molybdenite = dark grey, Cu-sulphides (cpy = chalcopyrite) = yellow. Green shaded areas = quartz-sericite alteration. The typical locations of each vein type are shown in the top left of each diagram: Proximal = <50 m from intrusion, distal = >50 m.

Fluid-wallrock interactions may have also played an important role in the sequential deposition of Mo and Cu. As fluids migrated outwards through the TMC, interaction with reduced iron-bearing silicates is likely to have led to fluid reduction. Previous studies have demonstrated that as log fO_2 decreases below NNO+1, molybdenite saturation is favoured over chalcopyrite (e.g. Audétat and Pettke, 2006; Seo *et al.*, 2012). This could explain the early deposition of Mo in type 6a veins proximal to the intrusion margins, and the outboard deposition of chalcopyrite (Figure 4.21).

The formation of the relatively rare, type 7a molybdenite veins can be explained by upward/outward adiabatic fluid flow down pressure gradients leading to retrograde quartz solubility (e.g. Vry *et al.*, 2010). The fact that the type 7a veins are commonly surrounded by significant disseminated chalcopyrite suggests that they were formed from Cu-bearing

fluids, with relatively high temperature and fO_2 conditions inhibiting Cu-precipitation proximal to the intrusions. Alternatively, the formation of type 7a veins could be the result of the exsolution of separate pulses of Mo-rich and relatively Cu-poor fluids from the magmatic source. Further fluid inclusion analysis is required to test this hypothesis.

The presence of numerous, thick, type 7b veins within the TMC suggests that fluid-wallrock interactions played an important role in triggering the precipitation of chalcopyrite (Figure 4.21). However, previous fluid inclusion studies also revealed an apparent increase in the abundance of boiling assemblages in Cu-rich type 6b-8 veins (Cannell, 2004; Klemm *et al*., 2007; Vry, 2010), so that vapour-brine partitioning may also have played a role in Cu deposition, perhaps via loss of sulphur species to the low density vapour and consequent destabilisation of Cu-sulphide complexes. The comparative rarity of brine-vapour assemblages reported in Mo-rich type 6a veins suggests that vapour-brine separation was less likely to have been important in controlling Mo deposition.

Type 8 veins display the strongest decoupling between Mo and Cu grades of any main mineralisation-type vein (Figures 4.10G-H, 4.11G-H). The rarity of type 8 veins containing molybdenite, and the fact that these rare examples commonly contain unaltered feldspars in their halos, suggests that most Mo was deposited prior to significant acid dissociation, whereas Cu was frequently deposited under cooler and more acidic conditions (Figure 4.21). A detailed fluid inclusion LA-ICP-MS study is presented in Chapter 5 in an attempt to test the proposed vein evolution model and to assess the conditions under which Mo and Cu were deposited as hydrothermal fluids migrated outward from each intrusion.

The abundance of Cu sulphide (especially bornite)-bearing main mineralisation-type veins surrounding the Teniente Dacite Porphyry suggests that this intrusion was responsible for much of the shallow level Cu mineralisation in this part of the deposit (Cuadra, 1975; Maksaev *et al*., 2004; Cannell *et al*., 2005; Vry *et al*., 2010). In contrast, Mo grades in this area are strongly controlled by late mineralisation stage veins and breccias that overprint Cu mineralisation and which have been dated at approximately 4.6 Ma (Figure 4.18). The relatively Cu-poor nature of late mineralisation stage veins and breccias is interpreted to be the result of the earlier extraction of Cu from the underlying magma chamber by previous

cycles of release of S-rich magmatic fluids (e.g. Zajacz and Halter, 2009). This could have created a Cu-poor residual melt that became progressively enriched in incompatible Mo during the final stages of crystallisation (e.g. Candela and Holland, 1984; Audétat, 2010).

The late exsolution of Mo-rich fluids from a highly fractionated magma chamber could explain why Mo grades associated with late mineralisation stage veins and breccias are typically two to three times higher than those associated with main mineralisation stage veins. Late pulses of deep-sourced, oxidised, Mo-rich fluids may have exploited recently-opened faults to form the concentric and northwest-trending configuration of anhydrite-dominated, late mineralisation stage veins and breccias at shallow mine levels. This focusing of Mo into structural traps may explain the unusually high Mo grades of up to 0.35 wt.% recorded in some drillcore intersections at shallow mine levels. Alternatively, Mo may have been significantly enriched by remobilisation as previously suggested (Vry *et al*., 2010). Mo remobilisation could explain the apparent rarity of Mo-rich main mineralisation stage veins associated with the Teniente Dacite Porphyry which, according to the proposed model of transitional vein development, should occur below Cu-rich veins in this part of the deposit. In addition, this process may explain why peak Mo grades occur slightly outboard of the Braden Breccia pipe margin. Although both mechanisms are possible, the physical and chemical characteristics of late mineralisation stage fluids remain poorly constrained. Further fluid inclusion studies are presented in the following chapter to try to identify the origin and reasons for the high Mo contents of these late stage fluids, which, to-date have not been studied in detail.

Summing up, the combination of geochronological, vein distribution and grade data suggest that magmatic processes probably do not control the spatial and temporal decoupling of Cu and Mo at El Teniente, although the late, high Mo grades could be attributed to the long-term evolution of Mo:Cu ratios in the underlying magma reservoir. In general, Cu and Mo were probably transported by the same fluids, with their tendency to precipitate in distinct vein types being related to varying temperature, pressure (e.g. Ulrich *et al*., 2002; Redmond *et al*., 2004; Landtwing *et al*., 2005; Ulrich and Mavrogenes, 2008; Rusk *et al*., 2008) and redox state of fluids (e.g. Phillips *et al*., 1974; Sillitoe 2010; Seo *et al*., 2012) as they exited the porphyry intrusive conduits and migrated out into fractured mafic rocks of the TMC.

4.6 Conclusions

Combined grade and vein distribution analysis and high-precision Re-Os dating at El Teniente provide valuable insights into the genetic links between different intrusions, breccias and vein types and enable a quantitative assessment of their importance with respect to economic mineralisation. Mo and Cu grades both show a strong spatial-temporal relationship with the A-Porphyry, diorites and Teniente Dacite Porphyry, which acted as conduits for pulses of magmatic-hydrothermal fluids. These each developed their own, relatively localised, main mineralisation-type vein halos that closely followed the same breccia and vein chronology. Re-Os dating provides evidence that there was no single, deposit-wide evolution in vein types and their associated fluids as previously proposed. Results are indicative of the systematic development of relatively localised ore shells surrounding each intrusion which developed during and immediately after their crystallisation. Intrusion-mineralisation pulses appear to be relatively short-lived (<100,000 years), with more prolonged mineralisation surrounding the Teniente Dacite Porphyry attributed to its extended intrusion history. The emplacement of this northward-trending intrusion is likely linked to the development of northwest trending faults that underwent dextral strike slip displacement at approximately 5.0 Ma. Individual pulses of magmatic-hydrothermal activity are separated by quiescent periods of up to 300,000 years, documented by distinct gaps in the ages of shallow level molybdenite mineralisation.

Vein distribution analysis reveals that type 6a quartz-molybdenite veins are the most important control on deposit-wide Mo grade distributions. The importance of these veins is particularly notable in close proximity to the felsic-intermediate intrusions and at deep mine levels, where their abundance controls typical grades of 0.01 to 0.06 wt.% Mo. In contrast, Cu grades of up to 2.4 wt.% are principally controlled by the abundances of type 6b, 7b and 8 veins that occur in more distal positions relative to the porphyry intrusions. These vein types appear to be upward and outward transitional veins from higher temperature 6a veins, suggesting that sequential deposition of metals, as a result of decreasing temperature and fO_2, was the main driving force in Mo-Cu decoupling during each cycle of main mineralisation-type veining.

Mo grades >0.06 wt.% are controlled by the presence of late mineralisation stage veins and breccias that show a close spatial association with faults and fractures surrounding the Braden pipe at shallow mine levels. The generally Cu-poor nature of this paragenetic stage is attributed to the prior preferential extraction of Cu from the underlying magma chamber in the previous mineralising events. This led to the development of a Mo-rich residual melt phase that exsolved oxidised, Mo-rich fluids that overprinted Cu mineralisation at approximately 4.60 Ma. During this event, remobilisation of Mo may have also increased Mo concentrations in late mineralisation stage fluids, explaining the apparent lack of molybdenite-bearing main mineralisation-type veins at depth proximal to the Teniente Dacite Porphyry. The late mineralisation stage was terminated by the formation of the Braden Breccia pipe in a single explosive event at approximately 4.58 Ma. With the exception of minor mineralisation associated with small dacitic dykes, this event marked the termination of Mo and Cu-sulphide deposition at the deposit.

Chapter 5. Magmatic-Hydrothermal Fluid Evolution at El Teniente

5.1 Introduction

To date, three substantive fluid inclusion studies have been completed at El Teniente (Cannell, 2004; Klemm *et al*., 2007; Vry, 2010), the latter two of which used LA-ICP-MS analysis to determine the chemistry of individual fluid inclusions. These studies revealed that there is a broad range of fluids present within the system, represented by vapours, brines and aqueous fluids of variable salinity, density and metal concentration. Understanding the controls on Mo transport and the reasons for the decoupled mineralisation of Mo and Cu relies on identification of the hydrothermal fluids responsible for the transport and deposition of both metals. This requires the recognition of different fluid generations, an assessment of their relative fluxes and an understanding of how they physically and chemically evolved during deposit formation.

By combining fluid inclusion microthermometry with SEM-cathodoluminescence (CL) petrography and individual fluid inclusion LA-ICP-MS analysis, this chapter identifies the different fluids present at El Teniente and how they evolved in space and time. By analysing samples from a range of depths and from multiple mineralised centres, new insights into the magmatic-hydrothermal evolution of El Teniente can be gleaned. This includes a discussion of the relationships between different vein and breccia types: testing the different hypotheses for the links between potentially related vein types, such as the evolution of type 6a veins outward into Cu-rich vein types (see Figure 4.24).

5.2 Methods

5.2.1 Sample Collection and Preparation

Two hundred representative and well-constrained vein and breccia samples from multiple mineralised intrusions and the TMC were collected. These extended over a broader area and greater range of depths than the previous fluid inclusion studies, which were focused on a few shallow drillcore sections (e.g. Cannell *et al*., 2005; Klemm *et al*., 2005) or were restricted between 50 and 550N (Vry, 2010: Figure 5.1). Simple samples that had no overprinting veins or alteration were selected so that primary inclusions could be identified and analysed with confidence. The variable intensity of Cu and Mo mineralisation in these samples allows some assessment of the importance of different fluid generations for metal transport and deposition. Key features of each sample, including size, mineralogy, associated alteration and evidence of overprinting and/or reopening were recorded.

Forty-eight samples were selected for fluid inclusion analysis (blue squares: Figure 5.1). These were prepared as doubly-polished sections of 120-150 μm thickness and were studied using conventional transmitted and reflected light petrography. Notes were taken on the abundance and petrographic relationships of different ore and gangue minerals. Areas containing large and/or abundant fluid inclusion populations were also marked for analysis. Sections were dismounted by soaking in acetone overnight and were cut into smaller wafers that could fit onto a 7 mm diameter sample holder for fluid inclusion microthermometry. These were mapped and studied in order to assess the relative abundances of different fluid inclusion types and the potential timing relationships between different populations and with sulphide mineralisation.

In each wafer, 2-5 regions of interest (ROIs) were selected to provide good sample coverage and to measure fluid inclusions in multiple host crystals. During this study, fluid inclusion populations were predominantly quartz-hosted, although some anhydrite- and gypsum-hosted inclusions were also measured. In the selected ROIs, inclusions of each type were described, measured and grouped into their corresponding fluid inclusion assemblages (FIAs; see Goldstein and Reynolds, 1994) FIAs were defined based on the very close proximity of fluid inclusions along unifying features (growth zones, fluid inclusion trails, and fractures) and

their identical vapour fractions and daughter phases at room temperature (c.f. Goldstein and Reynolds, 1994). Each assemblage typically consists of 2-10 inclusions; however, single fluid inclusions were also measured in some cases where there was a lack of fluid inclusions that could be confidently attributed to the same assemblage. The validity of FIA selections was tested using the results of subsequent heating and freezing tests (microthermometry). Inclusions were denoted with an x (e.g. inclusion 1b became 1b-x) in cases where microthermometric data showed they must be from a separate assemblage.

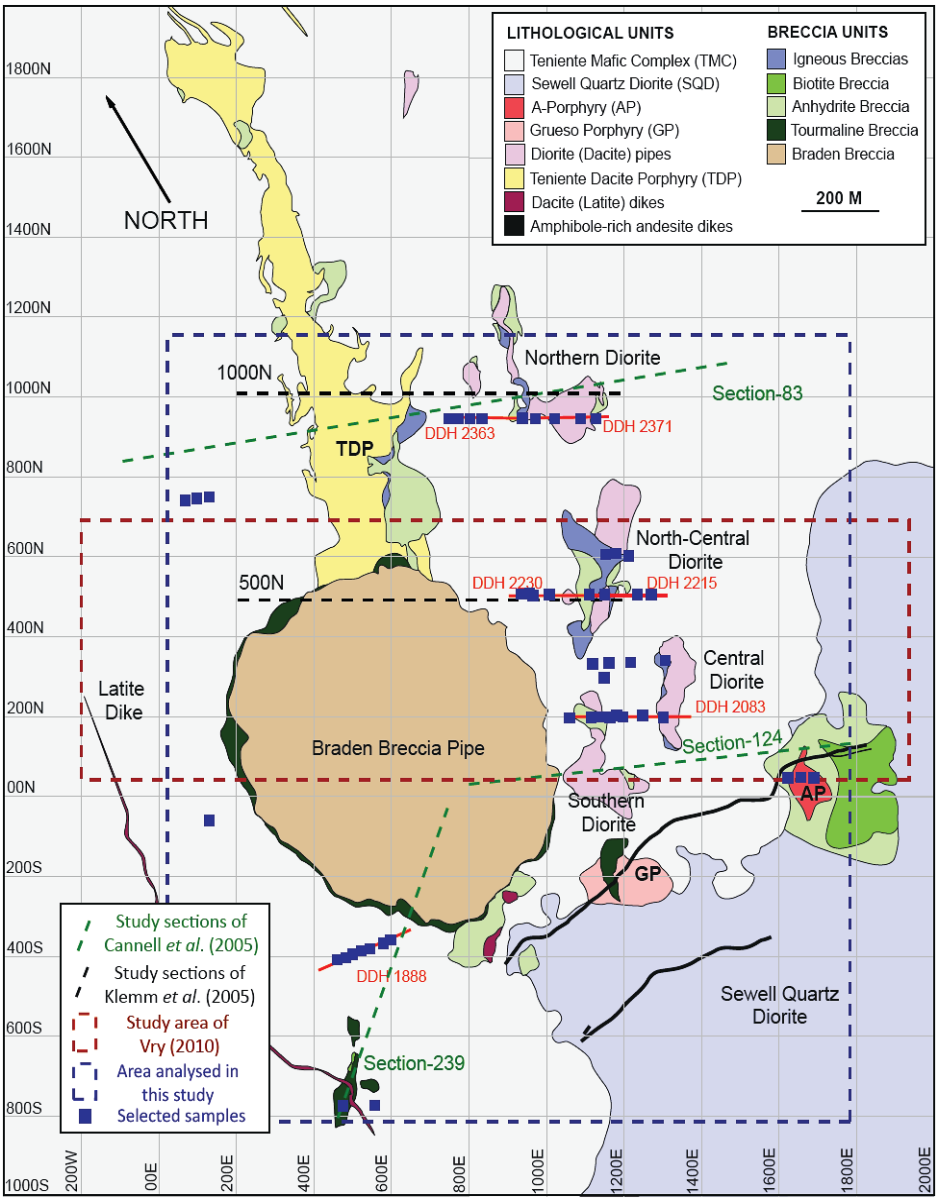


Figure 5.1: Geological map of El Teniente at 2165 m asl showing the sections and areas studied in this and previous fluid inclusion studies (Cannell *et al.*, 2004; Klemm *et al.*, 2007; Vry, 2010: see key). Samples analysed in this study are shown (blue squares). For sample descriptions refer to Appendix 2. Original map provided by CODELCO Chile Division El Teniente. The local mine grid is oriented approximately 14.5° from true north.

5.2.2 Microthermometry

Microthermometry was carried out using a Linkam MDS600 heating-freezing stage with operating temperatures between -190°C and 600°C and heating/cooling rates of 0.1–50°C/minute. Freezing tests were completed first by cooling samples to approximately -110°C, and then heating at rates of 30°C to 0.1°C/minute. All phase transition measurements were made during heating cycles with heating rates of ≤1°C/minute providing the most accurate measurements. Final ice melting (Tm_{ice}) was recorded first in order to determine the salinity of salt-undersaturated inclusions, reported as $NaCl_{eq}$ wt.% (Bodnar *et al*., 1985, 1989; Bodnar, 1993; Bodnar and Vityk, 1994). For saline inclusions, metastable freezing temperatures, first ice melting temperatures and hydrohalite disappearance temperatures were also noted to help determine fluid composition. Heating tests were then completed up to a maximum temperature of 590°C. The temperature was only elevated to approximately 30°C higher than the homogenisation temperatures of the 90th percentile in any one sample chip so that inclusion decrepitation due to overheating was minimised. For each inclusion, the homogenisation mode was also recorded, where; L = homogenised to liquid, V = to vapour, LV = by critical behaviour/meniscus fading, and H = by halite dissolution.

Heating experiments were also used to determine the salinities of salt oversaturated fluid inclusions based on their halite dissolution (Tm_{Halite}) temperatures (c.f. Bodnar, 1993; Bodnar and Vityk, 1994). Where brine inclusions homogenised by vapour disappearance ($Th_{L+V\rightarrow L}$), fluid inclusion salinity, density and minimum trapping pressure were obtained using existing experimental (Hass, 1976; Bodnar and Sterner, 1985; Sterner *et al*., 1988; Bodnar, 1992) and theoretical data (Bischoff and Pitzer, 1989; Anderko and Pitzer, 1993; Driesner, 2007) for the vapour-saturated halite solubility curve and liquid-vapour surfaces in the H_2O-NaCl system (c.f. Becker *et al*., 2008). For brine inclusions that homogenised by halite dissolution, minimum trapping pressures and salinities were interpreted based on previous experimental data (Bodnar, 1994; Becker *et al*., 2008) and the relationship between Tm_{Halite} and $Th_{L+V\rightarrow L}$ for a solution of 40 wt% $NaCl_{eq}$ as derived by Becker *et al*. (2008). Trapping conditions for brine inclusion assemblages that homogenised by halite disappearance between 100 and 600°C were also interpreted using a recently proposed set of equations for the NaCl-H_2O system (Lecumberri-Sanchez *et al*., 2012), building on the work of Becker *et al*., (2008).

3.3 SEM-CL Petrography

Scanning Electron Microscope-cathodoluminescence (SEM-CL) petrography was completed on selected vein and breccia samples to assess the relative timing of different fluid inclusion populations and their relation to host-mineral growth zones and sulphides. SEM-CL was adopted instead of cold-cathode CL due to its increased sensitivity for weakly luminescent quartz (ref.). All samples were analysed at the Natural History Museum, London, using a Zeiss EVO 15LS SEM and Zeiss variable pressure secondary electron detector operated with Oxford INCA software (working distance 20 mm, beam accelerating voltage of 20 kV and current of 3 nA). SEM backscattered electron images and CL maps were captured for each fluid inclusion ROI. Chroma-CL (CCL), three-band colour images were also acquired for selected samples (Gatan ChromaCL system with DigiScan II software) in order to better resolve complex host mineral zonation patterns.

3.4 LA-ICP-MS Analysis

Representative vein and breccia samples containing measured and mapped fluid inclusions were analysed in the LODE Laboratory at the Natural History Museum, London, using a New-Wave 213 nm solid state UV laser coupled to an Agilent 7700 quadrupole ICP-MS. Fluid inclusion assemblages were relocated using maps prepared during microthermometry and SEM-CL analyses. Individual fluid inclusions were ablated at a repetition rate of 10 Hz, ensuring that the beam size was large enough to encompass the entire inclusion. Prior to ablating each inclusion, trials were carried out on an area of sacrificial host mineral in order to ensure coupling between the laser and sample surface at different beam diameters and laser fluence. Tests revealed that low fluence of 2.2-2.5 J/cm^2 was suitable for surface-beam coupling with a beam diameter ≥30 μm, whereas slightly higher fluence of 2.6-3.1 J/cm^2 was optimal for spot sizes <30 μm. Once coupling was achieved, beam power was rapidly increased so that inclusions were breached at a fluence of ≥9 J/cm^2. For each run, approximately 30 seconds of background signal was acquired prior to starting ablation of the host mineral. Then, ideally, data for a stable period of host mineral ablation were collected prior to breaching of the inclusion (Figure 5.2). Each isotope was analysed with a dwell time of 10 ms with the exception of Cu, Mo and Au, where dwell times were doubled. Element concentrations were then quantified from natural isotopic abundances.

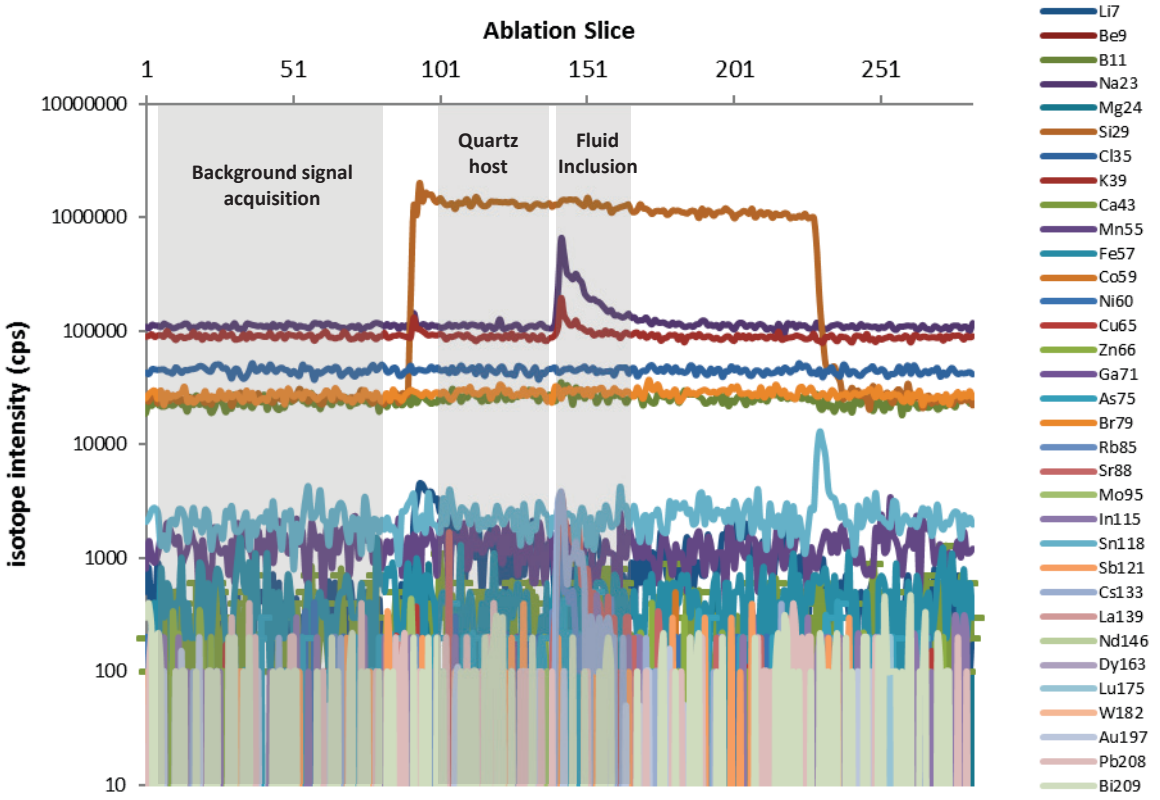


Figure 5.2: Example ablation of a high salinity (49.8 wt.% $NaCl_{eq}$) fluid inclusion processed using ExLAM2000 (Zachariáš and Wilkinson, 2007). Background signal = measurement slices 5 to 80. Quartz host mineral signal = slices 101-140. Fluid inclusion = slices 141 to 161 (Run JN21C17).

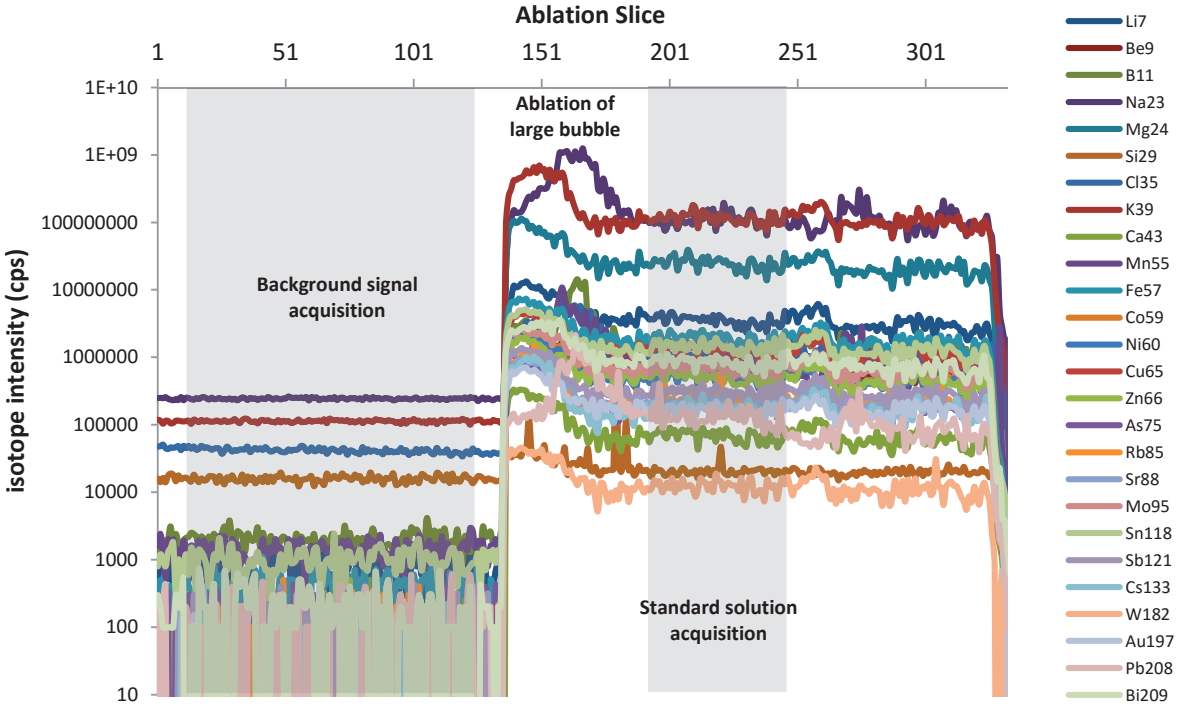


Figure 5.3: Example ablation of a microwell-hosted standard solution processed using ExLAM2000 (Zachariáš and Wilkinson, 2007). A bubble formed and burst at the start of the ablation resulting in significant Pb, Na and Zn fractionation. Grey highlighted section = slices integrated (Run NO19A05).

In order to quantify absolute element concentrations in each inclusion, an external standard of known composition must be ablated before and after each sample run. This is used to determine instrument sensitivity for each isotope (counts per second per ppm) and correct for machine drift during the course of a run. In this study, a customised in-house standard solution with a salinity of 5.0 wt.% NaCl+KCl+$CaCl_2$ at ratios of 10:2.5:1 was adopted as the primary external standard (Figure 5.3). Previous work has demonstrated that these solutions can yield more accurate analytical data than solid standards (such as NIST612 glass), which are not matrix-matched or, for many elements, are not concentration-matched to fluid inclusions (Stoffell, 2007; Buckroyd, 2008; Vry, 2010).

In a previous study, Vry (2010) prepared microwells to host the standard solutions using a micro-corer mounted on a rotating microscope stage. This was used to drill 1.5-2 mm wide and ~1 mm deep conical microwells into an extra thick (2 mm) glass slide. Due to the time-consuming nature of this technique, microwells in this study were prepared by creating 12 guide-holes of approximately 50 µm depth and width in an extra thick glass slide using a tungsten-carbide glass drill. A tungsten carbide masonry drill was then used to widen and deepen the microwells to the same depth and diameter as used in the previous study. Each microwell slide was prepared so that 4-6 inclusion wafer samples could be mounted on the opposing end. Individual microwells were filled with approximately 0.5 µl of the solution standard using an adjustable microliter pipette with disposable tips. The microwells were immediately sealed using standard laboratory PARAFILM M® to prevent evaporation or contamination.

A series of trial ablations were completed on the microwell-hosted solutions. These revealed that the most accurate and reproducible microwell ablations were achieved when microwells were opened using a 65 µm spot at a repetition rate of 20 Hz and a laser fluence of approximately 5.5 J/cm^2. The solution was then ablated through the hole using a 40 µm spot size and low laser fluence of 1.0-1.5 J/cm^2. These settings produced steady signals for most elements with limited fractionation effects. However, Pb, Na and to a lesser extent Au and Zn sometimes fluctuated due to the coalescence and ablation of vapour bubbles (e.g. Figure 5.3). During analytical runs, if a steady ablation signal was not obtained for at least 10 seconds, runs were restarted. Each microwell was ablated for a maximum of four times to avoid time-

related fractionation effects after the initial opening (Vry, 2010). Three successful microwell solution ablations were collected before and after the analysis of each sample.

In order to test the validity of microwell solutions for external standardisation, NIST612 glass was selected as a secondary standard. This has good ablation reproducibility, signal stability and is suitable for monitoring long-term instrument sensitivity drift (e.g. Buckroyd, 2008). Prior to each NIST analysis, background gas signal was acquired for approximately 30 seconds followed by 60 seconds of signal acquisition during ablation. All ablations were conducted using a 55 µm spot size, a frequency of 10 Hz and a laser fluence of 5.0 J/cm^2. Three ablations were run prior to and after the analysis of the microwell solution standards.

In LA-ICP-MS analysis, an internal standard (an element of independently known concentration) is required to determine the relative sensitivity factor between inclusions and external standard analyses. This is required in order to calculate absolute element concentrations in each fluid inclusion (e.g. Pettke *et al*., 2012). Cl and Na concentrations, derived from microthermometric $NaCl_{eq}$ values, are typically used to quantify solute concentrations in fluid inclusions (e.g. Heinrich *et al*., 2003; Stoffell *et al*., 2004). Previous studies have shown that Cl concentrations are more reliably determined from microthermometric measurements than Na, especially when considering salt-undersaturated inclusions (e.g. Stoffell *et al*., 2004; Pettke *et al*., 2012). However, preliminary tests show that microwell solution Cl concentrations can vary significantly. Furthermore, Na signals are generally larger than Cl signals in most fluid inclusions (e.g. Heinrich *et al*., 2003; Klemm *et al*., 2007). Therefore, despite uncertainty in Na values from microthermometry, it is perhaps the most reliable internal standard element to use. As a result, Na concentrations derived from microthermometric $NaCl_{eq}$ values were used as the internal standard. These values were corrected for concentrations of other major Cl-species including KCl, $FeCl_2$, $MnCl_2$, CuCl and $PbCl_2$ (c.f. Heinrich *et al*., 2003) using major element ablation data and iterative reduction in the ExLAM2000 (Zachariáš and Wilkinson, 2007) processing software used in this study. Limits of detection (LOD) were calculated for each element in each inclusion by EXLAM2000, using the 3 standard deviation criterion of Longerich *et al*. (1996).

5.3 Microthermometry and Fluid Inclusion Petrography

5.3.1 Fluid Inclusion Types

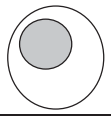
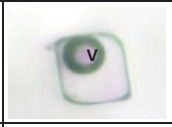
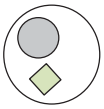
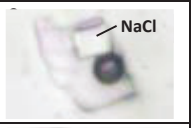
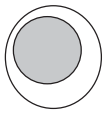
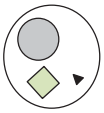
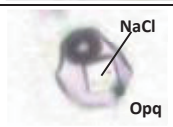
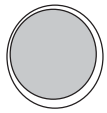
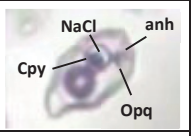
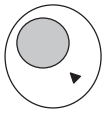
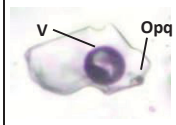
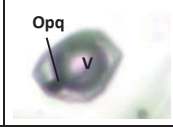
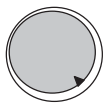
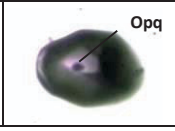
Nine fluid inclusion types were defined during this study, based on vapour fraction, salinity and contained accessory phases (Table 5.1). Of these, 6 types were salt undersaturated (type A) and 3 were salt saturated (type B) at room temperature. The salt saturated inclusions have fairly uniform vapour fractions of 15-30% and salinities exceeding 30 wt.% $NaCl_{eq}$ whereas type A inclusions display highly contrasting vapour fractions and salinities. Consistent with previous studies (Cannell, 2004; Klemm *et al*., 2007; Vry 2010), the presence of liquid CO_2 and formation of CO_2 clathrate on freezing were rarely observed in all inclusion types, indicating that CO_2 was not an important component. Halite (NaCl) was the primary dissolved salt species in all brine inclusions, although some populations also contained sylvite (KCl) daughter crystals. Based on the dominance of NaCl as the primary salt, the following interpretations are based on the simplifying assumption of a NaCl-H_2O system.

5.3.2 Appraisal of Microthermometric Measurements

The fluid inclusion stage accuracy is estimated at ±0.1°C from -100 to +30°C, and at ±0.5°C at higher temperatures, based on annual calibration using an in-house synthetic H_2O-CO_2 fluid inclusion standard. A correction was applied to all microthermometric data to account for the small difference in temperature between the thermocouple in the fluid inclusion stage heating block and the sample. For most inclusions, phase changes were successfully recorded at low rates of increasing temperature resulting in typical precision of ±0.1-0.2°C. Homogenisation temperatures were recorded with typical precision of ±0.5°C. However, homogenisation temperatures were sometimes difficult to observe for rounded inclusions that homogenised to vapour (see Appendix 4 notes). All fluid inclusions within the same assemblage typically homogenise within ±10°C of one another, although several FIAs contain inclusions that homogenise over a greater temperature range ~10-20°C. This was mainly attributed to minute P-T variations during the roughly coeval entrapment of fluids along the same growth zones. In several assemblages, a single fluid inclusion produced significantly different results. These were denoted with an ‘x’ and were omitted when calculating average FIA microthermometric and laser ablation data.

Repeat heating and freezing tests conducted on randomly selected, quartz-hosted fluid inclusions produced results that were within error in almost all cases. By contrast, repeat heating tests on anhydrite- and gypsum-hosted inclusions sometimes produced anomalous results, particularly for inclusions that homogenised at low temperatures (100-300°C). This was attributed to the fact that sulphate-hosted fluid inclusions are prone to stretching when heated to >10°C above their homogenisation temperature (c.f. Vanko and Bach, 2005). To limit this problem, subsequent heating tests on anhydrite- and gypsum-hosted samples were conducted sequentially with a very low rate of increasing temperature (<2°C/min). However, some samples, in particular the late stage anhydrite-carbonate ±gypsum breccias, were still prone to fluid inclusion stretching, decrepitation and sample disintegration.

Table 5.1: Classification scheme of fluid inclusion types found at El Teniente based on phases present and vapour fraction (V*f*) at room temperature.

T.	Characteristics		Example	T.	Characteristics		Example
A_L	V*f* = 10-40%			B_H	V*f* = 5-30% + halite crystal		
A_{ID}	V*f* = 40-70%			B_{HO}	V*f* = 5-30% + halite + opaque daughter mineral (typically Cpy)		
A_V	V*f* = 70%-100%			B_M	V*f* = 5-30% + multiple daughter phases (NaCl, KCl, cpy, py, mo, hm, anh)		
A_{LO}	V*f* = 5-40% + opaque daughter mineral (typically cpy)			TYPE A -Salt Undersaturated at Room Temperature A_L Inclusion 7a (2672-99.95) - anhydrite hosted A_{ID} Inclusion 5a 2215-151.9 - quartz hosted A_V Inclusion 9a 1034-E - quartz hosted A_{LO} Inclusion 5a 2371-183.25 - anhydrite hosted A_{IDO} Inclusion 15a 1034-H - quartz hosted A_{VO} Inclusion 5a 2661-223.2 - quartz hosted TYPE B - Salt Saturated at Room Temperature B_H Inclusion 1a 2371-183.25 - anhydrite hosted B_{HO} Inclusion 10a 2371-183.25 - anhydrite hosted B_M Inclusion 9a 1034-E - quartz hosted		
A_{IDO}	V*f* = 40-70% + opaque daughter mineral						
A_{VO}	V*f* = 70%-100%						

Notes: Type A inclusions = salt undersaturated at room temperature. Type B inclusions = salt saturated at room temperature. These inclusions have relatively uniform V*f* of 5-30% and always contain a halite daughter phase. Fluid inclusion types are based on the classification scheme of Vry (2010) with the addition of type A_{IDO} inclusions, which were not previously classified. Abbreviations: T. = Fluid inclusion type, A = Aqueous inclusions, B = Brine inclusions, L = Liquid, V = Vapour, Opq = Opaque daughter crystal, cpy = chalcopyrite, py = pyrite, mo = molybdenite, hm = hematite.

5.3.3 Premineralisation Veins and Breccias

Due to the low abundances of type 1, 2 and 4b veins observed in the studied transects (Chapter 4) these vein types were not studied during microthermometry (Appendix 4).

Biotite Breccias and Type 3 Veins

Type 3 veins and associated biotite breccias are dominated by high salinity B_H, B_{HO} and B_M inclusions (Figure 5.4A-B) that commonly occur within primary quartz growth zones without coexisting low density inclusions (e.g. Figure 5.5A-C). These typically homogenise by halite dissolution at temperatures between 350 and 450°C (Figure 5.4). A few rare brine inclusions also contain sylvite daughter crystals that dissolve at temperatures between 100 and 245°C. Approximately half the brine inclusions contain small opaque daughter crystals (Figure 5.5C) that are interpreted to be chalcopyrite. These opaque-bearing inclusions are particularly abundant along primary quartz growth zones in the biotite breccia sample.

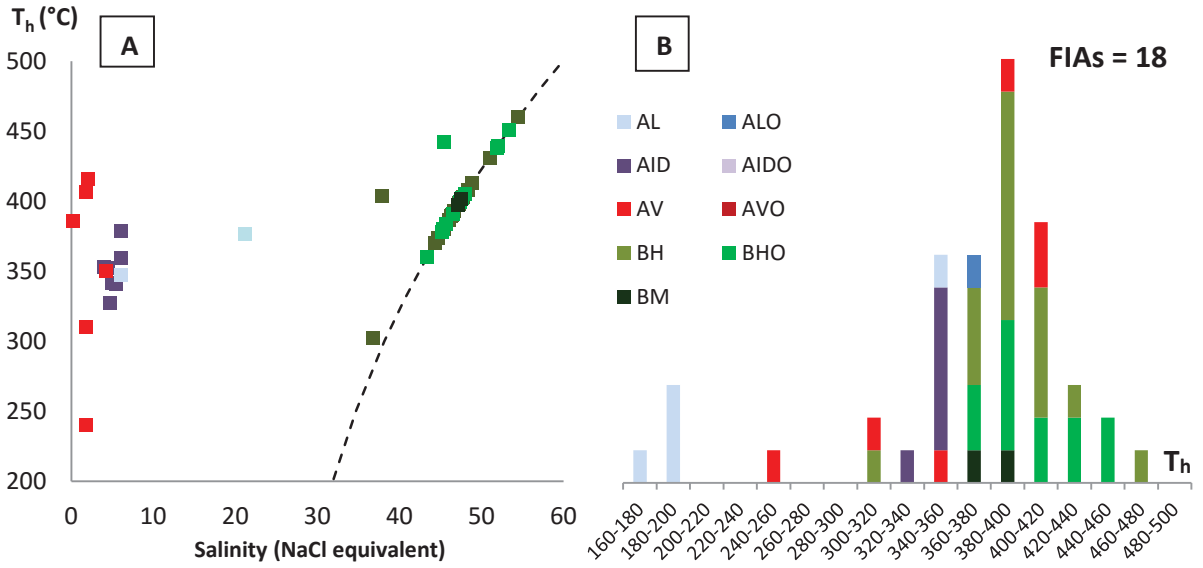


Figure 5.4: Fluid inclusion microthermometric data for type 3 veins and biotite breccias. (A) Fluid inclusion homogenisation temperature (T_h) versus salinity (wt% $NaCl_{eq}$) plot for salt undersaturated (grey) and salt saturated (black) fluid inclusions. Dotted line = Halite saturation curve for the system NaCl-H_2O determined in previous fluid inclusion studies (Bodnar *et al.*, 1985; Driesner and Heinrich, 2007; Becker *et al.*, 2008). (B) Fluid inclusion types versus homogenisation temperatures. The number of fluid inclusion assemblages (FIAs) measured is given at the top right of B. All halite saturated fluid inclusions are displayed in green.

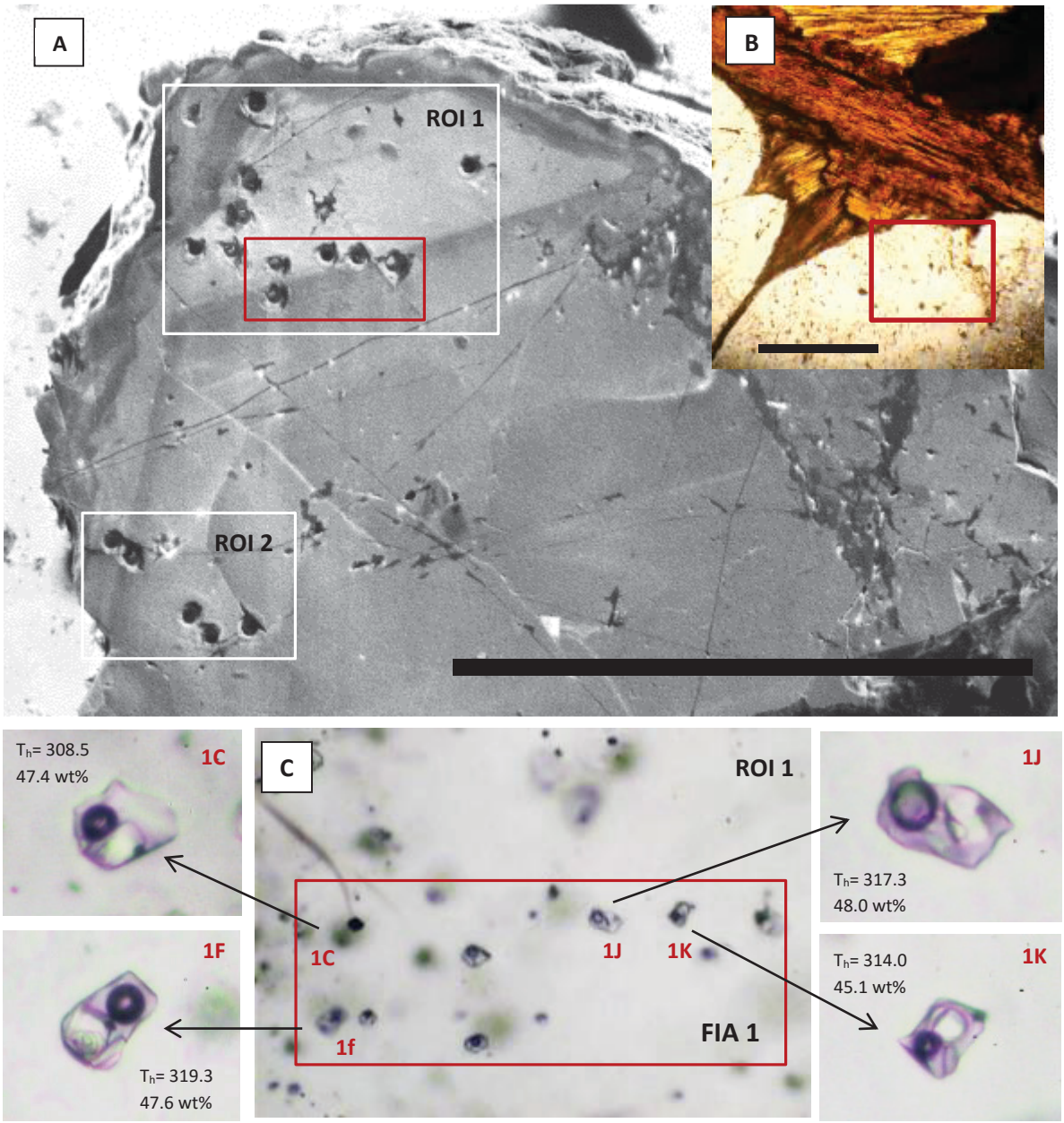


Figure 5.5: Quartz SEM-CL image and plane polarised light photomicrographs of fluid inclusions in a biotite breccia inferred to be associated with type 3 veins (sample Bt Bx 1). (A) Quartz SEM-CL image of sample Bt Bx 1 showing distinctive compositional zonation within quartz. Fluid inclusions in regions of interest 1 and 2 are concentrated in the two outer growth zones of the quartz crystal. Ablation holes are 20-35 µm in diameter. Scale bar = 1 mm. (B) Plane polarised light photomicrograph of sample Bt Bx 1 showing the location of the analysed quartz wafer. Scale bar = 1 mm. (C) Region of interest 1 cut from the sample Bt Bx 1 surrounded by zoomed in photomicrographs of highly saline fluid inclusions in FIA 1. Microthermometric data for each inclusion are shown on their respective photomicrographs. Black scale bars = 100 µm.

Moderate-low salinity A_{ID}, A_L and A_V inclusions are randomly distributed throughout the samples or occurring on secondary inclusion trails that cross the primary growth zones and brine assemblages. The A_{ID} inclusions have low salinities of 3-6 wt.% $NaCl_{eq}$ and homogenise

to liquid at temperatures between 350-380°C whereas the A_V inclusions have lower typical salinities of 0.5–3 wt.% $NaCl_{eq}$ and homogenise over a broad temperature range (Figure 5.4A-B). A_L inclusions are most abundant within the type 3 veins where they clearly occur on secondary inclusion trails. These have very low vapour fractions (10-20%), salinities of 5–7 wt.% $NaCl_{eq}$ and homogenise to liquid at lower temperatures to the other inclusion types.

Type 4a Veins

The studied type 4a vein sample is dominated by moderate-low salinity A_L inclusions and high salinity B_H and B_{HO} inclusions. The brine inclusions typically occur along primary quartz growth zones at the vein margins and typically display lower homogenisation temperatures than those recorded in the biotite breccia and type 3 vein samples (Figure 5.6). The brine inclusions commonly contain chalcopyrite daughter crystals (B_{HO}) and homogenise by halite dissolution at similar temperatures to rare A_V inclusions that occur along the same growth zones. The A_L inclusions usually homogenise between 340 and 360°C and have relatively uniform salinities of 7 wt.% $NaCl_{eq}$. These were particularly abundant in quartz crystals at the vein centre implying that these inclusions represent an overprinting, lower salinity fluid generation. Lower temperature A_L and A_V inclusions with salinities of 0-5 wt.% $NaCl_{eq}$ were also observed occurring along secondary inclusion trails.

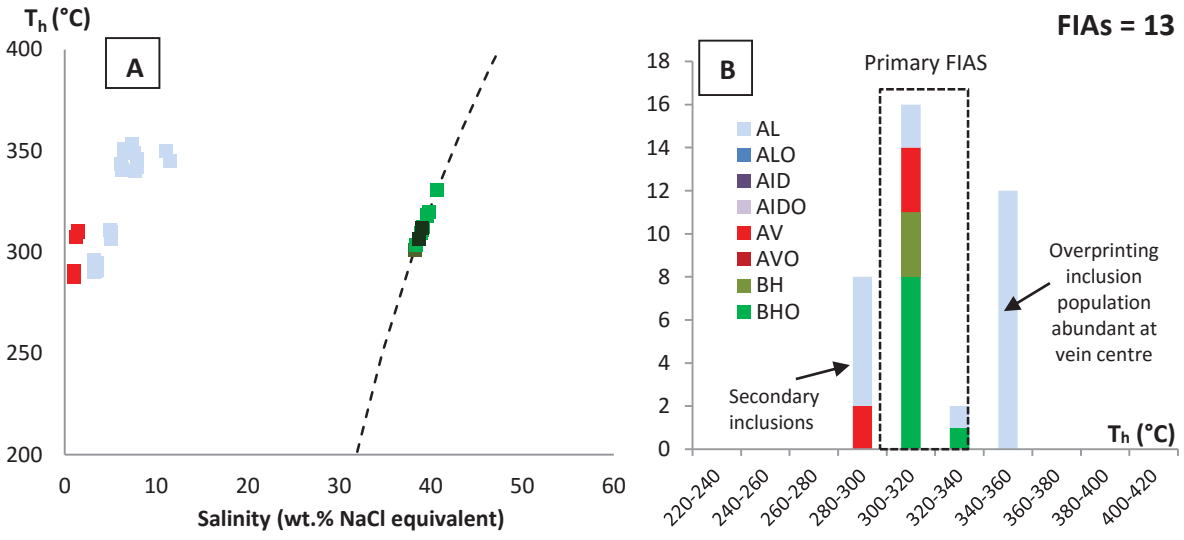


Figure 5.6: Fluid inclusion microthermometric data for different inclusion types in a type 4a vein sample. (A) Fluid inclusion total homogenisation temperature (T_h) versus salinity ($NaCl_{eq}$) plot. Dotted line = Halite saturation curve for the system NaCl-H_2O (Bodnar *et al.*, 1985; Driesner and Heinrich, 2007; Becker *et al.*, 2008). (B) Individual fluid inclusion homogenisation temperatures for each inclusion type with number of fluid inclusion assemblages (FIAs) measured. Dotted box surround the oldest primary inclusions.

5.3.4 Main Mineralisation Veins and Breccias

Main-stage mineralisation samples were analysed that contained highly variable amounts of molybdenite and Cu-sulphides and were obtained from a range of depths and multiple intrusive centres. This allows for the assessment of how fluids evolved during ascent and how different vein types developed in each intrusive centre.

Anhydrite Breccias and Type 5 Veins

Fluid inclusions in the type 5 veins and associated anhydrite breccias (e.g. Vry *et al.*, 2010) were predominantly measured in coarse anhydrite crystals that overgrow minor quartz that is particularly abundant at the vein and margin edges. Similar to the premineralisation stage veins and breccias, the anhydrite breccia sample is dominated by B_H and B_{HO} inclusions that typically homogenise between 310 and 360°C by halite dissolution (Figure 5.7).

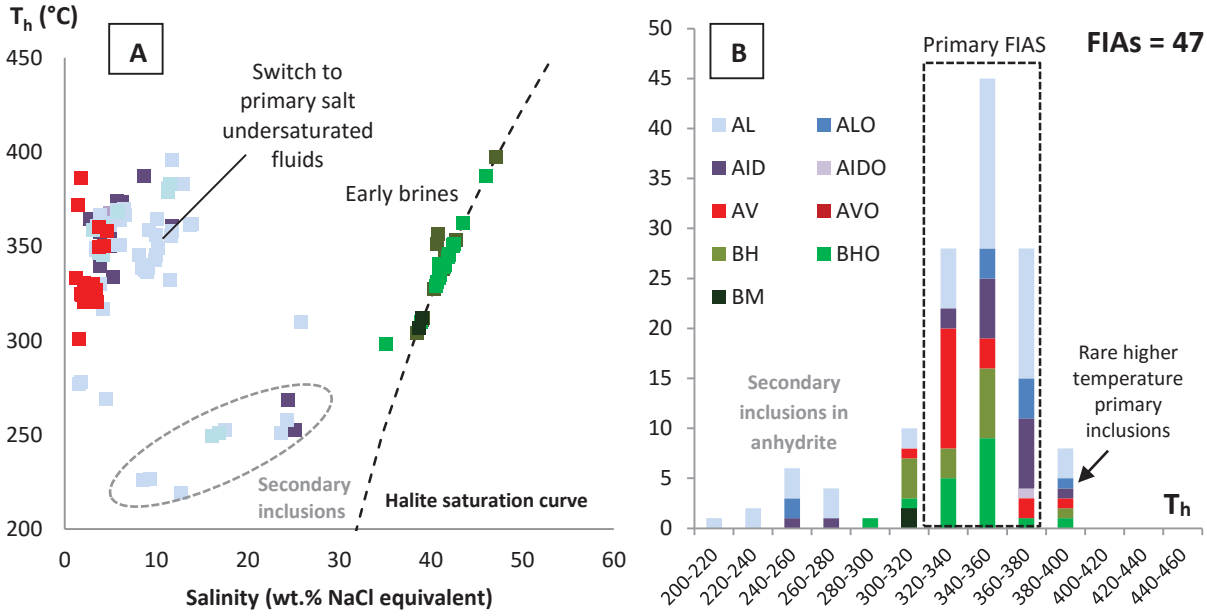


Figure 5.7: Fluid inclusion microthermometric data for different fluid inclusion types in type 5 veins and associated anhydrite breccias. (A) Individual fluid inclusion total homogenisation temperature (T_h) versus salinity ($NaCl_{eq}$). Dotted line = Halite saturation curve for the system NaCl-H_2O (Bodnar *et al.*, 1985; Driesner and Heinrich, 2007; Becker *et al.*, 2008). (B) Individual fluid inclusion homogenisation temperatures for each inclusion type with number of fluid inclusion assemblages (FIAs) measured. Box surround the oldest primary inclusions. All halite saturated fluid inclusions are displayed in green. Primary brine inclusions are particularly abundant in the type 5 breccia samples occurring alongside rare A_V inclusions. Primary A_{ID} and A_L inclusions are the predominant primary inclusions in the type 5 veins. These overprint the anhydrite breccia samples suggesting they represent an overprinting fluid generation to the brines.

In the anhydrite breccias, salt-undersaturated fluid inclusions have highly variable vapour fractions (0-95%) and salinities (1.2-25.8 wt.% $NaCl_{eq}$). This variability is less pronounced in the type 5 veins, which contain a far higher proportion of low to moderate salinity (3.3-8.7 wt.% $NaCl_{eq}$) inclusions with vapour fractions of 30-50% (e.g. Figure 5.8B). These inclusions are particularly abundant along primary growth zones in the subordinate quartz crystals (Figure 5.8B) but are also abundant along planar growth zones in the anhydrite-dominated type 5 veins. Anhydrite crystals are also cut by numerous secondary inclusion trails consisting of low salinity A_V inclusions and high salinity A_L inclusions that homogenised between 215-270°C (e.g. Figure 5.8D).

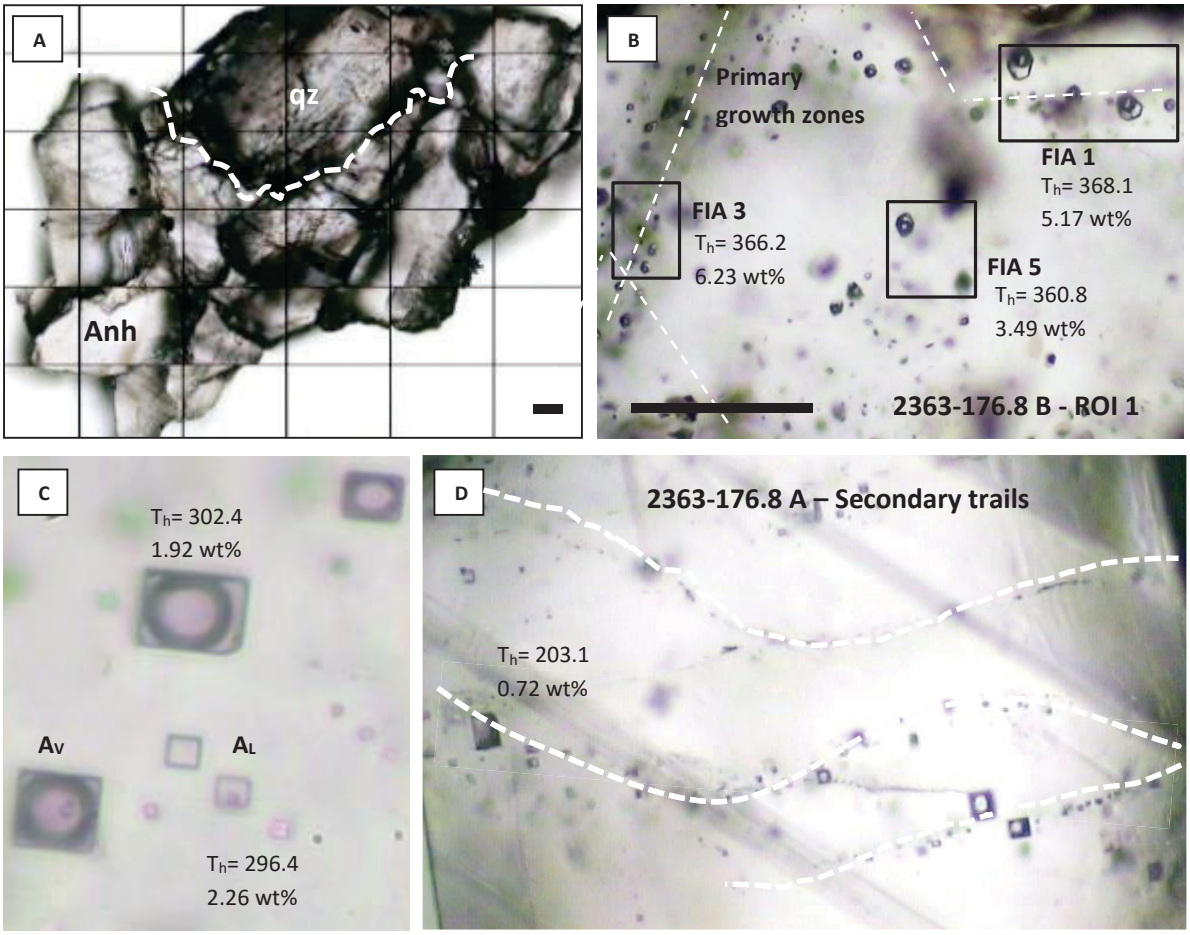


Figure 5.8 Transmitted light photomicrographs of fluid inclusions hosted in type 5 veins and associated anhydrite breccia cements. (A) Compiled map showing coarse anhydrite and overprinted subordinate quartz within a type 5 vein (sample 2363-176.8A). (B) Abundant intermediate density and moderate salinity fluid inclusions hosted in minor quartz in a type 5 vein sample (Region of interest 1 - sample 2363-176.8 B). (C) Lower temperature aqueous inclusions with highly variable vapour fractions in an anhydrite breccia sample proximal to the A-porphyry (sample 2305-191.7) possibly produced by heterogeneous inclusion entrapment or post-entrapment leakage (D) Low salinity A_V secondary inclusion trails in a type 5 vein (Region of Interest 2363-176.8 A). Scale bars = 100 µm.

Type 6a Veins

Type 6a veins were analysed from various mine levels and distances from their respective neighbouring - and possibly source - intrusions. These are subdivided into four categories: (1) deep-proximal 6a veins, from below 1470 m asl within and proximal to the North Central Diorite (Figure 5.9A-B); (2) intermediate 6a veins, formed between 1450 and 1700 m asl in a slightly more distal setting of the mafic complex to the east of the North Central Diorite (Figure 5.9C-D); (3) shallow 6a veins from above 1900 m asl (Figure 5.9E-F), which contain variable amounts of molybdenite (0-5%) and chalcopyrite (1-4%) and were obtained from within and surrounding several mineralised intrusions (A-Porphyry, Southern Diorite, North-Central Diorite, Northern Diorite and the Teniente Dacite Porphyry); and (4) transitional 6a-7a veins from above 1900 m asl, which were obtained from the A-Porphyry and Northern Diorite and contain increasing molybdenite from 40 to 90%. These samples contain minor Cu-sulphides (<1%) but are commonly surrounded by significant disseminated chalcopyrite.

The deep-proximal 6a veins are dominated by quartz and sometimes contain minor K-feldspar and plagioclase. The quartz crystals occur in a coarse mosaic with typical crystal sizes of 100 to 700 µm (e.g. Figure 5.10A-B). Crystals commonly display a core of highly luminescent quartz surrounded by zones of dully-luminescent quartz. All samples were dominated by A_{ID} inclusions (e.g. Figure 5.10C-D) with high vapour fractions (60-70%) and salinities of 3-9 wt.% $NaCl_{eq}$. These almost always homogenise to vapour (83% → V) between 420 and 500°C and sometimes occur on the same growth zones as A_V inclusions that have similar microthermometric properties (e.g. Figure 5.10A-B). Approximately 15% of the A_{ID} inclusions measured contain opaque daughter crystals that did not dissolve during heating tests and were interpreted to be chalcopyrite.

Rare A_L inclusions are randomly distributed throughout the samples, have a range of salinities (2-25 wt.% $NaCl_{eq}$) and homogenise at slightly lower temperatures to most A_{ID} and A_V inclusions (Figure 5.9B). Brine inclusions are also rare and are randomly distributed throughout the quartz crystals. These inclusions commonly contain chalcopyrite daughter crystals and homogenise by vapour-bubble disappearance at lower temperatures than the other inclusion types (Figure 5.9B). No evidence of fluid phase separation was observed.

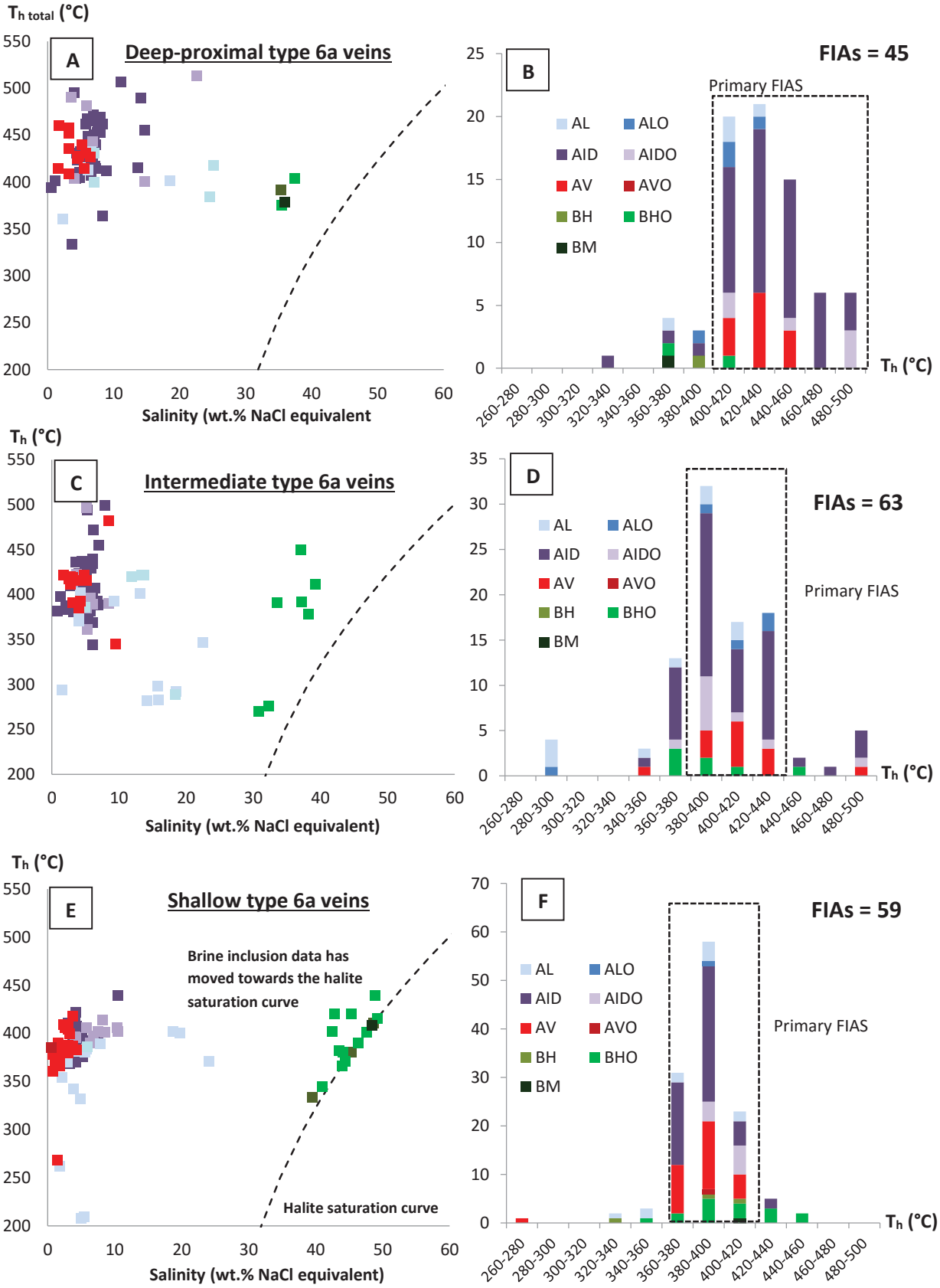


Figure 5.9: Fluid inclusion total homogenisation temperatures ($T_{h\ total}$) versus salinity ($NaCl_{eq}$) plots and homogenisation temperature histograms for different fluid inclusion types in type 6a veins from various depths. (A-B) Deep-proximal veins obtained from below 1470 m asl within and proximal to the North Central Diorite. (C-D) Intermediate depth (1500-1700) veins obtained from the Teniente Mafic complex to the east of the North Central Diorite. (E-F) Shallow 6a veins from above 1900 m asl, containing 1-5% molybdenite.

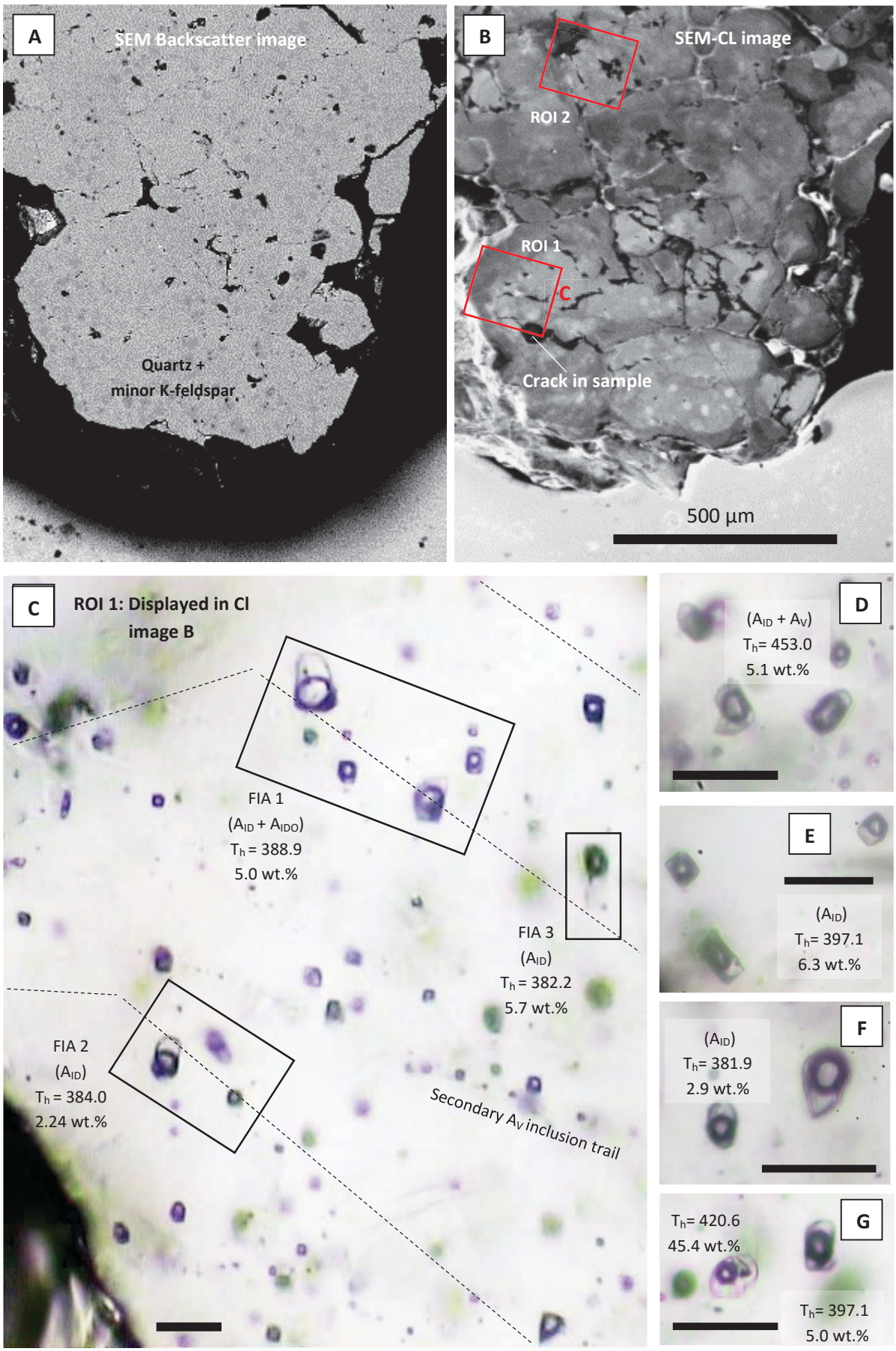

A
SEM Backscatter image
Quartz +
minor K-feldspar
B
SEM-CL image
ROI 2
ROI 1
C
Crack in sample
500 µm
C
ROI 1: Displayed in CI
image B
FIA 1
(AID + AIDO)
Th = 388.9
5.0 wt.%
FIA 3
(AID)
Th = 382.2
5.7 wt.%
FIA 2
(AID)
Th = 384.0
2.24 wt.%
Secondary AV inclusion trail
D
(AID + AV)
Th= 453.0
5.1 wt.%
E
(AID)
Th= 397.1
6.3 wt.%
F
(AID)
Th= 381.9
2.9 wt.%
G
Th= 420.6
45.4 wt.%
Th= 397.1
5.0 wt.%

Figure 5.10: SEM and fluid inclusion photomicrographs of type 6a veins from various mine levels. (A) SEM backscatter image of a deep level type 6a vein proximal to the North Central Diorite (sample 1034-988). (B) SEM-CL image of the same sample showing prominent quartz growth zones and the location of fluid inclusion ROI 1. (C) ROI 1 containing typical fluid inclusions present within deep level type 6a veins with a dominance of primary A_{ID} and A_{IDO} inclusions. Dashed lines = primary quartz growth zones containing abundant large A_{ID} inclusions. (D) A_{ID} and A_V inclusions in the same assemblage from 1313 m asl (ROI 1 - sample 1034-988.3). (E) Typical A_{ID} inclusions observed at depths of 1450-1700 m asl (FIA 14 – sample 1805-397.4). (F) Primary A_{ID} inclusions in a shallow (2045 m asl) type 6a vein proximal to the Teniente Dacite Porphyry (FIA 8 – 2661-139.1). (G) B_{HO} and A_{VO} fluid inclusions in a shallow type 6a vein containing 4% molybdenite and <1% chalcopyrite obtained from 1997 m asl (FIA 1 – sample 2215-33.9). Average microthermometric T_h and salinity values are displayed on selected FIAs. Scale bars = 25 µm.

The intermediate depth (1450-1650 m asl) type 6a veins are also composed of zoned quartz crystals dominated by A_{ID} inclusions with salinities of 2-8 wt.% $NaCl_{eq}$ (e.g. Figure 5.10E). Unlike the deep-proximal veins, the majority of these inclusions homogenise to liquid (43% → V) over a lower temperature range of 370-450°C (Figure 5.9C-D). Several inclusions with vapour fractions of 50-60% homogenise by critical behaviour in which their vapour bubble meniscus fades during heating. Brine and A_V inclusions are rare and again appear to be randomly distributed throughout the samples. These inclusions do not occur on obvious boiling trails and display similar homogenisation temperatures of ~400°C (Figure 5.9C). Two samples also contain secondary inclusion trails of intermediate-high salinity A_L inclusions and brine inclusions that homogenise to liquid between 260 and 310°C (Figure 5.9C-D).

Shallow 6a veins are composed of coarse mosaic quartz with similar typical crystal sizes of 100-700 µm (Figure 5.11A-B). In general, the quartz crystals are equant and more luminescent at the vein edges and grade inwards to larger, zoned, dull quartz crystals that are commonly intergrown with anhydrite (Figure 5.11A-B). Similar to the deeper type 6a veins, A_{ID} inclusions are the dominant fluid inclusion type (e.g. Figure 5.9F). These occur within quartz growth zones and exhibit trends of decreasing homogenisation temperature with decreasing quartz luminescence, typically towards the vein centres (e.g. Figure 5.11). The A_{ID} inclusions have lower typical vapour fractions (45-55%) than in the deep type 6a veins and almost always homogenise to liquid (13.2% → V) between 360 and 410°C. A greater proportion of A_V inclusions and brine inclusions also occur in close proximity to the A_{ID} inclusions (e.g. Figure 5.10G) or on the same primary quartz growth zones (Figure 5.11C). These inclusions homogenise at similar temperatures to the A_{ID} inclusions (Figure 5.9E-F) and may represent

inclusions produced by the onset of vapour-brine phase separation. The A_V inclusions typically have vapour fractions of 80-95% and are 4-5 times more abundant than the brine inclusions (Figure 5.9E-F). Opaque-bearing A_{VO} inclusions are rare with only a few chalcopyrite-bearing inclusions observed in the shallow molybdenite-bearing sample proximal to the North Central Diorite (e.g. Figure 5.10G).

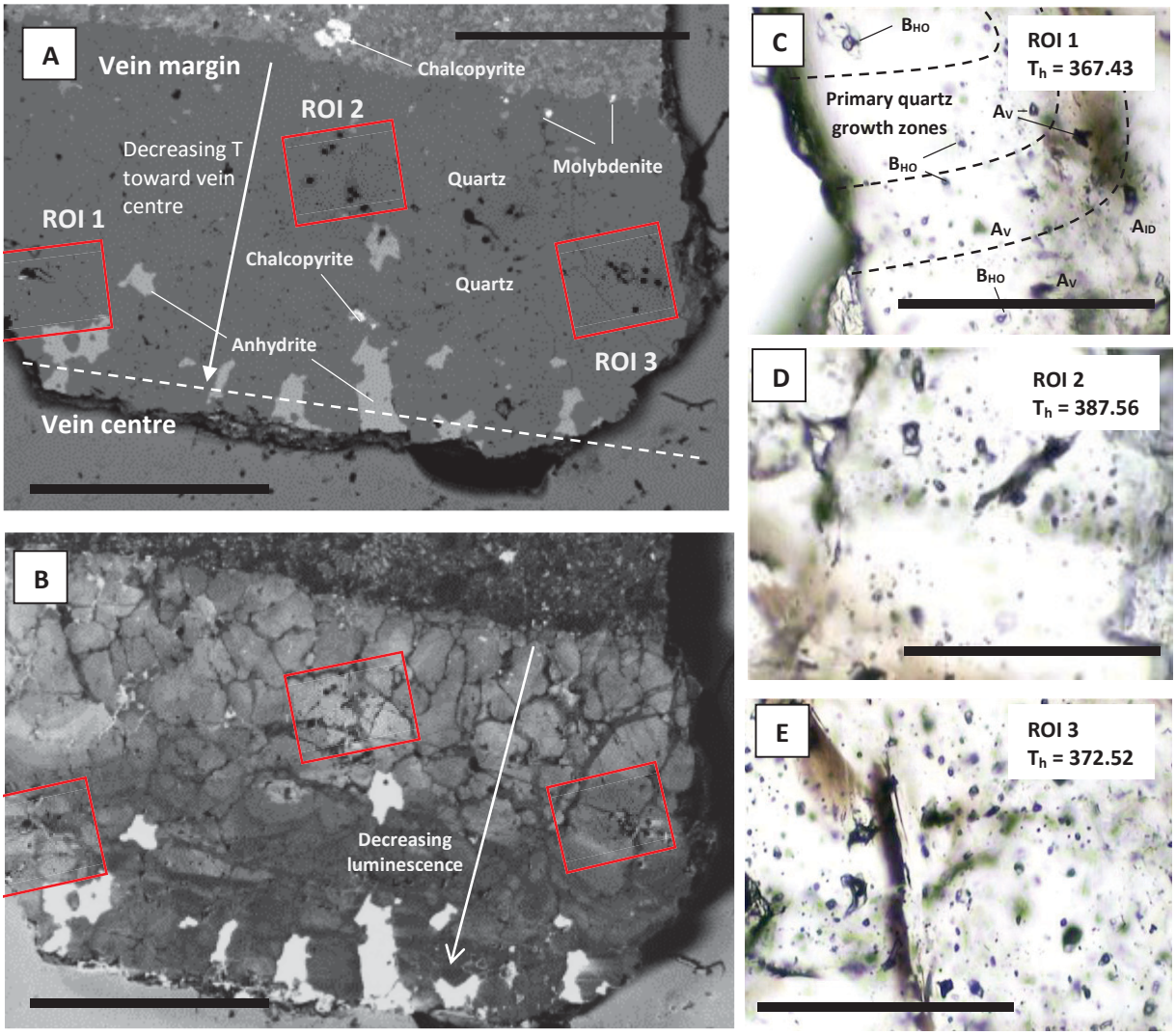


Figure 5.11: SEM images and fluid inclusion photomicrographs of a typical shallow type 6a vein proximal to the Teniente Dacite Porphyry (2661-131.9). (A) SEM backscatter image of vein showing the locations of fluid inclusion regions of interest 1-3 (red boxes). Dashed white line = vein centre. (B) SEM-CL image showing zoned mosaic quartz that grades from luminescent quartz at the vein edges to dull quartz at the vein centre. The vein centre is composed of intergrown quartz and anhydrite. Scale bars = 1 mm (C-E) Photomicrographs of fluid inclusion regions of interest 1-3 showing average homogenisation temperature (T_h) for primary fluid inclusions. Region of interest 1 (D) occurs closest to the vein centre, exhibits the lowest average homogenisation temperature for primary inclusions and contains the greatest abundance of apparently coexisting vapour and brine inclusions. Photomicrograph scale bars = 100 µm.

Microthermometric data for the transitional type 6a-7a veins (Figure 5.12A-B) were collected from quartz crystals surrounded by molybdenite or containing small molybdenite crystals as these were interpreted to contain inclusions that best represent Mo-depositing fluids. SEM-CL petrography revealed that these veins are typically composed of 100-300 µm crystals that exhibit clear compositional zonation (Figure 5.13A-C). Molybdenite is typically associated with patches of moderately luminescent quartz that predominantly occur near the vein margins and are overgrown by larger equant crystals of dully-luminescent quartz (e.g. Figure 5.13A-B). Molybdenite commonly occurs along the quartz growth zones but in areas is also found cutting large equant crystals (e.g. Figure 5.13C). This suggests that Mo in several veins is both present as co-precipitated molybdenite and quartz and also as a molybdenite replacement.

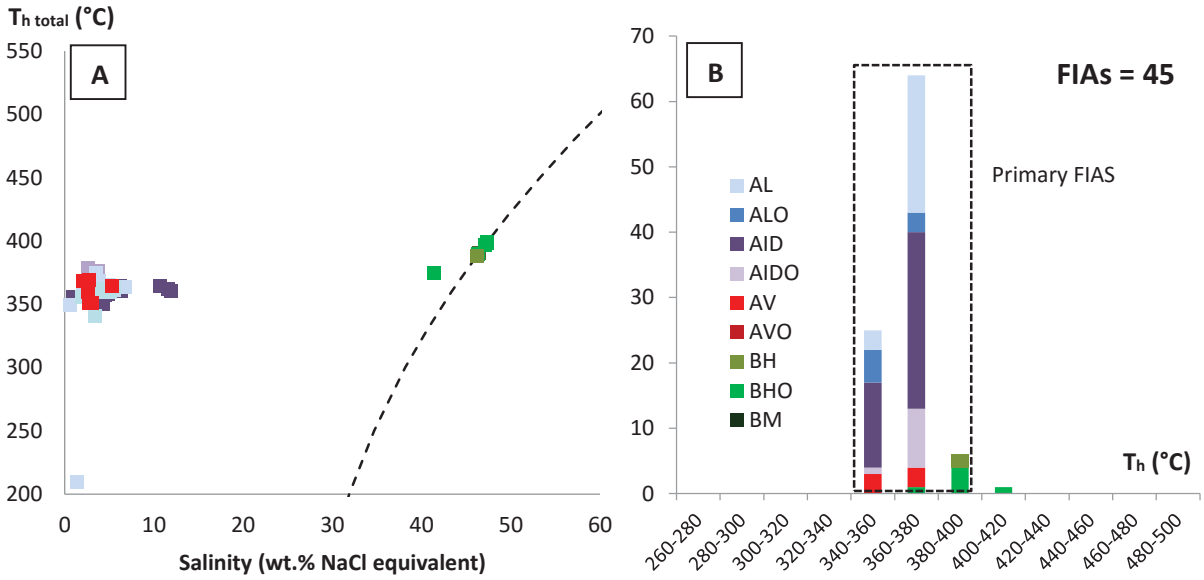


Figure 5.12: Summary fluid inclusion data for transitional type 6a-7a veins associated with the A-Porphyry and Northern Diorite. All inclusions are hosted in quartz veins that develop into pure molybdenite type 7a veins (e.g. Figure 12A). (A) Fluid inclusion homogenisation temperatures (T_h) versus salinities ($NaCl_{eq}$) for different fluid inclusions of each type. Dotted line = Halite saturation curve for the system NaCl-H_2O (Bodnar *et al.*, 1985; Driesner and Heinrich, 2007; Becker *et al.*, 2008). (B) Individual fluid inclusion homogenisation temperatures for each inclusion type and number of fluid inclusion assemblages (FIAs) measured.

Similar to the shallow 6a veins, A_{ID} inclusions are abundant and typically display low vapour fractions of 40-50% (e.g. Figure 5.12A-B, Figure 5.13E). These inclusions occur on the same growth zones as abundant A_L and A_{LO} inclusions, all of which homogenise to liquid over a narrow temperature interval of 355 to 380°C (Figure 5.12A-B). A_V inclusions are rare (Figure 5.13B), have uniform salinities of 1.5-2 wt.% $NaCl_{eq}$ and homogenise to vapour at similar temperatures to the A_{ID} and A_L inclusions (Figure 5.12A-B).

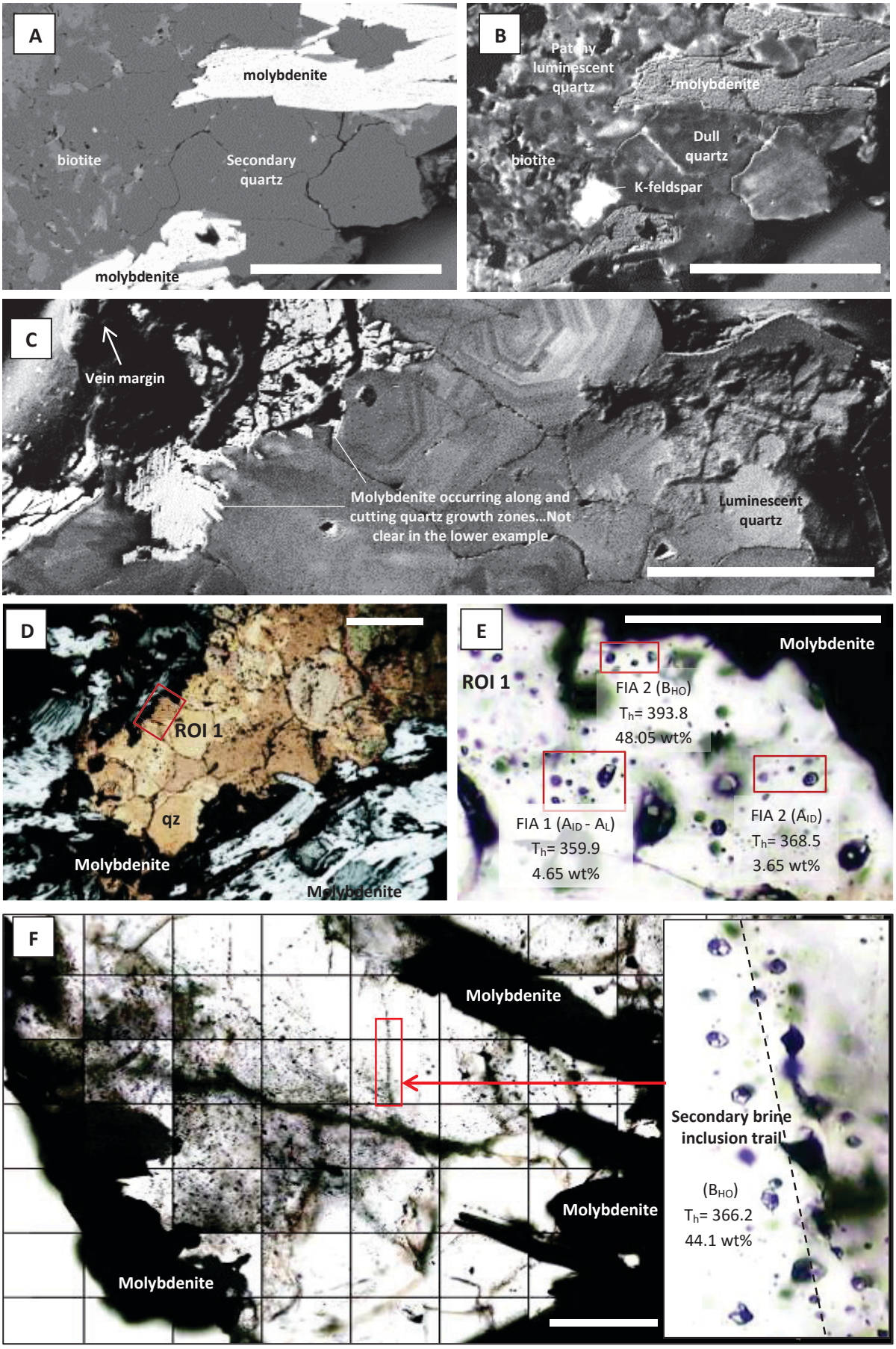
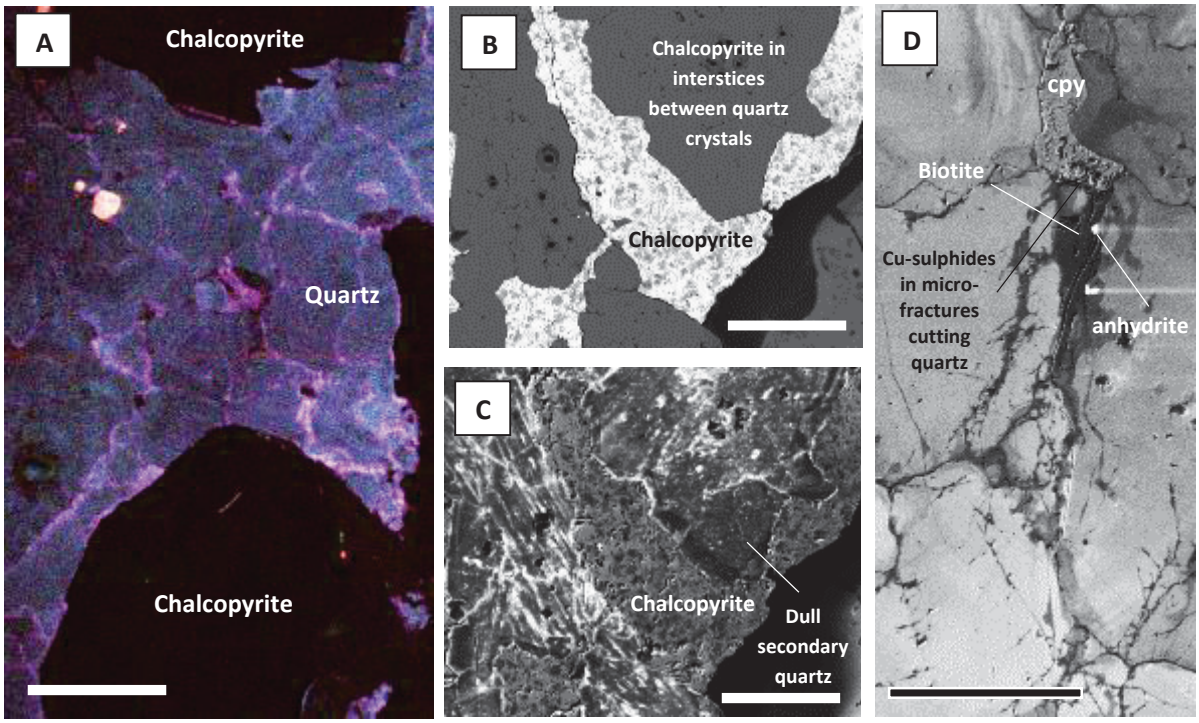

A
molybdenite
biotite
Secondary quartz
molybdenite
B
Patchy luminescent quartz
molybdenite
Dull quartz
biotite
K-feldspar
C
Vein margin
Molybdenite occurring along and cutting quartz growth zones...Not clear in the lower example
Luminescent quartz
D
ROI 1
qz
Molybdenite
Molybdenite
E
Molybdenite
ROI 1
FIA 2 (B_{HO})
T_h= 393.8
48.05 wt%
FIA 1 (A_{ID} - A_L)
T_h= 359.9
4.65 wt%
FIA 2 (A_{ID})
T_h= 368.5
3.65 wt%
F
Molybdenite
Molybdenite
Molybdenite
Secondary brine inclusion trail
(B_{HO})
T_h= 366.2
44.1 wt%

Figure 5.13 (previous page): SEM-CL images and reflected and transmitted light and photomicrographs of transitional 6a-7a veins. (A) SEM backscatter image of molybdenite in a transitional 6a-7a vein proximal to the A-Porphyry (sample 2305-82.0b). (B) SEM-CL image of same sample showing complex compositional zonation within the vein. Molybdenite is associated with highly luminescent quartz and K-Feldspar crystals at the vein edges that overprint large equant quartz crystals. (C) SEM-CL image of molybdenite cutting the edges of compositionally zoned quartz crystals at the vein edges (2371-79.6b). (D) Composite plane polarised and reflected light photomicrograph of a molybdenite type 7a vein with approximately 15% interstitial quartz on which fluid inclusion analysis was completed (Sample 2371-79.6a). (E) Transmitted light photomicrograph of coexisting A_{ID} and A_{LO} inclusions and small B_{HO} inclusions with corresponding assemblage microthermometric properties (ROI 1 - sample 2371-79.6b). (F) Compiled photomicrograph map and photomicrograph of a secondary trail consisting of B_{HO} inclusions (Sample 2305-82.0a). These inclusions were typically found in zones of brightly luminescent quartz. Scale bars = 300 μm.

Primary brine inclusions are also relatively rare and predominantly occur in the zones of highly luminescent quartz near the vein margins. The brine inclusions plot near the halite saturation curve and exhibit the highest average total homogenisation temperatures of any inclusions in this vein type (Figure 5.12A-B). Opaque-bearing brine inclusions that homogenise at slightly lower temperatures also occur along several secondary inclusion trails (e.g. Figure 5.13F). These trails run oblique to the vein edges and are commonly associated with minor chalcopyrite.

Type 6b Veins

SEM-CL analysis of type 6b veins reveals complex quartz zonation patterns and overgrowths indicative of multiple generations of crystallisation (Figure 5.14A-D). Veins contain highly variable abundances of Cu-sulphides (10-70%) and molybdenite (0-15%). Similar to the transitional 6a-7a veins, molybdenite is typically associated with zoned quartz crystals near the vein margins (e.g. Figure 5.14E). By comparison, chalcopyrite and minor bornite are usually present as large crystals that overgrow quartz or infill crystal interstices (e.g. Figure 5.14A). Additional chalcopyrite is also present in minor fractures that cut the quartz crystals where it commonly occurs with minor anhydrite, biotite and sericite (e.g. Figure 5.14D). In some samples, the Cu-sulphides are surrounded by streaks of highly luminescent quartz that cut the primary crystal growth zones (e.g. Figure 5.14B-C). In order to ascertain which fluids are the most important with respect to Mo and Cu transport, fluid inclusions were analysed in a number of quartz crystals that contain sulphide inclusions or were intergrown with or surrounded by significant chalcopyrite (e.g. Figure 5.14E).


A
Chalcopyrite
Quartz
Chalcopyrite
B
Chalcopyrite in interstices between quartz crystals
Chalcopyrite
C
Chalcopyrite
Dull secondary quartz
D
cpy
Biotite
Cu-sulphides in micro-fractures cutting quartz
anhydrite

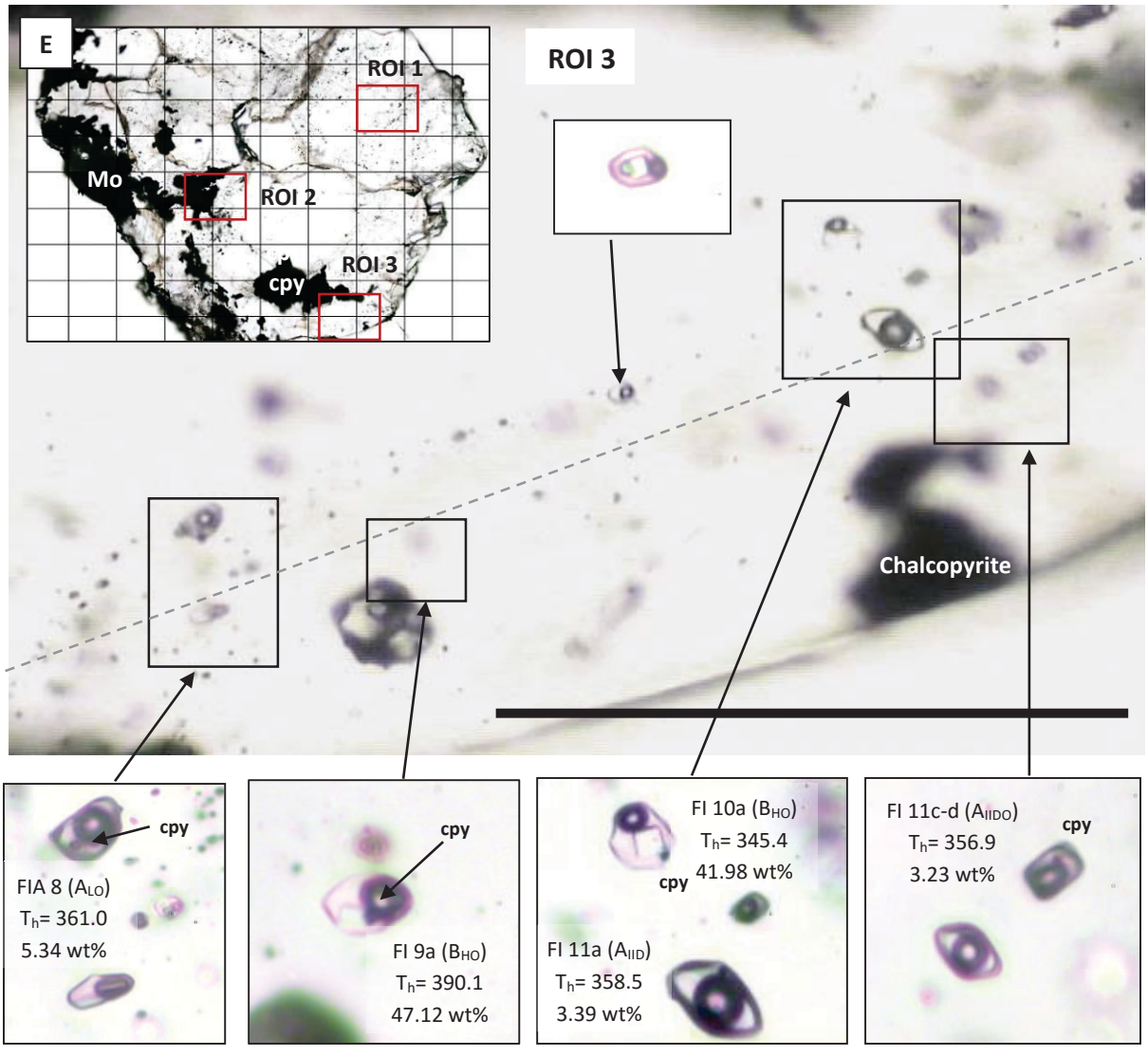

E
ROI 1
Mo
ROI 2
ROI 3
cpy
ROI 3
Chalcopyrite
cpy
FIA 8 (A_{LO})
T_h= 361.0
5.34 wt%
cpy
FI 9a (B_{HO})
T_h= 390.1
47.12 wt%
FI 10a (B_{HO})
T_h= 345.4
41.98 wt%
cpy
FI 11a (A_{IID})
T_h= 358.5
3.39 wt%
FI 11c-d (A_{IIDO})
T_h= 356.9
3.23 wt%
cpy

Figure 5.14 (previous page): SEM images and reflected and transmitted light and photomicrographs of type 6b veins. (A) Chroma-CL image of large chalcopyrite crystals overgrowing zoned quartz crystals in a type 6b vein proximal to the Southern Diorite (2083-162.5). (B) SEM backscatter image of region of a transitional type 6b-7b vein proximal to the North Central Diorite (region of interest 2 – sample 2230-1.5. (B) SEM-CL image of same region of interest showing complex compositional zonation within quartz associated with the edges of large chalcopyrite crystals. (C) SEM-CL image of chalcopyrite within a dull-CL veinlet that cuts quartz crystals in sample 2230-1.5. Minor biotite and anhydrite also occur within the annealed fracture. (E) Fluid inclusions in a molybdenite- and chalcopyrite-bearing type 6b vein from a shallow mine level proximal to the Northern Diorite (region of interest 3 - sample 2371-183.25). The sample contains A_{ID}, A_V, B_{HO} and B_H inclusions that often appear to occur on the same primary quartz growth zones, suggesting phase separation. These growth zones often contain small chalcopyrite inclusions. All scale bars = 300 µm.

Type 6b veins host all fluid inclusion type in relatively uniform proportions when compared to the other vein and breccia types (Figure 5.15A-B). A ~35% increase in the abundance of A_L inclusions is coupled with a marked decrease in the relative abundance of A_{ID} inclusions when compared to the shallow type 6a veins. These inclusion types homogenise at similar temperatures (350-420°C) and commonly occur on the same quartz growth zones (Figure 5.14E), suggesting that they represent similar fluids that are became progressively denser. Similar to the transitional 6a-7a veins, inferred primary A_L and A_{ID} inclusions frequently have salinities of 2.5 to 7 wt.% $NaCl_{eq}$ (Figure 5.13A) and almost always homogenise to liquid.

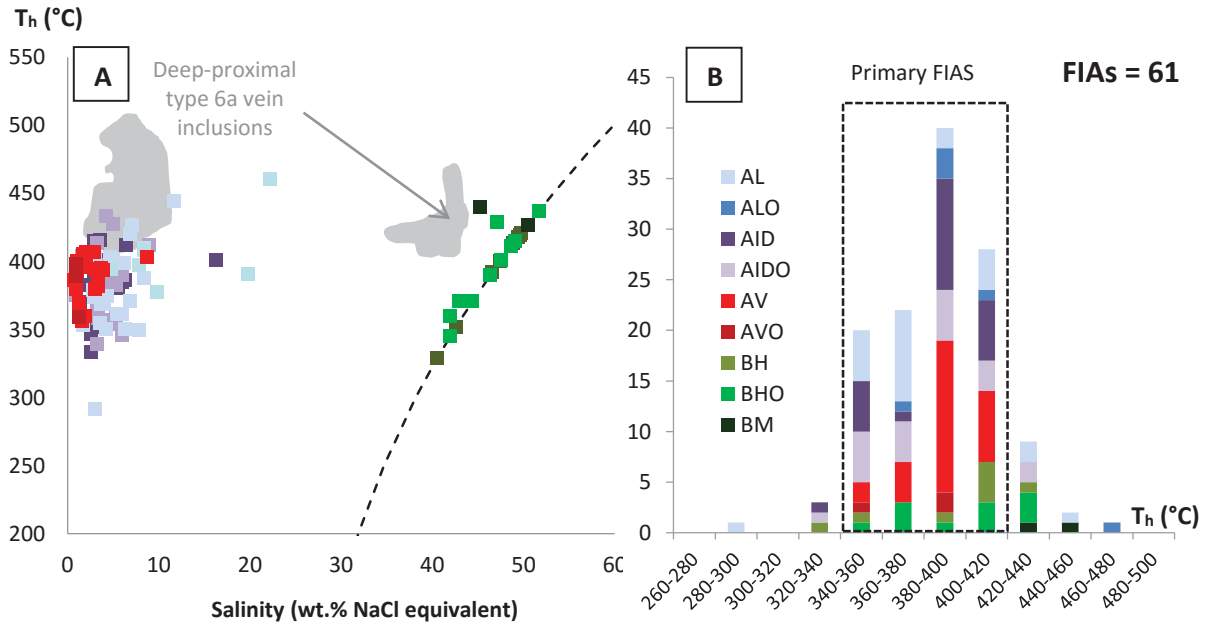


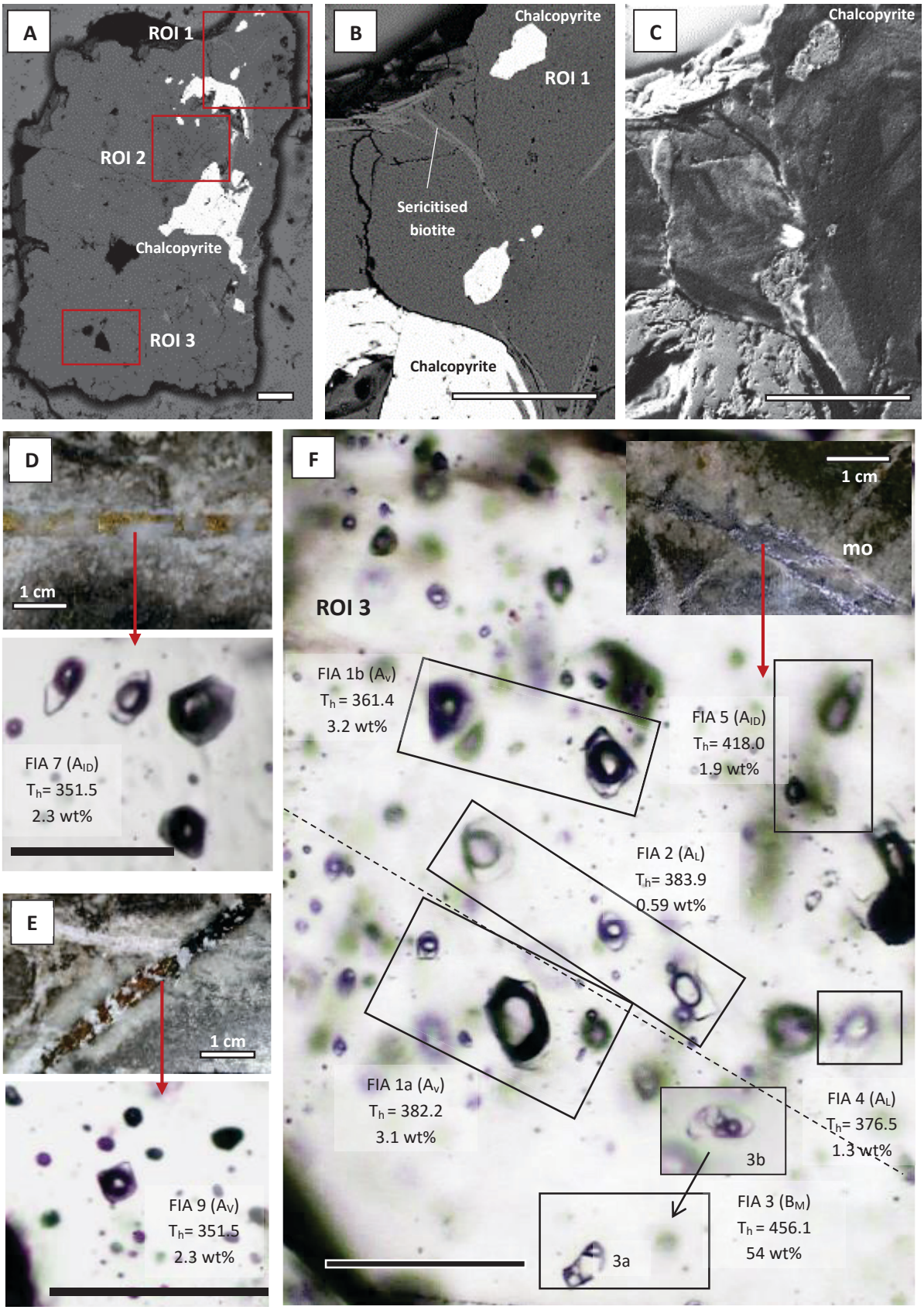
Figure 5.15: Summary fluid inclusion microthermometric data for different fluid inclusion types in type 6b veins associated with several intrusions and containing between 10 and 70% Cu-sulphides. (A) Fluid inclusion homogenisation temperatures (T_h) versus salinities ($NaCl_{eq}$) for different fluid inclusions of each type. Dotted line = Halite saturation curve for the system NaCl-H_2O (Bodnar *et al.*, 1985; Driesner and Heinrich, 2007; Becker *et al.*, 2008). (B) Histogram showing individual fluid inclusion homogenisation temperatures for each inclusion type and number of fluid inclusion assemblages (FIAs) measured.

Vapour and brine inclusions are far more abundant than in the type 6a veins and commonly occur on the same quartz growth zones as the A_L and A_{ID} inclusions where they homogenise at similar temperatures (Figure 5.14D). This suggests that the AID and AL inclusions are undergoing phase separation at temperatures <420 °C. The A_V inclusions are characterised by high vapour fractions (80-95%) and very low salinities of 0.5-1.5 wt.% $NaCl_{eq}$ (Figure 5.15A). Several opaque-bearing A_{VO} inclusions were also observed in the two most chalcopyrite-rich samples. The brine inclusions have a broader range of salinities (33-52 wt.% $NaCl_{eq}$) than in the type 6a veins (Figure 5.15A) and exhibit halite dissolution temperatures that are similar to those of vapour bubble homogenisation, implying fluid boiling. The vast majority of brine inclusions contain at least one opaque daughter phase.

Type 8 Veins

The type 8 veins consist of a far higher proportion of highly luminescent anhydrite than the type 6a-6b veins making it difficult to obtain clear SEM-CL images. As with the type 6b veins, SEM analysis reveals that chalcopyrite is usually present in clusters of grains that occur along the contacts between large quartz and anhydrite crystals or within microfractures where it is sometimes associated with minor sericitised biotite and/or anhydrite (e.g. Figure 5.16B). Small chalcopyrite crystals are also present dispersed throughout the large zoned crystals. In a molybdenite-rich type 8 vein sample, molybdenite predominantly occurs at the vein edges (e.g. Figure 5.16F) where it is intergrown with large crystals of zoned, luminescent quartz. Molybdenite was seldom observed in close proximity to anhydrite crystals. By contrast, bornite occurs in large (>300 µm) clusters throughout the type 8 veins, where it appears to be intergrown with large anhydrite crystals (e.g. Figure 5.16E).

Figure 5.16 (next page): SEM images, sample photographs and fluid inclusion photomicrographs of type 8 veins containing variable sulphide abundances. (A) SEM backscatter image of a type 8 vein wafer showing the location of fluid inclusion regions of interest 1-3 (2371-149.0). (B) SEM backscatter image of region of interest 1 showing abundant chalcopyrite mineralisation and minor sericitised biotite. (C) SEM-CL image of region of interest 1 showing chalcopyrite mineralisation along the edges of large, compositionally zoned quartz crystals. (D) Typical, chalcopyrite-rich, type 8 vein proximal to the Teniente Dacite Porphyry containing abundant coexisting A_{ID} and A_V inclusions (FIA 1 – sample 2661-223.2). (E) Bornite-rich type 8 vein proximal to the North-Central Diorite, dominated by A_V inclusions with typical vapour fractions >80% (FIA 9 – sample 2230-101.9). (F) Molybdenite-rich type 8 vein proximal to the North-Central Diorite containing B_{HO}, A_V, A_{ID}, A_L and A_{LO} inclusions in close proximity to one another (region of interest 1 - sample 2215-151.9). Average total homogenisation temperatures (T_h) and salinities (wt.% $NaCl_{eq}$) are displayed next to each measured fluid inclusion assemblage. SEM scale bars = 300 µm. Photomicrograph scale bars = 50 µm.


A
ROI 1
ROI 2
Chalcopyrite
ROI 3
B
Chalcopyrite
ROI 1
Sericitised biotite
Chalcopyrite
C
Chalcopyrite
D
1 cm
FIA 7 (AID)
Th= 351.5
2.3 wt%
E
1 cm
FIA 9 (AV)
Th= 351.5
2.3 wt%
F
1 cm
mo
ROI 3
FIA 1b (AV)
Th = 361.4
3.2 wt%
FIA 5 (AID)
Th= 418.0
1.9 wt%
FIA 2 (AL)
Th= 383.9
0.59 wt%
FIA 1a (AV)
Th = 382.2
3.1 wt%
FIA 4 (AL)
Th= 376.5
1.3 wt%
3b
FIA 3 (BM)
Th = 456.1
54 wt%
3a

Similar to the type 6b veins, the type 8 veins contain relatively uniform abundances of each fluid inclusion type (Figure 5.17B). The A_{ID} and A_L inclusions are present along the same mineral growth zones, display relatively uniform vapour fractions of 30-50% and typically homogenise to liquid between 340 and 410°C (Figure 5.17A-B). The modal homogenisation temperature is ~60°C cooler than that recorded for the A_{ID} inclusions in the deep 6a veins (Figure 5.17B). Fluid inclusions in a quartz and molybdenite-rich sample homogenised at greater temperatures than those in the Cu-sulphide-rich veins (e.g. Figure 5.16D-F). Molybdenite- and chalcopyrite-rich type 8 veins contain similar proportions of brine and A_V inclusions that sometimes occur on boiling trails, particularly in Mo-rich samples (e.g. Figure 5.16F). The A_V inclusions typically have low salinities of <1.8 wt.% $NaCl_{eq}$ and almost always homogenise to vapour between 345 and 395°C (Figure 5.17). The brine inclusions exhibit the largest range of salinities of any main mineralisation inclusion type and commonly homogenise by halite dissolution between 310 and 460°C. Some hypersaline inclusions are so saline that total homogenisation temperatures and salinities could not be measured. Bornite-rich type 8 veins contain a greater abundance of A_V inclusions than molybdenite and chalcopyrite-rich examples. These inclusions homogenise at lower temperatures suggesting greater degree of phase separation prior to bornite deposition (e.g. Figure 5.16E).

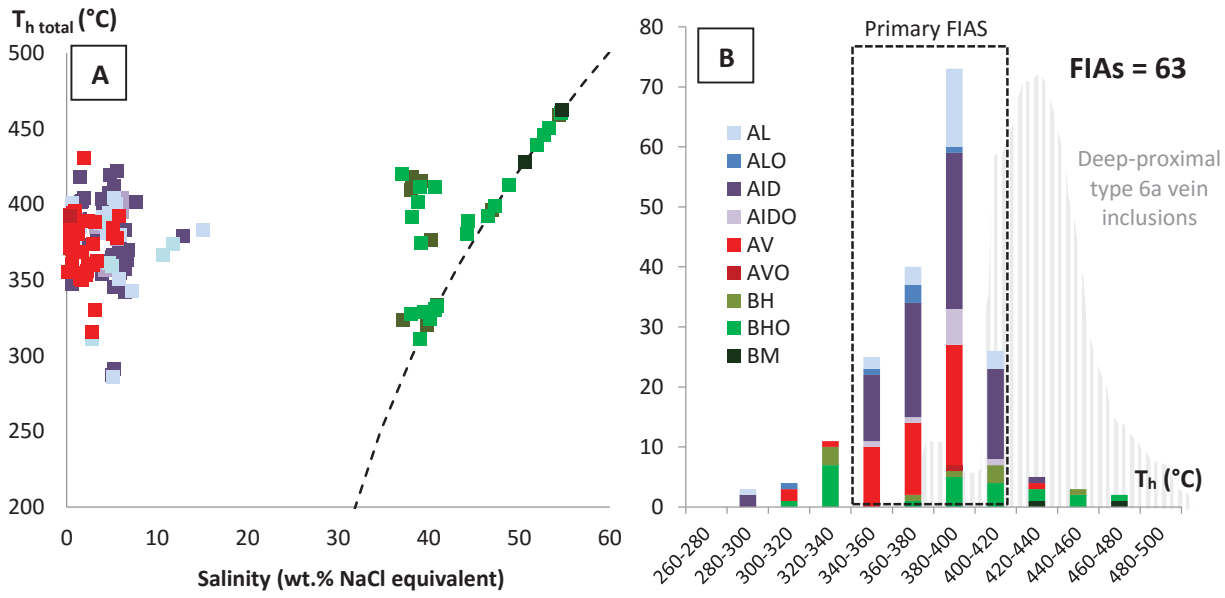


Figure 5.17: Summary fluid inclusion microthermometric data for different fluid inclusion types in type 8 veins containing chalcopyrite, bornite and molybdenite. (A) Homogenisation temperature (T_h) versus salinity for different fluid inclusions of each type. Dotted line = Halite saturation curve for the system NaCl-H_2O (Bodnar *et al.*, 1985; Driesner and Heinrich, 2007; Becker *et al.*, 2008). (B) Individual fluid inclusion homogenisation temperatures for each inclusion type and number of fluid inclusion assemblages (FIAs) measured.

5.3.5 Late Mineralisation Veins and Breccias

Tourmaline Breccias and Type 9 Veins

SEM-CL analysis of type 9 veins and breccias reveals that they are dominated by large (~500 µm) quartz and anhydrite crystals that exhibit distinct growth zonation (Figure 5.18A-B). Molybdenite and chalcopyrite are commonly associated with zones of highly luminescent quartz that occur along microfractures and in interstices between quartz crystals. This suggests a late input of Mo and Cu-rich fluids that may overprint main mineralisation type veins. The type 9 veins are dominated by low salinity A_V inclusions and high salinity brines that homogenise over a broad temperature range (Figure 5.19A-B). The A_V inclusions have low salinities of 0.4-3 wt.% $NaCl_{eq}$ and occur in clusters or along primary growth zones in quartz and anhydrite crystals. Unlike the main mineralisation samples, moderate salinity (3-10 wt.% $NaCl_{eq}$) A_{ID} inclusions are extremely rare.

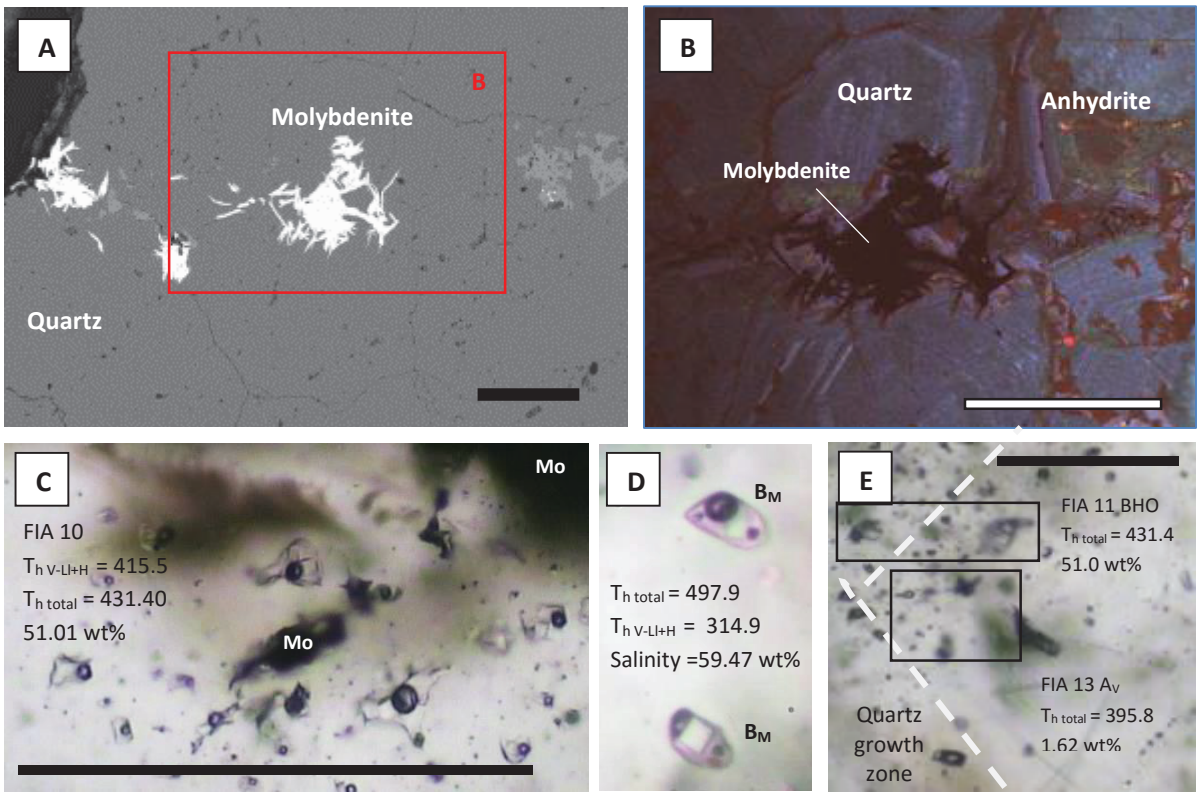


Figure 5.18: SEM images, sample photographs and fluid inclusion photomicrographs of type 9 veins and breccias. (A-B) SEM backscatter and chroma-CL image images of rod-like molybdenite and zoned quartz in a type 9 vein to the south of the Braden Breccia pipe (region of interest 1 – sample 1888-205.5). (C) Large, irregularly-shaped, high salinity brine inclusions alongside significant molybdenite mineralisation (region of Interest 2 - sample 2083-168.2). (D) High salinity, opaque-bearing B_M and B_{HO} brine inclusions (FIA 13, sample 2083-63.4). Quartz growth zone containing A_V and B_{HO} Inclusions (region of interest 3 – sample 2083-168.2).

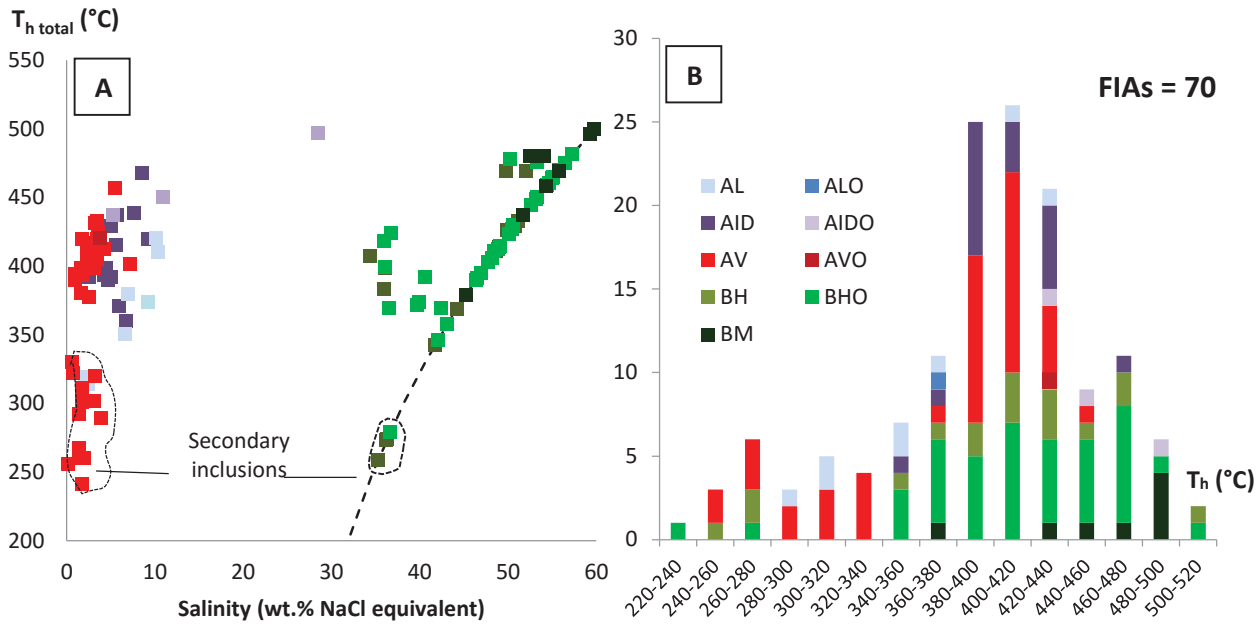


Figure 5.19: Summary fluid inclusion microthermometric data for different fluid inclusion types in type 9 veins and breccias. (A) Fluid inclusion homogenisation temperatures (T_h) versus salinities ($NaCl_{eq}$) for fluid inclusions of each type. Dotted line = Halite saturation curve for the system NaCl-H_2O (Bodnar *et al.*, 1985; Driesner and Heinrich, 2007; Becker *et al.*, 2008). (B) Histogram showing individual fluid inclusion homogenisation temperatures for each inclusion type and number of fluid inclusion assemblages (FIAs) measured.

The brine inclusions exhibit the highest and broadest range of salinities of any inclusion type in any vein type. Two types of brine inclusions were recognised: abundant, rounded B_{HO} and B_M inclusions that are randomly distributed throughout all samples (e.g. Figure 5.18D); and less common, irregularly-shaped B_{HO} and B_H inclusions that occur in clusters or on possible pseudosecondary trails, have salinities of >50 wt.% $NaCl_{eq}$ and commonly homogenise by halite dissolution (e.g. Figure 5.18C). The rounded brine inclusions homogenise at temperatures between 380 and 420°C and commonly occur along the same mineral growth zones as abundant A_V inclusions that exhibit similar homogenisation temperatures. This suggests trapping of a fluid undergoing phase separation. The opaque-bearing brine inclusions that homogenise by halite dissolution at temperatures >440°C commonly exhibit liquid-vapour homogenisation temperatures that are >100°C lower (e.g. Figure 5.18D). These inclusions often occur in close proximity to abundant A_V inclusions that typically homogenise at lower temperatures, similar to the vapour bubble homogenisation range of a number of brine inclusions (e.g. Figure 5.18E). A number of secondary B_H inclusions with salinities of ~36 wt.% $NaCl_{eq}$, small (<5 µm) A_V inclusions and low salinity (<2 wt.% $NaCl_{eq}$) A_L inclusions are also present throughout the samples (Figure 5.19A).

Anhydrite-Carbonate ±Gypsum Breccias and Type 10 Veins

In the type 10 veins and anhydrite-carbonate ±gypsum breccias, fluid inclusions were measured in quartz, anhydrite and gypsum (Figure 20A-B). Most samples could not be photographed well using SEM-CL due to the abundance of highly luminescent sulphates. Overall fluid inclusion type abundances are comparable to those recorded for the type 6b veins but the inclusions exhibit a far greater range of homogenisation temperatures and salinities (Figure 5.20A-B). The inclusions with the highest homogenisation temperatures are hosted by quartz, with lower temperatures characterising the anhydrite- and gypsum-hosted inclusions (Figure 5.20A).

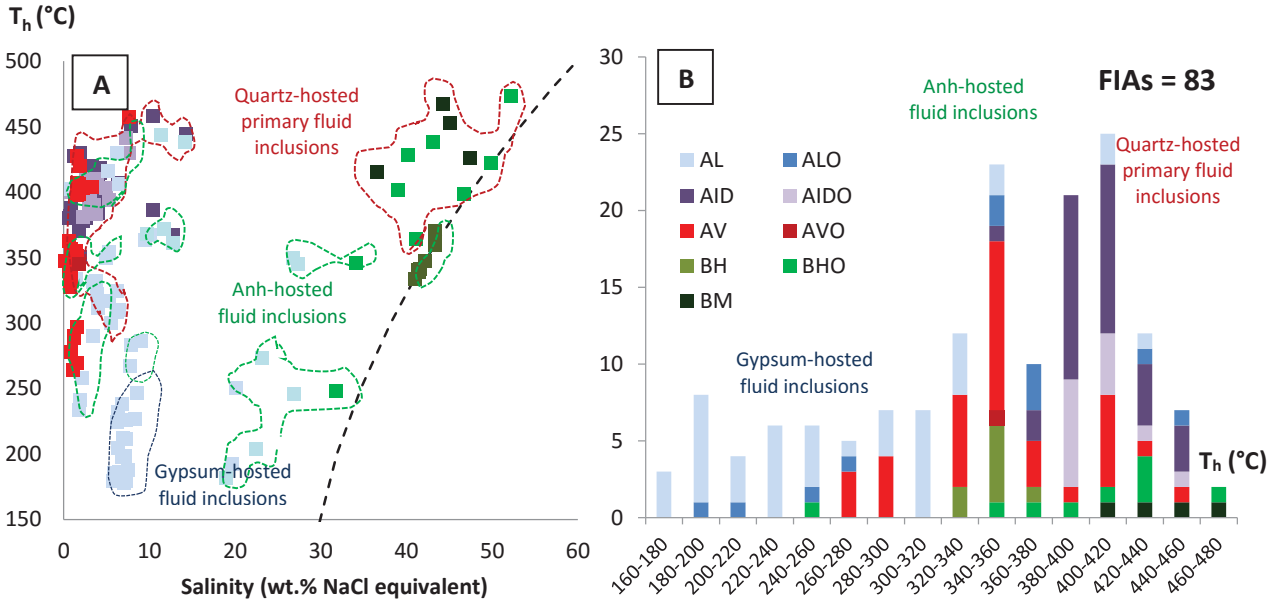


Figure 5.20: Summary fluid inclusion microthermometric data for different fluid inclusion types in the type 10 veins and breccias. (A) Fluid inclusion total homogenisation temperature (T_h) versus salinity ($NaCl_{eq}$) for each inclusion type in different host minerals. Dotted line = Halite saturation curve for the system NaCl-H_2O (Bodnar *et al.*, 1985; Driesner and Heinrich, 2007; Becker *et al.*, 2008). (B) Individual fluid inclusion homogenisation temperatures for each inclusion type and number of fluid inclusion assemblages (FIAs) measured.

Quartz-rich type 10 veins contain 200-600 µm comb-quartz crystals that meet at vein centres where they are commonly truncated by carbonate ±sulphate (e.g. Figure 5.21A-B). Similar to the type 6a veins, the quartz is dominated by primary A_{ID} inclusions (e.g. Figure 5.21E) that homogenise between 380 and 430°C. High salinity brine and low salinity A_V inclusions are also relatively abundant and commonly occur along the same quartz growth zones (e.g. Figure 5.21D). These inclusions typically contain at least one opaque-daughter phase and usually homogenise by vapour bubble disappearance at temperatures >350°C (Figure 5.20B).

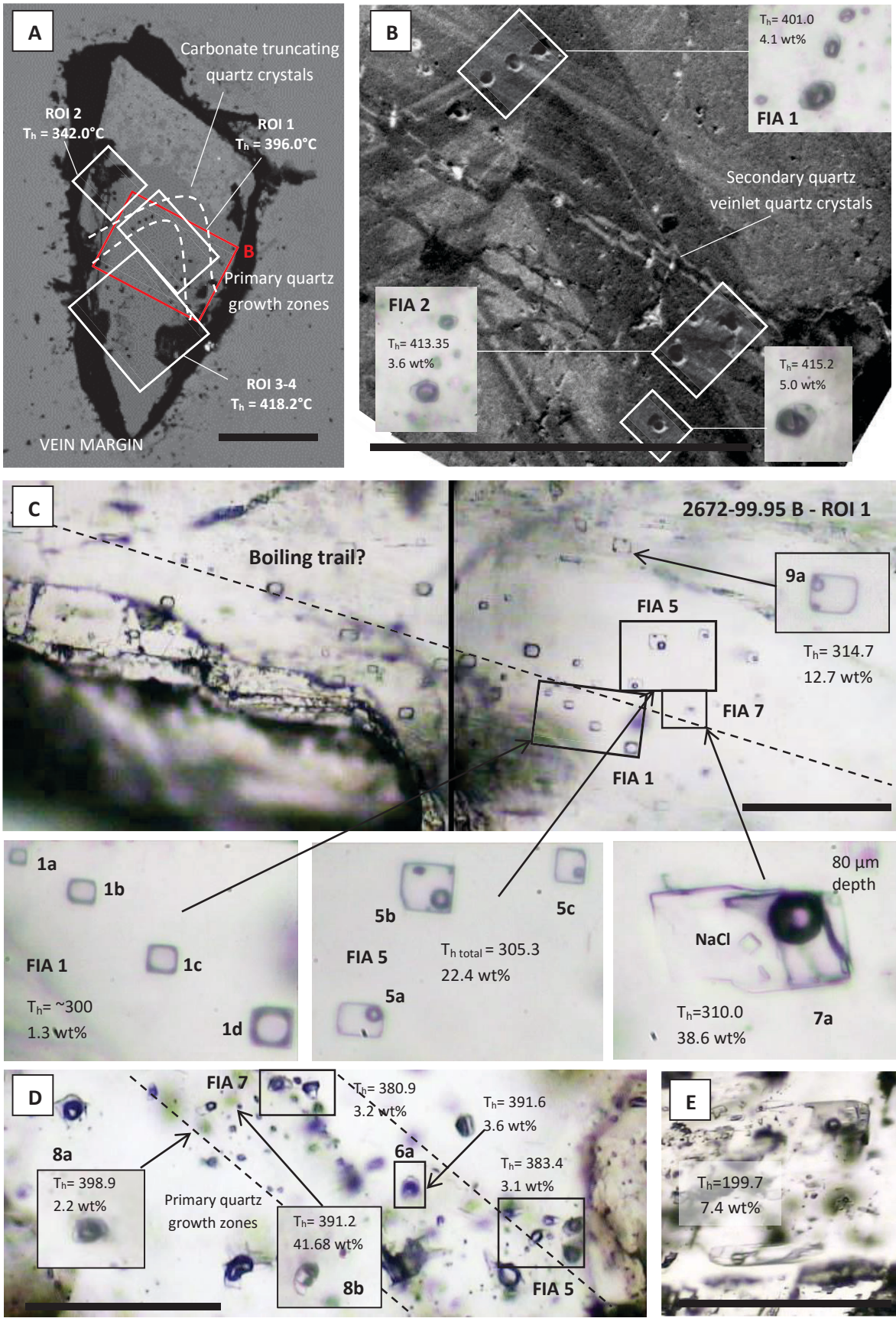

A
Carbonate truncating quartz crystals
ROI 2
Th = 342.0°C
ROI 1
Th = 396.0°C
B
Primary quartz growth zones
ROI 3-4
Th = 418.2°C
VEIN MARGIN
B
Th= 401.0
4.1 wt%
FIA 1
Secondary quartz veinlet quartz crystals
FIA 2
Th= 413.35
3.6 wt%
Th= 415.2
5.0 wt%
C
Boiling trail?
2672-99.95 B - ROI 1
9a
FIA 5
Th= 314.7
12.7 wt%
FIA 7
FIA 1
1a
1b
FIA 1
1c
Th= ~300
1.3 wt%
1d
5b
5c
FIA 5
Th total = 305.3
22.4 wt%
5a
80 µm depth
NaCl
Th=310.0
38.6 wt%
7a
D
FIA 7
Th= 380.9
3.2 wt%
Th= 391.6
3.6 wt%
8a
Th= 398.9
2.2 wt%
6a
Th= 383.4
3.1 wt%
Primary quartz growth zones
Th= 391.2
41.68 wt%
8b
FIA 5
E
Th=199.7
7.4 wt%

Figure 5.21 (previous page): SEM images, sample photographs and fluid inclusion photomicrographs of type 10 veins and anhydrite-carbonate ±gypsum breccias. (A) SEM backscatter image of sample 2230-180.15 showing quartz and carbonate vein centre and the location of fluid inclusion regions of interest 1-4. (B) SEM-CL image of region of interest 1 showing large quartz crystal with prominent zonation. Photomicrographs of analysed fluid inclusions are shown with corresponding microthermometric data. These occur on a single dull quartz growth zone. Scale bars = 500 µm. (C) Photomicrograph of possible boiling trail hosted in an anhydrite breccia to the south of the Braden Breccia pipe (sample 2672-99.95b). Zoomed in photomicrographs of fluid inclusion assemblages are shown below. (D) Primary A_{ID}, A_V and B_{HO} inclusions occurring in the same quartz growth zone in a vein proximal to the North Central Diorite (1754-183.9). (E) Irregularly-shaped A_L inclusions with very low vapour fractions (10%) hosted by gypsum in a reopened type 10 vein proximal to the B-fault (region of Interest 1 - sample 2083-191.7). Scale bars = 100 µm.

Anhydrite crystals are dominated by relatively equal proportions of A_V and A_L inclusions as well as randomly distributed brine assemblages (Figure 5.20A-B). In the type 10 vein samples the A_V inclusions homogenise at similar temperatures (330-410°C) to a number of A_{ID} inclusions present within the anhydrite and surrounding quartz. By contrast, A_V inclusions in the anhydrite breccias typically homogenise between 270 and 360°C and sometimes occur on the same inclusion trails as elevated salinity (17-27 wt.% $NaCl_{eq}$) A_L and A_{LO} and rare B_H inclusions that homogenise at similar temperatures (e.g. Figure 5.21C). Both the anhydrite veins and breccias contain abundant secondary A_L inclusions with a range of salinities that homogenise to the liquid at <290°C. Similar inclusions dominate the gypsum type 10 veins (e.g. Figure 5.21E), where they homogenise to liquid between 140 and 230°C (Figure 5.20A-B). These irregularly-shaped inclusions typically occur along cleavage planes within the gypsum crystals and have relatively uniform salinities of 6-10 wt.% $NaCl_{eq}$. (e.g. Figure 5.21F).

5.3.6 Fluid Inclusion Densities and Minimum Trapping Pressures

Due to the lack of an external fluid inclusion thermometer or barometer, minimum trapping pressures derived for dilute inclusions (Driesner, 2007) could only be calculated for most inclusions. By contrast, absolute trapping conditions could be constrained for boiling assemblages. Trapping conditions of brines that homogenised by halite disappearance were estimated using a recent set of numerical equations (c.f. Lecumberri-Sanchez *et al*., 2012). This technique is interpreted to give accurate trapping pressures for inclusions that show liquid-vapour homogenisation temperatures of 100-600°C and pressures of 10-300 MPa. All halite homogenising inclusions fell within these windows suggesting that the calculated trapping conditions were accurate. All pressure-density data are tabulated in Appendix 4.

Premineralisation Type Veins and Breccias

The abundant primary brine inclusions have relatively uniform densities of 1.1-1.21 g/cm^3 and yield high minimum trapping pressures of >50 MPa. In the biotite breccia sample, several brine inclusions that homogenise by halite dissolution yield a high absolute trapping pressure of ~90 MPa (Figure 5.22). By contrast, lower minimum trapping pressures of 1-32 MPa are recorded for the secondary A_L inclusions and rare A_V inclusions.

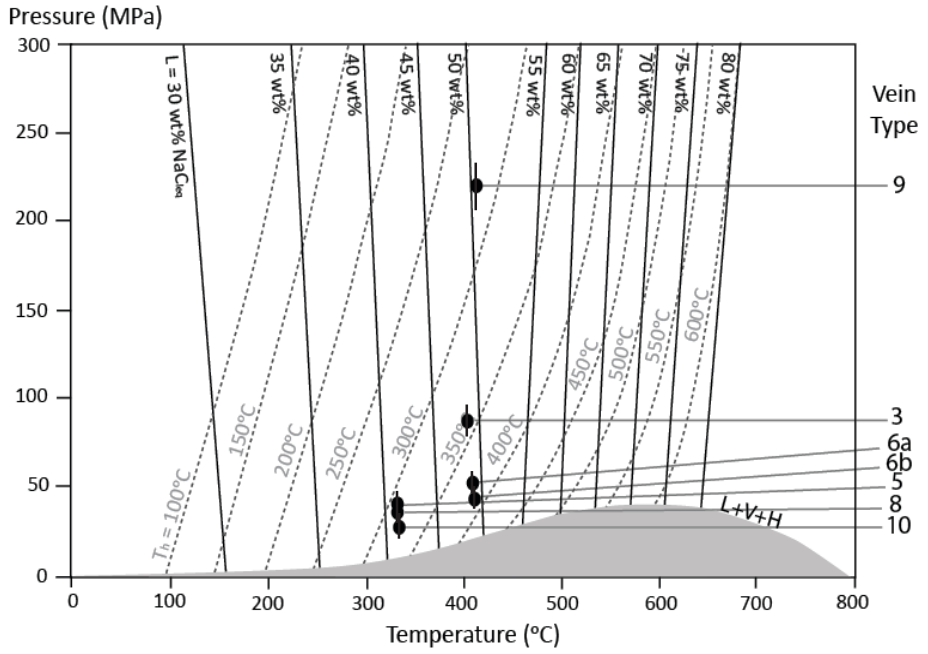


Figure 5.22: Pressure-temperature projection of isochore T_h (L–V) lines calculated for the H_2O-NaCl system using a numerical model (dotted lines: Lecumberri-Sanchez *et al.*, 2012) and previously proposed halite liquidus isopleths (solid lines: Bodnar, 1994). This diagram can be used to estimate the trapping conditions of inclusions that homogenise by halite disappearance. Plot shows the minimum average trapping conditions for selected brine assemblages in each sample type. Pressure error bars = ± 1 standard deviation. Temperature errors are within circular symbols. An average pressure estimate for the type 3 vein – biotite breccia stage was recorded using a brine assemblage in a biotite breccia sample from proximal to the A-Porphyry (FIA 1, Bt Bx 1). An average pressure estimate for the type 10 vein – anhydrite-carbonate ±gypsum breccia stage was recorded using two brine assemblages in an anhydrite-carbonate cemented breccia proximal to the latite dike in the southern part of the mine area (FIA 11 and 12, 2672-99.95A).

*Main Mineral*isa*tion Type Veins and Breccias*

Primary brine inclusions in the type 5 veins and associated anhydrite breccias yield low minimum trapping pressure estimates (10-20 MPa) and high inclusion densities (0.6-1.1 g/cm^3). The brine inclusions that homogenise by halite dissolution yield a high average trapping pressure of ~40 MPa (Figure 5.22). These data are consistent with a sudden drop in pressure related to brecciation and explain the transition to predominantly dilute fluids.

In the deep type 6a veins, the primary A_V and A_{ID} inclusions that homogenise at the highest temperatures yield the lowest densities of 0.3-0.5 g/cm^3 (Figure 5.23A-B) and highest minimum trapping pressures (30-60 MPa). In the shallow 6a veins, similar A_{ID} inclusions display slightly higher densities 0.5 to 0.6 g/cm^3 but yield lower minimum trapping pressures of 20-40 MPa. These inclusions plot along an apparent trend of increasing density with decreasing pressure suggestive of vapour contraction as a function of relatively rapid cooling. Coexisting brine and vapour inclusions are rare in the deep type 6a veins. However, a trapping pressure estimate of 49 MPa was calculated for an inferred primary brine assemblage in an intermediate depth type 6a veins (Figure 5.22). In the transitional 6a-7a veins, A_{ID} and A_L inclusions have higher densities of 0.55-0.7 g/cm^3 suggesting continued fluid contraction (Figure 5.23). These inclusions yield consistently low minimum trapping pressures of 14-22 MPa. No clear primary boiling assemblages could be used to assess absolute trapping pressure. In the chalcopyrite-rich type 6b and type 8 veins boiling assemblages yield relatively consistent and low trapping pressures of 10-23 MPa (Figure 5.23). However, slightly higher trapping pressure of 30-34 MPa were calculated for brine inclusions that homogenise by halite dissolution (Figure 5.22).

Late Mineralisation Type Veins and Breccias

In the type 9 veins all inclusions, including the primary A_V inclusions record low minimum trapping pressures of <35 MPa (Figure 5.24). However, brine assemblages that homogenise by halite dissolution gave a far higher trapping pressure estimate of 220 MPa (Figure 5.22), which greatly exceeds inferred lithostatic load. A cluster of primary A_{ID} inclusions in the type 10 veins record similar densities (0.44-0.64 g/cm^3) and minimum pressures (37-47 MPa) to those measured in the type 6a veins (Figure 5.24). Possible boiling assemblages that are present in the quartz type 10 sample yield an average trapping pressure of 23 MPa. This corresponds well with a minimum trapping pressure of 22 MPa calculated for two brine inclusion assemblages using the method of Lecumberri-Sanchez *et al*. (2012). In the gypsum samples, the abundant secondary A_L inclusions exhibit the highest densities of any salt-undersaturated inclusion type (Figure 5.24). These inclusion yield the lowest minimum trapping temperature estimates (3-12 MPa) of any inclusion type and appear to plot along an apparent trend of fluid contraction or fluid mixing with the primary A_{ID} inclusions.

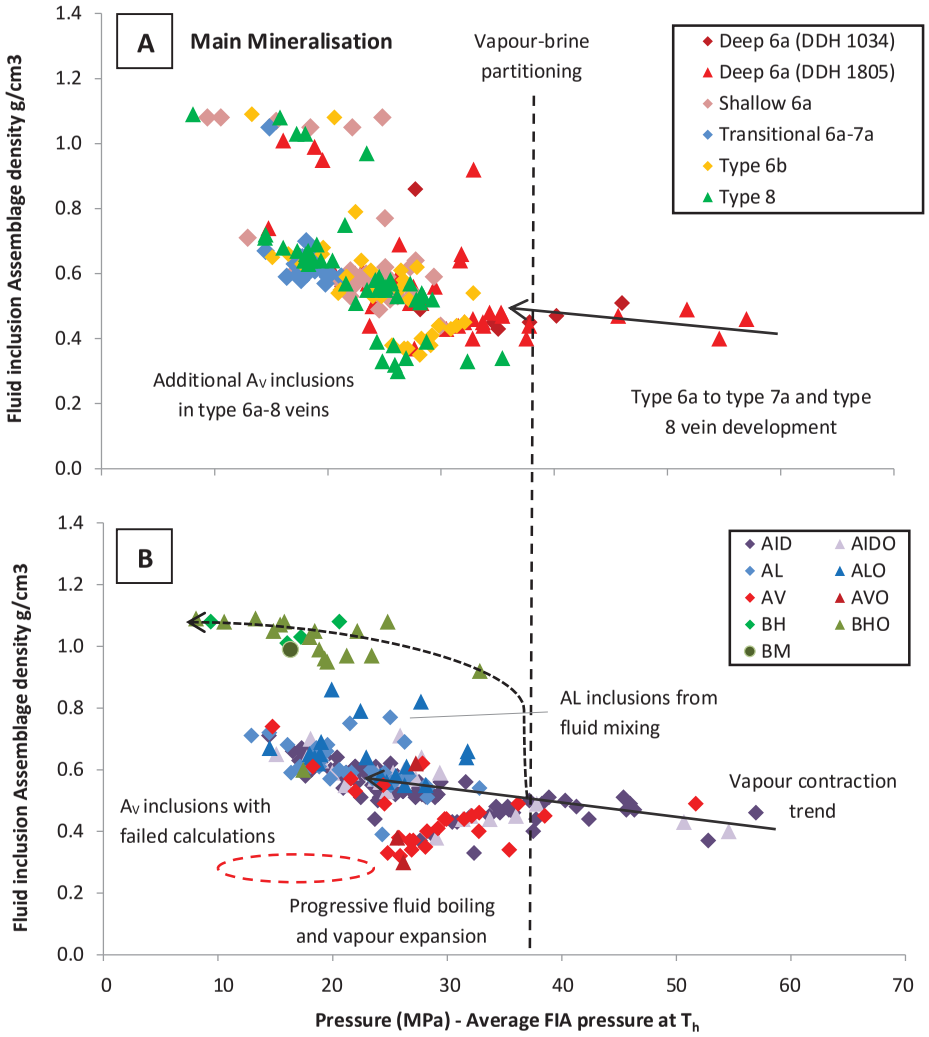


Figure 5.23: Fluid inclusion density versus minimum trapping pressure plots for different main mineralisation vein types (A) and fluid inclusion types (B). Results show an overall trend of decreasing pressure and increasing density between the development of deep type 6a and shallow type 7a and type 8 veins. A_{ID} inclusions plot on an apparent vapour contraction trend and partition as pressure drops below 350 MPa.

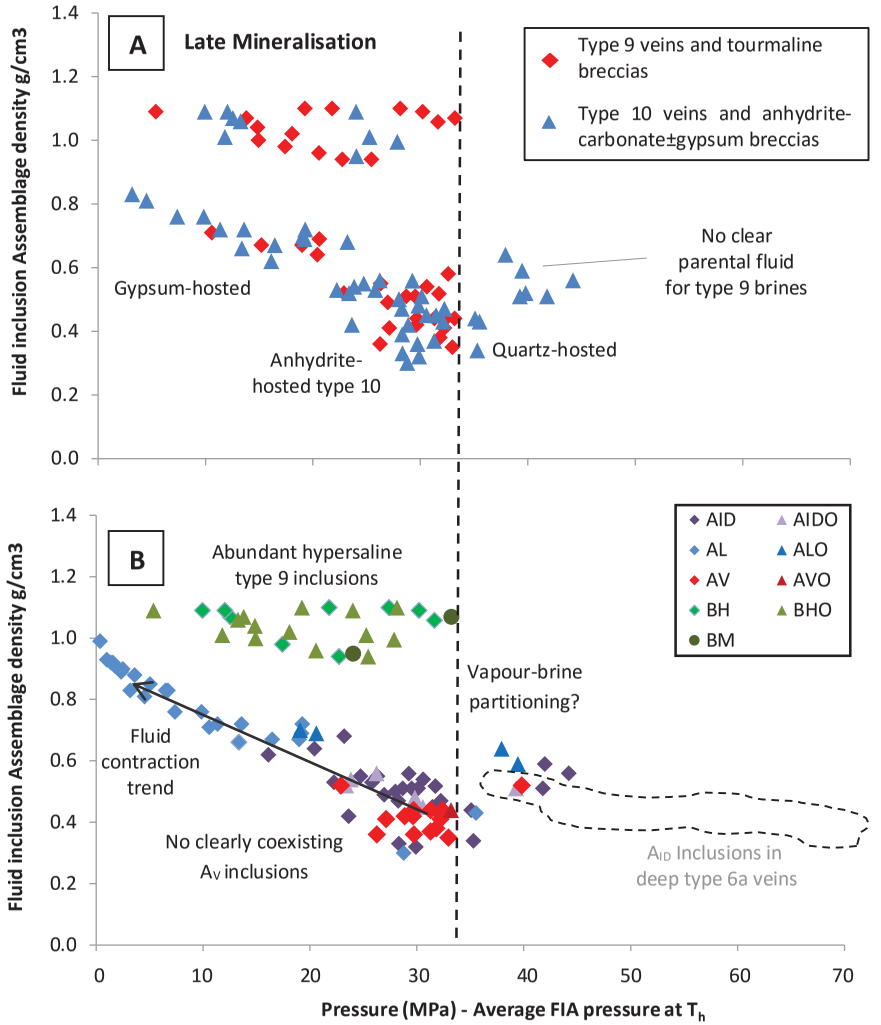


Figure 5.24: Fluid inclusion density versus minimum trapping pressure plots for different late mineralisation vein and breccias types (A) and fluid inclusion types (B). Fluid inclusions in type 9 and 10 veins overlap and show evidence of prolonged entrapment of boiling assemblages at pressures of 4-35 MPa. A clear vapour contraction trend extends from the partitioned A_V inclusions to the shallow A_L inclusions.

5.3.7 Spatial-Temporal Variations in Microthermometric Properties

Primary fluid inclusions in equivalent vein and breccia types from each intrusion overlap in terms of their homogenisation temperatures and salinities (Figure 5.25). With the exception of two brine assemblages, fluid inclusions in the type 5 veins from the A-Porphyry, Northern Diorite and Teniente Dacite Porphyry record low homogenisation temperatures, indicating that they formed under relatively similar conditions in pulses over a ~2 My period. Primary A_{ID} inclusions in shallow type 6a veins from each intrusion record considerable increases in homogenisation temperature relative to those in the anhydrite veins and breccias (Figure 5.25B). In all intrusive centres type 6a-hosted primary A_{ID} inclusions record apparent trends of decreasing salinity with homogenisation temperature. However, this trend is not apparent for the primary A_{ID} and A_L inclusions in the transitional 6a-7a veins, which record lower homogenisation temperatures proximal to the A-Porphyry and Northern Diorite (Figure 5.25C).

Primary fluid Inclusions in the type 6b veins record the largest range of homogenisation temperatures. Similarly to the type 5 and 6a veins, samples from the Northern Diorite record the lowest temperatures. Inclusions from opposing sides of this intrusion record average homogenisation temperatures that differ by ~30°C suggesting that type 6b veins associated with this intrusion formed under changing P-T conditions. Apparent boiling assemblages in the type 6b veins record similar temperatures to those in the shallow type 6a and transitional 6a-7a veins and are typically between 370 and 400°C (Figure 5.25D).

Primary fluid inclusions in type 8 veins from each intrusion also overlap in terms of homogenisation temperature and salinity (Figure 5.25E). However, salt-undersaturated fluid inclusions in a vein containing minor molybdenite from the eastern side of the Northern Diorite usually homogenise at lower temperatures and are similar to those present the transitional 6a-7a veins. The abundant primary brine inclusions in this sample homogenise at higher temperatures than the salt-undersaturated inclusions, possibly indicating boiling in response to a drop in pressure. Similar to the type 6b veins, apparent boiling assemblages typically homogenise at temperatures below 400°C (Figure 5.25E).

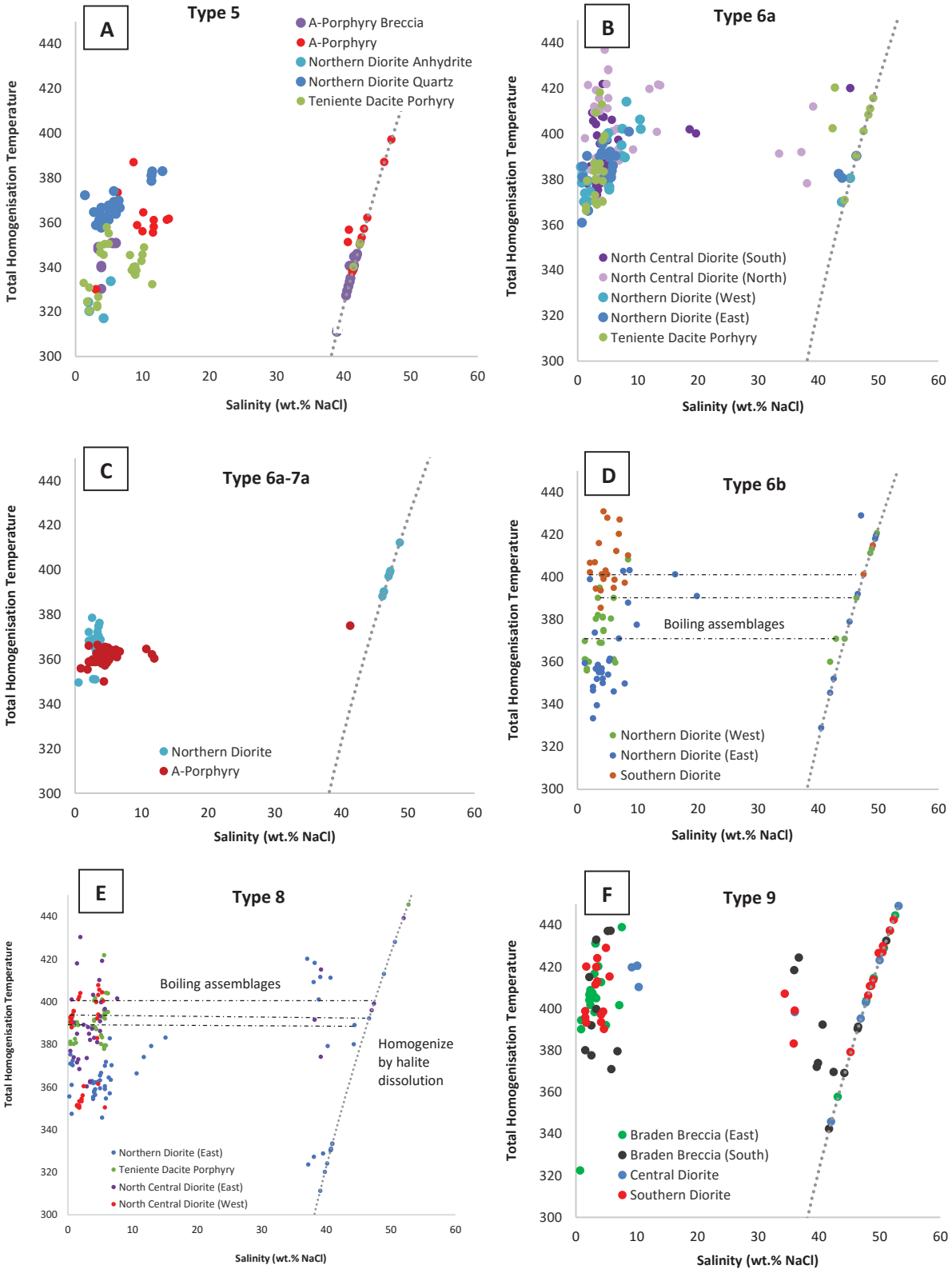


Figure 5.25: Fluid inclusion salinity versus total homogenisation temperature plots for similar main and late mineralisation type veins from different mineralised intrusions. (A) Type 5 veins and anhydrite breccias. (B) Shallow type 6a veins from between 2000 and 2200 m asl. (C) Transitional type 6a-7a veins. (D) Type 6b veins. (E) Type 8 veins containing variable amounts of chalcopyrite, bornite and molybdenite (F) Type 9 veins from opposing sides of the Braden Breccia pipe. Dotted lines = Fluid inclusion boiling assemblages.

Type 9 veins contain fluid inclusions that have overlapping homogenisation temperatures and salinities. Despite this, considerable variations in inclusion characteristics are observed within single samples, suggesting that they were trapped under fluctuating pressure-temperature conditions. Similar variations in fluid inclusion characteristics are recorded for fluid inclusions in the type 10 veins and anhydrite-carbonate ±gypsum breccias as a function of the entrapment of multiple fluid generations in different gangue minerals (e.g. Figure 5.20). This is consistent with petrological and evidence for multiple stages of vein opening associated with many of the type 10 veins.

In a previous study, Vry (2010) suggested that fluid inclusion densities varied significantly between each mineralised intrusion as a function of intrusion emplacement depth. However, this was based on relatively limited data. By combining data from this study with data from the study of Vry (2010), subtle distinctions in average fluid inclusion type densities can be observed between each intrusion (Figure 5.26). Primary A_{ID} inclusions in each mineralised centre exhibit low densities in deep type 6a veins and higher densities in the shallow mineralised veins, providing further evidence for contracting parental fluids prior to metal deposition. There is no clear evidence for decreasing or increasing parental fluid densities with decreasing intrusion age (A-Porphyry → the diorites → Teniente Dacite Porphyry). The average densities of the primary A_{ID} and A_V inclusions appear to decrease between the development of the A-Porphyry to North Central Diorite suggesting shallower intrusion emplacement, but then revert back following the emplacement of the Northern Diorite and Teniente Dacite Porphyry (Figure 5.26). This evolution must be linked to changes in the contraction of fluids in supercritical space during each intrusion-mineralisation cycle.

Primary salt-undersaturated fluid inclusion assemblages associated with the North Central Diorite generally have the highest and lowest densities. The dense A_L inclusions typically have higher salinities (8.4-18.5 wt.% $NaCl_{eq}$) than those associated with the other intrusions and are interpreted to represent intermediate density fluids that partially reequilibrated with early partitioned brines. The overall spectrum of fluid inclusion type densities in each system implies that even though fluid inclusion type development is linked in all the systems, fluid phase separation and the evolution from A_V to A_L inclusions (or vice versa) occurs through different depth intervals in different parts of the deposit.

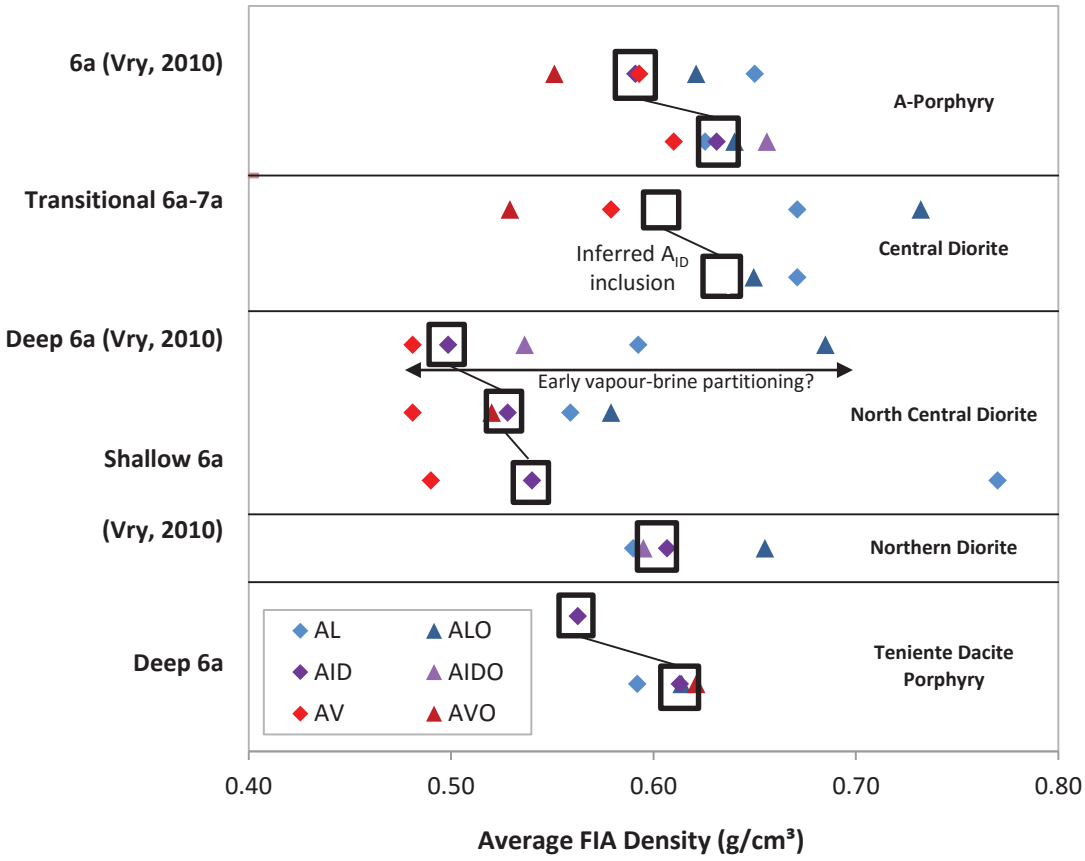


Figure 5.26: Average fluid inclusion type densities in type 6a veins from different intrusions and different mine levels calculated from microthermometric data from this and a previous study (Vry, 2010). Black boxes show the average densities of inferred parental A_{ID} inclusions. These show trends of increasing density with decreasing depth in each mineralised centre. A_V, A_{ID} and A_L inclusions in transitional type 6a-7a veins proximal to the A-Porphyry and Northern Diorite and in shallow type 6a veins proximal to the Teniente Dacite Porphyry (Vry, 2010) have similar densities.

5.3.8 Evolution of Fluids in Each Mineralised Centre

Fluid inclusion microthermometry indicates that each mineralised centre was subject to three fluid regimes (Figure 5.27). Premineralisation and main mineralisation vein types were formed in repeat cycles of fluid release during the emplacement of each felsic-intermediate intrusion (Figure 5.27A-B) whereas the late mineralisation vein types crosscut all intrusions and vein halos, implying a deposit-wide fluid evolution (Figure 5.27C). Similar vein and breccia types in each temporally separate mineralised system contain primary fluid inclusion assemblages that show a consistent fluid entrapment chronology and overlap in terms of their relative abundances and microthermometric properties. This, combined with the consistent vein and breccia chronologies, vein abundances and spatial distributions of vein and alteration types surrounding each intrusion, implies that fluids in each temporally separate system evolved along similar P-T-X pathways. Therefore, the following fluid chemistry sections first address the variations in fluid chemistry associated with each distinct vein type and then assess whether there are any distinct variations in input fluid chemistry or fluid evolution associated with each temporally separate system.

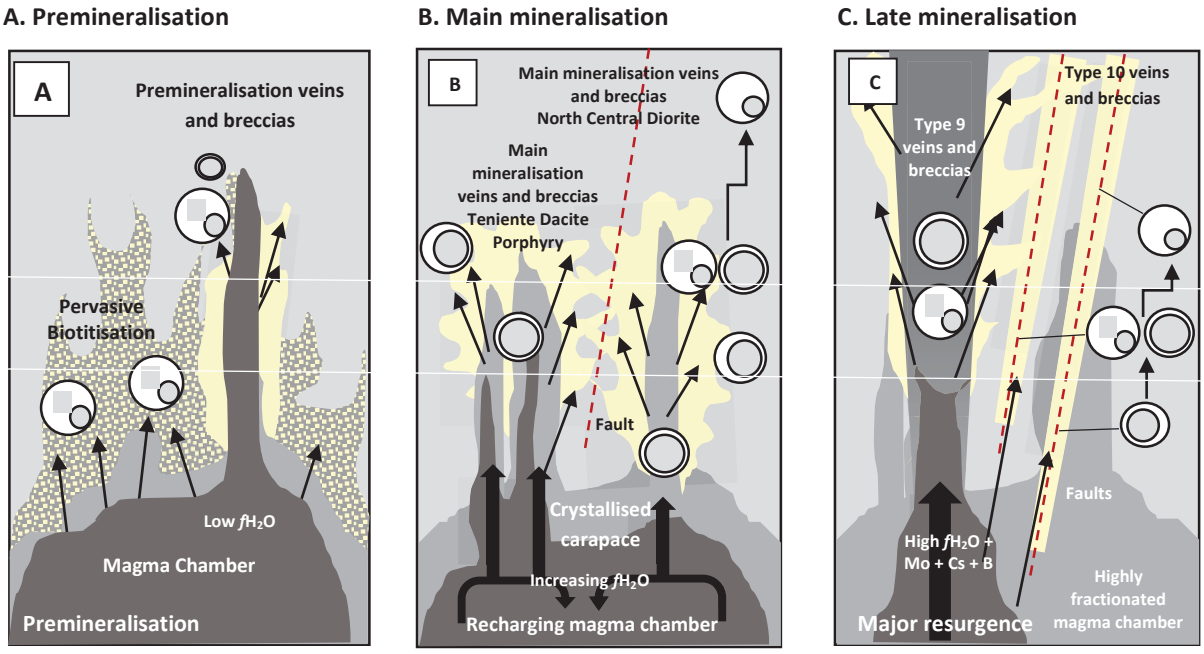


Figure 5.27: Schematic diagram showing the different fluid regimes that operate in each intrusion. (A) Premineralisation fluid regime associated with the exsolution of hypersaline fluids before and during the emplacement of each intrusion. (B) Main mineralisation fluid regime associated with the deep exsolution of multiple pulses of low salinity (~6 wt.% $NaCl_{eq}$), vapour-like fluids (C) Late mineralisation fluid regime associated with the direct exsolution of type 9 brines (that boil off minor vapour) and moderate-low salinity, ID fluids associated with type 10 vein development. White lines = main sampling depths (1800-2200 m asl).

5.4 LA-ICP-MS Fluid Chemistry

5.4.1 Appraisal of LA-ICP-MS Method

The LA-ICP-MS technique adopted usually produced stable ablation into quartz and anhydrite host minerals. In most cases, fluid inclusion fluid release intervals could be selected at a high level of confidence (e.g. Figure 5.2; Appendix 5) and were particularly easy to define for high salinity inclusions. However, consistent with previous studies, it was difficult to accurately select ablation intervals for low density inclusions with diameters <10 µm (Allan *et al*., 2005; Stoffell, 2007; Buckroyd, 2008). Problems also arose when ablating inclusions that were <10 µm from the sample surface. In these cases, inclusion signals sometimes coincided with the ablation of surface contaminates, or were compromised by pulses of elevated signal intensity produced by the initial, uncontrolled sharding of the host mineral (e.g. Figure 5.28). For inclusions within 30 µm of the sample surface, mineral ablation intervals for background subtraction also commonly needed to be selected following the ablation of the inclusion, taking care that the tail of the fluid inclusion signal was not incorporated.

The main problem faced during this study was the selection of stable mineral ablation signals in sulphide-rich veins in which quartz was commonly contaminated with small inclusions of molybdenite, Cu-sulphides and other minerals (e.g. Figure 5.28). In several examples, the synchronous ablation of sulphide and fluid inclusions produced anomalously high fluid inclusion metal concentrations (e.g. Figure 5.28). Steady mineral ablation signals were also difficult to obtain for the anhydrite and gypsum samples due to relatively high and variable concentrations of several elements including Sr and the REEs, possibly as a function of natural zoning. Despite this, most sulphate samples yielded sufficient steady mineral signals to quantify fluid inclusion compositions (e.g. Figure 5.29).

Due to the aforementioned complications, each inclusion analysis was given a confidence rating of 1-5. Inclusions with confidence ratings of 0-1 were not used when calculating average fluid inclusion assemblage data and were not plotted in subsequent LA-ICP-MS plots and inclusions with confidence ratings of 2-3 were reviewed if they proved to be significantly different to other inclusions in the same assemblage or sample. Inclusions with confidence ratings of 4-5 were always plotted and assumed to be accurate results.

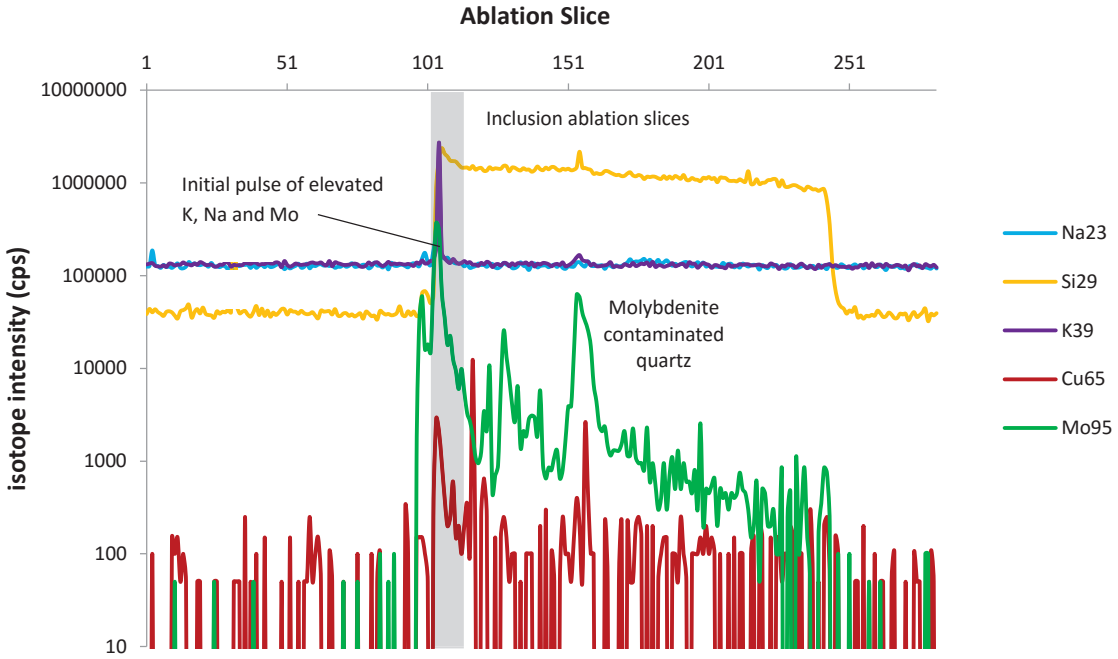


Figure 5.28: Poor ablation of a small (9 µm), shallow (5 µm deep), low salinity (0.5. wt.% $NaCl_{eq}$) A_L inclusion (3a: 2371-79.6a). The quartz in this transitional type 6a-7a sample was contaminated with abundant molybdenite inclusions. One of these was ablated alongside the small inclusion leading to an anomalous apparent molybdenum concentration in the fluid of approximately 10 wt.%. The slices integrated for the fluid inclusion are shown in grey. The ablation was given a confidence rank of 0 and data were deleted.

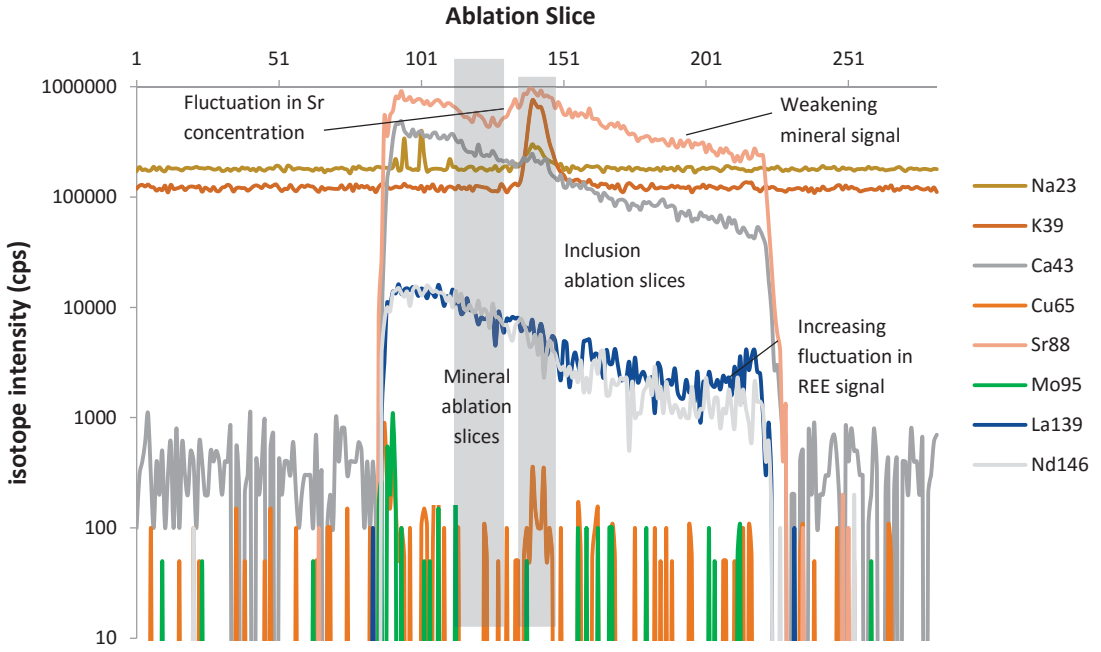
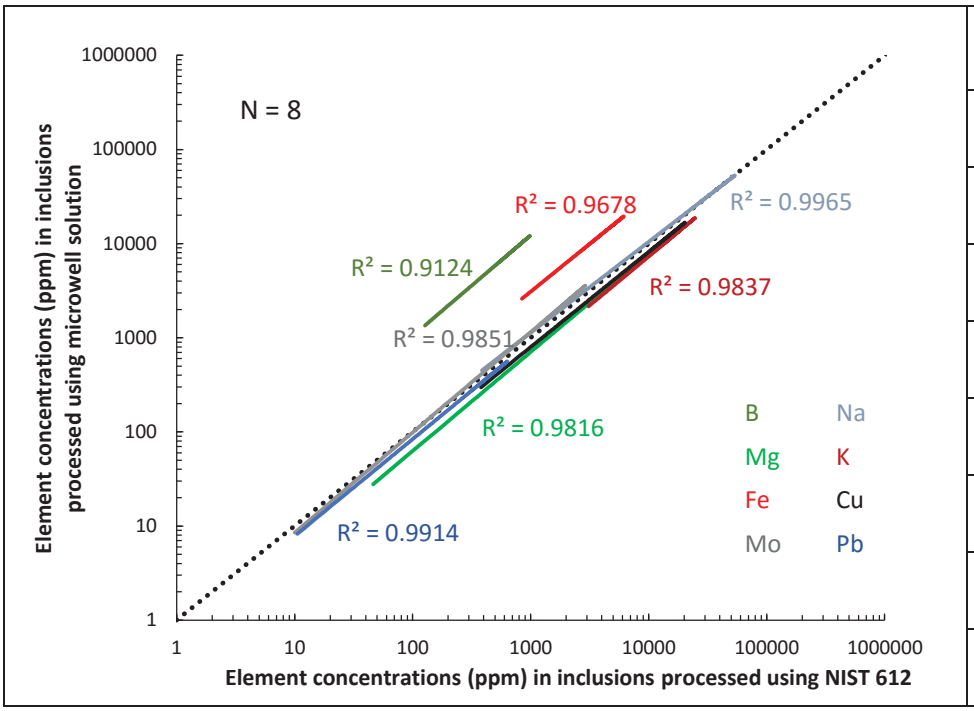


Figure 5.29: Ablation of inclusion 2a (2083-11.3). This was a large (15 µm), deep (35 µm deep), low salinity (1.5 wt.% $NaCl_{eq}$) A_V inclusion hosted in anhydrite. During ablation, the mineral background signal intensity gradually decreased and became slightly variable. The ablation was given a confidence rank of 2.

Fluid inclusion concentrations are relatively uniform for individual inclusions measured in the same assemblage (Appendix 4), with the majority of elements typically producing relative standard deviations of <25%. This is deemed a satisfactory level of precision for the technique (c.f. Heinrich *et al*., 2003; Stoffell, 2007). Despite this, several elements exhibit considerable variability within inclusions of the same assemblage. These include Li, B and Br which commonly vary by an order of magnitude. Of these, Br displays particularly bad fractionation effects characterised by elevated signal intensity when bursting bubbles that form during external standard ablations. Cl concentrations are usually below limits of detection but, where determined, typically yield variable concentrations that do not correspond to Cl concentrations derived from fluid inclusion salinities. This combined with the fact that inclusion Cl has a lower ionisation potential than Na (e.g. Heinrich *et al*., 2003; Stoffell, 2007; Buckroyd, 2008), supports the use of Na as the primary internal standard. Na concentrations were confidently obtained due to the low errors associated with microthermometric measurements (±0.1°C) and salinity calculations used (±0.05 wt.%: Bodnar, 1993). Realistic estimates of internal standard Na concentrations were also endured by applying a $NaCl_{eq}$ correction during processing that took into account the combined contributions of mixed salts (e.g. Na, Ca, K, Mg chlorides) to the freezing point depression determined for the simplified binary NaCl-H_2O system.

Ablation of the microwell-hosted external standard solutions often resulted in the formation of bubbles that burst producing significant fluctuations in element concentrations. In addition, elements including Pb and Mn fluctuated considerably as a result of fractionation during the formation of large vapour bubbles. Despite this, almost all ablations produced sufficient intervals of homogeneous and steady element signals suitable for quantifying fluid inclusion data (e.g. Figure 5.3). To test the bias when processing the samples using the external standard solution in producing accurate and reproducible data, selected samples were reprocessed using NIST-612 glass as the external standard. Most elements yield $NIST/Solution$ ratios between 0.9 and 1.4 (Figure 5.30). Charge balances indicate that the solutions are generally better for use as an external standard than NIST and allow for higher, more realistic B and Fe concentrations to be calculated. Plots of X^{NIST} against $X^{Solution}$ ratios for inclusions in an example type 6a vein yield R^2 values >0.91 (Figure 5.30), indicating that the $NIST/Solution$ ratios are not affected by absolute inclusion element concentrations.



NIST/Solution	
B	0.1
Na	1.0
Mg	1.3
K	1.4
Fe	0.3
Cu	1.2
Mo	1.0
Pb	1.2

Figure 5.30: Selected element concentrations calculated using different internal standards (microwell standard solution and NIST-612 glass) for primary A_{ID} inclusions from a deep level, type 6a quartz vein (1034-830b). A total of 8 individual fluid inclusions are represented. All slopes have constant ratios and high R^2 values. Microwell solutions tend to produce high Fe and B results relative to NIST-612. Similar ratios and R^2 values were produced for all other inclusion types in the other studied samples.

5.4.2 Premineralisation Type Veins and Breccias

In the biotite breccia, all fluid inclusion types are predominantly composed of Na, K, Fe, Ca, and Mn (Figure 5.31) and commonly contain high concentrations of Mg, As, Zn, Rb and Pb (Table 5.3). Concentrations of Au, Be, Bi, Br, Ni and the REEs are usually below limits of detection. In all inclusions, Na is the dominant cation and most inclusion types, whether primary or secondary, exhibit Na:K:Ca ratios in the order 5:2:1 (Figure 5.31A-D).

The primary brine inclusions contain the highest Cu concentrations (Figure 5.31F) with the B_{HO} inclusions recording an average Cu concentration of 1750 ppm (Table 5.3). Despite this, a higher concentration of 7970 ppm was recorded for an inferred secondary, high salinity (21.2 wt.% $NaCl_{eq}$) A_{LO} inclusion. Mo concentrations are comparatively low in all inclusion types but are also generally highest in the B_{HO} inclusions (Table 5), which yield an average Mo concentration of 101 ppm (Figure 5.31G). Plots of Mo versus Cu show that Cu is approximately 30 times more enriched in the early primary brines as well as in secondary A_{LO} and A_{ID} inclusion (Figure 5.31H). Mo shows a slightly stronger affinity for the secondary A_V inclusions, although Mo concentrations are still <130 ppm in these.

Fluid inclusions in the type 3 vein were hosted in anhydrite and therefore concentrations of Ca, Sr, and the REEs could not be accurately quantified. The predominant brine and vapour inclusion populations exhibit similar chemical characteristics to the primary brine inclusions in the biotite breccia (Table 5.3; Figure 5.32A). Unlike in the biotite breccia sample, Cu concentrations are relatively low in all inclusion types and do not show a clear positive relationship with Na concentrations (Figure 5.32E). Mo concentrations are similarly low, although a maximum of 485 ppm was recorded for a single inferred primary A_L inclusion.

Table 5.2: Average LA-ICP-MS element concentrations (ppm) and standard deviations for all fluid inclusion types in the premineralisation and main mineralisation type veins and breccias.

Sample Type	FI Type	Li	SD	N	1B	SD	N	Na	SD	N	Mg	SD	N
Biotite Breccia	ALO			0			0	65690		1	1213		1
	AID	8		1	556		1	12015	584	2	605		1
	AV	4	4	2			0	925	381	2	56	2	2
	BH	19		1	1572	338	2	115209	37017	2	238	215	2
	BHO	174	393	7	850	714	7	141136	11902	7	556	650	7
	BM	29		1	549		1	129656		1	308		1
Type 3	AL	74	15	2			0	14892	4848	3	90		1
	AV			0	141		1	3776	4003	2	2485		1
	BH	227	157	3	8360		1	149884	29654	4	4990	6981	2
	BHO	94		1			0	28875		1	110874		1
Type 5	AL	471	516	3	2237		1	15434	12333	9	2625	2727	10
	ALO	691	1257	4	1421		1	14002	12492	6	7768	11436	4
	AID	511	495	4	1822	814	3	15207	7879	7	1057	1884	4
	AV	493	517	2			0	1497	1820	2	2115	788	3
	BH	299	203	4	1908	630	2	91990	63097	5	1594	2129	5
	BHO	1072	516	2	10783		1	71709	72451	3	5935	6223	3
Deep Type 6a	AL	2781		1	10753		1	53634		1	10032		1
	ALO	27		1	19903	23281	3	29823	19543	4	53	56	2
	AID	277	418	13	2685	1408	8	22414	10849	27	559	1013	15
	AIDO	1315	1012	2			0	35381	27117	4	382	480	3
	AV			0	4815	4796	2	9361	3430	4	1488	1178	2
Int. depth Type 6a	AL	16	22	2			0	7326	7343	2	788	1058	2
	ALO	17	11	3	1515	279	2	41019	821	3	222	209	2
	AID	23	18	11	4817	6566	7	11966	6938	18	449	605	15
	AV	53	64	2			0	8403	7941	5	1288	1580	4
	BH			0			0	109378		1	5939		1
	BHO	29		1	2098		1	109755	5361	4	1182	1959	4
Shallow 6a	AL	169	158	3	3178	2258	2	24026	28135	4	151	126	4
	ALO			0			0	15883		1	1051		1
	AID	58	50	4	1339	1962	5	11427	5786	13	118	78	12
	AIDO	95		1			0	15945	5523	3	244	232	3
	AV	74	44	3	1439		1	6966	4566	10	163	183	10
	AVO			0			0	13563		1	3619		1
	BH			0	1043		1	120583		1	488		1
	BHO	263	377	5	2474	2843	6	127059	20316	9	1440	3004	9
Type 6a-7a	AL	67	108	3	21352	12521	3	15665	4227	10	549	1460	8
	ALO	136	60	2	11667		1	15844	5084	5	271	331	4
	AID	60	63	3			0	9513	4168	7	934	1754	6
	AIDO	86	124	4			0	24902	13726	7	74	118	7
	BH			0			0	72136		1	70669		1
	BHO	554	442	4	4729		1	104482	78324	5	1129	2070	5
Type 6b	AL	123	113	6	13502	18156	3	18181	6868	13	725	1139	9
	ALO	335	391	4	1419		1	39439	22546	5	1588	1674	5
	AID	311	495	5	2208	749	2	15613	11198	15	198	271	10
	AIDO	47	20	3	2691	2292	2	13285	6605	17	184	252	14
	AV	425	519	3	2073		1	6896	6096	14	324	412	12
	AVO			0	897		1	3269	207	3	35	7	2
	BH	82	74	5	7673	11020	6	133601	41128	9	664	845	5
	BHO	320	286	5	11434	15856	4	115622	56689	7	16367	41753	7
	BM	203		1	2039		1	120649	62479	2	3989	2917	2
Type 8	AL	132	35	3	20098		1	21507	13837	6	311	305	4
	ALO	83	55	2	4835	6211	3	25197	14595	4	167	95	4
	AID	503	551	6	7295	12049	12	16943	6769	28	585	880	17
	AIDO			0			0	3212	1731	2	63	84	2
	AV	192	209	3			0	5975	4349	14	750	1569	7
	AVO			0			0	1165		1	47		1
	BH	268	243	3			0	78952	38895	5	2104	2369	5
	BHO	641	894	4	22834	38617	5	96686	53382	11	2503	2847	11

Notes: Averages are reported for each fluid inclusion type with 1 standard deviation (SD). N = number of accurately interpreted concentrations used. Grey cells = Standard deviations that could not be calculated because all analyses were below LOD or the element was only determined in a single inclusion. For concentrations of Be, Co, Ga, Br, In, La, Nd, Dy, Lu, W and Au see Appendix 5.

Table 5.2: (Continued)

Sample Type	FI Type	K	SD	N	Ca	SD	N	Mn	SD	N	Fe	SD	N	Ni	SD	N
Biotite Breccia	ALO	22600		1			0	570		1	17817		1			0
	AID	1949	1246	2	6865	3211	2	50	15	2			0			0
	AV	589		1	8025		1	199		1	2013		1	36		1
	BH	48420	15748	2	17965	3836	2	13693	4810	2	66492	4029	2			0
	BHO	43571	10068	7	11305	3865	7	5210	1292	7	59401	15521	7	205	287	2
	BM	41140		1	12875		1	4774		1	72479		1			0
Type 3	AL	12742	13331	3			0	2149	646	2			0			0
	AV	4074		1			0	73		1	2380		1			0
	BH	52502	58822	4			0	6517	2374	4	26934		1	73	15	2
	BHO	54374		1			0			0	117474		1			0
Type 5	AL	9087	7288	8	35520	43289	2	559	477	7	20785	36782	8	304	383	7
	ALO	7974	5549	6	4446		1	602	504	5	11244	11891	5	163	199	3
	AID	10486	13727	5			0	2843	3210	5	8488	3864	3	583	801	2
	AV	9610	9443	3			0	3267	4521	2	3398		1	299	449	3
	BH	61137	28705	4	43837	52053	4	5192	5288	5	94894	45197	4	51	68	4
	BHO	91535	35076	3			0	13700	7037	3	181989	32241	2	635	425	2
Deep Type 6a	AL	19898		1			0	920		1			0	133		1
	ALO	15882	12230	4			0	3134	3614	4	55635	42275	4	1643		1
	AID	6067	3203	22			0	1028	619	20	10728	12455	14	31		1
	AIDO	19075	14669	4			0	4606	3210	3	3803		1	572	65	2
	AV	3703	698	3			0	1165	703	3	17837	13192	3			0
Int. depth Type 6a	AL	2350		1	11813	8191	2	108	146	2	4205		1	1		1
	ALO	6795	307	3			0	1990	79	3	14727	6671	3			0
	AID	1977	1561	15	17138	16696	6	515	438	11	4445	4381	11	30	22	5
	AV	1940	810	4	20600		1	389	311	4	6582	6811	4	54	57	2
	BH			0			0	619		1	80234		1			0
	BHO	17463	6308	4			0	6179	2636	4	44161	20127	4	38		1
Shallow 6a	AL	6368	5514	4	10264		1	4134	6734	3	15563	18256	2			0
	ALO	10139		1			0			0	5695		1			0
	AID	2790	1466	11	16784	6711	3	453	687	9	2535	2184	8	17	21	3
	AIDO	3024	505	3			0			0	3826	2047	3	80		1
	AV	1849	993	9			0	368	182	4	2888	2913	6	16	9	3
	AVO	38250		1			0			0	6411		1			0
	BH	41938		1	9306		1	16519		1	94087		1			0
	BHO	34431	14143	9	21235	10940	5	14366	12110	9	56529	21210	9	299		1
Type 6a-7a	AL	2359	2948	10			0	26	16	6	413		1			0
	ALO	3163	4453	4			0	28	21	3	1204		1	298		1
	AID	6955	7266	6			0	68	37	3	2754	2939	3			0
	AIDO	2198	2239	7			0	78	49	5	1272	760	2	38	41	2
	BH	67707		1			0	1463		1	66686		1	137		1
	BHO	93513	161328	5	87534		1	337	416	2			0	170	230	2
Type 6b	AL	6998	3812	11	3801	923	2	599	420	10	5059	3399	4			0
	ALO	18256	11779	5	7978		1	1846	1700	5	15103	5933	3	33	33	2
	AID	5666	4524	14			0	514	515	8	9893	9071	7	694	916	2
	AIDO	4850	2777	14	8496		1	293	242	12	7359	6386	10	432		1
	AV	5190	4159	11			0	564	728	7	6048	6393	5	18	16	2
	AVO	1071	677	3			0	72	34	2	1321		1			0
	BH	54476	29155	9	13465	10625	5	7874	10517	7	50041	41637	7	104	129	2
	BHO	51558	31298	7	15716		1	11233	12733	7	80518	83945	6			0
	BM	58335	26711	2	16681		1	10020	11987	2	74042	62769	2			0
Type 8	AL	7657	8450	5	19678	23469	2	539	941	4	3165	1278	2	2562		1
	ALO	11298	6768	4			0	807	673	4	12266		1			0
	AID	8306	7720	24			0	320	312	18	2826	2640	12			0
	AIDO	1733	2106	2			0			0	945		1	17		1
	AV	8060	16973	11			0	99	110	4	7096	8923	2	26	18	2
	AVO	509		1			0			0			0			0
	BH	62001	31725	5	37132	35641	2	6129	6290	5	103002	65613	4	77		1
	BHO	80378	57520	11	11167	6431	4	9750	8512	9	88570	65866	9	20		1

Table 5.2: (Continued)

Sample Type	FI Type	Cu	SD	N	Zn	SD	N	As	SD	N	Rb	SD	N	Sr	SD	N
Biotite Breccia	ALO	7972		1			0			0	84		1	5		1
	AID	55	67	2	14	10	2	55	36	2	18	9	2	10	5	2
	AV	27	36	2	45		1	30		1	9		1	3		1
	BH	148	131	2	2738	1079	2	461	282	2	488	125	2	483	90	2
	BHO	1731	724	7	1193	405	7	162	46	7	468	158	7	201	56	7
	BM	189		1	908		1	158		1	438		1	226		1
Type 3	AL	68		1	509	75	3	316	141	3	212	155	3			0
	AV	98	134	2	91		1	104	126	2	26	6	2	2171	2250	2
	BH	1482	1701	2	1566	584	4	2645	1319	3	436	240	4	5467	404	2
	BHO	950		1	1249		1	587		1	586		1			0
Type 5	AL	2499	2740	8	718	899	8	1371	2104	5	43	34	8	8933	23460	7
	ALO	2898	5081	6	360	267	5	309	233	3	40	44	5	67	89	6
	AID	2324	2120	6	2315	3639	4	697	980	4	94	147	5	8941	14871	6
	AV	2775	4458	3	225		1	5523		1	57	51	2	0.5		1
	BH	12380	23301	4	1704	1195	4	2783	4558	4	476	412	5	432	116	4
	BHO	14286	14984	3	6533	707	3	8519	9481	3	1064	511	3	1250	546	2
Deep Type 6a	AL	7934		1	780		1	987		1	80		1	64		1
	ALO	4729	6582	3	941	818	4	600	594	4	258	218	4	65	70	4
	AID	4409	4772	24	307	181	19	668	1074	12	58	72	23	22	27	25
	AIDO	3358	3419	4	1269	884	3			0	74	69	2	226	251	2
	AV	857	678	4	255	183	3	764		1	93	77	3	21	25	4
Int. depth Type 6a	AL	4617	6498	2	1518	2140	2	57		1	29	33	2	14	17	2
	ALO	3139	2751	3	216	23	3	97	70	3	81	27	3	5	4	3
	AID	792	1010	17	176	238	12	159	259	7	31	28	16	15	22	13
	AV	775	1042	5	433	595	3	286	294	3	84	85	5	12	11	4
	BH	182		1			0			0	160		1			0
	BHO	7823	13093	4	611	281	4	445	306	3	244	46	4	28	16	4
Shallow 6a	AL	1495	2124	3	993	1325	2	276	164	2	36	39	4	1915	2395	4
	ALO			0			0			0	64		1			0
	AID	2388	3127	13	153	101	8	82	73	7	12	9	10	352	962	10
	AIDO	2324	3161	3	76	30	3	302	202	2	37	41	2	14	10	3
	AV	4495	3090	10	78	49	5	28	22	2	15	15	6	14	16	6
	AVO	3762		1			0			0	116		1	53		1
	BH	3572		1	2512		1	318		1	214		1	243		1
	BHO	1083	978	6	2744	2114	9	540	343	9	220	84	9	448	398	8
Type 6a-7a	AL	92	127	10	86	142	7	31	20	4	23	30	7	1	0	5
	ALO	2035	3630	5	166	142	3	536	696	2	15	7	4	0	0	2
	AID	970	1985	6	30	51	4	29	20	2	18	15	6	19	28	7
	AIDO	183	98	7	18	14	3	79	49	6	21	12	5	9	13	5
	BH	9968		1	173		1			0	392		1			0
	BHO	6208	10593	3	4071	5853	3	5895	10763	4	122	84	4	208	404	4
Type 6b	AL	1334	1906	10	252	240	11	526	581	11	49	39	10	34	45	11
	ALO	12709	10838	4	1067	750	4	1043	993	5	112	42	5	82	79	5
	AID	4705	4205	10	282	490	10	606	777	10	42	49	11	28	40	14
	AIDO	6305	2981	11	131	77	8	291	227	6	35	28	14	15	18	13
	AV	2358	2101	11	267	375	9	258	229	5	42	35	9	16	19	12
	AVO	2688	3724	3	42	12	2	98		1	5	5	3	9	9	2
	BH	1313	3220	7	2152	2748	7	641	384	9	551	441	9	477	460	9
	BHO	1309	1698	6	1798	1096	7	2076	1830	7	432	431	7	722	866	7
	BM	1847	1316	2	2083	1643	2	1569	1422	2	546	427	2	356	126	2
Type 8	AL	1574	2665	5	284	382	5	172	143	4	42	32	4	25	37	6
	ALO	1136	1796	3	203	142	4	311		1	66	41	4	35	29	4
	AID	1332	1285	27	402	1071	15	288	259	12	46	39	22	78	283	19
	AIDO	507	408	2	13	13	1	62	49	2	6		1	4	5	2
	AV	941	1527	14	62	33	5	84		1	16	15	5	58	146	8
	AVO	36		1			0	41		1			0	1		1
	BH	1432	1940	4	2204	1799	4	749	790	4	795	702	4	316	271	5
	BHO	1927	2466	8	3241	2353	9	1465	1683	10	563	337	10	311	279	11

Table 5.2: (Continued)

Sample Type	Fl Type	Mo	SD	N	Sn	SD	N	Sb	SD	N	Cs	SD	N	Pb	SD	N
Biotite Breccia	ALO	235		1			0	98		1			0			0
	AID	9	9	2	101		1	2	1	2	14	6	2	51	12	2
	AV	99	43	2	13	12	2	2		1	5		1	156		1
	BH	4		1			0	62	5	2	582	73	2	**1466**	**458**	2
	BHO	101	66	7	51	52	5	14	7	7	208	87	7	**2521**	**1068**	7
	BM	1		1	43		1	20		1	224		1	**1858**		1
Type 3	AL	**485**		1			0			0	172	97	3	**608**	**560**	3
	AV	3		1			0			0	15	19	2	**406**	**533**	2
	BH			0			0	52	49	2	289	223	4	**5777**	**4259**	3
	BHO			0			0			0	99		1	**1083**		1
Type 5	AL	**168**	**303**	6	110		1	153	201	6	23	34	8	170	101	9
	ALO	104	114	2	6597		1			0	15	12	5	149	112	5
	AID	**363**	154	3			0	17		1	54	55	5	**346**	**513**	4
	AV			0	1210		1	538	608	2	1		1	**534**		1
	BH	**995**	**111**	3			0	172	275	4	343	243	5	**720**	**308**	5
	BHO			0	6595		1	703	648	3	947	292	3	**1847**	249	3
Deep Type 6a	AL			0			0	645		1	84		1	**594**		1
	ALO	62	70	3			0	37	43	2	1812	2717	4	**1037**	**802**	4
	AID	101	111	14			0	86	118	9	199	471	25	**369**	**549**	20
	AIDO	**314**	264	2			0			0	1636	2237	3	**1543**	**1594**	4
	AV	**36**		1			0	52	25	2	261	386	4	**346**	**343**	3
Int. depth Type 6a	AL	252	**323**	2	3		1	10	10	2	26	32	2	**1515**	**2133**	2
	ALO	4		1			0	3		1	42	10	3	**388**	112	3
	AID	43	50	11			0	10	10	7	43	84	15	158	176	14
	AV	**384**	**422**	2	160		1	11	7	3	57	85	5	193	192	5
	BH	70		1			0	71		1	220		1			0
	BHO	22	15	4			0	31	21	2	100	44	4	**1332**	**827**	4
Shallow 6a	AL	15		1			0			0	47	46	3	199	267	2
	ALO			0			0			0			0			0
	AID	137	162	3			0	3		1	7	8	6	31	29	9
	AIDO	**514**	**344**	2	459		1	76		1	12	5	2	12	1	3
	AV	140	99	5			0	3	3	2	9	5	3	30	23	5
	AVO			0			0			0	34		1			0
	BH	188		1			0	30		1	228		1	**1119**		1
	BHO	**469**	**975**	5			0	34	25	3	209	175	9	**651**	**358**	9
Type 6a-7a	AL	**285**	**431**	3	535		1	45	104	7	5	3	9	17	6	7
	ALO			0	3016		1	10	13	2	8	6	4	32	26	3
	AID	**576**	**735**	6	86		1	30	43	3	8	9	4	41	34	6
	AIDO	**3**	**2**	4			0	16	13	5	9	4	6	56	32	7
	BH			0			0			0	47		1	**495**		1
	BHO			0			0	2		1	91	103	4	**567**	**752**	4
Type 6b	AL	**187**	**268**	5	706	965	2	25	28	2	44	49	10	127	229	8
	ALO	**476**	**692**	3	149		1	34	38	3	107	51	5	**632**	**685**	5
	AID	**196**		1			0	13	13	3	37	54	11	75	56	9
	AIDO	105	119	6			0	21	15	3	14	14	12	61	42	10
	AV	**85**	**72**	7	797	1035	2	18	20	5	21	30	11	73	67	7
	AVO	**35**		1	186		1			0	5	4	3	18	16	2
	BH	**426**	233	2	18		1	48	33	7	653	749	9	**850**	**743**	7
	BHO	**124**		1			0	81	47	5	528	618	7	**1229**	**644**	7
	BM			0			0	136	137	2	629	673	2	**1666**	**320**	2
Type 8	AL	152	205	3			0	16	7	2	72	90	4	**5382**	**5809**	3
	ALO			0			0	132		1	29	16	4	57	16	3
	AID	72	**126**	4	17		1	16	20	9	25	16	18	**1618**	**3853**	14
	AIDO	170		1			0	13	8	2	2		1	149		1
	AV	**199**	**356**	5			0	19	13	2	9	5	7	**8448**	**9546**	6
	AVO	51		1			0	15		1			0	21		1
	BH			0	1750	69	2	182	155	3	503	665	5	**7320**	**7922**	4
	BHO			0			0	179	236	6	360	334	10	**5104**	**6870**	10

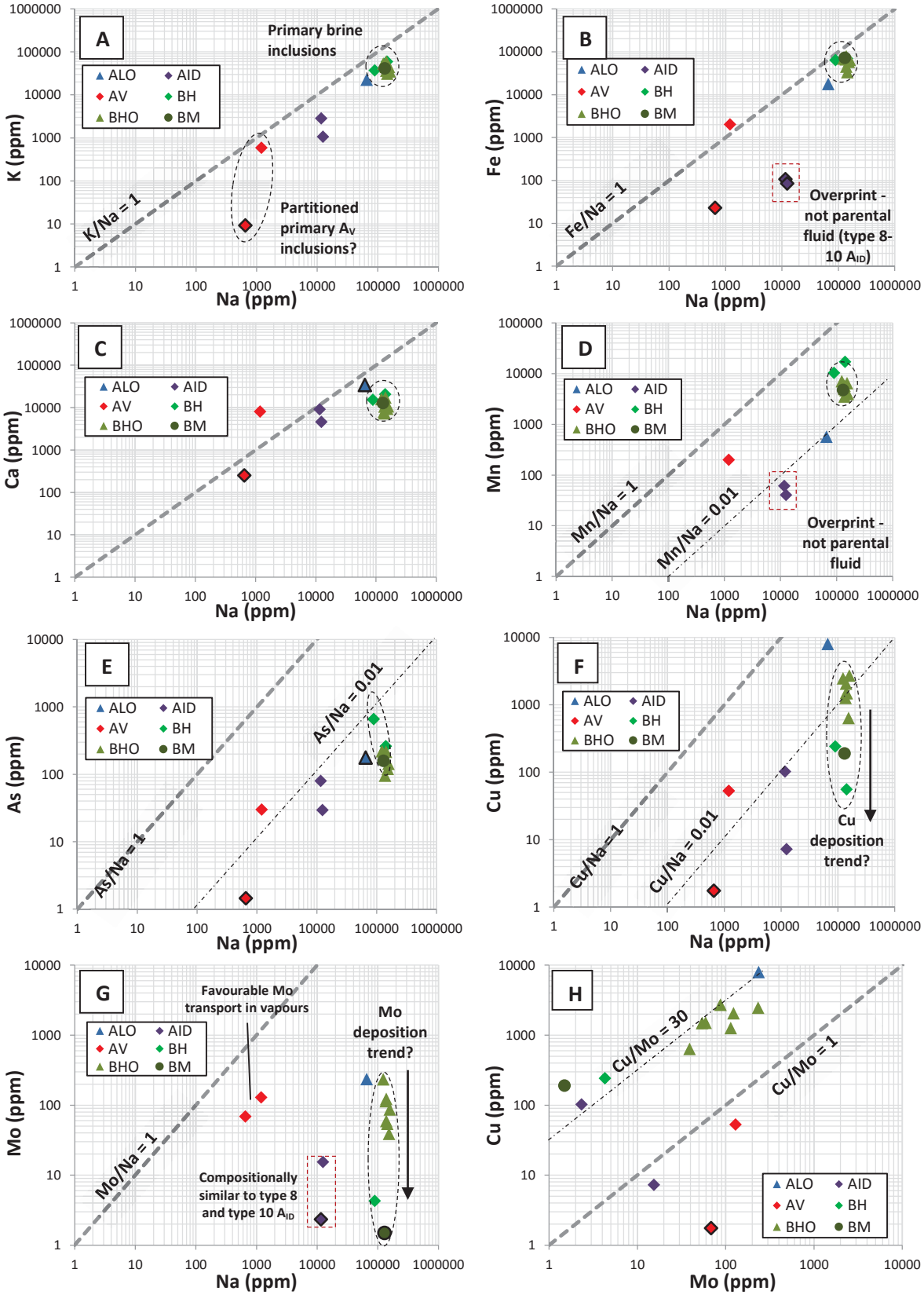


Figure 5.31: LA-ICP-MS major element geochemistry for individual fluid inclusions in a biotite breccia proximal to the A-Porphyry (sample Bt Bx. 1). Results are given for individual fluid inclusions. (A-G) Plots of K, Fe, Ca, Mn, As, Cu and Mo versus Na. (H) Cu versus Mo plot showing an average 30:1 Cu:Mo ratio in saline aqueous fluid and brine inclusions. Data with black borders = 0.5*LOD values.

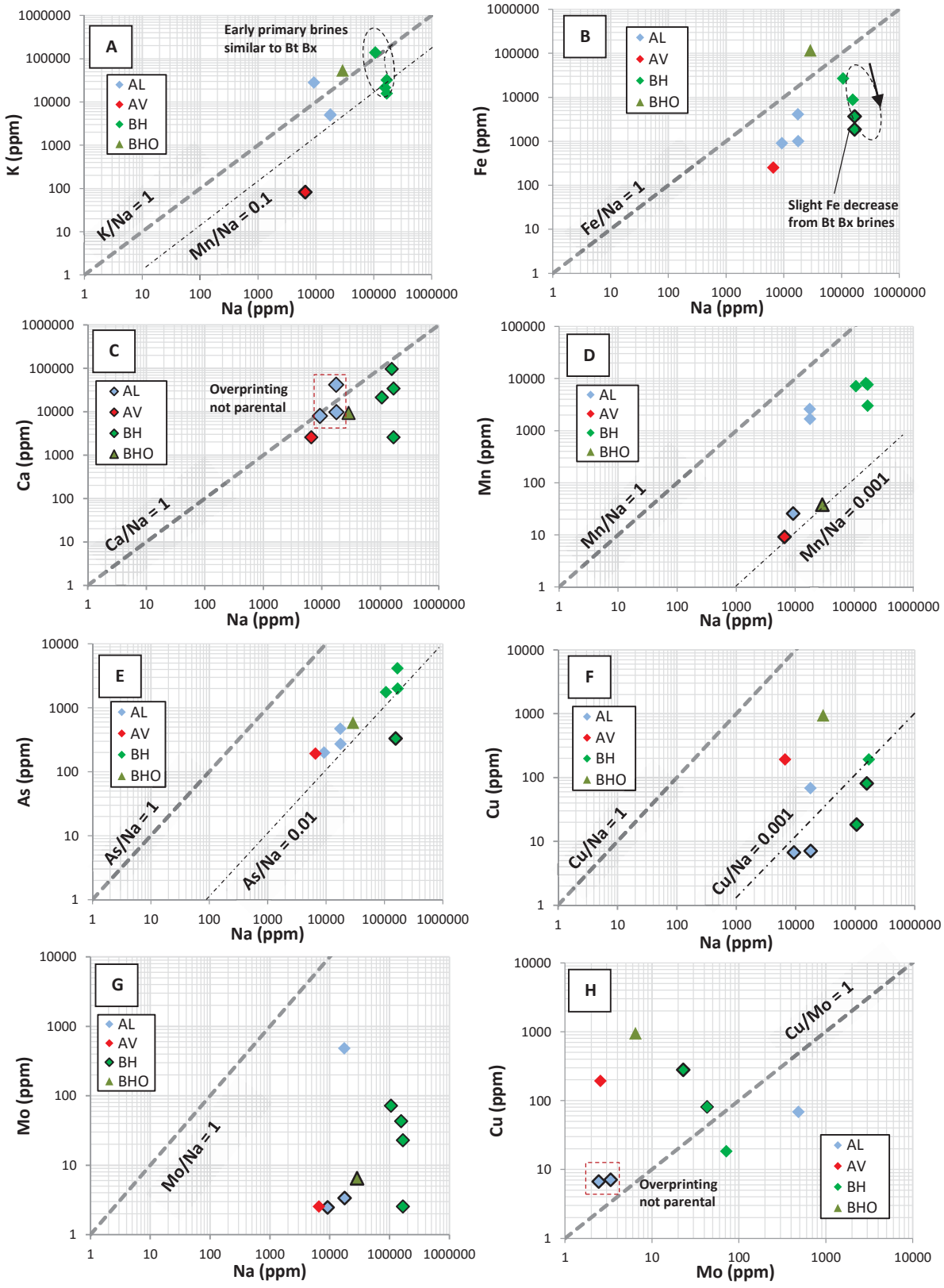


Figure 5.32: LA-ICP-MS major element geochemistry for individual fluid inclusions in a type 3 vein proximal to the Southern Diorite (2083-11.3). (A-G) Plots of K, Fe, Ca, Mn, As, Cu and Mo versus Na. (H) Cu versus Mo plot. Ca concentrations could not be quantified in these anhydrite-hosted inclusions. Due to the extremely low Mo concentrations, Mo was not plotted against Na. Data with black borders = 0.5*LOD values.

5.4.3 *Main Mineralisation Type Veins and Breccias*

Similarly to the premineralisation type samples, all inclusion types are dominated by Na, K, Fe, Ca and Mn and contain high yet variable concentrations of Mg, Ni, As, Pb (Table 5.2). Concentrations of Li, B, Be, Au and the REEs are typically below limits of detection

Type 5 Veins

Primary brine and A_L inclusions hosted by type 5 veins from the margins of the A-Porphyry (crosses) and North Central Diorite (diamonds) yield similar major element ratios (Figure 5.33A-D), even though they are hosted by different minerals. These inclusions contain higher relative proportions of Fe, Ni, As, Sn and Sb than the primary brine inclusions in the premineralisation samples (Table 5.2). The brine inclusions also contain Ca concentrations that are typically an order of magnitude greater, whereas Na displays a slightly lower relative abundance than in the premineralisation samples (Figure 5.33A-C).

Consistent with Vry (2010) the type 5 veins record a switch in fluid inclusion type from primary brines to predominant salt-undersaturated $A_L \pm A_{ID}$ inclusions. These commonly contain higher relative proportions of B, Li, Mg, Ni, Cu and Sr and are characterised by low Mn/Na ratios (Figure 5.33A-D). These inclusions record high Cu concentrations of 300 ppm to 1.2 wt.% (Figure 5.33E). The quartz-hosted fluid inclusions exhibit a weak trend of increasing Cu with increasing Na, but this is not apparent for the anhydrite-hosted inclusions (Figure 5.33E). Mo concentrations are up to two orders of magnitude greater than in the premineralisation samples although the vast majority still contain <100 ppm Mo (Figure 5.33F). Similar to Cu, Mo displays a weak positive correlation with Na and is commonly enriched in moderate salinity A_{ID} and A_L inclusions and high salinity brines. High Cu/Mo ratios of around 100 are recorded for both the brine inclusions and the A_{LO} inclusions.

Only three inferred secondary A_V inclusions were measured. These have high K/Na, Fe/Na and Ca/Na ratios >1 suggesting that, unlike the brines, they were not involved in potassic/magnetite alteration (Figure 5.33A-D). Similarly to the secondary A_V inclusions in the premineralisation samples, these low salinity (1.7 wt.% $NaCl_{eq}$) vapours contain low concentrations of both Mo and Cu (Figure 5.33F).

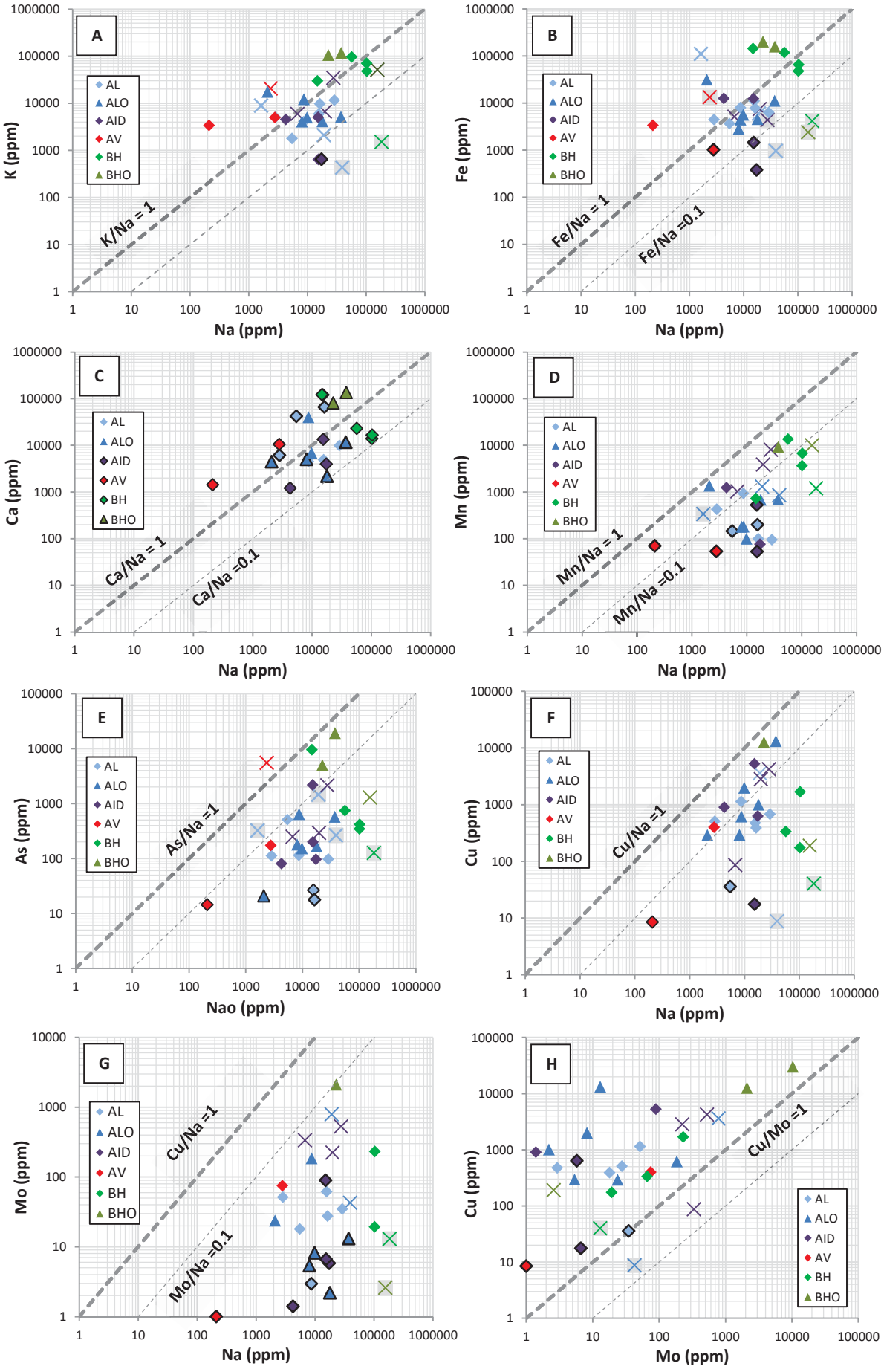

A
K (ppm)
Na (ppm)
K/Na = 1
B
Fe (ppm)
Na (ppm)
Fe/Na = 1
Fe/Na =0.1
C
Ca (ppm)
Na (ppm)
Ca/Na = 1
Ca/Na =0.1
D
Mn (ppm)
Na (ppm)
Mn/Na = 1
Mn/Na =0.1
E
As (ppm)
Nao (ppm)
As/Na =1
F
Cu (ppm)
Na (ppm)
Cu/Na =1
G
Mo (ppm)
Na (ppm)
Cu/Na =1
Mo/Na =0.1
H
Cu (ppm)
Mo (ppm)
Cu/Mo =1
AL
ALO
AID
AV
BH
BHO

Figure 5.33: Major element geochemistry for individual fluid inclusions in type 5 veins from the margins of the A-Porphyry and North Central Diorite. Crosses = anhydrite-hosted fluid inclusions. All other fluid inclusions are hosted in quartz. Data from both intrusions plot in the same area suggesting that type 5 veins were produced by similar hydrothermal fluids during the asynchronous development of the anhydrite veins and breccias surrounding these intrusions. Data with black outlines or grey backgrounds = 0.5*LOD.

Type 6a to Type 8 Veins

Deep and intermediate depth type 6a veins are dominated by primary A_{ID} inclusions that contain relatively uniform concentrations of K and Na (Figure 5.34A-B). These inclusions also contain high but variable concentrations of Fe, Mn, As and Zn (Figures 5.34-5.35). In general the primary A_{ID} inclusions in the intermediate depth samples record lower concentrations of K, Mn and As than the deeper type 6a veins. The rare partitioned brine in the intermediate depth samples contain elevated concentrations of Mn, and Fe relative to Na than the parental fluids. These inclusions also commonly contain highly elevated Cs concentrations relative to the other inclusion types (Table 5.2). The rare A_V inclusions are compositionally similar to the A_{ID} inclusions suggesting that they represent the same fluids trapped with a slightly lower density and not partitioned vapours (Figure 5.34, Table 5.2).

In the shallow type 6a and transitional 6a-7a veins the abundant primary A_{ID} and inferred contracted A_L inclusions yield similar major element ratios to the A_{ID} inclusions hosted in the deeper 6a veins (Figure 5.34). However, a number of these inclusions in the Mo-rich type 6a-7a veins contain far lower concentrations of K, Fe, Mn, Mg and Zn relative to Na (Figures 5.34-5.35). Several partitioned brine inclusions also contain low concentrations of K, Mn, Fe and Mg suggesting their involvement in the formation of ferromagnesian silicates. The brines yield far higher Mn+Fe/Na and lower As/Na ratios than their parental A_{ID} fluids.

In the type 6b and type 8 veins the abundant primary, salt-undersaturated Inclusions that have not yet undergone phase separation contain similar major and trace element ratios to the parental A_{ID} inclusions in the shallow type 6a veins (e.g. Figures 5.34-5.35). Unlike in the type 6a veins, the abundant A_V inclusions are clearly distinguishable from the A_{ID} inclusions in terms of their chemistry. All A_V inclusions contain higher relative proportions of As and lower abundances of Mn and Fe when compared to the primary A_{ID} inclusions (Figure 5.34). By contrast, the partitioned brine inclusions record the lowest As/Mn ratios and highest K concentrations (20000 to 120000 ppm) of any main mineralisation inclusion type.

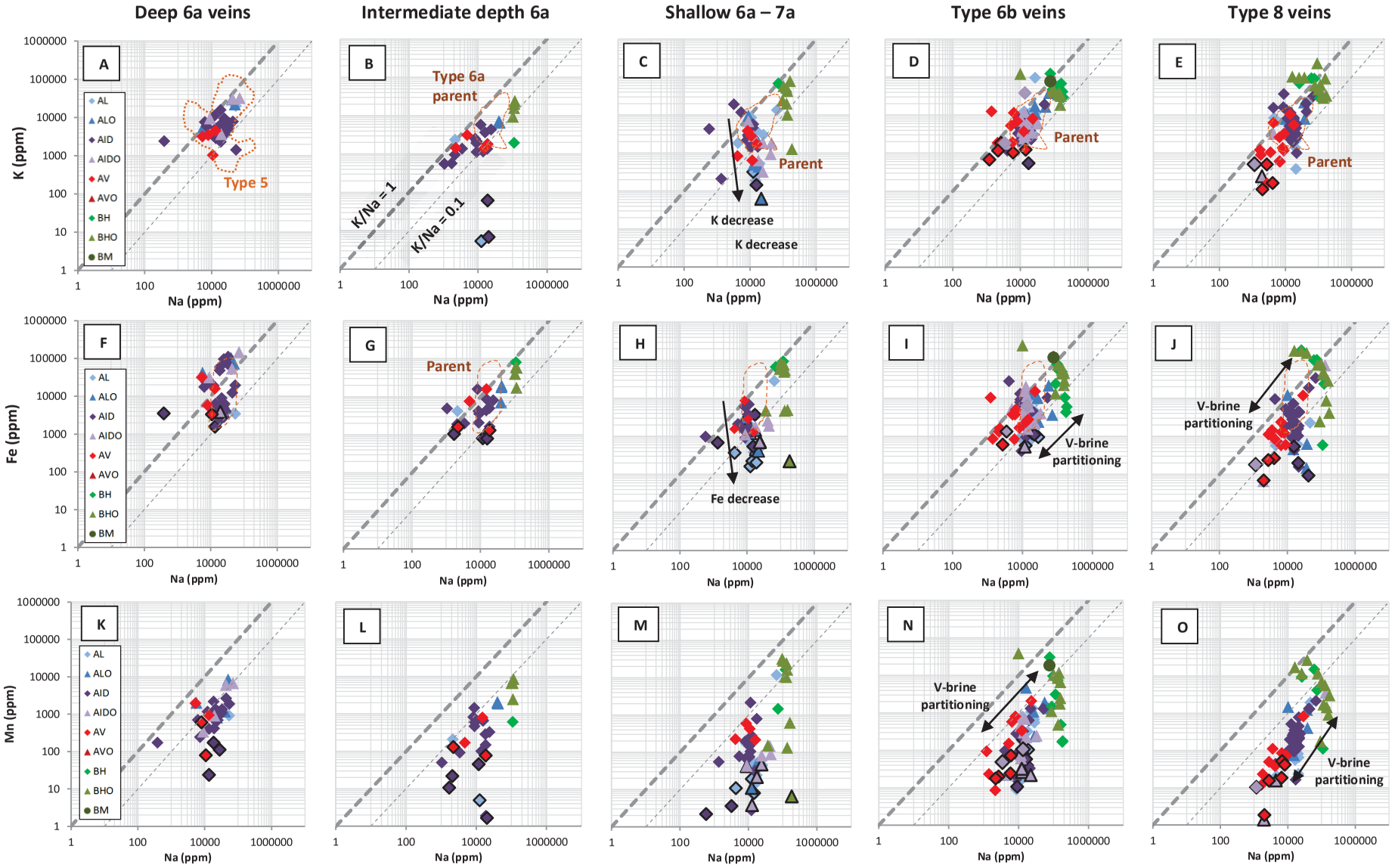


Figure 5.34: Major element ratios for individual fluid inclusions of each type in type 6a veins from variable depths, type 6b veins and type 8 veins. Figure shows fluid inclusion data from multiple intrusive centres. Data with black borders = 0.5*LOD values.

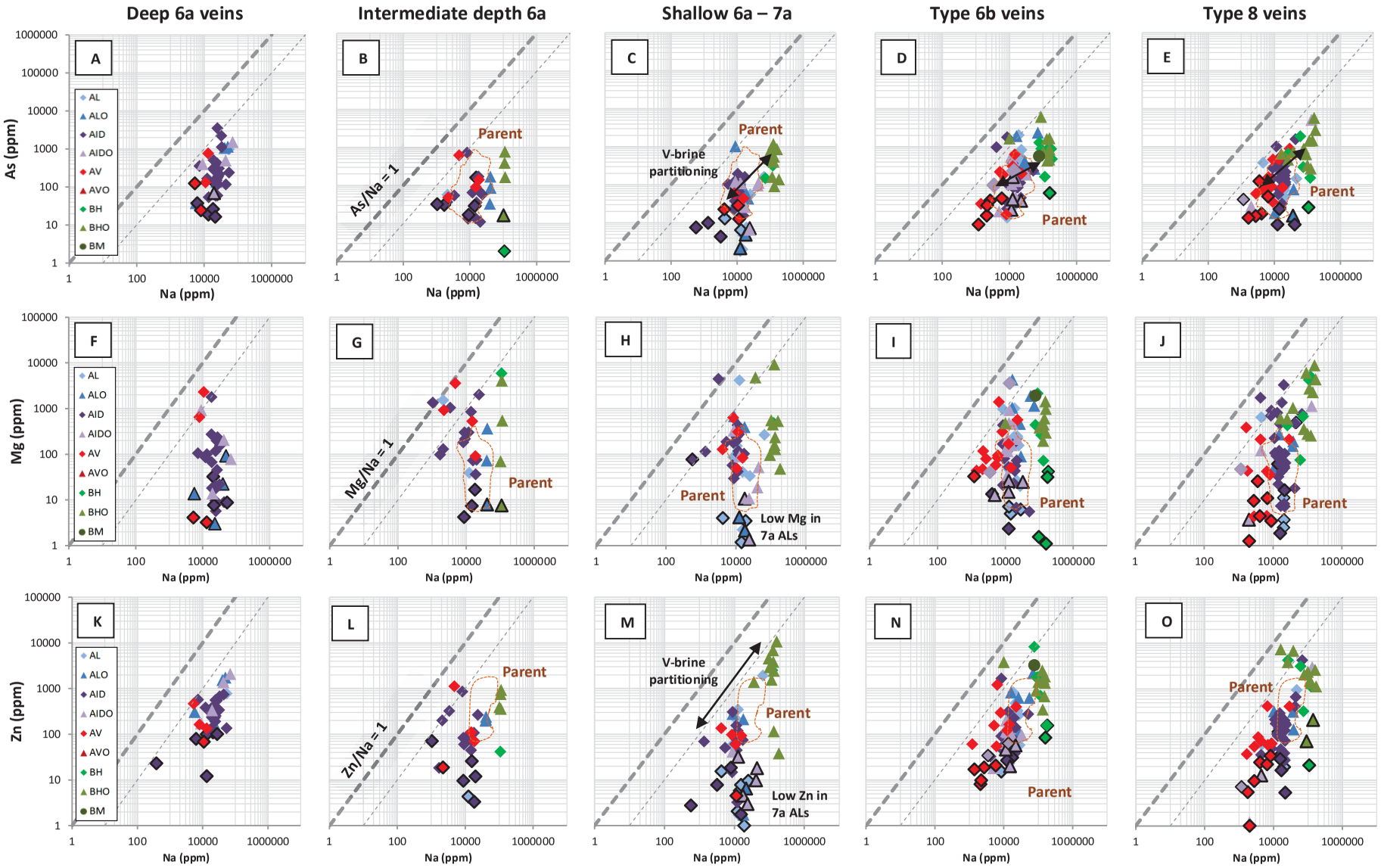
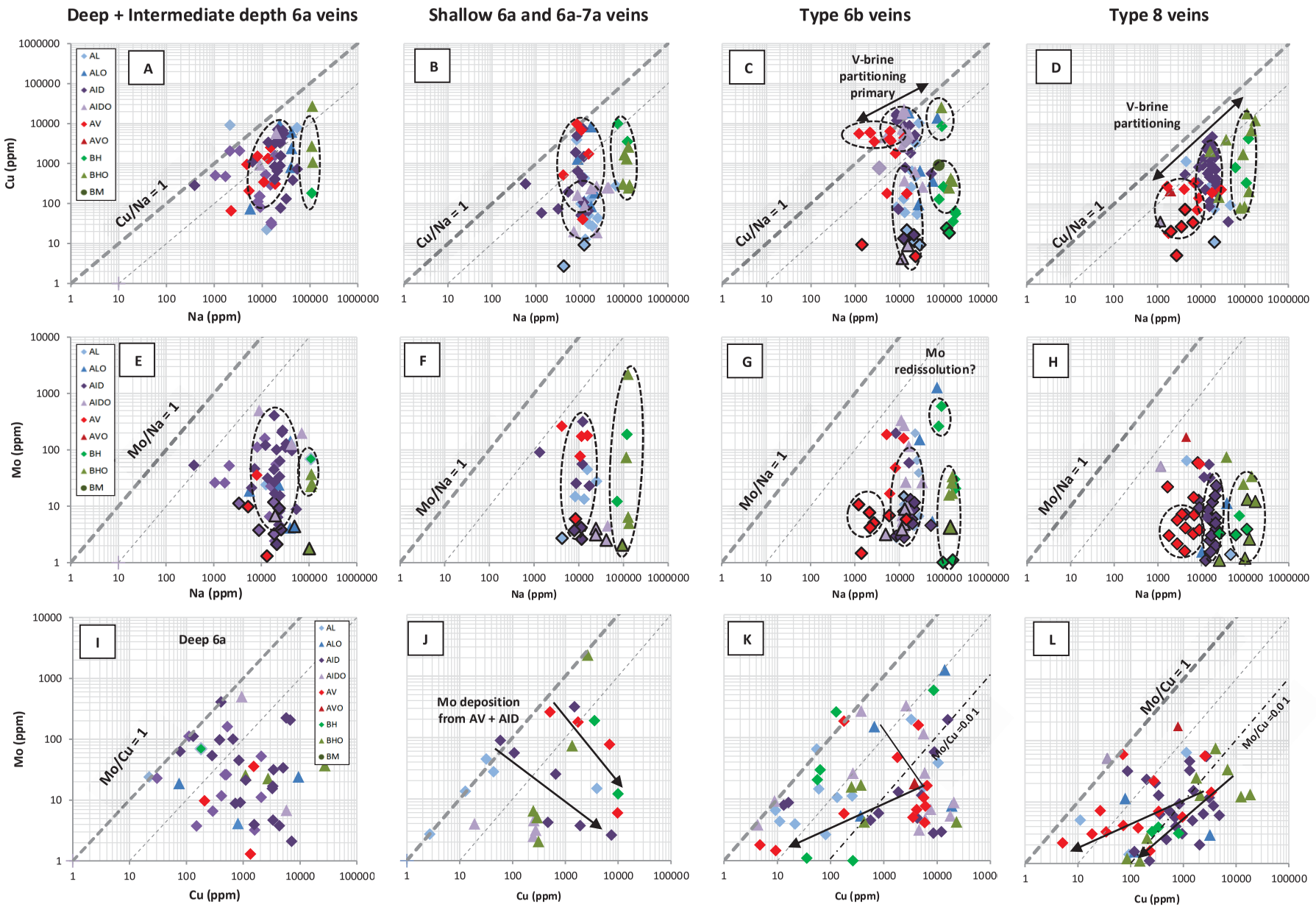


Figure 5.35: Minor element ratios for individual fluid inclusions of each type in type 6a veins from variable depths, type 6b veins and type 8 veins. Figure shows data from multiple intrusive centres. Data with black borders = 0.5*LOD values.

Fluid inclusions in the main mineralisation veins contain Mo and Cu concentrations that vary by 4 orders of magnitude (Mo = 1-2000 ppm, Cu = 5-20000 ppm). In the type 6a veins, Cu concentrations exhibit a weak positive correlation with inclusion Na concentrations (Figure 5.36B). Cu Concentrations of 200-10000 ppm are recorded for the rare brine inclusions whereas concentrations are commonly an order of magnitude lower in low salinity A_L inclusions in the transitional 6a-7a veins. Mo concentrations are relatively uniform (4-400 ppm) for all inclusion types and do not display a clear relationship with Na (Figure 5.36E). Highest Mo concentrations are usually recorded for the moderate salinity (5-8 wt.% $NaCl_{eq}$) A_{ID} and A_{IDO} inclusions that homogenise at temperatures >430°C. With the exception of two inclusions, Mo concentrations are below 100 ppm in the rare brine and A_V inclusions (Figure 5.36). Overall, Mo:Cu ratios are ≤1 for all inclusion types but exhibit a broad range of values between 1 and 0.0001 (Figure 5.36I-J).

In the type 6b veins the parental A_{ID} and contracted A_L inclusions are generally more Cu-rich (Figure 5.36C) and Mo-poor (Figure 5.36G) than in the primary type 6a inclusions. Highest Cu concentrations are recorded for a cluster of A_{ID}, A_{IDO} and B_{HO} inclusions that have typical Cu concentrations of 3000-15000 ppm. A cluster of A_V inclusions also contain high Cu concentrations, which is at variance with the general weak positive correlation between Cu and Na concentrations. Although most inclusions contain >3000 ppm Cu, there is a clear bimodality in the data with a numerous inclusions also containing 10-1000 ppm Cu (Figure 5.36C). These inclusions include abundant A_L and A_{ID} inclusions and less abundant brines that homogenise at lower temperatures and may represent a type 8 fluid overprint (Figure 5.36C). There is also a clear bimodality in Mo concentrations (Figure 5.36G). Several interpreted primary salt-undersaturated inclusions contain >100 ppm Mo, whereas the majority contain <50 ppm Mo and yield very low Mo/Cu ratios of ~0.001. A series of B_H inclusions with high salinities (~45 wt.% $NaCl_{eq}$) contain >200 ppm Mo, whereas the inferred overprinting, Cu-poor, B_{HO} inclusions are also clearly depleted in Mo (Figure 5.36K).

Figure 5.36 (next page): Mo and Cu concentrations in individual fluid inclusions of each type in type 6a veins from variable depths, type 6b veins and type 8 veins associated with multiple intrusions. Circles encircle the typical Mo and Cu concentration ranges of each fluid inclusion types. Data with black borders = 0.5*LOD values. Mo versus Cu plots (I-L) contain true and 0.5*LOD data.


Deep + Intermediate depth 6a veins
Shallow 6a and 6a-7a veins
Type 6b veins
Type 8 veins
A
B
C
D
E
F
G
H
I
J
K
L
AL
ALO
AID
AIDO
AV
AVO
BH
BHO
BM
Cu (ppm)
Na (ppm)
Mo (ppm)
Cu/Na = 1
Mo/Na = 1
Mo/Cu = 1
V-brine partitioning primary
V-brine partitioning
Mo redissolution?
Deep 6a
Mo deposition from AV + AID
Mo/Cu =0.0 1

In the type 8 veins, all fluid inclusion types contain lower average concentrations of Cu and Mo than in the type 6a and 6b veins (Table 5.2). Cu concentrations are less variable and exhibit a far stronger relationship with inclusion Na concentrations (Figure 5.36D). The inferred primary A_{ID} and A_L and brine inclusions contain similar Cu concentrations to those measured in the type 6a and 6b veins with maximum Cu concentrations of ~1 wt.% Cu recorded for a cluster of B_{HO} inclusions. Unlike in the type 6b boiling assemblages, Cu displays a stronger affinity for the partitioned brines relative to the A_V inclusions. The partitioned vapours typically contain Cu concentrations that are two orders of magnitude lower than in the type 6b veins (Figure 5.36D). Fluid inclusions in the type 8 veins yield the lowest Mo concentrations of any vein or breccia type. With exception to a single A_{VO} inclusion (170 ppm Mo) all inclusions contain < 100 ppm Mo (Figure 5.36H). As a result, inclusions in the type 8 veins yield the lowest average Mo/Cu ratios of any vein type (Figure 5.36L). Unlike the type 6b veins most inclusions yield Mo/Cu ratios of ~0.01 including the brine inclusions.

5.4.4 Late Mineralisation Type Veins and Breccias

Type 9 Veins

Primary fluid inclusions in the type 9 veins are dominated by Na, K, Mn, Fe, As and Pb and commonly contain significant Mg, Ca, Zn, Rb, Sr and Cs (Table 5.3). Unlike the other premineralisation and main mineralisation vein types, most inclusions contain Ca concentrations that are below limits of detection or are over ten times lower than Na. The primary, rounded B_M and B_{HO} inclusions contain similar major and trace element concentrations to the irregular shaped B_H inclusions that commonly occur in clusters (e.g. Figure 5.18C). This suggests that these separate brine generations are closely related. The separate brine generations also record far higher B and Cs concentrations than in similar inclusions in the main mineralisation samples. A maximum B value of 3887 ppm was recorded for a very high salinity (61.0 wt.% $NaCl_{eq}$) B_{HO} inclusion. The rarity of B-rich inclusions in the main mineralisation veins suggests that the inclusions in these veins do not represent a type 9 overprint. Unlike the premineralisation and main mineralisation brines, type 9 brines also contain higher average concentrations of As, Mg, Rb, Sb and Sn (e.g. Table 5.3; Figure 5.37G). As concentrations are typically orders of magnitude higher and can explain the presence of As-bearing sulphosalts in the late mineralisation veins and breccias (e.g. Camus, 1975; Vry *et al*. 2010). Unlike most other elements, these elevated concentrations do not correlate well with inclusion Na concentrations (Figure 5.37C, E, H).

Table 5.3: Average LA-ICP-MS element concentrations (ppm) and standard deviations for all fluid inclusion types in the late mineralisation type veins and breccias.

Vein Type	*FI Type*	*Na*	*SD*	*N*	*Mg*	*SD*	*N*	*K*	*SD*	*N*	*Ca*	*SD*	*N*	*Mn*	*SD*	*N*	*Fe*	*SD*	*N*	*Cu*	*SD*	*N*
Type 9	AL	12970		1	363		1	8002		1			0	577		1	22981		1	2180		1
	ALO	25275		1			0	5072		1			0	2193		1	17998		1	91		1
	AID	18239	8083	7	965	1384	5	6515	4222	7			0	1152	1036	7	22094	22785	4	728	415	5
	AIDO	10737		1	143		1	4034		1			0	1235		1	17389		1			0
	AV	6595	2784	7	487	597	2	4491	2955	6			0	351	290	3	6029	2978	3	1017	830	4
	BH	84938	63974	8	3439	4875	8	42932	27878	8	73332	138093	4	4443	3011	8	127032	133266	7	5633	4142	6
	BHO	117747	52810	19	3779	8633	18	52270	39823	17	10979	17128	4	3860	3344	19	113301	78702	17	2519	2345	10
	BM	55520	30958	7	1673	3282	7	45840	32701	7	75954	149511	4	3570	2721	7	244054	124127	7	7919	5258	4
Type 10 gypsum	AL	18575	5708	4	267		1	9452	7137	2			0	745	124	2	21264		1	130		1
	ALO	40431	8754	2	81	51	2	12461	4091	2			0	2179	660	2	8722	6511	2	2390	2234	2
	AID	9777	7825	16	494	1181	14	5955	4536	13			0	449	403	6	7113	5962	6	943	1623	12
	AIDO	12196	2475	5	551	322	3	4667	3360	4			0	169	108	3	6057	5688	2	8107		1
	AV	3426	3395	2			0	4262	5235	2			0			0	1901		1	354		1
	BH	135214	19574	3	457	336	3	31340	14776	3			0	2559	1355	3	41971	38120	3	3629	3715	2
	BHO	86474	47797	3	636	397	3	74253	73929	3	7018		1	20968	27286	3	90381	51698	3	2320	5	2
	BM	99494	931	3	3069	2941	3	57070	23498	3	13225		1	9179	2703	3	83740	26982	3	3301	1606	3
Type 10 anhydrite	AL	11048	8070	4	63	48	2	2565	544	4			0	41	12	2	3295		1	120	57	4
	ALO	9307	8584	3	242	332	2	1837	2382	2			0			0	157		1	178	234	2
	AIDO	2911		1			0			0			0	237		1			0			0
	AV	11118	9165	6	2100	2156	4	6983	8881	2			0	137		1			0	2067	3510	3
	BHO	5515		1	8		1	1345		1			0	188		1	7432		1	438		1
Gypsum	AL	10020	9414	12	13970	7981	9	7354	9501	10			0	16422	17148	8	15755	6320	7	453	319	8

Notes: averages are reported for each fluid inclusion type with 1 standard deviation (SD) and the numbers of significant concentrations used are shown in column N. Grey cells = Standard deviations that could not be calculated as element concentrations were <limits of detection using the 3σ criterion or only a single inclusion was measured. For concentrations of Be, Co, Ga, Br, In, La, Nd, Dy, Lu, W and Au see Appendix 5.

Table 5.3 (continued)

Vein Type	*FI Type*	*Zn*	*SD*	*N*	*As*	*SD*	*N*	*Rb*	*SD*	*N*	*Sr*	*SD*	*N*	*Mo*	*SD*	*N*	*Cs*	*SD*	*N*	*Pb*	*SD*	*N*
Type 9	AL	940		1			0	23		1	70		1	713		1			0	178		1
	ALO	252		1	286		1	14		1	42		1			0	26		1	173		1
	AID	574	395	5	10828	14021	4	39	27	7	22	26	6	252	128	2	98	106	6	2081	2676	6
	AIDO	285		1			0	25		1	28		1	37		1	12		1	451		1
	AV	730	505	5	1600		1	24	14	6	6	7	4	294	407	2	103	84	4	1051	1035	5
	BH	2570	2430	8	5451	7889	7	512	304	8	255	417	8	79	51	5	1390	2148	8	2359	1280	7
	BHO	2020	2239	18	4375	5119	14	552	405	16	257	364	18	281	226	10	1248	1879	19	3094	3270	17
	BM	3672	2701	7	4068	3223	7	694	614	7	559	1263	7	701	484	5	9802	13929	7	3745	2845	7
Type 10 Quartz	AL	423		1	91		1	75	61	4	87	66	3	184	97	3	49	14	3	153	45	2
	ALO	627	371	2	38		1	81	54	2	10	3	2			0	33	4	2	226	150	2
	AID	213	208	8	77		1	25	21	12	11	15	13	266	286	7	14	13	8	99	204	10
	AIDO	205	42	4	403	492	2	24	14	4	6	3	4	126	169	2	22	17	3	54	25	4
	AV			0	419		1			0	7		1	120	84	2			0			0
	BH	1129	874	3	1457		1	672	514	3	310	288	3			0	136	36	3	321	209	3
	BHO	5880	7784	3	177		1	549	590	3	310	340	3	160	59	2	380	491	3	1412	1214	3
	BM	3281	511	3	498	609	2	276	137	3	231	16	3	680	800	3	84	25	3	1153	605	3
Type 10 anhydrite	AL	152	6	2	84	50	2	48	50	3	20168		1			0	19	7	2	24	15	4
	ALO	194		1			0	17	21	2	107		1			0	10	13	2	33	35	3
	AIDO			0	87		1	14		1	72276		1			0	10		1	25		1
	AV	1484		1	856		1	61	23	3	76970	37352	3	76		1	69	28	2	326	290	4
	BHO	105		1	574		1	33		1			0	50		1	22		1	44		1
Gypsum	AL	451	1062	9	22	27	2	11	15	10	4195	3816	9	134	313	7	10	12	8	217	324	10

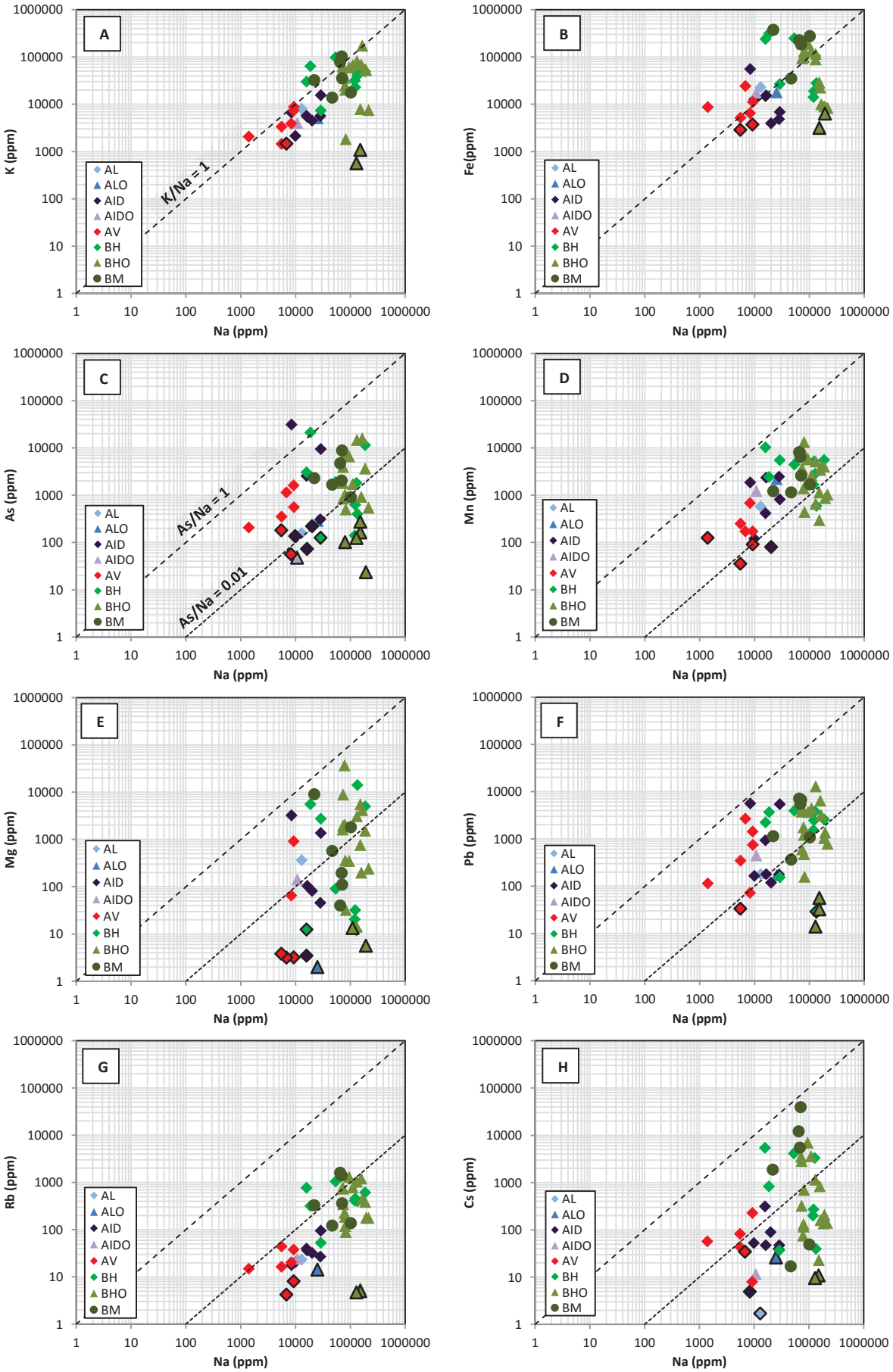

A
K (ppm)
Na (ppm)
K/Na = 1
B
Fe(ppm)
Na (ppm)
C
As (ppm)
Na (ppm)
As/Na = 1
As/Na = 0.01
D
Mn (ppm)
Na (ppm)
E
Mg (ppm)
Na (ppm)
F
Pb (ppm)
Na (ppm)
G
Rb (ppm)
Na (ppm)
H
Cs (ppm)
Na (ppm)
AL
ALO
AID
AIDO
AV
BH
BHO
BM
1
10
100
1000
10000
100000
1000000

Figure 5.37 (previous page): Major and trace element concentrations of individual fluid inclusions of each type in type 9 veins to the south and east of the Braden Breccia pipe at various mine levels. Data with black borders = 0.5*LOD values.

In the type 9 samples the partitioned A_V inclusions and rare A_{ID} inclusions have similar compositions and exhibit relatively consistent Fe/Na ratios of ~1 and Mn/Na and Pb/Na ratios of 0.05 (Figure 5.37D, F). This, and their clear overlap in microthermometric properties (Figure 5.19), suggests that some rare A_{ID} inclusions represent contracted vapours. However, a few A_{ID} assemblages overlap with the brine inclusions, particularly with respect to Pb and Mn. These assemblages may represent parental fluids. However, their low homogenisation temperatures relative to a number of the primary brines indicates that they are likely to represent vapours that have partially reequilibrated with the brines. Similar to the type 6b-8 veins, the A_V inclusions contain proportionately high As/Na and Mg/Na ratios when compared to the brines. Unlike the brines, B concentrations are commonly below limits of detection due to their low densities. However, Cs concentrations are typically >100 ppm, strongly suggesting that the A_V inclusions were boiled off the late Cs-rich brines.

Fluid inclusion Cu concentrations in the type 9 veins are comparable to those recorded for the type 8 veins, with typical Cu/Na ratios of ~0.1 (Figure 5.38A). Highest Cu concentrations of 10,000 ppm are recorded for the Fe-rich primary brine inclusions (Figure 5.38B). These inclusions display diverse Cu/Fe ratios as a function of ranging Fe concentrations in the B_H, B_{HO} and B_M populations (Table 5.3). These primary brine inclusions contain the highest Mo concentrations of any inclusion type in any vein or breccia type (Figure 5.38C). Mo concentrations are particularly high in the primary B_{HO} and B_M inclusions, which record a maximum concentration of 2090 ppm. By contrast, Mo concentrations are commonly an order of magnitude lower in the irregular shaped inferred pseudosecondary B_H inclusions. The partitioned vapours and rare A_{ID} inclusions also contain low Mo concentrations that are comparable with concentrations recorded for partitioned A_V inclusions in the type 6a-6b veins. When compared to other vein and breccia stages, a far greater proportion of inclusions contain Mo/Cu ratios that are >0.01 (Figure 5.38D). These include the primary B_{HO} and B_M inclusions, which exhibit typical Mo/Cu of ~0.1, which is an order of magnitude greater than the average Mo/Cu ratios recorded for brine inclusions in the type 8 veins (Figure 5.36L).

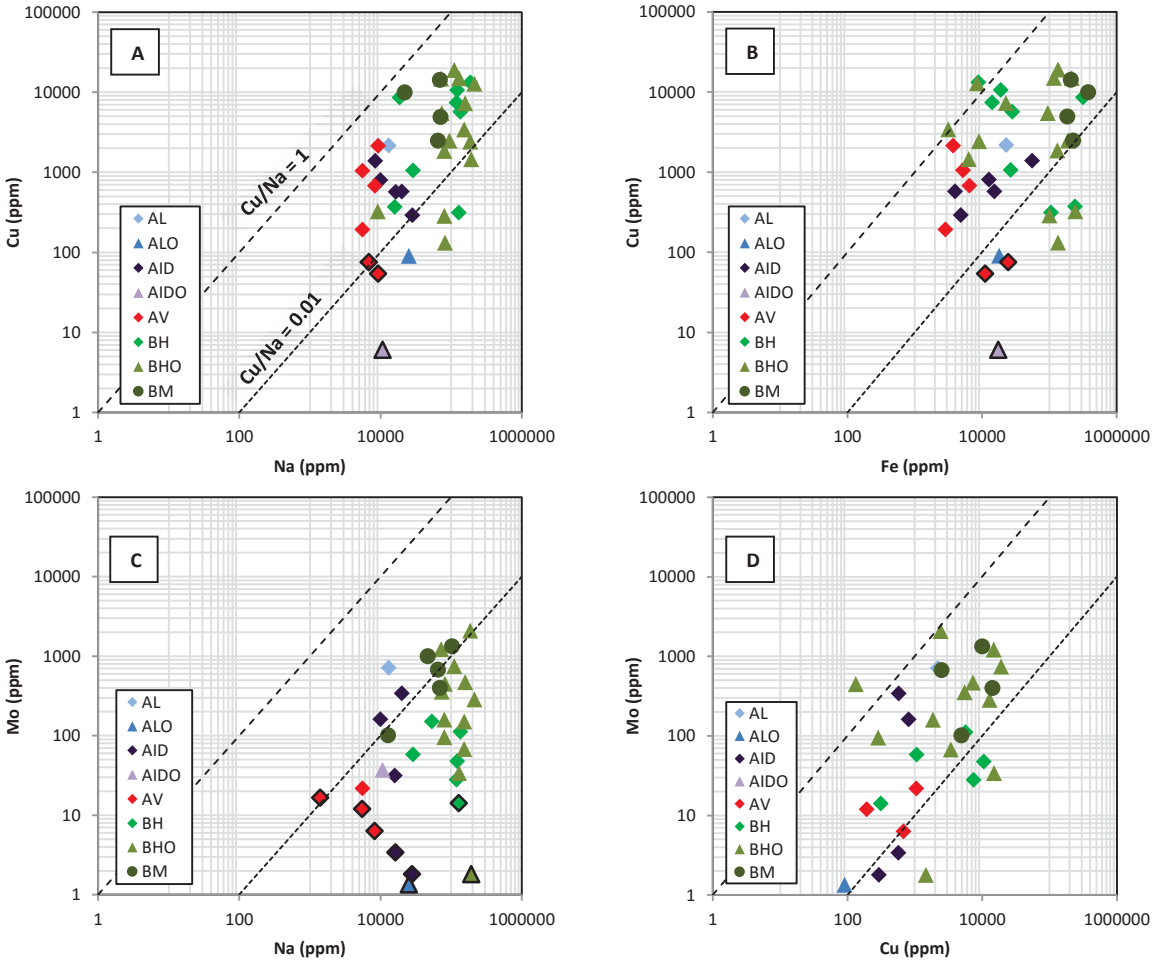


Figure 5.38: Mo and Cu concentrations in different fluid inclusion types in type 9 vein to the south and east of the Braden Breccia pipe at various mine levels. Data with black borders = 0.5*LOD values. Half LOD values are incorporated in plot D, refer to plots A and C.

Type 10 veins

Fluid inclusions in the type 10 veins are dominated by Na, K, Mn, Fe As and Pb and contain significant Mg, Ca, Zn and Rb (Table 5.3). The primary brine inclusions that homogenise at >380°C (Figure 5.20) contain similar concentrations of K, Fe and Mg to the primary brines in the type 9 veins (Figure 5.39A-B). Despite this, the brine inclusions in the type 10 brines typically contain lower concentrations of As, Mn and Pb that are commonly typically <1000 ppm (Figure 5.39 C, D, F). Cs concentrations are also far lower and rarely exceed 100 ppm (Figure 5.39H). In addition to this, a far higher proportion of inclusions in the type 10 veins contain concentrations of B, Co and Ni that are below limits of detection. These differences make the type 10 brines more compositionally similar to the main mineralisation brines.

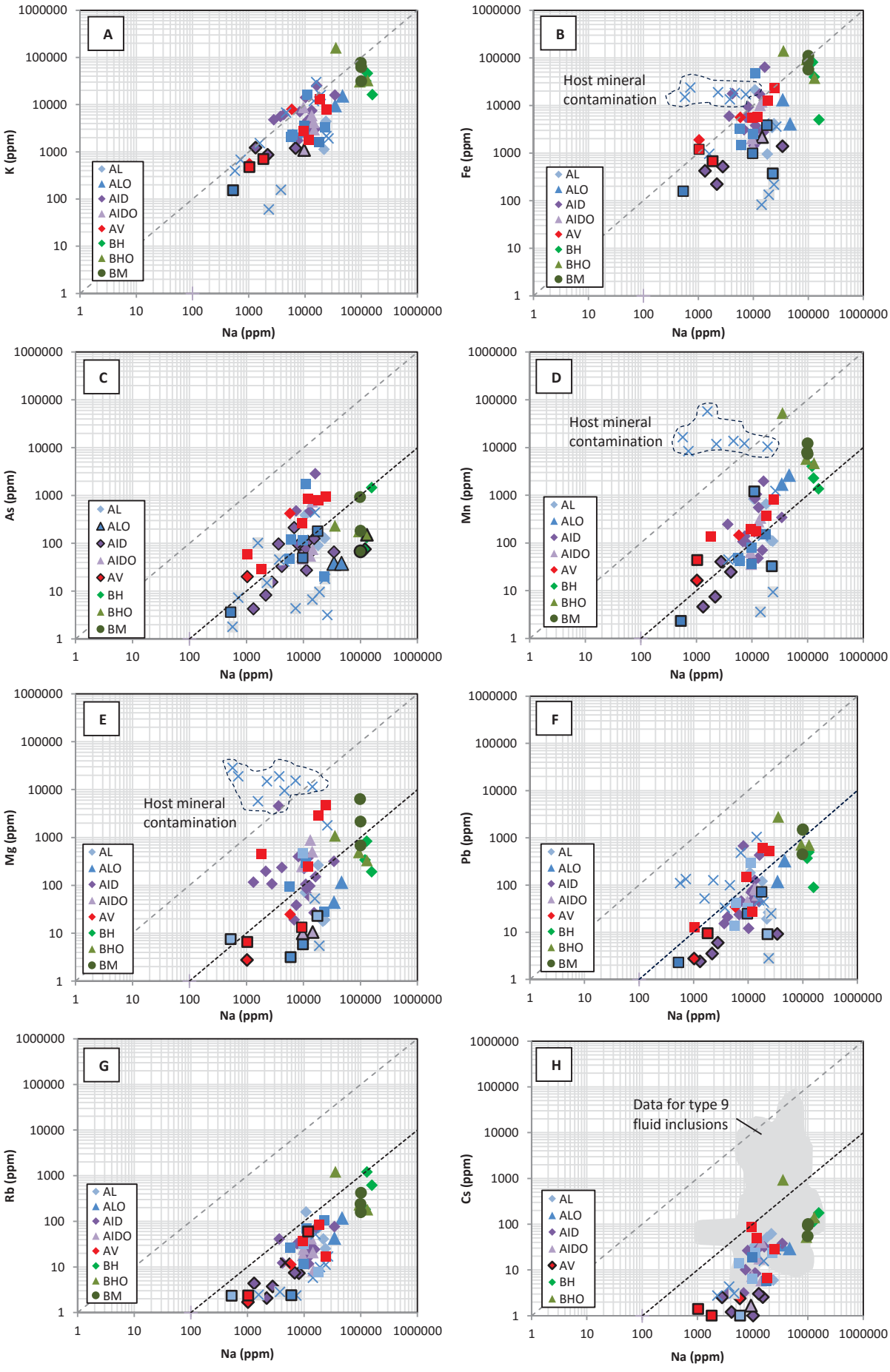

A
K (ppm)
Na (ppm)
B
Fe (ppm)
Host mineral contamination
C
As (ppm)
D
Mn (ppm)
Host mineral contamination
E
Mg (ppm)
Host mineral contamination
F
Pb (ppm)
G
Rb (ppm)
H
Cs (ppm)
Data for type 9 fluid inclusions
AL
ALO
AID
AIDO
AV
BH
BHO
BM
1
10
100
1000
10000
100000
1000000

Figure 5.39 (previous page): Major and trace element concentrations of different fluid inclusion types in different host minerals in type 10 veins and anhydrite-carbonate ±gypsum breccias. Triangles and diamonds = quartz-hosted inclusions. Squares = anhydrite-hosted inclusions. Crosses = gypsum-hosted inclusions. Data with black borders or grey shaded backgrounds = 0.5*LOD values.

Similar to the type 9 veins, several A_V inclusion assemblages yield elevated As/Na ratios relative to the A_L, A_{ID} and brine inclusions (Figure 5.39E), suggesting that they may be the product of fluid phase separation. These A_V inclusions typically homogenised between 320 and 370°C (Figure 5.20). Several higher temperature A_V inclusion assemblages hosted in the quartz samples contain similar element concentrations to the primary A_{ID} inclusions and A_L inclusions (Figure 5.39) suggesting that they represent similar fluids trapped with different densities. In the quartz- and anhydrite-dominated type 10 samples, these salt-undersaturated primary inclusion assemblages are compositionally similar to those hosted in the type 6a-6b veins. This suggests that the type 10 veins were either formed by late pulses of similar fluids or represent overprinted and reopened main mineralisation veins.

The gypsum-hosted A_L inclusions contain similar concentrations of Na, As, Pb, Rb and Sr to the anhydrite- and quartz-hosted A_L and A_{ID} inclusions. However, concentrations of Fe, Mn and Mg are usually far higher and cluster at ~10000 ppm (Figure 5.39 B, D, E). Unlike most other elements, these high concentrations of Mn, Mg and Fe do not correlate well with Na and may be the result of host mineral contamination.

All quartz-, anhydrite- and gypsum-hosted inclusions yield typical average Cu/Na ratios of 0.033 and Cu/Fe ratios between 1 and 0.01 (Figure 5.40A-B). The highest Cu concentrations of >1000 ppm are predominantly recorded for a number of opaque-bearing liquid and brine inclusions, whereas all anhydrite- and gypsum-hosted A_V inclusions contain <710 ppm Cu. Mo concentrations in the quartz-hosted primary A_{ID} and A_V inclusions are comparable to those recorded for the primary A_{ID} inclusions in the shallow type 6a veins (Figure 5.40C). These inclusions record Mo concentrations of up to 740 ppm and generally yield the highest Mo/Cu ratios of any inclusion types. Far lower Mo concentrations are recorded for the lower temperature A_V inclusions and the secondary A_L inclusions (Figure 5.40D). Similarly to the type 9 samples, partitioned brine inclusions in the quartz samples contain a range of Mo concentrations, with highest Mo concentrations occurring in the high temperature B_M

inclusions (Figures 5.20, 5.40C). By contrast all primary A_V and A_L inclusions in the anhydrite and gypsum samples contain <100 ppm Mo. The lower As concentrations of the A_L inclusions (Figure 5.39C) suggests that these Mo-poor fluids are not related.

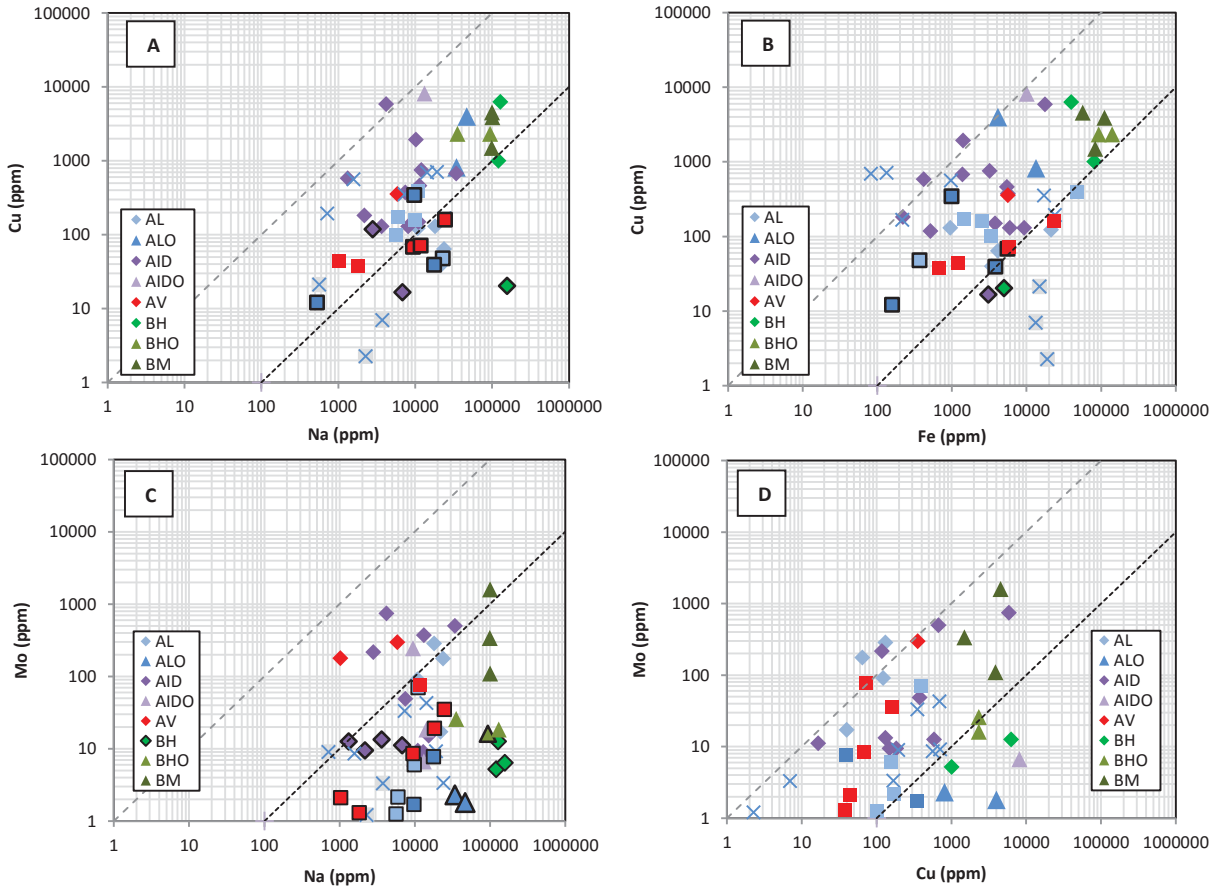


Figure 5.40 (previous page): Mo and Cu concentrations in individual fluid inclusions of each type in different host minerals in type 10 veins and anhydrite-carbonate ±gypsum breccias. Triangles and diamonds = quartz-hosted inclusions. Squares = anhydrite-hosted inclusions. Crosses = gypsum-hosted inclusions. For quartz hosted inclusions triangle symbols signify the presence of an opaque daughter crystal. Data with black borders or grey shaded backgrounds = 0.5*LOD values. These are incorporated in plot D.

5.4.5 Spatial-Temporal Variations in Fluid Chemistry

Variations in Primary Fluid Chemistry

Primary fluid inclusion populations in similar main mineralisation vein and breccia types from each intrusion display subtle variations in major, minor and trace element signatures that provide further evidence that each mineralised centre evolved separately. These chemical signatures are recorded in primary fluids in type 6a veins in each centre and are also reflected in primary ore fluids in outboard type 6b-8 veins in the same system with modifications superimposed due to precipitation of minerals and wallrock reactions (Figures 5.41-5.42). The broad similarity in inclusion chemistry irrespective of vein and inclusion type in each system strongly supports a continuous evolution of fluids within each centre.

Primary A_V and contracted A_{ID} inclusions in the deep type 6a veins proximal to the North Central Diorite tend to be enriched in Fe relative to the other major fluid components (Figure 5.41). These inclusions also have the highest relative proportions of Cs (Figure 5.42), suggesting that fluid entrapment in the deepest type 6a veins occurred prior to the deposition of significant Fe- and Cs-bearing phases associated with potassic alteration. Primary A_L and A_{ID} inclusions in shallow type 6a veins proximal to the North Central Diorite contain lower average proportions of Fe and Cs and higher proportions of Cu, Zn and Pb. Similar low concentrations are recorded for primary A_L and A_{ID} inclusions that homogenise at temperatures >390°C associated with the Northern Diorite and Teniente Dacite Porphyry (Figures 5.41-5.42). These shallow type 6a veins are commonly surrounded by diffuse biotite halos and typically contain negligible amounts of chalcopyrite. The remarkably similarity in major element concentration ratios, implies that the input fluid compositions and early type 6a vein development was extremely similar in each spatially-temporally separate system.

Primary A_L and A_{ID} inclusions that homogenise >390°C in shallow 6a and 6b veins display far greater variations in fluid chemistry. In the Southern Diorite, trace element ratios are similar to those recorded for the deep A_{ID} inclusions associated with the North Central Diorite (Figure 5.42) suggesting that the Southern Diorite may have been emplaced at a higher elevation. By contrast far higher relative Mo and As concentrations are recorded for the North Central Diorite. These high ratios are not apparent in the deeper 6a veins associated

with this intrusion and therefore are most likely to be a manifestation of the dissolution of molybdenite that deposited at >390°C.

Primary A_L inclusions associated with the Northern Diorite contain relatively low proportions of Cu relative to those associated with the other intrusions. The high Cu ratios recorded for higher temperature inclusions in type 6a veins in this part of the deposit indicate that this is not a system characteristic but the result of Cu deposition prior to fluid entrapment in this part of the deposit. With exception to As and Zn, absolute trace element concentrations are low for all inclusion types associated with the Northern Diorite when compared to the other intrusions. This is a system characteristic as opposed to the result of element fractionation processes such as fluid boiling. In contrast to the other veins, primary A_{ID} and A_L inclusions associated with the Teniente Dacite Porphyry contain extremely high concentrations Mn, Zn and Pb (Figures 5.41-5.42).

In the type 6a-6b veins the partitioned brine inclusions exhibit overall increasing proportions of Fe, Mn and Zn and decreasing K and As with decreasing intrusion age (Figures 5.41-5.42). The high Mn and Zn ratios in brine inclusions associated with the Teniente Dacite Porphyry conform to high proportions of these elements recorded in the parental A_L fluids indicating a system characteristic. The partitioned A_V inclusions also record trends of decreasing K ratios with interpreted intrusion age. This is coupled with a general trend of increasing Cu concentrations whereas Mo shows an increasingly strong affinity for the partitioned brines.

Primary salt-undersaturated inclusions and partitioned vapour and brine assemblages in the type 8 veins proximal to the North Central Diorite, Northern Diorites and Teniente Dacite Porphyry record extreme variability in major and minor element ratios (Figures 5.41-5.42. This is attributed to variable degrees of fluid mixing, mineral precipitation, redissolution and wallrock-reactions that obscure trends in fluid chemistry or links between type 8 fluids and those present in type 6a-6b veins in the same system. For example, the extremely high Mo ratios in A_L inclusions in type 6b and type 8 veins proximal to the North Central Diorite are clearly the result of molybdenite dissolution. Unlike in the type 6b veins the type 8 inclusions record increases in the overall proportions of K and As as a function of large drops in Cu, Mo and Pb concentrations linked to metal sulphide precipitation.

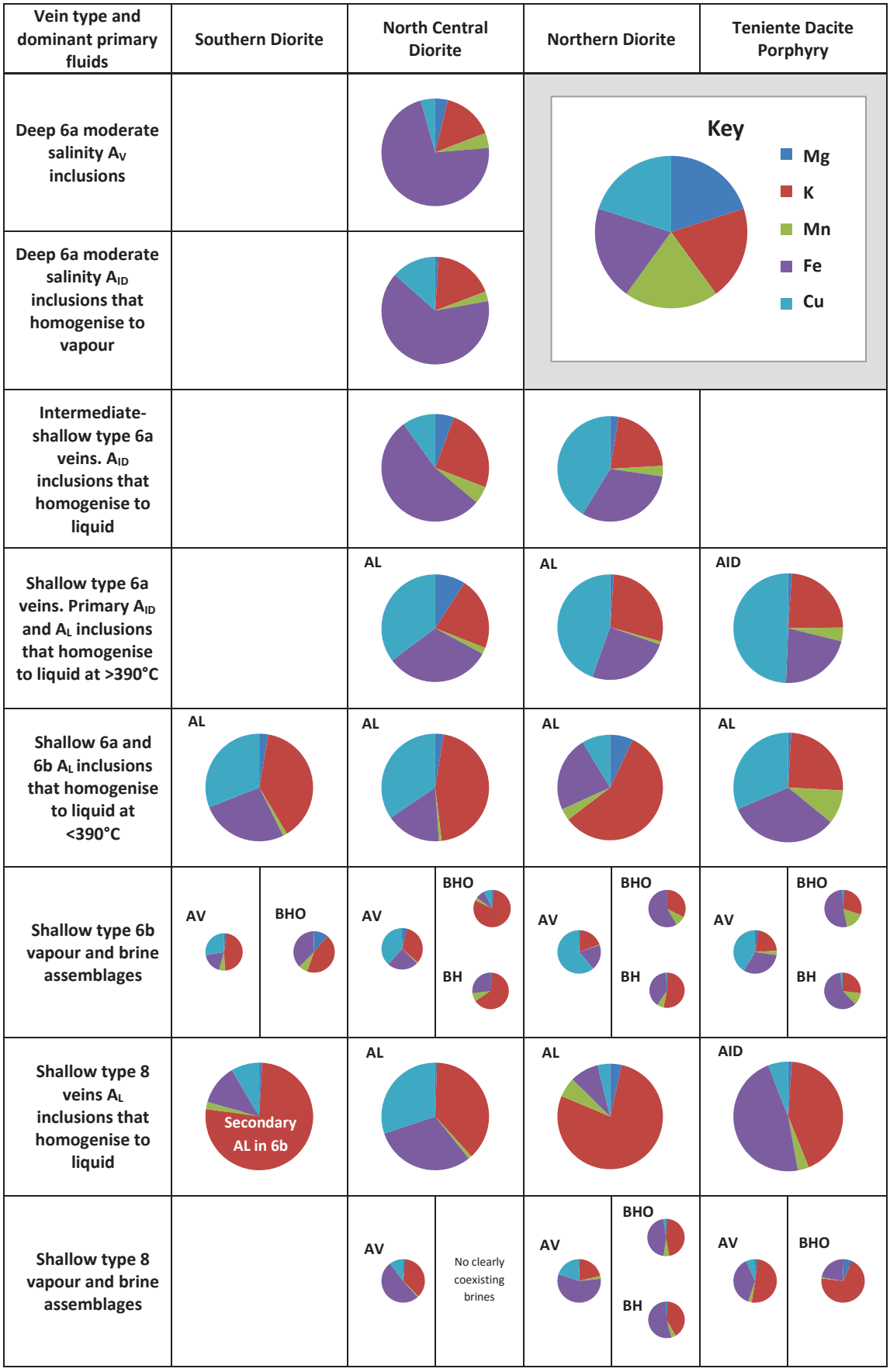


Figure 5.41: Major element ratios in primary inclusions associated with different vein types in multiple intrusions. Figure represents the overall evolution of fluids in each system.

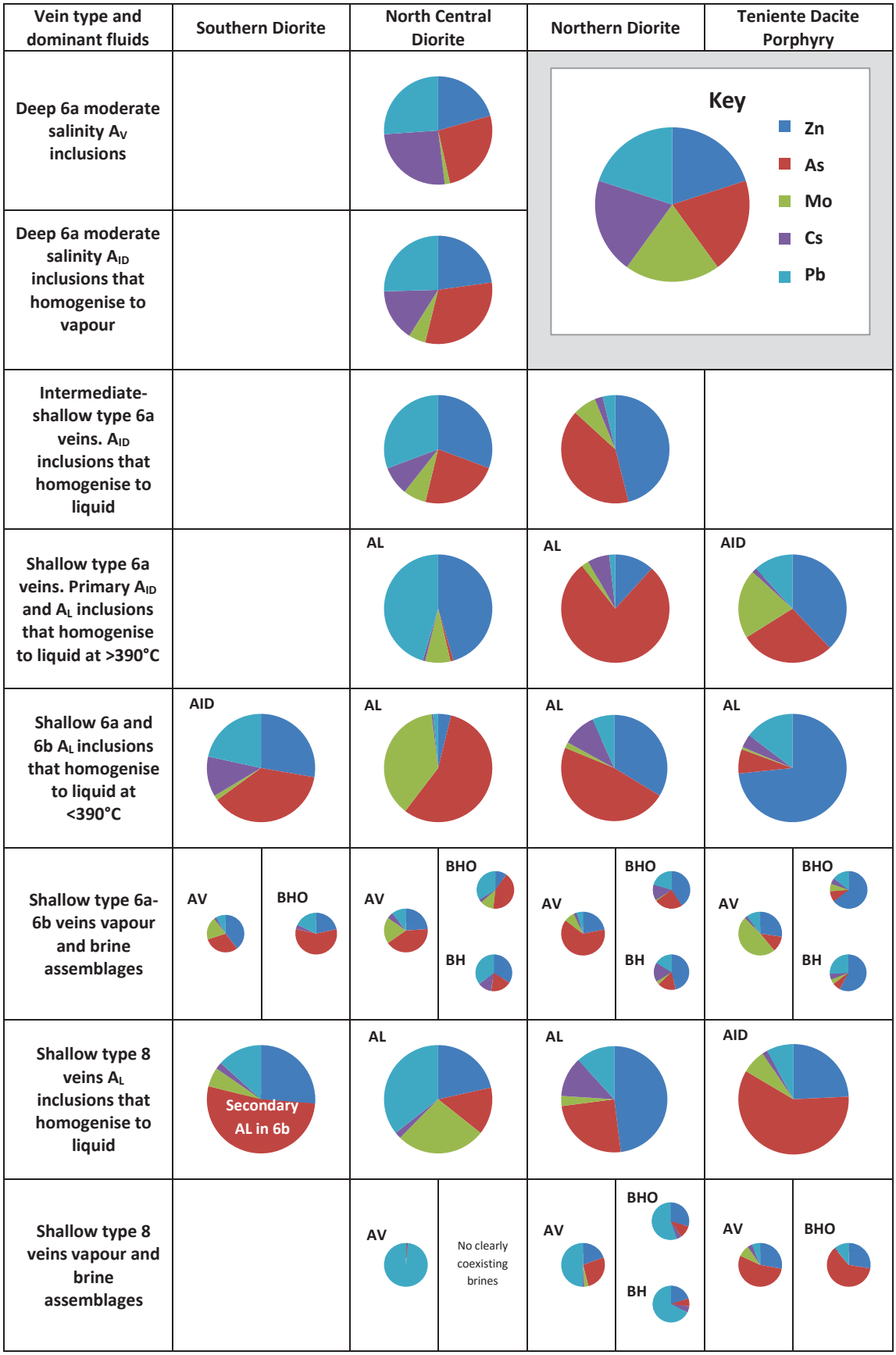


Figure 5.42: Minor and trace element ratios in primary inclusions associated with different vein types in multiple intrusions. Figure represents the overall evolution of fluids in each system.

Overall Variations in Brine Composition

Brine inclusion compositions are similar in vein-types associated with each intrusion. However, overall variations in brine compositions can be observed for the premineralisation, main mineralisation and late mineralisation-type samples implying that the development of these hypersaline fluids is linked in each paragenetic stage in each intrusion (Figure 5.43). Brine inclusions in the premineralisation veins and breccias typically contain high concentrations of Na and Fe but relatively low concentrations of As, Cu and Mo compared to brines in the type 6a-6b veins and late mineralisation type veins and breccias. Vry (2010) reported elevated Mn and Zn concentrations in type 8 brines relative to premineralisation brines. This was attributed to the fact that the type 8 brines were produced by vapour-brine partitioning and therefore are more enriched in elements that preferentially partition into the high salinity phase. In this study, the main mineralisation brines contain similar Zn values, but more varied Mn (Figure 5.43A). These brines also contain higher As concentrations that are on average approximately three times higher than in the premineralisation samples (Figure 5.43C). This is likely attributed to the fact that the partitioning of As was favoured during the deep exsolution of the parental intermediate density fluids relative to the shallow exsolution of premineralisation brines.

Brine inclusions in the late mineralisation type veins and breccias record the highest concentrations of Fe, As, Cs and Mn (Figure 5.43). These all display a bimodality in which the highest concentrations of As, Fe and Cs are usually recorded for the brine inclusions in the type 9 vein samples. Slightly lower concentrations of these elements recorded for the type 10 brines are similar to concentrations recorded for brine inclusions in the main mineralisation samples. High Mo concentrations are recorded for both the type 9 and 10 brines hosted in quartz and anhydrite (Figure 5.43F). However, there is a clear bimodality in brine Mo concentrations, with a number of brines in the type 10 samples recording Mo concentrations of <100 ppm. By contrast, Cu concentrations are relatively consistent in all type 9 and 10 samples and overlap well with main mineralisation brine concentrations (Figure 5.43E). The lack of Cu-depleted brine inclusions suggests that, unlike Mo, the trapped hypersaline fluids in the type 10 veins and associated breccias had not yet deposited their Cu.

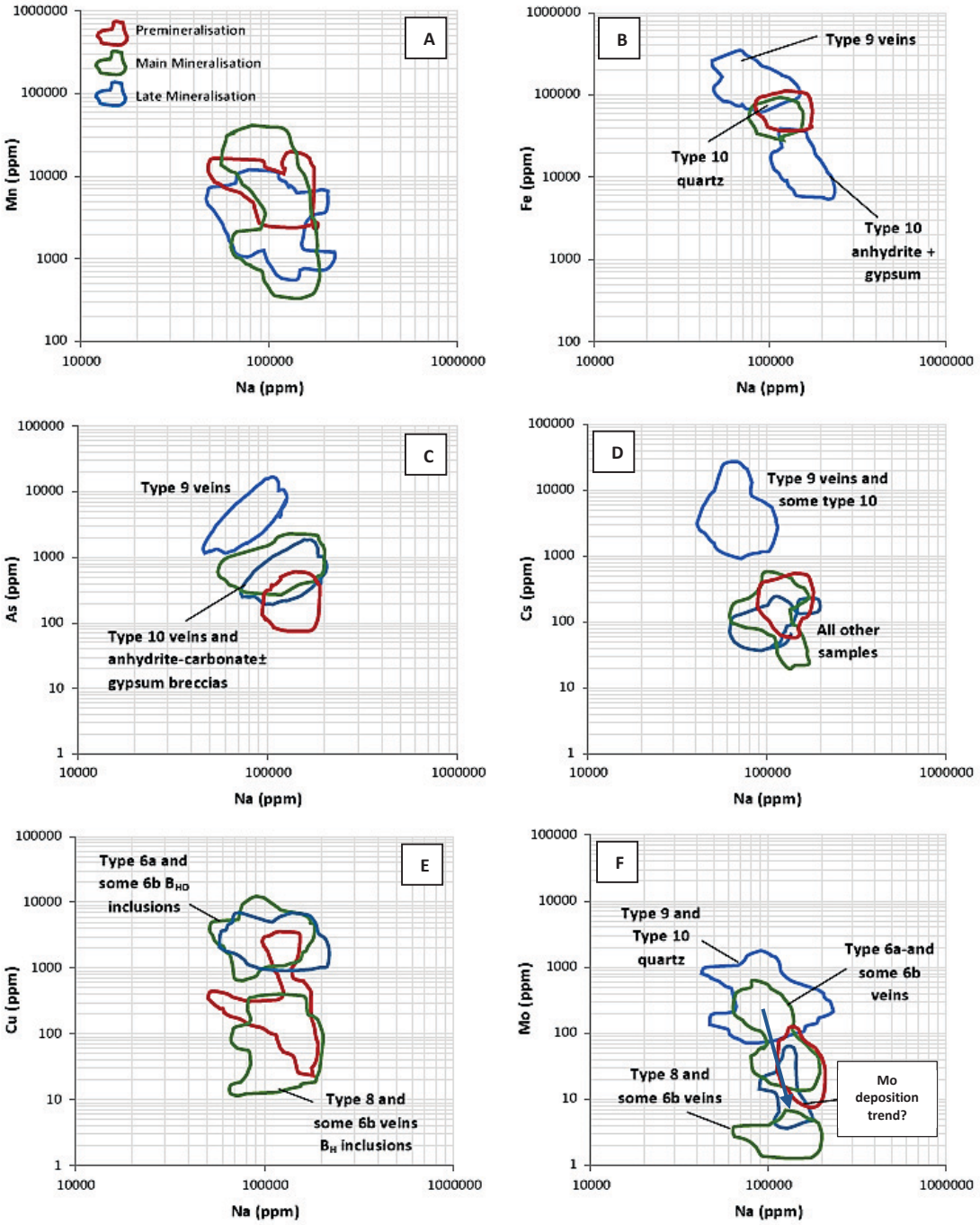


Figure 5.43: Compositions of primary brine inclusions in premineralisation (red), main mineralisation (green) and late mineralisation (blue) type veins and breccias. (A) Mn versus Na, showing clear overlap in brine concentrations for all mineralisation types. (B-D) Major element plots that show clear variations in each mineralisation type stage. (E-F) Mo and Cu concentrations plotted against brine Na concentrations. Each circle encompasses > 90 % of primary fluid inclusion data.

5.5 Discussion

SEM-CL petrography, microthermometric data minimum trapping pressure estimates (Driesner and Heinrich, 2007; Becker *et al*., 2008; Lecumberri-Sanchez *et al*., 2012) and LA-ICP-MS data for fluid inclusions in veins and breccia from multiple intrusions can be combined to constrain the physical and chemical evolution of magmatic-hydrothermal fluids at El Teniente. This information will help ascertain whether fluids evolved in a single, deposit-scale evolutionary sequence (e.g. Cannell, 2004; Klemm *et al*., 2007) or in more complex, potentially chemically distinct, cycles associated with each intrusion (Vry *et al*., 2010).

5.5.1 Premineralisation Type Vein and Breccia Development

Biotite breccias and type 3 veins are dominated by abundant, primary Na-K-Ca-Cl-rich brine inclusions with similar salinities (~47.0 wt.% $NaCl_{eq}$: Figure 5.4), densities (1.14-1.25 g/cm^3), and compositions (Table 5.3; Figures 5.31-5.32). Vry (2010) suggested that similar brine inclusions in early breccia samples proximal to the A-Porphyry are most strongly related to the crystallising parental magma in space and time. The similarity between brine inclusions in the type 3 veins proximal to the Central Diorite and the biotite breccias proximal to the A-Porphyry and the rare occurrence of type 3 veins overprinting main mineralisation type veins associated with younger intrusions (Figure 4.17) suggest that multiple pulses of hypersaline fluids occurred early in the evolution of each mineralised intrusion.

Primary brine inclusions in the biotite breccia sample homogenise by halite dissolution at temperatures that typically exceed vapour-bubble homogenisation temperatures by ~90°C. Brine inclusions in the type 3 veins typically display similar halite dissolution temperatures but vapour-bubble homogenisation temperatures that are ~150°C lower. This suggests that the hypersaline fluids in the type 3 veins were trapped after cooling at near-isobaric conditions (Figure 5.44A). Alternatively, the hypersaline fluids may have been trapped at relatively constant temperature and increasing pressure induced by the annealing of fractures created during the formation of the biotite breccias.

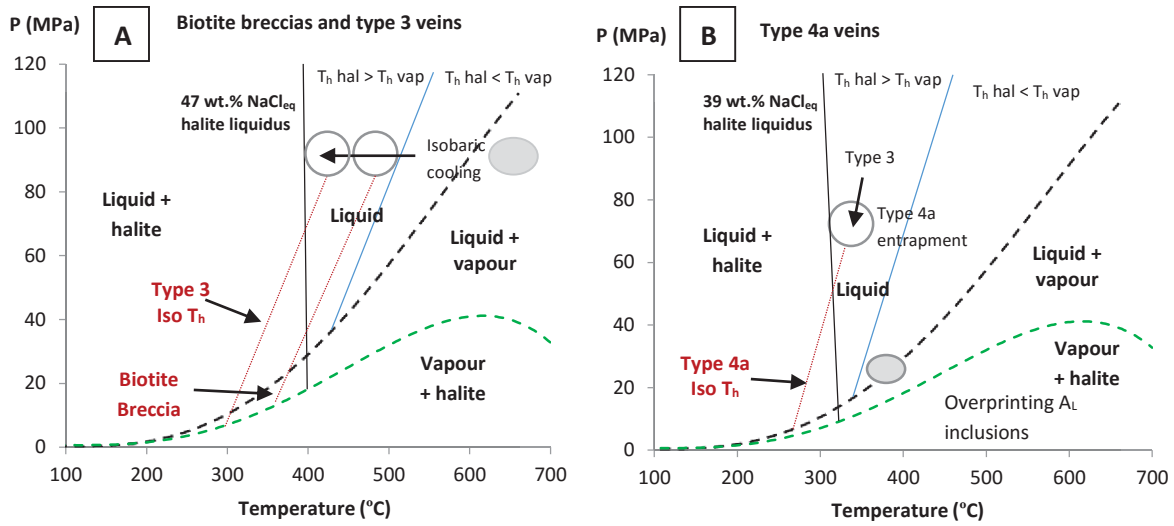


Figure 5.44: Pressure (MPa) versus temperature plot showing the different homogenisation modes of fluid inclusions in the premineralisation type veins and breccias. Figure after Bodnar and Vityk (1994) and the three-dimensional H_2O-NaCl phase diagram of Driesner and Heinrich (2007). Dotted black line = Two phase surface for a 45 wt.% $NaCl_{eq}$ fluid. Dotted green line = the halite-liquid-vapour surface. The 47 wt.% $NaCl_{eq}$ halite liquidus and isochores are drawn approximately based on data from Bodnar (1994) and Cline and Bodnar (1994). (A) Homogenisation modes of brine inclusions in the biotite breccia and type 3 veins showing lines of constant liquid-vapour homogenisation temperature (red lines). Blue line separates inclusions that homogenise to halite (left) from those that homogenise by vapour bubble disappearance (right). Circles = estimated trapping conditions based on microthermometric data. (B) Entrapment conditions of halite-homogenising brine inclusions in type 4a veins, and lower pressure, higher temperature, secondary liquid and vapour inclusions.

Brine inclusions in the biotite breccia yield a high minimum trapping pressure of 90 MPa (Figure 5.20) and are best preserved at the deepest mine levels (e.g. Skewes *et al.*, 2006; Vry *et al.*, 2010). Considering a broadly andesitic composition for the TMC (e.g. Lindgren and Bastin, 1922; Cannell *et al.*, 2005; Vry *et al.*, 2010), equating to a density of 2.6 g/cm^3 for the overlying rock column, this suggests that inclusions were trapped at depths of at least 3.5 km below the paleosurface. This conforms to previous estimations based on exhumation rates (Skewes and Holmgren, 1993; Kurtz *et al.*, 1997; Rivera and Falcon, 1998).

At a depth of 3.5 km it is possible that the halite-homogenising brine inclusions were produced by the direct exsolution of hypersaline fluids from the crystallising magma (e.g. Roedder, 1992; Wilson, 2003; Heinrich, 2007: Figure 5.45C). Experimental studies have demonstrated that the partitioning of Cl from silicate melts into an exsolving fluid is enhanced at high pressure (Shinohara, 1989; Cline and Bodnar, 1991, 1994; Webster, 1997). For example, a degassing magma chamber at a lithostatic pressure of ~200 MPa and 700°C

would produce a fluid with a salinity of ~50 wt.% NaCl that would be stable in the single phase field (Cline and Bodnar, 1991, 1994; Webster, 1997). The Cl concentration of exsolving fluids is also a function of Cl/H_2O in the residual melt, which is typically between 0.03 and 0.1 in porphyry melts, but can increase during progressive fractionation (e.g. Cline and Bodnar, 1991). The low concentrations of incompatible elements including Mo and Cs relative to Na in the premineralisation brines (Table 5.2) suggest that the high Cl concentrations of these fluids is not controlled by high degrees of fractionation. Based on a low Cl/H_2O ratio of ~0.05, a high average brine salinity of ~47 wt.% NaCl and a lack of clearly coexisting vapour inclusions it is likely that the early premineralisation brines were exsolved as single phase hypersaline fluids at >550°C and pressures >90 MPa (Figure 5.46).

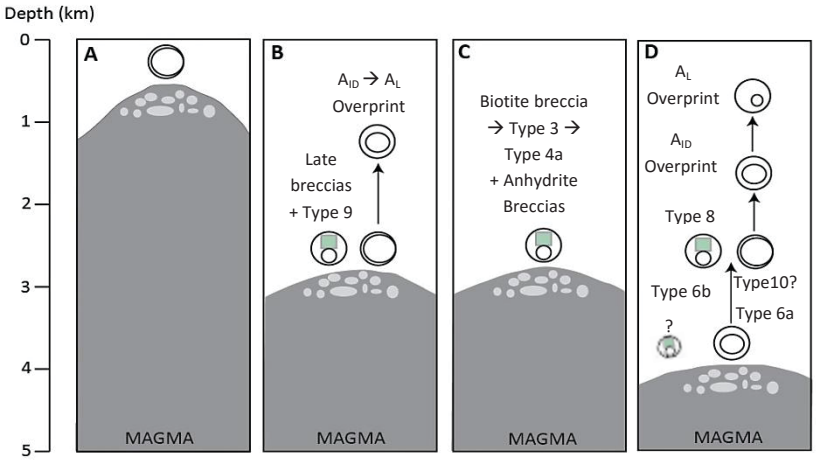


Figure 5.45: Models for the exsolution of different fluids from a magma intruded to varying depths (after Cline and Bodnar, 1994; Heinrich, 2007). (A) direct exsolution of a magmatic vapour at shallow depths; (B) direct exsolution of coexisting brine and vapour; (C) direct exsolution of a brine with high pressure and high Cl activity, also a function of degree of melt crystallisation; and (D) direct exsolution of a single-phase, intermediate density, low-salinity fluid and subsequent evolution during ascent. Premineralisation veins and breccias were likely produced by fluids exsolved in accordance with model C. Main mineralisation fluids are inferred to have been exsolved after contraction of the magmatic-hydrothermal system and associated deepening of the fluid exsolution horizon which, combined with a potential switch from a lithostatic to hydrostatic pressure regime, favoured the deeper exsolution of intermediate density fluids. The late mineralisation fluids appear to be the product of model B and/or the top half of model D in which vapours and brines formed by phase separation.

Type 4a veins are associated with weaker potassic alteration (diffuse biotite halos) and typically postdate the final emplacement of each felsic-intermediate intrusion (Chapter 4; Vry *et al*., 2010). These veins also contain brine inclusions that homogenise by halite dissolution and yield similar minimum trapping pressure estimates (70-90 MPa) to the type 3 veins. However, unlike the type 3 veins, the difference between average vapour bubble

homogenisation temperature and halite dissolution temperature is low, possibly due to a decreasing temperature at relatively constant and high pressure (Figure 5.44B). In accordance with the study of Vry (2010), the brine inclusions appear to be trapped in the single phase field (Figure 5.44B) suggesting that they are the product of the simple cooling of early magmatic brines at relatively constant pressure. Such cooling explains why type 4a veins are predominantly found at the fringes of each mineralised system where they grade outwards into type 4b veins with associated with propylitic alteration (epidote halos).

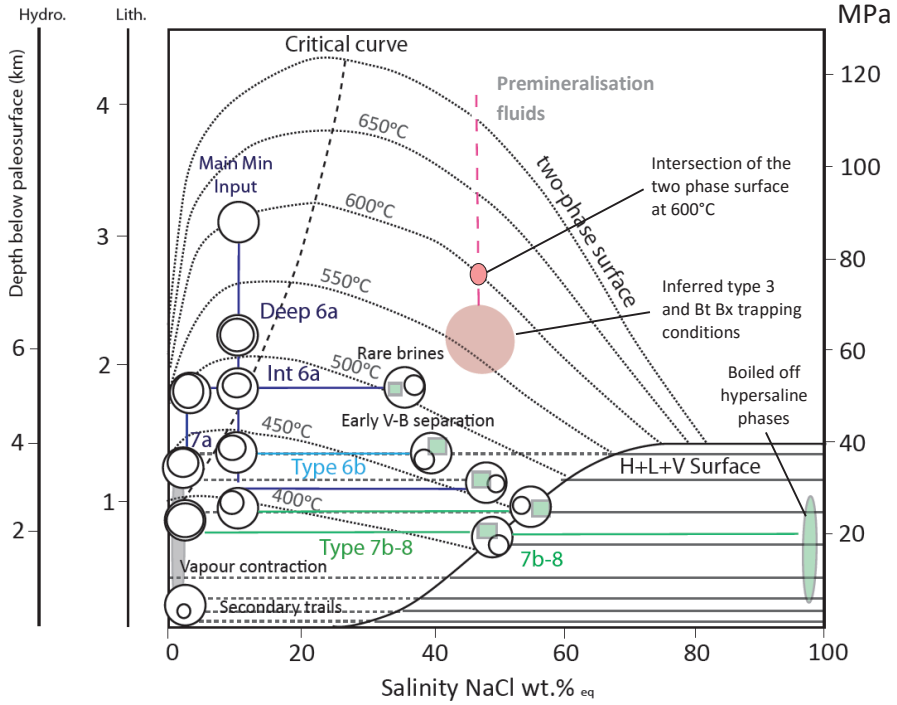


Figure 5.46: Pressure versus salinity phase diagram for the NaCl-H_2O system (after Driesner and Heinrich, 2007) illustrating the evolution of pre- and main mineralisation type fluids. The two phase surface divides the single phase field at high pressures from the two phase field at lower pressures. The critical curve defines the crest of the two phase surface and represents the locus of critical points for fluids of different salinities. Premineralisation stage fluids were generated by high pressure exsolution of brine from a magma. Main mineralisation stage fluids result from a second stage of fluid exsolution that commenced during the development of each type 5 vein halo. Aqueous, intermediate density fluids forming deep type 6a veins crossed the critical isochore from the vapour-like side to the liquid-like side trapping first A_V/A_{ID} inclusions then primary A_L inclusions in the shallow level type 6a veins and lower temperature type 6b veins. The density of these primary inclusion assemblages is similar with vapour fractions controlled by fluctuations in P-T conditions during repeated fracturing and annealing. Depressurisation of the ascending fluids led to the progressive boiling of the contracting liquid-like fluids leading to the subsequent formation of type 6b, 7 and 8 veins containing increasingly abundant coexisting brine and vapour inclusions. Dense brines recorded in type 8 veins that show similar microthermometric properties to those recorded in type 3 veins, biotite breccias and some anhydrite breccias are likely produced by phase separation at lower P-T. However, these fluids may also be related to the input of new magmatic brines into the system during the latter stages of crystallisation. In these cases accumulated concentrations of Cl, built up by prolonged degassing of low salinity liquids, may have been exsolved (c.f. Cline and Bodnar, 1991).

Fluid inclusion microthermometric data and the presence of rare type 3 veins cutting main mineralisation veins associated with younger intrusions provide strong evidence that each intrusive cycle commenced with the exsolution of premineralisation hypersaline solutions. However, the possibility that the TMC underwent extensive deposit-wide biotitisation as a result of degassing of the underlying magma chamber cannot be ruled out (Cannell, 2004; Klemm *et al*., 2007; Vry, 2010). Premineralisation veins and breccias commonly contain overprinting salt-undersaturated inclusions that have salinities of 5-8 wt.% $NaCl_{eq}$ and predominantly homogenise at higher temperature (Figure 5.6). These fluids are interpreted to be main mineralisation type fluids exsolved at greater depth following the final emplacement of each intrusion.

5.5.2 Main Mineralisation Type Vein and Breccia Development

As discussed in the previous chapter, the main mineralisation type veins and breccias developed within and surrounding several intrusions in short-lived pulses of hydrothermal activity immediately following intrusion emplacement. Cannell *et al*. (2005) and Klemm *et al*. (2007) stated that inclusions in each vein type are similar across the deposit indicating a single, deposit-wide evolution in fluid chemistry. However, Vry (2010) suggested that veins associated with each intrusion exhibit distinct physical and chemical characteristics. In this study, similar microthermometric (e.g. Figure 5-38-40) and major element ratios (e.g. Figure 5.41) are recorded for primary inclusion in similar vein types in each temporally separate mineralised halo suggesting that each main mineralisation vein halo formed as a result of the exsolution and evolution of similar fluids from the parental magma chamber. However, subtle variations in inclusion salinities, homogenisation temperatures and densities and minor and trace element signatures associated with each inclusion (e.g. Figure 5.26, 5.42) confirm that each main mineralisation halo evolved separately.

The anhydrite breccias contain primary magmatic brine inclusions that are compositionally similar to those present in the premineralisation type veins and breccias. These also have similar salinities to brine inclusions in the type 4a veins but, instead of displaying homogenisation by halite dissolution, these inclusions have similar vapour bubble disappearance and halite dissolution temperatures of 300-360^{o}C (Figure 5.7). This is possible

if there was a significant pressure drop during brecciation. As reported by Vry (2010), fluid inclusions in the type 5 veins document a distinct change in fluid properties, with a switch to abundant A_L and A_{ID} inclusions with a range of densities (0.67-1.0 g/cm^3) and salinities (1.2-25.8 wt.% $NaCl_{eq}$). The A_{ID} inclusions typically homogenise at higher temperatures than the type 5 brines and are similar to those measured in the type 6a veins, with high concentrations of Fe, Cu, Ni, As, Mo, Sn and Sb relative to Na (Table 5.3). The high metal concentrations of these fluids may be derived from the digestion of previously deposited sulphides, but may be attributed to the enhanced partitioning of metals into single-phase, vapour-like A_{ID} fluids at depth following extensive fracturing of the overlying rock column during anhydrite breccia formation (Figure 5.45D).

Vein distribution data provide strong evidence that type 6a veins represent feeder veins for outboard chalcopyrite-rich type 6b-8 veins (e.g. Figure 4.21) and therefore should contain parental fluids for the outboard vein types. Consistent with this, primary fluid inclusions in the deepest type 6a veins record the highest homogenisation temperatures (~500°C: Figure 5.9), whereas inclusions in outboard type 6b and type 8 veins homogenise at lower temperatures and display clear evidence of progressive fluid boiling (Figure 5.47).

Type 6a veins are dominated by primary A_{ID} inclusions that have relatively uniform bulk salinities of 5-8 wt.% $NaCl_{eq}$ (e.g. Figure 5.25B) and compositions (Figure 5.41) across the deposit. These parental fluids are similar to ≤7.5 wt.% $NaCl_{eq}$ parental fluids identified in two other studies (Cannell, 2004; Vry, 2010) but are considerably less saline than 12 wt.% $NaCl_{eq}$ parental fluids recorded by Klemm *et al*. (2007). The rarity of fluids with similar intermediate salinities (e.g. Figure 5.47) suggests that the apparent parental fluids identified by Klemm *et al*. (2007) were produced by the mixing of intermediate density fluids with small amounts of hypersaline fluids that condensed at high temperature (>400°C). In the deepest type 6a veins, these inclusions yield the highest minimum trapping pressures of any main mineralisation stage inclusions (40-60 MPa: Figure 5.23). The overlying host rock would have a density of ~2.8 g/cm^3 (i.e. basaltic andesite) equating to a minimum lithostatic depth estimate of 1.4-2.0 km and a minimum hydrostatic depth estimate of 4.0-5.6 km for the deepest type 6a veins.

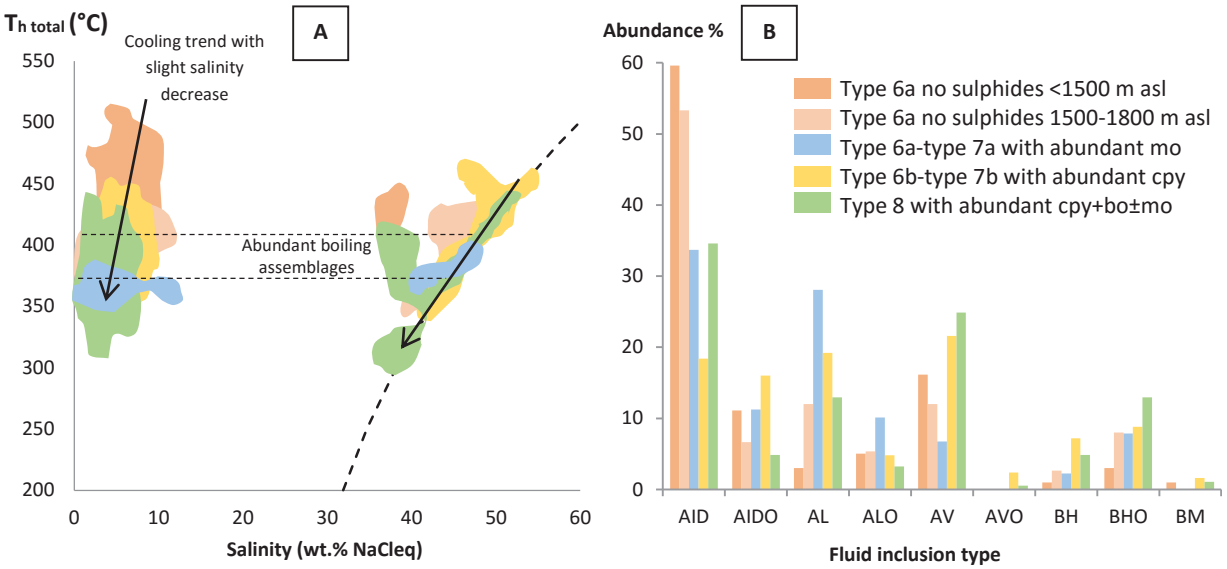


Figure 5.47: Summary of microthermometric data showing the temperature-salinity evolution of fluids in type 6a-8 veins. (A) Homogenisation temperature (T_h) versus salinity plot for all recorded primary inclusions. (B) Relative abundances of different fluid inclusion types recorded in each vein type. Type 6a and 6b veins are subdivided based on depth and contained sulphides. The apparent decrease in the salinity of the primary A_{ID} inclusions may be an artefact of decreasing CO_2 content resulting in less depression of ice melting as a result of clathrate formation. Due to a lack of clathrate in the deepest A_{ID} inclusions this trend is more likely to be a manifestation of the boiling off of hypersaline fluids in response to pressure fluctuations.

Primary A_{ID} inclusions in the deepest type 6a veins proximal to the North Central Diorite have low densities of ~0.4 g/cm^3 and homogenise to vapour, whereas primary A_{ID} and A_L inclusions in the shallower type 6a veins are compositionally similar (Figure 5.41-5.42) but have higher densities of ~0.65 g/cm^3 (Figure 5.23) and predominantly homogenise to liquid (Cannell, 2004; Klemm *et al.*, .2007; Vry, 2010; This study). Based on this, it is thought very likely that vapour-like, supercritical fluids were produced at depth and contracted during ascent to form liquid-like supercritical fluids, trapped in the form of A_{ID} and A_L inclusions (Figure 5.46). This is supported by density versus trapping pressure data for inclusions in the type 6a veins (Figure 5.23). A change in A_{ID} inclusion homogenisation mode was documented in type 6a veins at elevations of ~1800 m asl proximal to the North Central Diorite. In these samples, the A_{ID} inclusions homogenise by supercritical behaviour, have salinities of 4.8-6.7 wt.% $NaCl_{eq}$ and yielded minimum trapping pressures of 27-35 MPa. These characteristics suggest that ascending vapour-like fluids in each system evolved below the ~6 wt.% critical isochore and crossed the critical isochore in response to decreasing pressure at relatively constant temperatures of ~470°C (Figure 5.46).

Klemm *et al*. (2007) proposed a fluid evolution pathway in which intermediate density fluids were exsolved and depressurised so that they entered the two phase field (Figure 5.48A). This pathway explains the presence of abundant A_{ID} inclusions in the deep 6a veins but can only produce the initial stage of vapour contraction if the fluids initially cool above the two-phase surface (e.g. Cline and Bodnar, 1994; Heinrich *et al*., 2004; Heinrich, 2007: Figure 5.48B). This is likely to have occurred relatively rapidly following the final emplacement and crystallisation of each intrusion. The direct exsolution of vapour-like fluids is supported by a lack of clear evidence for phase separation in the deepest type 6a veins (e.g. Figure 5.9-5.10) as well as the apparent occurrence of primary A_{ID} inclusions coexisting with silicate melt inclusions (Cannell, 2004). Furthermore, the A_{ID} inclusions have higher concentrations of Mn/Na and Fe/Na and lower relative concentrations of Cu/Na and As/Na when compared to the partitioned vapours in the shallower type 6a-8 veins (Figures 5.34, 5.41-5.42). This suggests that the parental A_{ID} fluids are not the product of deep vapour-brine partitioning.

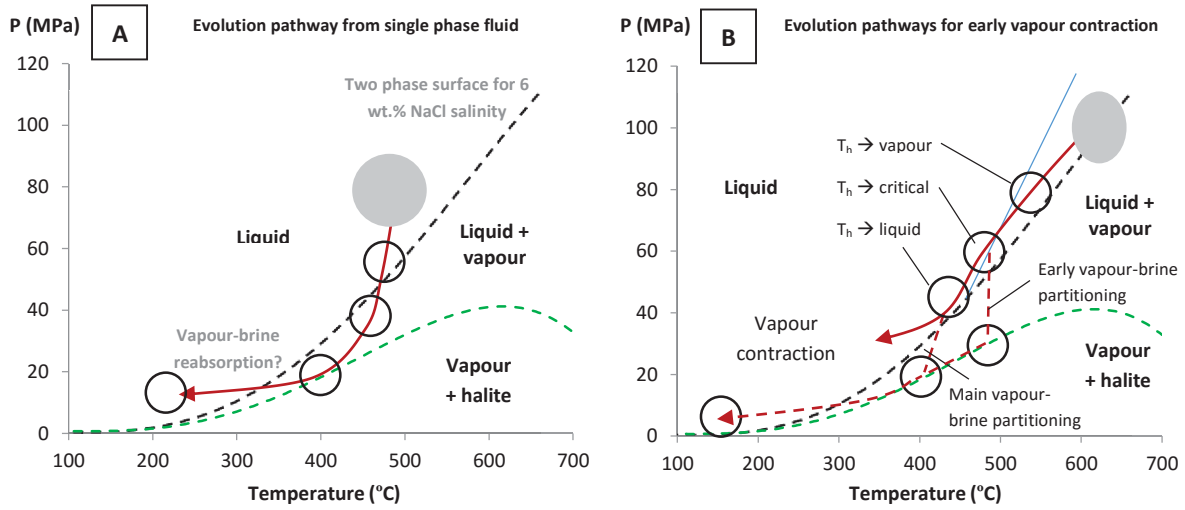


Figure 5.48: Pressure (MPa) versus temperature plot showing alternative evolution pathways for main mineralisation type fluids based on the vapour limb of the solvus of the three-dimensional H_2O-NaCl phase diagram of Driesner and Heinrich. (2007). Dotted black line = Two phase surface for a 6 wt.% NaCl fluid. Dotted green line = the halite-liquid-vapour surface. (A) Overall fluid pathway for main mineralisation type fluids according to Klemm *et al*. (2007). (B) Alternative evolution pathway based on early vapour contraction trend for the intermediate density parental fluids in the type 6a veins. Temperature decrease dominates first followed by pressure decrease with circles showing the entrapment conditions of primary inclusion populations recorded in this study. The partitioned vapours and brines are plotted on evolution projections (dotted lines) as they no longer fall on this salinity slice. The approximate trend of the 6 wt.% salinity critical isochore is shown in blue above the two phase (liquid+vapour) surface. The inclusions trapped in the wedge between this and the two phase surface will homogenise to vapour.

The brine distillation model of Klemm *et al*. (2007: Figure 5.48A) requires a fluid evolution path that is initially dominated by decreasing pressure. However, primary brine inclusions in the type 6a veins record an initial evolution path that is dominated by temperature decrease. The entrapment of different primary inclusion types within single type 6a-6b veins is best explained by the fact that the wedge between the two phase surface and critical isochore is narrow so that the fluids evolving along this proposed evolution path (Figure 5.48B) can easily cross over the critical isochore and two-phase surface in response to small changes in P-T conditions. Small pressure drops may cause the parental intermediate density fluids (within the wedge) to condense small amounts of brine. If the partitioned brines remain separated from the low density vapour-like fluids, they will plot along an apparent trend of decreasing salinity with decreasing homogenisation temperature. This general trend is recorded for primary fluids inclusions in the type 6a-6b veins (Figure 5.47A).

Vry (2010) stated that the development of type 6b veins occurred as a continuation of vein development from type 6a to 7a veins. Consistent with this, LA-ICP-MS data reveal clear compositional similarities between inclusions in the type 6a and type 6b veins (Figure 5.34-5.36). Despite this, the presence of type 6a veins developing into type 7a veins (Chapter 4) indicates that type 6b vein development can be omitted and may even occur after the local development of type 7a veins. Fluid inclusions in the type 6b veins have a broad range of salinities, homogenisation temperatures (Figure 5.15), densities (Figure 5.23) and compositions (Figure 5.41-5.42) indicative of the entrapment of multiple fluid generations under variable P-T conditions. For example, moderate salinity (~20 wt.% $NaCl_{eq}$) inclusions (Figure 5.15) are interpreted to represent fluids produced by the mixing of partitioned hypersaline fluids with low salinity fluids (e.g. Cannell, 2004; Vry 2010: Figure 5.23). The bimodality in Mo and Cu concentrations (Figure 5.36) is suggestive of the presence of both metal-rich and spent ore fluids. SEM-CL reveals that quartz crystals in type 6b veins are commonly dull, with lighter streaks of brighter alteration (e.g. Figure 5.14C). This is possibly the result of preferential partitioning of Al in quartz from fluids that became increasingly acidic (c.f. Rusk *et al*., 2008) as the fluids cooled. Vry (2010) stated that the formation of Mo-rich type 6b veins was linked to the influx of late, Mo-rich magmatic brines. However, such inclusions are rare (Figure 5.36) suggesting that Mo-rich type 6b veins are more likely to represent reopened or overprinted type 6a veins.

Unlike in the type 6a veins, most primary A_{ID} and A_L inclusions in the type 6b veins were trapped on the liquid-like side of the critical isochore (Figure 5.46) and sometimes occur in the same growth zones as A_V and B_{HO} inclusions that homogenise at similar temperatures (e.g. Figure 5.15). This implies the A_{ID} and A_L inclusions were generally being trapped very close to the two-phase surface. In the type 6b veins apparent boiling assemblages document a range of trapping temperatures between 370 and 420°C and typical trapping pressures of ~30 MPa (Figure 5.48B). Following phase separation, cooling under low confining pressure would have caused the partitioned vapours to contract small amounts of liquid leading to subsequent entrapment of low salinity A_L inclusions with densities of approximately 0.85 g/cm^3 at temperatures of 300°C and 0.97 g/cm^3 at temperatures of ~200°C (e.g. Anderko and Pitzer, 1993; Fournier, 1999; Driesner, 2001; Heinrich, 2005). These inclusions are present overprinting primary assemblages in all the main mineralisation veins.

Vry (2010) suggested that the formation of sulphide-dominated type 7a-7b veins must have occurred in response to a distinct change in fluid properties. In the transitional 6a-7a veins the abundant A_L inclusions (Figure 5.47) have similar salinities and overlapping but slightly higher densities than the A_{ID} inclusions in the shallow type 6a veins (Figure 5.11-5.12, 5.23). If these fluids are related, near-isobaric cooling can account for this transition in fluid properties (Figure 5.49). Previous studies have demonstrated that silica solubility in hydrothermal fluids is strongly controlled by temperature and pressure and that quartz is readily soluble in low-moderate salinity fluids at <375°C and <30 MPa that cool along an isobaric path (e.g. Anderson & Burnham, 1967; Hemley *et al*. 1980; Fournier *et al*. 1982; Xie & Walther 1993; Fournier, 1998; Akinfiev and Diamond, 2009; Steele MacInnis *et al*., 2012). Given this, the A_L-dominated type 7a veins may have formed by cooling of type 6a fluids at higher constant pressures than the type 6b veins (Figure 5.49). This may explain the lower average homogenisation temperatures of primary inclusions in the transitional 6a-7a veins and the rarity of boiling assemblages compared to the type 6b veins (Figure 5.47).

No fluid inclusions were measured in the chalcopyrite-dominated type 7b veins. However, the most sulphide-rich (~60% chalcopyrite) type 6b vein contains abundant brine inclusions and low salinity (1-2 wt.% $NaCl_{eq}$) A_V inclusions that homogenise at ~370°C and constrain trapping pressure to ~20 MPa. Phase separation and salinity variations have been shown to

strongly influence quartz solubility by affecting the density and dielectric constant of water (c.f. Cline *et al*., 1992; Xie and Walther 1993; Schmulovish *et al*., 2006). Quartz solubility is lower in low density vapours than in moderately saline fluids which, combined with the different flow dynamics of vapour and brine, can result in considerable silica remobilisation (Bischoff and Rosenbauer, 1989; Fontaine and Wilcock, 2006). Recent experimental studies have shown that quartz is readily soluble in high salinity fluids at 350°C and 30 MPa, with a maximum solubility at ~25 wt.% $NaCl_{eq}$ (Steele MacInnis *et al*., 2012). Considering this, it is possible that the formation of abundant type 7b veins was partly controlled by the cooling of partitioned, Cu-rich, silica-undersaturated brines produced by boiling of moderate-low salinity parental fluids in the type 6b veins in each mineralised centre.

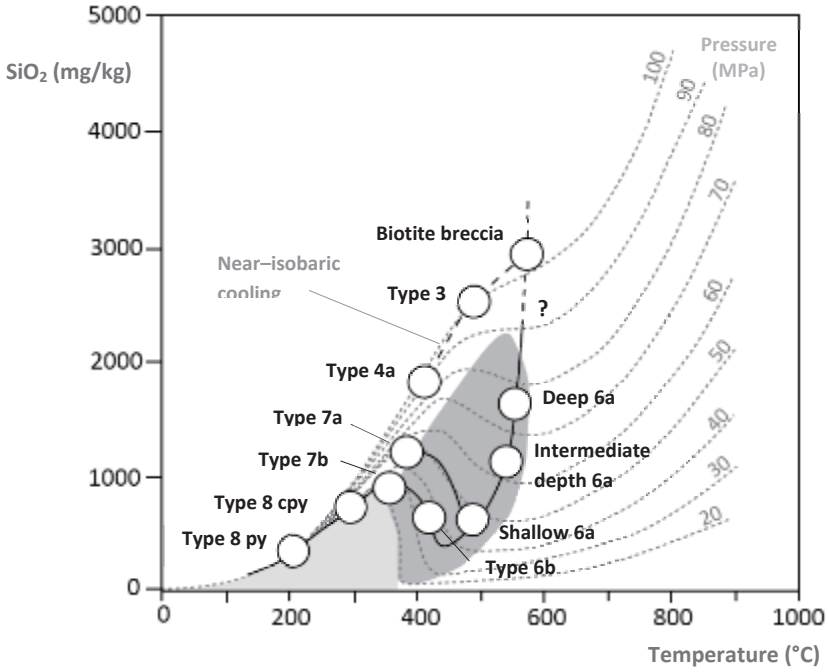


Figure 5.49: Quartz solubility in pure water as a function of temperature and pressure showing the general interpreted fluid evolution pathways for the development of pre- and main mineralisation vein types (white circles) in each mineralised centre. An initial reduction in pressure in the cooling fluids decreased quartz solubility generating quartz-rich type 6a-6b veins in the grey shaded area. Fluid cooling at near-constant pressure can then increase quartz solubility resulting in the formation of type 7a and/or type 7b veins. Continued cooling and depressurisation eventually allows minor quartz precipitation to recommence in the type 8 veins. Neutralisation and reduction of fluids associated with fluid interactions with the TMC leads to the outward formation of sulphate and pyrite dominated type 8 veins. Adapted from Fournier (1998).

Type 8 veins contain fluid inclusions with similar compositions and salinities to those present in the type 6b veins (Figure 5.34). Consistent with the study of Vry (2010), the type 8 veins contain abundant brine inclusions that either occur independently or with clearly

coexisting vapour inclusions. Apparent boiling assemblages constrain trapping temperatures fairly tightly to between 360 and 390°C (e.g. Figure 5.25E). These temperatures are consistent with the presence of sericitic alteration halos surrounding the type 8 veins, which form in response to increasing fluid acidity as a function of magmatic sulphur disproportionation and acid dissociation at temperatures below 400°C (e.g. Giggenbach, 1992; Rye, 1993; Ohmoto and Lasaga, 1997 Heinrich *et al*., 2004; Reed *et al*., 2005; Rusk *et al*., 2008). Trapping pressures are also well constrained to 10-25 MPa (Figure 5.23) corresponding to depths of approximately 2.5 km under hydrostatic pressure. This matches previous depth estimates of 2.5-4.0 km documented in two previous studies (Cannell 2004; Vry, 2010). Under these conditions, quartz exhibits strong retrograde solubility (Figure 5.49), which combined with neutralisation of ore fluids associated with sericitic alteration explains the switch from quartz-sulphide rich veins to outboard sulphate-dominated type 8 veins.

Boiling assemblages in the type 8 veins are produced by the phase separation of intermediate density fluids in response to pressure drops associated with brittle fracturing of the host rock at temperatures <400°C (Figure 5.48B). Similar to the type 6b veins, slight variations in primary boiling assemblages are attributed to variable P-T conditions produced by multiple episodes of localised fracturing and fracture annealing (e.g. Klemm *et al*., 2007; Vry, 2010). Cannell (2004) stated that a pronounced pressure drop occurred across the deposit at approximately 5.0 Ma in response to a switch from lithostatic to hydrostatic pressure conditions. This is extremely unlikely considering the low pressure estimates for inclusions in the type 6a-6b veins that formed significantly before this. It is suggested instead that cyclic transitions into the hydrostatic domain occurred during the evolution of each magmatic-hydrothermal pulse, perhaps with an evolution toward increasingly hydrostatically-dominated late stage veins as the system was gradually exhumed.

5.5.3 Late Mineralisation Type Vein and Breccia Development

The type 9 veins contain abundant primary brine inclusions that contain extremely high concentrations of Rb, Cs, As and Mo (Table 5.4, Figure 5.43) and rare low salinity vapours that homogenise over a broad temperature range (Figure 5.19). The absence of clear boiling assemblages and an obvious parental fluid (Figure 5.23) suggest that the brines may have been exsolved directly from the cooling magma (i.e. Figure 5.50A). This can occur at ~600°C under relatively low confining pressure (e.g. <60 MPa: Cline and Bodnar, 1994; Heinrich, 2007) possibly produced by late brecciation events and progressive deposit exhumation (e.g. Cannell, 2004; Maksaev *et al*., 2004; Camus, 2005). Low pressures of 15-30 MPa are recorded for most salt undersaturated fluid inclusions and brine assemblages (Figure 5.24), although the halite homogenising inclusions yield anomalously high average trapping pressures that greatly exceed the likely lithostatic load (e.g. Figure 5.22). These anomalously high pressures are interpreted to be the result of salt entrapment from brines boiling on the L+V+H curve. However, the generation of these hypersaline fluids as a result of the sporadic and short-lived development of supralithostatic pressure regimes during brecciation (e.g. Hezarkhani and Williams-Jones, 1998; Lai *et al*., 2007) cannot be fully discounted.

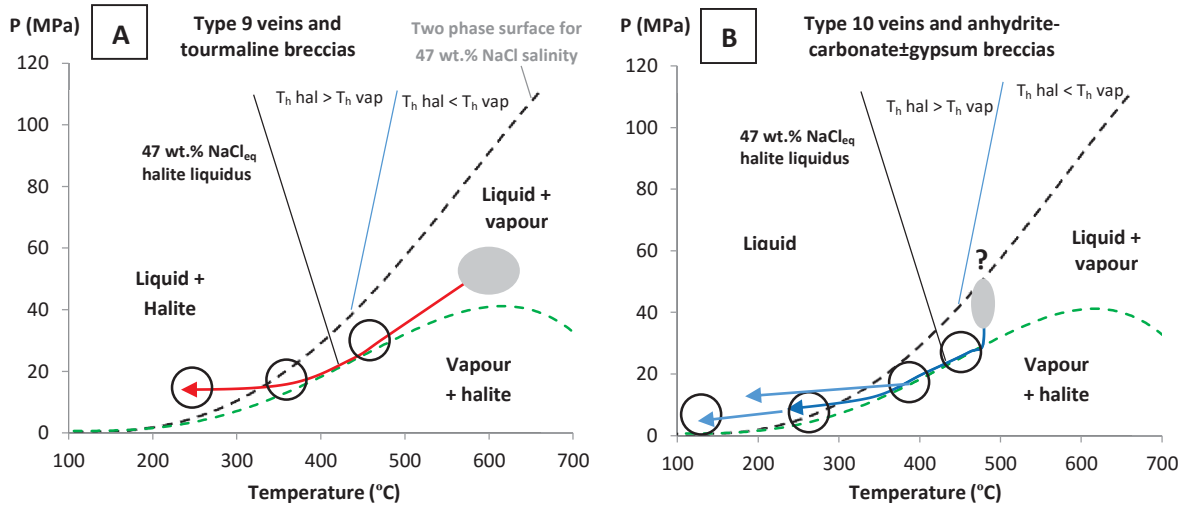


Figure 5.50: Pressure versus temperature plot showing the likely evolution pathways for late mineralisation type fluids based on the three-dimensional H_2O-NaCl phase diagram of Driesner and Heinrich. (2007). Dotted black line = Two phase surface based on a fluid with a 47 wt.% $NaCl_{eq}$ salinity. Dotted green line = the halite-liquid-vapour surface. (A) Overall fluid pathway for the generation of type 9 veins and tourmaline breccias (B) Fluid pathway for the generation of type 10 veins and anhydrite-carbonate ±gypsum breccias. The 47 wt.% $NaCl_{eq}$ halite liquidus and isochores are drawn approximately based on data from Bodnar (1994) and Cline and Bodnar (1994). Circles represent the interpreted trapping conditions of fluid inclusions recorded in this study.

In each type 9 vein sample the primary brine and vapour inclusions homogenise over a broad temperature range (Figure 5.25F) suggesting that they were trapped during rapid cooling and/or depressurisation. The rarity of boiling assemblages and presence of abundant halite-homogenising brine inclusions suggests that the fluids may have cooled at relatively constant pressure, thus departing from the liquid-vapour-halite surface (Figure 5.50A). This evolution pathway is similar to the primary fluids in the type 8 veins and may explain the switch from quartz-sulphide to sulphate-dominated type 9 veins surrounding the Braden Breccia pipe as a result of quartz undersaturation and ore fluid neutralisation (Figure 5.49). The presence of rare A_L and A_{ID} inclusions with salinities of 7-11 wt.% $NaCl_{eq}$ that homogenise at lower temperatures (Figure 5.19) and commonly occur on secondary trails are interpreted to be the product of the mixing of hypersaline fluids with partitioned vapours and/or low salinity groundwater.

The type 10 veins and anhydrite-carbonate ±gypsum breccias contain primary fluid inclusions that homogenise over a broad range of temperatures depending on host mineral (Figure 5.20) and contain highly variable concentrations of As, Mn, Pb and Cs relative to Na (Figure 5.39). SEM-CL analysis reveals that quartz crystals in the type 10 veins are commonly truncated by carbonate or sulphate crystals and microveinlets (e.g. Figure 5.21) and host to primary inclusions that are similar to those present in the type 6a veins with the exception that they contain a far greater presence of apparently coexisting brine and vapour inclusions (Figure 5.20) that yield lower trapping pressures and commonly contain elevated Mo and Cs concentrations relative to Na (e.g. Figure 5.40). Based on this, it is likely that the fluids responsible for the formation of the type 10 veins were late Mo-rich fluids that evolved along similar evolution pathways to the main mineralisation type 6b-8 fluids (Figure 5.50B). The exsolution of the intermediate density fluids following the exsolution of the type 9 brines is similar to the separate cycles of pre-main mineralisation vein formation and therefore may represent a late mega-magmatic cycle that occurred at shallower paleodepths across the entire deposit prior to the formation of the Braden Breccia pipe.

In the sulphate-dominated samples, coexisting vapour and brine inclusions are relatively rare but, in an anhydrite breccia sample, constrain trapping temperatures to approximately 350°C (Figure 5.20). Salt undersaturated inclusions occur throughout the sulphate crystals

that yield the lowest average homogenisation temperatures (Figure 5.20) and trapping pressures of any inclusions at El Teniente (Figure 5.24). Cannell (2004) identified an apparent linear relationship between inclusion salinities and homogenisation temperatures and proposed that inclusions in the type 10 veins may be produced by the mixing of low salinity (<8 wt.% $NaCl_{eq}$), low temperature (200–280°C) fluids with high temperature (up to 530°C), high salinity (60 eq. wt.% $NaCl_{eq}$) brines similar to those present in the type 9 veins.

The gypsum samples contain abundant A_L inclusions that are similar to large, 'ragged' inclusions described by Cannell (2004). The shapes of these inclusions are indicative of fluid entrapment at low temperature (Bodnar *et al*., 1985) or post-entrapment stretching (e.g., Bodnar, 2003). The A_L inclusions have similar compositions to the anhydrite-hosted inclusions, including similar Na, As, Pb and Rb concentrations (Figure 5.39) and plot along an apparent trend of increasing density that extends from the partitioned vapour inclusions in the quartz- and anhydrite-dominated samples (Figure 5.24). This suggests that the A_L inclusions may represent vapours that partitioned at depth and contracted as the fluids cooled at low pressure (Figure 5.50A). This is consistent with high (vapour-like) As/(Na+K+Mn+Fe) and B/(Na+K+Mn+Fe) ratios in low temperature liquid inclusions observed in this and a previous study, (Klemm *et al*., 2007). Klemm *et al*. (2007) stated that these vapours were produced by the fractionation of the main mineralisation stage fluids at depth. However, dating evidence and subtle differences in trace element chemistry (e.g. Figure 5.39-5.40) suggest that they are more likely produced by separate fluids that evolved along a similar evolution pathway to the main mineralisation-type fluids (Figure 5.50B).

5.5.4 Magmatic Evolution

The differences in trace element ratios in fluid inclusions hosted in similar vein types in each magmatic-hydrothermal centre (Figures 5.41-5.42) suggest that there were only subtle changes in the chemistry of the evolving parental magma during the emplacement of each intrusion. Variations in parental fluid chemistry can be attributed to changes in magma chemistry as a result of magma mixing and fractionation. For example, it has been suggested that fluid Rb and Cs concentrations can be used to assess the degree of crystallisation of a single source magma chamber in an evolving granitic system (e.g. Armbrust *et al*., 1977;

Audétat and Pettke, 2003). Rb and Cs ions are marginally larger than the K ion and therefore form slightly weaker bond energies with O when substituting into crystallising K-bearing minerals. This means that the crystallisation of K-bearing minerals will result in decreasing K/Rb and K/Cs in the residual melt and exsolving fluids (Armbrust *et al*., 1977). Caesium also exhibits relatively uniform ratios in partitioned vapours and brines, meaning that it can see through the fractionation effects of boiling to reveal the underlying magmatic controls on fluid composition.

Klemm *et al*. (2007) stated that the presence of similar Cs/(Na+K+Mn+Fe)-ratios for fluid inclusions in all the vein stages indicate that the underlying magma chamber did not undergo significant fractionation during the lifespan of overlying hydrothermal activity. However, this interpretation was based on a deposit-wide vein evolution model, meaning that early vein types associated with the oldest intrusions would have higher Cs concentrations than late vein types associated with the earlier intrusions. In this study, Cs/Na ratios are relatively uniform for parental A_{ID} inclusions in the type 6a veins from across the deposit largely due to the low concentrations of Cs in these inclusions (Figures 5.41-5.42). Despite this, previous whole rock and mineral isotopic analysis studies reveal an apparent general increase in the extent of crystal fractionation between the emplacement of the Sewell Quartz Diorite and Teniente Dacite Porphyry (e.g. Cannell, 2004; Kay *et al*., 2005; Stern *et al*., 2010; Vry *et al*., 2010; Munoz *et al*., 2012).

A clear change in fluid inclusion Cs concentrations is recorded for the stage 9 and 10 veins and breccias. In the type 9 veins, Cs concentrations are commonly an order of magnitude greater than in equivalent inclusion types from the main mineralisation type veins (Figure 5.37H; Figure 5.43). Contrary to the study of Klemm *et al*. (2007), the clearly elevated Cs concentrations are most likely explained by the release of magmatic-hydrothermal fluids from a highly fractionated magma chamber in the final stages of crystallisation. As the extent of crystal fractionation appears to be a key control on the mineral affinities of different systems (Figure 2.2), this means that the extent of magma fractionation and the evolution of the geochemically unique pulses of main and late mineralisation type fluids need to be reviewed in the following discussion section.

5.7 Conclusions

This section provides a detailed summary of the evolution of fluids at El Teniente and outlines the reasons for the development of different vein and breccia types. Veins associated with each mineralised intrusion contain similar fluid inclusion type abundances with similar microthermometric properties and compositions. These inclusions represent separate pulses of pre- and main mineralisation-type fluids that record no clear evidence for significant changes in source magma evolution. By contrast, overprinting late-mineralisation type fluids record clearly different metal affinities indicative of a late deposit-wide cycle of fluids exsolved from the fractionating magma source. The highly contrasting Mo and Cu concentrations associated with the pre-main mineralisation pulses and late-mineralisation-type fluids (Figure 5.51) means that these separate regimes need to be addressed when assessing the controls on Mo enrichment and Mo and Cu decoupling. Based on the evolution of fluids summarised in Figure 5.51 the following discussion needs to assess:

- Whether or not the evolution of parental fluids reflect changes in the underlying magma and whether these changes control metal partitioning into exsolving fluids.
- How Mo and Cu fractionate when ore fluids boil and whether these differences can decouple Mo and Cu in the main and late mineralisation-type fluids.
- How fluid chemistry changes between the type 6 and type 8 veins and how these changes are linked to metal sulphide/gangue mineral precipitation, alteration and fluid boiling from one vein to the next.
- Whether or not the type 9-10 veins are linked to another mega-magmatic cycle, produced at a shallower paleodepth in which the cycle of direct brine (+/-vapour) to intermediate density fluids is repeated in a similar fashion to each pre-main mineralisation cycle.
- The main controls on the decoupled deposition of Mo and Cu from the main mineralisation and late mineralisation fluids.

By combining this information with data from other natural and experimental systems the discussion will then evaluate the main magmatic and hydrothermal processes and variables that control the formation of Mo-rich porphyries and Mo-Cu decoupling.

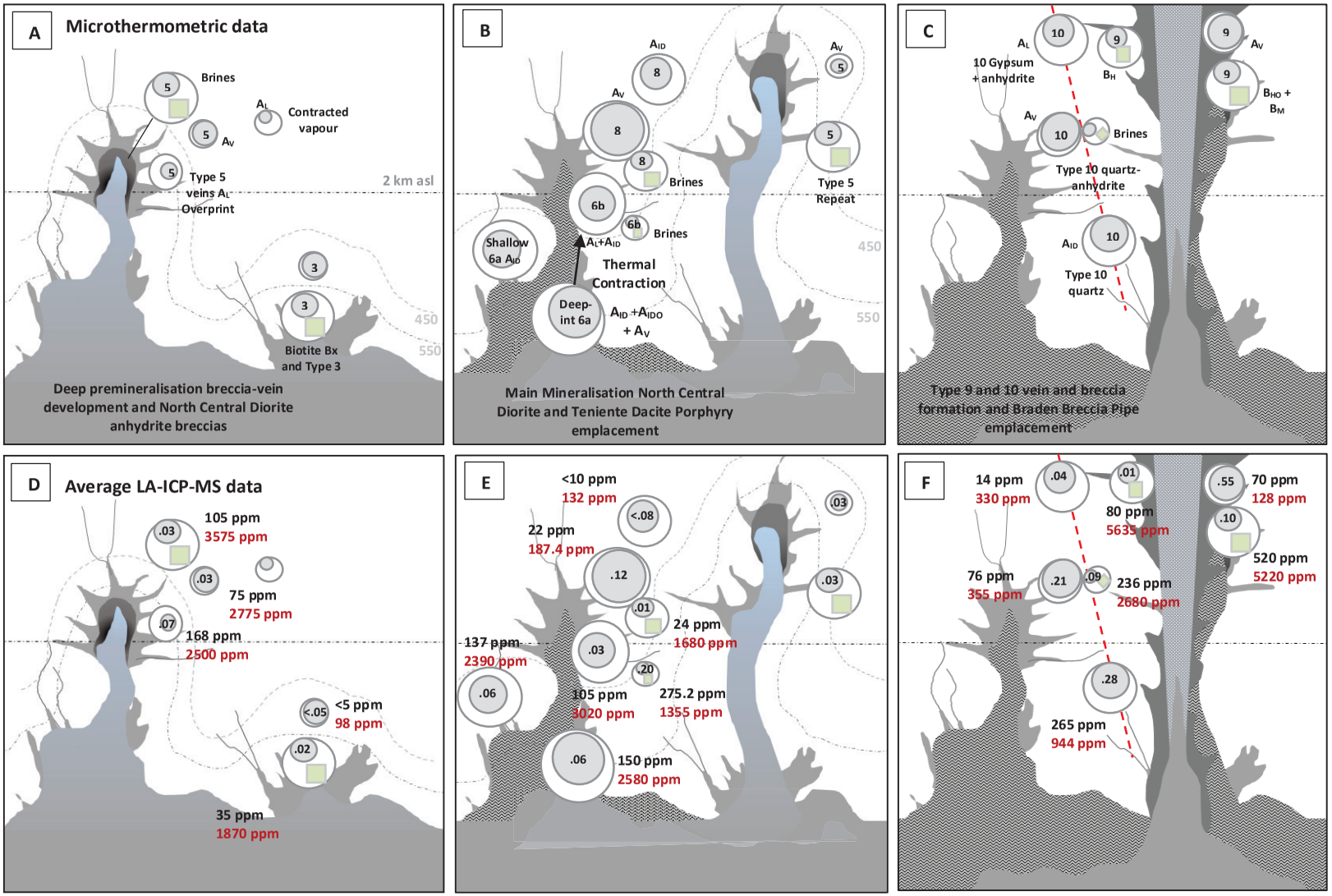


Figure 5.51. Schematic diagram summarising different magmatic-hydrothermal fluid regimes during the emplacement and mineralisation of the North Central Diorite (~5.3 Ma), the Teniente Dacite Porphyry (~5.0 Ma) and the Braden Breccia pipe (~4.6Ma). (A-C) Interpreted primary inclusion populations in each vein type at different depths with vein number shown in each vapour bubble. (D-F) Average Mo (black numbers) and Cu (red) concentrations derived from inclusion population averages. Mo/Cu ratios are shown within each inclusion. Clearly anomalous Mo and Cu concentrations were not considered.

Chapter 6. Discussion

6.1 Introduction

In the previous chapters, constraints were provided for the distribution and timing of mineralisation at El Teniente and the magmatic-hydrothermal evolution of the deposit. Based on these findings, this chapter assesses the most important processes and variables responsible for Mo transport and Mo-Cu decoupling at El Teniente. This information is presented chronologically, addressing the key differences in fluid inclusion chemistry associated with each temporally and geochemically distinct magmatic-hydrothermal fluid regime. This chapter addresses the key controls on the partitioning and solubility behaviour of Mo and Cu at El Teniente and the reasons for Mo and Cu decoupling within the system.

By comparing results from this study with data from a number of natural fluid inclusion (e.g. Ulrich *et al*., 1999, 2001; Harris *et al*., 2003; Landtwing *et al*., 2005, 2010; Rusk *et al*., 2004; Klemm *et al*., 2008; Seo *et al*., 2012) and experimental studies (e.g. Holzheid *et al*., 1994; Tacker and Candela, 1987; Candela and Bouton, 1990; Štemprok, 1990; O'Neill and Eggins, 2002; Farges *et al*., 2006a, 2006b; Rempel *et al*., 2006, 2009; Ulrich and Mavrogenes, 2008; Mengason *et al*., 2011; Zhang *et al*., 2012), this chapter then constrains the most important processes and variables responsible for the formation of Mo-rich porphyries.

6.2 Magmatic Controls on the Formation of Mo-rich Porphyries

6.2.1 Source Magma Composition and Intrusion Emplacement

Several studies have suggested that the formation of Mo-rich porphyries may rely on the presence of a source magma that is unusually enriched in Mo (Sinclair, 2007; Zhu *et al*., 2009; Pettke *et al.,* 2010). Based on total deposit S and Cu at El Teniente, a parental magma volume in excess of 600 km^3 has been estimated (Skewes and Stern, 2007). Considering a current and mined resource total in excess of 2.5 Mt Mo (Camus, 2002; Stern *et al*., 2010), this would equate to a minimum Mo concentration in the melt of 1.4 ppm considering 100% extraction and deposition of Mo by the ore fluids. Consequently, the Mo-rich nature of Cu-Mo systems appears to be the result of long-lived magmatic-hydrothermal activity and effective deposition mechanisms as opposed to the generation of Mo-rich magmas.

Primary, parental fluids in the separate pulses of main mineralisation-type fluids contain average Mo and Cu concentrations of ~0.015 wt.% and ~0.25 wt.% respectively (Figure 5.51). Given this, a total fluid mass of 17 or 38 Gt would be required to produce the aforementioned metal tonnages of Mo and Cu respectively. Assuming an average fluid density of 0.55 g/cm^3 for the metal-bearing fluids (e.g. Figure 5.23) and the inference that all transported Mo and Cu was deposited within the confines of the mineralised system, a total fluid volume of 31 or 69 km^3 would be required to produce Mo and Cu mineralisation respectively. The larger magma volume estimate for Mo suggests that considerable amounts of Mo may be hosted at depth at El Teniente, or that more Mo was transported beyond the system confines.

The close association of Mo and Cu mineralisation with each intrusion at El Teniente (Figure 4.2-4.3) indicates that these intrusions acted as effective, heated fluid conduits for multiple pulses of metal-bearing fluids (Figure 5.51A). Consistent with recent predictions (von Quadt *et al*., 2011), these mineralised systems had relatively short lifespans of <100,000 years. Consequently, the cyclic episodes of Mo and Cu mineralisation over ~1.9 Myr (Figure 4.19) would require periodic recharging and thermal rejuvenation of the underlying parental magma chamber, probably by more mafic magma. This rejuvenation explains why main mineralisation-type fluids associated with each intrusion contain similar Mo concentrations.

Petrological and isotopic studies of several other Mo-rich porphyries reveal clear evidence for the periodic recharging of parental magma chambers by multiple injections of mafic melt (e.g. Keith *et al.,* 1986; Audétat and Pettke, 2003; Klemm *et al.,* 2008; Audétat, 2010). Furthermore, Re-Os molybdenite dating reveals long-lived, episodic mineralisation in all Mo-rich porphyry subtypes including Climax-type deposits (e.g. Questa = 250 kyr: Rosera *et al*., 2013), low-F type deposits (e.g. Endako = ~9 Myr: Selby and Creaser, 2001) and Cu-Mo porphyries (e.g. El Salvador, Chile = 0.6 Myr: Zimmerman *et al*., 2014). Therefore, prolonged magmatism appears to be essential in favouring the formation of Mo-rich deposits.

6.2.2 Magmatic Controls on Mo-Cu Decoupling

At El Teniente, Mo and Cu are spatially associated with different intrusions and breccia types (Figures 4.2-4.5). Primary fluid inclusion types in each temporally separate main mineralisation halo have broadly similar compositions (e.g. Figures 5.41-5.42) suggesting that significant changes in parental magma chemistry did not occur during the emplacement of each intrusion. However, parental main mineralisation-type fluids associated with each intrusion and late mineralisation vein and breccia development exhibit clear variations in Mo/Cu ratios as well as clear variations in element concentrations including K, Cs (e.g. Figures 5.41-43, 6.1). This suggests that, although magmatic processes and variables played a negligible role in decoupling metals in each main mineralisation halo, they still may have exerted an overriding control on the extent of Mo and Cu mineralisation associated with the main and late mineralisation-type fluids.

The association of Mo and Cu mineralisation with different vein and breccia types associated with different intrusive units are described at a number of other world-class porphyry deposits (e.g. Gustafson and Hunt, 1975; Ulrich and Heinrich, 2001; Redmond *et al*., 2004; Rusk *et al*., 2008; Landtwing *et al*., 2010; Redmond and Einaudi, 2010; Sillitoe, 2010; Seo *et al*., 2012). For example, the generation of decoupled pulses of Cu- and Mo-stage ore fluids at Bingham were interpreted to be produced by variations in source magma chemistry (Redmond *et al*., 2004), and redox potential as the system evolved (Seo *et al*., 2012). This suggests that, similarly to El Teniente, changes in magma chemistry may be important in producing broad scale spatial-temporal decoupling in Mo and Cu.

Table 6.1. Summary of porphyry deposits with available fluid inclusion LA-ICP-MS data.

Deposit	Type	Depth	Mo and Cu Contents	Metal Grades	Simplified ore fluid evolution	References
Questa	Mo	3-5 km	0.64 Mt Mo - -	0.14 % Mo	Intermediate density, low salinity parental fluid underwent phase separation due to cooling and decompression. Mo was concentrated in the brine. Extent of fractionation allows for the exsolution of late Mo-rich fluids relative to early breccias.	Cline and Bodnar, 1994; Klemm, 2005; Klemm *et al.*, 2008; Seo, 2014
Cave Peak	Mo	>3 km	0.5 Mt Mo 0.17 Mt	0·25% Mo 0·05% Cu	Exsolution of an intermediate density, moderate salinity (15-19 wt.% $NaCl_{eq}$) fluid that separated to form dense brine and low density vapour. Mo deposition occurred as fluids cooled from 550 to 450°C.	Audétat, 2010
Bingham	Cu-Mo-Au	>3 km	0.81 Mt Mo 28.5 Mt Cu	0.053% Mo 0.88% Cu 0.5 g/t Au	Exsolution of an intermediate density, low salinity fluid that separated to form dense brine and S-bearing vapour. Sulphide precipitation inferred to be principally from vapour as a function of fluid cooling. The decoupled mineralisation of Mo and Cu is possibly related to compositional and fO_2 changes in the parental magma.	Redmond *et al.*, 2004; Klemm, 2005; Landtwing *et al.*, 2005, 2010; Redmond and Einaudi, 2010; Seo *et al.*, 2012
Andacollo	Cu-Mo-Au	~2 km	0.05 Mt Mo 2.43 Mt Cu	0.05% Mo 0.45% Cu 0.25 g/t Au	Dominated by brine and vapour although no definitive fluid evolution presented.	Oyarzun *et al.*, 1996; Klemm, 2005
Butte	Cu-Mo	~7.5 km	1.44 Mt Mo 35.1 Mt Cu	0.028% Mo 0.67% Cu 0.04 g/t Au	Ore deposition occurred from a single phase parental ore fluid of low salinity and intermediate density, which subsequently underwent phase separation to produce coexisting brine and vapour. Pressure played an important role in instigating Mo deposition.	Reed and Rusk, 2002; Rusk *et al.*, 2004, 2008; Buckroyd, 2008
El Teniente	Cu-Mo	> 5 km	2.5 Mt Mo 95.0 Mt Cu	0.019% Mo 0.064% Cu 0.04 g/t Au	Three distinct fluid regimes. Premineralisation…..Main mineralisation fluids were Intermediate density, low salinity parental fluids that partitioned into brine and vapour. Late Mineralisation parental fluids were either exsolved as similar single phase fluids or as brines and minor vapours. In both regimes temperature is the overriding control on metal deposition.	Klemm, 2005; Cannell *et al.*, 2005, 2007; Klemm *et al.*, 2007; Vry, 2010; This study
Los Pelambres	Cu-Mo	> 3 km	0.67 Mt Mo 26.8 Mt Cu	0.015% Mo 0.62% Cu 0.02 g/t Au	Dominated by brine and vapour although no definitive fluid evolution was presented. These may have partitioned rapidly following exsolution from the magma.	Sillitoe, 1973; Atkinson *et al.*, 1996; Frikken *et al.*, 2005
Granisle	Cu-Au	3-5 km	0.02 Mt Mo 1.8 Mt Cu	0.009% Mo 0.44% Cu 0.12 Mt Au	Dominated by brine and vapour although no definitive fluid evolution was presented.	Wilson *et al.*, 1980; Klemm, 2005
Bajo de la Alumbrera	Cu-Au	2.5 km	- 2.87 Mt Cu	- 0.53% Cu 0.67 g/t Au	Parental ore fluid was a high salinity, high-temperature brine with moderate Mo concentrations. This fluid underwent phase separation generating even higher salinity brines and coexisting vapours. Cu-sulphide deposition was inferred to be driven by fluid cooling.	Ulrich *et al.*, 2001; Proffett, 2003; Halter *et al.*, 2004; Harris *et al.*, 2005
Grasberg	Cu-Au	2 km	- 28.02 Mt Cu	- 0.6% Cu 1.05 g/t Au	Dominated by high temperature brine and coexisting vapour, possibly exsolved in the two phase field.	MacDonald and Arnold, 1994; Ulrich *et al.*, 1999

Notes: Table is listed in terms of decreasing Mo grades and deposit classifications and grades are given in accordance to figures reported in the 2008 USGS Porphyry-Cu database. Table adapted from Vry (2010) and including additional information.

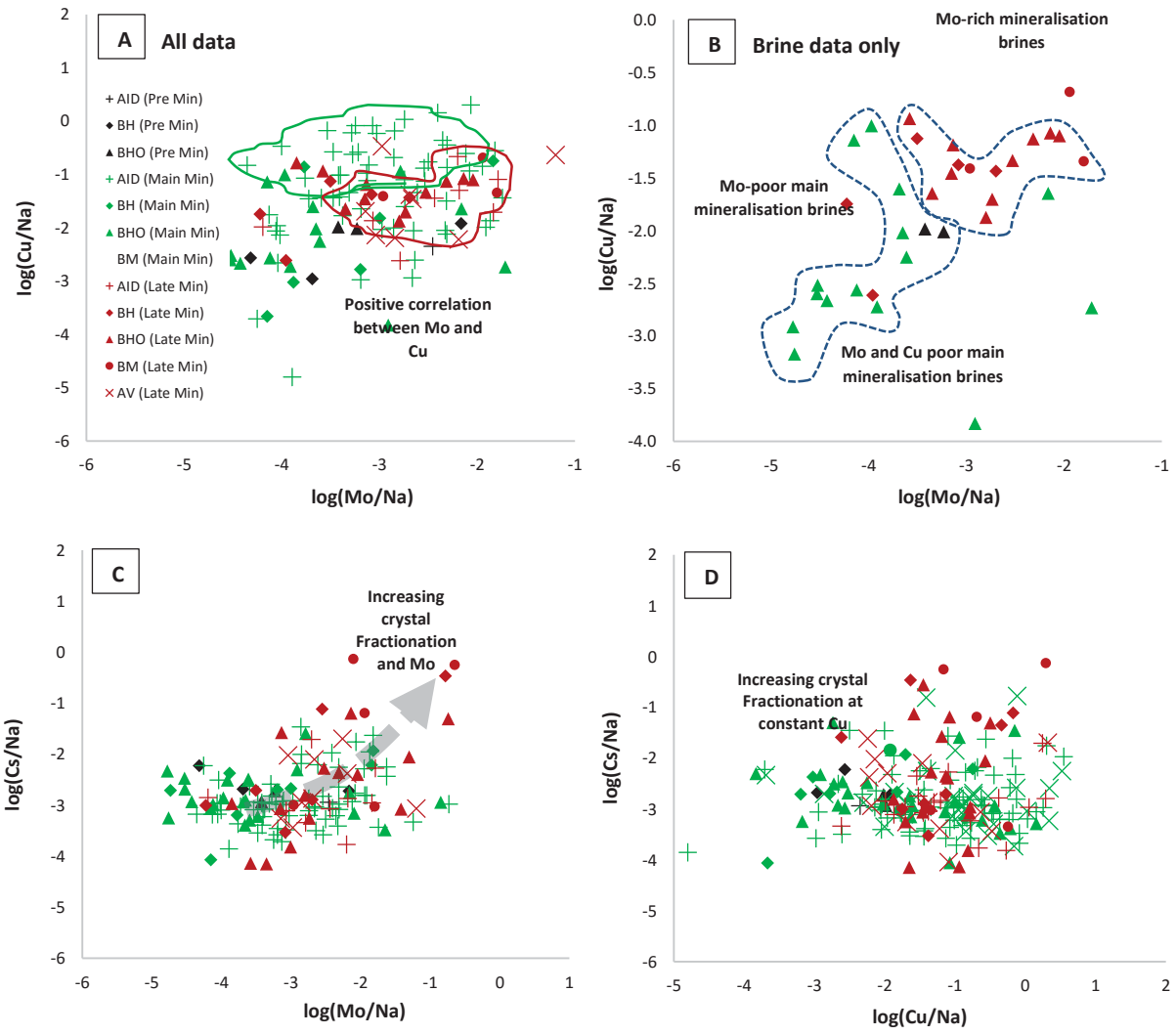


Figure 6.1: Mo, Cu and Cs versus Na concentrations for different inclusion types in the premineralisation-type (black), main mineralisation-type (green) and late mineralisation-type (red) fluid inclusion assemblages at El Teniente. Different fluid inclusion types are shown in plot D. (A-B) Average FIA Cu/Na versus Mo/Na for all fluid inclusion types in each fluid regime (A) and just primary brine inclusions (B). (C-D) Grey arrow marks the fractionation trend and positive relationship between Cs/Na against Mo/Na.

In addition to source magma generation and shallow intrusion emplacement, evolving magma chemistry may also strongly control the metal contents of exsolving fluids. To assess these controls on the formation of molybdenite-mineralising fluids the following sections discuss how the Mo-poor premineralisation-type fluids, Mo- and Cu-rich main mineralisation-type fluids and Mo-rich and relatively Cu-poor late mineralisation-type fluids (Figure 5.51) were generated and how these fluids evolved in space and through time.

6.3 Fluid Exsolution and Metal Partitioning in Mo-rich Porphyries

6.3.1 Premineralisation-Type Fluid Exsolution

The first major fluid regime associated with each mineralised intrusion at El Teniente involved the direct exsolution of hypersaline fluids prior to the final emplacement of each intrusion (Figure 5.27). Consistent with previous experimental studies (e.g. Candela and Holland, 1984; Candela 1992, 2007; Simon *et al*., 2006), the low Mo/Cu ratios of these fluids indicate that Cu was preferentially extracted from the melt by early exsolved pulses of Cl-rich fluids that accumulated in the carapace of the crystallising magma chamber and each individual porphyry intrusion. This behaviour conforms to the observation of increasing $D_{Cu}^{fluid/melt}$ and decreasing $D_{Mo}^{fluid/melt}$ values with increasing fluid inclusion salinity recorded for coexisting melt and fluid inclusions in several granitic systems (e.g. Zajacz *et al.,* 2008).

Even though absolute Cu concentrations are relatively high in the early hypersaline fluids, the premineralisation brine inclusions commonly record Cu/Na and Mo/Na ratios that are an order of magnitude lower than those recorded for the lower salinity main mineralisation fluids (Figure 6.1A). This suggests that variables other than fluid Cl concentration strongly controlled the partitioning of both metals. Previous studies have demonstrated that Mo and Cu are both highly soluble in oxidised magmas that have relatively low fH_2O at pressures of ~100 MPa (e.g. Rybachikov *et al*., 1980; Khitarov *et al*., 1982; Candela and Holland, 1984; Keppler and Wyllie, 1991). The premineralisation brine inclusions yield trapping pressure estimates of 90 MPa (Figure 5.22) whereas compositionally similar brines associated with the anhydrite breccias surrounding each intrusion record far lower trapping pressures of ~25 MPa (Figure 5.22) and contain Cu and Mo concentrations that are 2-3 times higher (Figure 5.51A). This suggests that drops in pressure related to the fracturing of host rocks surrounding each intrusion may have significantly aided in the partitioning of both metals.

6.3.2 Main Mineralisation-Type Fluid Exsolution

Type 5 veins and associated anhydrite breccias record a switch from brine (±vapour) FIAs to intermediate density (Figure 5.51A-B), low-moderate salinity (average 6.5 wt.% $NaCl_{eq}$) fluids (Figure 5.9-5.10) that contain typical Mo and Cu concentrations of ~150 ppm and ~2500 ppm (Figures 5.33, 5.51E). Similar single-phase, low salinity (3–10 wt.% $NaCl_{eq}$)

parental fluids with comparable Mo and Cu concentrations are recognised at a number of other Cu-Mo porphyries (e.g., Ulrich *et al*., 2001; Williams-Jones and Heinrich, 2005; Landtwing *et al*., 2005; Audétat *et al*., 2008; Rusk *et al*., 2004, 2008; Seo *et al*., 2012, Table 6.1). For example, Mo-stage ore fluids at Bingham are interpreted to contain ~200 ppm Mo and ~2000 ppm Cu respectively (Seo *et al*., 2012). Low-moderate salinity ore fluids (5–15 wt.% $NaCl_{eq}$) have also been recognised in Climax type (e.g. Climax: Hall, 1974; Henderson: Carten, 1987; Seedorf and Einaudi, 2004; Questa: Bloom, 1981; Cline and Bodnar 1994; Klemm *et al*., 2008; Cave Peak: Audétat, 2010) and Low-F type (e.g. Endako: Selby and Creaser, 2001) porphyry Mo deposits. These fluids also contain comparable Mo concentrations to those at El Teniente (e.g. 216 ppm at Cave Peak: Audétat, 2010; and 70 ppm at Questa: Klemm *et al*., 2008). These results suggest that the deep exsolution of intermediate density fluids with relatively low Mo and Cu concentrations may favour the formation of Mo-rich porphyries.

The A_{ID} inclusions in the deepest type 6a veins record higher homogenisation temperatures (>480°C) but lower trapping pressures (>50 MPa) than the premineralisation inclusions (Figure 5.23) suggesting that they were exsolved following thermal recharging of the parental magma chamber but drops in pressure associated with localised fracturing and anhydrite breccia formation (Figure 5.51). The rarity of reverse crosscutting vein relationships (Figure 4.17) indicates that each intrusion underwent relatively rapid thermal contraction following anhydrite breccia formation. This would have led to progressive deepening of the fluid-melt partitioning surface resulting in the deep exsolution of fluids with higher fH_2O and lower Cl/H_2O ratios (Figure 5.51B). Previous studies have demonstrated that $D_{Mo}^{fluid/melt}$ values increase with decreasing salinity (Keppler and Wyllie, 1991), increasing fluid temperature and pressure (e.g. Khitarov *et al*., 1982; Webster, 1997; Bai and Koster van Groos, 1999) and increasing fH_2O of vapour-like fluids (e.g. Ulrich and Mavrogenes, 2008; Audétat, 2010). Therefore, this may explain the strong association of Mo with the deepest emplaced porphyries (Figure 2.4, Table 6.1).

Based on an initial Mo concentration of 2.5 ppm in the parental source magma and the assumption that Mo was not significantly sequestered by early crystallising phases and premineralisation fluids, 80-90% crystal fractionation of a fluid saturated magma would

generate a residual melt containing 9.0-11.0 ppm Mo (e.g. Audétat and Pettke, 2003). If these assumptions are valid, a $D_{Mo}^{fluid/melt}$ value of 13.6 to 16.5 would be required to produce a single-phase parental ore fluid with an average Mo concentration of 150 ppm (Figure 5.51E). This estimate correlates with the most conservative $D_{Mo}^{fluid/melt}$ values calculated for coexisting melt and fluid inclusions at the Rito del Medio pluton, New Mexico (14-23: Zajacz *et al.,* 2008) and the Cave Peak Climax type Mo deposit (17-20: Audétat, 2010) but is higher than $D_{Mo}^{fluid/melt}$ values of 0.8-7.2 calculated for coexisting silicate melts and aqueous fluids synthesised at 750°C and 1-2 kbar pressure (Candela and Holland, 1984; Keppler and Wyllie, 1991). The similarity in $D_{Mo}^{fluid/melt}$ values recorded for barren and Mo-rich systems suggests that the mineralisation potential of granitic systems strongly hinges on the extent of crystal fractionation prior to water saturation (e.g. Audétat, 2010).

Main mineralisation-type parental fluids contain Cu concentrations that are roughly equivalent to those recorded in the premineralisation brines (Figure 5.51D-E) even though salinities are approximately seven times lower. This suggests that factors other than Cl concentration must be responsible for maintaining relatively high $D_{Cu}^{fluid/melt}$ values. Most measured element concentrations are similar in the pre- and main mineralisation-type fluids (e.g. Figures 5.31-5.32) suggesting that other fluid components enhanced the partitioning of Cu. The lack of CO_2 observed in this and previous studies (Cannell, 2004; Klemm *et al*., 2007; Vry 2010) suggests that Cu was not partitioned into carbonic solvents as has been suggested for other Cu-rich systems (Pokrovski *et al*., 2008; Wilkinson, 2013). By contrast, the abundance of sulphides in the main mineralisation veins suggests that there may have been a pronounced increase in sulphur contents of the exsolving fluids. Previous experimental studies show that $D_{Cu}^{fluid/melt}$ values can undergo a five-fold increase in the presence of S-bearing fluids, possibly due to the formation of CuHS complexes (e.g. Shea and Helz, 1988; Helz *et al*., 1993; Thompson and Helz, 1994; Mountain and Seward, 1999, 2003; Simon *et al*., 2006; Seo *et al*., 2009). This suggests that the shallow exsolution of high salinity fluids and the deep exsolution of S-rich fluids can both favour the formation of Cu-rich porphyry deposits.

6.3.3 Late Mineralisation-Type Fluid Exsolution

The late mineralisation veins and breccias are responsible for the most Mo-rich drillcore intervals (>0.06 wt.% Mo) and contain fluid inclusions with the highest Mo concentrations and Mo/Cu ratios (Figure 5.38D, 5.40D). Unlike the main mineralisation samples, the type 9 veins are dominated by high salinity brines and coexisting vapours (Figure 5.19) that lack of a clear parental, intermediate density fluid (e.g. Figure 5.24). This suggests either that phase separation had already occurred at depth so that such parental fluids are not observed at the current mining level or that the brines were exsolved directly in the two phase field, possibly in response to considerable pressure release during tourmaline breccia formation and faulting surrounding the Braden Breccia pipe (Figure 5.51).

Abundant B_{HO} and B_M inclusions yield an average Mo concentration of 520 ppm (Figure 5.35C) and Na concentrations that are typical of the most enriched brine inclusions present in porphyry Cu-Mo and Climax-type porphyry Mo systems (Figure 6.2C). If these hypersaline fluids were exsolved directly from a parental magma with typical Mo content, an extremely high $D_{Mo}^{fluid/melt}$ value of ~33 would be implicated, which exceeds previous estimates of 17-20 made for the Cave Peak Climax-type deposit (Audétat, 2010). Consistent with previous experimental data this implies that Mo may be strongly partitioned into high salinity brines (Webster, 1997). Alternatively, it could be explained by a considerable increase in the Mo content of the residual magma, which can be produced by minor degrees (1-2%) of crystal fractionation during the final stages of magma differentiation (Audétat and Pettke, 2003).

Even though Mo/Cu ratios are extremely low in the type 9 brines (Figure 5.40D) they still contain similar high Cu concentrations to the upper end of the range recorded for the main mineralisation stage parental fluids and partitioned brines (Figure 5.38A). The late partitioning of Cu-rich brines is consistent with general trends of increasing fluid salinity and fluid metal contents with time calculated for crystallising silicate magmas at <1.3 km depth (Cline and Bodnar, 1991). This means that Cu partitioning is also strongly controlled by extent of crystal fractionation as well as fluid salinity (Table 2.3; Candela and Holland, 1984; Simon *et al*., 2006). Similar high Cu and Na concentrations recorded in brine inclusions from highly fractionated porphyry Mo systems (Klemm *et al*., 2008; Audétat, 2010; Figure 6.2F).

The type 10 veins and breccias contain inclusion population that are analogous to those present in the main mineralisation samples (e.g. Figure 5.20), including apparent parental fluids represented by A_{ID} inclusions. This suggests that the type 10 fluids followed similar evolutionary paths to those in the main stage cycles (e.g. Figure 5.50). However, vein crosscutting relationships, elevated Mo and Cs concentrations (e.g. Figure 6.2E) and low Cu concentrations (Figure 5.51F) confirm their late mineralisation association. In the type 10 samples the parental A_{ID} inclusions record a higher average Mo concentration than the main mineralisation parental fluids (265 ppm: Figure 5.51F). The similar compositions, salinities and temperatures of these inclusions relative to the main mineralisation samples (Figure 6.2) imply these fluids followed very similar P-T-X paths. Consequently, it is suggested that the increased Mo content in these fluids is due to increasing Mo in the residual melt prior to fluid exsolution. The salt-undersaturated inclusions in the late mineralisation veins record similar Mo and Na concentrations to those measured at Questa and Cave Peak (Figure 6.2E), which are interpreted to have been produced by the deep exsolution of similar intermediate salinity fluids from a highly evolved magma (Klemm *et al*., 2008; Audétat, 2010).

Assuming $D_{Mo}^{fluid/melt}$ values of 14-17 still apply at the late stage, it is possible that the parental magma chamber produced a residual melt with a Mo concentration of 16-20 ppm. This is approaching the top end estimate of ~20 ppm Mo concentrations recorded for highly fractionated pegmatite liquids (Zajacz *et al*., 2008; Audétat, 2010) The lower estimate of 16 ppm is more realistic and is consistent with models for fluids exsolved from a residual melt phase created by ~95% crystallisation of a fluid saturated silicate magma with an initial Mo concentration of 2.5 ppm (Audétat and Pettke, 2003). It is possible that the evolving magma chamber had undergone a lower degree of magma fractionation, which would require increasing $D_{Mo}^{fluid/melt}$ values. This may have occurred as a function of the preferential extraction of Mo during sudden pressure release from the parental magma linked with fracturing of the host rocks associated with the formation of the Braden Breccia pipe. Alternatively, the preferential partitioning of Mo may be explained by the increased acidity of the late mineralisation fluids, as documented by a marked increase in the extent of sericitic alteration associated with all type 10 samples. Increased acidity can aid Mo partitioning at 750-800°C and 1-2 kbar as a function of increased fluid *m*HCl and the favourable formation of Mo-chloride complexes (Bai and Koster van Groos, 1999).

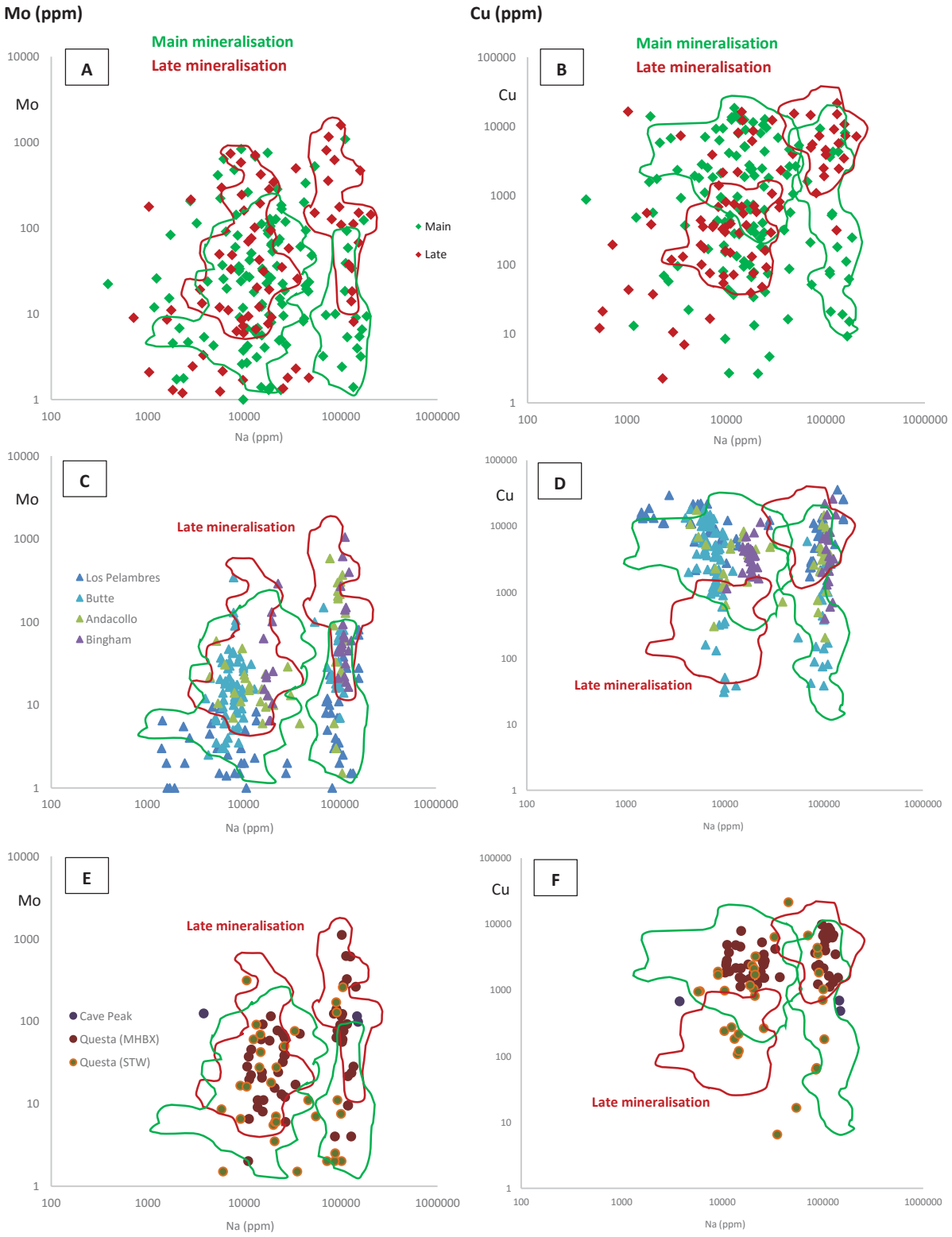
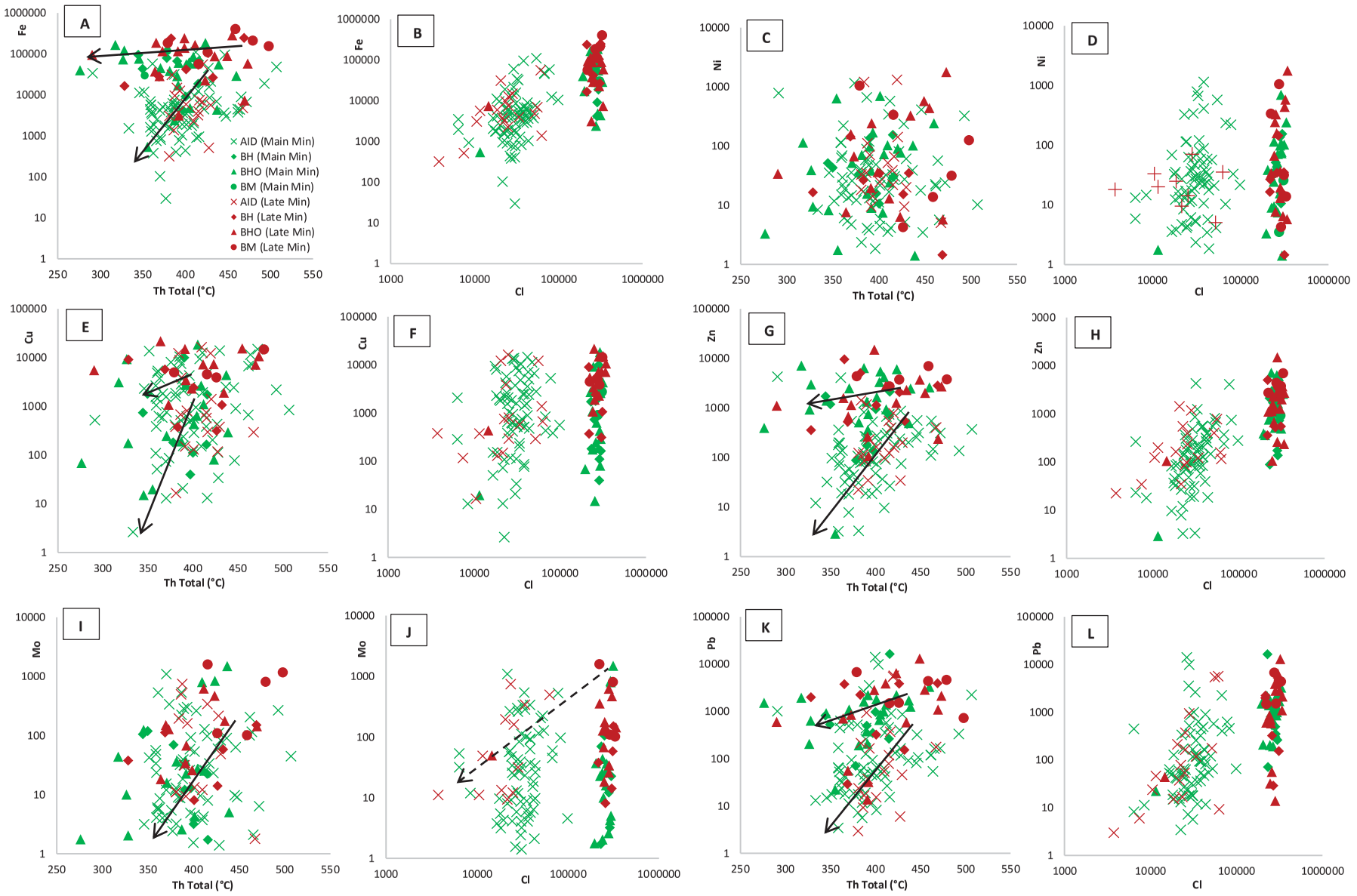


Figure 6.2: (A-B) Mo and Cu versus Na concentrations for the main mineralisation-type and late mineralisation-type fluid inclusion assemblages at El Teniente. (C-D) Comparison of fluid populations at El Teniente with inclusions measured in other Mo-Cu porphyries. (E-F) Comparison plot of fluid populations at El Teniente with inclusions measured in Mo porphyries. Main mineralisation Cu and Na concentrations show an excellent correlation with Cu-Mo porphyry data. Main and late mineralisation Mo versus Na data show an excellent correlation with porphyry Mo data.

In accordance with this, Klemm *et al*. (2007) suggested that the late mineralisation fluids represent contracted vapours produced by downward regression of fluid boiling as a function of thermal contraction during the main mineralisation stage. This was based on the presence of a limited number of A_L inclusions that exhibit elevated As/(Na+K+Mn+Fe) and B/(Na+K+Mn+Fe) ratios. However, in this study, similar A_L inclusions occurring on primary growth zones in the type 10 samples (Figure 5.21) yield comparable Cs/Na and As/Na ratios to the main mineralisation-type A_V inclusions suggesting that the Mo-rich type 10 veins may have been produced by fluids that were exsolved and partitioned at considerable depth. Alternatively, low Cs/Na and As/Na ratios may be the result of the mixing of late stage fluids with shallow meteoric waters (e.g. Cannell, 2004).

In the late mineralisation samples the salt-undersaturated inclusions record far lower Cu concentrations than those measured in the main mineralisation samples and from mineralised veins at a number of Cu-Mo porphyries (Figure 6.2D). In the type 10 samples, the inferred parental A_{ID} inclusions yield an average Cu concentrations of 944 ppm (Figure 5.51F) that is over two times lower than the average recorded for pulses of parental main mineralisation-type fluids (Figure 5.51E). Assuming that the type 10 fluids were exsolved from the underlying magma under similar conditions to the main stage cycles, the comparable compositions and temperatures of these parental fluids (e.g. Figure 6.3E-F) suggest that the average $D_{Cu}^{fluid/melt}$ value for the type 10 fluids may be similar to the one recorded for the main mineralisation fluids. If this is true the decrease in Cu concentrations could be accounted for by a 73% loss of Cu in the parental magma prior to the exsolution of the type 10 fluids. However, less favourable partitioning of Cu could also be attributed to the deep exsolution of fluids with low Cl/fH$_2$O ratios. A factor that may explain the less favourable association of Cu than Mo with the deepest formed and most fractionated porphyry deposits (Figures 2.3-2.4).

Figure 6.3 (next page): Average FIA metal concentrations versus total homogenisation temperature and average chlorine concentrations (ppm) calculated using microthermometry and LA-ICP-MS analysis. Arrows represent overall inferred deposition trends for selected elements from the low salinity, intermediate density fluids and brines.


A
B
C
D
E
F
G
H
I
J
K
L
Fe
Ni
Cu
Zn
Mo
Pb
Th Total (°C)
Cl
AID (Main Min)
BH (Main Min)
BHO (Main Min)
BM (Main Min)
AID (Late Min)
BH (Late Min)
BHO (Late Min)
BM (Late Min)

6.4 Crystal Fractionation as a Key Control on the Formation of Mo-rich Porphyries

Klemm *et al*., (2007, 2008) stated that element concentrations normalised against the major fluid components Na+K+Mn+Fe reveal true trends in the compositional evolution of fluids. Based on this approach fluid inclusions associated with all the fluid regimes reveal no trends between crystal fractionation and normalised Mo and Cu concentrations (Figure 6.2C-D). Despite this, the poor relationship between Cs/(Na+K+Mn+Fe) and Mo/(Na+K+Mn+Fe) may purely be a manifestation of the moderately siderophile behaviour of Mo, which will cause it to be comparatively enriched in Fe- and Mn-rich fluids. This means that normalisation by these elements will mask any trends in absolute Mo concentrations. In addition, natural and experimental studies indicate that progressive fractionation of a felsic-intermediate magma may produce increasingly Fe-rich single-phase fluids (Audétat and Pettke, 2003; Cline and Bodnar, 1991). Therefore dividing Cs by an expression containing Fe may hide trends in magma fractionation. Given this, plots of absolute concentrations or metal and Cs concentrations normalised to Na should give far better indications.

Premineralisation fluid inclusion Cs/Na concentrations (limited data) overlap with main mineralisation inclusion data suggesting that there was limited evolution of the underlying magma source between these stages (Figure 6.2 E-F). However, absolute Cs versus Mo and Cu concentrations associated with each intrusion do reveal subtle changes (Figure 6.4) that are indicative of subtle but progressive crystal fractionation during the development of each main mineralisation halo. For example, fluid inclusions in type 6a veins associated with the A-Porphyry are relatively Cs and Cu poor, whereas inclusions in the younger Northern Diorite and Teniente Dacite Porphyry are commonly more Cs and metal rich (Figure 6.4A-B).

Parental A_{ID} inclusions in the type 6a veins from across the deposit contain relatively low Cs concentrations (Figure 6.4C-D) making trends in Cs concentrations difficult to identify. By contrast, brine inclusions in the same samples (produced by partitioning of the parental fluids) contain Cs concentrations that are commonly an order of magnitude greater. These inclusions document an increase in Cs with decreasing intrusion age (A-Porphyry/Diorites/ Teniente Dacite Porphyry: Figure 6.4E-F). In accordance with their close spatial and temporal relationships, fluid inclusions from the Teniente Dacite Porphyry and the type 10

samples contain similar Cs concentrations. However, several inclusions contain elevated Cs/Na and Mo/Na ratios (Figure 6.4C), suggesting that multiple pulses of type 10 fluids were exsolved during the latter stages of magma fractionation. This may explain the variable Mo and Cu-sulphides associated with the type 10 veins and breccias (e.g. Figure 4.7L-N).

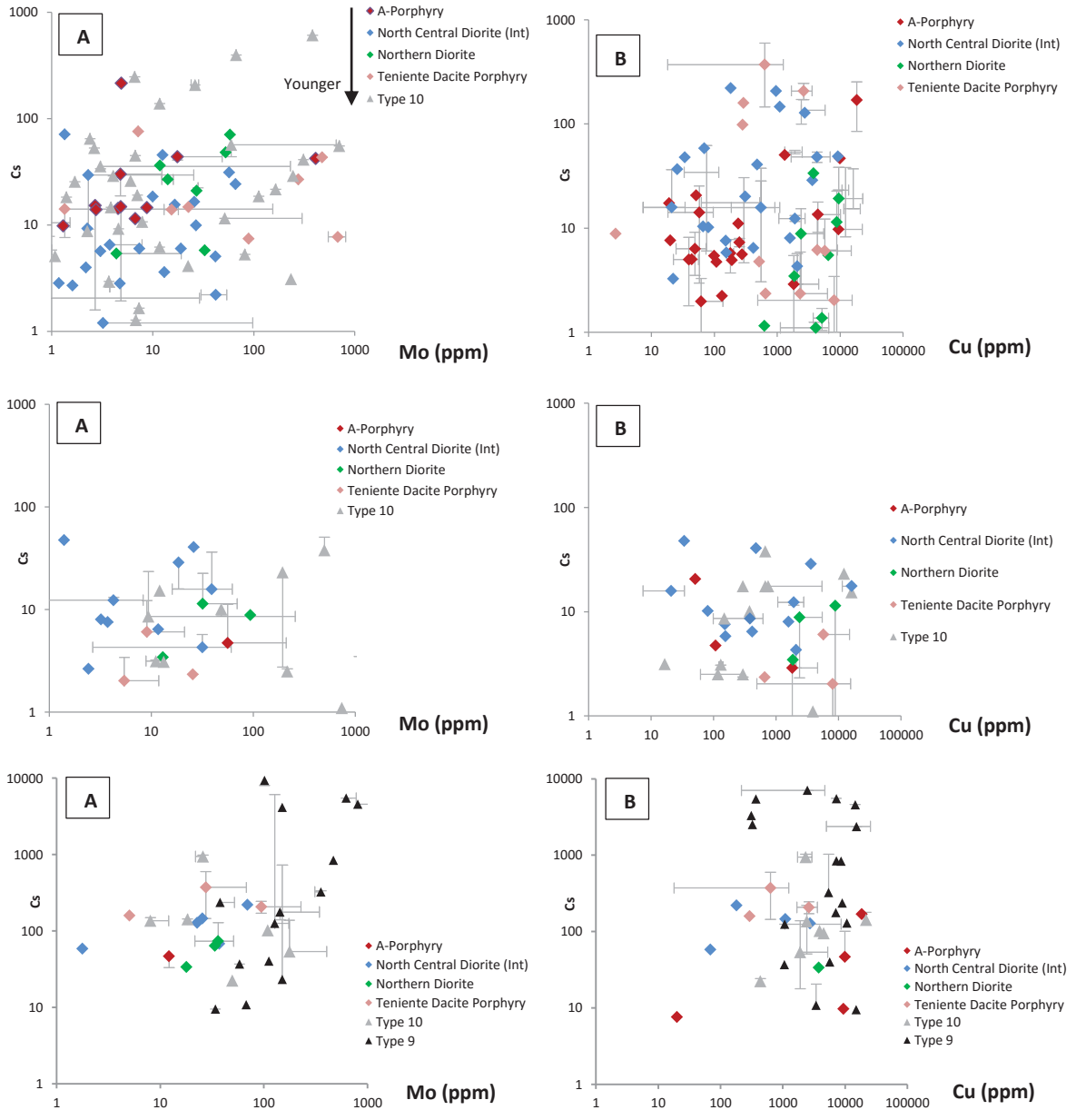


Figure 6.4: Average Cs versus Mo and Cu concentrations for fluid inclusion assemblages in type 6a veins associated with different intrusions at El Teniente (error bars = ±1 standard deviation). (A-B) Cs versus Mo and Cu for all fluid inclusions in type 6a veins from different intrusions. Type 10 vein data are also plotted in plot A. (C-D) Plots for just parental A_{ID} inclusions in type 6a veins from different intrusions and the type 10 veins. (E-F) Plots for just brine inclusions in type 6a veins from different intrusions and in type 9 and type 10 veins and associated breccias from across the deposit.

The type 9 brine inclusions commonly yield highly elevated Cs concentrations (Figure 6.4D) and also record the highest Mo concentrations (Figure 5.37H; Figure 5.38C; Figure 5.43) and highest Mo/Na and Cs/Na ratios of any inclusion (Figure 6.1C). This is consistent with strong evidence that exsolution from a highly fractionated magma during the final stages of crystal fractionation (e.g. Keppler and Wyllie, 1991; Audétat, 2010). The extremely high Mo concentrations of these fluids may be in part attributed to an increase in fO_2 during subsolidus cooling of the parental magma (e.g. Zhang *et al*., 2012), which would have favoured Mo speciation as melt-soluble Mo^{6+}, thus postponing aqueous phase partitioning until the final stages of crystallisation activity (e.g. Candela and Holland, 1984 Webster, 1997). This could also explain the abundant sulphate mineralisation associated with the marginal tourmaline breccias surrounding the Braden Breccia pipe (Figures 4.3-4.4), which formed during the final major pulses of magmatic-hydrothermal activity (Figure 4.19).

Unlike Mo, Cu concentrations in the main and late hydrothermal fluids show no clear relationship with Cs/Na ratios (Figure 6.1D) suggesting that degree of fractionation did not play a significant role in enriching Cu. In the late mineralisation inclusions Cu/Na ratios are commonly lower than in the main mineralisation A_{ID} inclusions (Figure 6.1A). The overall increase in Mo/Cu ratios of these fluids (e.g. Figure 5.51) is interpreted to reflect the residual melt composition during the final stage of magma fractionation and implicate crystal fractionation as an important control on the overall decoupling of Mo and Cu at El Teniente.

Intermediate density fluid inclusions from several other Mo-rich porphyries exhibit strong positive correlations between their Cs/Na and Mo/Na ratios (Figure 6.5C), but no clear relationships when normalising Mo and Cs with Na+K+Mn+Fe (Figure 6.5A). High temperature A_{ID} inclusion assemblages from the Teniente Dacite Porphyry and diorites plot on similar trends to fluid inclusions from Butte (Rusk *et al*., 2004; Buckroyd, 2008) and Bingham (Landtwing *et al*., 2005), whereas several A_{ID} assemblages in the late mineralisation samples yield high Cs/Na and Mo/Na ratios that are comparable to those recorded for the stockwork veins at Questa (Figure 6.5C). At Questa, high Cs concentrations in fluid inclusions in the stockwork veins that host 60-70% of Mo (Ross *et al*., 2002) were interpreted to be the product of high degrees of fractionation of the parental magma chamber following the

formation of the relatively Mo-poor magmatic hydrothermal breccias MHBX (Figure 6.5C: Klemm *et al*., 2008). The similar Mo and Cs concentrations recorded for the late mineralisation fluids at El Teniente suggest that the parental magma chamber had, by this time, undergone a similar degree of crystal fractionation to those associated with porphyry Mo systems (e.g. Blevin, 2003).

Similarly to El Teniente, Cu/Na ratios in intermediate density fluid inclusions show no clear relationship with Cs/Na in any of the studied deposits (Figure 6.5D). The A_{ID} inclusions in main and late mineralisation samples at El Teniente exhibit variable Cu/Na and Cs/Na ratios that are most similar to ranges recorded for parental inclusions at Butte. The highest Cu/Na ratios are recorded for low density fluid inclusions at Los Pelambres, whereas Cu/Na ratios are typically one to two orders of magnitude lower at the Questa porphyry Mo deposit (Figure 6.5D). This suggests that the residual melts in granitic systems may become Cu-poor during the latter stages of crystal fractionation. This may be due to the earlier extraction of Cu by S-rich volatiles (Zajacz and Halter, 2009; Seo *et al*., 2012) or by incorporation into crystallising mineral phases such as biotite, magnetite, amphiboles, feldspar and ilmenite (Ewart *et al*., 1973; Ewart and Griffin, 1994). Therefore, results of this and several other fluid inclusion studies indicate that the timing of fluid exsolution relative to extent of fractional crystallisation plays an integral role in controlling the metal affinities of granitic systems.

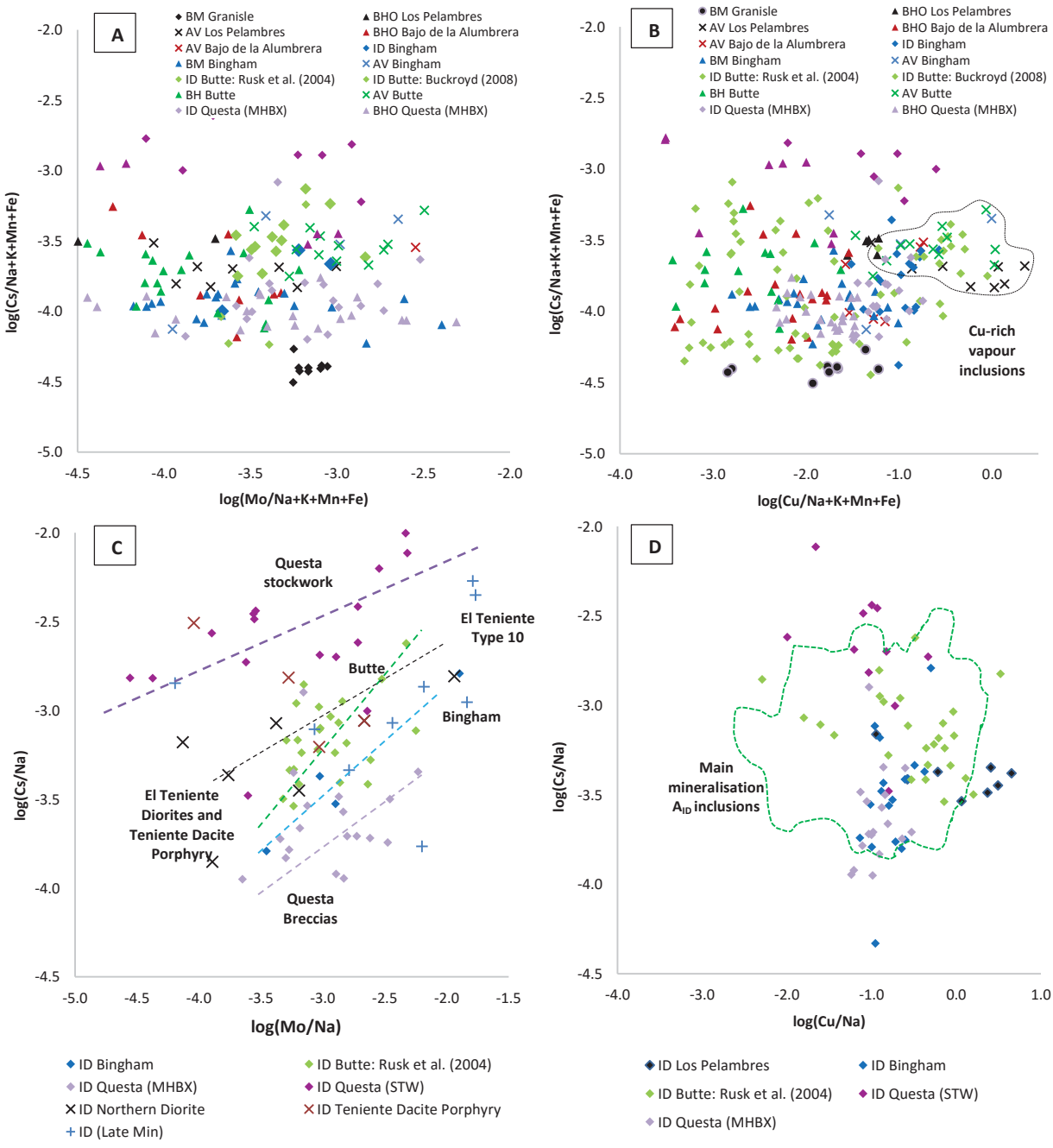


Figure 6.5: Mo versus Cs concentrations for fluid inclusions from several porphyry Cu-Au, Cu-Mo and Mo deposits. (A-B) Plots of Mo and Cu versus Cs plotted as ratios to the major fluid components (Na+K+Mn+Fe). (C-D) Plots of Cs/Na against Mo/Na and Cu/Na for intermediate density (ID), parental fluid inclusions showing an apparent positive relationship between Mo concentrations and degree of fractional crystallisation. Average intermediate density FIA data for type 6a veins from the Northern Diorite and Teniente Dacite Porphyry and late mineralisation type 10 veins are plotted as crosses. The dotted green line in plot D encompasses all main mineralisation A_{ID} inclusions. Data from Questa are subdivided into STW (stockwork vein data) and MHBX (Magmatic hydrothermal breccia data). References: Granisle, Klemm (2005); Los Pelambres, Klemm (2005); Bajo de la Alumbrera, Ulrich *et al.* (2001); Bingham, Landtwing *et al.* (2005); Butte, Rusk *et al.* (2004), Buckroyd (2008); Questa, Klemm *et al.*, (2008); Data from at Bajo de la Alumbrera (Ulrich *et al.*, 2001) and El Teniente from this study are given as FIA averages. For details about each ore deposit refer to Table 6.1.

6.5 The Hydrothermal Transport of Metals in Mo-rich Porphyries

6.5.1 The Speciation and Transport of Mo

The deep exsolution of fluids with relatively low Cl/H_2O ratios and relatively high Na and K concentrations in the main mineralisation-type and type 10 veins at El Teniente (e.g. Figure 5.34), is likely to have favoured the formation of non-chloride Mo complexes including $KHMoO_4$ and Na_2MoO_4 (Cao, 1989; Ulrich and Mavrogenes, 2008). However, the poor correlation between fluid inclusion Mo and Na and K concentrations in these veins (e.g. Figure 5.36E) suggests that the formation of such ion pairs was not a prerequisite for favourable Mo partitioning and transport. In accordance with Vry *et al*., (2010), the abundance of sulphide mineralisation associated with main mineralisation-type veins is interpreted to be the result of enhanced sulphur partitioning from melt into the main mineralisation fluids. Based on this interpretation, it is possible that dissolved ion pairs were modified to molybdite species such as $NaHMoO_2S_2$ (Zhang *et al*., 2012). This speciation is most likely to have predominated in the type 10 fluids, which are linked to abundant sulphide, sulphate and sulphosalt precipitation indicative of excess fluid S concentrations.

In accordance with previous predictions Mo is more likely to have been transported as Mo oxy-chloride complexes in fluids containing >7wt.% $NaCl_{eq}$, Mo (Yokoi *et al*., 1993; Ulrich and Mavrogenes, 2008). These complexes may be present in partitioned brines and moderate salinity liquids in the main mineralisation-type and type 10 samples, but are only likely to have predominated during type 9 breccia-vein development. In these samples, Mo concentrations correlate with inclusion Na (Figure 5.38C, 5.40C) and Cl (Figure 6.3J) concentrations, implying a strong salinity control on Mo solubility and transport. Previous XANES analyses on the structure of Mo^{6+} in Cl-bearing solutions have shown that Mo can be dissolved as MoO_2Cl^+, MoO_2Cl_2, or $MoO_2Cl_3^-$, depending on the number of Cl atoms surrounding the MoO_2^{2+} structure (Yokoi *et al*., 1993). In the type 9 samples, the moderate-high salinity fluid inclusion assemblages that were interpreted to be trapped prior to Mo deposition record ~150 ppm Mo at 2.5 wt.% Cl, ~490 ppm Mo at 6.3 wt.% Cl and ~1500 ppm at ~22.2 wt.% Cl (Figure 6.3J). These concentrations are consistent with a one to one molar relationship between Mo and Cl, consistent with the predominance of MoO_2Cl^+.

6.5.2 The Speciation and Transport of Cu

Unlike Mo the positive correlation between premineralisation fluid Cu and Na concentrations (Figures 5.31-5.32) suggests that salinity played an important role in controlling Cu solubility in these fluids. In accordance with previous speciation studies this suggests that Cu was initially transported as highly soluble $[CuCl_3]^{2-}$ and $[CuCl_4]^{3-}$ complexes in each system (Berry *et al*., 2006; 2009). In the main mineralisation-type samples, Cu fluid inclusion concentrations also correlate positively with inclusion Na (Figure 5.36A-D) and Cl (Figure 6.3F) concentrations. This again implies that Cu may have been predominantly dissolved as Cl complexes, even in the relatively Cl-poor (6.5 wt.% NaCleq) parental fluids. The spread of Cu concentrations recorded in the salt-undersaturated inclusions in the main mineralisation samples makes identification of the exact dissolved species difficult. However high pressure fluids with relatively low Cl/H_2O ratios are likely to be dominated by $CuCl^0$ and $[CuCl_2]^-$ complexes based on solubility, spectroscopic and speciation experiments completed at comparable temperatures and pressures (e.g. Hemley *et al*., 1992; Seyfried and Ding, 1993; Xiao *et al*., 1998; Liu *et al*., 2002; Archibald *et al*., 2002; Hack and Mavrogenes 2006; Simon *et al*., 2006; Berry *et al*., 2006; 2009).

Copper concentrations in the late mineralisation samples also exhibit clear positive relationships with inclusion Na (Figures 5.38A, 5.40A) and Cl concentrations (Figure 6.3F). Similarly to Mo, Cu speciation in the low salinity type 10 fluids is most likely to match that in the main mineralisation A_{ID} inclusions, whereas Cu is likely to have been dissolved as Cl-rich $[CuCl_3]^{2-}$ and $[CuCl_4]^{3-}$ complexes in the type 9 brines with high chlorinities. Unlike Mo, Cu concentrations are also relatively high in the lowest salinity A_{ID} and A_V inclusions (Figure 5.51). Previous experimental studies have shown that Cu can complex with HS^- in reduced, alkaline, sulphur-rich vapours (Heinrich *et al*., 1999; Mountain and Seward, 1999, 2003; Simon *et al*., 2006; Pokrovski *et al*., 2008; Seo *et al*., 2009; Landtwing *et al*., 2010). These complexes are interpreted to be more stable than chloride complexes in lower temperature fluids (Lui *et al*., 2001; Archibald *et al*., 2002), suggesting they may have been important following phase separation of the cooling parental fluids. The formation of $Cu(HS)_2^-$ may explain the high Cu/Na ratios of the A_V inclusions at El Teniente (Figure 6.1D) and the high Cu/Na+K+Mn+Fe recorded at a number of other porphyry Cu-Mo porphyries (Figure 6.5B).

6.6 Vapour-Brine Partitioning in Mo-rich Porphyries

6.6.1 Mass and Volume Proportions

The predominant co-transportation of Mo and Cu in the same parental fluids suggests that the spatial decoupling of Mo and Cu surrounding each intrusion at El Teniente is primarily the result of hydrothermal processes. Small variations in salinity, pressure and temperature can significantly alter the mass and volume proportions of brines and vapours produced during phase separation (e.g. Driesner and Heinrich, 2007), which may, in turn, strongly control the vapour-brine partitioning behaviour of Mo and Cu. The mass proportions of brine and vapour produced during phase separation can be estimated using their compositions relative to the parental fluid using the following mass conservation formula:

$$(100 \cdot A_{ID}\ conc) = (V\% \cdot [xA_V\ conc]) + (B\% \cdot [xB_H\ conc])$$

Where V% and B% are the relative mass percentages of vapour and brine and [xA_V conc] and [xB_H conc] are the concentrations of different elements in each phase derived from LA-ICP-MS analysis of partitioned inclusions. In In this study, mass and volume proportions were derived using the mass balance approach of Landtwing *et al*. (2010) with the Lever rule applied to the model H_2O-NaCl system (Driesner and Heinrich, 2007).

In the type 6a veins the parental A_{ID} inclusion assemblages that homogenise at >410°C have an average salinity of 6.59 wt.% $NaCl_{eq}$ (standard deviation = 2.8). Only three boiling assemblages were confidently measured in the main mineralisation-type samples (Table 6.2). These yield an average trapping temperature of 382.2°C and an average brine salinity of 43.3 wt.% $NaCl_{eq}$. The coexisting vapour inclusions record rather high and variable salinities (Table 6.2), possibly as a result of partial reequilibration with the hypersaline fluids immediately after boiling. In accordance with Dreisner (2007), a vapour separating at this temperature in the NaCl-H_2O system should have a salinity of ~ 0.01 wt.% $NaCl_{eq}$. This inferred vapour salinity and the measured average brine salinity of 43.3 wt.% $NaCl_{eq}$ gives an average vapour/brine mass ratio of 85:15. This is higher than a previous estimate of 77:23 (Klemm *et al*., 2007) that was based on a higher average input fluid salinity of 12.5 wt.% $NaCl_{eq}$. Such moderate salinity fluid inclusions were rare in this study and were interpreted to be produced by the mixing of early brines with later, lower salinity input fluids.

Based on the new estimated 85:15 mass ratio and average densities of 1.05 g/cm^3 and = 0.3 g/cm^3 for the partitioned brines and vapour respectively (Figure 5.23B) it is likely that the vapours would have had a volume approximately 40 times greater than the brines. This, combined with the lower viscosity of vapours suggests that this phase may have had the potential to infiltrate and potentially deposit metals in larger volumes of the TMC.

Table 6.2: Average fluid inclusion microthermometric properties and Mo concentrations for three apparent boiling assemblages in type 6b-8 veins and quartz- and anhydrite-dominated type 10 veins and breccias.

Sample	Vein	FIA	Type	Th (L+V→L/V)	T_m Halite (°C)	Salinity	Pressure	Density	Mo (ppm)
2363-149.0	Type 6b	1	Brine	368.1	365.7	43.9	13.3	1.09	15.9
	Type 6b	2	Vapour	357.5		1.68	13.3		< LOD
2371-149.0	Type 8	1	Brine	393.7	338.9	41.6	18.0	1.03	20.8
	Type 8	2	Vapour	399.0		0.18	18.0		< LOD
2371-77.4	Type 8	10	Brine	384.5	369.7	44.3	15.8	1.08	
	Type 8	9	Vapour	390.1		2.80	15.8		
1754-183.9	Type 10	8	Brine	391.2	342.1	41.7	18.2	1.00	1594.7
	Type 10	8	Vapour	398.9		2.20	18.2		296.4
1754-183.9	Type 10	14	Brine	364.2	335.4	41.1	17.0	1.02	< LOD
	Type 10	14	Vapour	366.0		3.23	17.0		< LOD
2083-251.6 anhydrite	Type 10	12	Brine	347.2	240.9	34.12	11.8	1.01	< LOD
	Type 10	12	Vapour	346.2		0.18	11.8		< LOD
2672-99.95 anhydrite	Type 10	11	Brine	339.7	325.6	40.23	12.5	1.07	< LOD
	Type 10	10	Vapour	340.2		0.60	12.5		< LOD
2672-99.95 anhydrite	Type 10	14	Brine	340.0	321.1	39.9	12.4	1.07	< LOD
	Type 10	13	Vapour	341.0		0.88	12.4		< LOD

Notes: Mo concentrations are given as fluid inclusion assemblage averages. Anhydrite-hosted type 10 were not considered when assessing the vapour-brine partitioning behaviour of Mo.

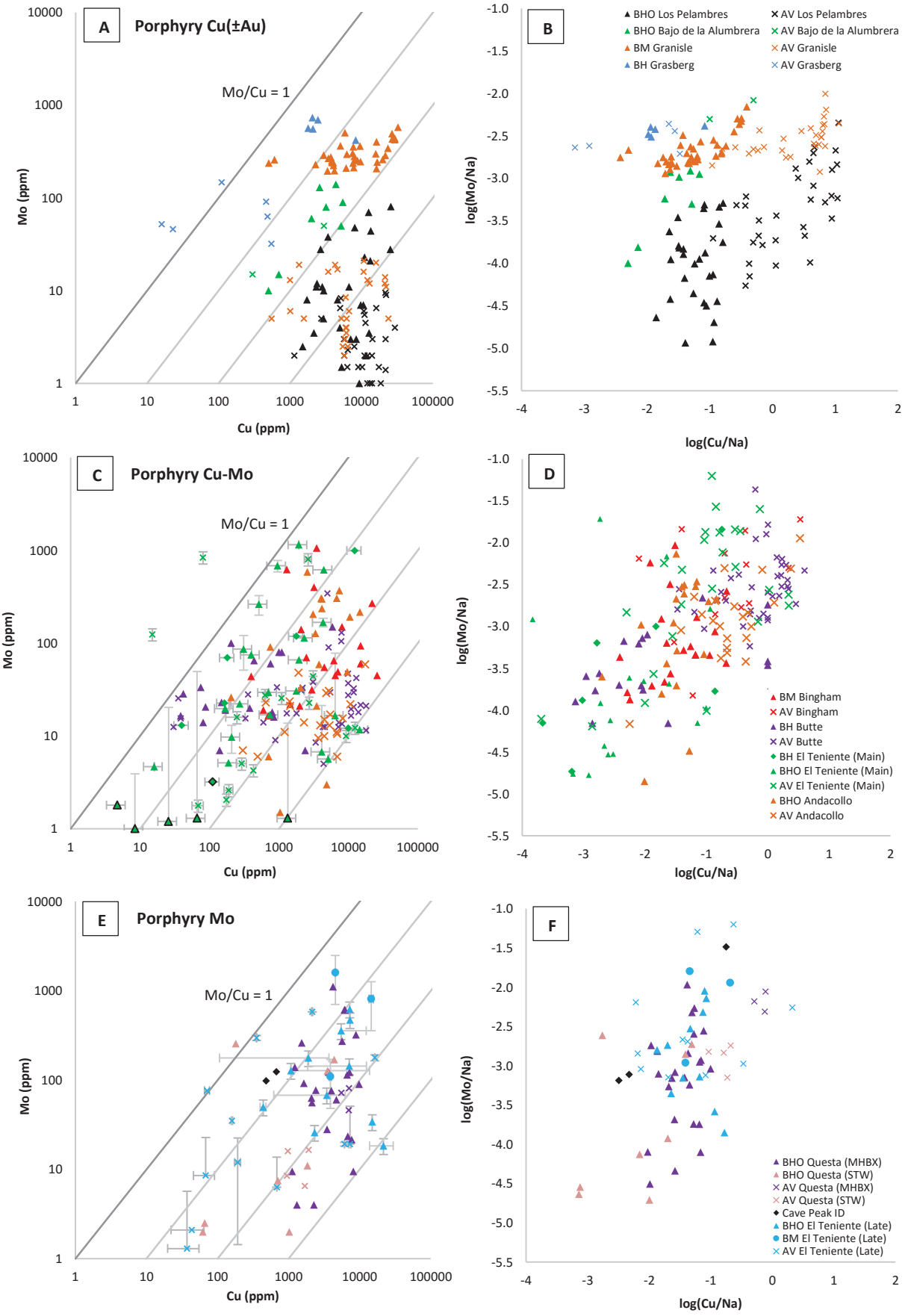
Boiling assemblages in the type 10 samples record a range of trapping temperatures (Figure 5.21) indicative of progressive fluid boiling of ascending intermediate fluids. In the anhydrite samples, apparent boiling assemblages were trapped at ≤350°C and contain low Mo concentrations (Table 6.2). By contrast, the highest temperature quartz-hosted boiling assemblages yield comparable trapping conditions to those characteristic of the main mineralisation-type fluids (Table 6.2). Based on this and the similar salinity of the inferred parental fluids to those in the type 6a veins, the type 10 fluids are also interpreted to have undergone phase separation into the approximate mass proportion of 85% vapour and 15% brine.

6.6.2 Vapour-Brine Partitioning of Mo

Previous studies at El Teniente concluded that phase separation may have been a primary control on Mo-Cu decoupling as a function of their contrasting complexation behaviour (e.g. Klemm *et al*., 2007; Vry, 2010). The interpreted preferential partitioning of Mo into brines led to the interpretation that a considerable proportion of main mineralisation-type Mo was transported and precipitated from these high salinity fluids. Consistent with this, main mineralisation-type brine inclusions measured in this study commonly yield the highest Mo concentrations (Figure 5.36) and vapour and brine inclusions in the type 6b and type 8 veins that homogenise between 375-405°C yield an average $DMo^{vapour/brine}$ = 0.28. This partitioning behaviour is consistent with previous experimental studies (Cao, 1989; Kudrin, 1989).

Despite this, the small mass ratio of the brines relative to partitioned vapours and the common occurrence of Mo-depleted brines in the main mineralisation-type veins (Figure 6.3J) suggest that these fluids may have played a limited role in transporting Mo. Recent LA-ICP-MS studies of boiling assemblages in other porphyry systems may also undermine the importance of brines in producing Mo-rich deposits (Figure 6.6A, C, E). At Questa, coexisting vapour and brine inclusions yielded an average $D_{Mo}^{vapour/brine}$ value of 0.32 (Klemm *et al*., 2008), whereas far lower $D_{Mo}^{vapour/brine}$ values of ~0.10 were recorded at the Grasberg Cu-Au deposit (Ulrich *et al*., 1999) and the Rito del Medio barren pluton (Audétat and Pettke, 2003). Given this, the strong preferential partitioning of Mo into high salinity fluids may favour Mo solubility to the extent that it prevents its deposition in exploitable ore shells.

Vapour inclusions in Mo-rich porphyries usually contain <100 ppm Mo (Figure 6.6C-F) but higher Mo/Na ratios than the partitioned brines (Figure 6.6D, F) and vapour inclusions in Cu-Au systems (Figure 6.6B). The higher Mo concentrations in vapour inclusions in Mo-rich porphyries may be a function of higher parental fluid input Mo concentrations, but also may be a manifestation of the deeper emplacement of Mo-rich systems (Figure 2.4). This would promote Mo partitioning into the vapours as a function of elevated vapour fH_2O (e.g. Audétat, 2010). The main mineralisation-type fluids are interpreted to be exsolved from a parental magma chamber emplaced at >5km (Table 6.1), raising the possibility that phase separated vapours produced at depth played an important role in transporting Mo.


A
Porphyry Cu(±Au)
Mo/Cu = 1
Mo (ppm)
Cu (ppm)
B
BHO Los Pelambres
BHO Bajo de la Alumbrera
BM Granisle
BH Grasberg
AV Los Pelambres
AV Bajo de la Alumbrera
AV Granisle
AV Grasberg
log(Mo/Na)
log(Cu/Na)
C
Porphyry Cu-Mo
Mo/Cu = 1
Mo (ppm)
Cu (ppm)
D
BM Bingham
AV Bingham
BH Butte
AV Butte
BH El Teniente (Main)
BHO El Teniente (Main)
AV El Teniente (Main)
BHO Andacollo
AV Andacollo
log(Mo/Na)
log(Cu/Na)
E
Porphyry Mo
Mo/Cu = 1
Mo (ppm)
Cu (ppm)
F
BHO Questa (MHBX)
BHO Questa (STW)
AV Questa (MHBX)
AV Questa (STW)
Cave Peak ID
BHO El Teniente (Late)
BM El Teniente (Late)
AV El Teniente (Late)
log(Mo/Na)
log(Cu/Na)

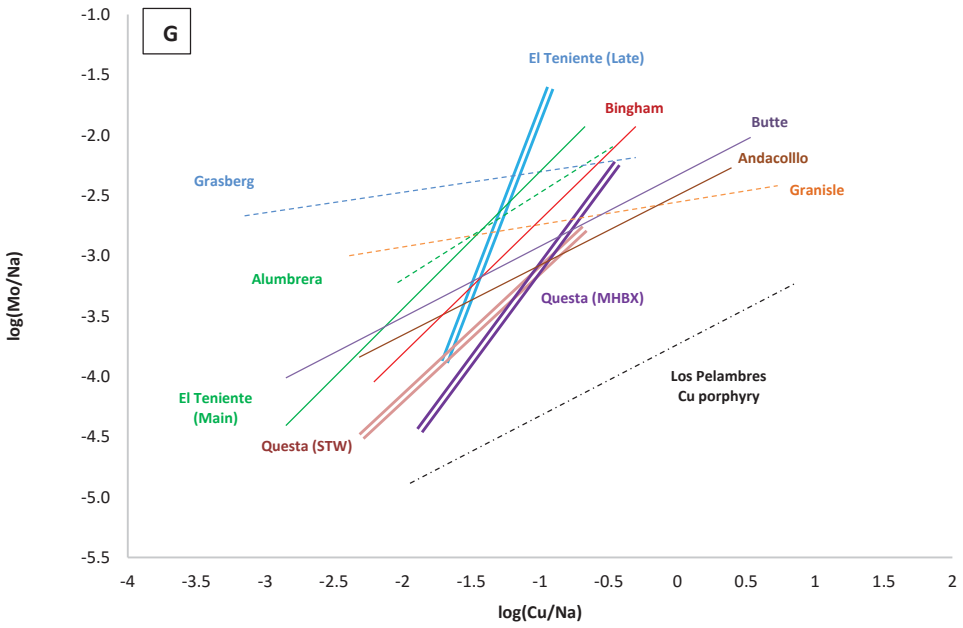


Figure 6.6: Cu versus Mo and Cu/Na versus Mo/Na ratios for vapour and brine inclusions at El Teniente and in a series of porphyry Cu±Au (A-B), porphyry Cu-Mo±Au (B-C) and porphyry Mo deposits. A summary of main mineralisation data for El Teniente are plotted as FIA average on plot B (error bars = 1 standard deviation). Data with black borders = Late mineralisation data for El Teniente are plotted as FIA averages on plot C and show a good correlation with inclusion concentrations recorded for Questa and Cave Peak. Plot G summarises lines of best fit connecting vapour and brine inclusion assemblages in each Cu/Na versus Mo/Na ratios plot as a function of intrusion type. Dotted lines = porphyry Cu-Au deposits. Solid lines = porphyry Cu-Mo deposits. Double lines = porphyry Mo deposits and late mineralisation inclusions at El Teniente. Data from Questa are subdivided into STW (stockwork vein data) and MHBX (Magmatic hydrothermal breccia data). References: Los Pelambres, Klemm (2005); Bajo de la Alumbrera, Ulrich *et al*. (2001); Granisle, Klemm (2005); Bingham, Landtwing *et al*. (2005); Andacollo, Klemm (2005); Grasberg, Ulrich *et al*., (1999); Butte, Rusk *et al*. (2004), Buckroyd (2008); Questa, Klemm (2005). For additional information regarding each deposit refer to Table 6.1.

Even though Mo concentrations are low in the partitioned main mineralisation-type A_V inclusions formed by phase separation (Figure 5.51; Table 6.2), a recent study concluded that vapours with Mo concentrations as low as 0.5 ppm may have the potential to form porphyry Mo deposits if fluid regimes operate over a ~115,000 year period (Rempel *et al.,* 2006). This is comparable to the predicted lifespans made for each intrusion at El Teniente (Figure 4.19), suggesting that the relatively Mo-poor vapours (Figure 6.6B) may have played an important role in transporting Mo. At Bingham, vapour and brine inclusions in the Mo-stage veins were interpreted to be produced by the separation of single-phase, intermediate density fluids into ~90% vapour and ~10% brine by mass (Seo *et al*., 2012). Based on this ratio and measured Mo concentrations in two boiling pairs it was suggested

that at least 70% of the Mo may have been transported in the vapour phase, possibly as hydroxyl species including $HMoO_4^-$ (e.g. Candela and Holland, 1984; Seo *et al*., 2009). Even though similar mass ratios and initial Mo concentrations are recorded in this study, vein distribution data indicate that type 6a veins are the most important veins with respect to controlling the deposit-wide distribution of Mo grades (Figure 4.10A-B). The rarity of boiling assemblages in molybdenite-rich type 6a-7a veins (Figure 5.9-5.12) and the very low Mo concentrations recorded in both vapour and brine assemblages in the type 6b-8 veins (Table 6.2) suggest that most Mo was deposited prior to phase separation. In accordance with several other studies (e.g**.,** Rusk *et al*., 2004; Landtwing *et al*., 2005; Seo *et al*., 2012) the onset of Mo deposition commonly occurs at temperatures that exceed phase separation. This therefore undermines the importance of both partitioned phases in transporting Mo.

By contrast, high Mo concentrations are recorded in both vapour and brine inclusions in the late mineralisation-type samples (Figure 6.3J) suggesting that less Mo was deposited prior to phase separation. Average partitioned brine and vapour concentrations in the type 10 samples yield a $D_{Mo}^{vapour/brine}$ value of 0.32. This is slightly higher than the $DMo^{vapour/brine}$ = 0.28 estimated for the main mineralisation fluids and is identical to a previous value of 0.32 recorded for boiling assemblages at Questa (Klemm *et al*., 2008). This and the high Mo/Na ratios recorded for the late mineralisation vapours relative to the brines suggests that the type 10 fluids may be similar to those produced in porphyry Mo systems (Figure 6.2E). Assuming an 85:15 mass ratio and an average $DMo^{vapour/brine}$ value of 0.32, it is possible that the type 10 vapours transported nearly twice as much Mo as the brines, possibly as hydroxyl complexes including H_2MoO_4 (e.g. Seo *et al*., 2012). However, in the type 10 samples, average Mo concentrations in the partitioned brines (236 ppm) and A_V inclusions (76 ppm) are still lower than the interpreted input fluid Mo concentration of ~270 ppm (Figure 5.51) and are commonly below limits of detection in boiling assemblages (Table 6.2). This suggests that, here too, considerable Mo was lost (~63%) before or during phase separation.

6.6.3 Vapour-Brine Partitioning of Cu

The relatively high Cu concentrations recorded in partitioned vapour and brine inclusions from boiling assemblages in the type 6b and type 8 veins (Figure 5.36C-D, Figure 6.3E-F)

suggest that, unlike Mo, abundant Cu was still being transported during the main phases of fluid boiling (Table 6.2). This implies that fluid phase separation played a far more important role in partitioning and concentrating Cu. Main mineralisation-type brine inclusions record the highest Cu concentrations (20000 ppm: Figure 5.36A-D, Figure 6.6), suggesting that Cu is preferentially partitioned into brines. However, vapour and brine inclusions in the in the type 6b and type 8 veins that homogenise between 375 and 405°C yield a relatively high average $DCu^{vapour/brine}$ value of 0.60. Consequently, on average, around 77% of the onward transport of Cu may have occurred in the vapour phase. The effective dispersion of large volumes Cu-bearing low viscosity vapours into the surrounding host-rock may explain the broader halos of elevated Cu grades surrounding each intrusion (e.g. Figure 4.2-3) and the presence of abundant disseminated chalcopyrite throughout the TMC (Cannell *et al*., 2005; Vry *et al*., 2010) and surrounding Mo rich type 7a veins (e.g. Figure 4.7I).

Vapour transport of Cu has been proposed in a number of other studies, with the suggestion that Cu may be predominantly transported as non-chloride aqueous complexes, such as $Cu(HS)_2^-$ following phase transition (e.g. Heinrich *et al*., 1992, 1999; Audétat *et al*., 1998; Ulrich *et al*., 2001; Williams- Jones and Heinrich, 2005; Klemm *et al*., 2007; Seo *et al*., 2009; Murakami *et al*., 2010). Despite this, most partitioned vapours recorded in this study contain relatively high Cl concentrations, possibly due to partial reequilibration of the vapours with higher salinity fluids. This suggests that even in the low density vapours, significant Cu may still be transported as chloride complexes, particularly at lower temperatures ≤350°C (Lui *et al*., 2001; Archibald *et al*., 2002; Zhong *et al*., 2015). Plots of Mo/Na versus Cu/Na for vapour and brine inclusions from a series of porphyry Cu-Au, Cu-Mo and Mo deposits reveal a steepening in the line of best fit that connects partitioned vapour and brine inclusions (Figure 6.6G). This means that in Mo-rich systems, Cu shows an apparent preference for the brines (Figure 6.6C-F), whereas it displays a preference for the vapour phase in Cu-Au systems (Figure 6.6A-B). However, these extremely high values have to be treated with caution as they may be the result of the post-entrapment, inward Cu diffusion (Lerchbaumer and Audétat, 2012: Figure 2.8).

In the quartz-rich type 10 samples, average Cu concentrations of 350 and 2680 ppm were recorded for vapour and brine inclusions produced via phase separation (Figure 5.51), which equates to a low $D_{Cu}^{vapour/brine}$ value of 0.13. A similar low value of 0.16 is recorded for a single anhydrite-hosted B_{HO} (438 ppm Cu) and A_V (71 ppm Cu) inclusions in a single type 10 boiling trail. Anhydrite does not permit the post-entrapment diffusion of Cu^+ suggesting that this value is likely to accurately reflect the true partitioning behaviour of Cu. These values are far lower than the $DCu^{vapour/brine}$ value of 0.60 recorded for the main mineralisation-type vapours and brines and the >1 values recorded for several Cu-Au systems (e.g. Heinrich *et al*., 1999; Ulrich *et al*., 1999; Ryan *et al*., 2001). The apparent limited partitioning of Cu into the late mineralisation vapours is consistent with observations from a number of porphyry Mo deposits, where vapour inclusions display similar low Cu/Na ratios (Figure 6.6) and suggests that partitioning of Cu into vapours is inhibited in these deeply emplaced systems (Table 6.1). Alternatively, vapour inclusions in the late stage fluids and Mo-rich systems may be less prone to post-entrapment inward Cu^+ diffusion as a function of the weaker Cu^+ to H^+ gradients than in lower temperature, more acidic Cu and Cu±Au systems.

6.6.4 Post-Entrapment Modification of Cu Partition Coefficients

The main mineralisation $DCu^{vapour/brine}$ value of 0.60 calculated in this study is considerably higher than typical values of ~0.1 determined via experimental studies conducted at similar pressure and temperature conditions (Williams *et al*., 1995; Simon *et al*., 2006; Pokrovski *et al*., 2008; Frank *et al*., 2011). One explanation for this is that the high vapour inclusion Cu concentrations are a manifestation of the post-entrapment inward diffusion of Cu through quartz (Zajacz *et al*., 2009; Lerchbaumer and Audétat, 2012; Seo and Heinrich, 2013: Figure 2.8). In this study, quartz-hosted A_V inclusions in the type 6b veins commonly contain high Cu concentrations of 900-7000 ppm that deviate markedly from the broad correlation observed in the remaining data between Cu and Na concentrations (Figure 6.7A). A_V inclusions in the type 8 veins yield consistently lower Cu concentrations of 20-300 ppm that are consistent with the predominant correlation with Na concentrations (Figure 6.7B). This is permissive evidence that the A_V inclusions in the type 6b veins have undergone post-entrapment modification suggesting that $DCu^{vapour/brine}$ values may be overestimated.

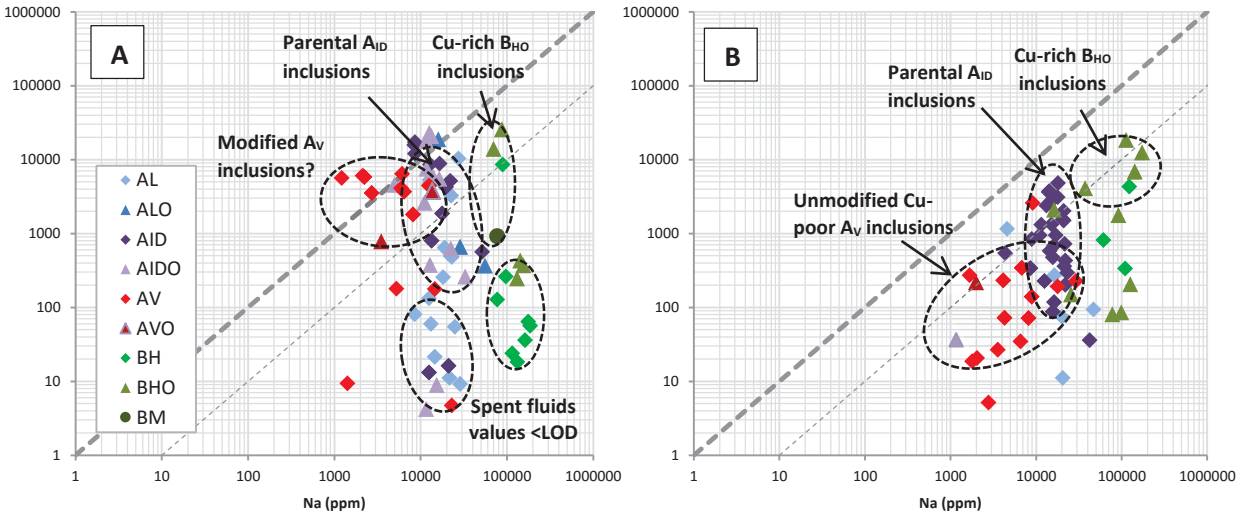


Figure 6.7. Individual fluid inclusion LA-ICP-MS data for different fluid inclusion types in quartz-chalcopyrite (type 6b) veins and sericite-altered quartz-chalcopyrite (type 8) veins at El Teniente. Data are presented for veins from several of the mineralised intrusions at El Teniente.

The inward Cu diffusion process is believed to depend on the presence of Cu-bearing external fluids and the establishment of an H^+ activity gradient out of the fluid inclusion (Lerchbaumer and Audétat 2012; Seo and Heinrich, 2013). At El Teniente, the quartz-dominated type 6a-6b veins are interpreted to develop outwards and upwards into type 8 veins with associated sericitic halos (Figure 4.21). The presence of intense sericitic alteration and abundant chalcopyrite in the type 8 veins suggests that the ore fluids responsible for the formation of these veins had already undergone acid dissociation and were by then increasingly H^+-rich and Cu-poor. This would have inhibited inward Cu diffusion meaning that the type 8 A_V inclusions are more likely to contain unmodified Cu concentrations.

Based on an average Cu concentration of 187 ppm in the A_V inclusions in the type 8 veins and an average Cu concentration of 1680 ppm in the coeval brine inclusions (Figure 5.51, Figure 6.7B) a more realistic $DCu^{vapor/brine}$ value of 0.11 is determined. This matches recent $DCu^{vapour/brine}$ values of 0.11 to 0.15 derived for reequilibrated coexisting vapour and brine inclusions calculated using vapour/brine mass ratios of 4:1 to 9:1 (Lerchbaumer and Audétat, 2012). Assuming that the vapour phase formed ~85% of the total fluid by mass, these D values would imply roughly equal amounts of Cu were transported in the brine and vapour phases after phase separation.

6.7 Mo Deposition in Porphyry Systems

6.7.1 Main Mineralisation-Type Mo Deposition

Results of this study indicate that the input Mo and Cu concentrations of each fluid regime are controlled by the extent of crystal fractionation. However, the co-transportation of both metals suggests that partitioning and depositional processes were the main controls on the localised decoupled mineralisation of Mo-Cu. Previous fluid inclusion studies have shown that ore fluids in Climax-type systems tend to be relatively Cu-rich (e.g. Klemm *et al*., 2008: Figure 6.6E-F) whereas brine inclusions in Cu-Au systems commonly contain higher Mo concentrations than those recorded in Mo-rich systems (e.g. Ulrich *et al*., 1999; Ulrich *et al*., 2001; Klemm, 2005: Figure 6.6A-B). This suggests that depositional processes are also important in controlling the mineralisation potential and metal affinities of granitic systems.

Approximately 60% of Mo is hosted within the TMC suggesting that this unit may have acted as an effective chemical trap for molybdenite mineralisation (Vry *et al*., 2010). However, significant Mo also occurs within the late mineralisation breccias (~20%) and felsic-intermediate intrusions (~20%) implying that fluid-rock interaction between hydrothermal fluids and the TMC was not the only control on molybdenite deposition. This is consistent with numerous other Mo-rich porphyries, where Mo grades are either sub-equally distributed across multiple host rocks (e.g. Bingham: Landtwing *et al*., 2005, 2010; or are focused within felsic intrusions that predominate in the centre of each system (e.g. Questa: Carten *et al*., 1993). Given this host rock independence, it is more likely that Mo deposition was primarily driven by drops in temperature, pressure (e.g. Cao, 1989; Kudrin 1989; Ulrich and Mavrogenes, 2008) and/or chemical changes associated with phase separation.

At the Butte Cu-Mo porphyry, significant amounts of Mo were interpreted to have been deposited in response to a switch from near-lithostatic to near-hydrostatic pressure regimes (Rusk and Reed, 2002; Rusk *et al*., 2008). However, fluid inclusion boiling assemblages in the main mineralisation-type veins record relatively low and consistent pressures <40 MPa. The vertical pressure gradient is likely to be far more subtle than a vertical temperature gradient of 15°C/100 m gradient predicted in a previous S-isotope study (Cannell, 2004). This, combined with the strong temperature-dependent solubility of Mo in S-bearing fluids at

temperatures of ~400°C (e.g. Ivanova *et al*., 1975, Wood *et al*., 1987; Cao, 1989, Gu, 1993; Ulrich and Mavrogenes, 2008; Rempel *et al*., 2009: Table 2.4), suggests that temperature may have exerted a stronger control on Mo deposition. However, it is likely that pressure fluctuations produced by repeated fracturing and annealing of the overlying host rock affected the local temperatures at which Mo was deposited (Cannell, 2004; Vry *et al*., 2010).

Vein distribution data and fluid inclusion evidence show that the type 6a veins probably represent higher temperature parental veins for outboard type 6b-8 veins (e.g. Figure 4.21). In these veins, different inclusion types reveal clear decreases in average Mo concentrations with decreasing homogenisation temperature, providing a proxy that temperature was a key control on Mo deposition (Figure 6.8E). This apparent temperature relationship is far stronger than those displayed by most other elements including Na, Cu, Zn and As (Figure 6.8A-D) and implies that most main mineralisation Mo was deposited directly from the parental intermediate density fluids at >390°C. The low Mo concentrations recorded in partitioned vapour and brine inclusions in the type 6b-8 veins (Figure 5.51) and the three measured boiling assemblages (Table 6.2) suggest that most Mo was deposited prior to or during fluid boiling at ~390°C and ~15 MPa (Table 6.2). The deposition of Mo prior to significant vapour-brine partitioning is similar to recent interpretations made at Butte (Rusk *et al*., 2004, 2008) and Bingham (Landtwing *et al*., 2005; Seo *et al*., 2012). At Bingham and Questa, Mo-stage ore fluids were also almost always trapped at temperatures >390°C (Landtwing *et al*., 2005; Klemm *et al.,* 2008). Based on the presence of different dissolved Mo species in the different fluids and vapours the most likely reactions that drive Mo precipitation at El Teniente and in other porphyry systems are:

$H_2MoO_4 + H_2 + 2H_2S \rightarrow MoS_2 + 4H_2O$ *(1)* [low salinity fluids/vapours]

$Na_2MoO_4 + 2H_2S + 2HCl \rightarrow MoS_2 + 3H_2O + 2NaCl + ½\ O_2$ *(2a)*

$NaHMoO_2S_2 + HCl \rightarrow MoS_2 + H_2O + NaCl + ½\ O_2$ *(2b)*

[Intermediate density, moderate-low salinity fluids]

$MoO_2Cl_2 + H_2 + 2H_2S \rightarrow MoS_2 + 2H_2O + 2HCl$ *(3)* [Partitioned brines]

Reactions 2a and 2b do not require an external reducing agent and involve acid consumption. The lack of wallrock alteration associated with Mo-rich type 6a-7a veins and the apparent overriding temperature control on Mo solubility implicates reactions 2a-2b as the most important with respect to main mineralisation Mo deposition.

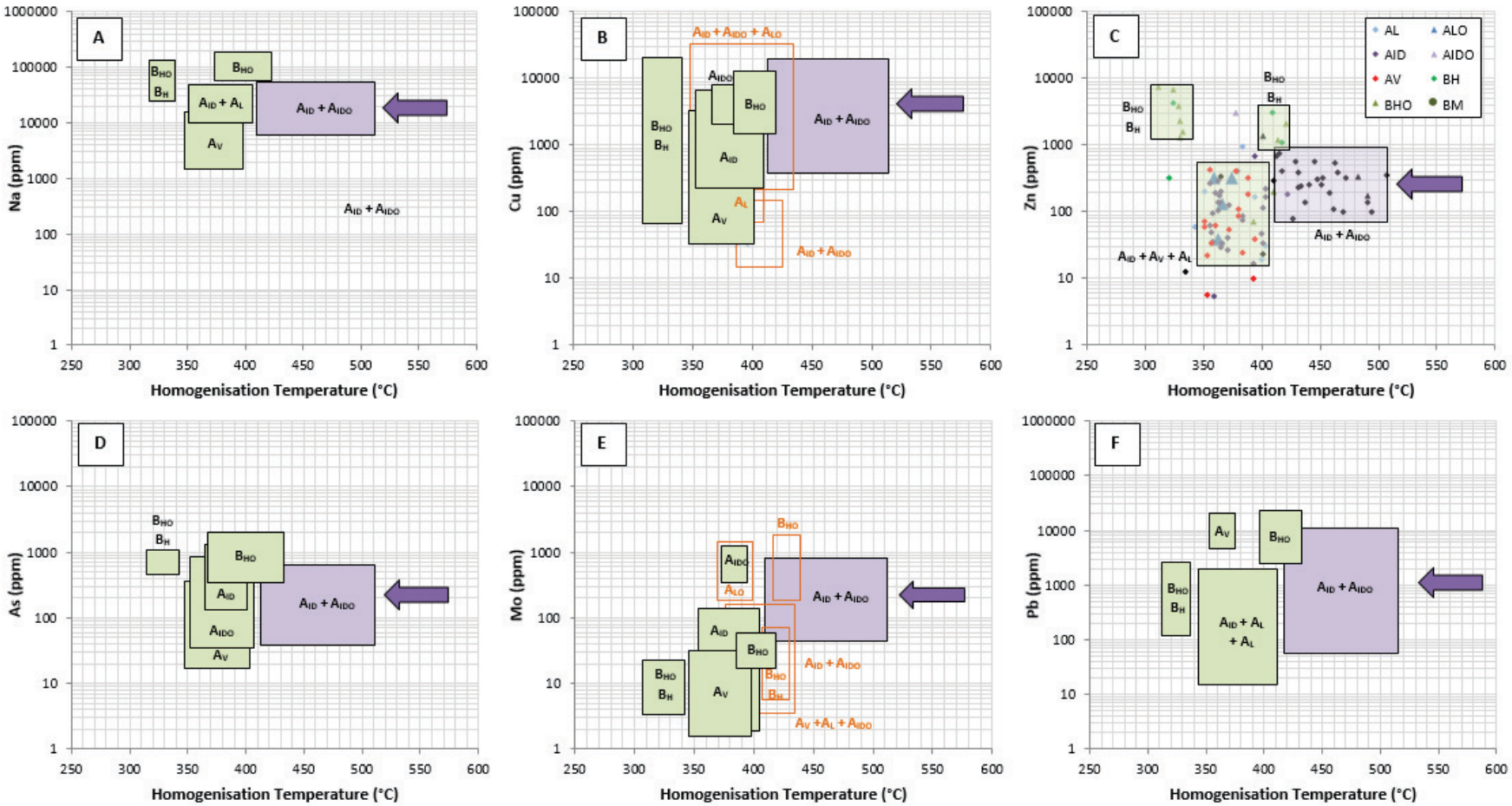


Figure 6.8: Total homogenisation temperature versus individual fluid inclusion element concentrations for type 6a, 6b and type 8 veins. Purple boxes represent ≥90% of intermediate density fluid inclusions in the deep type 6a veins. Green boxes represent ≥90% of each fluid inclusion type in all type 8 veins. Orange boxes in plots B and E represent ≥90% of each fluid inclusion type in the type 6b veins. Example inclusion clusters are shown in plot C. Purple arrows indicate average element concentrations for the input A_{ID} fluids. Mo concentration shows strong temperature dependence and a weak salinity dependence. Cu partitioning and solubility behaviour shows weak temperature dependence and is comparable to As and Pb in the type 6a-type 8 veins.

In accordance with previous experimental studies (e.g. Kudrin, 1985; Cao, 1989; Ulrich and Mavrogenes, 2008) and the deposition of Mo via reactions (1-4), molybdenite mineralisation at El Teniente is likely to have been favoured by decreasing fO_2, increasing H_2S and increasing HCl in the ore fluids. In addition, fO_2 is likely to have decreased as a function of oxidation of Fe^{2+} in the surrounding iron-rich host-rocks(e.g. Cannell, 2004) and anhydrite precipitation following the disproportionation of dissolved magmatic sulphur dioxide as fluids cooled below ~400°C (e.g. Giggenbach, 1992; Rye, 1993). This may explain why reduced Mo in the form of molybdenite ($Mo^{4+}S_2$) is strongly associated with the transition from quartz-dominated type 6a veins to more sulphate-rich type 6b veins.

Cooling to 400°C will also have initiated the dissociation of dissolved acid species in the outward and upward migrating ore fluids (Reed *et al*., 2005; Rusk *et al*., 2008) leading to decreases in pH and an increase in the activity of HS^-, both of which favour molybdenite saturation (e.g. Tingle and Fenn, 1984; Gu, 1993; Vigneresse, 2007). The very low Mo contents of most vapour inclusions that homogenise below <400°C (Figure 6.8E) are consistent with the efficient deposition of molybdenite from fluids with high reduced sulphur contents as is inferred for the low density vapours based on measured partition coefficients for S (Drummond and Ohmoto, 1985; Seo *et al*., 2009). Previous experimental studies have shown that molybdenite displays a minimum solubility at a pH value of ~3 in S-bearing hydrothermal fluids at 400°C (Kudrin, 1985). This suggests that increasing acidity at the onset of acid dissociation may have been extremely effective in depositing Mo. The rarity of molybdenite in the chlorite-quartz-sericitic-altered type 8 veins (Figure 5.16F; Figure 5.36L) suggests that most Mo was deposited prior to acid attack of the surrounding wallrocks, possibly when fluid pH was at its lowest.

Therefore, main mineralisation-type Mo deposition at El Teniente is likely to have occurred in a narrow temperature window (390-430°C) as a manifestation of the interplay of decreasing temperature with decreasing fO_2 (wallrock-driven reduction), increasing $a.HS^-$ (SO_2 disproportionation) and decreasing pH (acid dissociation). The combined effects of these variables may explain similar narrow precipitation temperature ranges (360-440°C) recorded at a number of other Mo-rich porphyries, where abundant molybdenite is associated with the transition from potassic to early sericitic alteration (e.g. Questa: Klemm

et al., 2008; Bingham Canyon, Utah: Landtwing *et al*., 2005; and Endako, British Colombia: Selby *et al*., 2000). Indeed main mineralisation Mo deposition at El Teniente appears to occur following an initial drop in fluid K and Mn concentrations (Figure 5.34). The absence of significant molybdenite in porphyry Cu-Au systems is not thought to be due to a lack of Mo in the magmatic fluids but is more likely to be a manifestation of the high solubility of Mo in the phase separated brines (e.g. Figure 6.6A).

6.7.2 Late Mineralisation-Type Mo Deposition

Unlike in the main mineralisation-type veins and breccias, late mineralisation molybdenite deposition is coupled with intense quartz-sericite alteration suggesting that temperatures were <400°C. In accordance with this, a previous sulphur isotope study of 42 sulphide and 31 anhydrite samples from El Teniente indicated a drop in ore deposition temperatures from approximately 410°C in the type 7-8 veins to ~360°C in the late mineralisation veins (Kusakabe *et al*., 1984). In the type 9 samples, high Mo concentrations >500 ppm are recorded in partitioned brine inclusions that were trapped at temperatures as low as 360°C (Figure 6.3IA). Interpreted coexisting vapour inclusions trapped at similar temperatures (350-375°C) usually record Mo concentrations that are below limits of detection. Therefore, the most likely explanation for the lower temperature of molybdenite deposition is that Mo was primarily transported in high salinity fluids in which it is highly soluble (e.g. Cao, 1989; Yokoi *et al*., 1993; Ulrich and Mavrogenes, 2008). Drillcore intervals associated with the tourmaline breccias record average Mo grades of up to 0.35 wt.%, indicating an extremely effective deposition mechanism for Mo from the very Mo-rich, type 9 brines.

Similar to the main mineralisation-type fluids, the salt-undersaturated inclusions in the type 10 samples record an overall decrease in Mo with decreasing homogenisation temperature (Figure 6.9A). However, as with the type 9 samples, the co-entrapment of both Mo-rich and Mo-poor inclusion assemblages suggest that rapid pressure drops may have favoured sudden molybdenite saturation (Figure 6.9A). These low pressures can be attributed to the exploitation of northward-trending faults and fractures, including the B-Fault, and the concentric and radial fractures and fault swarms surrounding the Braden Breccia pipe (Cannell, 2004; Figures 3.8-3.10) that opened between 5.0 and 4.58 Ma (Figure 4.19).

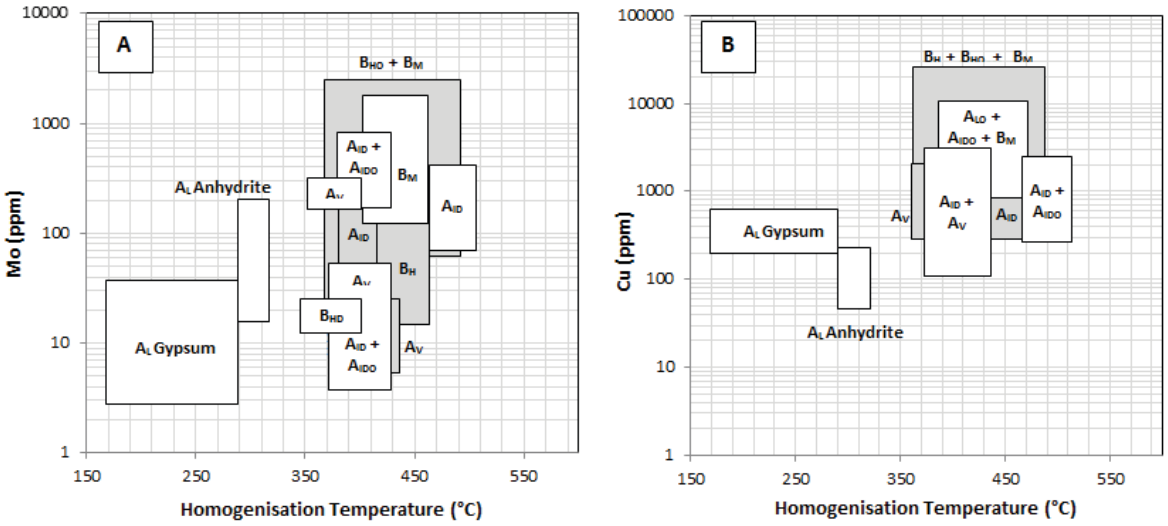


Figure 6.9: Total homogenisation temperature versus individual fluid inclusion element concentrations for late mineralisation veins and breccias. Grey boxes represent ≥90% of each fluid inclusions type in the type 9 veins. White boxes represent ≥90% of each fluid inclusion types in all type 10 veins and anhydrite-carbonate±gypsum breccias. Arrows indicate average element concentrations for the inferred input fluids. Mo concentration shows strong homogenisation temperature dependence and a strong salinity dependence. Moderate Cu concentrations are also recorded for the low salinity gypsum-hosted inclusions.

Drillcore intersections in the faults typically yield average Mo grades 0.06-0.15 wt.% (e.g. Figure 4.16), whereas ore grades associated with the abundant type 6a veins are typically between 0.01 and 0.04 wt.%. These high Mo grades may be in part due to the two-fold increase in Mo concentrations of the parental fluids (e.g. Figure 5.51E-F). But it is likely that Mo grades were enhanced by the focusing of multiple pulses of late Mo-rich fluids through these structural traps. This is supported by the diverse range of inclusions hosted within these samples (Figures 5.20-5.21).

The presence of boiling assemblages with variable trapping temperatures of 350-410°C in molybdenite-rich type 10 veins (Table 6.2) suggests that progressive boiling during rapid ascent played a significant role in instigating molybdenite saturation by destabilising species including H_2MoO_4 (e.g. Seo *et al.*, 2012) and $NaHMoO_2S_2$ (Zhang *et al.*, 2012) as a function of decreasing fH_2O. Similar to the type 9 samples, these Mo-rich veins develop into sulphate-dominated type 10 veins with intense quartz-sericite alteration halos that contain Mo-depleted fluid inclusion assemblages (Figure 6.9A) and boiling assemblages (Table 6.2).

6.8 Cu Deposition in Porphyry Systems

6.8.1 Main Mineralisation-Type Cu Deposition

Vein distribution data indicate that Cu is predominantly hosted in type 7b and sericite-altered type 8 veins that generally occur in more distal settings of the TMC relative to the felsic-intermediate intrusions and their Mo-rich, type 6a vein halos (e.g. Figure 4.21). The sequential deposition of Mo followed by Cu is similar to a recent model proposed for the hydrothermal evolution of Butte, in which fluids with relatively uniform compositions are interpreted to have been capable of producing potassic alteration at 600°C, alteration-free quartz-molybdenite veins at ~400°C and even advanced argillic alteration at 200°C (Reed *et al*., 2013).

Cannell (2004) suggested that the decoupled mineralisation of Mo and Cu was a function of the temperature of the system, which created a circular configuration of zoned metal grades centred on the Braden Breccia pipe (Figure 3.10). Although this deposit-wide configuration is clearly an oversimplification, similar zonation patterns do occur around each intrusion (Figures 4.3-4.4), suggesting that decreasing temperature (plus decreasing fO_2 and increasing pH) away from each centre may have led to the sequential deposition of Mo followed by Cu. In accordance with this, main mineralisation fluid inclusions record a decrease in Cu concentrations in inclusions that homogenise at temperatures of between 395° and 345°C (Figure 6.3E).

A strong temperature-control on Cu solubility is known from experimental studies that document steep drops in chalcopyrite solubility at temperatures of 390-410°C (Hezarkhani and Williams-Jones, 1999: Figure 6.10). A similar precipitation temperature range is proposed for Bingham, where most Cu was interpreted to have been deposited between 320–430°C and low pressures of 9–26 MPa (Figure 6.10: Landtwing *et al*., 2005; Seo *et al*., 2012). Temperature is also interpreted to have been the overriding control on the deposition of Cu at the Sungun porphyry Cu deposit, Iran, where Cu concentrations are thought to have decreased from 1000 to 25 ppm between 400 and 350°C (Hezarkhani *et al*., 1999). However, chalcopyrite deposition windows as high as 475-650°C (e.g. Butte: Rusk *et*

al., 2008) and <300°C (e.g. Grasberg: Ulrich *et al*., 1999) have been reported in other porphyry systems, indicating that pressure may strongly influence Cu deposition.

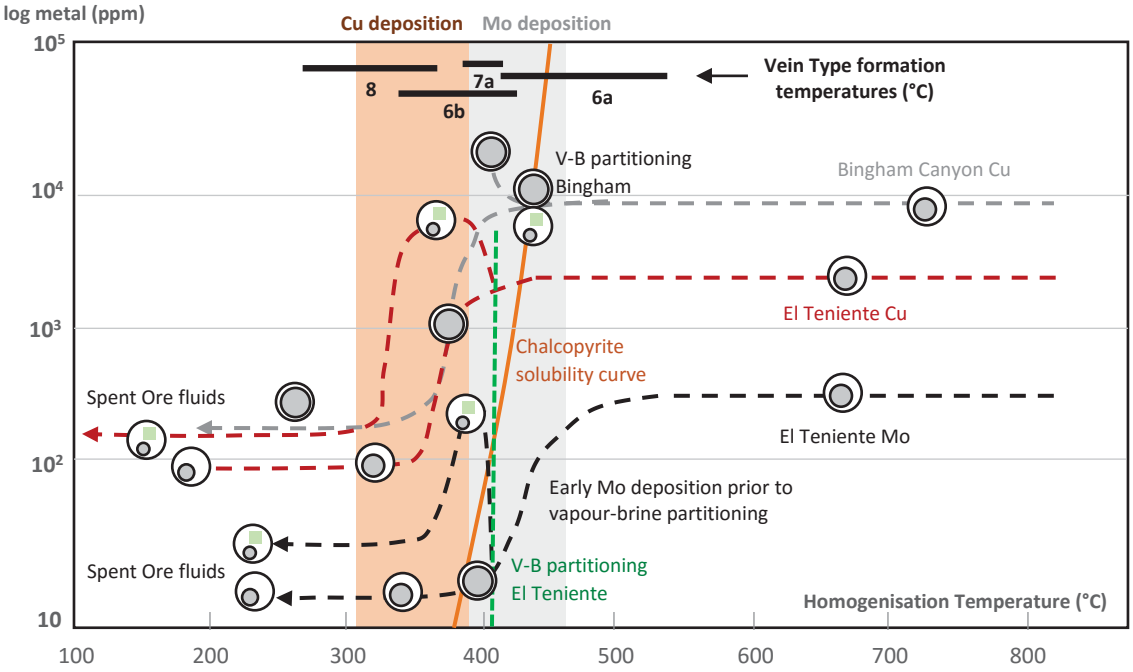


Figure 6.10. Copper and molybdenum concentrations as a function of homogenisation temperature and fluid inclusion type in main mineralisation-type veins. Red lines = Cu concentrations showing weak enrichment in brine inclusions. Black lines = Mo concentrations at El Teniente showing preferential partitioning and solubility in brine inclusions. Grey lines = Cu concentrations in fluid inclusions at Bingham Canyon (Landtwing *et al*., 2005). The deposition of Cu from separated vapour and hypersaline fluids is interpreted to run parallel to the temperature-solubility curve for chalcopyrite (orange line), predicted in a previous experimental study (Hezarkhani and Williams-Jones, 1999). The steep temperature dependence of the solubility curve is relatively constant at low to moderate pressure.

Previous studies at El Teniente concluded that most main-stage Cu was deposited from low-salinity fluids and vapours between 400 and 320°C (Klemm *et al*., 2007; Vry, 2010). Vry (2010) suggested that the onset of chalcopyrite deposition correlates well with fluid boiling, possibly as a result of the effective precipitation of Cu from low density vapours by the destabilisation of dissolved metal-sulphide complexes during volatile loss (Pokrovski *et al*., 2005). Consistent with this, fluid inclusion data record a significant decrease in Cu concentrations at ~390°C (Figure 6.3E), reflecting the trapping temperatures of the measured boiling assemblages (Table 6.2). Cu mineralisation at Bingham also appears to have coincided with the onset of vapour-brine separation (Figure 6.10), suggesting that this process may play an important role in promoting Cu-sulphide saturation.

In the type 8 veins, both the partitioned vapours and brines contain lower Cu concentrations than the inferred input fluid indicating that considerable Cu (>80%) was lost prior to inclusion entrapment. However, it is unclear whether this Cu was lost by deposition from the parental fluid prior to phase separation, during the initial stages of fluid boiling, or during cooling of the phase separated fluids prior to trapping.

At El Teniente the partitioned brine inclusions record elevated Cu concentrations at trapping temperatures as low as 310°C suggesting that the partitioning of Cu into the hypersaline fluids may have played an important role in exaggerating the extent of Mo-Cu decoupling by enhancing the solubility of Cu as highly soluble CuCl complexes (e.g. Hezarkhani and Williams-Jones, 1998; Berry *et al*., 2006, 2009). This may therefore explain the broad ranges in Cu deposition temperatures (~100°C) recorded at El Teniente and other porphyry deposits (e.g. Rusk *et al*., 2008; Ulrich *et al*., 1999; Seo *et al*., 2012). In accordance with previous speciation and solubility studies (Berry *et al*., 2006, 2009; Pokrovski *et al*., 2008; Seo *et al*., 2009; Seo *et al*., 2012), it is likely that Cu was deposited from Cl-poor vapours via reactions similar to (4) and from Cl-bearing fluids via reaction (5) or similar derivatives involving $CuCl_2$-$CuCl_4$:

$$2Cu(HS)(H_2S) + 2FeCl_2 \rightarrow 2CuFeS_2 + 4HCl + H_2 \quad (4) \quad \text{[very low salinity vapours]}$$

$$CuCl + FeCl_2 + 2H_2S \rightarrow CuFeS_2 + 3HCl + 0.5\ H_2 \quad (5) \quad \text{[moderate-high salinity fluids]}$$

Based on these equations, it has been suggested that changes in fO_2 and pH play significant roles in controlling chalcopyrite solubility (e.g. Hemley *et al*., 1992; Hezarkhani *et al*., 1999; Landtwing *et al*., 2005) and the order in which Mo and Cu are deposited (e.g. Dilles and Einaudi, 1992; Seo *et al*., 2012). Both reactions are favoured if fluids encounter an oxidised environment and where the acid generated can be consumed by hydrogen metasomatism (sericitisation or argillisation).

At El Teniente, the abundance of Cu-rich inclusions in the anhydrite-bearing type 6b veins and sericite-altered type 8 veins (e.g. Figure 6.7A-B) indicates that significant amounts of Cu were still dissolved following the onset of SO_2 disproportionation and acid dissociation at ~400°C (Giggenbach, 1992; Rye, 1993; Reed *et al*., 2005; Rusk *et al*., 2008). Cannell (2004)

suggested that high H_2S concentrations in the partitioned vapours may have favoured the early deposition of significant Cu via reaction (4). This may have contributed to the pronounced decrease in Cu concentrations in the low salinity inclusions at ~400°C (Figure 6.3E). By contrast, the favourable solubility of Cu in the acid volatile-poor partitioned brines may have resulted in favourable Cu solubility leading to the asynchronous deposition of Cu from the different fluid types. This may explain the broad (~100°C) temperature deposition windows for Cu reported in this (e.g. Figure 6.8) and several other porphyry systems (e.g. Landtwing *et al*., 2005; Rusk *et al*., 2008 Seo *et al*., 2012).

Grade distribution data indicate that ~80% of Cu at El Teniente is hosted within the TMC in relatively tight ore shells surrounding each individual intrusion. This suggests that fluid-wallrock reactions may have played an important role in depositing Cu without significant outward dispersion. Similar fluid-wallrock interactions may explain why a number of other world-class porphyry Cu deposits are hosted in mafic complexes, including Resolution, Arizona (Manske and Paul 2002; Ballantyne *et al*., 2003), and Oyu Tolgoi, Mongolia (Kirwin *et al*., 2005; Sillitoe, 2010). Following acid dissociation, acid attack of the surrounding TMC will have gradually neutralised the outward migrating ore fluids (e.g. Hemley *et al*., 1992) as a function of the reaction of fluid H^+ with biotite and plagioclase to produce the early chlorite-quartz halos (e.g. Eggleton and Banfield, 1985). This, combined with decreasing pressure will have favoured chalcopyrite saturation explaining why abundant chalcopyrite is typically associated with the onset of chlorite-sericite alteration associated with the type 7b and type 8 veins (Figure 3.7) at ~100 m from the margins of each intrusion (e.g. Figure 4.12).

6.8.2 Late Mineralisation-Type Cu Deposition

The late mineralisation samples host primary inclusions that contain highly variable Cu concentrations. In the type 9 samples, almost all the brine inclusions contain highly elevated Cu concentrations (Figure 6.9B) that are similar to those recorded in porphyry Mo systems (Figure 6.6F). Unlike the main mineralisation-type brines, these inclusions do not record a decrease in Cu concentrations with decreasing homogenisation temperature and the B_H inclusions that homogenise between 360 and 460°C record a high average Cu concentration (5630 ppm: Figure 5.51). This suggests that Cu was highly soluble in the type 9 fluids and

failed to precipitate effectively within the confines of the system. The high Cu solubility is most likely due to the high solubility of Cu in Cl-rich fluids that became increasingly acidic at low temperatures.

Copper concentrations are relatively depleted in the type 10 fluids relative to the main mineralisation-type and type 9 fluids (Figure 5.51F). However, the salt-undersaturated inclusions in the type 10 veins record relatively consistent Cu concentrations, even in the gypsum-hosted inclusions that homogenise at temperatures as low as 170°C (Figure 6.9B). This suggests that the relatively Cu-poor nature of the type 10 samples is due to the combined effects of low Cu input due to earlier Cu extraction (e.g. Figure 6.1F) and a lack of an effective mineralisation trap for Cu-sulphide deposition. High Cu solubility is likely to have been initially maintained by decreasing pH as fluids cooled below 400°C. This is supported by the presence of minor tennantite, the presence of which is indicative of As-rich fluids with low Cu^{+} activity and higher H^{+} ion activity ratios (Schwartz, 1995). High Cu solubility is also likely to have been the result of the precipitation of molybdenite followed by abundant anhydrite from the type 10 fluids. This would have reduced fluid sulphur concentrations favouring Cu solubility by reversing reactions (5-6) and can explain the presence of minor bornite (Cu_5FeS_4) rather than abundant chalcopyrite ($CuFeS_2$).

6.9 Metal Remobilisation

Evidence for metal sulphide redissolution has been reported at a number of other deeply emplaced Mo-rich porphyries, including Butte (Brimhall, 1980), Andacollo (Klemm, 2006) and Bingham (Landtwing *et al*., 2005; Seo *et al*., 2012) and has been proposed as a potentially important process in producing the final ore configurations of porphyry systems (Carten *et al*., 1988; Sillitoe, 2010). At El Teniente, the presence of multiple mineralisation events associated with multiple intrusions (Figure 5.51) over a 1.9 My period (Figure 4.19), raise the possibility that metal remobilisation played an important role in redistributing and potentially enriching Mo and Cu grades across the deposit.

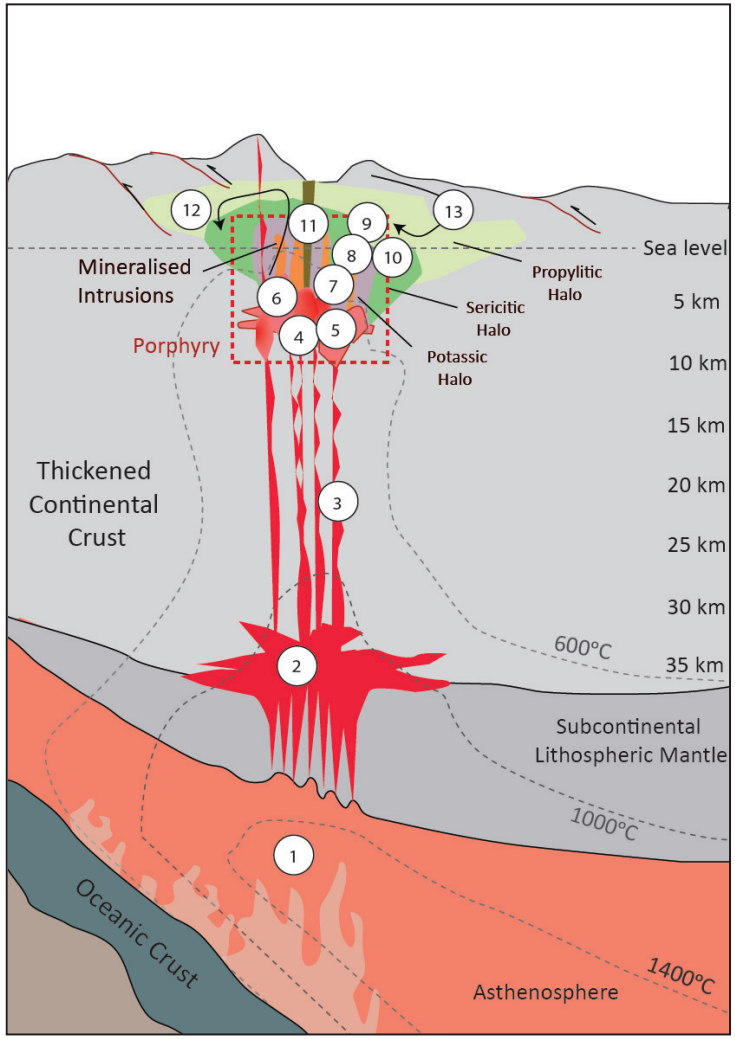
In the main mineralisation samples a number of inclusions contain unusually high concentrations of Cu (>2 wt.%) and Mo (>2000 ppm: Appendix V), suggesting that these may contain remobilised Mo and Cu. However, the extremely high metal concentrations of these fluids (often several wt.%) imply that these high values are more likely to be the result of the accidental ablation of sulphide microinclusions. In addition, the rarity of reverse crosscutting relationships (Figure 4.17) indicates that each main mineralisation-stage halo was subject to extremely limited overprinting by later pulses of main mineralisation-type fluids associated with younger intrusions. In addition, thermal contraction of each system (Figure 4.19) means that Mo and Cu mineralisation was predominantly overprinted by cooler and predominantly lower salinity fluids. As these variables strongly control Mo and Cu-sulphide solubility (Figures 6.8-6.9) it is likely that only a limited degree of metal remobilisation occurred surrounding the Braden Breccia pipe.

Unlike the main mineralisation veins, type 9 and 10 veins and associated breccias cut mineralisation associated with other intrusions, suggesting that they may have metal remobilised Mo and Cu (e.g. Figures 4.14-4.16). High Mo concentrations exceeding 10000 ppm are particularly common in the brine inclusions (Appendix V) suggesting that the late hypersaline fluids may have been particularly effective in redistributing metals (Figure 5.20). Consistent with previous studies (Klemm, 2006; Vry, 2010) the limited flow of high salinity, metalliferous fluids through the TMC (Cannell, 2004) means that metal redistribution may have been restricted to the margins of the Braden Breccia pipe.

6.10 Conclusions

Results of this study combined with previous natural and experimental studies indicate that a number of magmatic and hydrothermal variables can favour the formation of Mo-rich porphyries over Cu-rich and molybdenite-poor deposits. These are summarised in Figure 6.11. Fluid inclusion and petrological evidence indicate that Mo mineralisation at El Teniente resulted from multiple generations of Mo-bearing magmatic-hydrothermal fluids associated with the emplacement of multiple intrusion-mineralisation cycles. The extent of mineralisation is attributed to the efficient extraction of Mo and Cu from a long-lived magma chamber, as opposed to the generation of anomalously metal-rich arc magmas. The extent of fractionation of the underlying parental magma chamber and changes in the composition of exsolving fluids control the overall spatial and temporal variations in Mo and Cu mineralisation within a single system. The preferential partitioning of Cu into high salinity brines and S-rich fluids can lead to the generation of residual melts that become increasingly enriched in Mo. This led to the exsolution of late Mo-rich fluids at El Teniente and explains the high Mo grades in highly fractionated porphyry Mo systems.

Dissolved species of Mo and Cu in ore fluids are strongly controlled by fluid salinity, which governs the formation of different ion pairs and chloride complexes. Previous studies suggested that the different complexation behaviour of Mo and Cu during vapour-brine partitioning may be a key control on main mineralisation decoupling (Klemm *et al*., 2007; Vry 2010). However, results of this and previous studies indicate that significant amounts of molybdenite are commonly deposited prior to fluid phase separation. Consequently, decoupled Mo and Cu deposition appears to be the result of sequential deposition of Mo then Cu as a function of the interplay of decreasing temperature with evolving fluid fO_2 and acidity during ascent. Combined LA-ICP-MS and microthermometric data from this study and a number of other Mo-rich porphyries indicate that most molybdenite is precipitated between 370 and 440°C under relatively low, hydrostatic pressures. The common deposition of Mo just before the onset of sericite alteration suggests that Mo is typically deposited in response to decreasing pH following the onset of acid dissociation. By contrast, Cu is usually deposited at lower temperatures during fluid neutralisation, largely due to its favourable solubility in phase separated brines as well as in acidic aqueous liquids and vapours.



Process	Key Variables	Mo-rich Porphyries	Cu-rich porphyries
1) Magma generation and Mo source	Tectonic setting, distance from ridge, subducting material, incorporation of the lower continental crust	Established continental arc to rift-related settings with continental crust component	Island arc and juvenile continental arc settings with primitive crustal component
2) MASH zone interactions	Longevity of MASH zone, Lower crustal metal anomaly	Long-lived MASH zone to liberate Mo from lower crust	Long-lived MASH zones may help liberate more Cu
3) Magma ascent	Water content, magma host rock interactions	Buoyant ascent of a water-rich mafic magma (>4% H_2O)	Buoyant ascent of a water-poor mafic magma (<4% H_2O)
4) Magma chamber emplacement	Magma composition, fH_2O, extent of crystallisation, tectonic regime	Deep emplacement (~3-7 km) of a water-rich magma of intermediate composition	Shallower emplacement (~1-5 km) of an intermediate calc-alkali magma
5) Magma recharging and intrusion emplacement	Longevity of system, composition of mixing magmas, fH_2O, extent of crystallisation, temperature	**Strongly favoured by the formation of long-lived fertile systems that is periodically recharged by mafic magma**	**Strongly favoured by the formation of long-lived fertile systems that is periodically recharged by mafic magma**
6) Fractional crystallisation	Magma composition, temperature, pressure, fH_2O	**High degree (80-90%) crystal fractionation prior to saturation**	**Lower degree of fractional crystallisation (~60-70%).**
7) Magmatic volatile exsolution	Pressure, temperature,fO_2, magma and fluid composition and fH_2O	**Deep exsolution of intermediate density (vapour-like) fluids with high fH_2O and fO_2**	**Shallow brines and vapours or deep vapour-like fluids that co-transport Mo**
8) Mo transport in hydrothermal fluids	Fluid composition and salinity, temperature, pressure, fH_2O, pH, fO_2	**Transported well in fluids with high salinity fH_2O and fO_2**	**High salinity brines and acid volatile and S-rich vapours**
9) Vapour-brine partitioning	Pressure, temperature, fH_2O, fluid density and salinity	**Mo may be enriched in partitioned brines, but this is not a prerequisite for the formation of Mo-rich deposits**	**Cu partitions into brine and vapour in relatively equal proportions based on mass balance**
10) Metal deposition	Temperature, pressure, fH_2O, pH, fO_2, fS^{2-}, fluid-wallrock interactions, fluid mixing, S02 disproportionation and acid dissociation	**Mo deposited with decreasing temperature to 400°C as pH and fO_2 decrease with acid dissociation and SO_2 disproportionation.**	**Typically deposited at lower T from neutralising fluids with moderate-high fO_2, wallrock reactions can aid deposition**
11) Mineralisation (veins+breccias)	Vein density, fault and fracture controls, breccia formation, sequential vein formation and disseminations	**Mo systems favoured by the formation of dense quartz stockwork veins and late hydrothermal breccias.**	**Veins more distal to heat source. qz redissolution and anhydrite deposition can be important + disseminations**
12) Metal remobilisation	Composition of fluids, metal carrying capacity of fluids, volumes and lateral movement	**Late fluid pulses may remobilise Mo in multi-intrusion systems. i.e. brines with high fO_2**	**Late fluids may remobilise Cu in multi-intrusion systems. i.e. brines or acidic vapours**
13) Supergene enrichment	Depth, composition of fluids, pH, fO_2, exhumation and age of deposit	Mo-systems are commonly deeper than the supergene enrichment blanket	Supergene enrichment can play an important role in increasing shallow Cu grades

Figure 6.11. Summary of the main processes and variables that govern the formation of Mo-rich porphyries over Cu-rich and Mo-poor porphyries, adapted from Figure 1.1. Bold cells in table are conclusions made from evidence presented in this and previous studies. Non-bold cells are interpretations made from previous studies.

Chapter 7. Conclusions

7.1 Main Conclusions

This study has elucidated details of the complex evolution of El Teniente and has helped constrain the magmatic and hydrothermal controls on the formation of Mo mineralisation and the processes and variables that govern the decoupled mineralisation of Mo and Cu in porphyry ore systems. By combining results with previous natural and experimental data, this study has also critically assessed the likely speciation of Mo and Cu in hydrothermal fluids and has evaluated the roles of different fluid types in transporting and depositing metals as a function of their metal carrying capacities, masses and volumes. The key findings of this study are summarised below.

7.1.1 The Evolution of El Teniente

- Geological relationships, Re-Os dating and fluid inclusion LA-ICP-MS data provide definitive evidence that there was no deposit-wide evolution in fluid type and breccia-vein development as previously proposed. Instead, metal-bearing fluids were exsolved in multiple pulses of hydrothermal activity linked to the emplacement of multiple felsic-intermediate intrusions.
- Mo and Cu grades both show strong spatial-temporal relationships with the A-Porphyry, diorite intrusions and Teniente Dacite Porphyry. These intrusions are therefore considered to have acted as conduits for pulses of magmatic-hydrothermal fluids leading to the formation of localised, pre- and main mineralisation breccia-vein halos. Intrusion-mineralisation pulses appear to be relatively short-lived events (<100,000 years), with multiple phases associated with the composite Teniente Dacite Porphyry. Individual pulses of magmatic-hydrothermal activity are separated by quiescent periods of up to 300,000 years, documented by distinct gaps in the ages of shallow level molybdenite mineralisation.
- Vein distribution data indicate that type 6a quartz-molybdenite veins are the most important vein type with respect to deposit-wide Mo grades of (0.02-0.06 wt.%). Cu grades are principally controlled by the abundances of type 6b, 7b and 8 veins that occur in more distal positions of the TMC relative to the felsic-intermediate intrusions. Fluid inclusion data indicate that type 6a veins, which are dominated by intermediate density fluids with typical salinities of ~6.5 wt.% $NaCl_{eq}$, develop outwards into the Cu-rich type 6b-8 veins, which are dominated by denser aqueous fluids and coexisting vapour and brine assemblages.

- Fluid cooling, progressive boiling and then increasing pH following acid dissociation were the main driving forces for the sequential deposition of Mo and then Cu. Most main mineralisation Mo was deposited at >400°C from the intermediate density, parental fluids. Cu was predominantly deposited at lower temperature following vapour-brine partitioning. The strong association of Cu with sericitic alteration suggests implies that increasing pH as a function acidic fluids with the TMC was a key driving force for chalcopyrite deposition.
- The intermediate density fluids predominantly partitioned at ~390°C following the formation of type 6a veins in each mineralised centre. Partitioned vapours and brines are interpreted to have a high average mass ratio of approximately 85:15 and volume ratio of 40:1.
- Very high Mo grades (>0.06 wt.%) are controlled by the presence of late mineralisation stage veins and breccias. The high Mo concentrations in the type 9 veins are the result of the late exsolution of high salinity, Mo-bearing brines from a highly fractionated magma chamber. The Mo-rich nature of the type 10 veins is attributed to the deep exsolution of lower salinity Mo-rich fluids during the final stages of magma fractionation. These fluids are commonly focused into radial faults and fractures associated with the margins of the Braden Breccia pipe. Only minor amounts of Mo and Cu were remobilised by the latest pulses of hydrothermal fluids. Based on the preservation of main mineralisation-type grade halos, remobilisation is likely to have operated on a relatively localised scale.
- Extensive shallow-level Mo and Cu mineralisation terminated with the formation of the Braden Breccia pipe in a single explosive event at approximately 4.59 Ma. This event effectively extracted any remaining volatiles from the parental magma chamber at which point it was almost completely crystallised. Only minor mineralisation followed this event and is linked to the emplacement of volumetrically minor dacitic dikes.

7.1.2 Magmatic Controls on the Formation of Mo-rich Porphyries

Based on the results of this and previous studies, the main magmatic and hydrothermal controls on the formation of Mo-rich porphyries are summarised in Figure 6.11.

- The emplacement of multiple porphyry intrusions at shallower crustal depths provides effective fluid-transport pathways for deeply exsolved, Mo-rich fluids. Multiple Mo and Cu mineralised intrusions can form if both metals are replenished in the parental magma chamber and subsequently enriched in new batches of residual melt prior the next phase of intrusion emplacement and breccia-formation.

- The formation of Mo-rich porphyries appears to be favoured by the deep exsolution of large volumes of fluids with relatively low Cl concentrations and high fH_2O.
- Extent of fractional crystallisation is a key control on the metal contents of exsolving fluids. High degrees of fractional crystallisation prior to fluid exsolution can result in the late exsolution of fluids with high Mo/Cu ratios and high Cs/Na. Such fluids are a feature of several Mo-rich porphyries including El Teniente, Questa and Bingham. The generation of late veins and breccias via the overpressuring of a highly fractioned magma chamber during the final stages of crystallisation can produce extremely Mo-rich grades within a deposit.

7.1.3 Hydrothermal Controls on the Formation of Mo-rich Porphyries

- In Mo-rich porphyry systems, intermediate-low salinity parental fluids with high fH_2O typically transport 70-300 ppm Mo. Depending on the Cl concentration of the fluid, Mo will form different ion pairs and oxy-chloride complexes. In S-rich fluids with salinities <7 wt.% $NaCl_{eq}$, Mo is most likely transported as $NaHMoO_2S_2$. In fluids with salinities >7 wt.% $NaCl_{eq}$ Mo is most likely transported as MoO_2Cl^+ or MoO_2Cl_2 at higher Cl concentrations.
- The direct exsolution of high salinity fluids (>40 wt.% $NaCl_{eq}$) can result in very high fluid Mo concentrations (500-1100 ppm) that can produce high Mo grades (>0.06 wt.%) in systems that have an effective fluid-focusing structures (such as faults or breccias). However, the high solubility of Mo as highly soluble oxy-chloride complexes may inhibit the formation of Mo-rich porphyries by dispersion, particularly if the exsolving fluids have high fO_2 and low S concentrations (such as in Cu-Au systems).
- If Mo is not deposited directly from parental intermediate density fluids, it may become enriched via phase separation, in which Mo is preferentially partitioned into Fe and Cl-rich brines with an estimated $DMo^{vapour/brine}$ value of 0.1 being typical for most Mo-rich systems. The absolute amount of Mo that is transported in partitioned vapours and brines is strongly controlled by the mass proportions of each phase. Several studies report similar vapour-brine mass proportions to the average 85:15 estimate for partitioning main mineralisation fluids at El Teniente. This implies that large volumes of low density vapour may be equally as important as partitioned brines in transporting and depositing Mo.
- The temperature at which Mo is deposited is strongly temperature controlled. In porphyry Cu-Mo systems Mo is typically deposited after the onset of SO_2 disproportionation and prior to significant acid alteration of the surrounding host rocks at temperatures of ~400°C. Mo deposition can occur at lower temperatures if cooling fluids are subject to a high lithostatic

pressures (increasing Mo solubility as in high fH_2O fluids), if the fluids are relatively S-poor or there is competition for S, or if fluids are highly oxidised favouring Mo solubility as Mo^{6+}.

7.1.4 The Decoupled Mineralisation of Mo and Cu

- The decoupled mineralisation of Cu and Mo is a common feature of porphyry systems and is the result of both magmatic and hydrothermal processes. Magmatic processes determine the metal affinities of a granitic system and can produce significant variations in the metal affinities of different intrusions within in a single system. These variations are most pronounced in systems that operate over long time periods (>100,000 Kyr). By contrast, hydrothermal processes control localised and temporally restricted separation of Mo and Cu associated with a single intrusion.
- The Mo/Cu ratios of fluids that exsolved within a single porphyry system are controlled by exsolving fluid composition and the timing of fluid exsolution relative to crystal fractionation. The early exsolution of high salinity fluids or S-rich vapours (favoured at shallow emplacement depths) will preferentially remove Cu from the melt leading to an increase in the Mo/Cu ratio of the parental magma. Fluids exsolved during the final stages of crystallisation of such a magma therefore will be more Mo-rich. This may explain the presence of late Mo-rich vein and breccias at El Teniente as well as at several other Mo-rich porphyry deposits including Bingham and Questa.
- Vapour-brine partitioning affects Mo and Cu in different ways in different systems. In porphyry Mo systems Cu shows a stronger affinity for partitioned brines than Mo. In shallowly emplaced Cu-Au systems, Mo shows a stronger affinity to the brines, probably due to the greater contrast in fluid densities produced by partitioning at shallow mine levels. The high solubility of Mo as oxy-chloride complexes in these S-poor fluids may result in the failed deposition of Mo within the confines of the system. In Cu-Mo systems, both metals are partitioned in a similar manner, with Cu exhibiting a slight preference for the vapour phase. The timing of vapour-brine partitioning relative to metal deposition can exaggerate the extent of decoupling in these systems. If Mo is deposited prior to or during the onset of fluid boiling then Cu may be deposited in more distal settings as a function of its enhanced solubility in partitioned brines or acidic S-rich vapours.
- Sequential metal deposition as a function of the different solubilities of dissolved Mo and Cu species is the main control on the local decoupling of Mo and Cu surrounding individual intrusions within a porphyry system.

7.2 Future Work

During this project, several areas of further work have been identified that would improve our understanding of the evolution of El Teniente, the magmatic controls on the formation of Mo-rich porphyries and the hydrothermal transport and deposition of Mo.

7.2.1 The Evolution of El Teniente

- A systematic bulk geochemical study of variably altered rocks should be completed to assess and quantify element mobility during alteration. Linking fluid inclusion trace element concentrations with alteration assemblages would give a much better insight into the cycling of metals through alteration halos and will help ascertain whether significant outward loss of Cu and Mo occurred during the formation of any pulses of mineralisation.
- Further host rock geochronology and Re-Os molybdenite dating is required to better link the timing of mineralisation with each intrusion. Additional U-Pb zircon dates and Re-Os molybdenite dates for the Southern and Northern Diorites and the separate intrusion phases of the Teniente Dacite Porphyry will help ascertain whether intrusion emplacement and mineralisation migrated to the north. Better time constraints for these intrusions alongside further fluid inclusion analysis will help identify any clear temporal changes in geochemistry. In addition, at least two Re-Os molybdenite ages should be provided for premineralisation type veins from different parts of the deposit (e.g. A-Porphyry and Teniente Dacite Porphyry) to provide definitive evidence that there were spate episodes of premineralisation breccia-vein development associated with each mineralised intrusion.
- A study of silicate melt inclusion compositions can be compared with coexisting parental fluids to assess the accuracy of $DMo^{fluid/melt}$ and $DCu^{fluid/melt}$ values predicted in this study and in previous experimental studies. Results will help identify the key physical and chemical controls on metal partitioning associated with each intrusive centre.
- Detailed isotope (S, O) and Ti thermometry on quartz study should be undertaken to further constrain the absolute formation temperatures and pressures of each vein and alteration assemblage in each intrusive centre, this will help identify trends in intrusion emplacement depths or system exhumation throughout the formation of the deposit.
- A detailed comparative study of the formation of the tourmaline breccias should be made with other well mineralised breccias such as those at Los Bronces and Los Pelambres, to assess how these breccias form and why they are typically highly enriched in Mo and/or Cu.

7.2.2 Magmatic Controls on the Formation of Mo-rich Porphyries

- A comparative study of parental ore fluid compositions should be completed in other porphyry Mo (Low-F and Climax Type) systems, porphyry Cu-Mo systems and Mo-rich Sn-W greisen systems. This will help identify whether or not there are any unifying processes or variable that govern the transport and deposition of Mo in different Mo-rich granitic systems. This study will also help determine why Cu concentrations are so variable in these deposit types and whether the failed deposition of significant Cu-sulphides in porphyry Mo systems is a manifestation of magmatic processes (e.g. the generation of Cu-poor magmas and the sequestration of Cu in mineralising phases) or hydrothermal processes (e.g. failed deposition of Cu due to high solubility in exsolved fluids or the lack of an effective physical or chemical fluid trap for mineralisation). The chemistry of ore fluids in porphyry Mo systems remain poorly constrained and to-date no study has used LA-ICP-MS to constrain the chemical evolution of fluids in Low-F systems.

7.2.3 Hydrothermal Transport of Mo

- Speciation studies should be conducted on natural fluid inclusions with variable salinities and densities using XANES analysis to ascertain the dominant Mo species in intermediate density fluids, vapours and brines. A comparative study should be completed between porphyry Mo, Cu-Mo and Cu-Au deposits to see whether dissolved Mo speciation vary in each system and how different ligand concentrations affect the solubility of Mo and Cu. To date no LA-ICP-MS study has been undertaken to assess the chemistry of fluids in Low-F type systems and therefore the hydrothermal transport of Mo in these systems and the reasons for their characteristically low Cu grades remain poorly understood.
- Coexisting silicate melt and fluid and fluid boiling assemblages should be synthesised under known conditions to help ascertain the true partitioning behaviour of Mo and Cu over a greater range of physical and chemical conditions. This should include a study the fluid-melt partitioning behaviour of Mo at high pressures >100 MPa and fO_2 and the vapour-brine partitioning behaviour of Mo and Cu in fluids with high fH_2O. To date most partitioning studies have been conducted at temperatures below typical phase separation temperatures of ≥400°C inferred for most Mo-rich systems.
- Fluid inclusions hosted in other gangue minerals including carbonate, anhydrite and gypsum should be studied to assess the extent of post-entrapment inclusion modifications via gangue mineral recrystallisation and Cu^+ and H^+ diffusion in natural samples.

References

Acocella, V., Cifelli, F., and Funiciello, R., 2000, Analogue models of collapse calderas and resurgent domes: Journal of Volcanology and Geothermal Research, v. 104, p. 81–96.

Annen, C., Blundy, J., and Sparks, R.S.J., 2006, The genesis of intermediate and silicic magmas in deep crustal hot zones: Journal of Petrology, v. 47, p. 505–5 39.

Archibald, S.M., Migdisov, A.A., and Williams-Jones, A.E., 2002, An experimental study of the stability of copper chloride complexes in water vapor at elevated temperatures and pressures: Geochimica et Cosmochimica Acta, v. 66, p. 1611-1619.

Arévalo, A., and Floody, R., 1995, Estúdio Geometallúrgico del mineral a explotar a mediano y largo plazo. Chapter 1, Modelo Global de Alteración y Mineralización: Internal report, Superintendencia de Geología, El Teniente, CODELCO-Chile, p. 16.

Arévalo, A., Floody, R., and Oliveras, A., 1998, Modelo geometalurgico. Estudio geometalurgico del mineral a explotar a mediano y largo plazo: Internal report GL-133/98, Superintendencia Geologia de El Teniente, Rancagua. CODELCO-Chile, 76 p.

Astudillo, N., Roperch, P., Townley, B., Arriagada, C., and Chauvin, A., 2010, Magnetic polarity zonation within the El Teniente copper-molybdenum porphyry deposit, central Chile: Mineralium Deposita, v. 45, p. 23–41.

Atkinson, W.W., Souviron, S., Vehrs, T.I., and Faunes, A., 1996, Geology and mineral zoning of the Los Pelambres porphyry copper deposit, Chile. *In*: Camus, F., Sillitoe, R. H. And Petersen, R. (Eds) Andean Copper Deposits: Society of Economic Geologists Special Publication, v. 5, p. 131-155.

Audétat, A., 2010, Source and evolution of molybdenum in the porphyry Mo(-Nb) deposit at Cave Peak, Texas: Journal of Petrology. v. 51, p. 1739–1760.

Audétat A., and Pettke, T., 2003, The magmatic-hydrothermal evolution of two barren granites: A melt and fluid inclusion study of the Rito del Medio and Cañada Pinabete plutons in northern New Mexico (USA): Geochimica et Cosmochimica Acta, v. 67, p. 97–121.

Audétat, A., and Pettke T., 2006, Evolution of a porphyry-Cu mineralized magma system at Santa Rita, New Mexico (USA): Journal of Petrology, v. 47, p. 2021−2046.

Audétat, A., Günther, D., and Heinrich, C.A., 1998, Formation of a magmatic-hydrothermal ore deposit: Insights with LA-ICP-MS analysis of fluid inclusions: Science, v. 279, p. 2091-2094.

Audétat, A., Günther D., and Heinrich, C.A., 2000, Causes for large-scale metal zonation around mineralised plutons: fluid inclusion LA-ICP-MS evidence from the Mole Granite, Australia: Economic Geology, v. 95, p. 1563-1581.

Audétat, A., Dolejš, D., and Lowenstern, J.B., 2011, M olybdenite Saturation in Silicic Magmas: Occurrence and Petrological Implications: Journal of Petrology, v. 52, p. 891-904.

Bai, T.B., and Koster van Groos, A.F.K., 1999, The distribution of Na, K, Rb, Sr, Al, Ge, Cu, W, Mo, La, and Ce between granitic melts and coexisting aqueous fluids: Geochimica et Cosmochimica Acta, v. 63, p. 1117–1131.

Baker, T., van Achterberg, E., Ryan, C.G., and Lang, J.R., 2004, Composition and evolution of ore fluids in a magmatic–hydrothermal skarn deposit: Geology, v. 32, p. 117–120.

Baker, M.J., Hollings, P.N., and Cooke, D.R., 2013, Development of fertile magma at El Teniente, Chile: implications for porphyry-style mineralisation [abs]: Goldschmidt Conference, 23rd, Florence, Italy, 25-30 August 2013, Abstract Volume, p. 645.

Ballard, J.R., Palin, J.M., Williams, I.S., Campbell, I.H., and Faunes, A., 2001, Two ages of porphyry intrusion resolved for the super-giant Chuquicamata copper deposit of northern Chile by ELA-ICP-MS and SHRIMP: Geology, v. 29, p. 383–386.

Berry, A.J, Hack, A.C., Mavrogenes, J.A., Newville, M., and Sutton, S.R., 2006, A XANES study of Cu speciation in high-temperature brines using synthetic fluid inclusions: American Mineralogist, v. 91, p. 1773-1782.

Berry, A.J., Harris, A.C., Kamenetsky, V.S., Newville, M., and Sutton, S.R., 2009, The speciation of copper in natural fluid inclusions at temperatures up to 700 ˚C: Chemical Geology, v. 259, p. 2-7.

Best, M.G., and Christiansen, E.H., 2001, *Igneous Petrology*. Blackwell Science.

Bingen, B., and Stein, H., 2003, Molybdenite Re-Os dating of biotite dehydration melting in the Rogaland high-temperature granulites, S Norway: Earth and Planetary Science Letters, v. 208, p. 181–195.

Bingen, B., Davis, W.J., Hamilton, M.A., Engvik, A.K., Stein, H.J., Skar, O., and Nordgulen, O., 2008, Geochronology of high-grade metamorphism in the Sveconorwegian nelt, S. Norway; U-Pb, Th-Pb, and Re-Os data: Norwegian Journal of Geology, v. 88, p. 12–42.

Blevin, P., 2003. Metallogeny of granitic rocks. In: Blevin, P., Jones, M. and Chappell, B. (Eds) Magmas to mineralization. The Ishihara symposium, B. 1–4. GEMOC MacQuarie University, 22-24 July 2003. Geoscience Australia.

Blevin, P L., and Chappell, B.W., 1992, The role of magma sources, oxidation states and fractionation in determining the granite metallogeny of eastern Australia: Transactions of the Royal Society of Edinburgh, Earth Sciences, v. 83, p. 305-316.

Bloom, M.S., 1981, Chemistry of inclusion fluids: Stockwork molybdenum deposits from Questa, New Mexico, and Hudson Bay Mountain and Endako, British Columbia: Economic Geology, v. 76, p. 1906-1920.

Bodnar, R.J., 1993, Revised equation and table for determining the freezing point depression of H2O-NaCl solutions: Geochimica et Cosmochimica Acta, v. 57, 683-684.

Bodnar, R.J., 1995, Fluid inclusion evidence for a magmatic source for metals in porphyry copper deposits. In: Thompson, J.F.H. (Ed), Magmas, Fluids and Ore Deposits. Mineralogical Association of Canada Short Course Volume, v. 23, p. 39-152.

Bodnar, R.J., and Vityk, M.O., 1994, Interpretation of Microthermometric data for H2O-NaCl fluid inclusions. *In* De Vivo, B., and Frezzotti, M.L. (Eds), *Fluid inclusions in Minerals: Methods and Applications*. Blacksburg, VA: Virginia Tech, pp. 117-130.

Bodnar, R.J., Bumham, C.W., and Sterner, S.M., 1985, Synthetic fluid inclusions in natural quartz. III. Determination of phase equilibrium properties in the system HrO-NaCl to 1000 qc and 1500 bars: Geochimica et Cosmochimica Acta, v. 49, p. 186l-1873.

Bodnar, R.J., Binns, P.R., and Hall, D.L., 1989, Synthetic fluid inclusions-Vl Quantitative evaluation of the decrepitation behavior of fluid inclusions in quartz at one atmosphere confining pressure: Jounal of Metamorphic Geology, v. 7, p. 229-242.

Brugger, J., Etschmann, B., Liu, W., Testemale, D., Hazemann, J.L., Emerich, H., van Beek, W., and Proux, O., 2007, An XAS study of the structure and thermodynamics of Cu(I) chloride complexes in brines up to high temperature (400°C, 600 bar): Geochimica et Cosmochimica Acta, v. 71, p. 4920-4941.

Buckroyd, C.C., 2008, Development of the 213nm UV Laser Ablation ICP-MS Technique for Fluid Inclusion Microanalysis and Application to Contrasting Magmatic-Hydrothermal Systems. Unpublished PhD Thesis, Imperial College London: 480 pp.

Burnham, C.W., 1979, Magmas and hydrothermal fluids, *in* Barnes, H.L., (Ed), Geochemistry of hydrothermal ore deposits, 2nd edition.: New York, John Wiley & Sons, p. 71−136.

Burnham, C.W., 1981, Physicochemical constraints on porphyry mineralization. Arizona Geological Society Digest, v. 14, p. 71-77.

Burnham, C.W., 1997, Magmas and hydrothermal fluids. In: H.L. Barnes (Ed), Geochemistry of Hydrothermal Ore Deposits, 3rd Edition. John Wiley and Sons, New York: 63-123.

Burnham, C. W., and Ohmoto, H., 1980. Late-stage processes of felsic magmatism. In: Ishihara, S., and Takenouchi, S. (Eds) Granitic magmatism and related mineralization: 1-12.

Cahill, T., and Isaacs, B., 1992, Seismicity and shape of the subducted Nazca plate: Journal of Geophysical Research, v. 97, p. 503-529.

Camus, F., 1975, Geology of the El Teniente orebody with emphasis on wallrock alteration: Economic Geology, v. 70, p. 1341−1372.

Camus, F., 2002, The Andean Porphyry Systems. In Porter, T. M., Ed., Super Porphyry Copper and Gold Deposits: A Global Perspective, 1st ed.: Adelaide, PGC Publishing, p.45−63.

Camus, F., 2003, Geología de los Systemas Porfíricos en los Andes de Chile: Santiago, Chile, Servicio Nacional de Geología y Minería, 267 p.

Candela, P.A., 1997, A review of shallow, ore-related granites: Textures, volatiles and ore minerals: Journal of Petrology, v. 38, p. 1619-1633.

Candela, P.A., and Bouton, S.L., 1990, The influence of oxygen fugacity on tungsten and molybdenum partitioning between silicate melts and ilmenite. Economic Geology, v. 85, p. 633-640.

Candela, P.A., and Holland, H.D., 1984, The partitioning of copper and molybdenum between silicate melts and aqueous fluids: Geochimica et Cosmochimica Acta, v. 48, p. 373–380.

Candela, P.A., and Holland, H.D., 1986, A mass transfer model for copper and molybdenum in magmatic-hydrothermal systems; the origin of porphyry-type ore deposits: Economic Geology, v. 81, p. 1-9.

Candela, P.A., and Piccoli, P.M., 1995, Model Ore-metal Partitioning from Melts into Vapour and Vapour/Brine Mixtures. In: Thompson, J. F. H. (Ed), Magmas, Fluids and Ore Deposits. Mineralogical Association of Canada Short Course Volume Short Course Volume, v. 23, p. 101-127.

Cannell, J., 2004, El Teniente porphyry copper-molybdenum deposit, central Chile: Unpublished Ph.D. thesis, Hobart, Australia, University of Tasmania, 299 p.

Cannell, J., Cooke, D.R., Walshe, J.L., and Stein, H., 2005, Geology, mineralization, alteration, and structural evolution of the El Teniente porphyry Cu-Mo deposit: Economic Geology, v. 100, p. 979−1003.

Cannell, J., Cooke, D.R., Walshe, J.L., and Stein, H., 2007, Geology, mineralization, alteration and structural evolution of the El Teniente porphyry Cu-Mo deposit - a reply: Economic Geology, v. 102, p. 1171−1180.

Cao, X., 1989, Solubility of molybdenite and the transport of molybdenum in hydrothermal solutions. Unpublished PhD thesis, Ames, USA, Iowa State University. 53 p.

Carroll, M.R., and Rutherford, M.J., 1988, Sulfur speciation in hydrous experimental glasses of varying oxidation state: Results from measured wavelength shifts of sulfur X-rays: American Mineralogist, v. 73, p. 845–849.

Carten, R.B., Geraghty, E.P., and Walker, B.M., 1988, Cyclic development of igneous features and their relationship to high-temperature hydrothermal features in the Henderson porphyry molybdenum deposit, Colorado: Economic Geology, v. 83, p. 266-296.

Carten, R.B., White, W.H., and Stein, H.J., 1993, High-grade granite-related Mo systems; Classification and Origin. In: Kirkham, R.V., Sinclair, W.D., Thorpe, R.I. and Duke, J.M. (Eds). Mineral Deposit Modeling, Geological Association of Canada Special Paper, v. 40, p. 521-554.

Cathles, L.M., 1977, An analysis of the cooling of intrusives by ground-water convection which includes boiling: Economic Geology, v. 72, p. 804-826.

Cathles, L.M., and Shannon, R., 2007, How potassium silicate alteration suggests the formation of porphyry ore deposits begins with the nearly explosive but barren expulsion of large volumes of magmatic water: Earth and Planetary Science Letters, v. 262, p. 92–108.

Charrier, R., Baeza, O., Elgueta, S., Flynn, J.J., Gans, P., Kay, S.M., Muñoz, N., Wyss, A.R., and Zurita, E., 2002, Evidence for Cenozoic extensional basin development and tectonic inversion south of the flat-slab segment, southern central Andes, Chile (33°-36°S): Journal of South American Earth Sciences, v. 15, p. 117–139.

Clark, A.H., Farrar, E., Camus, F., and Quirt, S., 1983, K-Ar age data for the El Teniente porphyry copper deposit, central Chile: Economic Geology, v. 78, p. 1003−1006.

Cloos, M., 2001, Bubbling magma chambers, cupolas, and porphyry copper deposits: International Geology Review, v. 43, p. 285-311.

Cooke, D.R., Hollings, P., and Walshe, J., 2005, Giant porphyry deposits: Characteristics, distribution, and tectonic control: Economic Geology, v. 100, p. 801-818.

Cox, D.P., and Singer, D.A., 1988, Distribution of gold in porphyry copper deposits: U.S.G.S Open File Report, p. 88-46.

Creaser, R.A., and Selby, D., 2002, Re-Os molybdenite analysis–Considerations for accurate and reproducible dates [abs]: Goldschmidt Conference, 12th, Davos, Switzerland, 18th–23rd August 2002, Abstract Volume, p. A156.

Cuadra, P.C., 1986, Geochronologia K-Ar del yacimiento El Teniente y areas adyacentes: Revista Geológica de Chile, v. 27, p. 3−26.

Dilles, J. H., 1987, Petrology of the Yarrington Batholith, Nevada: Evidence for the evolution of porphyry copper ore fluids: Economic Geology, v. 82, p. 1750-1789.

Dilles, J.H., and Einaudi, M.T., 1992, Wall-rock alteration and hydrothermal flow paths about the Ann-Mason porphyry copper deposit, Nevada- a 6 km vertical reconstruction: Economic Geology, v. 87, p. 1963-2001.

Driesner, T., 2007, The System H_2O-NaCl. II. Correlation Formulae for Phase Relations in Temperature-Pressure-Composition Space from 0 to 1000°C, 0 to 5000 bar, and 0 to 1 X_{NaCl}: Geochimica et Cosmochimica Acta, v. 71, p. 4902-4919.

Driesner, T., and Geiger, S., 2007, Numerical simulation of multiphase fluid flow in hydrothermal systems, in Liebscher, A., and Heinrich, C.A., eds., Fluid-fluid interactions: Reviews in Mineralogy and Geochemistry, v. 65, p. 187–212.

Driesner, T., and Heinrich, C.A., 2007, The System H_2O-NaCl. I. Correlations for molar volume, enthalpy, and isobaric heat capacity from 0 to 1000 degrees C, 1 to 5000 bar, and 0 to 1 X-NaCl: *Geochimica et Cosmochimica Acta,* v. 71, p. 4880-4901.

Duarte, P.O., 2000, Caracterización geológica y geotécnica del pórfido dacitico El Teniente: Unpublished Honours thesis, Santiago, Chile, Universidad de Chile, p. 80.

Eastoe, C.J., 1978, A fluid inclusion study of the Panguna Porphyry Cu Deposit, Bougainville, Papua New Guinea: Economic Geology, v. 73, p. 721-748.

Ewart, A., and Griffin, W.L., 1994, Application of Proton-Microprobe Data to Trace-Element Partitioning in Volcanic-Rocks: Chemical Geology, v.117, p. 251-284.

Ewart, A., Bryan, W.B., and Gill, J.B., 1973, Mineralogy and Geochemistry of the Younger Volcanic Islands of Tonga, S. W. Pacific: Journal of Petrology, v. 14, p. 429-465.

Farges, F., Siewert, R., Brown Jr, G.E. Guesdon, A., and Morin, M., 2006a, Structural environments around molybdenum in silicate glasses and melts. I. Influence of composition and oxygen fugacity on the local structure of molybdenum: The Canadian Mineralogist, v. 44, p. 731-753.

Farges, F., Siewert, R., Ponader, C.W., Brown Jr, G.E. Pichavant, M., and Behrens, H., 2006b, Structural environments around molybdenum in silicate glasses and melts. II. Effect of temperature, pressure, H_2O, halogens and sulphur: *The Canadian Mineralogist*, v. 44, p. 755-773.

Farmer, G.L., and DePaolo, D.J., 1984, Origin of Mesozoic and Tertiary granite in the western United States and implications for pre-Mesozoic crustal structure: 2. Nd and Sr isotopic studies of unmineralized and Cu - mineralized and Mo-mineralized granite in the Precambrian craton: Journal of Geophysical Reearch, v., 89, p., 141–160.

Field, C.W, Zhang, L., Dilles, J.H., Rye, R.O., and Reed, M.H., 2005, Sulfur and oxygen isotope record in sulphate and sulfide minerals of early deep pre-Main stage porphyry Cu-Mo and late Main Stage base metal mineral deposits, Butte district, Montana: Chemical Geology, v. 215, p. 61-93.

Fournier, R.O., 1999, Hydrothermal processes related to movement of fluid from plastic into brittle rock in the magmatic-epithermal environment: Economic Geology, v. 94: p. 1193–1212.

Frank, M.R., Simon, A.C., Pettke, T., Candela, P., and Piccoli, P. M., 2011, Gold and copper partitioning in magmatic-hydrothermal systems at 800 C and 100MPa: Geochimica et Cosmochimica Acta, v. 75, p. 2470–2482.

Freydier, C., Ruiz, J., Chesley, J., Candless, T., and Munizaga, F., 1997, Re-Os isotope systematics of sulfides from felsic igneous rocks: Application to base metal porphyry mineralisation in Chile: Geology, v. 25, p. 775-778.

Frikken, P. H., Cooke, D. R., Walshe, J. L., Archibald, D., Skarmeta, J., Serrano, L., and Vargas, R., 2005, Mineralogical and Isotopic Zonation in the Sur-Sur Tourmaline Breccia, Río Blanco-Los Bronces Cu-Mo Deposit, Chile: Implications for Ore Genesis: Economic Geology, v. 100, p. 935-961.

Frost, D.J., and McCammon, C.A., 2008, The redox state of Earth's mantle: Annual Reviews in Earth and Planetary Sciences, v. 36, p. 389-420.

Garrido, I., Riveros, M., Cladouhos, T., Espineira, D., and Allmendinger, R., 1994, Modelo geologico estructural yacimiento El Teniente: 7th Congreso Geologico Chileno, Concepcion, 1994, Abstacts, - v. 2, p. 1553-1558.

Garrido, I., Cembrano, J., Siña, A., Stedman, P., and Yañez, G., 2002, High magma oxidation state and bulk crustal shortening: key factors in the genesis of Andean porphyry copper deposits, central Chile (31-34°S): Revista Geológica de Chile, v. 29, p.43-54.

Giggenbach, W.F., 1987, Redox processes governing the chemistry of fumerolic gas discharges at White Island, New Zealand: Applied Geochemistry, v. 2, p. 143–161.

Giggenbach, W.F., 1992, Magma degassing and mineral deposition in hydrothermal systems along convergent plate boundaries: Economic Geology, v. 87, p. 1927−1944.

Giles, D. L., and Schilling, J. H., 1972, Variation in rhenium content of molybdenite: International Geological Congress, 24th, Montreal, Proceedings, v. 10, p. 145–152.

Godoy, E., Yañez, G., and Vera, E., 1999, Inversion of an Oligocene volcano-tectonic basin and uplifting of its superimposed Miocene magmatic arc in the Chilean central Andes: first seismic and gravity evidences: Tectonophysics, v. 306, p. 217-236.

Godstein, R.H., and Reynolds, T.J., 1994, Systematics of fluid inclusions in diagenetic minerals. Society for Sedimentary Geology Short Course 31, SEPM, Tulsa, OK, 199 p.

González, R. A., 2006, Petrografía geoquímica y microtermometría de los intrusivos félsicos del sector norte del yacimiento El Teniente. Unpublished Memoria de Título, Concepción, Chile, Universidad de Concepción, 140 p.

Gu, Y., 1993, Theoretical and experimental studies of the hydrothermal geochemistry of molybdenum. Unpublished Ph.D. thesis, Melbourne, Australia, Monash University.

Guzmán, C. G., 1991, Alteración y mineralización de los Pórfidos Dioriticos del sector centrál, yacimiento El Teniente: Unpublished honours thesis, Santiago, Universidad de Chile: 143 pp.

Gustafson, L. B., and Hunt, J.P., 1975, The porphyry copper deposit at El Salvador, Chile. Economic Geology, v. 70, p. 857-912.

Hack, A.C., and Mavrogenes, J.A., 2006, A synthetic fluid inclusion study of copper solubility in hydrothermal brines from 525 to 725 °C and 0.3 to 1.7 GPa: Geochimica et Cosmochimica Acta, v. 70, p. 3970–3985.

Harris, A.C., Kamenetsky, V.S., White, N.C., van Achterbergh, E., and Ryan, C.G., 2003, Melt inclusions in veins: Linking magmas and porphyry Cu deposits: Science, v. 302, p. 2109-2111.

Harris, A.C., Golding, S.D., and White, N.C., 2005, Bajo de la Alumbrera Copper-Gold Deposit: Stable Isotope Evidence for a Porphyry-Related Hydrothermal System Dominated by Magmatic Aqueous Fluids: Economic Geology, v. 100, p. 863-886.

Harris, A.C., Dunlap, W.J., Reiners, P.W., Allen, C.M., Cooke, D.R., White, N.C., Campbell, I.H., and Golding, S.D., 2008, Multimillion year thermal history of a porphyry copper deposit: Application of U-Pb, 40Ar/39Ar and (U-Th)/He chronometers, Bajo de la Alumbrera copper-gold deposit, Argentina: Mineralium Deposita, v. 43, p. 295−314.

Hattori, K.H., and Keith, J.,D., 2001, Contribution of Mafic Melt to Porphyry Copper Mineralization, Evidence from Mount Pinatubo, Philippines, and Bingham Canyon, Utah, USA: Mineralium Deposita, v. 36, p. 799-806.

Hedenquist, J.W., and Lowenstern, J.B., 1994,The role of magmas in the formation of hydrothermal ore deposits: Nature, v. 370, p. 519-527.

Hedenquist, J.W., and Richards, J.P., 1998, The Influence of Geochemical Techniques on the Development of Genetic Models for Porphyry Copper Deposits. In: Richards, J. P., and Larson, P. B. (Eds). Techniques in Hydrothermal Ore Deposits: Reviews in Economic Geology, v. 10, p. 235-256.

Hernández, E., Letelier, C., Letelier, O., Mestre, A., and Portigliati, C., 1980, Geología, distribución y cálculo de reservas de molibdeno en El Teniente: Anales del Congreso del Cincuentenario 1930–1980, Minería de cobres porfíricos: Santiago, Chile, Instituto de Ingenieros de Minas, v. 2, p. 364–383.

Heinrich, C.A., 2007, Fluid-Fluid Interactions in Magmatic-Hydrothermal Ore Formation. In: Liebscher, A. and Heinrich, C. A. (Eds). Fluid-Fluid Interactions: Reviews in Mineralogy and Geochemistry, v. 65, p. 363-387.

Heinrich, C.A., Ryan, C.G., Mernagh, T.P., and Eadington, P.J., 1992, Segregation of ore metals between magmatic brine and vapor: a fluid inclusion study using PIXE microanalysis: Economic Geology, v. 87, p. 1566-1583.

Heinrich, C.A., Günther, D., Audétat, A., Ulrich, T., and Frischknecht, R., 1999, Metal fractionation between magmatic brine and vapor, determined by micro-analysis of fluid inclusions: Geology, v. 27, p. 755–758.

Heinrich, C.A., Driesner, T., Stefansson, A., and Seward, T.M., 2004, Magmatic vapor contraction and the transport of gold from the porphyry environment to epithermal ore deposits: Geology, v. 32, p. 761−764.

Hemley, J.J., Cygan, G.L., Fein, J.B., Robinson, G.R., and d'Angelo, V.M., 1992, Hydrothermal ore-forming processes in the light of studies in rock buffered systems: I. Iron-copper-zinc-lead sulphide solubility relations: Economic Geology, v. 87, p. 1-22.

Herr, W., Wölfle, R., Eberhardt, P., and Kopp, E., 1967, Development and recent applications of the Re/Os dating method: International Atomic Energy Agency Radioactive Dating Proceedings Series, p. 499–508.

Hezarkhani, A., and Williams-Jones, A., 1998, Controls of Alteration and Mineralization in the Sungun Porphyry Copper Deposit, Iran: Evidence from Fluid Inclusions and Stable Isotopes: Economic Geology, v. 93, p. 651-670.

Hildreth, W., and Moorbath, S., 1988, Crustal Contributions to Arc Magmatism in the Andes of Central Chile: Contributions to Mineralogy and Petrology, v. 98, p. 455-489.

Hirt, B., Herr, W., and Hoffmeister, W., 1963, Age determination by the rhenium-osmium method: International Atomic Energy Agency Radioactive Dating Proceedings Series, p. 35–44.

Hitschfeld, M., 2006, Petrografía y geoquímica de los intrusivos leucocráticos del sector sur este del yacimento El Teniente, VI region, Chile: Unpublished Honours thesis, Concepción, Chile, Universidad de Concepción, 120 p.

Holzheid, A., and Lodders, K., 2001, Solubility of copper in silicate melts as function of oxygen and sulfur fugacities, temperature, and silicate composition: Geochimica et Cosmochimica Acta, v. 65, p. 1933–1951.

Holzheid, A., Borisov, A., and Palme, H., 1994, The effect of oxygen fugacity and temperature on solubilities of nickel, cobalt, and molybdenum in silicate melts: Geochimica et Cosmochimica Acta, v.58, p. 1975-1981.

Howell, F.H., and Molloy, J.S., 1960, Geology of the Braden orebody, Chile, South America: Economic Geology, v. 55, p. 863−905.

Introcaso, A., Pacino, M.C., and Fraga, H., 1992, Gravity, isostasy and crustal shortening between latitudes 30 and 35°S: Tectonophysics, v. 205, p. 31-48.

Ip, L.Y., 1987, Estudio de inclusiones fluidas en vetillas de la etapa hidrotermal temprana y principal del sector nor-oeste del yacimiento El Teniente: Santiago: Unpublished honours thesis, Universidad de Chile: 105 pp.

Isuk, E.E., and Carman, J.H., 1981, The system $Na_2Si_2O_5$ -$K_2Si_2O_5$ -MoS_2 -H_2O with implications for molybdenum transport in silicate melts: *Economic Geology*, v. 76, p. 2222-2235.

Ivanova, G.F., Lavkina, N.I., Nesterova, L.A., Zhudikova, A.P., and Khodakovskii, I.L., 1975, Equilibrium in the MoO_3-H_2O system at 25–300C: Geochemistry International, v. 12, p. 163–176.

Jenner, F.E., O'Neill, H.S.C., Arculus, R.J., and Mavrogenes, J.A., 2010, The magnetite crisis in the evolution of arc-related magmas and the initial concentration of Au, Ag and Cu: Journal of Petrology, v. 51, p. 2445-2464.

Johnston, W.D., and Chelko, A., 1966, Oxidation-reduction equilibria in molten $Na_2O.2SiO_2$ glass in contact with metallic copper and silver: Journal of the American Ceramic Society, v. 49, p. 562-564.

Kay, S. M., and Kurtz, A., 1995, Magmatic and tectonic characterization of the El Teniente region: Internal report, Superintendencia de Geología, El Teniente, CODELCO-Chile, 180 pp.

Kay, S.M., Godoy, E., and Kurtz, A., 2005, Episodic arc migration, crustal thickening, subduction erosion, and magmatism in the south-central Andes: Geological Society of America Bulletin, v. 117, p. 67−88.

Keith, J.D., Shanks, W.C., III, Archibald, D.A., and Farrar, E., 1986, Volcanic and intrusive history of the Pine Grove porphyry molybdenum system, southwestern Utah: Economic Geology, v. 81, p. 553-577.

Keppler, H., and Wyllie, P. J., 1991, Partitioning of Cu, Sn, Mo, W, U, and Th between melt and aqueous fluid in the systems Haplogranite–H2O-HCl and Haplogranite–H2O-HF: Contributions to Mineralogy and Petrology, v. 109, p. 139–150.

Kesler, S.E. 1973, Copper, molybdenum and gold abundances in porphyry copper deposits: Economic Geology, v. 68, p. 106–112.

Khitarov, N.I., Malinin, S.D., Lebedev, E.B., and Shibieva, N.P., 1982, Partition of Zn, Cu, Pb and Mo between the fluid phase and silicate melt of granitic composition under high-temperature and pressure: Geokhimiya, p. 1094–1107.

Kirwin, D.J., Forster, C.N., Kavalieris, I., Crane, D., Orssich, C., Panther, C., Garamjav, D., Munkhbat, T.O., and Niislelkhuu, 2005, The Oyu Tolgoi copper-gold porphyry deposits, South Gobi, Mongolia. In: Seltmann, R., Gerel, O., and Kirwin, D.J. (Eds) Geodynamics and metallogeny of Mongolia with special emphasis on copper and gold deposits. Society of Economic Geologists-International Association for the Genesis of Ore Deposits Field Trip, IAGOD Guidebook Series, London, Centre for Russian and Central EurAsian Mineral Studies, Natural History Museum, v. 11, p. 155−168.

Klemm, L.M., Pettke, T., Heinrich, C.A., and Campos, E., 2007, Hydrothermal evolution of the El Teniente deposit, Chile: Porphyry Cu-Mo ore deposition from low-salinity magmatic fluids: Economic Geology, v. 102, p. 1021−1045.

Klemm L.M., Pettke, T., and Heinrich, C.A., 2008, Fluid and source magma evolution of the Questa porphyry Mo deposit, New Mexico, USA: Mineralium Deposita, v. 43, p. 533–552.

Koide, H., and Bhattacharji, S., 1975, Formation of fractures around magmatic intrusions and their role in ore localization: Economic Geology, v. 70, p. 781−799.

Kudrin, A.V., 1989, Behavior of Mo in aqueous NaCl and KCl solutions at 300–450°C: Geochemistry International, 26, p. 87−99.

Kuroda. P.K. and Sandell, E.B., 1954, Geochemistry of molybdenum. Geochemica et Chosmochemica Acta: v. **6**, p. 35−63.

Kurtz, A. C., Kay, S. M., Charrier, R., and Farrar, E., 1997, Geochronology of Miocene plutons and exhumation history of the El Teniente region, Central Chile (34-35° S): Revista Geológica de Chile, v.16, p.145−162.

Kusakabe, M., Hori, M., and Matsuhisa, Y., 1990, Primary mineralization-alteration of the El Teniente and Río Blanco porphyry copper deposits, Chile. Stable isotopes, fluid inclusions, and $Mg^{2+}/Fe^{2+}/Fe^{3+}$ ratios of hydrothermal biotite. *In*: Herbert, H. K., and Ho, S.E. (Editors) Stable isotopes and fluid processes in mineralization: Perth, University of Western Australia Press: p. 244-259.

Landtwing, M.R., Pettke, T., Halter, W.E., Heinrich, C.A., Redmond, P.B., Einaudi, M.T., and Kunze, K., 2005, Copper deposition during quartz dissolution by cooling magmatic– hydrothermal fluids: the Bingham porphyry: Earth and Planetary Science Letters, v. 235, p. 229−243.

Landtwing, M.R., Furrer, C., Redmond, P.B., Pettke, T., Guillong, M., and Heinrich, C.A., 2010, The Bingham Canyon porphyry Cu–Mo–Au deposit. III. Zoned copper-gold ore deposition by magmatic vapor expansion: Economic Geology, v. 105, p. 91−118.

Lawley, C.J.M., and Selby, D., 2012, Re-Os geochronology of quartz-enclosed ultrafine molybdenite: Implications for ore deposit geology: Economic Geology, v. 107, p. 1499−1505.

Lecumberri-Sanchez, P., Steele-MacInnis, M., and Bodnar, R.J., 2012, A numerical model to estimate trapping conditions of fluid inclusions that homogenize by halite disappearance: Geochimica et Cosmochimica Acta, v. 92, p. 14–22.

Lerchbaumer, L., and Audétat, A., 2012, High Cu concentrations in vapor-type fluid inclusions: an artifact?: Geochimica et Cosmochimica Acta, v. 88, p. 255–274.

Liang, H.Y., Sun, W., Su, W.C., and Zartman, R.E., 2009, Porphyry copper-gold mineralization at Yulong, China, promoted by decreasing redox potential during magnetite alteration: Economic Geology, v. 104, p. 587-596.

Lindgren, W., 1933, Mineral Deposits, 4th Edition: McGraw-Hill Book Company, New York, 930p.

Lindgren, W., and Bastin, E. S., 1922, Geology of the Braden mine, Rancagua, Chile: Economic Geology, v. 17, p. 863−905.

Liu, W.H., Brugger, J., McPhail, D.C., and Spiccia, L., 2002, A spectrophotometric study of aqueous copper(I)-chloride complexes in LiCl solutions between 100 and 250 °C: Geochimica et Cosmochimica Acta, v. 66, p. 3615–3633.

Lodders, K., and Palme, H., 1991, On the chalcophile character of molybdenum: determination of sulfide/silicate partition coefficients of Mo and W: Earth and Planetary Science Letters, v. 103, p. 311-324.

Loucks, R.R., 2014, Distinctive composition of copper-ore-forming arc magmas: Australian Journal of Earth Sciences, v. 61, p. 5–16.

Lowell, J.D., and Guilbert, J.M., 1970, Lateral and vertical alteration-mineralization zoning in porphyry copper ore deposits: Economic Geology, v. 65, p. 373-408.

Lowenstern, J.B., Mahood, G.A., Hervig, R.L., and Sparks, J., 1993, The occurrence and distribution of Mo and molybdenite in unaltered peralkaline rhyolites from Pantelleria, Italy: Contributions to Mineralogy and Petrology, v. 114, p. 119 129.

Ludington, S.D., 1986, Descriptive model of Climax Mo deposits, in Cox, D.P., and Singer, D.A., eds., Mineral deposit models: U.S. Geological Survey Bulletin 1693, p. 73.

Ludington, S., and Plumlee, G.S., 2009, Climax-type porphyry molybdenum deposits. U.S.G.S Open-File Report, v. 1215, p. 1-16.

Lynton, S.J., Candela, P.A., and Piccoli, P.M., 1993, An experimenta l study of the partition ing of copper between pyrrhotite and a high-silica rhyolitic melt: Economic Geology, v. 88, p.901-915.

Maksaev, V., Munizaga, F., McWilliams, M., Fannning, M., Mathur, R., Ruiz, J., and Zentilli, M., 2004, New chronology for El Teniente, Chilean Andes, from U-Pb, 40Ar/39Ar, Re-Os, and fission-track dating: Implications for the evolution of a supergiant porphyry Cu-Mo deposit: Society of Economic Geologists Special Publication 11, p. 15−54.

Maksaev, V., Munizaga, F., Zentilli, M., and Charier, R., 2009, Fission track thermochronology of Neogene plutons in the Principal Andean Cordillera of central Chile (33-35°S): Implications for tectonic evolution and porphyry Cu-Mo mineralization, Andean Geology, v. 36, p. 153−171.

Manske, S.L., and Paul, A.H., 2002, Geology of a major new porphyry copper center in the Superior (Pioneer) district, Arizona: Economic Geology, v. 97, p. 197–220.

Markey, R., Stein, H.J., Hannah, J.L., Selby, D., and Creaser, R.A., 2007, Standardizing Re-Os geochronology: A new molybdenite Reference Material (Henderson, USA) and the stoichiometry of Os salts: Chemical Geology, v. 244, p. 74-87.

Mavrogenes, J.A., Berry, A.J., Newville, M., and Sutton, S.R., 2002, Copper speciation in vapor-phase fluid inclusions from the Mole Granite, Australia: American Mineralogist, v. 87, p. 1360–1364.

McCready, P., 2007, Molybdenum. Mining Journal Supplementary. London: Mining Communications Ltd, 16 p

McMillan, W.J., and Panteleyev, A., 1980. Ore deposit models – 1. Porphyry copper deposits: *Geoscience Canada*, **7:2**, 52-63.

Mengason, M.J., Candela, P.A., and Piccoli, P.M., 2011, Molybdenum, tungsten and manganese partitioning in the system pyrrhotite–Fe–S–O melt–rhyolite melt: impact of sulfide segregation on arc magma evolution: Geochimica et Cosmochimica Acta, v. 75, p. 7018-7030.

Meyer, C., and Hemley, J.J., 1967, Wall rock alteration, in: Barnes, H.L., ed., Geochemistry of Hydrothermal Ore Deposits. New York, Holt, Rinehart and Winston, Inc., p. 166–232.

Misra, K.C., 2000, Understanding mineral deposits. Kluwer Academic Publishers, 845 p.

Mountain, B.W., and Seward, T.M., 2003, Hydrosulfide complexes of copper (I): Experimental confirmation of the stoichiometry and stability of Cu(HS)2- to elevated temperatures: Geochimica et Cosmochimica Acta, v. 67, p. 3005-3014.

Mungall, J.E., 2002, Roasting the mantle: Slab melting and the genesis of major Au and Au-rich Cu deposits: Geology, v. 30, p. 915–918.

Muñoz, M., Charrier, R., Fanning, C.M., Maksaev, V., and Deckart, K., 2012, Zircon trace element and O-Hf isotope analyses of mineralized intrusions from El Teniente ore deposit, Chilean Andes: constraints on the Source and magmatic evolution of porphyry Cu-Mo related magmas: Journal of Petrology, v. 53, p. 1091-1122.

Murakami, H., Seo, J.H., and Heinrich, C.A., 2010, The relation between Cu/Au ratio and formation depth of porphyry-style Cu-Au±Mo deposits: Mineralium Deposita, v. 45, p. 11-21.

Nagaseki, H., and Hayashi, K.I., 2008, Experimental study of the behaviour of copper and zinc in a boiling hydrothermal system: Geology, v. 36, p. 27–30.

O'Neill, H.S.C., and Eggins S.M., 2002, The effect of melt composition on trace element partitioning: an experimental investigation of the activity coefficients of FeO, NiO, CoO, MoO_2 and MoO_3 in silicate melts. Chemical Geology, v. 186, p. 151–181.

Ootes, L., Lentz, D.R., Creaser, R.A., Ketchum, J.W.F., and Falck, H., 2007, Re-Os molybdenite ages from the Archean Yellowknife greenstone belt: Comparison to U-Pb ages and evidence for metal introduction at ~2675 Ma: Economic Geology, v. 102, p. 511–518.

Ossandón, G., 1974, Petrografía y alteración del Pórfido Dacitico, yacimiento El Teniente: Unpublished Honours thesis, Santiago, Chile, Universidad de Chile, p. 112.

Panteleyev, A., 1995, Porphyry Cu+/-Mo+/-Au. In: Lefebure, D.V. and Ray, G.E. (Eds). *Selected British Columbia Mineral Deposit Profiles, Volume 1 - Metallics and Coal*. British Columbia Ministry of Energy of Employment and Investment, Open File 1995, v. 20, p. 87-92.

Parada, M.A., López-Escobar, L., Oliveros, V., Fuentes, F., Morata, D., Calderón, M., Aguirre, L., Féraud, G., Espinoza, F., Moreno, H., Figueroa, O., Muñoz Bravo, J., Vásquez, R., and Stern, C.R., 2007, Andean Magmatism. *In*: Moreno, T., and Gibbons, W., (Eds), The Geology of Chile: Geological Society of London, p. 115-146.

Pettke, T., Oberli, F., and Heinrich, C.A., 2010, The magma and metal source of giant porphyry-type ore deposits, based on lead isotope microanalysis of individual fluid inclusions: Earth and Planetary Science Letters, v. 296, 267−277.

Pettke, T., Oberli, F., Audétat, A., Guillong, M., Simon, A.C., Hanley, J.L., and Klemm, L.M., 2012, Recent developments in element concentration and isotope ratio analysis of individual fluid inclusions by laser ablation single and multiple collector ICP-MS: Ore Geology Reviews, v. 44, p. 10−38.

Phillips, C.H., Gambell, N.A., and Fountain, D.S., 1974, Hydrothermal alteration, mineralization, and zoning in the Ray deposit: Economic Geology, v. 69, p. 1237−1250.

Pokrovski, G.S., Borisova, A.Y., and Harrichoury, J-C., 2008, The effect of sulfur on vapour-liquid fractionation of metals in hydrothermal systems: Earth and Planetary Science Letters, v. 266, p. 345–362.

Polyak, D., 2013, Molybdenum. *In*: U.S. Geological Survey. *Mineral Commodity Summaries* [online: cit. 2013-03-03]. Available from: http://minerals.usgs.gov/.../mcs-2013-molyb.pdf.

Proffett, J.M., 2003, Geology of the Bajo de la Alumbrera porphyry copper-gold deposit, Argentina: Economic Geology and the Bulletin of the Society of Economic Geologists, v. 98, p. 1535-1574.

Quirt, S., 1972, A potassium argon investigation of the Andean mobile belt of North and Central Chile: Unpublished Ph.D. thesis, Kingston, Ontario, Canada, Queens University, 240 p.

Rabbia, O. M., Hernández, L. B., French, D. H., King, R. W. and Ayers, J. C., 2009, The El Teniente Cu-Mo deposit from a hydrothermal rutile perspective: Mineralium Deposita, v. 44, p. 849−866.

Redmond, P.B., Einaudi, M.T., Inan, E.E., Landtwing, M.R., and Heinrich, C.A., 2004, Copper deposition by fluid cooling in intrusion-centered systems: New insights from the Bingham porphyry ore deposits, Utah: Geology, v. 32, p. 217−220.

Redmond, P.B., and Einaudi, M.T., 2010, The Bingham Canyon porphyry Cu-Mo-Au deposit. I. Sequence of intrusions, vein formation, and sulfide deposition: Economic Geology and the Bulletin of the Society of Economic Geologists, v. 105, p. 43−68.

Reed, M., and Rusk, B., 2001, Insights into supercritical hydrothermal processes from numerical models of potassic hydrothermal alteration, and SEM-CL imaging of vein quartz at Butte, Montana, in Toshiyuki, H., ed., *Proceedings from the Workshop on Potential Thermal Extraction from Deep-seated Rock Masses*: Sendai, Japan, Tohoku University, p. 37–53.

Reed, M.H., Rusk, B., Palandri, J., and Dilles, J., 2005, The Butte hydrothermal system: One magmatic fluid yielded all vein types [abs]: Geological Society of America Abstracts with Programs, v. 37, p. A315.

Reed, M., Rusk, B., and Palandri. J., 2013, The Butte magmatic-hydrothermal system: one fluid yields all alteration and veins: Economic Geology, v. 108, p. 1379–1396.

Rempel, K.U., Migdisov, A.A., and Williams-Jones, A.E., 2006, The solubility and speciation of molybdenum in water vapour at elevated temperatures and pressures: Implications for ore genesis: Geochimica et Cosmochimica Acta, v. 70, p. 687-696.

Rempel, K.U., Williams-Jones, A.E., and Migdisov, A.A., 2009, The partitioning of molybdenum(VI) between aqueous liquid and vapour at temperatures up to 370°C: Geochimica et Cosmochimica Acta, v. 73, p. 3381-3392.

Richards, J.P., 2003, Tectono-magmatic precursors for porphyry Cu-(Mo-Au) deposit formation: Economic Geology and the Bulletin of the Society of Economic Geologists, v. 98, p. 1515–1533.

Richards, J.P., 2009, Postsubduction porphyry Cu-Au and epithermal Au deposits: Products of remelting of subduction-modified lithosphere: Geology, v. 37, p. 247−250.

Rivera, O., and Falcón, M. F., 1998, Estudio Geológico distrital de la división El Teniente de CODELCO-Chile, Escala 1:25 000: Internal report, Superintendencia de Geología, El Teniente, CODELCO-Chile, p. 200.

Roedder, E., 1971, Fluid Inclusion Studies on the Porphyry-Type Ore Deposits at Bingham, Utah, Butte, Montana, and Climax, Colorado: Economic Geology, v. 66, p. 98-120.

Rojas, A., 2002, Petrografía y geoquímica del pórfido dacitico Teniente, yacimiento El Teniente, Provincia de Cachapoal, VI Región, Chile: Unpublished Honours thesis, Concepción, Chile, Universidad de Concepción, p. 118.

Rojas, A., 2003, Porfido Teniente: Dos fases intrusivas caracteristicas geológicas, petrográficas y geoquímicas, yacimiento El Teniente [abs]: Congreso Geológico Chileno, 10th, Concepción, Chile, 2003, Abstract volume, p. 9.

Rosenbaum, G., Giles, D., Saxon, M., Betts, P.G., Weinberg, R.F., and Duboz, C., 2005, Subductionof the Nazca Ridge and the Inca Plateau: Insights into the Formation of ore deposits in Peru: Earth and Planetary Science Letters, v. 239, p. 18-22.

Rusk, B.G., Reed, M.H., Dilles, J.H., Klemm, L.M., and Heinrich, C.A., 2004, Compositions of magmatic hydrothermal fluids determined by LA-ICP-MS of fluid inclusions from the porphyry copper–molybdenum deposit at Butte, Montana: Chemical Geology, v. 210, p. 173–199.

Rusk, B.G., Reed, M.H., and Dilles, J.H., 2008, Fluid inclusion evidence for magmatic-hydrothermal fluid evolution in the porphyry copper-molybdenum deposit at Butte, Montana: Economic Geology, v. 103, p. 307−334.

Ryabchikov, I.D., Rekharsky, V.I., and Kudrin, A.V., 1981, Mobilization of molybdenum by magmatic fluids in the process of crystallization of granite melts: Geokhimia, v. 8, p. 1243-1246.

Ryan, C.G., McInnes, B.M., Williams, P.J., Dong, G., Win, T.T., and Yeats, C.J., 2001, Imaging Fluid Inclusion Content using the New CSIRO-GEMOC Nuclear Microprobe: *Nuclear* Instruments and Methods, B181, p. 570-577.

Ryabchikov, I.D., Rekharsky, V.I., and Kudrin, A.V., 1981, Mobilization of molybdenum by magmatic fluids in the process of crystallization of granite melts: Geokhimia, v. 8, p. 1243-1246.

Rye, R.O., 1993, The evolution of magmatic fluids in the epithermal environment: the stable isotope perspective: Economic Geology, v. 88, p. 733−753.

Seedorff, E., Dilles, J.H., Proffett, J.M., Einaudi, M.T., Zurcher, L., Stavast, W.J.A., Johnson, D.A., and Barton, M.D., 2005, Porphyry deposits: Characteristics and origin of hypogene features: Economic Geology 100th Anniversary Volume, p. 251−298.

Seguel, J., Arévalo, A., and Skewes, M.A., 2006, Complejo de brechas hidrotermales en el flanco este de Mina El Teniente: Congreso Geológico Chileno, 11th, Antofagasta, Actas, v. 2, p. 351−354.

Selby, D., and Creaser, R.A., 2001, Re-Os geochronology and systematics in molybdenite from the Endako porphyry molybdenum deposit, British Columbia, Canada: Economic Geology, v. 96, p. 197–204.

Selby, D., and Creaser, R.A., 2004, Macroscale NTIMS and microscale LA-MC-ICP-MS Re-Os isotopic analysis of molybdenite; testing spatial restrictions for reliable Re-Os age determinations, and implications for the decoupling of Re and Os within molybdenite: Geochimica et Cosmochimica Acta, v. 68, p. 3897–3908.

Seo, J.H., and Heinrich, C.A., 2012, Copper partitioning during magmatic-hydrothermal phase separation — revisited: Fluid inclusions in coeval quartz, topaz and garnet [abs]: Goldschmidt Conference, 22nd, Montreal, Canada, 24-29 August 2013, Abstract Volume.

Seo, J.H., and Heinrich, C.A., 2013, Selective copper diffusion into quartz-hosted vapor inclusions: Evidence from other host minerals, driving forces, and consequences for Cu–Au ore formation: Geochimica et Cosmochimica Acta v. 113, p. 60–69.

Seo, J.H., Guillong, M., and Heinrich, C.A., 2009, The role of sulfur in the formation of magmatic–hydrothermal copper–gold deposits: Earth and Planetary Science Letters, v. 282, p. 323–328.

Seo, J.H., Guillong, M., and Heinrich, C.A., 2012, Separation of Molybdenum and Copper in Porphyry Deposits: The Roles of Sulfur, Redox, and pH in Ore Mineral Deposition at Bingham Canyon: Economic Geology, v. 107, p. 333−356.

Serrano, L., Vargas, R., Stambuk, V., Aguilar, C., Galeb, M., Holmgren, C., Contreras, A., Godoy S., Vela, I., Skewes, M.A., and Stern, C.R., 1996, The late Miocene to early Pliocene Río Blanco-Los Bronces copper deposit, central Chilean Andes: Society of Economic Geologists Special Publication, v. 5, p. 120–129.

Seyfried, W.E., Jr., and Ding, K., 1993, The effect of redox on the relative solubilities of copper and iron in Cl-bearing aqueous fluids at elevated temperatures and pressures: An experimental study with application to subseafloor hydrothermal systems: Geochimica et Cosmochimica Acta, v. 57, p. 1905-1917.

Shea, D., and Helz, G.R., 1988, The solubility of copper in sulfidic waters: Sulfide and polysulfide complexes in equilibrium with covellite: Geochimica et Cosmochimica Acta, v. 52, p. 1815--25.

Sillitoe, R.H., 1973, Tops and bottoms of porphyry copper deposits: Economic Geology, v. 68, p. 799-815.

Sillitoe, R.H., 1997, Characteristics and controls of the largest porphyry copper-gold and epithermal deposits in the circum-Pacific region: Australian Journal of Earth Sciences, v. 44, p. 373-388.

Sillitoe, R.H., 1998, Major regional factors favouring large size, high hypogene grade, elevated gold content and supergene oxidation and enrichment of porphyry copper deposits. In: Porter, T. M., (Editor) Porphyry and hydrothermal copper and gold deposits-a global perspective. Australian Mineral Foundation: 21-34.

Sillitoe, R.H., 2010, Porphyry copper systems: Economic Geology, v. 105, p. 3−41.

Simon, A.C., and Ripley, E.M., 2011, Sulfur in Magmas and Melts: Its Importance for Natural and Technical Processes, in: Behrens, H., and Webster, J.D., (Eds) *Reviews in Mineralogy and Geochemistry*, Mineralogical Society of America. *v.* 73, p. 513–578.

Simon, A.C., Pettke, T., Candela, P.A., Piccoli, P.M., and Heinrich, C.A., 2006, Copper partitioning in a melt–vapor–brine–magnetite–pyrrhotite assemblage: Geochimica et Cosmochimica Acta, v. 70, p. 5583–5600.

Sinclair, W.D., 1995, Porphyry Mo (low-F type). In: Lefebure, D.V. and Ray, G.E. (eds). *Selected British Columbia Mineral Deposit Profiles, Volume 1 - Metallics and Coal*. British Columbia Ministry of Energy of Employment and Investment, Open File 1995, v. 20, p. 93-96.

Sinclair, W.D., 2007, Porphyry deposits. In: Goodfellow, W.D., (Ed) Mineral Deposits of Canada: a Synthesis of Major Deposit-types, District Metallogeny, the Evolution of Geological Provinces, and Exploration Methods. Geological Association of Canada, Mineral Deposits Division, Special Publication, v. 5, p. 223-243.

Singer, D.A., Berger, V.I., and Moring, B.C., 2005, Porphyry copper deposits of the world: database, map, and grade and tonnage models: U.S.G.S Open-File Report 2005-1060. (http://pubs.usgs.gov/of/2005/1060).

Singer, D.A., Berger, V.I., and Moring, B.C., 2008, Porphyry copper deposits of the world: database and grade and tonnage models: U.S.G.S Open-File Report 2008-1155 (http://pubs.usgs.gov/of/2008/1155).

Skewes, A., 1996, Inclusiones fluidas de la sección 83 de El Teniente: Internal report, Superintendencia de Geología, El Teniente, CODELCO-Chile: 22 pp.

Skewes, A., 1997, Inclusiones fluidas de la sección 124 de El Teniente: Internal report, Superintendencia de Geología, El Teniente, CODELCO-Chile: 30 pp.

Skewes, A., and Holmgren, C., 1993, Solevantamiento andino, erosión y emplazamiento de brechas mineralizadas en el depósito de cobre porfídico Los Bronces, Chile Centrál (33°S): Applicación de geotermometria de inclusions fluidas: Revista Geólogica de Chile, v. 20, p. 71−83.

Skewes, A.M., and Stern, C.R., 1994, Tectonic trigger for the formation of late Miocene Cu-rich breccia pipes in the Andes of central Chile, v. 22, p. 551-554.

Skewes, A., and Stern, C.R., 1995, Genesis of the giant Late Miocene to Pliocene copper deposits of central Chile in the context of Andean magmatic and tectonic evolution: International Geology Review, v. 37, p. 71−84.

Skewes, A., and Stern, C.R., 2007, Geology, mineralization, alteration and structural evolution of El Teniente porphyry Cu-Mo deposit - a discussion: Economic Geology, v. 102, p. 1165–1170.

Skewes, A.M., Arévalo, A., Floody, R., Zuñiga, P.H., and Stern, C., 2002, The giant El Teniente breccia deposit: Hypogene copper distribution and emplacement: Society of Economic Geologists Special Publications, v. 9, p. 299−332.

Skewes, A., Arévalo, A., Floody, R., Zuñiga, P.H., and Stern, C., 2005, The El Teniente megabreccia deposit: The world's largest copper deposit, in Porter, T.M., ed., Super porphyry copper and gold deposits - a global perspective: Adelaide, Australia, Porter Geoscience Consultancy Publishing, v. 1, p. 83−114.

Smoliar, M.I., Walker, R.J., and Morgan, J.W., 1996, Re–Os ages of Group IIA, IIIA, IVA, and IVB iron meteorites: Science, v. 271, p. 1099−1102.

Spencer, E.T., Vry, V.H., Wilkinson, J.J., Berry, A.J., and Seguel, J., 2011, Molybdenum transport and mineralization at the El Teniente Cu-Mo porphyry deposit, Chile: 11th SGA Biennial Meeting on Let's Talk Ore Deposits, Publisher: Ediciones *Universidad Católica* del *Norte*, p. 374-376.

Spencer, E.T., Vry, V.H., Wilkinson, J.J., Creaser, R.A., and Seguel, J., 2015, The Distribution and Timing of Molybdenite Mineralization at the El Teniente Cu-Mo Porphyry Deposit, Chile: Economic Geology, v. 110**,** p. 387-421**.**

Stein H. J., Markey R. J., Morgan J. W., Du A., and Sun Y., 1997, Highly precise and accurate Re-Os ages for molybdenite from the East Qinling molybdenum belt, Shaanxi province, China: Economic Geology, v. 92, p. 827–835.

Stein, H.J., Sundbland, K., Markey, R.J., Morgan, J.W., and Motuza, G., 1998, Re-Os ages for Archean molybdenite and pyrite, Kuittila-Kivisuo, Finland and Proterozoic molybdenite, Kabeliai, Lithuania; testing the chronometer in a metamorphic and metasomatic setting: Mineralium Deposita, v. 33, p. 329–345.

Stein, H. J., Markey, R. J., Morgan, J. W., Hannah, J.L., and Scherstén, A., 2001, The remarkable Re-Os chronometer in molybdenite: how and why it works, Terra Nova, v 13, p. 479–486.

Stein, H.J., and Bingen, B., 2002, 1.05–1.01 Ga Sveconorwegian metamorphism and deformation of the supracrustal sequence at Saesvatn, South Norway: Re-Os dating of Cu-Mo mineral occurrences: Geological Society of London Special Publication, v. 204, p. 319-335.

Štemprok, M., 1990, Solubility of tin, tungsten and molybdenum oxides in felsic magmas: Mineralium Deposita, v. p. 25, 205-212.

Stern, C.R., 1989, Pliocene to present migration of the volcanic front, Andean Southern Volcanic Zone: Revista Geológica de Chile, v. 16, p. 145−162.

Stern, C.R., 1991, Role of subduction erosion in the generation of Andean magmas: Geology, v. 19, p. 78−81.

Stern, C., and Skewes, M.A., 1995, Miocene to present magmatic evolution at the northern end of the Andean Southern Volcanic Zone, central Chile: Revista Geológica de Chile, v. 22, p. 261-272.

Stern, C.R., and Skewes, M.A., 2005, Origin of giant Miocene and Pliocene Cu-Mo deposits in Central Chile: Role of ridge subduction, decreased subduction angle, subduction erosion, crustal thickening and long-lived, batholiths-size, open system magma chambers. in: Porter, T.M., ed., Super Porphyry Copper and Gold Deposits - A Global Perspective: Adelaide, Australia, Porter Geoscience Consultancy Publishing, v. 1, p. 65−82.

Stern, C. R., Skewes, M. A., and Arévalo, A., 2010, Magmatic evolution of the giant El Teniente Cu-Mo deposit, central Chile: Journal of petrology, v. 52, p. 1591−1617.

Stimac, J., and Hickmott, D., 1994, Trace-element partition-coefficients for ilmenite, ortho-pyroxene and pyrrhotite in rhyolite determined by micro-PIXE analysis: Chemical Geology, v. 117, p. 313-330.

Stoffell, B., Wilkinson, J.J. and Jeffries, T.E., 2004, Metal transport and deposition in hydrothermal veins revealed by 213nm UV laser ablation microanalysis of single fluid inclusions: American Journal of Science, v. 304, p. 533-557.

Stoffell, B., 2007, Metal Transport and Deposition Hydrothermal Fluids- Insights from Laser Ablation Microanalysis of Individual Fluid inclusions: Unpublished PhD Thesis, Imperial College London: 295 pp.

Streck, M.J., and Dilles, J.H. 1998, Sulfur evolution of oxidized arc magmas as recorded in apatite from a porphyry copper batholith: Geology, v. 26, p. 523-526.

Suzuki, K., Kagi, H., Nara, M., Takano, B., and Nozaki, Y., 2000, Experimental alteration of molybdenite: evaluation of the Re-Os system, infrared spectroscopic profile and polytype: Geochimica et Cosmochimica Acta, v. 64, p. 223–232.

Tacker, R.C., and Candela, P.A., 1987, Partitioning of molybdenum between magnetite and melt: A preliminary experimental study of partitioning of ore metals between silicic magmas and crystalline phases: Economic Geology, v. 82, p. 1827-1838.

Taylor, H.P. Jr., 1974, The application of oxygen and hydrogen isotope studies to problems of hydrothermal alteration and ore deposition: Economic Geology, v. 69, p. 843−883.

Thompson, R.A., and Helz, G.R., 1994, Copper speciation in sulfi dic solutions at low-sulfur activity—further evidence for cluster complexes: Geochimica et Cosmochimica Acta, v. 58, p. 2971–2983.

Tingle, *T.N., and Fenn, P.M., 1984,* Transport and concentration of molybdenum in granite molybdenite systems: Effects of fluorine and sulphur: *Geology*, v. 12, p. 156-158.

Ulrich, T., and Heinrich, C.A., 2001, Geology and alteration geochemistry of the porphyry Cu-Au deposit at Bajo de la Alumbrera, Argentina: Economic Geology, v. 96, p. 1719−1742.

Ulrich, T., Günther, D. and Heinrich, C.A., 2001. The Evolution of a Porphyry Cu-Au Deposit, Based on LA-ICPMS Analysis of Fluid Inclusions: Bajo de la Alumbrera, Argentina. Economic Geology, 96: 1743–1774.

Ulrich, T., Günther, D., and Heinrich, C.A., 2002, The evolution of a porphyry Cu-Au deposit, based on LA-ICP-MS analysis of fluid inclusions: Bajo de la Alumbrera, Argentina: Economic Geology, v. 97, p. 1888–1920.

Ulrich, T., and Mavrogenes, J., 2008, An experimental study of the solubility of molybdenum in H_2O and KCl–H_2O solutions from 500 degrees C to 800 degrees C, and 150 to 300 MPa: Geochimica et Cosmochimica Acta, v. 72, p. 2316–2330.

Valenzuela, R., 2003, Mineralización sulfurada hipógena de cobre en el sector central del yacimiento El Teniente, VI región: Unpublished B.Sc. thesis, Concepción, Universidad de Concepción, 118 p.

Vanko, D.A., and Bach, W., 2005, Heating and freezing experiments on aqueous fluid inclusions in anhydrite: Recognition and effects of stretching and the low-temperature formation of gypsum: Chemical Geology: v. 223, p. 35–45.

Vergara, M., Charrier, R., Munizaga, F., Rivano, S., Sepulveda, P., Thiele, R., and Drake, R., 1988, Miocene volcanism in the central Chilean Andes: Journal of South American Earth Sciences, v. 1, p. 199-209.

Vignaresse, J.L., 2007, The role of discontinuous magma inputs in felsic magma and ore generation: Ore Geology Reviews, v. 30, p. 181–216.

Vry, V.H., 2010, Geological and hydrothermal fluid evolution at El Teniente, Chile: Unpublished Ph.D. thesis, London, United Kingdom, Imperial College.

Vry, V.H., Wilkinson, J. J., Seguel, J., and Millán, J., 2010, Multistage intrusion brecciation and veining at El Teniente, Chile: evolution of a nested porphyry system: Economic Geology, v. 105, p. 119-153.

von Quadt, A., Erni, M., Martinek, K., Moll, M., Peytcheva, I., and Heinrich, C.A., 2011, Zircon crystallization and the life times of ore-forming magmatic-hydrothermal systems: Geology, v. 39, p. 731-734.

Watanabe, Y., and Stein, H. J., 2000, Re-Os ages for the Erdenet and Tsagaan Suvarga porphyry Cu-Mo deposits, Mongolia, and tectonic implications: Economic Geology, v. 95, p. 1537–1542.

Webster, J.D., 1997, Exsolution of magmatic volatile phases from Cl-enriched mineralizing granitic magmas and implications for ore metal transport: Geochimica et Cosmochimica Acta, v. 61, p. 1017-1029.

Westra, G., and Keith, S.B., 1981, Classification and genesis of stockwork molybdenum deposits: Economic Geology, v. 76, p. 844-873.

White, W.H., Bookstrom, A.A., Kamilli, R.J., Ganster, M.W., Smith, R.P., Ranta, D.E., and Steininger, R.C., 1981, Character and origin of Climax-type molybdenum deposits: Economic Geology, 75th Anniversary Volume, p. 270–316.

Wilkinson, J.J., 2013, Triggers for the formation of porphyry ore deposits in magmatic arcs: Nature Geoscience, v. 6, p. 917-925.

Wilkinson, J.J., Stoffell, B., Wilkinson, C.C., Jefferies, T.J., and Appold, M.S., 2009, Anomalously metal-rich fluids from hydrothermal ore deposits: Science, v. 323, p. 764-767.

Williams, T.J., Candela, P.A., and Piccoli, P.M., 1995, The partitioning of copper between silicate melts and 2-phase aqueous fluids – an experimental investigation at 1-kbar, 800 C and 0.5-kba r, 850 C: Contributions to Mineralogy and Petrology, v. 121, p. 388–399.

Williams-Jones, A.E., and Heinrich, C.A., 2005, Vapour Transport of Metals and the Formation of Magmatic-Hydrothermal Ore Deposits: Economic Geology, v. 100, p. 1287-1312.

Wood, S.A., Crerar, D.A., and Borcsik, M.P., 1987, Solubility of the assemblage pyrite–pyrrhotite–magnetite sphalerite–galena– gold–stibnite–bismuthinite–argentite–molybdenite in H2O– NaCl–CO2 solutions from 200 to 350°C: Economic Geology, v. 82, p. 1864–1887.

Yamamoto, H., and Kennedy, G.C., 1969, Stability relations in the system $CaSO_4$–H_2O at high temperatures and pressures: American Journal of Science, v. 267, p. 550-557.

Yokoi K., Matsubayashi, N., Miyanaga, T., Watanabe, I., and Ikeda, S., 1993, Studies on the structure of molybdenum (Vi) in acidic solution by XANES and EXAFS: Polyhedron, v. 12, p. 911-914.

Zachariáš, J., and Wilkinson, J.J., 2007. ExLAM 2000: Excel VBA application for processing of transient signal data from laser ablation (LA-ICP-MS) of fluid inclusions and solid phases. ECROFI-XIX Abstract volume: p. 194.

Zajacz, Z., Halter, W.E., Pettke, T., and Guillong, M., 2008. Determination of fluid/melt partition coefficients by LA-ICPMS analysis of co-existing fluid and silicate melt inclusions: Controls on element partitioning. Geochimica et Cosmochimica Acta, 72: 2169–2197

Zajacz, Z., and Halter, W., 2009, Copper transport by high temperature, sulfur-rich magmatic vapor: Evidence from silicate melt and vapor inclusions in a basaltic andesite from the Villarrica volcano (Chile): Earth and Planetary Science Letters, v. 282, p. 115-121.

Zajacz, Z., Candela, P.A., Piccoli, P.M., and Sanchez-Valle, C., 2012, The partitioning of sulfur and chlorine between andesite melts and magmatic volatiles and the exchange coefficients of major cations: Geochimica et Cosmochimica Acta, v. 89, p. 81–101.

Zhang, L., Audétat, A., and Dolejš, D., 2012, Solubility of molybdenite (MoS_2) in aqueous fluids at 600–800°C, 200 MPa: A synthetic fluid inclusion study: Geochimica et Cosmochimica Acta, v. 77, p. 175–185.

Zhong, R., Brugger, J., Chen, Y., and Li, W., 2015, Contrasting regimes of Cu, Zn and Pb transport in ore-forming hydrothermal fluids: Chemical Geology, v. 395, p. 154-164.

Zhu, L., Ding, Z., Yao, S., Zhang, G., Song, S., Qu, W., Guo, B., and Lee, B., 2009, Ore-forming event and geodynamic setting of molybdenum deposit at Wenquan in Gansu Province, Western Qinling: Chinese Science Bulletin, v. 54, p. 2309-2324.